

Development of an Intelligent Tire Based Tire - Vehicle State Estimator for Application to Global Chassis Control

Kanwar Bharat Singh

Thesis submitted to the faculty of the
Virginia Polytechnic Institute and State University
in partial fulfillment of the requirements for the degree of

Master of Science
In
Mechanical Engineering

Saied Taheri, Chair
Shashank Priya, Member
John B. Ferris, Member

January 17, 2012
Blacksburg, Virginia

Keywords: Intelligent/smart tire, state and parameter estimation, tire-road friction estimation, vehicle dynamics control, broadband vibration energy harvesting

Copyright © 2012, Kanwar B. Singh

Development of an Intelligent Tire Based Tire - Vehicle State Estimator for Application to Global Chassis Control

Kanwar Bharat Singh

Abstract

The contact between the tire and the road is the key enabler of vehicle acceleration, deceleration and steering. However, under the circumstances of sudden changes to the road conditions, the driver's ability to maintain control of the vehicle may be at risk. In many cases, this requires intervention from the chassis control systems onboard the vehicle. Although these systems perform well in a variety of situations, their performance can be improved if a real-time estimate of the tire-road contact parameters (ranging from kinematic conditions of the tire to its dynamic properties) are available. At the present stage of development, tire-road contact parameters are indirectly estimated using observers based on vehicle dynamics measurements (acceleration, yaw and roll rates, suspension deflections, etc). Although these methods present a relatively accurate solution, they rely heavily on tire and vehicle kinematic formulations and break down in case of abrupt changes in the measured quantities.

To address this problem, researchers have been developing certain sensor based advanced tire concepts for direct measurement of the tire-road contact parameters. Thus the new terms "Intelligent Tire" and "Smart Tire", which mean online tire monitoring are thus enjoying increasing popularity among automotive manufacturers and formed the motivation for this thesis to explore the possibility of developing an intelligent tire system. The development of the so called "intelligent tire/ smart tire system" is expected to spur the development of a new generation of vehicle control system with modified control strategies, leveraging information directly coming from the interface between the tire and the road, and in turn significantly reducing the risk of accidents.

The specific contributions of this thesis include the following:

- Development of an intelligent tire system, with a special attention to development of measurement and sensor feature extraction methodologies of acceleration signals coming from sensors fixed to the tire innerliner
- Design of an integrated vehicle state estimator for application to global chassis control
- Development of a model-based tire-road friction estimation algorithm
- Development of an intelligent tire based adaptive wheel slip controller for anti-lock brake system (ABS)
- Development of a piezoelectric vibration energy harvesting system with an adaptive frequency tuning mechanism for intelligent tires

Dedication

This thesis is dedicated to my parents, Vijay and Nandita Singh, who have always been incredibly supportive of my educational pursuits. Thank you for believing in me and pushing me to succeed in all my endeavors.

Acknowledgements

First and foremost I would like to express my gratitude to my advisor, Dr. Saied Taheri, for his guidance, support, and motivation throughout my Master's study. I really couldn't ask for a better advisor supervising my entirely enjoyable and successful graduate career. He has always been available for guidance as well as pushing me forward in research. He has given me the opportunity to work on several research problems other than the subject of this thesis. I would also like to express my deep appreciation to the other members of my committee, Dr. Shashank Priya and Dr. John Ferris for their valuable advice and comments, which helped guide the direction of my work.

I would like to acknowledge the support of our research sponsor: The Goodyear Tire and Rubber Company. Particularly, my gratitude goes to Anthony Parsons for his guidance, technical input on the research, especially in the areas of vehicle and tire modeling. In addition, I would like to thank Dr. Robert Benedict and Peter Suh at The Goodyear Tire and Rubber Company for their support, technical oversight of this research and for providing me with a wonderful opportunity to work on site at the Goodyear Innovation Center.

I am thankful to all of my current and past labmates, especially Mustafa Ali Arat and Joshua Caffee for the academic and non-academic discussions we shared.

Finally, I owe thanks to my parents who instilled in me an indelible love for learning and all members of my family, especially my brother, Gautam who included me in their prayers and gave me strength despite the distance.

Table of Contents

Acknowledgements	iv
Table of Contents	v
List of Figures.....	ix
List of Tables	xviii
Chapter 1: Introduction	
.....	1
1.1 Motivation	1
1.2 Objective and Approach.....	5
1.3 Contributions.....	6
1.4 Thesis Outline	7
1.5 List of Publications.....	9
Chapter 2: Development of an Intelligent Tire System – Technology Review, Sensing Principle, System Configuration and Algorithm Development	
.....	12
2.1 Background and Literature Review.....	13
2.2 Tire Instrumentation	18
2.3 Tire Testing	22
2.3.1 Testing at the Goodyear Innovation Center, Akron, Ohio	22
2.3.2 Testing Using the In-House Mobile Tire Test Rig at the Intelligent Transportation Laboratory (ITL), Virginia Tech	23
2.4 Data Acquisition.....	26
2.5 Measurements on the Tire	29
2.6 Tire Load Estimation Algorithm	32
2.6.1 Results for the Parameter Sensitivity Analysis.....	36
2.6.2 Summary of Parameter Sensitivity Analysis	51
2.6.3 Algorithm Development	57
2.6.4 Neural Network Details	62
2.6.5 Analysis Results	64
2.7 Tire Slip angle Estimation Algorithm	71
2.8 Tire Slip ratio Estimation Algorithm	73

2.9 Friction Estimation Algorithm	75
2.9.1 Classification Algorithm.....	76
2.9.2 Classification Methodology.....	77
2.9.3 Identification Process - Classifier Architecture.....	79
2.9.4 Classification Performance.....	80
2.10 Conclusion.....	80
Chapter 3:Design of an Integrated Vehicle State Estimator for Application to Global Chassis Control	87
3.1 Introduction	88
3.2 Observer Design.....	95
3.2.1 General Observer Flow Chart.....	95
3.2.2 Vehicle Chassis Roll Angle Estimator	96
3.2.3 Vehicle Chassis Pitch Angle Estimator	102
3.2.4 Vehicle Roll and Pitch Angle Estimator.....	110
3.2.5 Bias Compensation.....	118
3.2.6 Vehicle Longitudinal Velocity Estimator.....	120
3.2.7 Tire Vertical Load Estimator.....	123
3.2.8 Tire Longitudinal and Lateral Force Estimator	135
3.2.9 Vehicle Lateral and Longitudinal Velocity Estimator.....	152
3.2.10 Tire slip-ratio and slip-angle estimator.....	157
3.3 Conclusion.....	165
Chapter 4:Model-Based Tire-Road Friction Estimation	178
4.1 Introduction	179
4.2 Mechanics of Pneumatic Tire.....	181
4.2.1 Longitudinal Tire Characteristics	182
4.2.2 Lateral Tire Characteristics	183
4.2.3 Combined-slip Forces.....	184
4.3 Tire Model Selection.....	186
4.4 Brush Model Validation.....	189
4.5 Real-Time Implementation	191

4.6 Parameter Estimation Results	192
4.6.1 Estimation Based on Longitudinal Force-Slip Regression Method	193
4.6.2 Estimation Based on Lateral Force-Slip Regression Method.....	194
4.6.3 Estimation Based on Moment-Slip Regression Method.....	196
4.7 Conclusion.....	199
Chapter 5: An Intelligent Tire Based Tire-Road Friction Estimation Technique and Adaptive Wheel Slip Controller for Anti-lock Brake System.....	203
5.1 Introduction	204
5.2 System Dynamics	205
5.2.1 Wheel Dynamics.....	206
5.2.2 Vehicle Dynamics.....	209
5.2.3 Coupled Wheel and Vehicle Dynamics	210
5.2.4 Hydraulic Brake Dynamics	212
5.3 Controller Design	212
5.3.1. Road Surface Condition Estimation Algorithm.....	213
5.3.2 Wheel Slip Controller.....	231
5.4 Simulation Results.....	234
5.4.1 Baseline ABS Controller Model - Straight-Line Braking Simulation Results.....	237
5.4.2 Proposed Intelligent Tire Based ABS Control Model - Straight-Line Braking Simulation Results.....	239
5.4.3 Drawbacks of a Pure Sliding Mode Controller and Proposed Controller Modifications to Overcome These Drawbacks	241
5.4.4 Jump $-\mu$ Simulation Results.....	246
5.5 Conclusion.....	252
Chapter 6: Piezoelectric Vibration Energy Harvesting System with an Adaptive Frequency Tuning Mechanism for Intelligent Tires	257
6.1 Introduction	257
6.2 Principle of Operation	260
6.3 Energy Harvester Design	262
6.3.1 Target Energy Levels.....	262
6.3.2 Design Considerations	267

6.3.3 Harvester Configuration and Mounting Location	277
6.3.4 System Modeling	280
6.3.5 Numerical Studies.....	285
6.4 Harvester Fabrication and Performance Results	289
6.4.1 Fabrication Details.....	289
6.4.2 Performance Results and discussion.....	292
6.5 Power Processing Circuitry for Broad-Band Harvesting	294
6.6 Conclusion.....	311
Chapter 7: Conclusions and Future Work	316
7.1 Summary of the Work.....	316
7.2 Future Work	318

List of Figures

Fig. 1.1: Inherent weaknesses of indirect state estimation techniques	2
Fig. 1.2: Potential of intelligent tires in improving performance of anti-lock braking system (ABS)	3
Fig. 1.3: The envisioned architecture of an intelligent tire system	4
Fig. 1.4: Research activities undertaken as part of the development, testing and evaluation process.....	6
Fig. 2.1: Intelligent tire system sensor output	14
Fig. 2.2: Intelligent tire system – Products and Concepts	15
Fig. 2.3: Accelerometer (a) glued to the inner liner, and (b) sensor wires secured to the tire inner bulkhead connector	19
Fig. 2.4: Setup for the accelerometer shaker tests	19
Fig. 2.5: Sample results from the shaker tests	20
Fig. 2.6: (a) High speed slip ring, and (b) its placement on the metal plate.....	21
Fig. 2.7: Instrumented tire assembly.....	21
Fig. 2.8: Instrumented tire mounted on the Flat-Trac® machine.....	23
Fig. 2.9: Data for the dynamic tests collected using the in-house mobile tire test rig at the Intelligent Transportation Laboratory (ITL), Virginia Tech.....	24
Fig. 2.10: (a) Instrumented tire prototype mounted on the test trailer, and (b) equipment housed in a trailer attached to a tow vehicle	24
Fig. 2.11: Tire mounted on a force hub	25
Fig. 2.12: Outdoor testing locations	26
Fig. 2.13: Data acquisition equipment of the mobile test trailer	27
Fig. 2.14: (a) Tire sensor data acquisition setup, (b) tire vertical load control setup, and (c) tire steer control setup on the trailer.....	28
Fig. 2.15: Measured acceleration signal during straight track running conditons: (a) circumferential signal, (b) lateral signal, and (c) radial signal	29
Fig. 2.16: Input variables for the tire model.....	30
Fig. 2.17: Estimation of variables of interest (tire load, slip ratio, slip angle, and friction coefficient) made using on-board sensors and state observers	31
Fig. 2.18: Algorithm development process	31
Fig. 2.19: Magnified view of the radial acceleration signal for one cycle of rotation	32
Fig. 2.20: Cascade diagram showing the time series data for the tire radial acceleration at different rolling speeds	33
Fig. 2.21: Cascade diagram showing the dependency of the tire vibration spectra on the rolling speed	33
Fig. 2.22: Radial acceleration signal power on a per revolution basis	35
Fig. 2.23: Flowchart for the contact patch length estimation algorithm	35
Fig. 2.24: Patch length estimation algorithm.....	36

Fig. 2.25: Rolling speed dependence study- Frequency domain.....	37
Fig. 2.26: Rolling speed dependence study- Time Domain	37
Fig. 2.27: Rolling speed dependence study- Patch length.....	38
Fig. 2.28: Pressure dependence study- Frequency domain	39
Fig. 2.29: Pressure dependence study- Time Domain	39
Fig. 2.30: Pressure dependence study- Patch length	40
Fig. 2.31: Load dependence study- Frequency domain.....	41
Fig. 2.32: Load dependence study- Time domain	41
Fig. 2.33: Load dependence study- Patch length.....	42
Fig. 2.34: Camber angle dependence study- Frequency domain.....	43
Fig. 2.35: Camber angle dependence study- Time Domain	43
Fig. 2.36: Camber angle dependence study- Patch length.....	44
Fig. 2.37: Instantaneous slipangle and vertical load during the test.....	45
Fig. 2.38: Effect of slipangle maneuver on: (a) the radial acceleration signal, and (b) the lateral acceleration signal.....	45
Fig. 2.39: Effect of slipangle maneuver on: (a) the radial acceleration signal; (b) the lateral acceleration signal for one tire revolution	46
Fig. 2.40: Wavelet transform decomposition: (a) the radial signal, and (b) the lateral signal	47
Fig. 2.41: Effect of slipangle maneuver on (a) the radial acceleration signal; (b) the lateral acceleration signal- Frequency domain	48
Fig. 2.42: Slipangle dependence study- Time domain	48
Fig. 2.43: Slipangle dependence study- Patch length.....	49
Fig. 2.44: Road surface condition dependence study- Frequency domain.....	50
Fig. 2.45: Road surface condition dependence study- Time domain	50
Fig. 2.46: Road surface condition dependence study- Time domain	51
Fig. 2.47: Flowchart for the proposed tire normal load estimation algorithm	53
Fig. 2.48: Experimental data set.....	54
Fig. 2.49: Identifying regions of maximum difference in the frequency domain	55
Fig. 2.50: Domain extracted signal power.....	56
Fig. 2.51: Flowchart for the tire normal load estimation algorithm	57
Fig. 2.52: Neuron model with n inputs.....	58
Fig. 2.53: Architecture of proposed NN model.....	59
Fig. 2.54: Tan-Sigmoid activation function	60
Fig. 2.55: Neural network training procedure	61
Fig. 2.56: Neural network architecture selected.....	62
Fig. 2.57: Training data set.....	65
Fig. 2.58: Training performance- Mean square error (MSE)	65
Fig. 2.59: Training performance- Correlation coefficient (R).....	66
Fig. 2.60: Testing performance-30 mph	67
Fig. 2.61: Testing performance-45 mph	67

Fig. 2.62: Testing performance- 45 mph with camber angle ($+2^\circ$)	68
Fig. 2.63: Testing performance-65 mph	68
Fig. 2.64: Outdoor testing details	69
Fig. 2.65: Experimental data set	70
Fig. 2.66: Testing performance-30 mph	70
Fig. 2.67: (a) Lateral acceleration profile – slip angle sweep test, and (b) magnified view of the lateral acceleration signal for one tire revolution	71
Fig. 2.68: (a) Variation in the instantaneous amplitude of the lateral acceleration signal, (b) radial acceleration signal power on a per revolution basis	72
Fig. 2.69: Variation in instantaneous amplitude of the lateral acceleration signal as function of the tire-slip angle under different loading conditons	72
Fig. 2.70: Functional diagram of the tire slip angle estimation process	73
Fig. 2.71: Time history of the acceleration signal in the circumferential direction during: (a) low slip conditions, and (b) high slip conditons	74
Fig. 2.72: Functional diagram of the tire slip ratio estimation process	75
Fig. 2.73: Vibration-ratio estimation	76
Fig. 2.74: Road surface identification using a fuzzy logic classifier.....	77
Fig. 2.75: Fuzzy logic classifier architecture.....	79
Fig. 2.76: Fuzzy logic linguistic rules	79
Fig 2.77: Classification performance	80
Fig. 3.1: Block diagram representation of an integrated chassis control system	88
Fig. 3.2: Performance in tracking of the desired vehicle yaw rate for an evasive lane change maneuver; WITH a vehicle state feedback controller and WITHOUT a controller	89
Fig. 3.3: Functional diagram of the estimation process.....	96
Fig. 3.4: (a) Linear 3DOF yaw-roll vehicle model, and (b) 1DOF roll dynamics model	97
Fig. 3.5: Roll estimation based on a 1DOF model	98
Fig. 3.6: (a) Incorporating the effect of process noise (w) and sensor noise (Θ) in the system dynamics, and (b) a complete picture of the operation of the Kalman filter	100
Fig. 3.7: Estimator performance: (a) fishhook maneuver, and (b) double lane change maneuver	102
Fig. 3.8: Longitudinal vehicular load transfer under acceleration.....	103
Fig. 3.9: Parameter variations: mass can change.....	104
Fig. 3.10: (a) Longitudinal vehicle dynamics model, and (b) simplified wheel dynamics model	105
Fig. 3.11: Schematic diagram of the vehicle mass estimation process	107
Fig. 3.12: Longitudinal force (individual tire) estimator performance: a) high μ surface condition, and (b) low μ surface condition	108
Fig. 3.13: Vehicle mass estimation results (a) D-class vehicle (sedan) driving on low μ surface, and (b) B-class vehicle (hatchback) driving on high μ surface	109

Fig. 3.14: Estimator performance: (a) straight-line braking maneuver (constant μ condition), and (b) straight-line braking maneuver (varying μ condition)	109
Fig. 3.15: Vehicle roll model.....	110
Fig. 3.16: Vehicle pitch model	111
Fig. 3.17: Performance of the steady state vehicle roll angle estimator: (a) constant speed straight-line driving (steady state) on a banked road, and (b) double lane change maneuver (transient state) on a banked road	113
Fig. 3.18: Schematic diagram of the proposed vehicle roll/pitch angle estimation process	115
Fig. 3.19: Vehicle roll/pitch angle estimator performance (ref. Table 3.2 for a description of the simulation conditions).....	118
Fig. 3.20: Effect of gravity bias on the lateral acceleration signal	119
Fig. 3.21: Vehicle sideslip angle estimation using a simple integration method: (a) double lane change steering/high μ (0.85 / 120kph/ bank(0 - 18- 0 deg), and (b) fishhook steering/high μ (0.85 / 80kph/ flat surface).....	120
Fig. 3.22: Estimation algorithm data flow chart.....	121
Fig. 3.23: (a) Test conditions: straight-line braking maneuver (varying μ condition), (b) estimated vehicle speed compared with the reference vehicle speed, and (c) estimated wheel slip (top) and absolute error (bottom) compared with the reference wheel slip	123
Fig. 3.24: Load distribution of a vehicle on a graded road.....	125
Fig. 3.25: Load distribution of a vehicle on a banked road.....	125
Fig. 3.26: Test condition: double lane change maneuver (varying μ condition).....	129
Fig. 3.27: Test condition: fishhook maneuver (constant μ , banked (3°) and graded road (2°) condition)	130
Fig. 3.28: Test condition: slalom steering maneuver (low μ condition)	131
Fig. 3.29: Test condition: straight-line braking maneuver (varying μ condition).....	131
Fig. 3.30: Simplified roll dynamics model.....	132
Fig. 3.31: LTR based chassis roll angle estimates (ref. Table 5 for a description of the simulation conditions).....	134
Fig. 3.32: (a) Simulated longitudinal force curves as a function of wheel slip-ratio (λ) for varying surface conditions, and (b) simulated lateral force curves as a function of slip-angle (α) for varying surface conditions	135
Fig. 3.33: Some representative tire-road friction models	136
Fig. 3.34: (a) Tire forces calculated by the Dugoff and MF model, and (b) Tire forces calculated by the Modified Dugoff and MF model.....	137
Fig. 3.35: (a) Road surface condition (bottom) and the tire slip-ratio (top) during the simulation, and (b) longitudinal stiffness estimation result (bottom) and corresponding activation signal (top)	140
Fig. 3.36: (a) Road surface condition (bottom) and the tire slip-ratio (top) during the simulation, and (b) longitudinal stiffness estimation result (bottom) and corresponding activation signal (top)	141

Fig. 3.37: Longitudinal tire force in the small-slip region under different road conditions.....	142
Fig. 3.38: Observer Performance (ref. Table 7 for a description of the simulation conditions)	148
Fig. 3.39: Observer Performance (ref. Table 3.8 for a description of the simulation conditions)	152
Fig. 3.40: Four wheel vehicle model	154
Fig. 3.41: Schematic diagram of the vehicle longitudinal and lateral velocity estimation process	155
Fig. 3.42: Observer Performance (ref. Table 3.9 for a description of the simulation conditions)	157
Fig. 3.43: Observer Performance (ref. Table 3.10 for a description of the simulation conditions)	158
Fig. 3.44: Schematic diagram of the tire slipangle estimation process	161
Fig. 3.45: Observer Performance (ref. Table 3.11 for a description of the simulation conditions)	165
Fig. 4.1: Friction circle of a tire.....	179
Fig. 4.2: Simulated longitudinal force curves as a function of wheel slip-ratio (λ) for varying surface conditions	183
Fig. 4.3: Simulated lateral force curves as a function of slip-angle (α) for varying surface conditions.....	184
Fig. 4.4: (a) Normalized longitudinal tire force for combined braking and steering, and (b) normalized lateral tire force for combined braking and steering.....	185
Fig. 4.5: Friction circle diagram at a vertical load of 3000 N	185
Fig. 4.6: Tire and Brush model [10].....	186
Fig. 4.7: Adaptation of the brush-tire model to tire measurement data (ref.....)	191
Fig. 4.8: Tire parameter estimation algorithm - Lateral Force-Slip regression method.....	192
Fig. 4.9: Longitudinal stiffness and friction coefficient estimates from (F_x, λ) data: (a) high μ conditons, and low μ conditons	194
Fig. 4.10: Cornering stiffness and friction coefficient estimates from (F_y, α) data: (a) high μ conditons, and low μ conditons	196
Fig. 4.11: Cornering stiffness and friction coefficient estimates from (M_z, α) data: (a) high μ conditons, and low μ conditons	198
Fig. 5.1: Free body diagram of the quarter car model.....	205
Fig. 5.2: Simulated adhesion/friction coefficient (μ) versus longitudinal slip-ratio (λ) curve for varying surface conditions	207
Fig. 5.3: Wheel dynamics (refer to Equations (5.1)-(5.6)).....	209
Fig. 5.4: Vehicle dynamics (refer to Equations (5.7)-(5.8)).....	210
Fig. 5.5: Combined system dynamics.....	211

Fig. 5.6: Intelligent tire application: (a) sensor mounting location, (b) instrumented tire assembly, (c) mobile tire test rig, and (d) test rig attached to the towing vehicle	213
Fig. 5.7: Measured acceleration signal for one rotation	214
Fig. 5.8: Measured circumferential acceleration signal under free-rolling, traction, braking, and steering conditions	214
Fig. 5.9: Tire tested on different road surface conditions: (a) dry surface testing, and (b) wet surface testing; Roughness dependence study: (c) radial signal PSD, and (d) circumferential signal PSD.....	215
Fig. 5.10: Algorithm flowchart.....	216
Fig. 5.11: (a) Accelerometer signal domains; PSD waveforms using: (b) all the domains, (c) only the pre-trailing domain, and (c) only the post- trailing domain.....	217
Fig. 5.12: High and low frequency domains in the circumferential acceleration PSD	217
Fig. 5.13: Vibration ratio on dry and wet surface conditions for a range of tire speeds	218
Fig. 5.14: Fuzzy logic based controller architecture	219
Fig. 5.15: Membership functions for input variable-speed	219
Fig. 5.16: Membership functions for input variable-tire pressure.....	220
Fig. 5.17: Membership functions for input variable-vibration ratio.....	220
Fig. 5.18: Membership functions for output variable-terrain classification.....	221
Fig. 5.19: Flowchart of the proposed terrain classification algorithm	221
Fig. 5.20: Tire tested on different road surface conditions: (a) rough asphalt, (b) regular asphalt, (c) smooth asphalt, and (d) wet asphalt	222
Fig. 5.21: Performance of the Fuzzy Logic classifier - low-slip conditions	223
Fig. 5.22: Performance of the Fuzzy Logic classifier - high-slip conditions	223
Fig. 5.23: Circumferential acceleration signal under low-slip conditions (top), and increased vibration levels in the circumferential acceleration signal under high-slip conditions (bottom)	224
Fig. 5.24: Adaption of the brush model towards the magic formula.....	225
Fig. 5.25: Tire force estimator architecture	226
Fig. 5.26: Straight-line braking test - SMC observer - tire force estimates.....	226
Fig. 5.27: Straight-line braking test - estimated vehicle speed compared with the reference vehicle speed (top), and estimated wheel slip compared with the reference wheel slip (bottom)	227
Fig. 5.28: Measured radial and circumferential acceleration signal for one tire rotation	228
Fig. 5.29: Architecture of the proposed artificial neural network (ANN) model.....	229
Fig. 5.30: Artificial neural network (ANN) performance	230
Fig. 5.31: Friction estimation results using the brush model based algorithm under high-slip .	230
Fig. 5.32: Architecture of the proposed integrated approach using an intelligent tire based friction estimator and the model based estimator	231
Fig. 5.33: Sliding mode control law($U(t) = U_{eq} t + U_{sw} (t)$) model	234
Fig. 5.34: Baseline ABS model - design parameters.....	234
Fig. 5.35: Operation flowchart -baseline ABS algorithm.....	235

Fig. 5.36: Threshold value selection for the baseline ABS model - wheel-deceleration and slip curves for different initial braking velocities (top), and wheel-deceleration thresholds (bottom)	236
Fig. 5.37: Baseline ABS model performance: (a) high- μ condition, and (b) low- μ condition...	238
Fig. 5.38: SMC based ABS model performance: (a) high- μ condition, and (b) low- μ condition	239
Fig. 5.39: Comparison of performance of the two ABS algorithms: (a)-(b) high- μ condition, and (c)-(d) low- μ condition	240
Fig. 5.40: Implementation of the proposed FSP ABS	242
Fig. 5.41: ABS performance- PI v/s SMC	242
Fig. 5.42: Performance of Fuzzy-SMC-PI controller compared to SMC and PI controllers	243
Fig. 5.43: Fuzzy logic membership functions	244
Fig. 5.44: Fuzzy-SMC-PI controller implementation block diagram	244
Fig. 5.45: Supervisory Fuzzy controller block diagram	245
Fig. 5.46: FSP based ABS performance: (a) high- μ condition, and (b) low- μ condition.	246
Fig. 5.47: Jump- μ test	247
Fig. 5.48: Intelligent tire based ABS with road-condition estimator and brake preconditioning module	247
Fig. 5.49: Jump- μ test results.	249
Fig. 5.50: Jump- μ results for extreme surface friction conditions (high=1-low=0.2-high=1)	250
Fig. 5.51: Jump- μ results for extreme surface friction conditions (low=0.2-high=1-low=0.2)	251
Fig. 6.1: Intelligent tire system for online tire monitoring	258
Fig. 6.2: Tire vibration waveform arranged in time series: (top) circumferential, (middle) lateral, and (bottom) radial signals.	260
Fig. 6.3: Radial acceleration signal in frequency domain	261
Fig. 6.4: Typical wireless data transmission system for intelligent tires	262
Fig. 6.5: (a) Velocity profile for the city driving schedule, and (b) energy demand analysis for the city cycle	263
Fig. 6.6: (a) Velocity profile for the hwy driving schedule, and (b) energy demand analysis for the hwy cycle	264
Fig. 6.7: Equivalent battery model for a Li-ion cell created in matlab-simulink for analysis	266
Fig. 6.8: (a) Power limits as a function of the state of charge (SOC) of the cell, and (b) Charge-discharge current limits as a function of the state of charge (SOC) of the cell	266
Fig. 6.9: (a) Accelerometer glued to the inner liner, (b) static testing setup equipment, (c) instrumented hammer, and (d) free hanging hammer test setup	268
Fig. 6.10: Hammer test results for different pressure	268
Fig. 6.11: Test setup used to determine the natural modes of vibrations of the tire under static loading conditions	269
Fig. 6.12: Hammer test results for different tire vertical loading conditions	269

Fig. 6.13: Data for the dynamic tests collected using the in-house mobile tire test rig at the Intelligent Transportation Laboratory (ITL), Virginia Tech.....	270
Fig. 6.14: Cascade diagram showing the time series data for the tire radial acceleration at different translational speeds	270
Fig. 6.15: Cascade diagram showing the dependency of the tire vibration spectra on the translational speed.....	271
Fig. 6.16: Tire tested on different road surface conditions: (a) dry Asphalt, (b) wet Asphalt, and (c) gravel	272
Fig 6.17: Load dependence study.....	272
Fig. 6.18: Pressure dependence study.....	272
Fig. 6.19: Speed dependence study	273
Fig. 6.20: Roughness dependence study.....	273
Fig. 6.21: Time spent in the contact patch per revolution for different tire speeds, under different tire pressure and vertical load conditions: (a) 30 mph, (b) 45 mph, and (c) 60 mph.....	274
Fig. 6.22: Identifying ideal operating frequency band for the harvester	276
Fig. 6.23: Comparison between radial acceleration PSD plots for low and high- μ surface conditions	276
Fig. 6.24: Key design guidelines for selecting an appropriate harvester configuration for tires	277
Fig. 6.25: Cantilever beam with a tip mass under translational base motion	278
Fig. 6.26: The planned mounting location of the harvester is demonstrated	278
Fig. 6.27: (a) CAD drawing of the harvester casing, (b) drawing of the harvester placed inside the casing, and (c) drawing of the complete assembly. (Note: some components removed from model for clarity)	279
Fig. 6.28: Stress distribution along the length of the beam	280
Fig. 6.29: 31-direction: Charge collection in 3 direction and stress in 1 direction	281
Fig. 6.30: Schematic of the beam showing the parameters used in the simulations	286
Fig. 6.31: Connection method between the energy harvesting device and the rectification circuitry	287
Fig. 6.32: (a) Output power v/s electrical resistance, (b) output current v/s electrical resistance, and (c) output power v/s frequency	288
Fig. 6.33: (a) X-ray diffraction pattern of PZTZNN plates showing single phase perovskite structure, (b) sintering profile, and (c) microstructure of sintered PZTZNN plates	290
Fig. 6.34: (a) parallel bimorph configuration, (b) experimental setup, and (c) Frequency response function	291
Fig. 6.35: Voltage and power characteristics of the bimorph energy harvester at $1g_{rms}$ base excitation with a tip mass of 11.45 gm at: (a) 62.5 Hz, and (b) 80 Hz	294
Fig. 6.36: Harvester power dissipated in the optimal resistive load versus operating frequency and squared coupling factor	296
Fig. 6.37: Basic Buck-Boost AC-DC switch-mode power converter	297

Fig. 6.38: Proposed system architecture for real time control- A self-tunable system, combining both frequency detection and self-actuation	298
Fig. 6.39: Optimal load impedance selection	299
Fig. 6.40: (a) Power versus frequency for three cases, a constant resistance, the resistance matched to the capacitive piezoelectric materials, and the optimal resistance, and (b) additional power obtained (percentage) by using the optimal resistance instead of the matched resistance	299
Fig. 6.41: (a) Power output, (b) optimal resistance, (c) optimal current, and (d) voltage vs frequency of the parallel-connected and serial-connected systems	300
Fig. 6.42: Load impedance estimation via neural networks	301
Fig. 6.43: (a) Tire testing setup, and (b) Front panel of LabView VI - Instantaneous Force – Moment- Slip Angle Information	302
Fig. 6.44: Radial acceleration signal power on a per revolution basis: at 30 mph, 45mph and 65 mph	303
Fig. 6.45: Identifying regions of maximum difference in the frequency domain	304
Fig. 6.46: Identifying regions of maximum difference in the frequency domain	305
Fig. 6.47: (a) Sample experimental data set, and (b) System architecture for the ANN system	306
Fig. 6.48: Artificial training data set creation.....	306
Fig. 6.49: (a) Neuron model with R inputs, and (b) Tan-Sigmoid activation function	307
Fig. 6.50: Multi-layer Perceptron (Neural Network).....	308
Fig. 6.51: (a) Test Road in the Map, and (b) Remote desktop control setup	309
Fig. 6.52: Testing under dry and wet road surface conditons	309
Fig. 6.53: Comparison of experimental and ANN predicted results	310
Fig. 6.54: Neural network based impedance matching system for tire energy harvesting.....	310
Fig. 6.55: Key conclusions	311
Fig. 7.1: Sensor data fusion scheme	318

List of Tables

Table 2.1: APOLLO program findings on how information gained from an intelligent tire will affect vehicle control systems [20]	16
Table 2.2: Methods for measuring and analyzing various parameters of a tire	17
Table 2.3: Dytran 3023A5 tri-axial accelerometer characteristics	18
Table 2.4: Prototype tires with sensor type	22
Table 2.5: Frequency (Hz) bandwidth of decomposed components	47
Table 2.6: Results for the parameter sensitivity analysis	51
Table 2.7: Synaptic weights	63
Table 2.8: Synaptic weights	63
Table 2.9: Synaptic weights	63
Table 2.10: Bias details	64
Table 2.11: Training data set range	64
Table 2.12: ANN training performance	66
Table 2.13: ANN performance –Testing set	69
Table 3.1: State-of-the-Art Literature Review	91
Table 3.2: Simulation cases	116
Table 3.3: Estimation algorithm rules	122
Table 3.4: Simulation cases	128
Table 3.5: Simulation cases	134
Table 3.6: Simulation cases	140
Table 3.7: Simulation cases	147
Table 3.8: Simulation cases	150
Table 3.9: Simulation cases	156
Table 3.10: Simulation cases	157
Table 3.11: Simulation cases	161
Table 4.1: State-of-the-Art Literature Review	180
Table 4.2: Tire test conditions	189
Table 4.3: Required utilization of friction (in percent) to achieve a friction estimate within an accuracy of $\pm 10\%$	199
Table 5.1: Typical roads parameters	208
Table 5.2: Results for the parameter sensitivity analysis	228
Table 5.3: Triggering signals and threshold values	237
Table 5.4: Vehicle simulation parameters	237
Table 5.5: Straight line braking results comparison	246
Table 5.6: Jump- μ tests- results comparison	249
Table 6.1: Minimum energy required per tire revolution for different tire translational speeds	263
Table 6.2: Distribution of the power consumption for a TPMS [10]	264
Table 6.3: Battery specifications used for power analysis [12]	265

Table 6.4: Current consumption for sensors, microcontroller and wireless transmitter [13]	267
Table 6.5: Number of passages through the contact patch region in one second	275
Table 6.6: Geometry and material properties of the simulated system.....	286
Table 6.7: Piezoelectric properties of the synthesized material.....	290
Table 6.8: Test Matrix for creating the training data set.....	303

Chapter 1

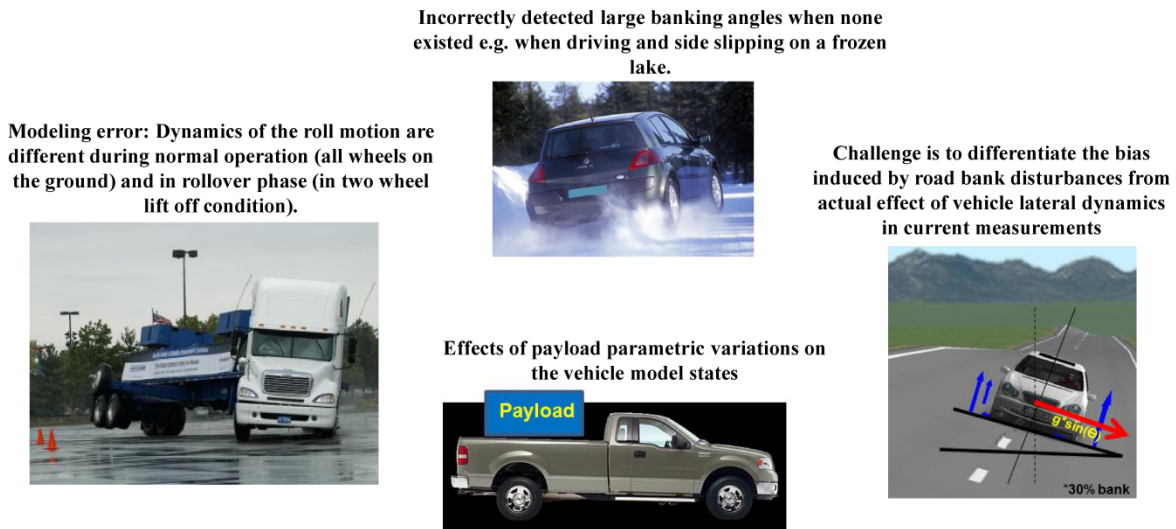
Introduction

1.1 Motivation

Vehicle dynamic performance is predominantly controlled by tire dynamic characteristics through the forces and moments generated at the tire-road contact patch. The control of the tire vertical force can improve the vertical vibration characteristics and ride behavior. The control of the tire lateral forces usually benefits the vehicle stability and handling characteristics, and an optimized tire longitudinal force control can improve braking performance. Consequently, in the case of modern day vehicle control systems employing a feedback control structure, a real-time estimate of the tire-road contact parameters is invaluable for enhancing the performance of the chassis control systems such as anti-lock braking systems and stability control systems. However, at present, the commercially available tire monitoring systems are not equipped to sense and transmit high speed dynamic variables used for real-time active safety control systems. Consequently, under the circumstances of sudden changes to the road conditions, the driver's ability to maintain control of the vehicle maybe at risk. One could possibly envision a methodology to circumvent this drawback in current control systems, provided an estimation scheme is developed to make real-time estimates of the tire-road contact parameters (ranging from kinematic conditions of the tire, tire-road contact forces and friction coefficient). This interest in estimating tire-road contact forces is mainly control oriented, because contact force estimation is not an intrinsic or a final objective, but it is functional to the implementation/improvement of vehicle stability control systems. Knowledge of the friction coefficient of the road is important for the design and analysis of vehicle control systems. Lack of knowledge about friction leads to conservative design rules for the controller, resulting in reduced performance.

At the present stage of development, tire-road contact parameters are indirectly estimated using observers based on vehicle dynamics measurements (acceleration, yaw and roll rates, suspension deflections, etc). Although these methods present a relatively accurate solution, they

rely heavily on tire and vehicle kinematic formulations and break down in case of abrupt changes in the measured quantities (Fig. 1.1). Hence, due to the significant nonlinear dynamics of a vehicle system, due to unknown and changing plant parameters, and due to the presence of unknown input disturbances, the design and implementation of observer based indirect estimation algorithms is challenging.



Uncertainty in Sensor Networks and State Estimators Currently Used in the Estimation of Tire-Vehicle States Reduces Their Accuracy and Reliability

Fig. 1.1: Inherent weaknesses of indirect state estimation techniques

To address this problem, researchers have been developing certain sensor based advanced tire concepts for direct measurement of the tire-road contact parameters. Thus, the new terms "Intelligent Tires" and "Smart Tires", which mean online tire monitoring, are enjoying increasing popularity among automotive manufacturers. The development of the so called "intelligent tire/smart tire system" is expected to spur the development of a new generation of vehicle control system with modified control strategies (Fig. 1.2), leveraging information directly coming from the interface between the tire and the road, and in turn significantly reducing the risk of accidents. Moreover, measured data directly available from the tire sensor module is expected to simplify and optimize the performance of current control systems, by eliminating uncertainty-adding procedures, inherent in most indirect estimation techniques.

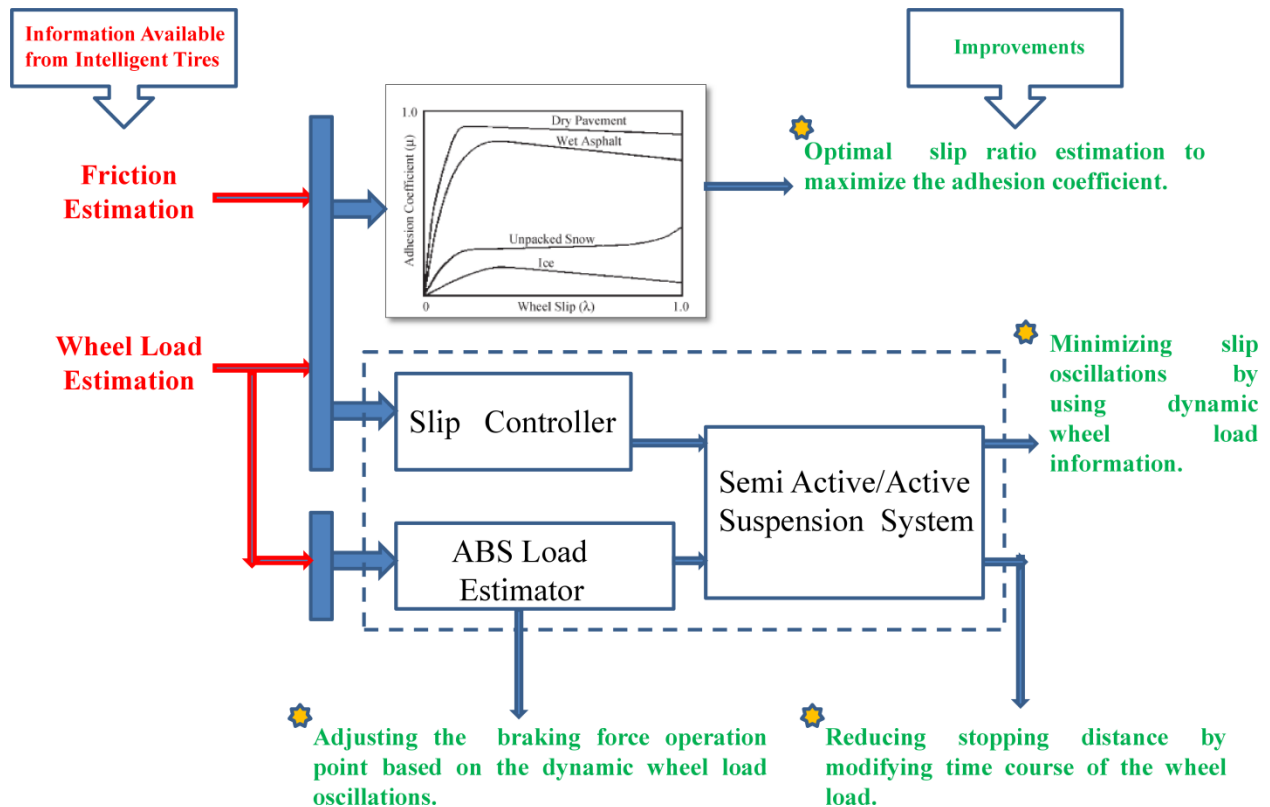


Fig. 1.2: Potential of intelligent tires in improving performance of anti-lock braking system (ABS)

Despite the plethora of advantages offered by the intelligent tire technology, some of the key technical challenges hindering large-scale commercialization of the intelligent tire technology in its present state include:

- Compatibility of the sensors with tire rubber i.e. stiffness issues.
- Robustness of the sensing element in the harsh internal environmental conditions within the tire.
- Availability of a ‘Low-Power-Consumption IC Chipset’ for supporting the complex signal processing algorithms for in-tire processing of the raw signal.
- Wireless transmission of gathered data and meeting the power supply needs of all the electronic components.
- Bandwidth limitations of a single-point sensing application (multi –point sensing architecture doesn’t seem a viable option, for both technical and economic reasons).
- Economic feasibility issues relating to the use of expensive sensors in a comparatively inexpensive product like tires.

Clearly, from a technical standpoint, the successful realization of the intelligent tire technology requires the simultaneous development of a number of other enabling technologies. These supporting technologies would play a vital role in overcoming some of the above-mentioned limitations of the current state-of-the-art tire sensing technologies. Currently, the state-of-the-art tire sensing technologies under development are not equipped to sense and transmit high speed dynamic variables used for real-time active safety control systems. Therefore, in order to exploit the fullest potential of the intelligent tire technology, a data fusion approach with more complex data processing algorithms would be required. These proposed systems would be capable of leveraging information from existing sensors onboard modern day vehicles and fusing them with information available from tire embedded sensors (Fig. 1.3). The end result will be a novel system capable of providing real-time information about the tire-vehicle states. The availability of this crucial piece of information about the tire-vehicle states is expected to potentially open a new era in design of vehicle control systems.

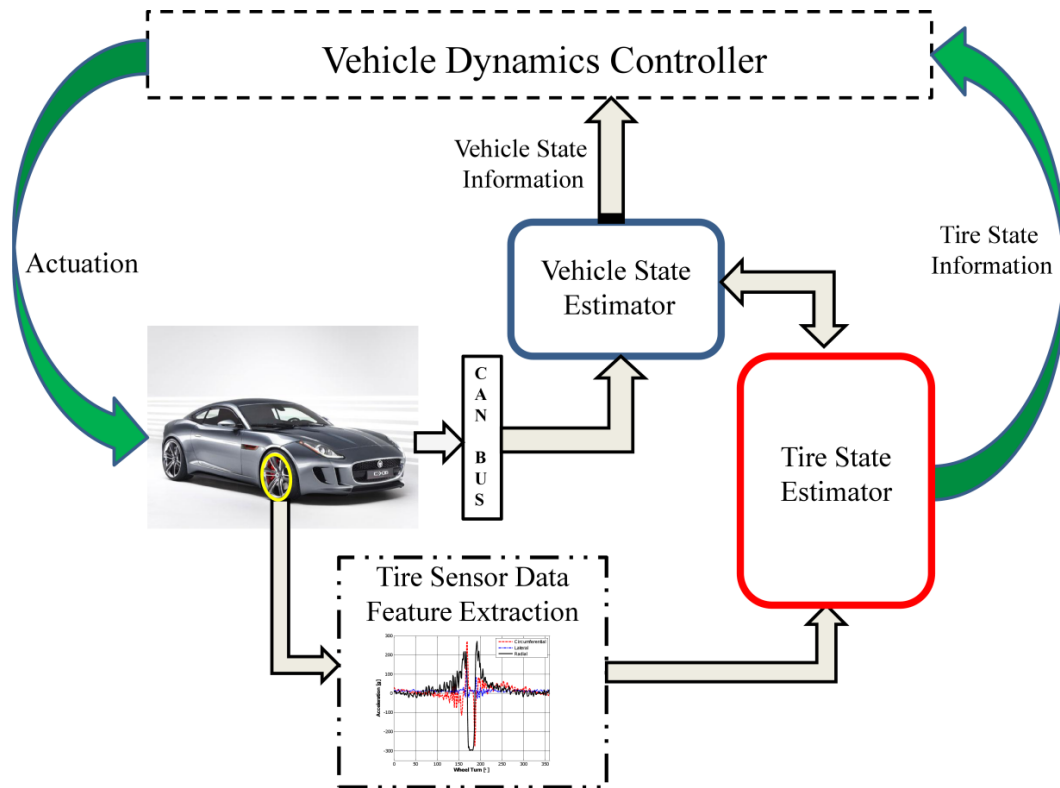


Fig. 1.3: The envisioned architecture of an intelligent tire system

1.2 Objective and Approach

The aim of this thesis is to test the following research hypothesis:

"If a tire attached sensor module unit could be developed to meet the undermentioned functional and operational specifications, and in addition have the following attributes:

- *Be capable of measuring/estimating several contact parameters ranging from the kinematic conditions of the tire (the longitudinal slippage and the side slip angle) to its dynamic properties (the contact area shape and dimensions as well as the longitudinal, lateral and vertical loads);*
- *Be capable of transmitting the measured data to the on-vehicle ECUs without the need of cables (wireless transmission);*
- *Need no external power supply;*
- *Not modify the tire performances such as its handling characteristics, comfort characteristics, acoustic emission, braking performances, fatigue resistance, wearing properties, etc.;*
- *Demonstrate reliability and robustness in the typically harsh and hostile tire environment;*
- *Have a life at least equal to that of the tire;*
- *Be modular, i.e. easily adjustable to fit any kind of tire.*

Then the developed tire attached sensor module could be used to:

- *Provide existing electronic control units (ECUs) with valuable information, as an actuator, which they could use to change vehicle–road interaction properties according to some control strategies thus improving vehicle safety and performance;*
- *Provide real time information about the tire condition to the driver;*
- *Provide information for services for external users e.g. vehicle-to-vehicle (V2V) communication or vehicle-to–infrastructure (V2I) communication”.*

Research activities undertaken as part of the development, testing and evaluation process can be broadly classified into four broad stages, as shown in Fig. 1.4.

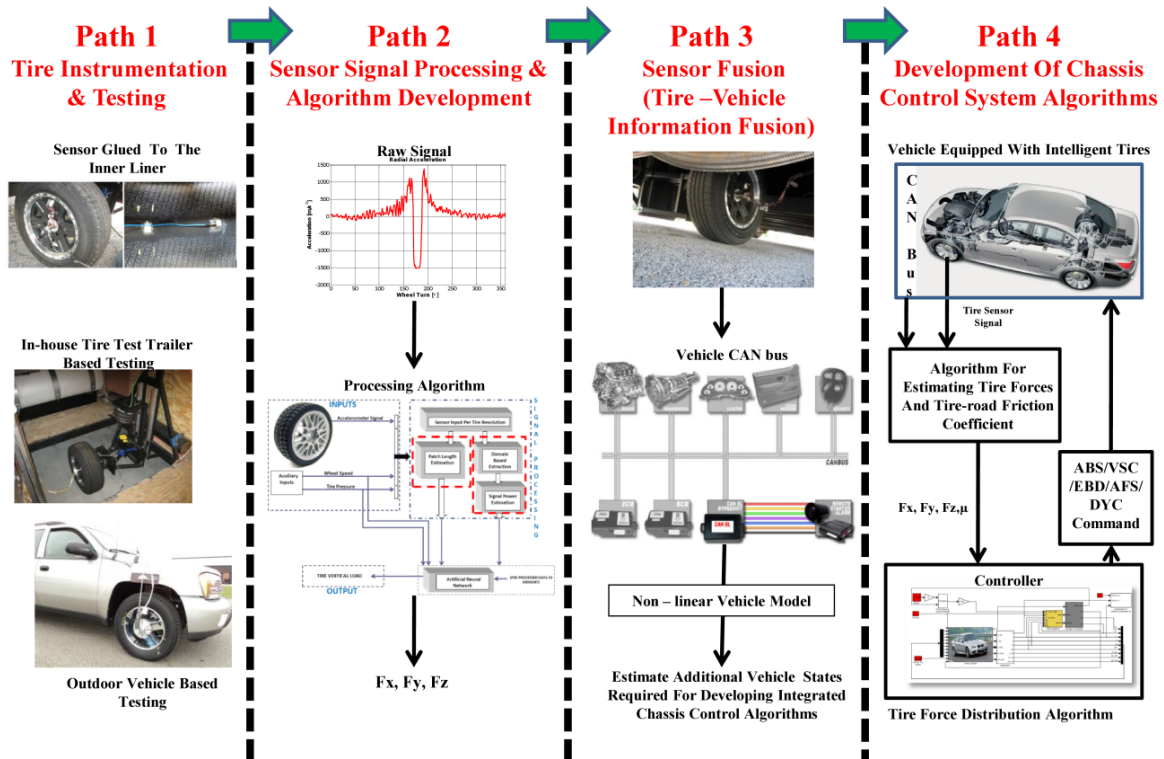


Fig. 1.4: Research activities undertaken as part of the development, testing and evaluation process

1.3 Contributions

Based on the motivation provided in the above sections, this thesis:

1. Develops an artificial neural network(ANN) based tire load estimation algorithm,
2. Develops a novel signal processing method to estimate the tire slip angle,
3. Develops a novel signal processing method to estimate the tire ratio,
4. Develops a fuzzy-logic based real-time terrain classification system using tire vibration pattern analysis,
5. Develops an integrated vehicle state estimator, comprising a series of model-based and kinematics-based observers, for estimating vehicle roll/pitch angles, road bank/grade angles, tire load, tire longitudinal/lateral forces, vehicle longitudinal/lateral velocity, tire slip ratio/slip angle,
6. Develops a model-based approach to estimate tire-road friction coefficient,

7. Develops a fuzzy/sliding mode/proportional integral control methodology based adaptive wheel slip controller for anti-lock brake system (ABS),
8. Develops a vibration energy harvesting system with an adaptive frequency tuning mechanism for intelligent tires.

Development of the above estimation algorithms presents state, parameter and unknown input estimation problems for linear and nonlinear systems. Thus, this thesis also makes significant contributions to state/parameter estimation techniques for linear and nonlinear systems.

1.4 Thesis Outline

The remainder of this thesis is organized as follows:

Chapter 2: Development of an Intelligent Tire System – Technology Review, Sensing Principle, System Configuration and Algorithm Development provides a state-of-the-art review of the intelligent tire technology and presents details regarding the procedure developed to instrument the tire, methodology for tire sensor data acquisition, tire testing, sensor data analysis and algorithm development. A description of the signal processing algorithms that can be used to extract information about the tire-road contact parameters from an intelligent tire system is included in this chapter. The results presented in this chapter demonstrate the feasibility of developing a sensorized tire system capable of providing real-time information about the tire-road contact parameters. Being able to leverage the plethora of information about the contact patch dynamic properties, an intelligent tire system is expected to stimulate the development of a new generation of traction (TCS), braking (ABS) and stability (ESP) control systems for improving vehicle safety and performance.

Chapter 3: Design of an Integrated Vehicle State Estimator for Application to Global Chassis Control introduces a new integrated vehicle state estimator, comprising a series of model-based and kinematics-based observers, for estimating unmeasurable vehicle states. Using an appropriate vehicle model, kinematic equations of motion, and available measurements from sensors potentially integrable or already integrated in current production vehicles, the unknown vehicle states as well as the tire-road contact forces are estimated by implementing a series of observers, arranged in a cascade structure. An effectively designed merging scheme ensures robust estimation performance even during the vehicle maneuvers which show highly

nonlinear tire characteristics, and in the existence of road inclination or bank angle. In this study, it is assumed that measurements from a 6-axis Inertial Measurement Unit (IMU) (3-axes of rotation rate measurement, and 3-axes of acceleration measurement), wheel speed sensors, and steering wheel angle sensor are available. The estimator is implemented in the Matlab/Simulink and CarSim software environment. Results presented in this chapter show the ability of cascaded estimators to provide accurate estimates of vehicle states. Improved information about the vehicle states can be used to develop more reliable and robust vehicle stability control systems.

Chapter 4: Model-Based Tire-Road Friction Estimation introduces a novel method for estimating the value of tire-road friction coefficient by using a well-defined accurate model for the “effect of the friction on the tire behavior”. The model adopted for this purpose is the physically based brush-tire model. Friction estimation using the real-time estimation technique presented in chapter is tested on tire measurement data. Knowledge of the shape of the friction characteristic, possibly obtained through estimation of both friction and tire stiffness using the brush model, provides information on the slip values for which maximum friction is obtained. This information could be used to generate slip references for slip controllers, for example in ABS. Tire stiffness estimates can also be used in vehicle models, such as the bicycle model, which are often used for reference generation and estimation.

Chapter 5: An Intelligent Tire Based Tire-Road Friction Estimation Technique and Adaptive Wheel Slip Controller for Anti-lock Brake System (ABS) presents a novel development and implementation of a real-time tire-road contact parameter estimation methodology using acceleration signals from an intelligent tire. Considering the strong interdependence between the operating road surface condition and the instantaneous forces and moments generated; this real time estimate of the tire-road friction coefficient is expected to play a pivotal role in improving the performance of a number of vehicle control systems. In particular, this study focuses on the possibility of enhancing the performance of the ABS control systems. In order to achieve the aforementioned objectives, the design and implementation of a Fuzzy/Sliding Mode/Proportional Integral (Fuzzy-SMC-PI (FSP)) control methodology is proposed. Fuzzy-SMC-PI is basically a combination of Sliding Mode Control (SMC) and PI control methodologies through fuzzy logic. The mathematical model of the vehicle-wheel system and the Fuzzy-SMC-PI control algorithm to regulate the wheel slip are presented. The results

show significant improvements in the stopping distance of a vehicle equipped with an intelligent tire based FSP controller as compared to a vehicle equipped with a standard ABS.

Chapter 6: Piezoelectric Vibration Energy Harvesting System with an Adaptive Frequency Tuning Mechanism for Intelligent Tires assesses the feasibility developing an onboard vibration energy harvesting system for tires. Various parameters such as tire speed, normal load, inflation pressure and road roughness conditions are investigated based on real-time accelerations measured inside a tire. To optimize the frequency band of operation, a novel artificial neural network (ANN) based feedback loop control system is developed. High energy density piezoelectric ceramic materials based bimorph harvesters are designed and characterized for the chosen frequency range. By presenting a battery-less power supply unit, the proposed system addresses one of the key challenges in the realization of the intelligent tire concept. These harvesters designed for the harsh tire environment provide a distinct advantage in cost and flexibility of installation, while extending the lifetime of the power supply for sensor data acquisition and communication.

1.5 List of Publications

This research has lead to a series of publications of which some of them are public, some internal and some in the form of patent applications/invention disclosures. The publications are listed below:

Journal Publications

1. Singh, K.B., Bedekar, V., Taheri, S. and Priya, S., *Piezoelectric Vibration Energy Harvesting System with an Adaptive Frequency Tuning Mechanism for Intelligent Tires*, Journal of Mechatronics,2011(accepted).
2. Singh, K.B. and Taheri, S., *Piezoelectric Vibration Based Energy Harvesters for Next Generation Intelligent Tires*, Journal of Tire science & Technology, 2011 (accepted).
3. Singh, K.B., Arat, M.A. and Taheri, S., *An Intelligent Tire Based Tire-Road Friction Estimation Technique and Adaptive Wheel Slip Controller for Anti-lock Brake System*, submitted to the Journal of Dynamic Systems, Measurement and Control, 2012 (manuscript ID: DS-11-1256).

4. Arat, M. A., Singh, K. B., and Taheri, S., *An Intelligent Tire Based Adaptive Vehicle Stability Controller*, submitted to the International Journal of Vehicle Design - Special Issue on Advanced Developments in Tire Modeling, Analysis and Dynamics, 2012 (manuscript ID: IJVD-31576).
5. Singh, K.B. and Taheri, S., *Design of a Nonlinear Observer for Vehicle State Estimation*, IEEE Transactions on Vehicular Technology, 2012 (in preparation).
6. Singh, K.B. and Taheri, S., *Model Based Strategies for Real Time Estimation of Tire-Road Friction Coefficient*, Journal of Dynamic Systems, Measurement and Control, 2012 (in preparation).

Conference Publications

1. Singh, K.B. and Taheri, S., *Anti-Lock Brake System Control Using An Innovative Intelligent Tire-Vehicle Integrated Dynamic Friction Estimation Technique*, 30th Annual Conference on Tire Science and Technology, September 13 & 14, 2011 Akron, Ohio, USA.
2. Singh, K.B. and Taheri, S., *Piezoelectric Vibration Based Energy Harvesters for Next Generation Intelligent Tires*, 29th Annual Conference on Tire Science and Technology, September 20 & 21, 2010 Akron, Ohio, USA. (* Won the 'Best Student Paper Award').
3. Singh, K.B. and Taheri, S., *Energy Harvesting From Tires: Feasibility Study Using Tire Test Data From Accelerometers*, 5th Annual Energy Harvesting Workshop, 3-4 March 2010 Roanoke, VA, USA.
4. Arat, M. A., Singh, K. B., and Taheri, S., *Intelligent Tire: Development and Application*, International Conference on Engineering and Meta-Engineering, ICEME 2012 (under review).
5. Singh, K. B., Arat, M. A., and Taheri, S., *Adaptive Control of Antilock Brake System Using a Tire-Vehicle Estimator*, FISITA 2012 World Automotive Congress (in preparation).
6. Arat, M. A., Singh, K. B., and Taheri, S., *An Intelligent Tire Based Adaptive Vehicle Stability Control System*, International Conference on Advanced Vehicle Technologies and Integration, VTI 2012 (in preparation).

Industrial Research Reports (Internal)

1. Singh, K.B. and Taheri, S., *An Artificial Neural Network Based Dynamic Tire Load Estimation Algorithm for an Intelligent Tire*, The Goodyear Tire and Rubber Company, Jan. 2011.

2. Singh, K.B. and Taheri, S., *An Intelligent Tire Based Adaptive Wheel Slip Controller for Antilock Brake System*, The Goodyear Tire and Rubber Company, Dec. 2010.
3. Singh, K.B. and Taheri, S., *Real Time Terrain Classification System for Ground Vehicles Using Tire Vibration Pattern Analysis*, The Goodyear Tire and Rubber Company, April. 2010.
4. Singh, K.B. and Taheri, S., *Dynamic Tire Characterization for Intelligent Tire Systems: Review and Implementation Strategy*, The Goodyear Tire and Rubber Company, Jan. 2010.

Posters

1. Singh, K.B. and Taheri, S., *Broad Band Energy Harvesting System for Next Generation Intelligent Tires*, Tire Research and Test Center Planning Conference, September 23 & 24, 2010 Akron, Ohio, USA.
2. Singh, K.B. and Taheri, S., *Piezoelectric Vibration Based Energy Harvesting System for In-Tire TPMS*, Tire Research and Test Center Planning Conference, September 23 & 24, 2010 Akron, Ohio, USA.

Chapter 2

Development of an Intelligent Tire System – Technology Review, Sensing Principle, System Configuration and Algorithm Development

Executive Summary

This research focuses on the development of an intelligent tire system, with a special attention to development of measurement and sensor feature extraction methodologies of acceleration signals coming from sensors fixed to the tire innerliner, with the final objective of developing a sensorized tire system capable of providing real-time information about the tire-road contact parameters. The identified sensing parameters/features of a tire include: tire load, slip angle, slip ratio and tire-road friction coefficient. A description of the signal processing algorithms that can be used to extract aforementioned features of interest from an intelligent tire system is included in this study.

The specific objectives of this study are:

- *Development of an artificial neural network(ANN) based tire load estimation algorithm,*
- *Development of a novel signal processing method to estimate the tire slip angle,*
- *Development of a novel signal processing method to estimate the tire ratio,*
- *Development of a fuzzy-logic based real-time terrain classification system using tire vibration pattern analysis.*

The first section of this chapter presents a state-of-the-art review of the intelligent tire technology. Thereafter, details regarding the procedure developed to instrument the tire, methodology for tire sensor data acquisition, tire testing, sensor data analysis and algorithm development are elaborated in the sections that follow.

Keywords: *intelligent tire system, artificial neural network (ANN), Fast Fourier transform (FFT), wavelet transforms, fuzzy logic*

2.1 Background and Literature Review

A vehicle's interaction with the road surface initiates at the contact patch of the tires. This small patch dictates the resulting motion of the vehicle and is a major governing factor of the vehicle's stability and control, especially under severe maneuvers. This underscores the importance of developing a tire contact patch monitoring system, capable of providing real-time estimates of the tire-road contact parameters to the vehicle control system. By having a thorough understanding of the tire-road interaction forces and other parameters at the contact patch, the state of the road surface can be derived which can play a pivotal role in improving the performance of a number of vehicle control systems [1]. Examples of vehicle control systems that can benefit from the knowledge of tire-road friction include anti-lock braking systems (ABS), electronic stability control (ESC), adaptive cruise control, and collision warning or collision avoidance systems. The quality of traffic management and road maintenance work (e.g., salt application and snow plowing) can also be improved if the estimated friction value is communicated to the traffic and highway authorities.

The new terms "Intelligent Tire" and "Smart Tire", which mean online tire monitoring are thus enjoying increasing popularity among automotive manufacturers and formed the motivation for this study to explore the possibility of developing an intelligent tire system. These next generation intelligent tires are expected to play a cardinal role in improving the overall drivability of a vehicle and contributing significantly in improving the performance of a number of active safety systems on board today's vehicles [2-6]. The stimulus for increased research into intelligent tires is attributed to the Bridgestone/Firestone recalls in 2000 [7]. As a result of the recalls, United States Transportation Recall Enhancement, Accountability, and Documentation (TREAD) legislation has mandated that every new automobile be equipped with a tire pressure monitoring system (TPMS) [8-10]. This legislation has given impetus to the development of advanced tire technologies for improved tire safety.

The Intelligent tire concept as envisioned by the tire researchers will have the capability to monitor in real time, the forces at tire-road interface, friction coefficient, slip conditions, temperature/pressure and tire wear (Fig. 2.1). The potential of this system can be judged by its ability to give exhaustive information about a tire in motion in terms of the sensor outputs. Being able to leverage the plethora of information about the contact patch dynamic properties, an

intelligent tire system is expected to stimulate the development of a new generation of traction (TCS), braking (ABS) and stability (ESP) control systems for improving vehicle safety and performance [11-13]. Moreover, as compared to a classical tire-pressure monitoring system (TPMS) mounted to the valve stem in the wheel, an intelligent tire sensor module being attached directly to the tire tread would allow the sensor to collect temperature and pressure data more accurately. This being achieved by making the sensor module less vulnerable to impacts during tire changes and heat radiated from the brakes and wheel, as in the case of valve mounted TPMS units [14].

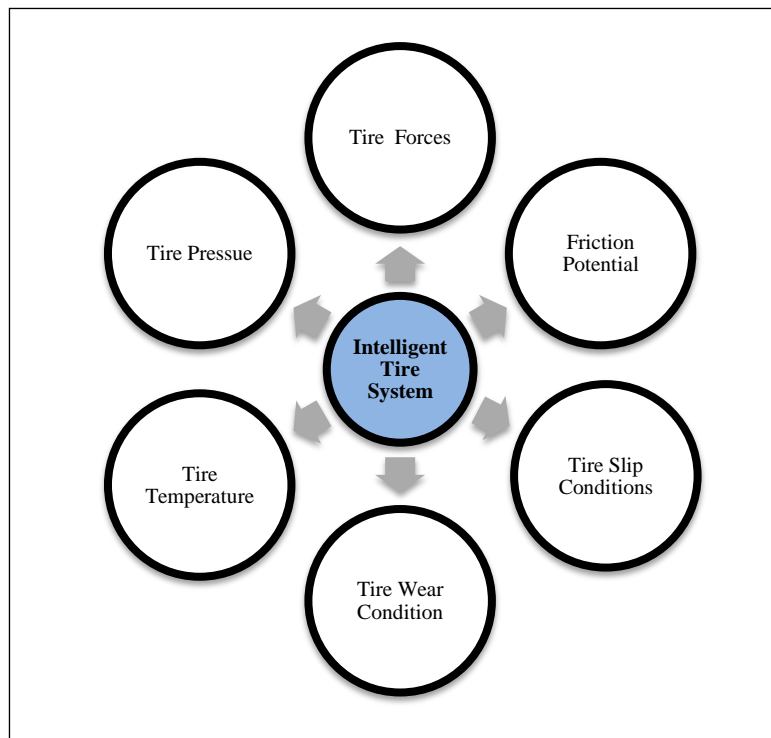


Fig. 2.1: Intelligent tire system sensor output

Most of the research over the past few decades in the field of advanced tire systems has been focused on developing techniques for both offline and online tire inspection. Intelligent tire system, which primarily consists of online tire monitoring systems, has garnered a lot of interest from both industry (Fig. 2.2) and academia, and there have been several architectures proposed in the past few years pertaining to these systems. Some of the concepts which have shown great potential include:

- (i) The APOLLO program - Developed a 3-in-1 intelligent tire [15];
- (ii) The FRICTI@N program - On-board system for measuring and estimating tyre-road friction[16];
- (iii) Contact area information sensing (CAIS) system being developed by Bridgestone [17];
- (iv) Cyber Tire being developed by Pirelli Tires [18];
- (v) Intelligent tire systems being developed by Continental AG [19].

The APOLLO program consortium, consisting of several tire and vehicle companies, performed a study to evaluate the potential benefits of using an intelligent tire system and its effects on accident free traffic [20]. Table 2.1 presents their findings on which control and driver assistance systems stand to benefit from information gathered from the tire.

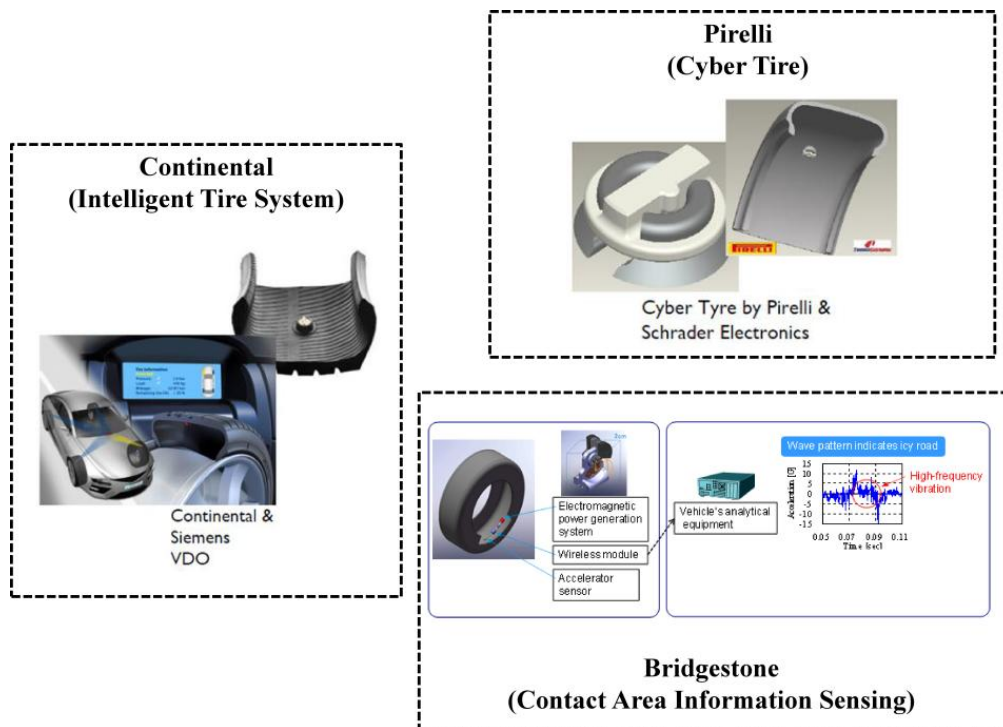


Fig. 2.2: Intelligent tire system – Products and Concepts

Table 2.1: APOLLO program findings on how information gained from an intelligent tire will affect vehicle control systems [20]

		Friction Information	Slip Angle	Wheel Forces	Tire Condition	Road Parameters
Vehicle Control	ABS	Red	Yellow	Yellow	Yellow	Yellow
	TCS	Red	Yellow	Yellow	Yellow	Yellow
	ESP	Red	Red	Yellow	Yellow	Yellow
	Rollover Avoidance	Blue	Yellow	Red	Yellow	Yellow
Advanced Driver Assistance System	ACC	Red	Blue	Yellow	Yellow	Yellow
	Emergency Braking	Red	Yellow	Yellow	Yellow	Yellow
	Collision Avoidance	Red	Yellow	Yellow	Yellow	Yellow
Driver Information	Information Level	Red	Blue	Yellow	Red	Yellow
	Warning Level	Red	Blue	Red	Red	Yellow
The application would benefit from the availability of the tire information		Greatly		Somewhat		Little

Some more recent studies [3-5] have evaluated the possibility of enhancing the performance of the ABS (Antilock Braking System)/EBD (electronic braking distribution) control systems by using the tire normal load and the tire-road friction coefficient information from the intelligent tire system. [4], examines the integration of accelerometer based tire sensors with lateral stability control system (ESP) and presents a preliminary study on potential performance improvements.

As part of this study, a preliminary research was devoted to the identification of a sensing technology suitable for tire applications. A number of advanced tire sensing technologies are currently under development. These sensing technologies can be broadly classified as: (1) Direct Methods and (2) Indirect Methods. These approaches are depicted in Table 2.2.

Table 2.2: Methods for measuring and analyzing various parameters of a tire

Direct Methods	Indirect Methods
These methods utilize :	These methods utilize :
<ul style="list-style-type: none">• Magnetic Sensors [21-22]• Surface Acoustic Wave (SAW) Sensors [23-24]• Accelerometers [25]• Ultrasonic Sensors [26]• Optical Sensors [27-29]• Piezoelectric Sensors [30-32]• Flexible Sensors [33-34]• Tire Steel Wires Being Used as Sensors [35-37]	<ul style="list-style-type: none">• Strain Gages [38-39]• Wavelet Sound Analysis [40-41]• GPS Velocity Data [42-46]• Slip Based Analysis [47-48]• Redundant Wheel Based Methods [49]• Tire Rotational Vibration Model [50]• Infrared Sensors [51-53]

This classification is primarily based on the fact that, indirect methods do not monitor tire deformation, while the direct methods do. Before choosing a sensing technology suitable for tire applications, it is necessary to specify the requirements for the measuring system. Ideally, a tire attached sensor module should meet the following functional and operational specifications:

- Should be capable of measuring/estimating several contact parameters ranging from the kinematic conditions of the tire (the longitudinal slippage and the side slip angle) to its dynamic properties (the contact area shape and dimensions as well as the longitudinal, lateral and vertical loads);
- Should be capable of transmitting the measured data to the on-vehicle ECUs without the need of cables (wireless transmission);
- Need no external power supply;
- Not modify the tire performances such as its handling characteristics, comfort characteristics, acoustic emission, braking performances, fatigue resistance, wearing properties, etc.;
- Demonstrate reliability and robustness in the typically harsh and hostile tire environment;
- Have a life at least equal to that of the tire;

- Be modular, i.e. easily adjustable to fit any kind of tire.

Based on their proven reliability for tire applications [54], it was decided to use tri-axial micro electro mechanical systems (MEMS) accelerometers in this study. These sensors offer the advantage of their tiny dimensions, low weight, wide passband, high reliability and robustness, all of which are necessary to withstand the impulses occurring when the accelerometers enter and exit the footprint.


The following sections elaborate on all the research activities undertaken as part of this study, aimed at developing an intelligent tire system.

2.2 Tire Instrumentation

The tire was instrumented with tri-axial accelerometers. These sensors were mounted radially on the centerline of the inner liner of the tire. The accelerometers being used were:

- Dytran 3023A5 (triaxial) with a 5000g peak measurement range (Table 2.3).

Table 2.3: Dytran 3023A5 tri-axial accelerometer characteristics

 Accelerometer Characteristics	
Range	± 5000 g
Sensitivity	1 mv/g
Frequency response	1.2 -10 kHz
Resonance frequency	30 kHz
Mass	3.0 g
Dimensions	17.7 x 9.02 x 9.14 mm

The accelerometers were enclosed in latex (rubber) and the latex part was glued to the inner liner (Fig. 2.3). This formed a stronger bond with the tire and reduced the chances of the accelerometer coming loose when the tire is rotated. In addition, duct tape (in combination with cyanoacrylate adhesive) was used to secure the wires of the accelerometers inside the tire. The idea is to prevent the wires pulling on the accelerometers and yanking them out during rotation.

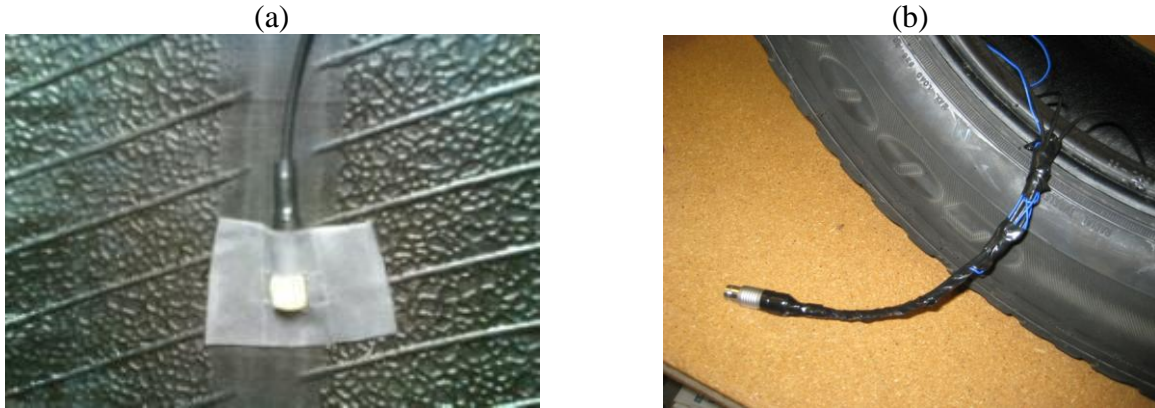


Fig. 2.3: Accelerometer (a) glued to the inner liner, and (b) sensor wires secured to the tire inner bulkhead connector

It should be observed that the connection of sensors to the liner is of crucial importance. It should not modify the local stiffness characteristics of the tire; also it should never break even in the presence of very high static (centrifugal) and dynamic (contact impulse) stresses.

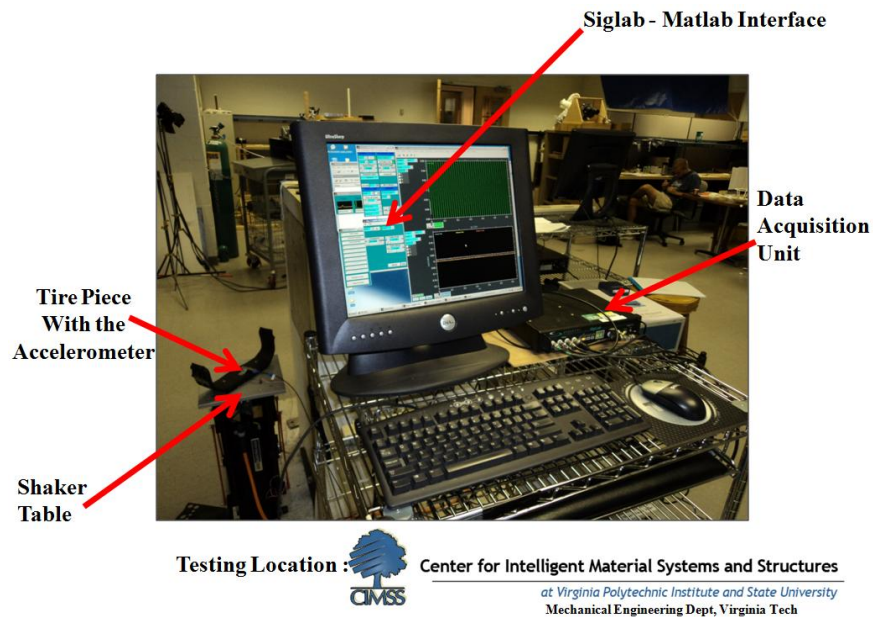


Fig. 2.4: Setup for the accelerometer shaker tests

To ensure that the use of latex was not modifying the local stiffness characteristics of the tire and the tire behavior/response to an external excitation, extensive shaker tests (Fig. 2.4) of an accelerometer mounted on a tire piece were carried out by subjecting the tire piece to a range of external excitation inputs (sine, saw-tooth, square etc). For the first set of tests, the accelerometer

was directly mounted on the tire piece without being enclosed in a latex glove. Thereafter these tests were repeated by enclosing the accelerometer in a latex glove and then mounting it on the tire piece.

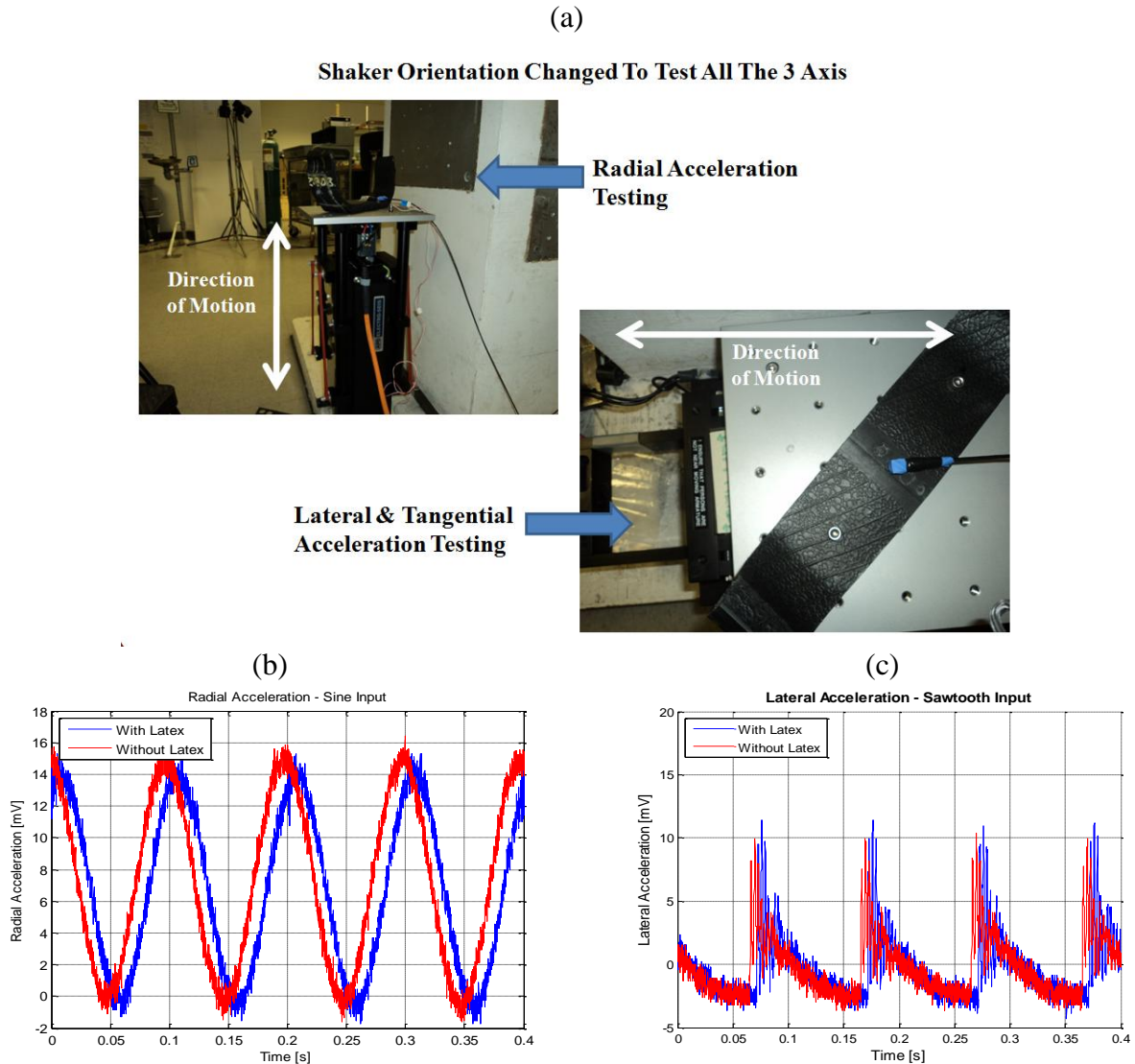


Fig. 2.5: Sample results from the shaker tests

The accelerometer output (Fig. 2.5c-Fig. 2.5d) in either case was found to be the same and hence the use of latex gloves was not modifying the local stiffness characteristics of the tire.

At this preliminary stage, power supply or wireless transmission problems have been neglected by connecting the sensors and the acquisition board through traditional cables using a bulkhead connector on the rim and a slip ring (Fig. 2.6). A slip ring assembly was placed at the

center of the wheel and allows for the free rotation of the tire-wheel assembly without entangling the wires.

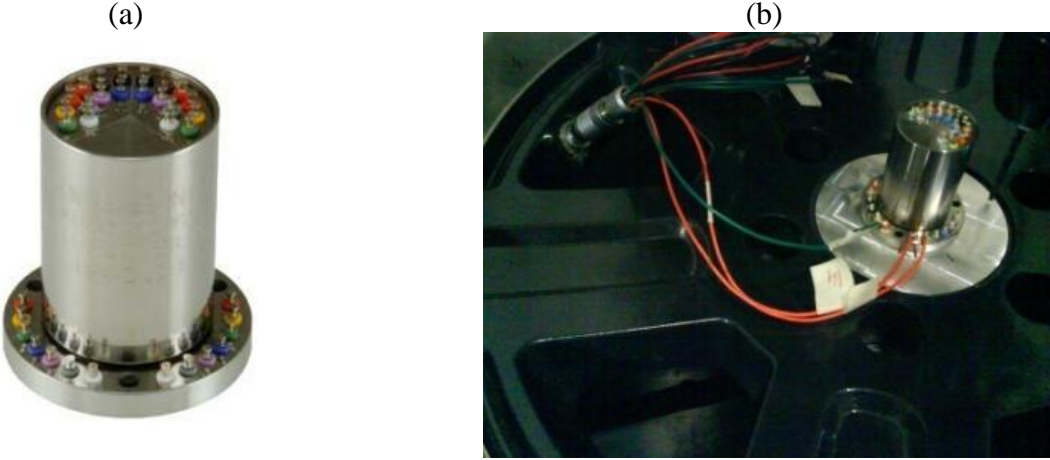


Fig. 2.6: (a) High speed slip ring, and (b) its placement on the metal plate

Fig. 2.7 shows the final assembly of the instrumented tire with the high speed slip ring attached to the wheel.



Fig. 2.7: Instrumented tire assembly

Data acquisition was accomplished using three tire prototypes. Table 2.4 lists the three tire prototypes and their sensor configurations. Multiple sensor configurations were tested in order to compare results for each type of sensor for a reliable and robust signal. Using several

prototypes ensured signals were consistent across multiple tires of the same type. The tire used for testing is the Goodyear Fortera P245/65R17.

Table 2.4: Prototype tires with sensor type

Prototype	Sensors used	Number of sensors	Location
P1	Tri-axial accelerometers	5	Inner Liner
P2	Tri-axial accelerometers	1	Inner Liner
P3	Tri-axial accelerometer & Acoustic sensor	3+1	Inner Liner

2.3 Tire Testing

The testing of the instrumented tire was carried out at two locations:

- a. Indoor Testing: Goodyear Innovation Center in Akron, Ohio. The tire was tested on a Flat-Trac® test machine.
- b. Outdoor Testing: Testing using the in-house mobile tire test rig at the Intelligent Transportation Laboratory (ITL), Virginia Tech, a part of the Institute for Advanced Learning and Research (IALR) at Danville, Virginia.

2.3.1 Testing at the Goodyear Innovation Center, Akron, Ohio

The Flat-Trac® machine (Fig. 2.8) was used to carry out tests under different inflation pressure, speed, load, camber angle and slip angle conditions.

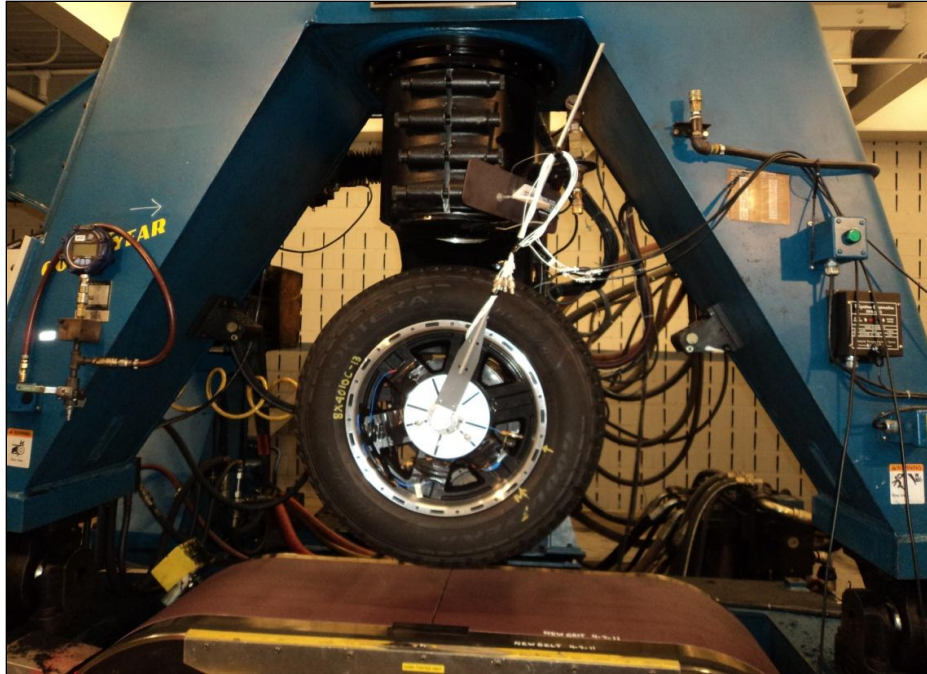


Fig. 2.8: Instrumented tire mounted on the Flat-Trac® machine

A test matrix was created that included the following information:

1. The speeds at which the tire would be run (10, 30, 45 and 65 mph)
2. The inflation pressures (28, 30, 32 and 35 psi)
3. The loads to which the tire is subjected (800, 1000, 1300, 1500 and 1800 lbs)
4. Slip angles (-8° to 8° sweep)
5. Camber angle (0° and $+2^{\circ}$)

2.3.2 Testing Using the In-House Mobile Tire Test Rig at the Intelligent Transportation Laboratory (ITL), Virginia Tech

Extensive outdoor testing of the instrumented tire was performed using the in-house mobile tire test trailer (TTT) (Fig. 2.9-Fig. 2.10). The in-house mobile tire test trailer gives us the capability to recreate real life driving conditions for the tire.

Portable Tire Test Rig



Test Rig Highlights

- 3-axis Force And Moment Hub
 - Max Vertical Load Capability Of 8000lbs
- Camber Sweep Of -16 to +16
- Slip Angle Sweep Of -30 to +30
 - High Speed Testing Capability (70 Mph)
- Onboard 500 Gallon Tank Provides Wet Testing Capabilities

Fig. 2.9: Data for the dynamic tests collected using the in-house mobile tire test rig at the Intelligent Transportation Laboratory (ITL), Virginia Tech

The objective of the trailer is to collect tire force and moment data for a variety of on and off-road surfaces. The TTT is a robust, standalone system capable of traversing smooth and rough surfaces under dry and wet conditions. The testing trailer was designed to test tires ranging from small passenger and motorcycle tires up to large semi-truck tires. The TTT is able to measure and control tire parameters including vertical load, slip angle and camber angle. These parameters can be adjusted to measure the tire's response to varying inputs and test conditions in order to quantify the performance of the tire.

(a)



(b)



Fig. 2.10: (a) Instrumented tire prototype mounted on the test trailer, and (b) equipment housed in a trailer attached to a tow vehicle

The tire was attached to a hub that had a wheel force transducer. The tire and hub assembly were loaded using an airspring filled with nitrogen gas. Fig. 2.11 shows how the airspring is mounted. Once the test assembly was lowered to the road surface using the screw actuator, the nitrogen tank forced nitrogen into the airspring until the desired vertical load was achieved.

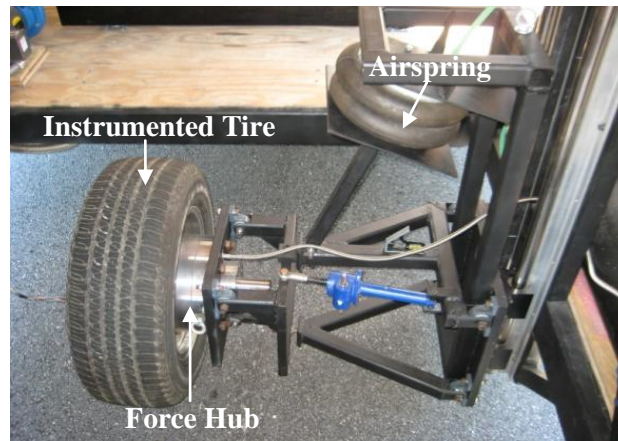


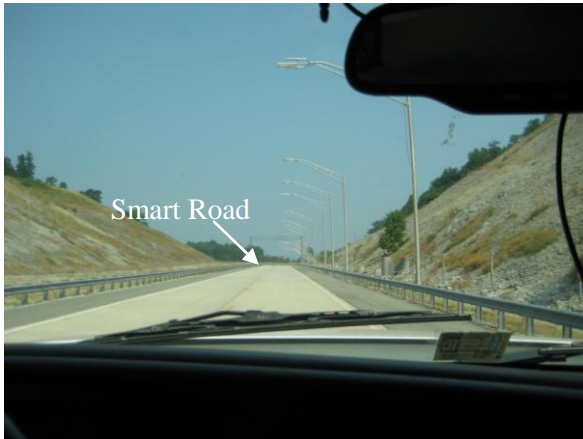
Fig. 2.11: Tire mounted on a force hub

Testing of the prototype tires with the mobile test trailer was carried out in three main locations (Fig. 2.12). The first tests were carried out at the Danville airport using prototype tires 1 and 2 at low speeds. The second tests were carried out at the Virginia Smart Road, VTTI in Blacksburg, Virginia using prototype tire 3. The most extensive testing was performed on US-58, Danville Expressway using prototype tire 3. The test matrices vary for each location tested, but all consist of speed, vertical load, tire pressure and surface type. Speed was varied between low speed and high speed, ranging from 15mph to 60mph in 15mph increments. Vertical loads of 800, 1000, 1300 and 1500lbs were tested at each speed. Tire pressure was varied between 26 psi and 40 psi in 4 psi increments. This complete test matrix was tested at two sampling rates, 2500Hz and 8000Hz, to record both the low frequency and high frequency response.

(a) Location: Danville Regional Airport



(b) Location: The Virginia Smart Road, VTTI,
Blacksburg



(c) Location: US-58, Danville Expressway



Fig. 2.12: Outdoor testing locations

2.4 Data Acquisition

Fig. 2.13 shows the data acquisition equipment housed inside the mobile tire test trailer.

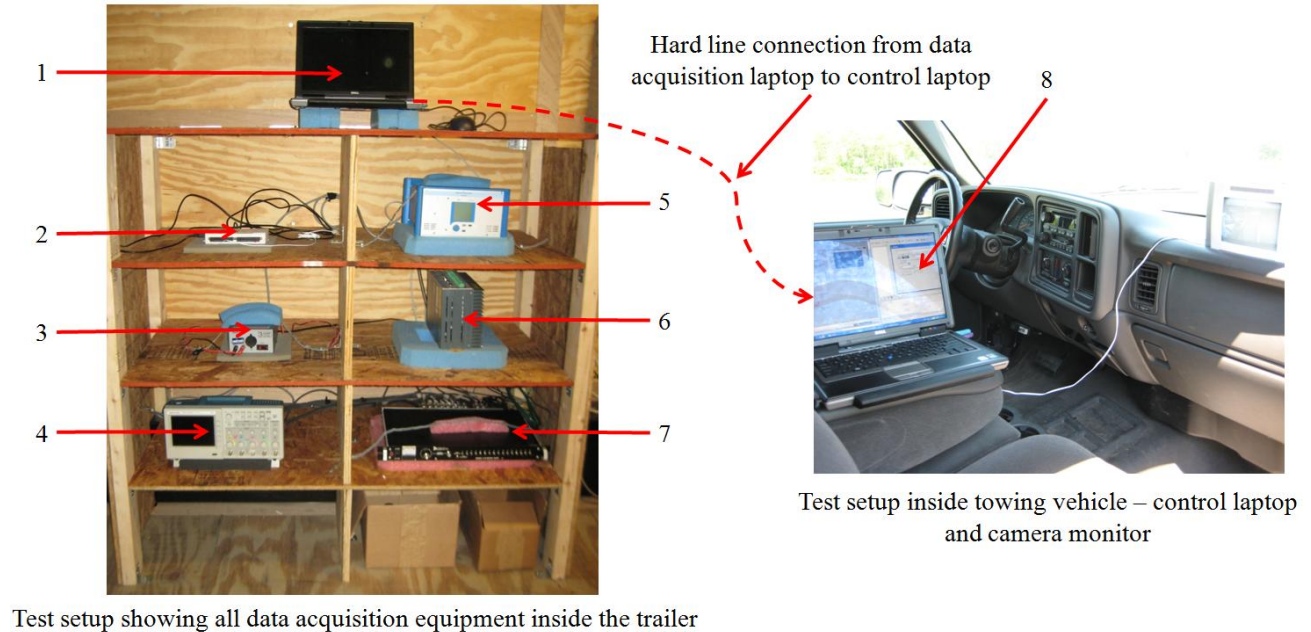


Fig. 2.13: Data acquisition equipment of the mobile test trailer

1. Laptop responsible for collecting and storing all data processed through LabView
2. National Instruments data acquisition board (NI USB 6212)
3. DC Voltage regulator to supply constant power to dSpace data acquisition unit
4. dSPACE Micro Auto Box data acquisition unit (DS 1401/1501)
5. Kistler power amplifier
6. Steering servo motor controller
7. 16-channel power source for the tire sensors (Dytran 4116)
8. Remote laptop for user control of data acquisition laptop and all control equipment

The tire sensor data acquisition equipment consisting of the power supply unit and the dSPACE data acquisition box collects and records the signal from the sensors mounted inside the tire (Fig. 2.14a). The Kistler hub is connected to a Kistler charge amplifier that outputs the signal to a National Instruments DAQ setup and transmits the data to a LabView VI (Fig. 2.14b).

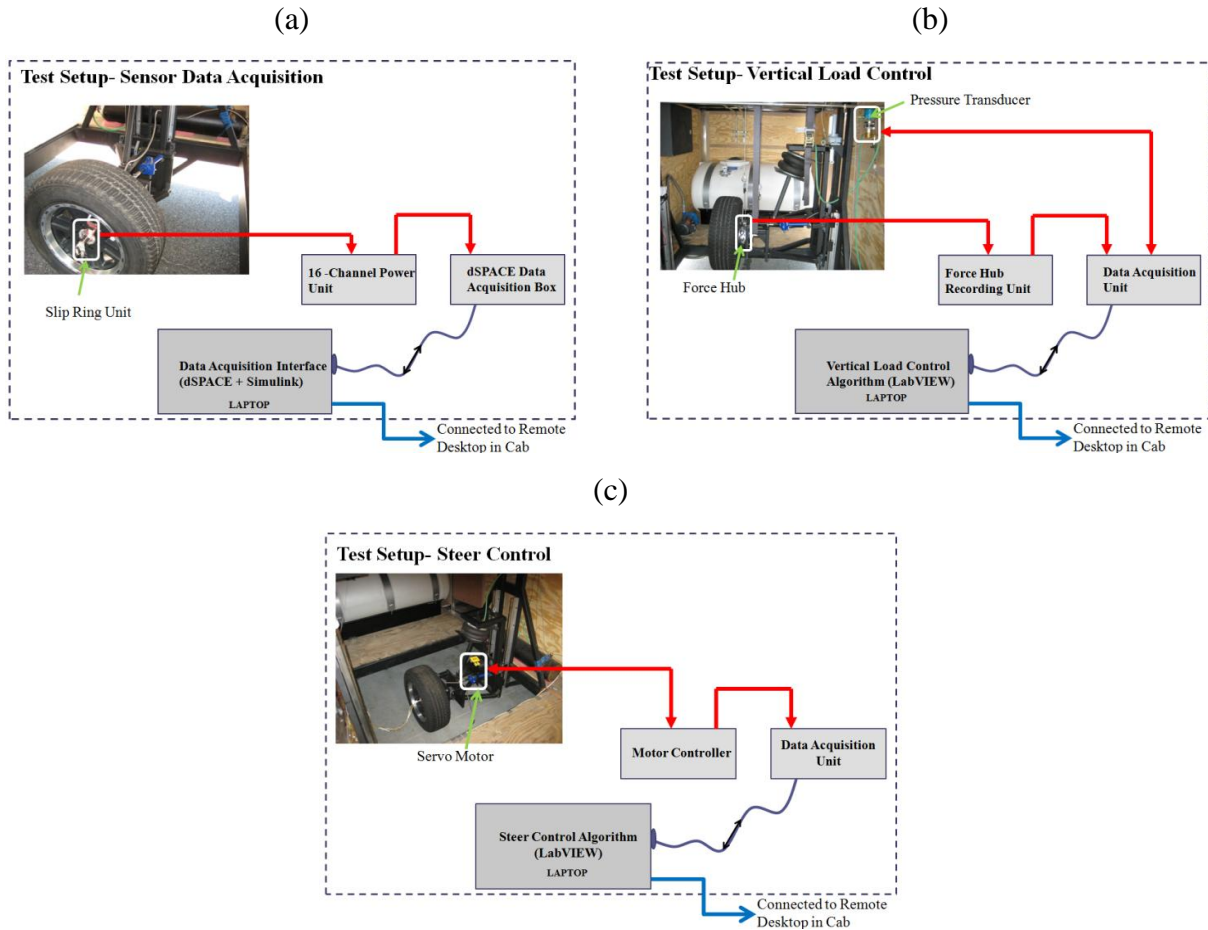


Fig. 2.14: (a) Tire sensor data acquisition setup, (b) tire vertical load control setup, and (c) tire steer control setup on the trailer

The servo controllers which are used to adjust the steer angle are connected to the National Instruments DAQ setup which transmits the data to a LabView VI (Fig. 2.14c). The control laptop is used to record the tire sensor signals and runs the LabView control program for vertical loading and steer control. The control laptop is accessed from the passenger cab of the truck using a remote VNC connection. This allows for the passenger to have complete control of the vertical loading, steer control and data acquisition from the cab of the tow vehicle. A remote monitor paired with a camera inside the test trailer allows the passenger to watch the tire during testing to ensure proper operation and control is achieved.

2.5 Measurements on the Tire

While the tire rotates, a region of the tire contacts with the road periodically. During this cyclic deformation, accelerations occur in three different directions, namely, circumferential, lateral and radial, due to rotation and deflection of the tire. Fig. 2.15 shows the acceleration profile for data collected from an accelerometer attached to the inner-liner of a tire.

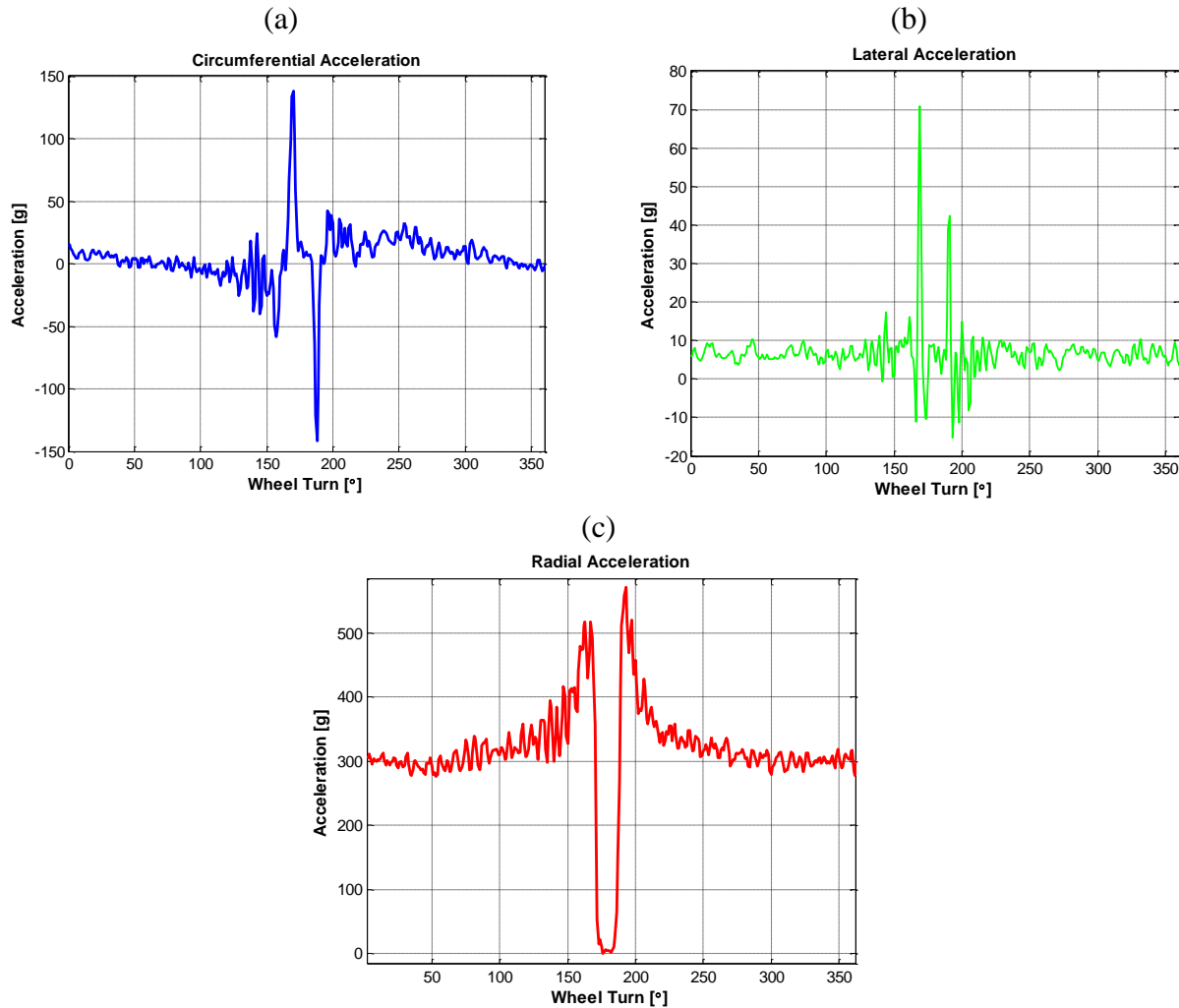


Fig. 2.15: Measured acceleration signal during straight track running conditions: (a) circumferential signal, (b) lateral signal, and (c) radial signal

The passage of the accelerometer in the contact patch is evidenced in the circumferential and the radial acceleration signals. As far as the circumferential acceleration is concerned, the entering and the exiting from the contact patch are highlighted by peaks having opposite signs, while the

radial acceleration shows values close to zero when the sensor is passing over the contact footprint.

As stated before, the underlying objective of this study is to develop an intelligent tire system capable of providing in real-time information about the forces at tire-road interface and the tire - road friction coefficient. Direct measurement/estimation of tire-road contact forces using the accelerometer signals may pose some challenges due to the complex nonlinear behavior of a tire. Instead, the approach adopted in this study is to measure/estimate the variables required to characterize the force generation capabilities of tire. A classical tire model characterizes forces as a function of four key variables: tire load, slip ratio, slip angle, and friction coefficient (Fig. 2.16).

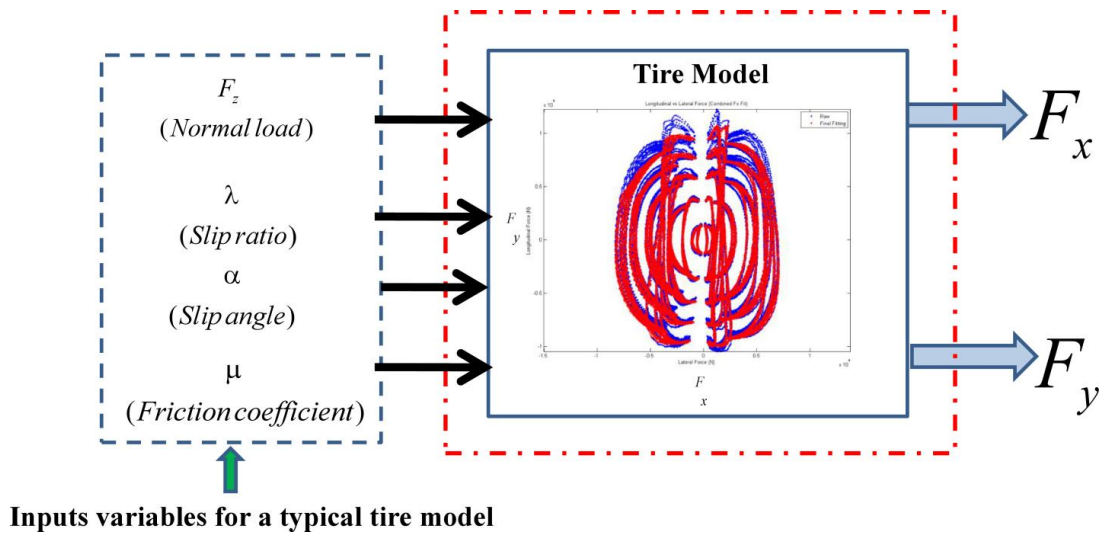


Fig. 2.16: Input variables for the tire model

Even though an estimate of these variables of interest can be made using on-board sensors and observers (Fig. 2.17) available in some modern vehicles, uncertainties of each of the sensors and state observers used in the estimation of these variables reduces the accuracy and reliability of the tire force estimates. Hence, the goal is to develop a system capable of providing robust and prompt information about these variables of interest, by eliminating uncertainty-adding procedures, inherent in most indirect estimation techniques.

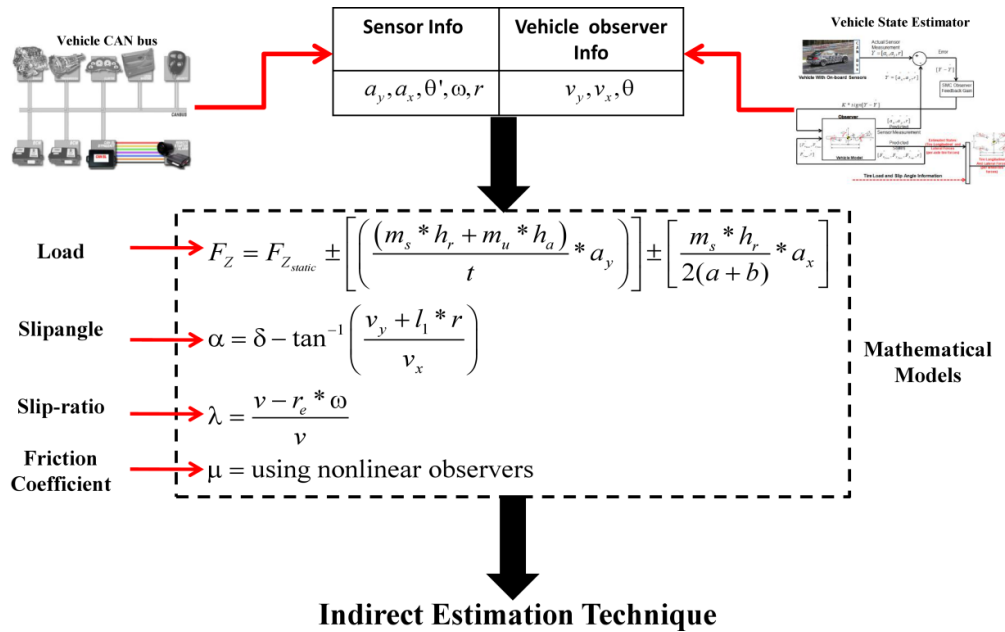


Fig. 2.17: Estimation of variables of interest (tire load, slip ratio, slip angle, and friction coefficient) made using on-board sensors and state observers

The following sections elaborate on the details of the signal processing algorithms (Fig. 2.18) developed to estimate previously identified variables from accelerometric signals coming from a tire attached sensor unit.

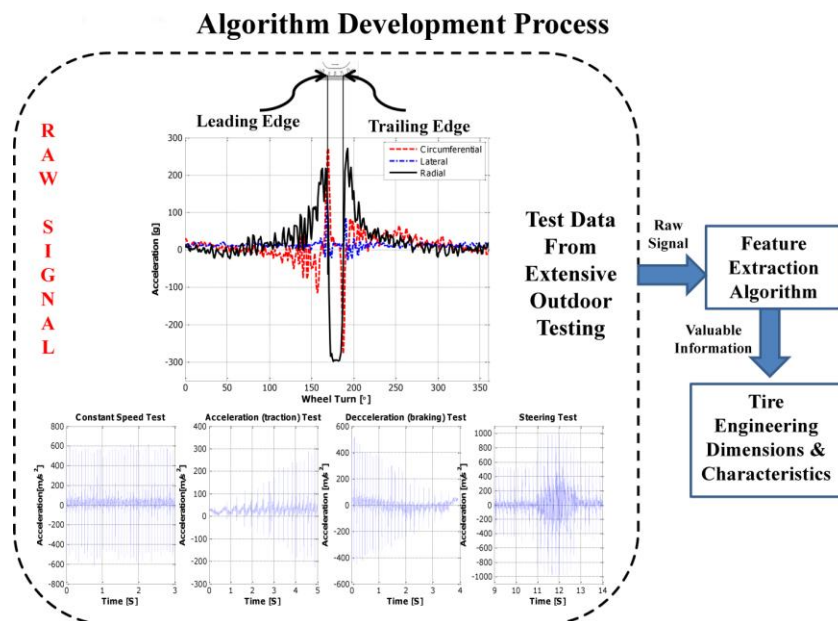


Fig. 2.18: Algorithm development process

2.6 Tire Load Estimation Algorithm

Although vibrations in the circumferential direction are possible alternatives, those in radial direction were preferred in our study for the development of a tire load estimation algorithm. A magnified view of the radial acceleration for one tire revolution is shown Fig. 2.19. As a point on a tire moves around, it is subject to an almost constant centrifugal acceleration due to the tire rotation. This is seen as the more or less horizontal line. When that point on the tire comes into contact with the ground, the centrifugal acceleration goes to zero for the short time that the point is translating along the surface of the ground. This happens after an initial increase in the acceleration levels due to deformation to which the tire is subjected during passage from a circumferential to a flat configuration, at the beginning of the contact region between the tire and the ground. A further increase in the acceleration levels are encountered when the tire exits from the contact region.

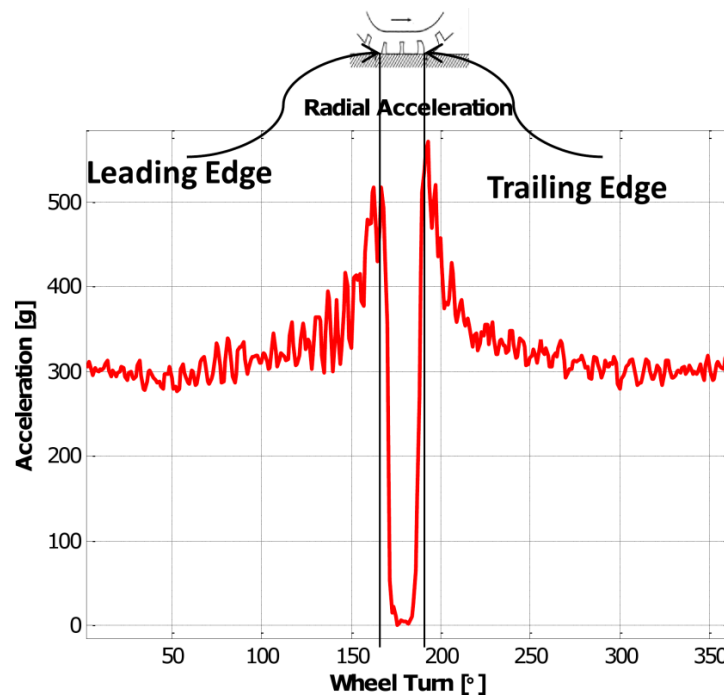


Fig. 2.19: Magnified view of the radial acceleration signal for one cycle of rotation

A plot of the typical time series data of the radial acceleration signal collected for a tire under a range of different rolling speed conditions is presented in Fig. 2.20.

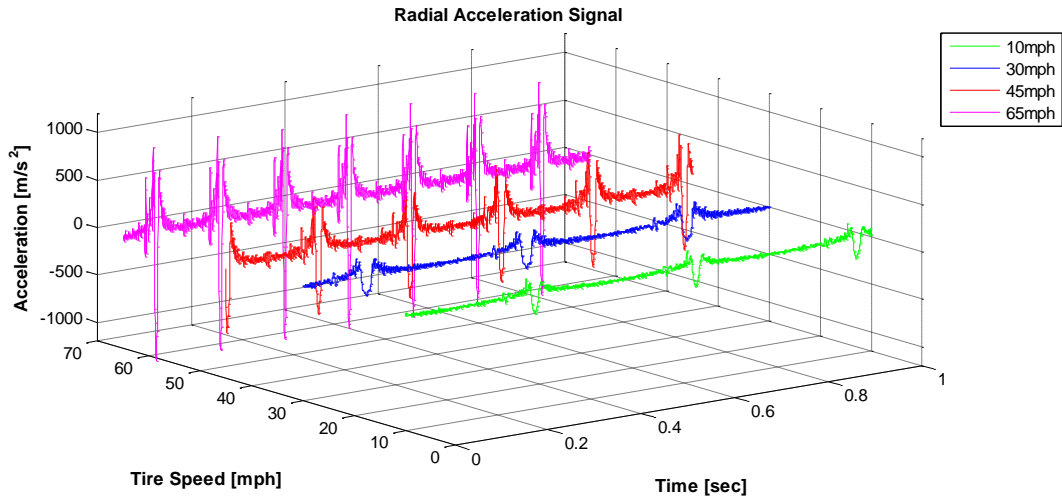


Fig. 2.20: Cascade diagram showing the time series data for the tire radial acceleration at different rolling speeds

By analyzing the FFT of the test data (Fig. 2.21), the fundamental frequencies at different translational speeds of a tire were identified.

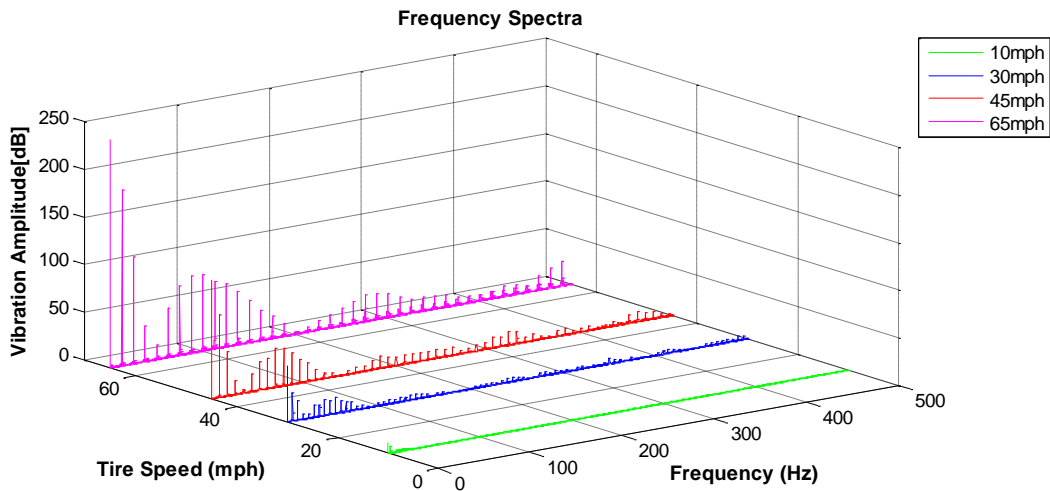


Fig. 2.21: Cascade diagram showing the dependency of the tire vibration spectra on the rolling speed

To better understand the effect of changes in working conditions of the tire on the radial acceleration signal, one would need to study the influence of the following parameters on the radial acceleration signal:

- Rolling speed
- Inflation pressure
- Load
- Camber angle
- Slip angle
- Road surface condition (dry, wet etc)
- Slippage
- Type and structure of the tire
- Tire wear

A detailed parametric sensitivity analysis was carried out using the exhaustive indoor and outdoor tire sensor data sets. In this study, it is assumed that the tire does not change during the tests. Thus, the influence of the type and structure of the tire are neglected. Also, the influence of tire wear on the measured accelerations has been neglected at the present stage of the research, but it is clear that further investigations are necessary. The influence of all other parameters, have been taken into account. From the measured acceleration time histories, a number of synthetic parameters have been extracted. The synthetic parameters can be subdivided into two different families: frequency domain parameters and time domain parameters.

Frequency domain parameter(s) analyzed:

- a) **Power Spectrum (PSD) of the Signal:** The power spectrum of each accelerometer signal from these tests was computed using Welch's averaged modified periodogram method for spectral estimation. The signal was divided into windows of length 256 and windowed using a hamming window with 50% overlap.

Time domain parameter(s) analyzed:

- a) **Signal power (estimated for a single cycle of rotation of the tire):** The magnitude of the radial acceleration signal is characterized by estimating the signal power (absolute amplitude of the signal) on a per revolution basis (Fig. 2.22).

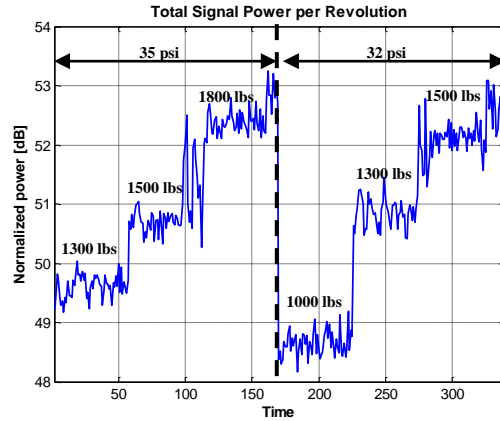


Fig. 2.22: Radial acceleration signal power on a per revolution basis

- b) **Contact patch length (estimated for a single cycle of rotation of the tire):** The tire-road contact patch length can be calculated as the product of the time spent by the accelerometer inside the patch and the speed of the vehicle.

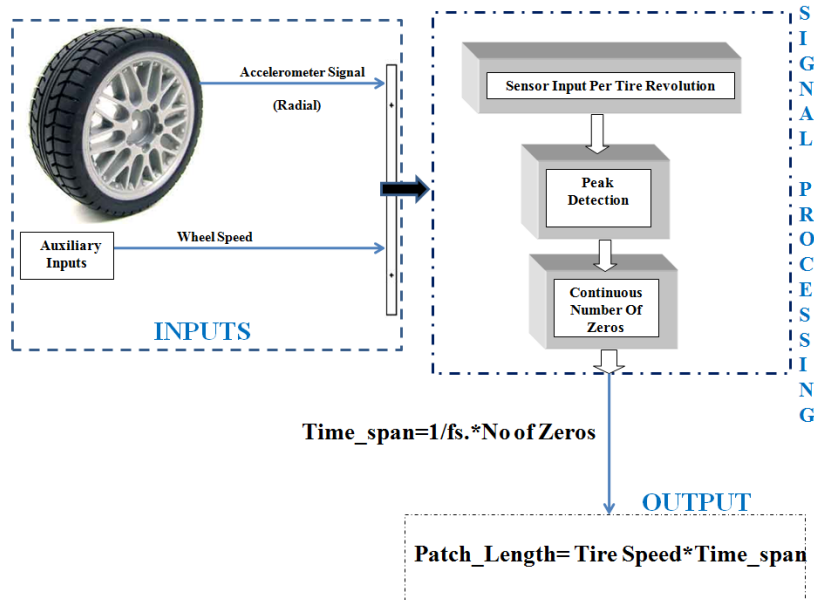


Fig. 2.23: Flowchart for the contact patch length estimation algorithm

The time spent inside the patch is estimated by counting the continuous number of zeros in the accelerometer signal on a per revolution basis (Fig. 2.23-Fig. 2.24). The zeros correspond to the pure linear motion of the sensor without any radial movement, as one expects the sensor to undergo in the flat contact patch region.

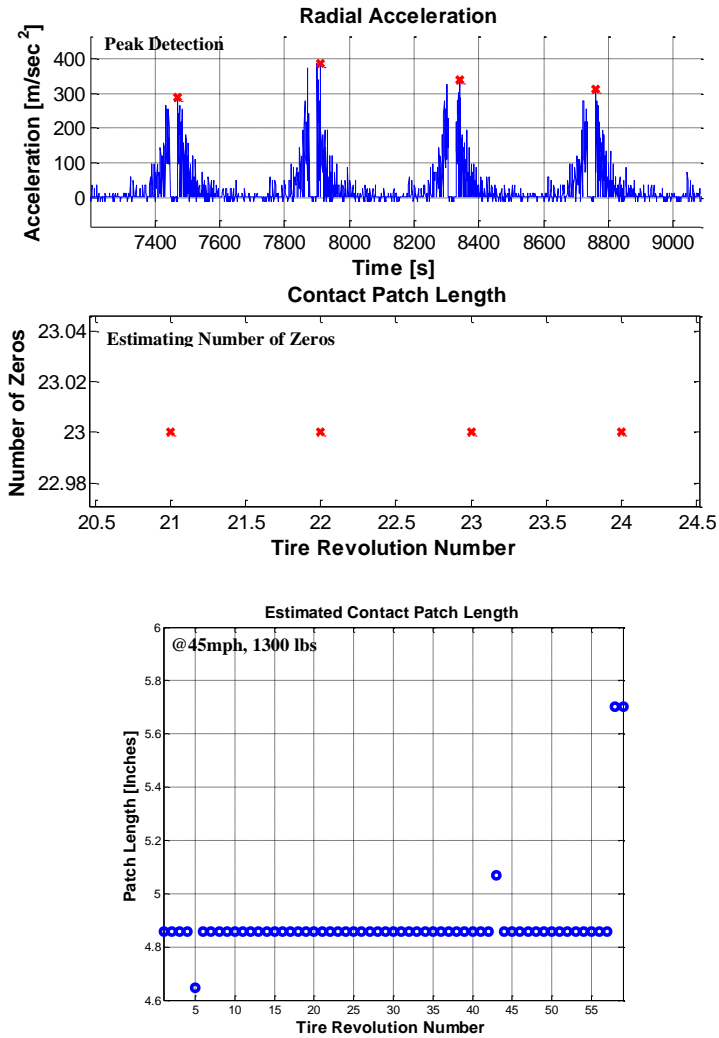


Fig. 2.24: Patch length estimation algorithm

2.6.1 Results for the Parameter Sensitivity Analysis

a) Effect of rolling speed

Speed	Load	Pressure	Camber Angle	Slip Angle	Road Surface Condition
Varying	1800 lbs	35 psi	0°	0°	Flat -Trac®

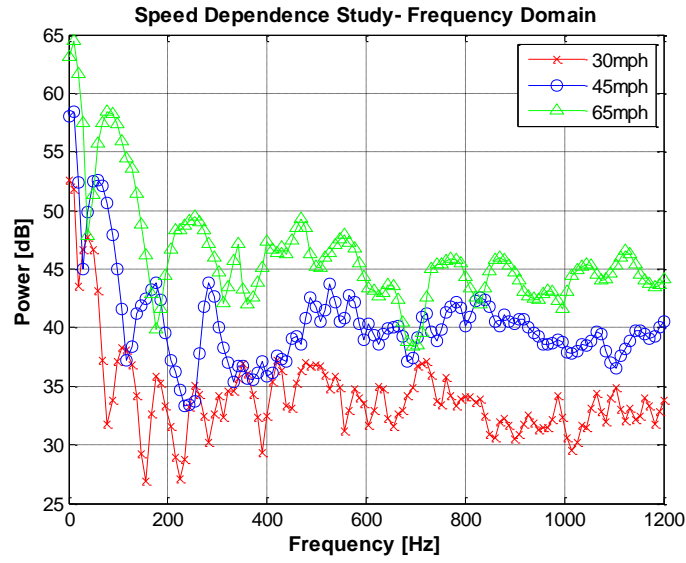


Fig. 2.25: Rolling speed dependence study- Frequency domain

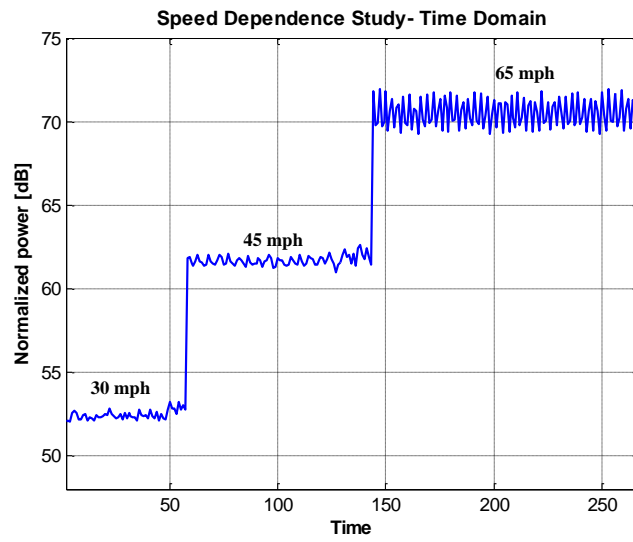


Fig. 2.26: Rolling speed dependence study- Time Domain

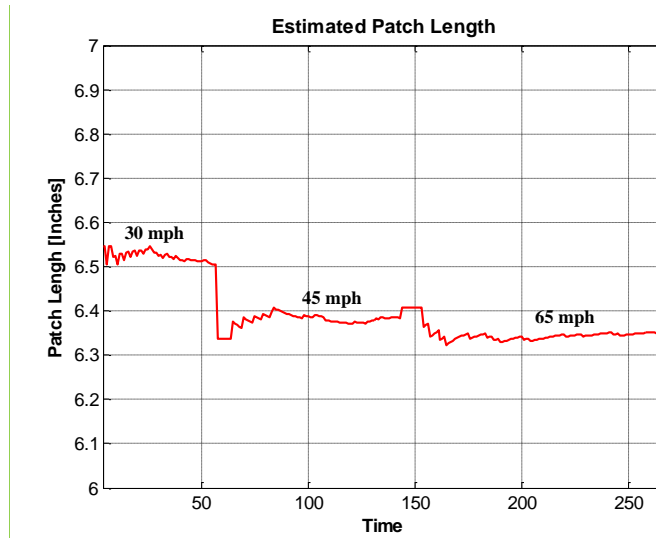


Fig. 2.27: Rolling speed dependence study- Patch length

Analyzing the dynamic test results, it was concluded that, a shift in the spectrum to higher frequencies was noticed with an increase in the tire speed (Fig. 2.25). Also, increasing the tire translational speed resulted in higher vibration levels (Fig. 2.26). With an increase in the rolling speed, the centrifugal forces increase. This is equivalent to a stiffer tire. Thus, the contact area dimensions decrease (Fig. 2.27).

Parameter sensitivity analysis summary: Effect of rolling speed

S. No	Parameter Under Study	Frequency Domain	Time Domain	
		Variation in Frequency Spectra	Variation in Signal Power	Variation in Contact Patch Length
1	Rolling Speed	Significant	Significant	Significant

b) Effect of inflation pressure

Speed	Load	Pressure	Camber Angle	Slip Angle	Road Surface Condition
Constant	1800 lbs	Varying	0°	0°	Flat –Trac®

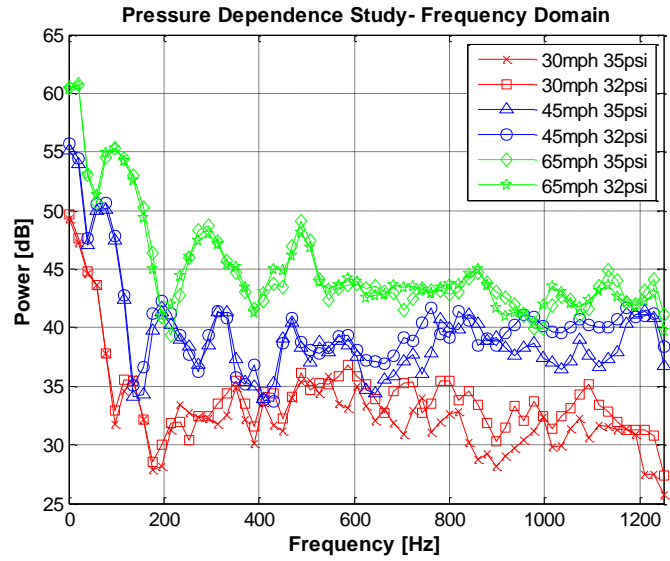


Fig. 2.28: Pressure dependence study- Frequency domain

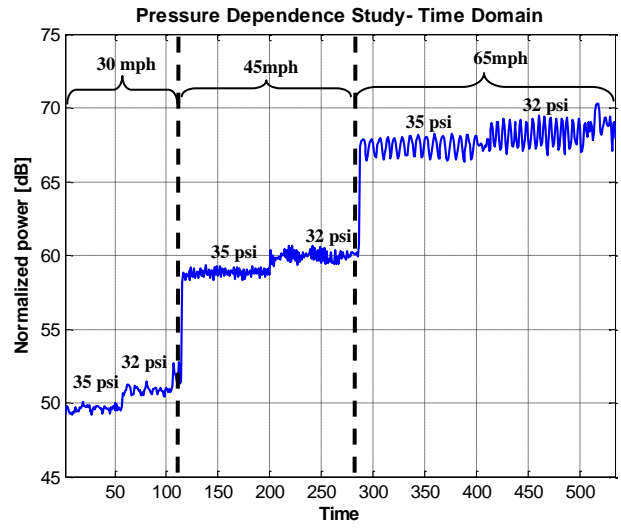


Fig. 2.29: Pressure dependence study- Time Domain

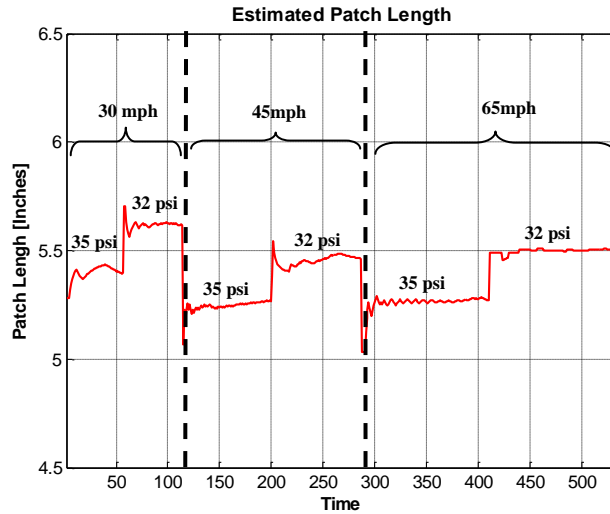


Fig. 2.30: Pressure dependence study- Patch length

The fundamental frequencies show close to negligible dependence on varying tire inflation pressure conditions (Fig. 2.28). The signal power changes significantly with a variation in inflation pressure (Fig. 2.29). Also, changing inflation pressure modifies the contact area dimensions: a higher inflation pressure means a smaller contact area (Fig. 2.30).

Parameter sensitivity analysis summary: Effect of inflation pressure

S. No	Parameter Under Study	Frequency Domain	Time Domain	
		Variation in Frequency Spectra	Variation in Signal Power	Variation in Contact Patch Length
2	Inflation Pressure	Negligible	Significant	Significant

c) Effect of load

Speed	Load	Pressure	Camber Angle	Slip Angle	Road Surface Condition
45 mph	Varying	35 psi	0°	0°	Flat –Trac®

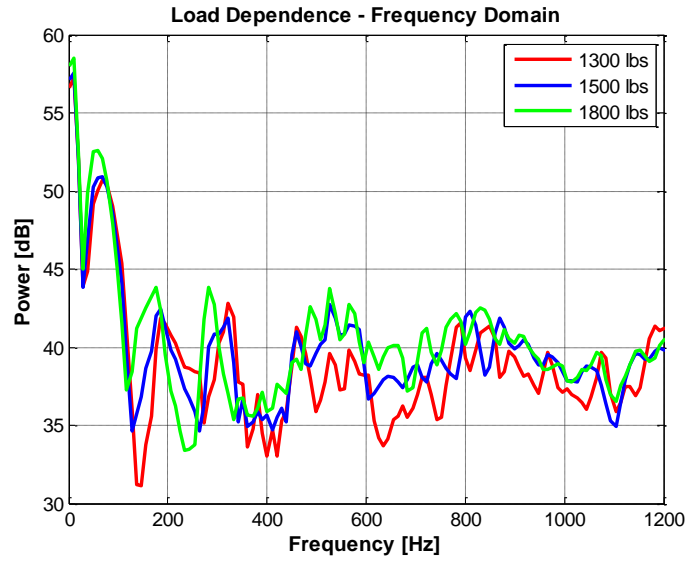


Fig. 2.31: Load dependence study- Frequency domain

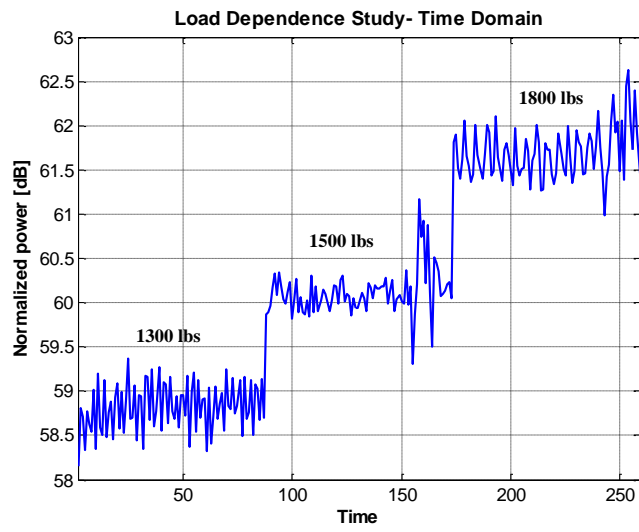


Fig. 2.32: Load dependence study- Time domain

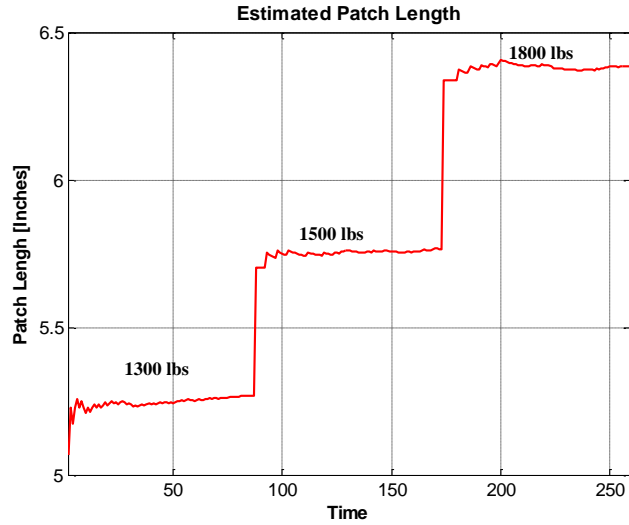


Fig. 2.33: Load dependence study- Patch length

The fundamental frequencies show marginal dependence on varying normal load conditions (Fig. 2.31). The vibration level changes significantly with varying load conditions (Fig. 2.32). Also, changing tire load modifies the contact area dimensions: a higher load means a larger contact area (Fig. 2.33).

Parameter sensitivity analysis summary: Effect of load

S. No	Parameter Under Study	Frequency Domain	Time Domain	
		Variation in Frequency Spectra	Variation in Signal Power	Variation in Contact Patch Length
3	Load	Marginal	Significant	Significant

d) Effect of camber angle

Speed	Load	Pressure	Camber Angle	Slip Angle	Road Surface Condition
Constant	Constant	Constant	2°	0°	Flat –Trac®

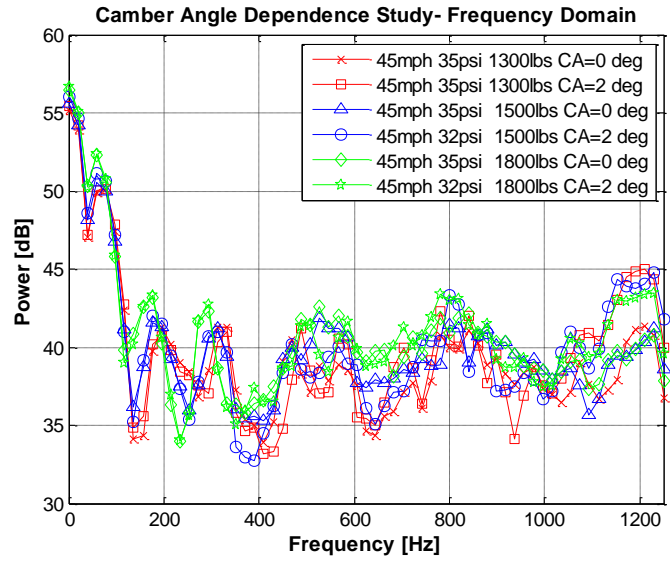


Fig. 2.34: Camber angle dependence study- Frequency domain

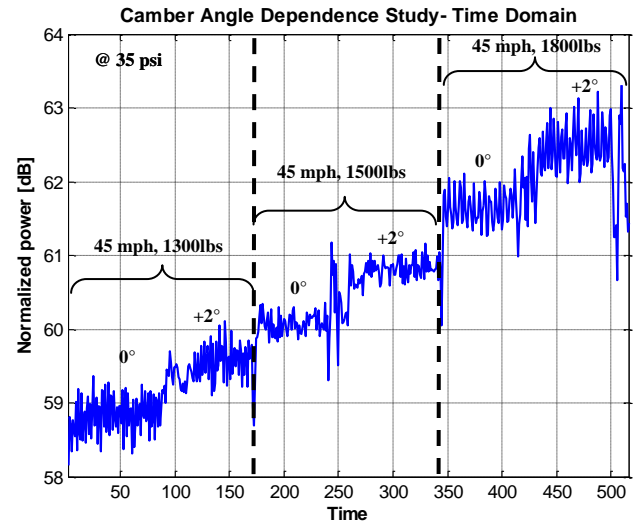


Fig. 2.35: Camber angle dependence study- Time Domain

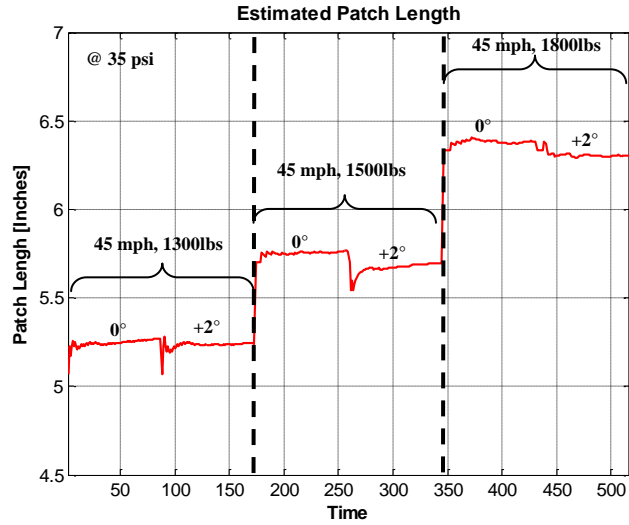


Fig. 2.36: Camber angle dependence study- Patch length

A change in the tire camber angle was found to only marginally affect the signal power magnitude (Fig. 2.35) and the contact patch length (Fig. 2.36).

Parameter sensitivity analysis summary: Effect of camber angle

S. No	Parameter Under Study	Frequency Domain	Time Domain	
		Variation in Frequency Spectra	Variation in Signal Power	Variation in Contact Patch Length
4	Camber Angle	Negligible	Marginal	Marginal

e) Effect of slip angle

Speed	Load	Pressure	Camber Angle	Slip Angle	Road Surface Condition
Constant	≈ Constant	35 psi	0°	Varying	Flat –Trac®

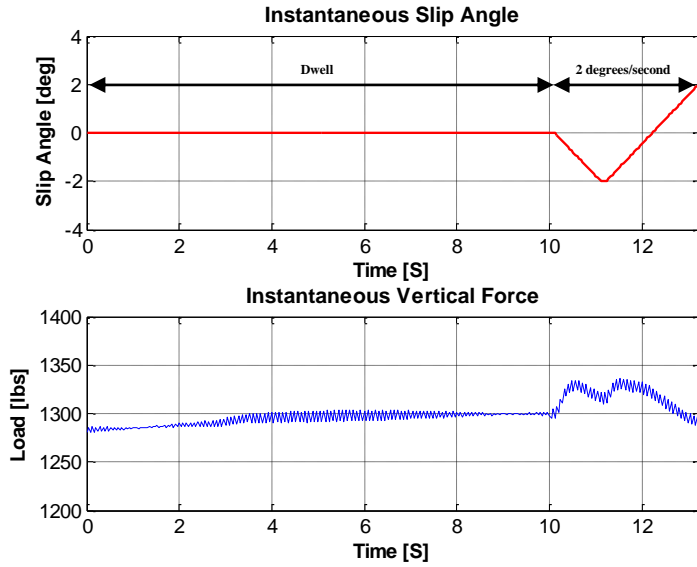


Fig. 2.37: Instantaneous slipangle and vertical load during the test

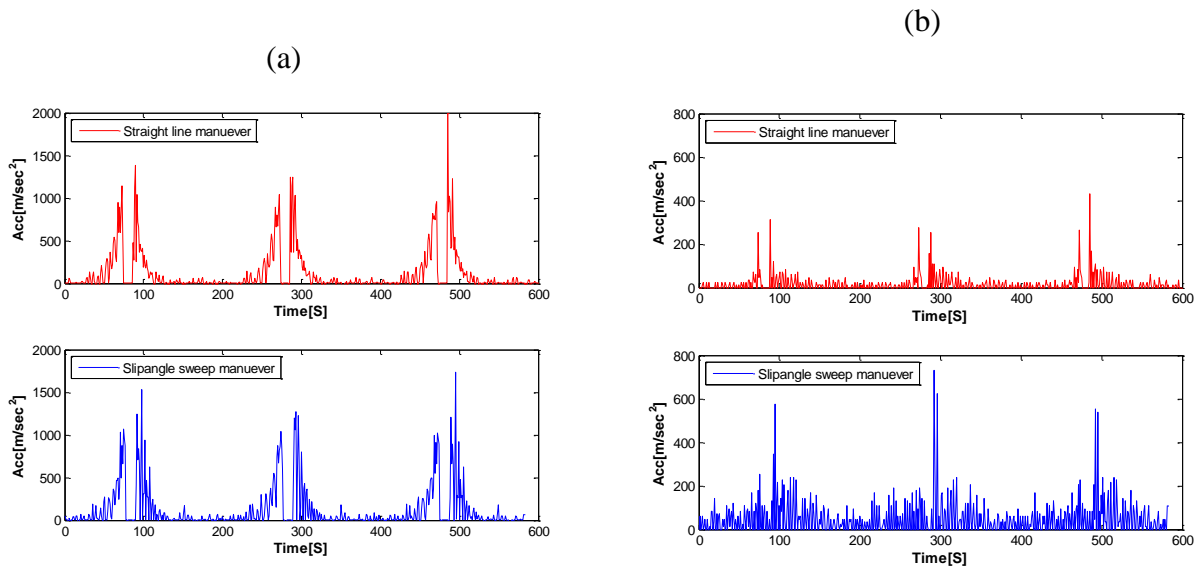


Fig. 2.38: Effect of slipangle maneuver on: (a) the radial acceleration signal, and (b) the lateral acceleration signal

The test involved a straight line run for 10 seconds and then a sweep maneuver in which the tire is moved from side to side up to slip angles of 2 degrees on either side of the straight line (Fig. 2.37). The effect of a slip angle maneuver on the time series data for the tire radial and lateral acceleration is shown in Fig. 2.38. A magnified view of the radial and lateral acceleration for one tire revolution is shown in Fig. 2.39.

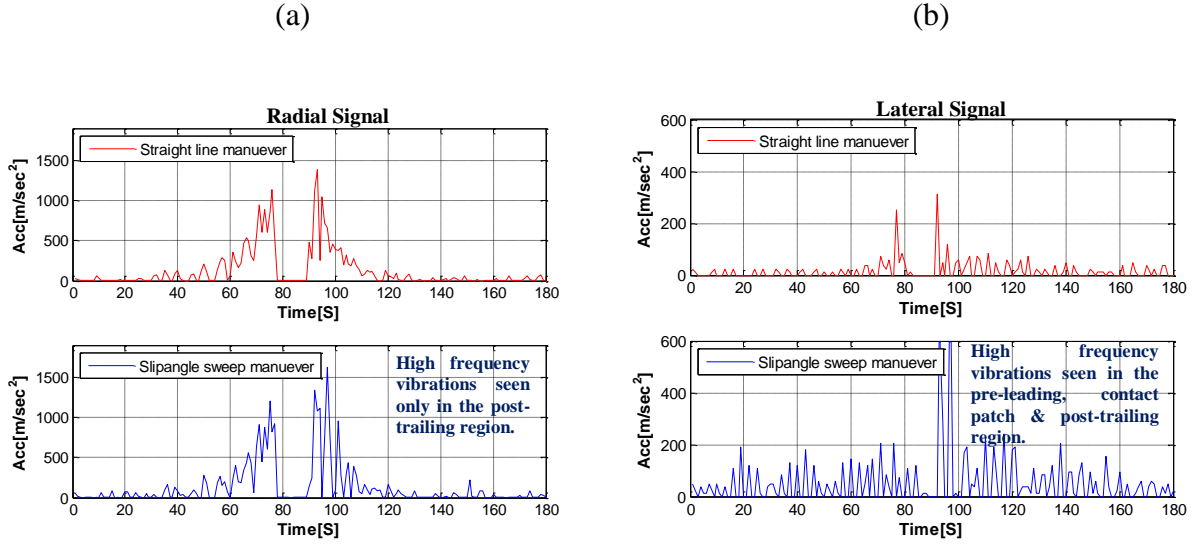


Fig. 2.39: Effect of slipangle maneuver on: (a) the radial acceleration signal; (b) the lateral acceleration signal for one tire revolution

High frequency vibrations were seen only in the post-trailing region of the radial acceleration signal (Fig. 2.39a). In the case of lateral acceleration signal, high frequency vibrations were seen in all the regions (i.e. in the pre-leading, contact patch and post-trailing region) (Fig. 2.39b). This observation was validated by analyzing the acceleration signal at different scales or resolutions using a discrete wavelet transform. Wavelets are a family of basis functions whose time–frequency scale is not the same in the entire time–frequency domain. Thus wavelets possess multiscale character and this property makes them capable of producing timescale (frequency) information as opposed to Fourier analysis which provides only frequency information. A Haar wavelet function was chosen for this analysis. Since the sensor data points were recorded at an interval of 0.0004 seconds, the highest frequency detectable was 1250 cycle/sec. Since a typical discrete wavelet transform (DWT) is computed on a dyadic grid, the number of data points is half at each lower octave band. As a result, maximum level of decomposition (M) of the acceleration signal with N number of samples (data points) can be calculated from $2^M \leq N$. The profile data used for this study comprised of sensor data points for one tire revolution (180 data points for the case under study as shown in Fig. 2.39). As a result, maximum level of decomposition for such signal is $M = 7$. Hence the signal has been expressed as the sum of the seven frequency sub-band signals (Fig. 2.40).

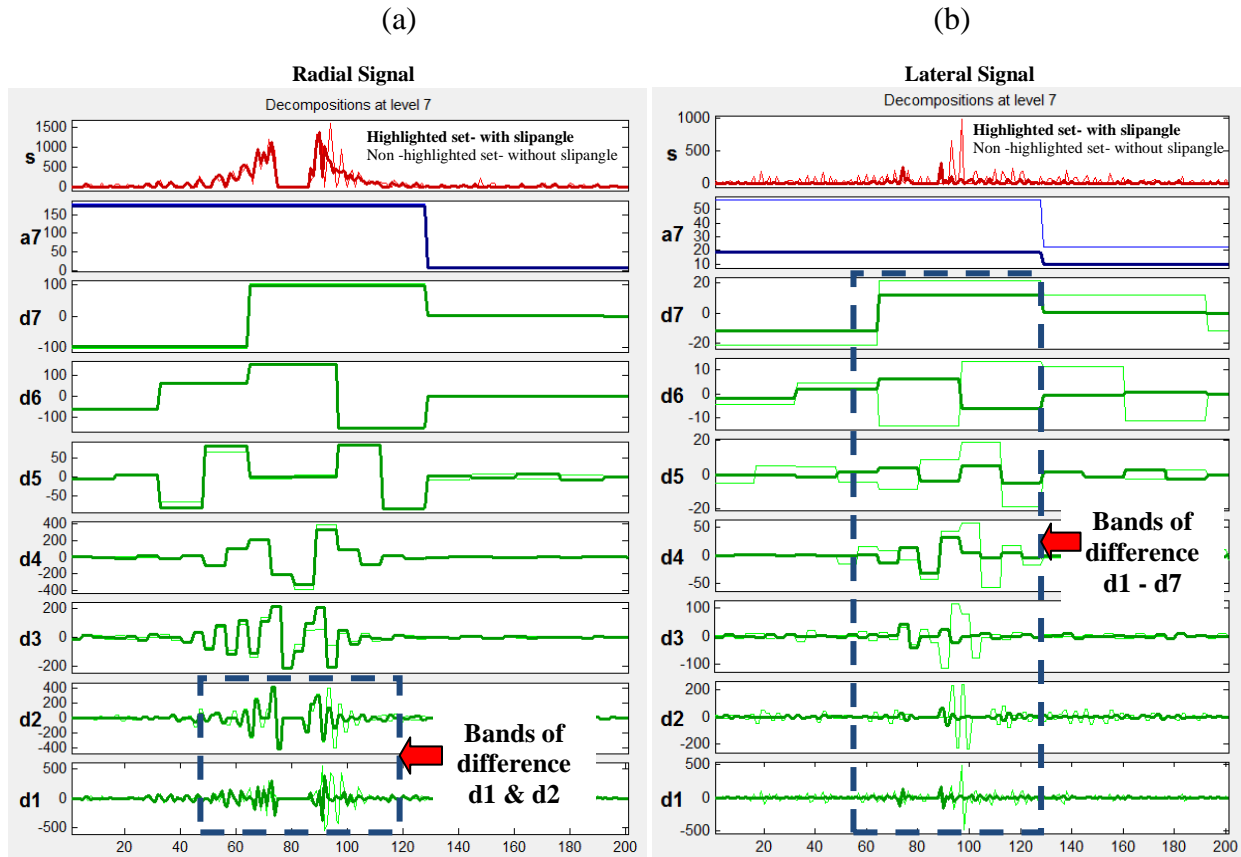


Fig. 2.40: Wavelet transform decomposition: (a) the radial signal, and (b) the lateral signal

The unfiltered profile (s) is shown at the top of the figure. The last remaining low-frequency component of the profile a7 and the successive higher-frequency components, namely d7, d6, . . . , d1, are also presented. The physical frequency bandwidth (Hz) corresponding to all components are given in Table 2.5.

Table 2.5: Frequency (Hz) bandwidth of decomposed components

Frequency Bandwidth of Wave Transform Decomposed Components	
Component	Frequency Bandwidth (Hz)
sa7	0-9.7
d7	9.7-19.7
d6	19.5-39.0
d5	39.0-78.1
d4	78.1-156.2
d3	156.2-312.5
d2	312.5-625
d1	625-1250

In the case of the radial acceleration signal, a difference in the signal components was seen in the subbands d1 and d2 (Fig. 2.40a), which represent the high frequency bands. In the case of the lateral acceleration signal, one could see a stark difference in the signal components of the tire signal collected during straight line tests and the tire signal collected while the tire was undergoing a slipangle sweep maneuver in almost all the subbands, d1-d7 (Fig. 2.40a).

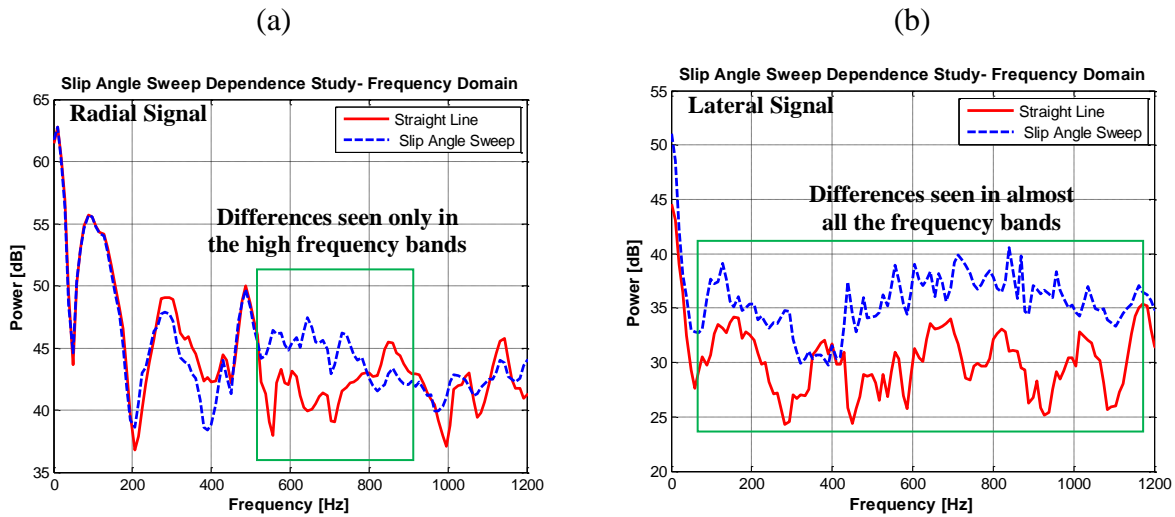


Fig. 2.41: Effect of slipangle maneuver on (a) the radial acceleration signal; (b) the lateral acceleration signal- Frequency domain

These results also explain the difference seen in FFT of the radial acceleration signal and the lateral acceleration signal for the two cases (Fig. 2.41).

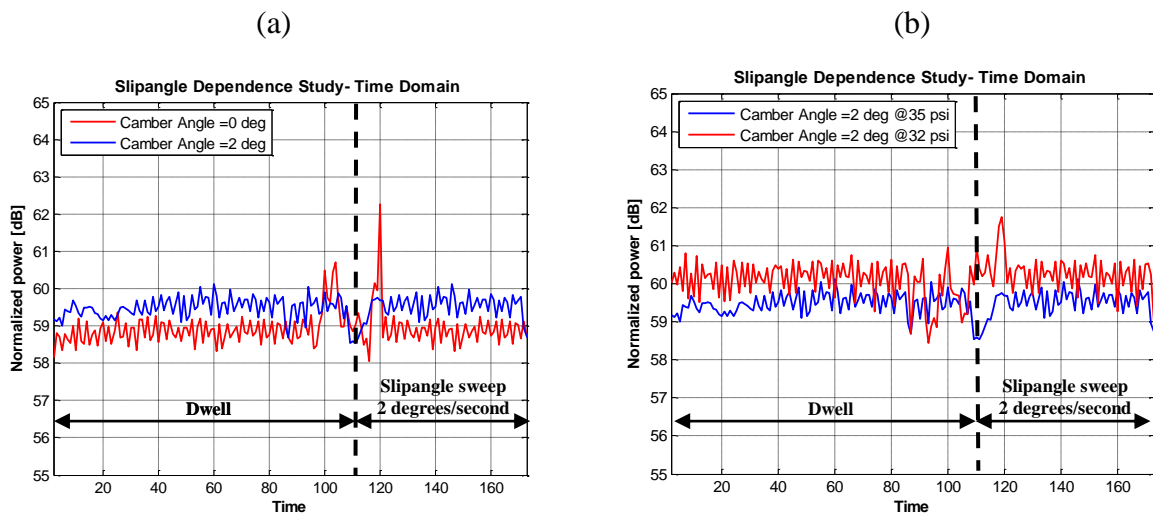


Fig. 2.42: Slipangle dependence study- Time domain

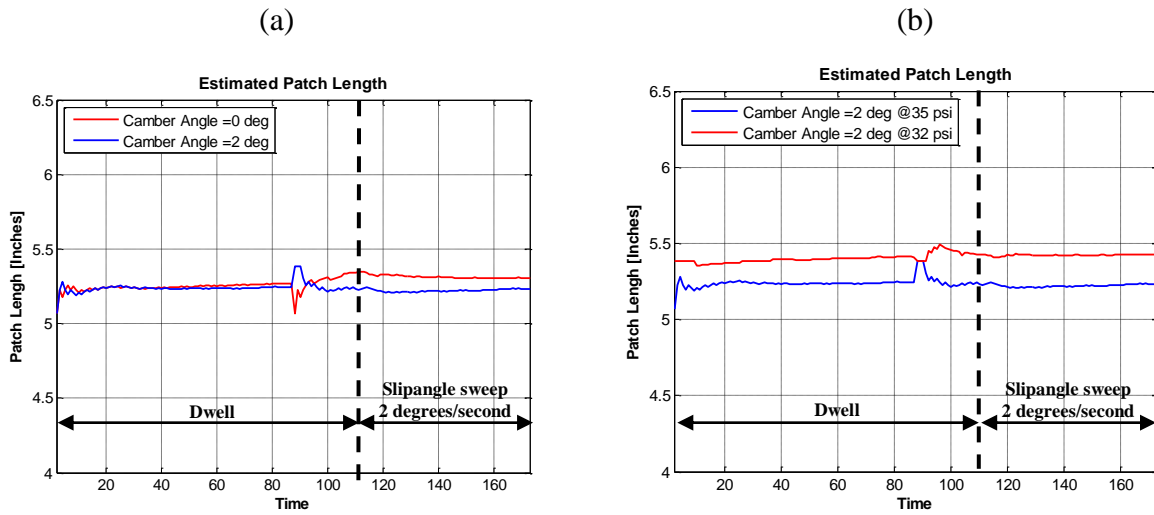


Fig. 2.43: Slipangle dependence study- Patch length

A change in the tire slipangle was found to only marginally affect the signal power magnitude (Fig. 2.42) and the centerline contact patch length (Fig. 2.43).

Parameter sensitivity analysis summary: Effect of slip angle

S. No	Parameter Under Study	Frequency Domain	Time Domain	
		Variation in Frequency Spectra	Variation in Signal Power	Variation in Contact Patch Length
5	Slip Angle	Marginal	Marginal	Marginal

f) Effect of road surface condition

Speed	Load	Pressure	Camber Angle	Slip Angle	Road Surface Condition
45 mph	1500 lbs	35 psi	0°	0°	Varying

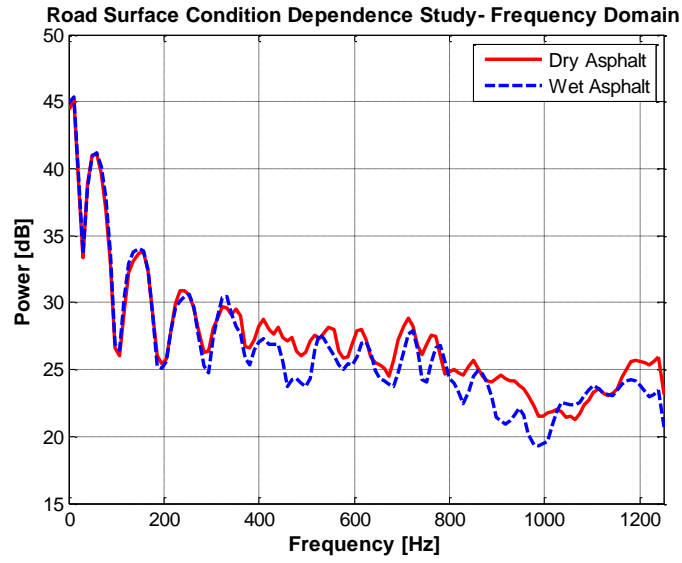


Fig. 2.44: Road surface condition dependence study- Frequency domain

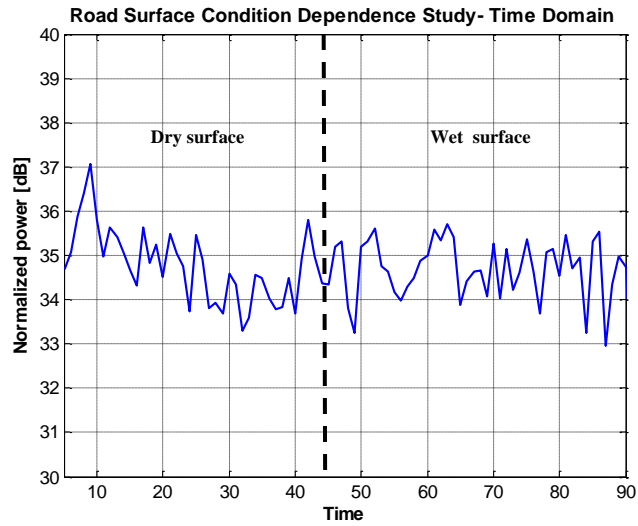


Fig. 2.45: Road surface condition dependence study- Time domain

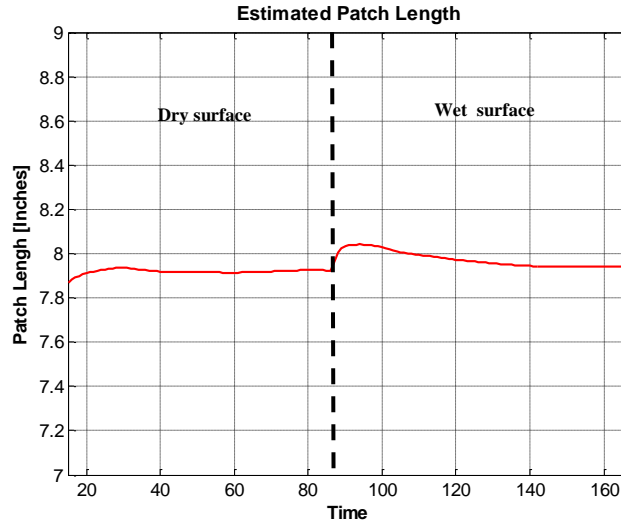


Fig. 2.46: Road surface condition dependence study- Time domain

A change in the road surface condition was found to have a negligible effect on the signal PSD (Fig. 2.44), the signal power magnitude (Fig. 2.45) and the contact patch length (Fig. 2.46).

Parameter sensitivity analysis summary: Effect of road surface condition

S. No	Parameter Under Study	Frequency Domain	Time Domain	
		Variation in Frequency Spectra	Variation in Signal Power	Variation in Contact Patch Length
6	Road Surface condition	Negligible	Negligible	Negligible

2.6.2 Summary of Parameter Sensitivity Analysis

Table 2.6: Results for the parameter sensitivity analysis

S. No	Parameter Under Study	Frequency Domain	Time Domain	
		Variation in Frequency Spectra	Variation in Signal Power	Variation in Contact Patch Length
1	Rolling Speed	Significant	Significant	Significant
2	Inflation Pressure	Negligible	Significant	Significant
3	Load	Marginal	Significant	Significant
4	Camber Angle	Negligible	Marginal	Marginal
5	Slip Angle	Marginal	Marginal	Marginal
6	Road Surface	Negligible	Negligible	Negligible

For developing a load estimation algorithm, we especially were interested in determining synthetic parameters that were sensitive only to normal load. The two parameters identified were: (a) the contact patch length (CPL) and (b) the signal power (Table 2.6). So one could possibly characterize the instantaneous tire normal load as a function of the CPL and signal power.

$$Tire_{load} \propto [Contact\ patch\ length, Signal\ power]$$

This doesn't present to us a realistic approach, keeping in mind the strong interdependence between other tire operating parameters (e.g. rolling speed, inflation pressure, slippage, slipangle, road surface condition) and the synthetic parameters (contact patch length and signal power) being used to characterize the normal load. Hence one needs to account for this interdependence. Based on the results obtained from the sensitivity analysis presented in the last section, it was concluded that, the synthetic parameters - contact patch length and signal power, were not dependent on the tire slipangle, camber angle and the road surface conditions for a centerline mounted accelerometer. However, a strong dependence of both these parameters was seen on the tire rolling speed and inflation pressure. Hence, one would need to take into account the effect of rolling speed and inflation pressure while estimating these parameters. Consequently, the modified tire normal load estimation algorithm would not only need information about the two synthetic parameters identified, i.e. contact patch length and signal power, but also would need information about the tire rolling speed, inflation pressure.

$$Tire_{load} \propto [Contact\ patch\ length, Signal\ power, Rolling\ speed, Inflation\ pressure]$$

Shown in Fig. 2.47 is a flowchart for the proposed tire normal load estimation algorithm.

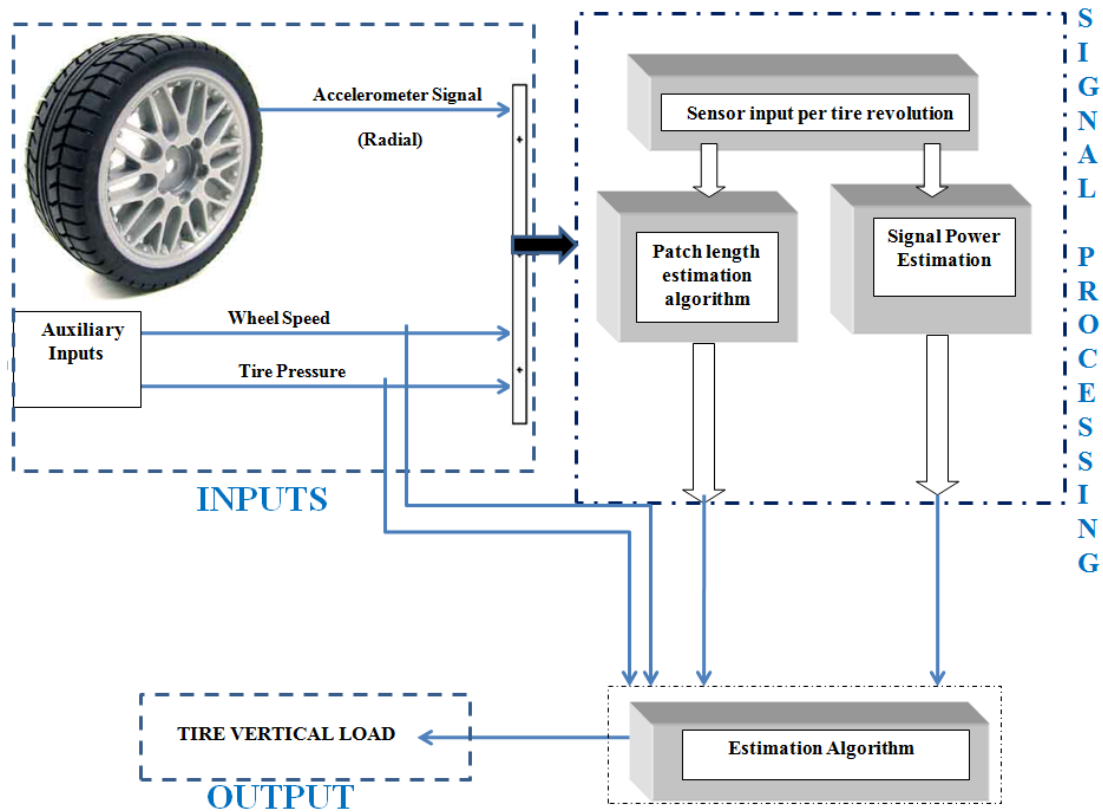
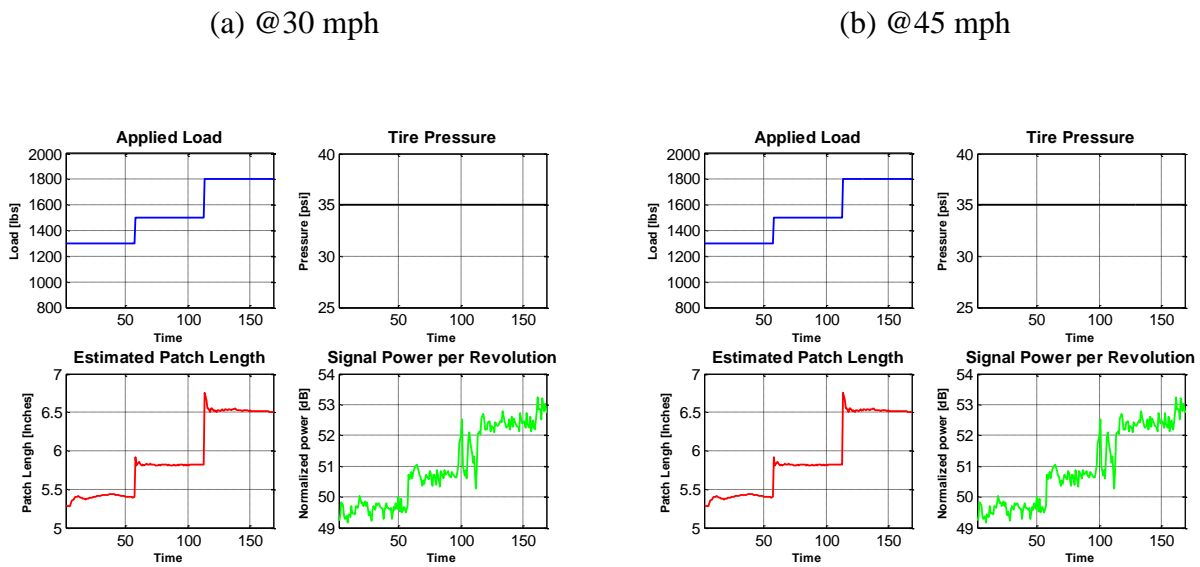


Fig. 2.47: Flowchart for the proposed tire normal load estimation algorithm

Having identified parameters that were sensitive to the tire normal load, the next task was to establish a relationship between these system inputs/parameters (rolling speed, inflation pressure, contact patch length and signal power) and the system output (tire normal load). To achieve the aforementioned objective, this study explored the possibility of using an artificial neural network (ANN) based estimation algorithm. Artificial Neural Networks is a class of flexible nonlinear models that can discover patterns adaptively from the data. A neural network is a form of artificial intelligence that imitates some function of the human brain and can be used as a computing tool that can solve complex non-linear problems. The network comprises a large number of simple processing elements linked to each other by weighted connections according to a specified architecture. These networks learn from the training data by adjusting the connection weights. ANN requires only a set of experimental results, numerical in nature and describes the relation by analyzing them. In other words, it only needs solution examples concerning the problem. Rather than determine an optimum neural network structure for this specific problem,

the scope of this work was to design a network capable of estimating the tire load for all possible tire operating conditions.

Typically, most modeling/classification algorithms like an ANN based approach works well if the input parameters don't have any overlapping/smooth boundaries. Analyzing the experimental data sets for a range of different tire operating conditions (Fig. 2.48), certain overlapping boundaries were noticed for the input parameter – signal power per revolution, especially at higher tire rolling speeds (Fig. 2.48c).



(c) @65 mph

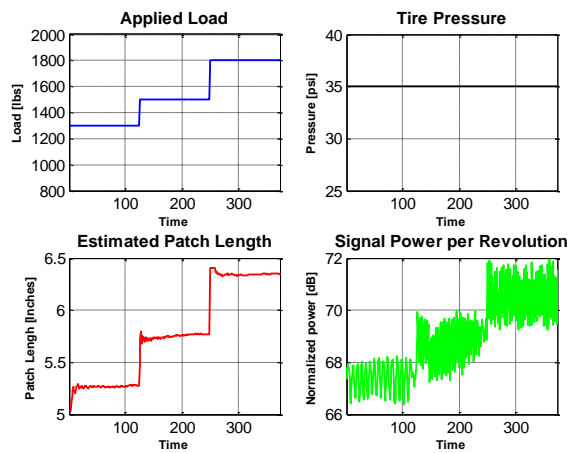


Fig. 2.48: Experimental data set

For the low speed tests (10-50 mph) (Fig. 2.48a), the signal power estimates were seen to correlate to the applied vertical load with distinct boundaries demarcating the change in the instantaneous load. For the high speed tests (>50 mph) (Fig. 2.48c), certain overlapping boundaries were noticed, which did not present an ideal scenario for a classification algorithm. To resolve this issue, the effect of change in normal load on the frequency domain of the radial acceleration signal was analyzed (Fig. 2.49). The sole purpose of this analysis was to try and analyze the regions showing maximum difference in the PSD with changing normal load conditions on the tire. For each tire speed, a ‘range of maximum difference’ was identified. The raw radial accelerometer signal was filtered using a band pass filter, with the filter range being same as the range identified in the aforementioned analysis and being changed adaptively as function of the tire speed.

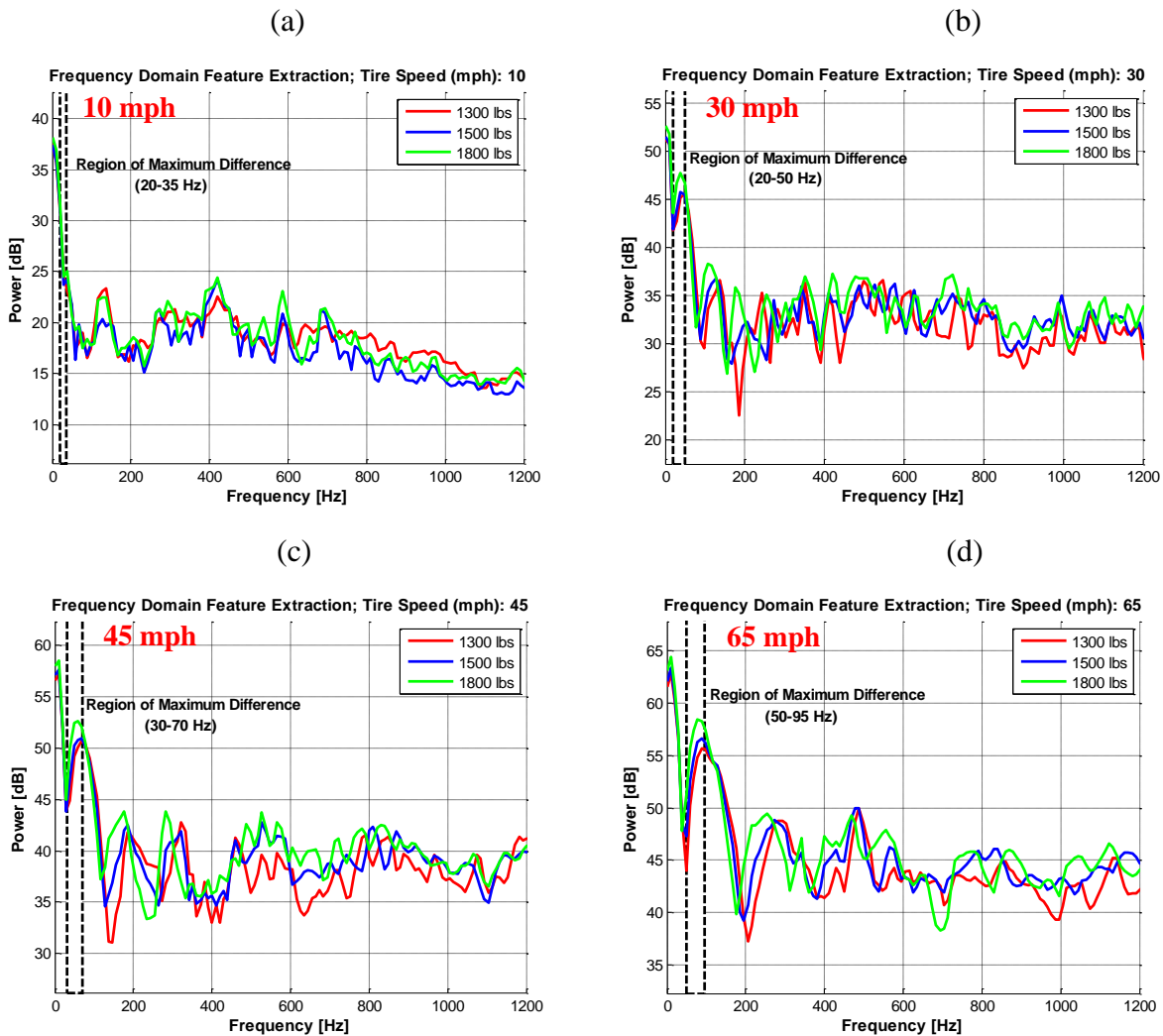


Fig. 2.49: Identifying regions of maximum difference in the frequency domain

Using this filtered signal, the signal power of this domain extracted signal was estimated on a per revolution basis (Fig. 2.50).

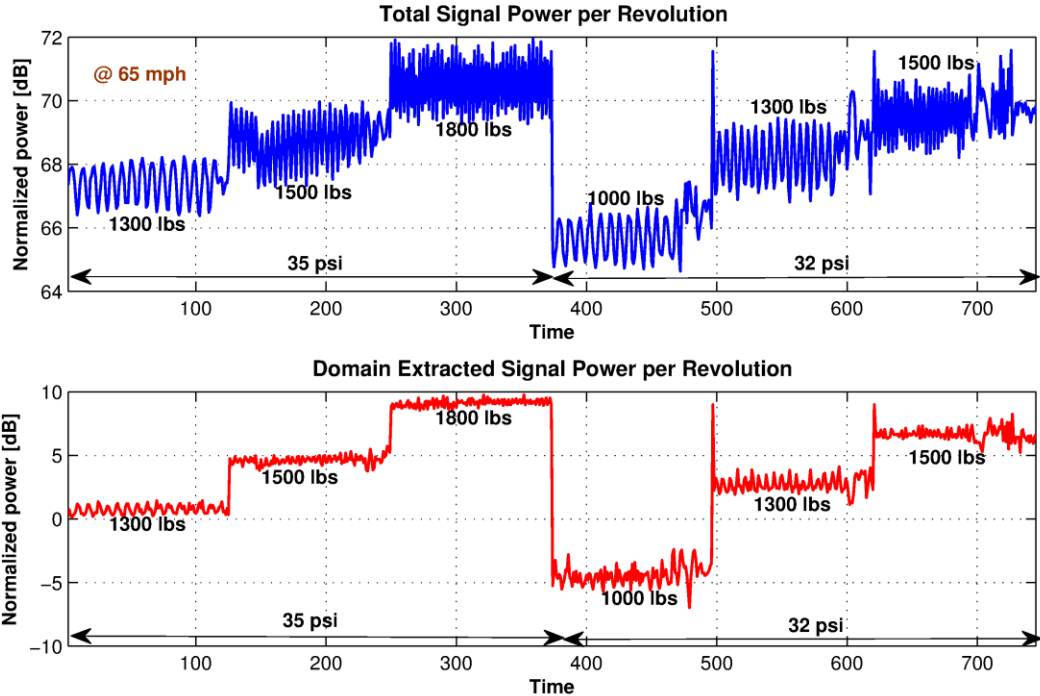


Fig. 2.50: Domain extracted signal power

Distinct boundaries demarcating the change in the instantaneous vertical load were noticed even for the high speed tests (Fig. 2.50). Hence the proposed tire normal load estimation algorithm as shown in Fig. 2.47 was modified by incorporating a domain extraction block, which was used to estimate the domain based signal power for the radial acceleration signal, as shown in Fig. 2.51.

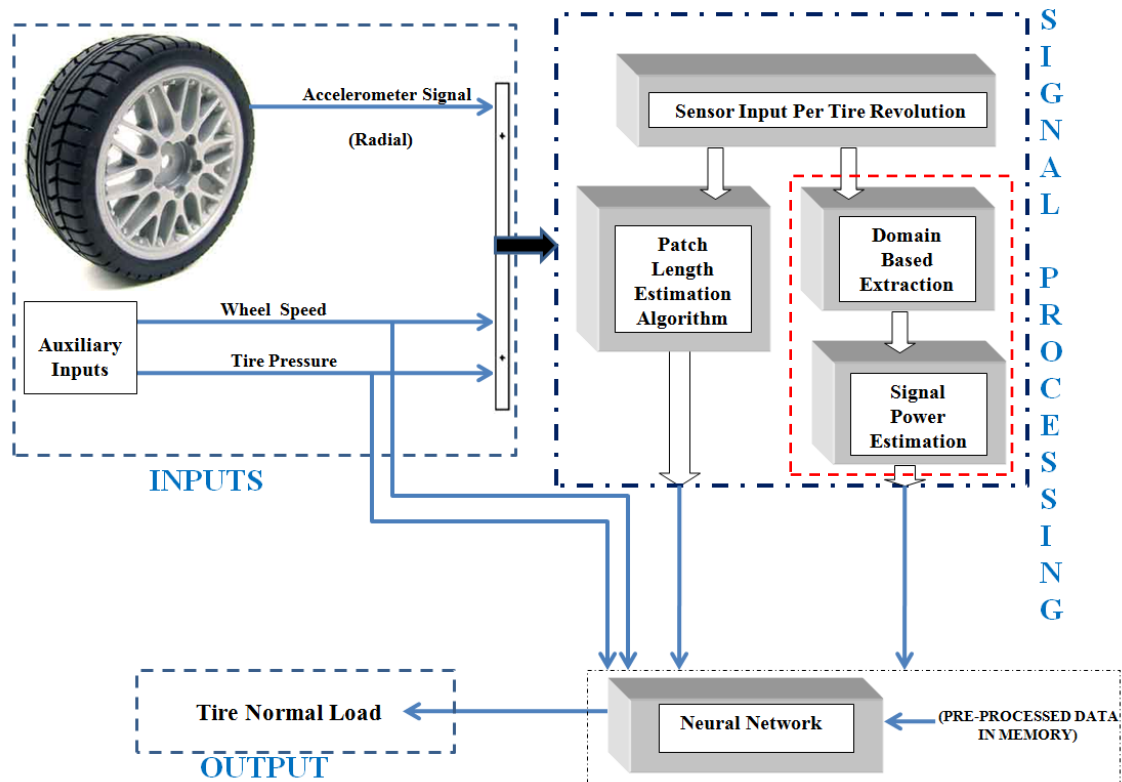


Fig. 2.51: Flowchart for the tire normal load estimation algorithm

Details regarding the architecture of the proposed neural network are given in the next section.

2.6.3 Algorithm Development

The goal is to develop an explicit ANN based formulation to estimate the tire normal load in terms of tire rolling speed, inflation pressure, contact patch length and signal power. Both indoor and outdoor tire tests were performed to obtain training and testing data sets for the neural network.

A neural network can be thought to be as a massively parallel distributed processor which resembles the human brain in two respects: the knowledge is acquired by the network through a learning process, and inter-neuron connection strengths known as synaptic weights are used to store the knowledge. Neural network operates like a “black box” model, and does not require detailed information about the system. Instead, it learns the relationship between the input parameters and the controlled and uncontrolled variables by studying previously recorded data,

in a similar way that a non-linear regression might be performed. Another advantage of using ANNs is their ability to handle large and complex systems with many interrelated parameters.

Neural network is composed of large numbers of highly interconnected processing elements known as neurons. The basic elements of an artificial neuron are shown in Fig. 2.52. Artificial neuron consists of weight, bias and activation function mainly. Each neuron receives inputs x_1, x_2, \dots, x_n , attached with a weight w_{ji} which shows the connection strength for a particular input (x_i) for each connection. Every input is then multiplied by the corresponding weight of the neuron connection. A bias b_j can be defined as a type of connection weight with a constant nonzero value added to the summation of inputs and corresponding weights u_j , given as follows:

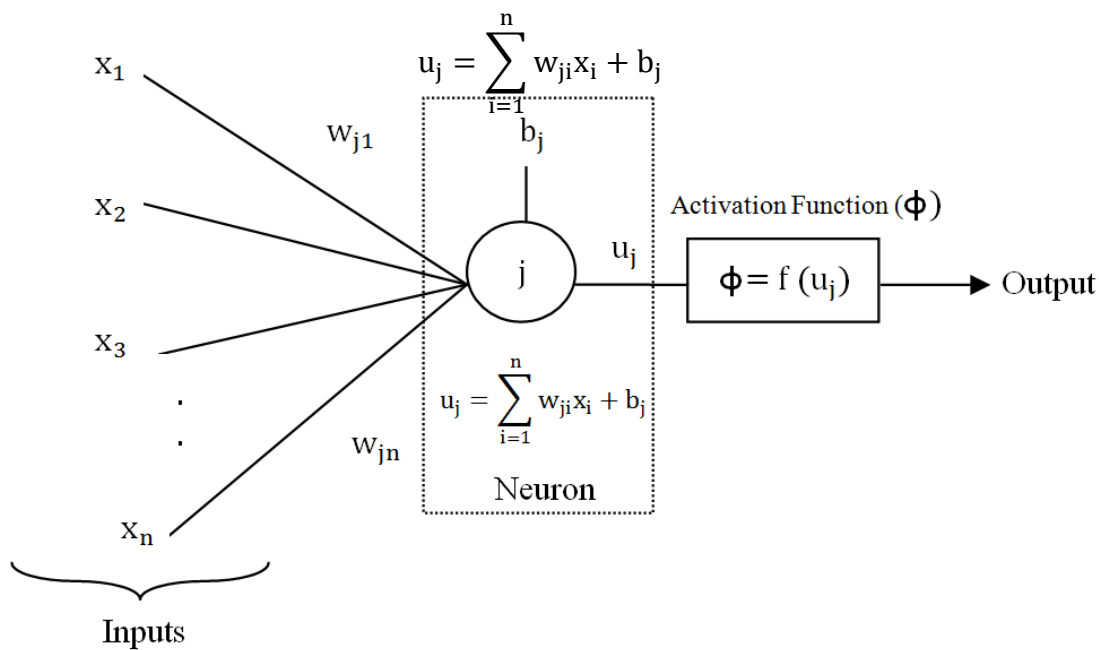


Fig. 2.52: Neuron model with n inputs

The summation u_j is transferred using a scalar-to-scalar function called an “activation or transfer function”, $f(u_j)$, to yield a value called the unit’s “activation”, given as:

$$y_j = f(u_j) \tag{2.1}$$

Activation functions serve to introduce nonlinearity into neural networks which makes it more powerful than linear transformation. The training of the network is accomplished by adjusting the weights and is carried out through a large number of training sets and training cycles (epochs). The goal of the learning procedure is to find the optimal set of weights, which in the ideal case would produce the right output for any input. The output of the network is compared with a desired response to produce an error. Once the ANN is adequately trained, it can generalize to similar cases, which it has never seen.

Choosing an appropriate architecture of ANN is dependent on the type of system being modeled. In this work, the MATLAB software was used to model the intended ANN. Rolling speed, inflation pressure, contact patch length and signal power have been used as input layer components, while the normal load was used as output layer component of the ANN (Fig. 2.53). One of the most important tasks in ANN studies is to determine the optimal network architecture which is related to the number of hidden layers and neurons in it.

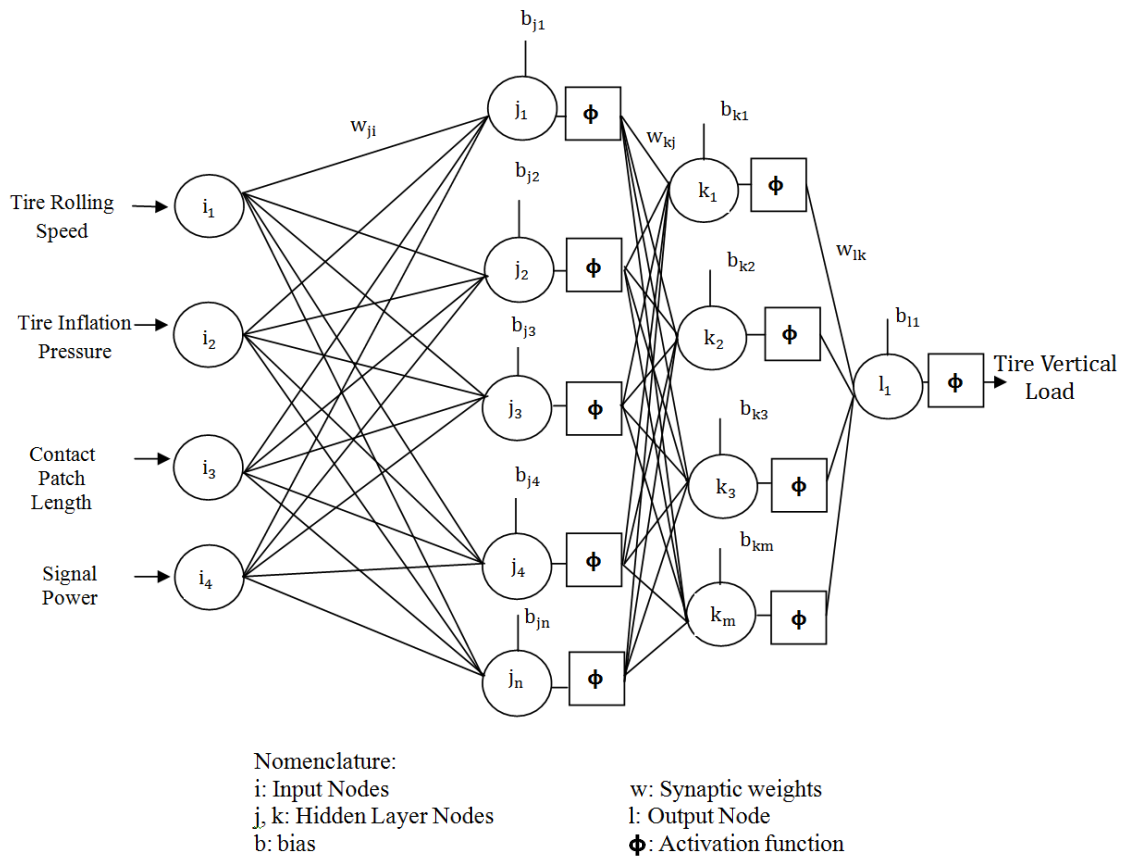


Fig. 2.53: Architecture of proposed NN model

In this study, the neural network structure was selected by using an evolutionary algorithm. The evolutionary algorithm tried different ANN structures having various hidden layers and various numbers of neurons in each hidden layers. After that, the selected ANN has been trained for various learning rate and termination criteria. The performance of each network was checked by estimating the correlation coefficient (R). The goal was to maximize correlation coefficient(R), to obtain a network with the best generalization.

To train the NN, a back-propagation learning algorithm was used in feed forward mode. The ANN was trained by adjusting the values of connections (synaptic weights). The ANN parameters (weights and biases) were adjusted to minimize the sum of the squares of the differences between the actual values and network output values. The performance index for the Back propagation algorithm is defined as:

$$E(n) = [d(n) - y(n)]^2 = e^2(n) \quad (2.2)$$

where $d(n)$ is the desired output value, $y(n)$ is the predicted value and $e(n)$ is the iteration for iteration n . A random sampling of the training data was used to divide the training data into three groups. The first group (60% of data) was used for the neural network training, the second group (20% of data) was used to cross-validate the results of the training and the third group (20% of the data) was used to test the neural network or generalize the error of the network. The differentiable activation function was specified as the tan sigmoid or hyperbolic tangent (Fig. 2.54), for all nodes: hidden layers, and output layer.

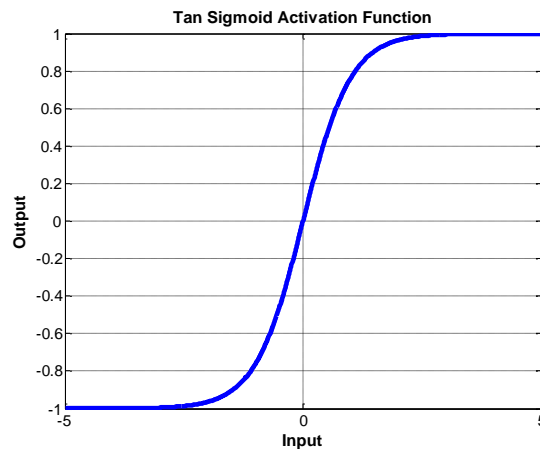


Fig. 2.54: Tan-Sigmoid activation function

The ANN was trained in a batch mode where its parameters were only updated after all the input-output pairs were presented.

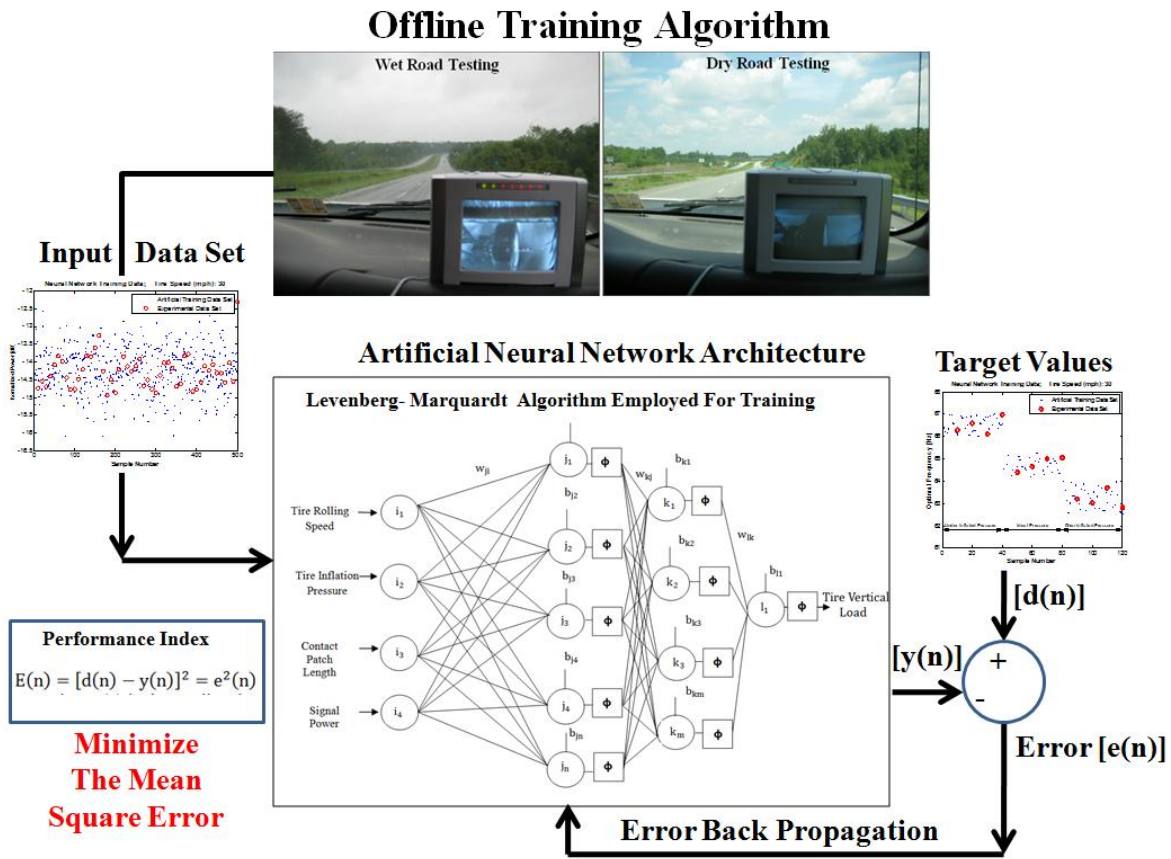
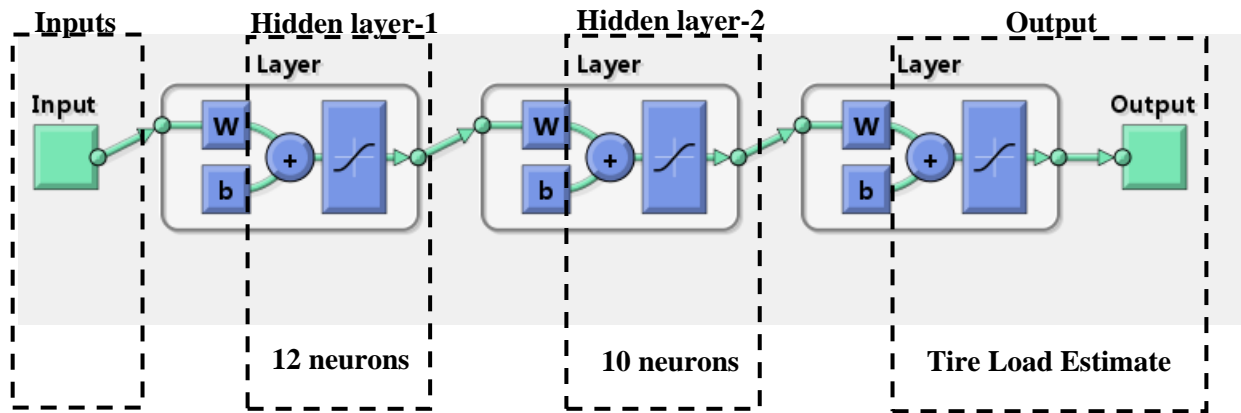


Fig. 2.55: Neural network training procedure

The Levenberg-Marquardt (L-M) algorithm was employed for the training and the target performance goal (mean square difference between ANN output and target output) was set at 0.001 (Fig. 2.55). The maximum number of epochs (representation of the input/output pairs and the adjustment of ANN parameters) was set at 1000. Effect of the number of neurons in the hidden layer in the ANN performance was analyzed. Based on this analysis, the optimal architecture of the ANN was constructed as 4–12–10–1 NN architecture (Fig. 2.56) representing the number of inputs, neurons in hidden layer-1, neurons in hidden layer-2, and outputs, respectively.



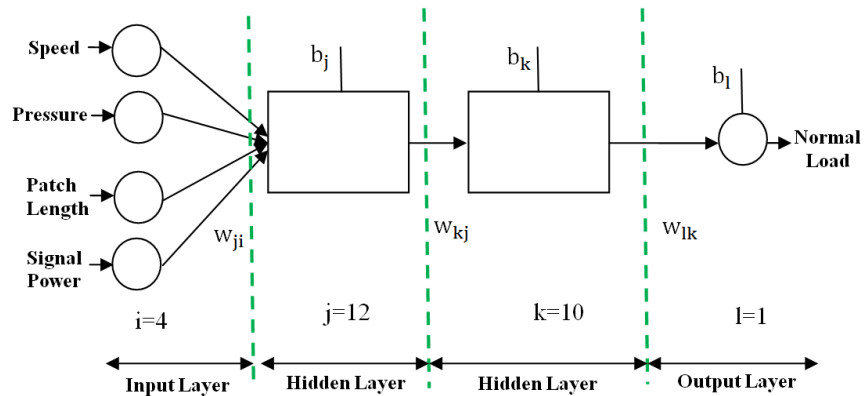
Algorithms		
Training:	Levenberg-Marquardt (trainlm)	
Performance:	Mean Squared Error (mse)	
Data Division:	Random (dividerand)	
Progress		
Epoch:	0	1000
	1000 iterations	
Time:	0:04:10	
Performance:	5.90e+04	2.86e-05
Gradient:	1.00	0.0223
Mu:	0.00100	1.00
Validation Checks:	0	6

Fig. 2.56: Neural network architecture selected

2.6.4 Neural Network Details

The synaptic weights (w) and biases (b) between input layer and hidden layers for the trained multi-layer feed-forward network are given below.

Nomenclature:



Synaptic weights:

Table 2.7: Synaptic weights

Input layer → Hidden layer 1

w_{ji}	$i =$	1	2	3	4
j=1		0.41125	0.40292	6.1525	2.0945;
2		-1.2114	1.6138	2.8838	0.93679;
3		-1.342	1.0119	-4.6893	-1.5662;
4		3.4936	1.4316	-8.029	-2.6727;
5		-1.4578	-0.69118	-1.5114	-0.24153;
6		4.7475	2.2621	-7.7934	-3.1402;
7		1.4864	-1.3265	-1.4466	-0.37843;
8		1.9416	-3.4698	9.7365	3.1955;
9		-1.5371	2.5674	0.038157	-0.020639;
10		-0.95951	1.3599	0.92153	2.0929;
11		-0.87652	1.597	1.004	2.461;
12		-0.00022248	-3.5002	-4.5291	-1.4864

Table 2.8: Synaptic weights

Hidden layer 1 → Hidden layer 2

w_{kj}	$j =$	1	2	3	4	5	6	7	8	9	10	11	12
k=		0.59196	0.0014513	0.12555	0.95588	1.3503	0.2932	-0.34876	-1.6389	1.1289	-0.16304	-0.49334	-1.2885;
1		-1.7899	-0.23625	1.796	-1.0935	0.64369	0.18295	-0.71838	0.68816	-0.038948	1.4414	0.94418	-2.3879;
2		-0.58	-0.61276	-2.9328	-3.1722	0.44023	0.5603	0.058161	-0.42047	-2.1532	0.19692	-0.3908	1.7549;
3		3.2296	-0.019984	2.7275	3.3809	0.85333	2.7004	-0.34381	0.64121	-0.39105	-0.60492	0.15751	-1.8666;
4		-1.4966	-1.7382	1.9741	-0.80385	0.15578	0.6127	1.5314	-0.42014	-1.0719	-0.93016	0.067935	-0.5812;
5		0.38679	0.10168	-0.4631	0.39399	0.012388	0.010619	0.099109	-1.5261	0.1711	0.44983	-0.23247	0.099255;
6		-2.7018	0.26454	-1.7867	0.5205	-0.37278	4.4702	3.9912	-6.5797	-2.1627	-0.5158	-0.10698	0.056457;
7		6.0149	-0.0531	1.5271	-2.8901	0.55535	1.5911	-0.048212	-1.5102	2.4035	-0.1197	-0.11866	-3.0729;
8		0.12008	-2.2759	1.1599	1.5245	0.41325	1.9485	-0.95869	1.2699	-0.39679	-1.3967	-3.2807	1.0523;
9		-0.31343	-0.55188	-0.52361	0.14386	2.0896	-0.36829	-0.036034	0.63813	0.41311	-0.83112	-0.070953	-
10							0.67522						

Table 2.9: Synaptic weights

Hidden layer 2 → Output layer

w_{lk}	$j =$	1	2	3	4	5	6	7	8	9	10
l=1		0.22887	0.27676	-3.1828	-3.4387	-0.28197	-0.33969	-0.28387	0.26258	-2.9603	1.7436

Table 2.10: Bias details

Biases

Hidden layer 1	Hidden layer 2	Output layer
b_j	b_k	b_l
[-4.2248; -2.7268; 2.313; 3.2972; 1.2733; -2.0491; -0.35925; 1.6147; -0.86193; -3.6604; -3.4631; -3.7645]	[-1.7563; 0.65537; 1.1689; -0.36634; 0.22565; -0.53214; -0.19077; 1.7229; 0.69619; 1.9565]	[1.0891]

2.6.5 Analysis Results

a) Neural Network Training Performance

Table 2.11: Training data set range

Speed	Pressure	Load
15-65 mph	32 psi and 35 psi	1000, 1300, 1500, 1800 lbs

(a)



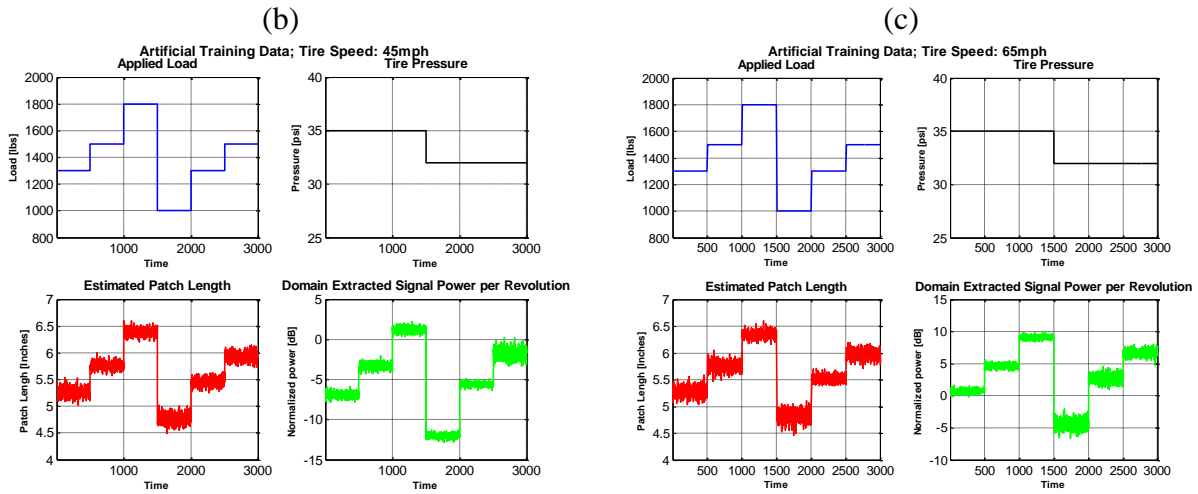


Fig. 2.57: Training data set

Mean square error (MSE)

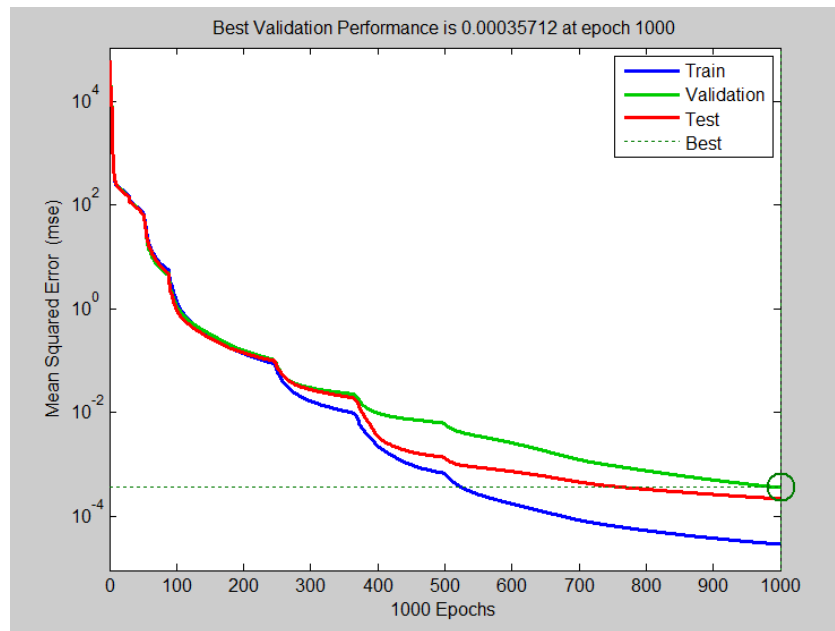


Fig. 2.58: Training performance- Mean square error (MSE)

Correlation coefficient (R)

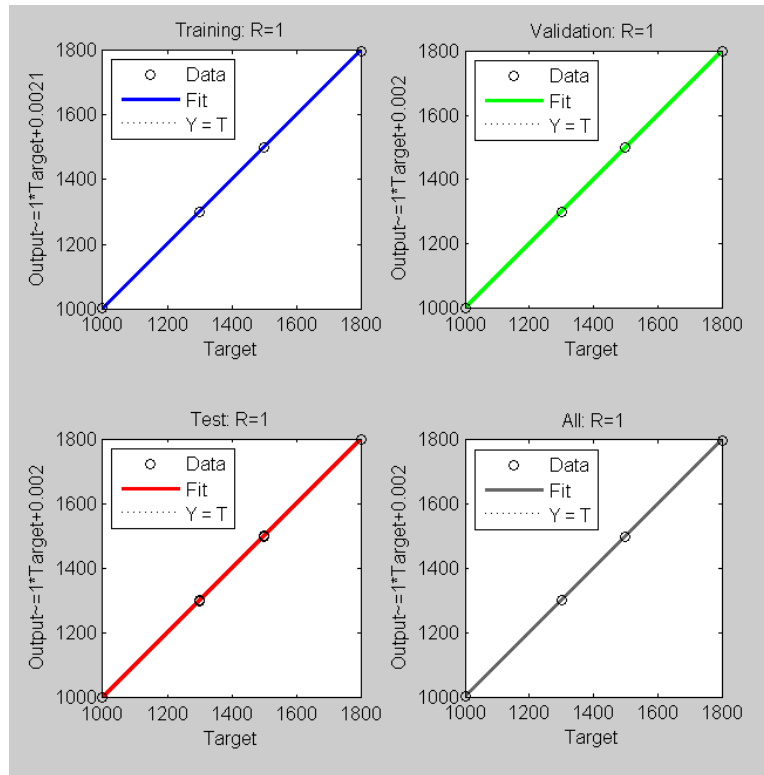


Fig. 2.59: Training performance- Correlation coefficient (R)

Table 2.12: ANN training performance

Mean square error (MSE)	Correlation coefficient (R)
0.0000286	1

From Fig. 2.58-Fig. 2.59, we can see that the neural network was successfully trained using the data set given in Fig. 2.57.

b) Neural Network Testing Performance

The neural network performance was validated using experimental data from both indoor and outdoor tests.

I. ANN performance using the indoor test data i.e. experimental data collected on the Flat-Trac® machine.

Case 1: Rolling speed: 30 mph, Camber angle: 0°

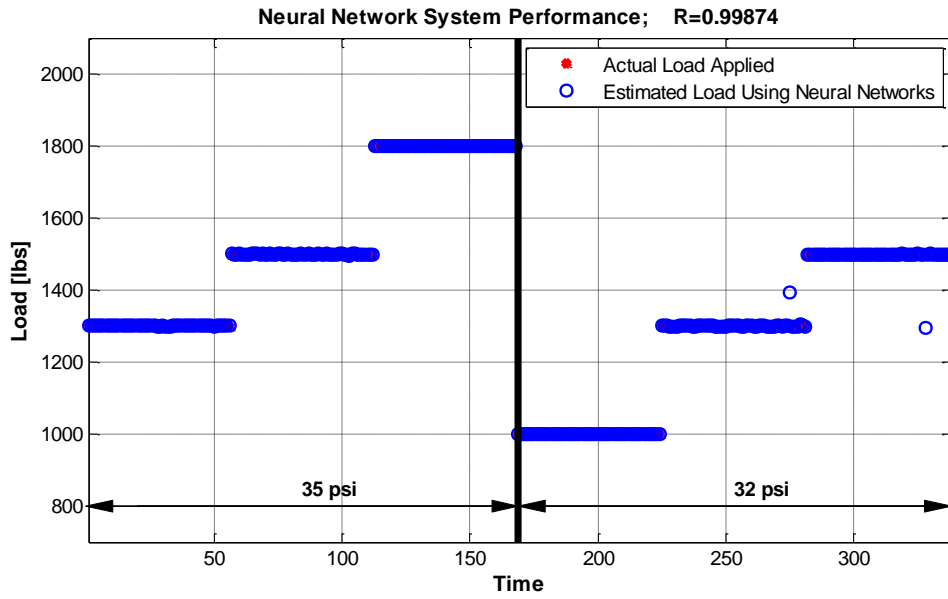


Fig. 2.60: Testing performance-30 mph

Case 2: Rolling speed: 45 mph, Camber angle: 0°

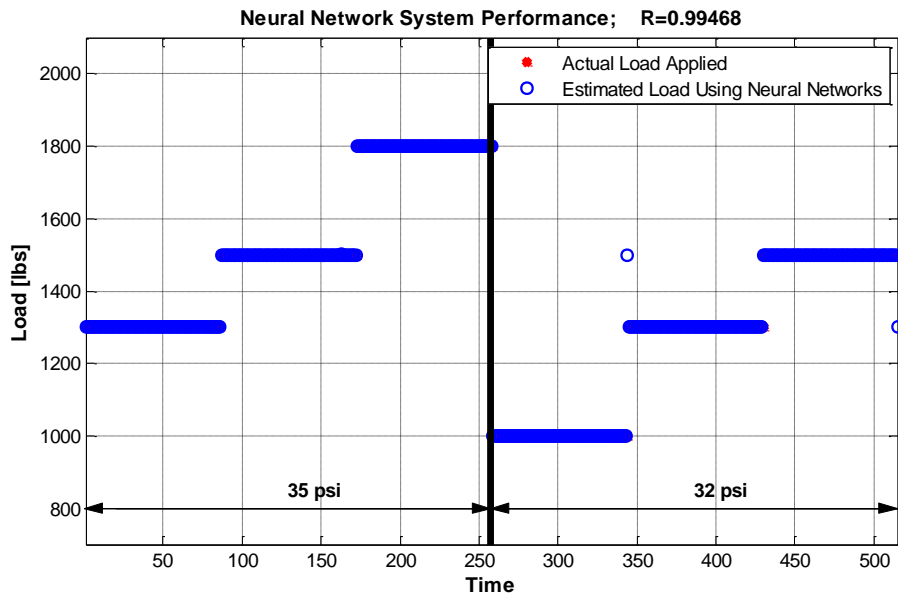


Fig. 2.61: Testing performance-45 mph

Case 3: Rolling speed: 45 mph, Camber angle: +2°

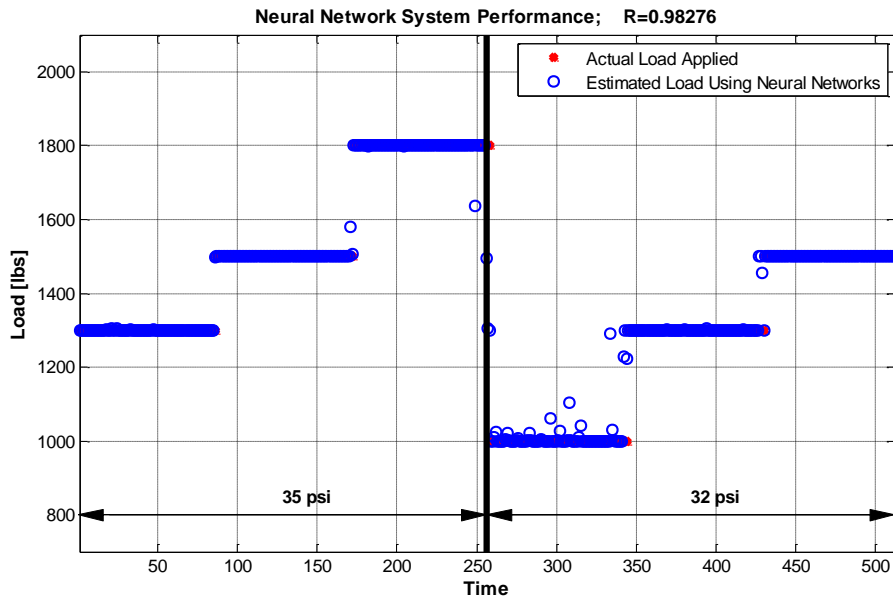


Fig. 2.62: Testing performance- 45 mph with camber angle (+2°)

Case 4: Rolling speed: 65 mph, Camber angle: 0°

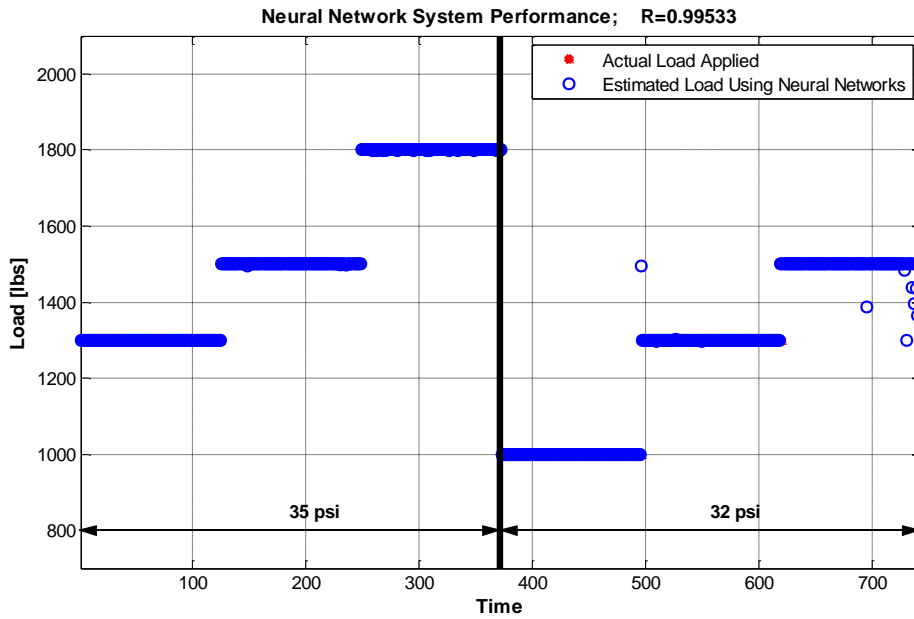


Fig. 2.63: Testing performance-65 mph

Summary:

Table 2.13: ANN performance –Testing set

Test case	Rolling speed [mph]	Correlation coefficient [R]
1	30	0.998
2	45	0.994
4	45 (with + 2° camber)	0.982
3	65	0.995

II. ANN performance using the outdoor test data i.e. experimental data collected using the mobile tire test trailer at ITL.

Testing Location: Danville Expressway

Dry Asphalt Testing



Temperature: 98°F

Total Test Runs: 80

Wet Asphalt Testing



Temperature: 86°F

Total Test Runs: 80

Fig. 2.64: Outdoor testing details

Case 1:

Rolling speed	Pressure range	Load range
30 mph	25- 35 psi	700-1600 lbs

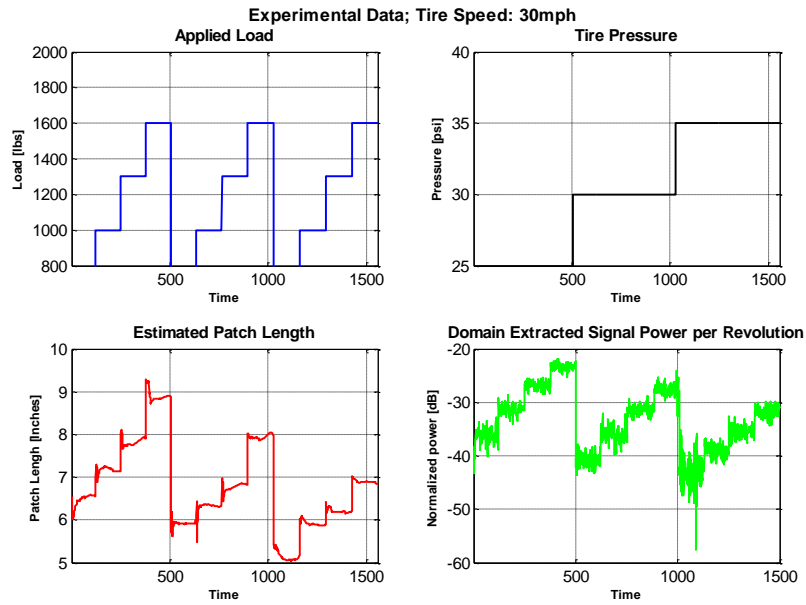


Fig. 2.65: Experimental data set

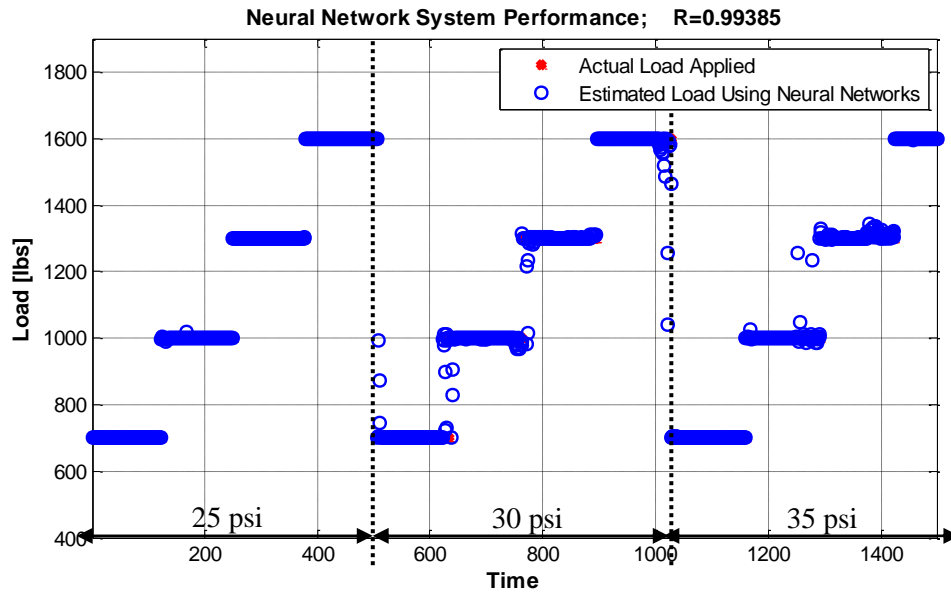


Fig. 2.66: Testing performance-30 mph

As we can see from Fig. 2.60-Fig. 2.66, the neural network model was able to make highly complex, nonlinear and multidimensional associations between selected input parameters and output to allow acceptable degree of accuracy in the estimation of the tire load across the full range of the tire operating conditions.

Hence, in this study, a new and efficient artificial neural network (ANN) based signal processing algorithm has been developed to estimate the normal load on a tire. The ANN predicted and experimental results were extensively compared under different working conditions of the tire. The findings of this study suggest the usefulness of an ANN technique in estimating the tire normal load successfully.

2.7 Tire Slip angle Estimation Algorithm

This section presents the development and implementation strategy for the real-time estimation of the tire slip angle using accelerometric signals from an intelligent tire. For developing a slip angle estimation algorithm, the underlying goal was to determine synthetic parameters that were sensitive to slip angle. Through extensive parametric studies, the key parameter identified was the magnitude of the lateral acceleration signal (Fig. 2.67).

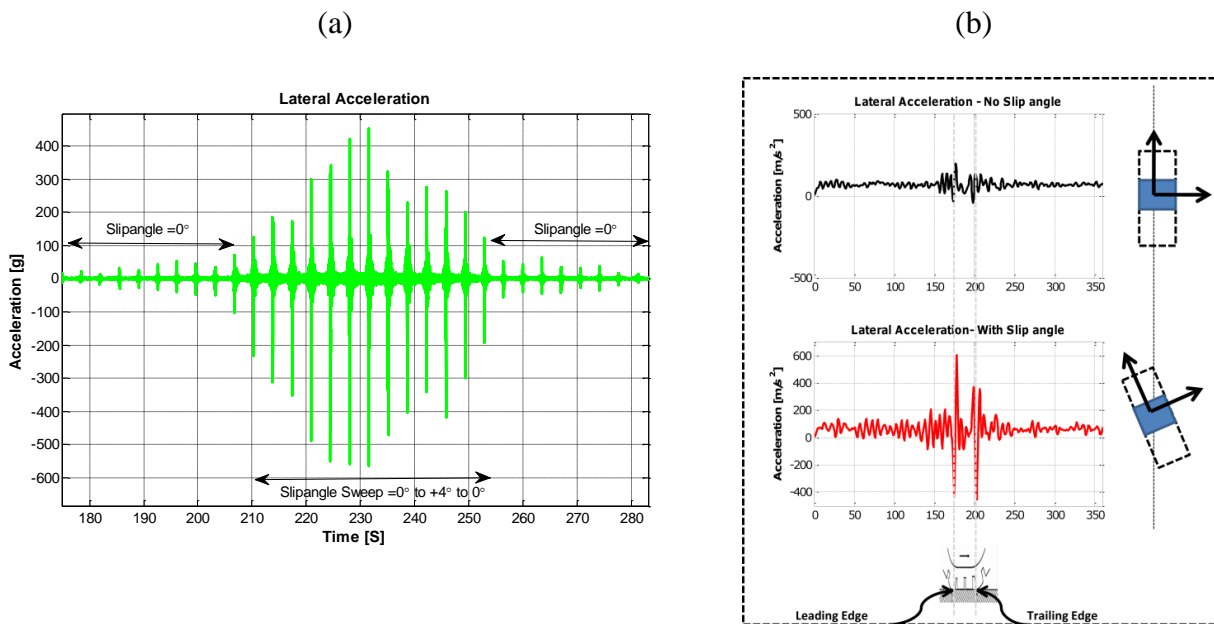


Fig. 2.67: (a) Lateral acceleration profile – slip angle sweep test, and (b) magnified view of the lateral acceleration signal for one tire revolution

The magnitude of the lateral acceleration signal was characterized by estimating the signal power (absolute amplitude of the signal) on a per revolution basis (Fig. 2.68a). A strong dependence of the identified parameter was also seen on the tire loading condition. Hence, one would need to take into account the effect of tire load while estimating the signal power. In the absence of the

vertical load information during the online estimation procedure, it became necessary to correlate the accelerometer signal to the instantaneous vertical load. To achieve this objective, the total radial acceleration signal power was estimated on a per revolution basis (Fig. 2.68b). From Fig. 2.68b, it can be seen that the signal power estimates correlate to the applied vertical load with distinct boundaries demarcating the change in the instantaneous load.

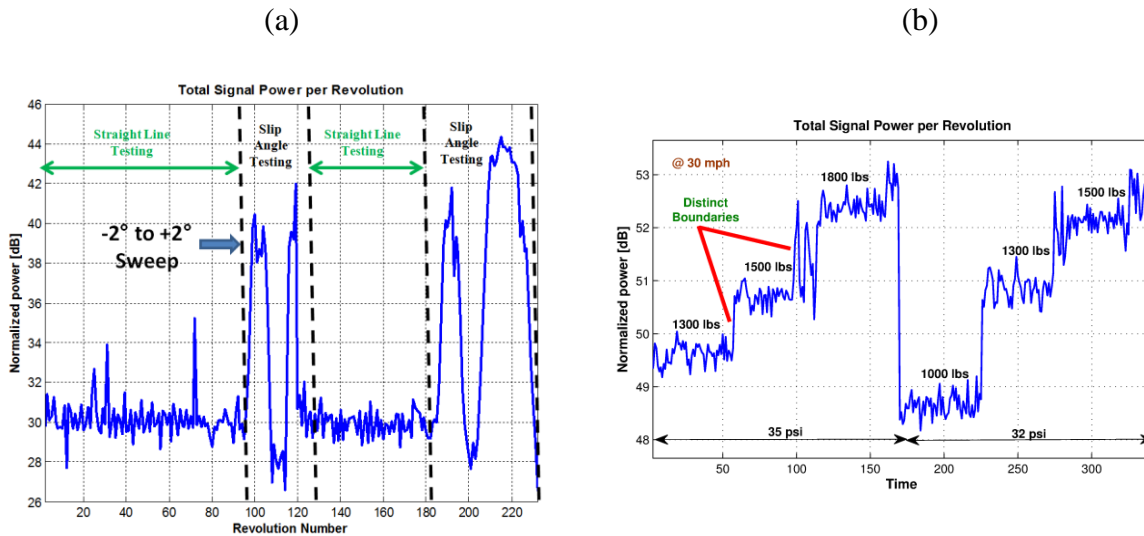


Fig. 2.68: (a) Variation in the instantaneous amplitude of the lateral acceleration signal, (b) radial acceleration signal power on a per revolution basis

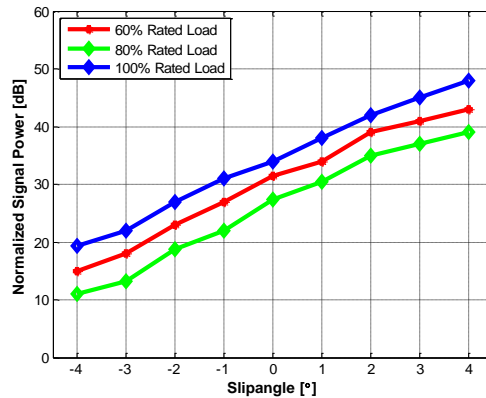


Fig. 2.69: Variation in instantaneous amplitude of the lateral acceleration signal as function of the tire-slip angle under different loading conditions

Finally, a line-fit algorithm was employed to estimate the slip angles. The tire-slip angles were estimated accurately up to a slip angle of 4° (Fig. 2.69). However, in the estimation of higher slip

angles the nonlinear characteristic of the tire dominates the results. To ensure robust performance even during the vehicle maneuvers which show highly nonlinear tire characteristics, a sensor fusion approach, combining the intelligent tire slip-angle estimate with a model based estimate is proposed (Fig. 2.70). The model based estimation methodology uses a tire force estimator in conjunction with a Luenberger observer to make dynamics estimates of the tire slip-angle.

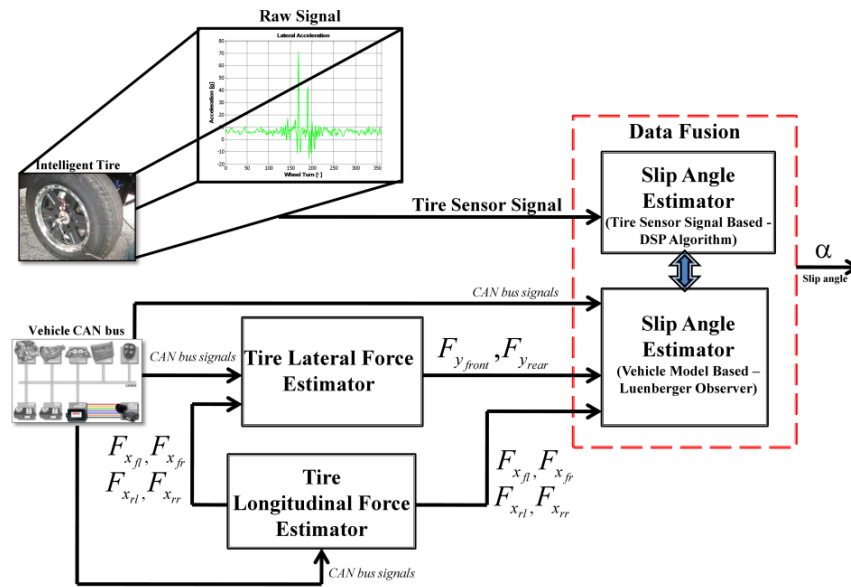


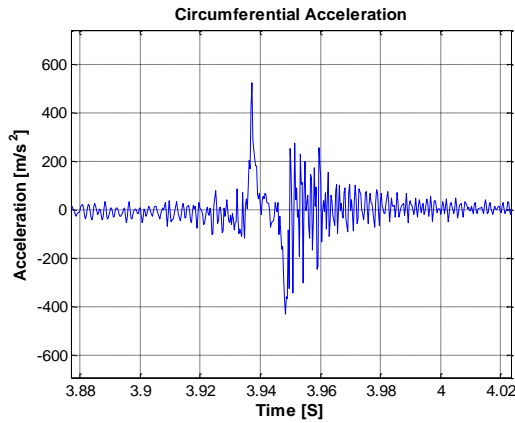
Fig. 2.70: Functional diagram of the tire slip angle estimation process

Details regarding the methodology adopted to estimate the tire slipangle using an observer based approach are presented in Chapter 3.

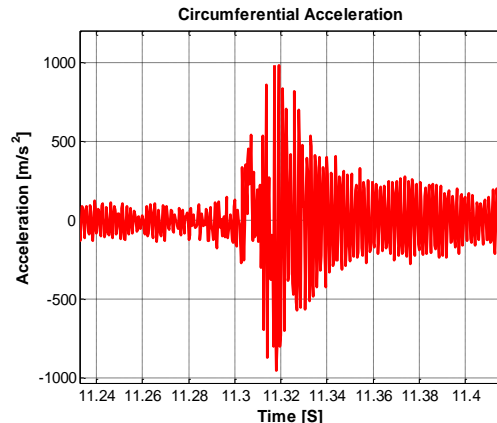
2.8 Tire Slip ratio Estimation Algorithm

This section presents the development and implementation strategy for the real-time estimation of the tire slip ratio using accelerometric signals from an intelligent tire.

(a) Tire under low-slip conditions



(b) Tire under high-slip conditions



Tire vibrations are dominated by high-frequency components

Fig. 2.71: Time history of the acceleration signal in the circumferential direction during: (a) low slip conditions, and (b) high slip conditons

Fig. 2.71 shows the time histories of the acceleration signal in the circumferential direction. It is evident from these plots that under high-slip conditons the level of the high frequency vibrations increase. This is in agreement with [55], where it was shown that the stick/slip phenomenon is linked to block vibration. These results show that there are particular frequency ranges where vibrations rise due to sliding, which could help recognize sliding conditions and get a measure of the slip state of the tire.

The dynamic slip state information from the intelligent tire could be used in conjunction with existing vehicle state observer based slip-ratio estimators (Fig. 2.72), which are known to exhibit unsatisfactory performance during a hard braking event.

A detailed description of the tire slip ratio estimation algorithm cannot be provided due to industrial privacy reasons.

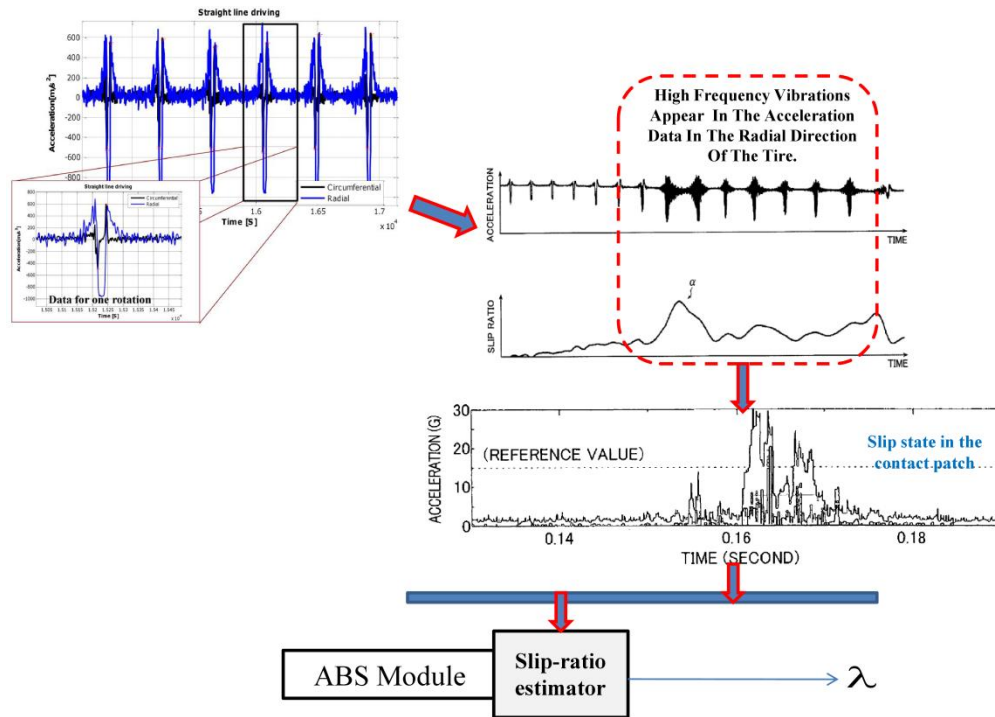


Fig. 2.72: Functional diagram of the tire slip ratio estimation process

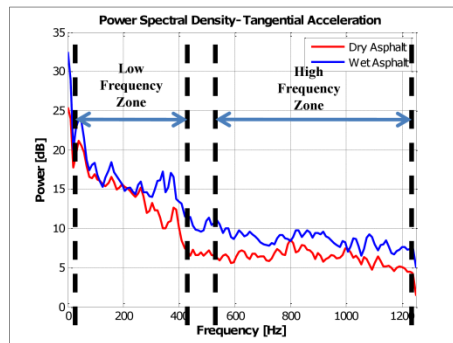
2.9 Friction Estimation Algorithm

Road surface friction coefficient is a variable of interest for enhancing the accuracy of vehicle chassis control systems such as anti-lock braking system (ABS) and stability control (VSC) system. This underlines the need to have a road surface condition/terrain classification system which has the capability to identify the changing road surface conditions in real time and make certain terrain-based adjustments to the vehicle control systems. This section provides an overview of the implementation strategy for a terrain classification system that utilizes sensor signals from an intelligent tire. A detailed description of the the classification algorithm cannot be provided due to industrial privacy reasons.

The proposed algorithm assumes that the tire vibrations are correlated to the terrain type and the terrain signature is given by the magnitude frequency responses of the tire attached vibration sensors. To do this, the signals of the tire vibration in a predetermined domain are extracted. The predetermined domain represents a certain portion of the tire signal per tire revolution. Based on the degree of temperature dependence of vibration level in different domains of a tire signal, we can identify certain regions in a tire signal which show least dependence on temperature and are most suited for our analysis and represent these so called

predetermined domains. The vibration levels of a predetermined frequency band within these domains are then calculated using the frequency spectrum of the time signal by passing the signals through a band-pass filter (Fig. 2.73). Based on the calculated vibration level, the road surface condition can be estimated using a supervised fuzzy logic classifier that characterizes the terrain using the measured frequency response of the instrumented tire. The fuzzy logic classifier classifies the road profile segments as members of pre-defined classes (such as asphalt, wet asphalt, gravel, etc).

Estimating the Vibration Amplitude Ratio (R)



Dry Asphalt:
R= 0.22

Wet Asphalt:
R= 0.31

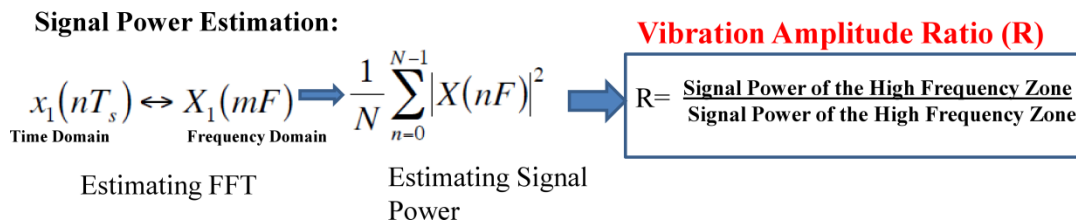


Fig. 2.73: Vibration-ratio estimation

The following sections elaborate on the details of the classification algorithm.

2.9.1 Classification Algorithm

A fuzzy logic-based classifier: The application of fuzzy logic to solve the classification problem is motivated by its noise tolerance to the vibration data retrieved from sensors, and its ability for real-time implementation while ensuring robustness with respect to imprecise or uncertain signal interpretation.

Fuzzy logic provides a linguistic-based method for modeling the relationship between vibration data input values and the terrain surface information. In fact, fuzzy logic is ideally

suited for this application because it naturally copes with ambiguities and imprecision's. This is accomplished by representing terrain information using ranges of values that are sectorized into several linguistic classes that have smooth overlapping boundaries. Fuzzy logic rule evaluation involves only simple arithmetic calculations that can be performed very rapidly. Therefore, the computational time is very small, making it feasible for real-time implementation.

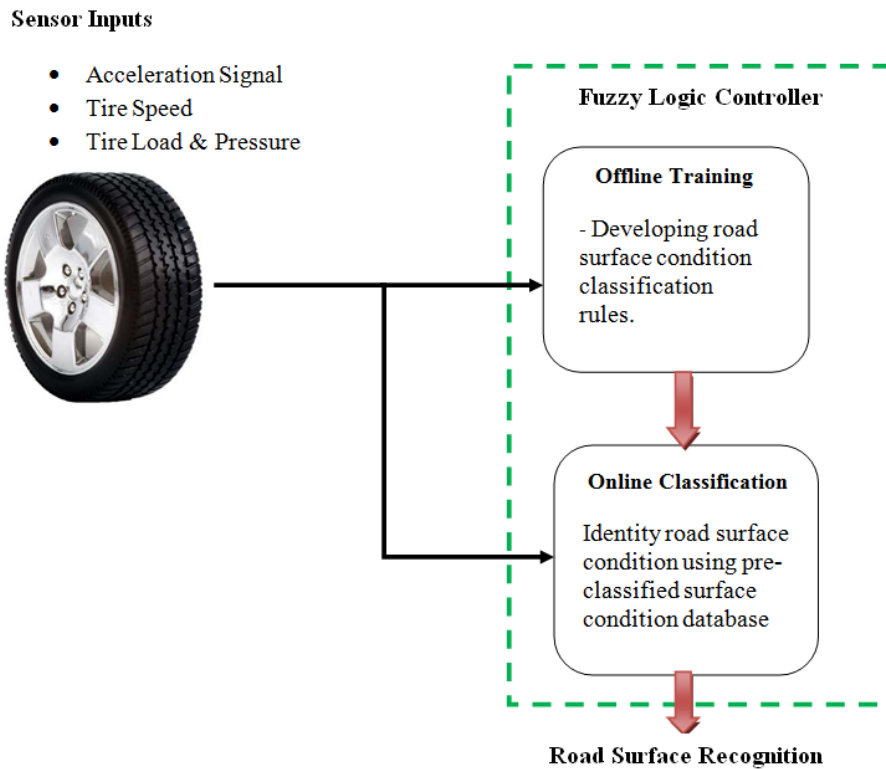


Fig. 2.74: Road surface identification using a fuzzy logic classifier

2.9.2 Classification Methodology

The road surface recognition process would consist of two stages:

1. Fuzzy logic set creation process
2. Identification process

Typically a fuzzy logic set creation process contains following steps: sampling, filtration, windowing, feature extraction.

a) Sampling

Sampling is a technique to convert an analog signal into a digital signal. It periodically samples an input signal and transforms into a sequence of intensity values. Desirable sampling frequency is 10000 Hz in road surface recognition application.

b) Filtration

Filtration is a very efficient way of removing the unwanted noise from the spectrum. It is used to modify the frequency domain of the input sample. The filtration is not necessary. However the usage of this can improve the efficiency of the recognition system.

c) Windowing

Windowing is a technique used to shape the time portion of measurement data, to minimize edge effects that result in spectral leakage in the FFT spectrum. By using window functions, the spectral resolution of frequency domain will be increased. There are different types of window functions available, each with their own advantage. The Hamming window is used to avoid distortion of the overlapped window functions.

d) Fast Fourier Transform (FFT)

The sequence of frequency of a signal obtained by FFT becomes the basis for extracting of the frequency-domain features. It is applied instead of discrete Fourier transform because of shorter time of calculation. Obtained coefficients create feature vectors which are used in calculations.

2.9.3 Identification Process - Classifier Architecture

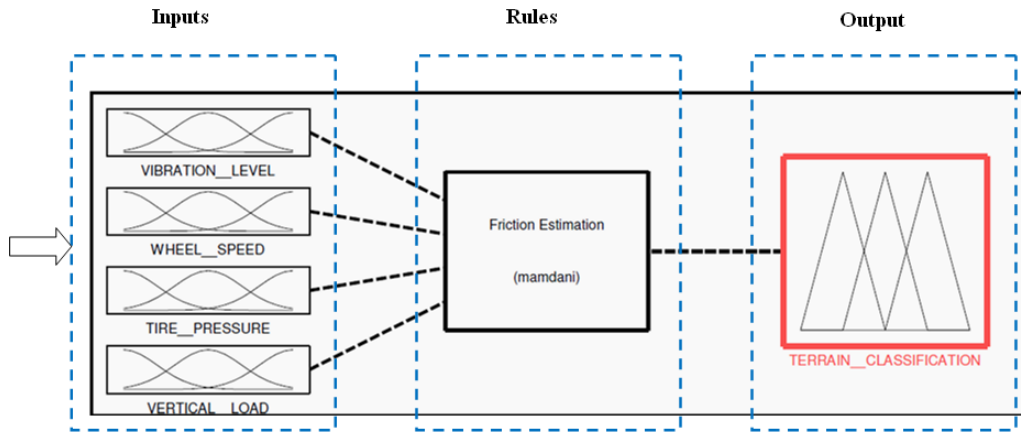


Fig. 2.75: Fuzzy logic classifier architecture

Fig. 2.75, shows the fuzzy logic classifier architecture. The input block has four variables, which have been identified based on the factor dependence study. Based on the interdependence of all the inputs for a given road surface condition and the way they effect the vibration spectra of a tire, a set of linguistic rules would be developed to identify the road surface condition (Fig. 2.76).

Developing Robust Linguistic Rules

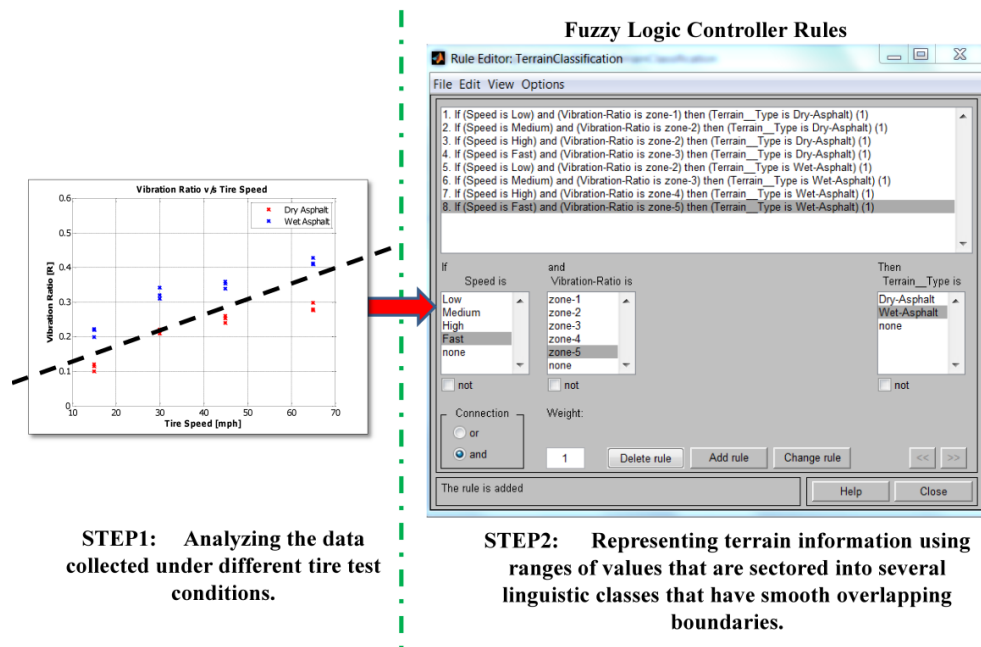


Fig. 2.76: Fuzzy logic linguistic rules

2.9.4 Classification Performance

The classifier performance was validated on dry and wet asphalt. The test involved testing the tire under free-rolling and low-slip conditions (low force utilization). The classifier was successfully able to distinguish between the different road surface conditions as shown in Fig 2.77

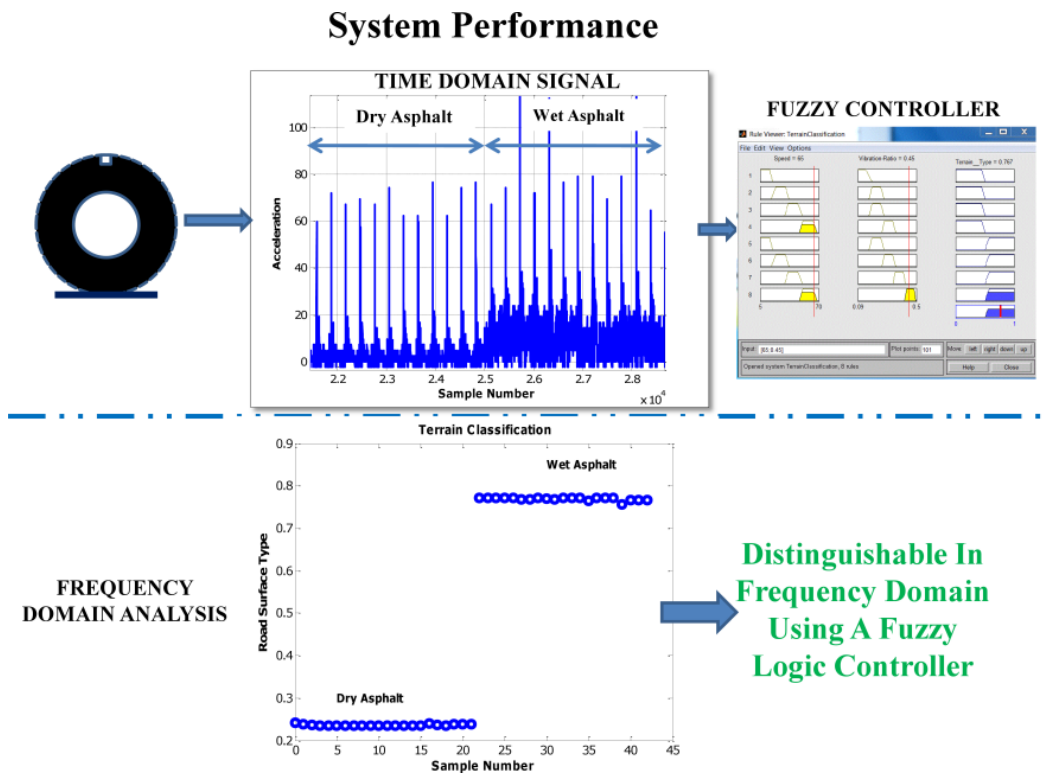


Fig 2.77: Classification performance

2.10 Conclusion

This study presents an innovative approach to obtain real-time information about the tire-road contact parameters from “in-tire” acceleration measurements. The development of a sensorized smart/intelligent system is expected to eliminate some of the vehicle sensors and provide accurate, reliable and real-time information about magnitudes, directions and limits of force for each tire. Moreover, direct measurement of tire variables using wireless sensors embedded inside the tire is expected to open a new era in design of vehicle control systems.

Acknowledgements

The intelligent tire based signal feature extraction and algorithm development work was performed under a research project with The Goodyear Tire and Rubber Company. The author would like to thank Peter Suh, Dr. Robert Benedict, Anthony Parsons and Marc Engel from The Goodyear Tire and Rubber Company for their enthusiasm and driving force in the project.

References

- [1] E. Sabbioni, L. Kakalis and F. Cheli, *On the Impact of the Maximum Available Tire-Road Friction Coefficient Awareness in a Brake-Based Torque Vectoring System*, in: SAE 2010 World Congress & Exhibition, Detroit, MI, USA, 2010.
- [2] F. Braghin, F. Cheli, S. Melzi, E. Sabbioni, F. Mancosu and M. Brusarosco, *Development of a cyber tire to enhance performances of active control systems*, in: 7th EUROMECH Solid Mechanics Conference, Lisbon, Portugal, 2009.
- [3] F. Cheli, E. Leo, S. Melzi and E. Sabbioni, *On the impact of 'smart tyres' on existing ABS/EBD control systems*, *Vehicle System Dynamics*. 48 (2010), pp. 255-270.
- [4] G. Erdogan, S. Hong, F. Borrelli and K. Hedrick, *Tire Sensors for the Measurement of Slip Angle and Friction Coefficient and Their Use in Stability Control Systems*, in: SAE 2011 World Congress & Exhibition, Detroit, MI, USA, 2011.
- [5] F. Cheli, E. Sabbioni, M. Sbroisi, M. Brusarosco, S. Melzi and V. d'alessandro, *Enhancement of ABS Performance through On-Board Estimation of the Tires Response by Means of Smart Tires*, in: SAE 2011 World Congress & Exhibition, Detroit, MI, USA, 2011.
- [6] F. Cheli, G. audisio, M. brusarosco, F. mancosu, D. Cavaglieri and S. melzi, *Cyber Tyre: A Novel Sensor to Improve Vehicle's Safety*, in: SAE 2011 World Congress & Exhibition, Detroit, MI, USA, 2011.
- [7] National Highway Traffic Safety Administration, *Proposed new pneumatic tires for light vehicles - FMVSS No.139*, 2001.

- [8] 106th Congress, Public Law 106-414, *Transportation Recall Enhancement, Accountability, and Documentation (TREAD) Act*, US, 2000.
- [9] National Highway Traffic Safety Administration Federal motor vehicle safety standards, *tire pressure monitoring systems; controls and displays - NHTSA-2000-8572*, 2000.
- [10] National Highway Traffic Safety Administration, Federal motor vehicle safety standards; *tire pressure monitoring systems; controls and displays - NHTSA-2005-20586*, 2005.
- [11] K.B. Singh, M.A. Arat and S. Taheri, *An Intelligent Tire Based Tire-Road Friction Estimation Technique and Adaptive Wheel Slip Controller for Anti-lock Brake System*, Journal of Dynamic Systems, Measurement and Control (2011). (under review)
- [12] M.A. Arat, K.B. Singh and S. Taheri, *Intelligent Tire: Development and Application*, International Conference on Engineering and Meta-Engineering (2012). (under review)
- [13] M.A. Arat, K.B. Singh and S. Taheri, *An Intelligent Tire Based Adaptive Vehicle Stability Controller*, International Journal of Vehicle Design - Special Issue on Advanced Developments in Tire Modeling, Analysis and Dynamics (2012). (under review)
- [14] Available online at: http://wardsauto.com/ar/Intelligent_tires_debut_100624/
- [15] Available online at: www.vtt.fi/apollo
- [16] Available online at: <http://friction.vtt.fi>
- [17] Available online at: <http://www.bridgestone.eu/press/press-releases/2011/bridgestone-announces-new-tyre-technology-for-determining-road-surface-conditions-based-on-the-concept-of-cais>
- [18] Available online at: http://www.motorauthority.com/news/1044745_pirelli-schrader-team-up-for-computerized-cyber-tire

- [19] Available online at: http://www.conti-online.com/generator/www/de/en/continental/automotive/themes/commercial_vehicles/chassis/chassis_control/intelligent_tire_system/intelligent_tire_system_en.html
- [20] Available online at: http://www.vehicledynamics-expo.com/05vdx_conf/pres/day2/hakanen.pdf
- [21] O. Yilmazoglu, M. Brandt, J. Sigmund, E. Genc and H.L. Hartnagel, *Integrated InAs/GaSb 3D magnetic field sensors for “the intelligent tire”*, Sensors and Actuators A: Physical. 94 (2001), pp. 59-63.
- [22] M. Brandt, V. Bachmann, A. Vogt, M. Fach, K. Mayer, B. Breuer and H.L. Hartnagel, *Highly sensitive AlGaAs/GaAs position sensors for measurement of tyre tread deformation*, Electronics Letters. 34 (1998), pp. 760-762.
- [23] A. Pohl, R. Steindl and L. Reindl, *The “intelligent tire” utilizing passive SAW sensors measurement of tire friction*, Instrumentation and Measurement, IEEE Transactions on. 48 (1999), pp. 1041-1046.
- [24] Z. Xiangwen, W. Zhixue, G. Leifu, A. Yunfeng and W. Feiyue, *Design considerations on intelligent tires utilizing wireless passive surface acoustic wave sensors*, in: Intelligent Control and Automation, 2004. WCICA 2004. Fifth World Congress on, 2004, pp. 3696-3700 Vol.3694.
- [25] S.M. Savaresi, M. Tanelli, P. Langthaler and L. Del Re, *New Regressors for the Direct Identification of Tire Deformation in Road Vehicles Via “In-Tire” Accelerometers*, Control Systems Technology, IEEE Transactions on. 16 (2008), pp. 769-780.
- [26] V. Magori, V.R. Magori and N. Seitz, *On-line determination of tyre deformation, a novel sensor principle*, in: Ultrasonics Symposium, 1998. Proceedings., 1998 IEEE, 1998, pp. 485-488 vol.481.
- [27] A.J. Tuononen, *Optical position detection to measure tyre carcass deflections*, Vehicle System Dynamics. 46 (2008), pp. 471-481.

- [28] A. Tuononen and L. Hartikainen, *Optical position detection sensor to measure tyre carcass deflections in aquaplaning*, International Journal of Vehicle Systems Modelling and Testing. 3 (2008), pp. 189 - 197.
- [29] A. Tuononen, *On-board estimation of dynamic tyre forces from optically measured tyre carcass deflections*, International Journal of Heavy Vehicle Systems. 16 (2009), pp. 362-378.
- [30] Y. Jingang, *A Piezo-Sensor-Based "Smart Tire" System for Mobile Robots and Vehicles*, Mechatronics, IEEE/ASME Transactions on. 13 (2008), pp. 95-103.
- [31] G. Erdogan, L. Alexander and R. Rajamani, *A novel wireless piezoelectric tire sensor for the estimation of slip angle*, Measurement Science and Technology. 21 (2010), pp. 015201.
- [32] R. Grossmann, *Quartz crystals as remote sensors for tire pressure*, in: Instrumentation and Measurement Technology Conference, 1999. IMTC/99. Proceedings of the 16th IEEE, 1999, pp. 1745-1749 vol.1743.
- [33] R. Matsuzaki and A. Todoroki, *Wireless flexible capacitive sensor based on ultra-flexible epoxy resin for strain measurement of automobile tires*, Sensors and Actuators A: Physical. 140 (2007), pp. 32-42.
- [34] R. Matsuzaki, T. Keating, A. Todoroki and N. Hiraoka, *Rubber-based strain sensor fabricated using photolithography for intelligent tires*, Sensors and Actuators A: Physical. 148 (2008), pp. 1-9.
- [35] A. Todoroki, S. Miyatani and Y. Shimamura, *Wireless strain monitoring using electrical capacitance change of tire: part I—with oscillating circuit*, Smart Materials and Structures. 12 (2003), pp. 403–409.
- [36] R. Matsuzaki and A. Todoroki, *Passive wireless strain monitoring of actual tire using capacitance–resistance change and multiple spectral features*, Sensors and Actuators A: Physical. 126 (2006), pp. 277-286.

- [37] M. Sergio, N. Manaresi, M. Tartagni, R. Guerrieri and R. Canegallo, *On road tire deformation measurement system using a capacitive-resistive sensor*, in: *Sensors*, 2003. Proceedings of IEEE, 2003, pp. 1059-1063 Vol.1052.
- [38] M. Otori, T. Ishizuka, T. Fujita, N. Masaki and Y. Suizu, *Fundamental study of smart tire system*, in: *Intelligent Transportation Systems Conference*, 2006. ITSC '06. IEEE, 2006, pp. 1519-1524.
- [39] A. Mishra, F.M. Gondal, A.A. Afrashteh, R.R. Wilson, R.D. Moffitt, R.K. Kapania and S. Bland, *Embedded wireless sensors for aircraft/automobile tire structural health monitoring*, in: *Wireless Mesh Networks*, 2006. WiMesh 2006. 2nd IEEE Workshop on, 2006, pp. 163-165.
- [40] M. Suido, T. Tabaru and S. Shin, *Estimating tire condition with wavelet analysis*, in: *SICE-ICASE*, 2006. International Joint Conference, 2006, pp. 5222-5226.
- [41] K. Seki, S. Shin and T. Tabaru, *Analysis of wavelet correlation between tyre sounds and tread patterns*, in: *Networking, Sensing and Control*, 2005. Proceedings. 2005 IEEE, 2005, pp. 241-246.
- [42] H. Jin-Oh, R. Rajamani and L. Alexander, *GPS-based real-time identification of tire-road friction coefficient*, *Control Systems Technology*, IEEE Transactions on. 10 (2002), pp. 331-343.
- [43] C.R. Carlson and J.C. Gerdes, *Nonlinear estimation of longitudinal tire slip under several driving conditions*, in: *American Control Conference*, 2003. Proceedings of the 2003, 2003, pp. 4975-4980 vol.4976.
- [44] S.L. Miller, B. Youngberg, A. Millie, P. Schweizer and J.C. Gerdes, *Calculating longitudinal wheel slip and tire parameters using GPS velocity*, in: *American Control Conference*, 2001. Proceedings of the 2001, 2001, pp. 1800-1805 vol.1803.
- [45] R. Daily and D.M. Bevly, *The use of GPS for vehicle stability control systems*, *Industrial Electronics*, IEEE Transactions on. 51 (2004), pp. 270-277.
- [46] D.M. Bevly, J.C. Gerdes and C. Wilson, *The Use of GPS Based Velocity Measurements for Measurement of Sideslip and Wheel Slip*, *Vehicle System Dynamics* 38 (2002), pp. 127-147.

- [47] F. Gustafsson, *Monitoring tire-road friction using the wheel slip*, Control Systems, IEEE. 18 (1998), pp. 42-49.
- [48] S. Muller, M. Uchanski and K. Hedrick, *Estimation of the Maximum Tire-Road Friction Coefficient*, Journal of Dynamic Systems, Measurement, and Control. 125 (2003), pp. 607-617.
- [49] G. Erdogan, L. Alexander and R. Rajamani, *Adaptive Vibration Cancellation for Tire-Road Friction Coefficient Estimation on Winter Maintenance Vehicles*, Control Systems Technology, IEEE Transactions on. 18 (2010), pp. 1023-1032.
- [50] T. Umeno, *Estimation of Tire-Road Friction by Tire Rotational Vibration Model*, RD Review of Toyota CRDL. 37 (2002), pp. 53-58.
- [51] Z. Zhao, Y. Li, Q. Wang, J. Li, L. Chu, Z. Ma and D. Liu, *Application of infrared thermometer in testing of temperature field for a rolling tire*, in: Vehicle Electronics Conference, 1999. (IVEC '99) Proceedings of the IEEE International, 1999, pp. 98-101 vol.101.
- [52] W. Tjiu, A. Ahanchian and B.Y. Majlis, *Development of tire condition monitoring system (TCMS) based on MEMS sensors*, in: Semiconductor Electronics, 2004. ICSE 2004. IEEE International Conference on, 2004, pp. 4 pp.
- [53] G. Danese, M. Giachero, F. Leporati, N. Nazzicari and M. Nobis, *An Embedded Acquisition System for Remote Monitoring of Tire Status in F1 Race Cars through Thermal Images*, in: Digital System Design Architectures, Methods and Tools, 2008. DSD '08. 11th EUROMICRO Conference on, 2008, pp. 432-437.
- [54] F. Braghin, M. Brusarosco, F. Cheli, A. Cigada, S. Manzoni and F. Mancosu, *Measurement of contact forces and patch features by means of accelerometers fixed inside the tire to improve future car active control*, Vehicle System Dynamics. 44 (2006), pp. 3-13.
- [55] B.N.J. Persson, O. Albohr, F. Mancosu, V. Peveri, V.N. Samoilov and I.M. Sivebaek, *On the nature of the static friction, kinetic friction and creep*, Wear. 254 (2003), pp. 835-851.

Chapter 3

Design of an Integrated Vehicle State Estimator for Application to Global Chassis Control

Executive Summary

Most modern day automotive control systems for vehicle handling and active safety usually employ a feedback control structure. Therefore, a real-time estimate of the vehicle handling dynamic states and tire-road contact parameters are invaluable for enhancing the performance of current vehicle control systems, such as ABS and the electronic stability program (ESP). Today's production cars are equipped with onboard sensors (e.g. a 3-axis accelerometer, a 3-axis gyroscope, steering wheel angle sensor) which provide some vehicle states and stability related information to the vehicle control systems. However, some key variables such as the tire forces, road bank/grade angles, and the tire-road friction coefficient, which have a significant impact on vehicle handling performance and safety, are difficult to measure using sensors already onboard vehicles. This study introduces a new integrated vehicle state estimator, comprising a series of model-based and kinematics-based observers, for estimating these unmeasurable states. Using an appropriate vehicle model, kinematic equations of motion, and available measurements from sensors potentially integrable or already integrated in current production vehicles, the unknown vehicle states as well as the tire-road contact forces are estimated by implementing a series of observers, arranged in a cascade structure. The performance of the proposed estimators have been evaluated via computer simulations conducted using the vehicle dynamics software CarSim.

Keywords: *state estimation, parameter estimation, sliding-mode observer (SMO), Kalman filter (KF), unscented Kalman filter (UKF), recursive least squares (RLS)*

3.1 Introduction

For implementation of automotive control algorithms, accurate information about the state of the vehicle and its surroundings is important. Real-time measurements of the vehicle handling dynamic states are extremely vital for the online computation of the optimized active longitudinal and lateral tire forces to be generated by electronic stability control modules (Fig. 3.1).

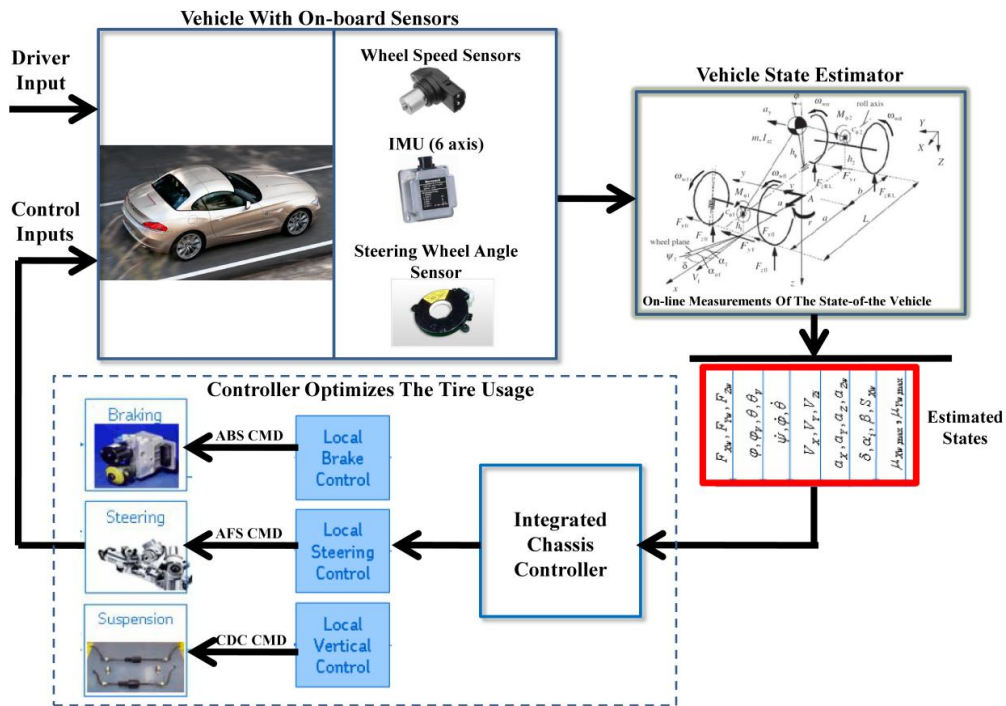


Fig. 3.1: Block diagram representation of an integrated chassis control system

Although some these states are easily measured, others are difficult to measure because of high cost or impracticality. As a consequence, vehicle-control systems currently available on production cars rely on available inexpensive measurements, such as longitudinal velocity, accelerations, and yaw-rate.

Knowledge about additional (currently unmeasurable) states of a vehicle (e.g. vehicle roll angle, side slip angle, lateral load transfer ratio etc.) can significantly reduce the risk of accidents, through effective design and implementation of advanced chassis control systems

(Fig. 3.2). As a result, the problem of vehicle state estimation has attracted considerable attention of many researchers, and many studies have been conducted to estimate vehicle states using model-based and/or kinematics-based estimation techniques.

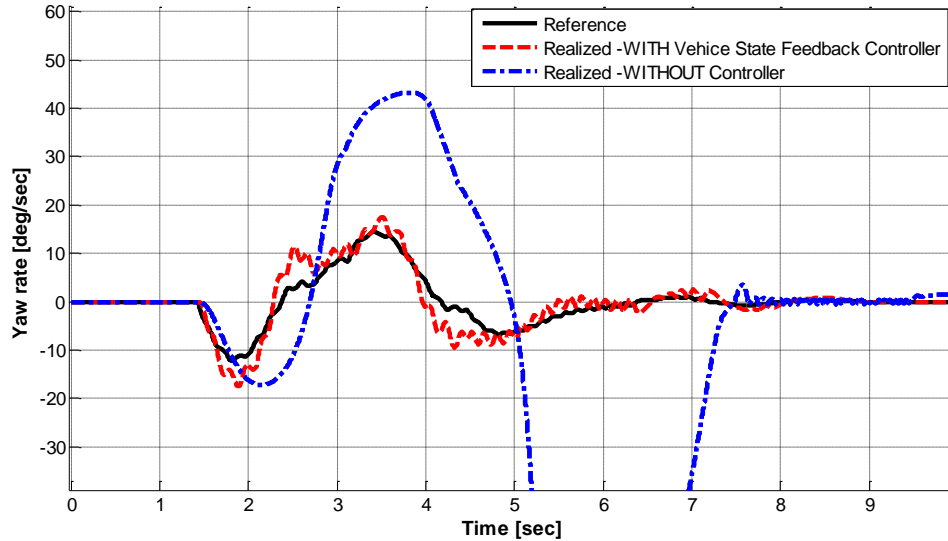


Fig. 3.2: Performance in tracking of the desired vehicle yaw rate for an evasive lane change maneuver; WITH a vehicle state feedback controller and WITHOUT a controller

A summary description of the state-of-the-art in the field of vehicle state estimation is given in Table 3.1. In [1-3], a sliding mode observer is proposed to estimate tire-road forces, while an extended Kalman filter estimates sideslip angle and cornering stiffness. [4-6], presents an extended Kalman filter based estimation process for lateral load transfer and wheel-ground contact normal forces. In [7-8], a recursive least square scheme for the online estimation of vehicle mass is examined. [9], presents a scheme for longitudinal/lateral tire-force estimation using a random-walk Kalman filter. In [10-14], two observers derived from extended and unscented Kalman filtering techniques are proposed and compared to estimate tire-road forces and vehicle sideslip angle. A method for the evaluation of a risk skid indicator based on the estimation of the maximum friction coefficient is proposed in [15-17]. [18], presents a method to estimate the road profile elevation based on a classical Kalman filter. [19], presents a nonlinear vehicle sideslip observer with reduced computational complexity compared to an extended Kalman filter. In [20-21], an extended Kalman filter based method is presented to estimate the dynamic state and tire-road forces for a nonlinear vehicle model. In [22-23], cascaded observers,

based on first or second order sliding modes, are used to estimate the contact forces. [24], presents a tire force estimator, designed by accounting for the dependency between the longitudinal and lateral tire forces by introducing the friction ellipse into the estimation algorithm. In [25-26], an extended Kalman filter and Luenberger observer based method for the estimation of the vehicle dynamics using a nonlinear vehicle model is proposed. [27-30], presents a nonlinear observer using unscented Kalman filter to estimate sideslip angle. In [31], lateral tire forces, obtained from a multi-sensing hub unit, are used to estimate vehicle lateral velocity and roll angle using a recursive least square algorithm and a Kalman filter. [32-33], presents a vehicle lateral and longitudinal velocity estimation method using an adaptive/unscented Kalman filter. In [34], an algorithm for the estimation of longitudinal vehicle speed, based on the measurements of the four wheel rotational speeds and of the longitudinal vehicle acceleration is presented. In [35], a fuzzy logic is used to get an estimate of the vehicle longitudinal velocity; together with the estimated vehicle longitudinal acceleration, a Kalman filter is used to estimate the velocity of vehicle for use in ESC control applications. [36-37], present a Kalman filter based approach to estimate roll angle and roll rate with either a three-degree-of freedom (3DOF) or 1DOF vehicle model. In [39], an estimator designed on the basis of a three-degree-of-freedom vehicle maneuvering model and a four-degree-of-freedom half-car suspension model is used to obtain estimates of the vehicle roll angle and roll rate in driving situations in which both maneuvering and road disturbances affect the vehicle roll motions. In [40], an approach using a closed-loop adaptive observer for estimating roll angle and roll rate of vehicle body with respect to the road is proposed. [41-42], focuses on algorithms to estimate roll angle and c.g. height. The algorithms investigated include a sensor fusion algorithm that utilizes a low frequency tilt angle sensor and a gyroscope and a dynamic observer that utilizes only a lateral accelerometer and a gyroscope. In [43], two rollover indexes are proposed and analyzed. The first rollover index estimates the actual Lateral Transfer Ratio (LTR) while the second, referred to as 'Predictive Lateral Transfer Ratio' (PLTR), incorporates the predictive influence of the driver's steering input. [44], focuses on the accurate estimation of the vehicle states, including the longitudinal, lateral, and vertical velocities, as well as the roll and pitch angles, using merging schemes, that combine the kinematic and model-based observer outputs. [45-47], present methods for estimation of road inclination and bank angle. In [48], a scheme for the vehicle roll angle is derived based on the combination of sensors from vehicle dynamics control

system and a rollover mitigation system. In [49-50], method for compensating the gravity components of the lateral acceleration is proposed. [51], presents a model based estimation method that utilizes pneumatic trail information in steering torque to identify a vehicle's lateral handling limits.

Table 3.1: State-of-the-Art Literature Review

Measurements Used	Estimated States	Model Used	Estimation Methodology	Reference
r, a_y, a_x, δ	Tire forces and vehicle sideslip angle	Single-track model	SMO, EKF	[1-3]
a_y, a_x, δ_{sus}	Tire normal force	Vehicle roll dynamic model	EKF	[4-6]
$a_x, v_x, r, \lambda, T_e, T_b$	Vehicle mass	Longitudinal dynamics	RLS	[7-8]
$r, a_y, a_x, \delta, \omega_w, T_e, T_b$	Tire forces	Wheel dynamics model, vehicle planar model	KF	[9]
$a_y, a_x, \delta_{sus}, r, p, \delta, \omega$	Tire forces and vehicle sideslip angle	Four-wheel vehicle model	EKF, UKF	[10-14]
$a_y, a_x, \delta_{sus}, r, p, \delta, \omega$	Tire-road friction coefficient and vehicle lateral skid indicator	Four-wheel vehicle model	EKF, UKF, NLLS	[15-16]
$a_y, a_x, \delta_{sus}, r, p, \delta, \omega$	LTR (Lateral load transfer) and LSI (Lateral skid indicator)-	Four-wheel vehicle model	EKF, UKF, NLLS	[17]

	Accident risk prediction			
a_y, δ_{sus}	Road profile and wheel load	Quarter-car model	KF	[18]
r, a_y, a_x	Vehicle sideslip angle	Kinematics model	Nonlinear observer	[19]
r, a_y, a_x, ω	Tire forces	Nonlinear vehicle model	EKF	[20-21]
T_w, v_x, θ_w	Velocities and accelerations of the wheels, tire forces (vertical and longitudinal) and friction coefficient	Wheel dynamics model	Robust differentiator and sliding modes	[22-23]
T_w, ω, r, a_x, a_y	Tire forces and vehicle parameter estimation	Wheel dynamics model, vehicle planar model, Friction ellipse	Model based	[24]
$r, a_x, a_y, \omega, \delta$	Tire forces and road grade	Four wheel vehicle model	EKF, Luenberger observer	[25-26]
a_x, a_y, ω, δ	Vehicle sideslip angle and yaw rate	Bicycle model	UKF	[27-28]
a_x, a_y, r	Vehicle sideslip angle	Kinematic model	EKF	[29]
a_x, a_y, v_x, δ, r	Vehicle sideslip angle, lateral tire road forces and tire road friction coefficient	Four-wheel vehicle model	UKF	[30]

F_y	Vehicle sideslip angle	Yaw plane model	RLS	[31]
$r, a_x, a_y, \omega, \delta$	Vehicle longitudinal and lateral velocity	Bicycle model	AKF, UKF	[32-33]
a_x, ω	Vehicle longitudinal velocity	Kinematics-based	Rule Based	[34]
a_x, ω	Vehicle longitudinal velocity	Yaw plane model	KF, Fuzzy logic	[35]
a_y, p	Roll angle	Vehicle roll dynamic model	KF	[36-37]
a_y, r, δ	Roll angle and roll rate	Lateral-dynamics-model a four-degree-of-freedom half-car suspension model	KF	[38-39]
a_y, p	Roll angle	Vehicle roll dynamic model	Closed loop adaptive observer	[40]
$a_y, p, \phi_{\text{tilt angle sensor}}$	Roll angle and center of gravity height	Kinematic sensor fusion, Vehicle roll dynamic model	Sensor fusion	[41-42]
a_y, p	Load Transfer Ratio	Vehicle roll dynamic	Model based	[43]

	(LTR) and Predictive Load Transfer Ratio (PLTR)	model		
a_x, a_y, a_z, p, q, r	Roll and pitch angles, longitudinal, lateral, and vertical velocities	Kinematic and model-based (bicycle model) observer	Merging schemes	[44]
a_y, r, δ	Road bank angle	Bicycle model	Transfer function approach, superposition	[45]
$a_x, a_y, p, q, r, \omega$	Vehicle roll and pitch angles	Kinematics-based observer	State observer	[46]
$r, a_x, a_y, \omega, \delta$	Road bank and grade angles	Kinematic model	Observers using time-varying gains	[47]
p	Roll angle	Vehicle roll dynamic model	Controlled integration	[48]
a_y, r, v_x, p	Roll angle	Vehicle roll dynamic model, Kinematic model	Vehicle state index based switching	[49]
$r, \omega, \delta, a_y, p$	Vehicle roll angle and Sideslip angle	Kinematic model	Weighting function	[50]
r, δ, a_y, v_x	Tire Slipangle	Bicycle model	State observer	[51]

SMO: Sliding mode observer, KF: Kalman Filter, EKF: Extended Kalman Filter, UKF: Unscented Kalman Filter, AKF: Adaptive Kalman Filter, RLS: Recursive least squares, NLLS: Nonlinear least squares.

This study introduces an integrated vehicle state estimator, comprising of a series of model-based and kinematics-based observers, and an effectively designed merging scheme, that ensures robust estimation performance even during the vehicle maneuvers which show highly nonlinear tire characteristics, and in the existence of road inclination or bank angle. In this study, it is assumed that measurements from a 6-axis Inertial Measurement Unit (IMU) (3-axes of rotation rate measurement, and 3-axes of acceleration measurement), wheel speed sensors, and steering wheel angle sensor are available.

The basic organization of this chapter is as follows: Section 3.2.1 contains information on the general layout of the observer with the data flow description. Section 3.2.2 denotes the principle behind the chassis roll angle estimator. Section 3.2.3 describes the method for chassis pitch angle estimation. Section 3.2.4 focuses on the vehicle roll (global roll) and pitch angle (global pitch) observer design. Section 3.2.5 describes the method to compensate the measured acceleration signals for gravity. Section 3.2.6 focuses on the method to estimate the vehicle longitudinal velocity. Section 3.2.7 describes the method to estimate the tire vertical load. Section 3.2.8 presents a scheme for longitudinal/lateral tire-force estimation. Section 3.2.9 describes a method for estimating the vehicle lateral and longitudinal velocity. Section 3.2.10 proposes an estimation procedure for the tire slip-ratio and slip-angle, and conclusions are finally given in Section 3.3.

3.2 Observer Design

3.2.1 General Observer Flow Chart

The block diagram in Fig. 3.3 explicitly shows the estimation process in its entirety. The entire process is separated into five blocks: the first block serves to identify the road bank and grade angles (using a kinematics-based observer) and vehicle chassis roll (using a Kalman filter) and pitch angles (with vehicle mass adaptation) , the second block contains a bias compensation algorithm (gravity compensation in accelerometer measurements), a vehicle longitudinal speed estimation algorithm (based on the measurements of the four wheel rotational speeds and the gravity-compensated longitudinal vehicle acceleration) and a tire load estimation algorithm (using gravity-compensated acceleration information and roll/pitch states), the third block contains a tire longitudinal/lateral force estimation observer (sliding-mode observer based),

while the fourth block contains a nonlinear vehicle longitudinal and lateral velocity observer (based on unscented Kalman filter), designed for the purpose of vehicle side-slip estimation. Finally, the fifth block makes use of the estimations provided by the third and the fourth block to estimate the tire slip-ratio and slip-angle (Luenberger observer based).

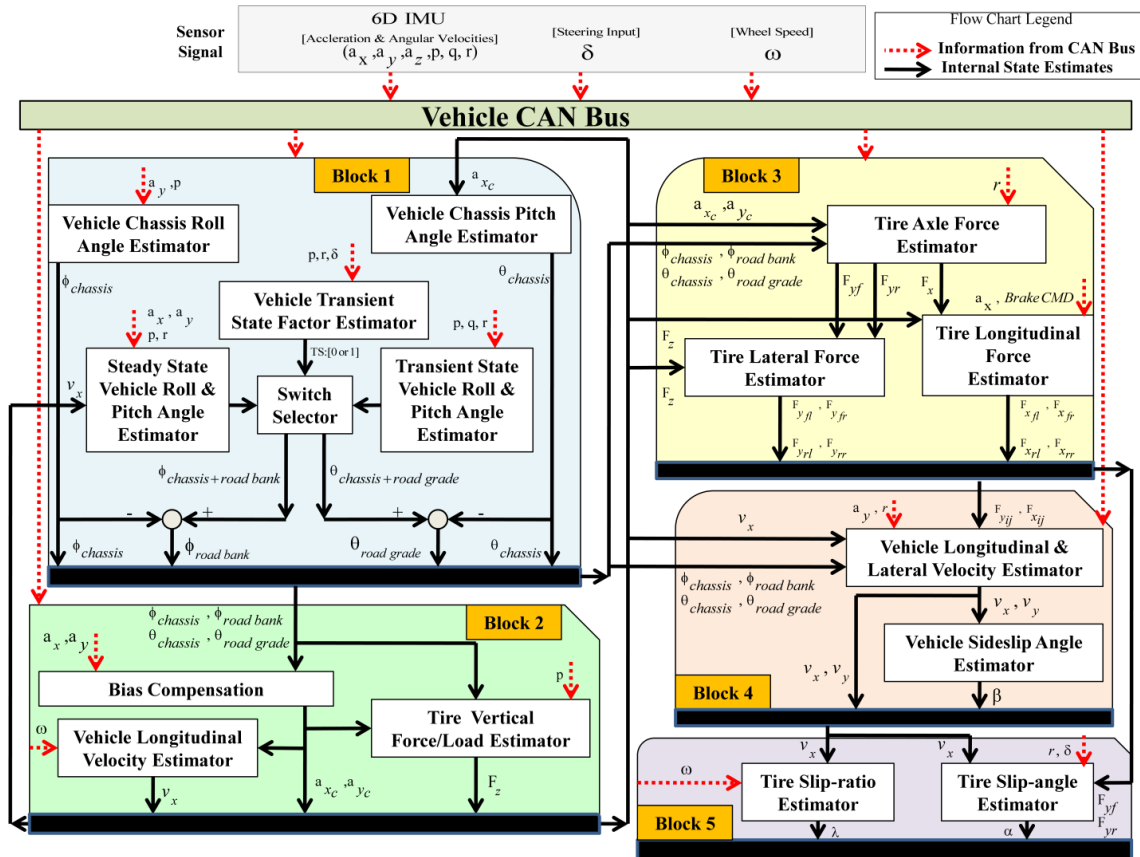


Fig. 3.3: Functional diagram of the estimation process

3.2.2 Vehicle Chassis Roll Angle Estimator

3.2.2.1 Modeling Approach

Roll angle is an important variable that plays a critical role in the calculation of real-time rollover index for a vehicle [39]. Vehicle models widely used to estimate roll angle and roll rate include: 1) 3DOF model, which represents yaw, lateral, and roll motions of a vehicle (Fig. 3.4a), and 2) 1DOF model, which represents only roll motion of a vehicle (Fig. 3.4b). As shown in previous work [36], roll-angle estimation accuracy using the 3DOF model is adversely affected by the linear tire model that it assumes. On the other hand, the 1DOF model, which does not rely on any

tire model, uses the lateral acceleration directly. Therefore, the 1DOF model is not sensitive to the nonlinear tire dynamics. Also, the 1DOF model has a practical advantage over the 3DOF model in terms of the required model parameters. The 3DOF model requires the cornering stiffness, which varies with road surface and tire condition and is not easy to estimate online. Although the 1DOF model also needs roll stiffness and damping coefficients, these parameters are usually available since vehicle manufacturers routinely measure them before production and they do not change significantly over the lifetime of the vehicle. With these considerations, in this study, a 1DOF model was considered for the purpose of designing a roll angle estimator.

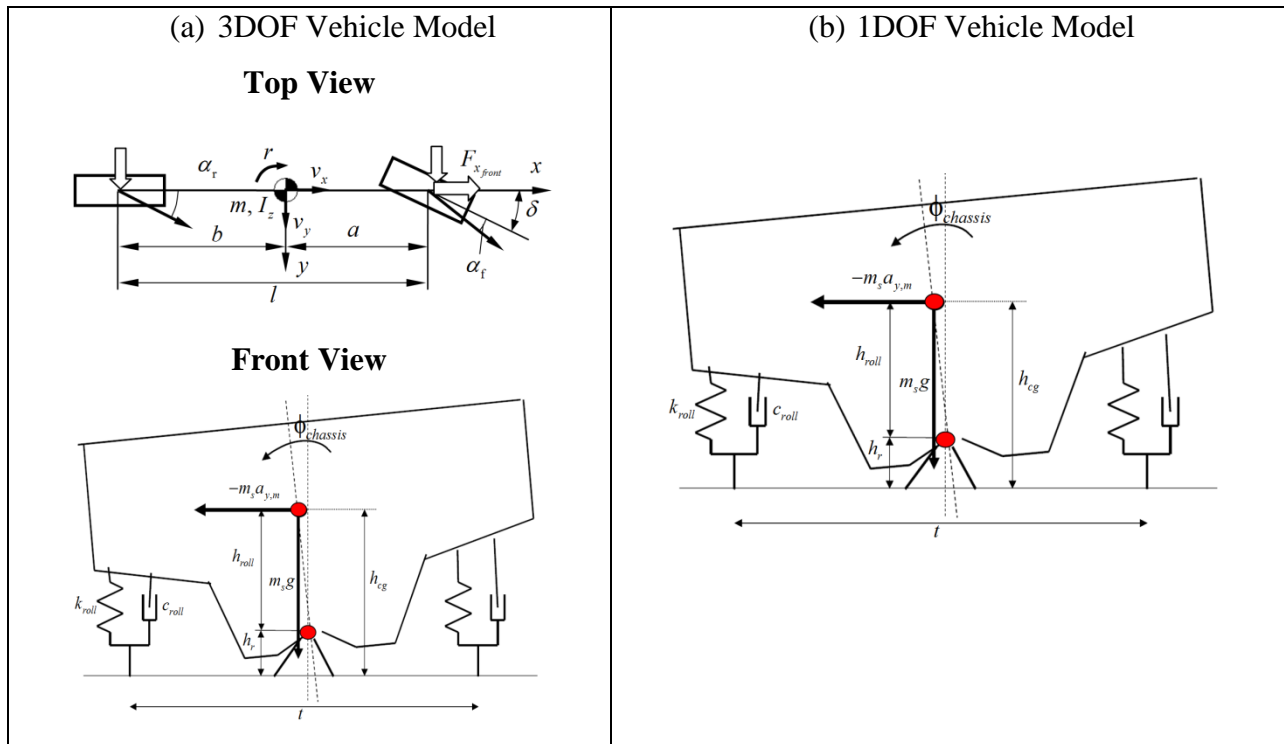


Fig. 3.4: (a) Linear 3DOF yaw-roll vehicle model, and (b) 1DOF roll dynamics model

The following assumptions are made in the case of a 1DOF roll dynamics model:

- The roll axis is fixed
- The roll angle does not change depending on payload
- The roll stiffness and damping coefficient are constants
- There is no vertical motion of the vehicle

Using these assumptions and also taking into account the effect of gravity, the equation of vehicle chassis roll motion (according to the torque balance about the roll axis) is:

$$(I_x + m_s h_{roll}^2) \ddot{\phi}_{chassis} + c_{roll} \dot{\phi}_{chassis} + k_{roll} \phi_{chassis} = -m_s h_{roll} a_{y,m} \quad (3.1)$$

Here $I_x + m_s h_{roll}^2$ is the moment of inertia of vehicle body with respect to the roll axis, c_{roll} is the combined roll damping of suspension and tires, and k_{roll} is the combined roll stiffness of suspension and tires. The lateral acceleration used in Equation (3.1) is the measured lateral acceleration, $a_{y,m} = a_y + g \sin(\phi_{chassis})$, which includes the effect of the gravity component, contributing to the roll moment.

The corresponding state-space realization of the model described by Equation (3.1) can be given as follows:

$$\begin{bmatrix} \dot{\phi} \\ \ddot{\phi} \end{bmatrix} = \begin{bmatrix} 0 & 1 \\ \frac{-k_{roll}}{I_x + m_s h_{roll}^2} & \frac{-c_{roll}}{I_x + m_s h_{roll}^2} \end{bmatrix} \begin{bmatrix} \phi \\ \dot{\phi} \end{bmatrix} + \begin{bmatrix} 0 \\ \frac{-m_s h_{roll}}{I_x + m_s h_{roll}^2} \end{bmatrix} a_{y,m} \quad (3.2)$$

Assuming roll rate measurement is available (from a 6-axis IMU), an estimator based on the Kalman filter is implemented to estimate vehicle states (Fig. 3.5). The states are roll angle and roll rate and the input is the measured lateral acceleration. The state feedback is the measured roll rate.

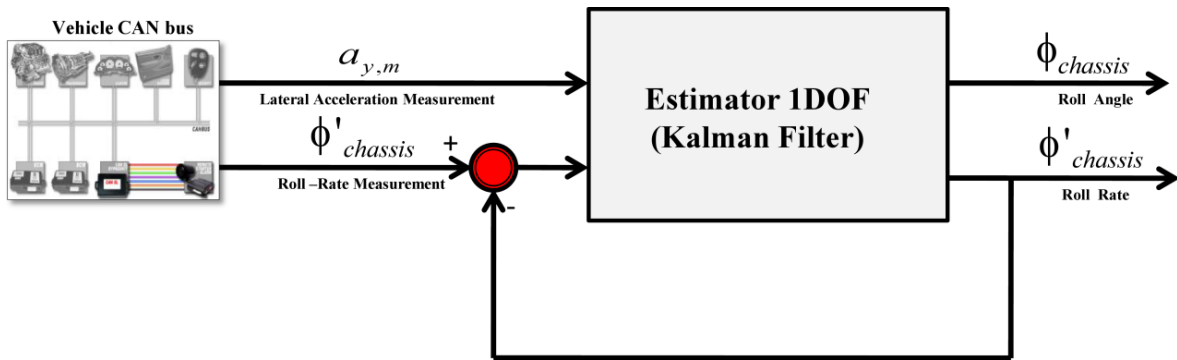


Fig. 3.5: Roll estimation based on a 1DOF model

3.2.2.2 Kalman Filter - Estimation Concept

The Kalman filter is essentially a set of mathematical equations that implement a predictor-corrector type estimator that is optimal in the sense that it minimizes the estimated error covariance—when some presumed conditions are met [52]. The Kalman filter addresses the general problem of trying to estimate the state of a discrete-time controlled process that is governed by the linear stochastic difference equation:

$$\begin{aligned}x_k &= Ax_{k-1} + BU_{k-1} \\y_k &= Cx_k + DU_k\end{aligned}\tag{3.3}$$

The matrix A in the difference Equation (3.3) relates the state at the previous time step to the state at the current step, in the absence of either a driving function or process noise. Note that in practice A might change with each time step, but here we assume it is constant. The matrix B relates the optional control input to the state. The matrix C in the measurement equation relates the state to the measurement. In practice C might change with each time step or measurement, but here we assume it is constant. The matrix D in the measurement equation relates the control input to the measurement.

The real dynamic systems are subjected to a variety of “noise” signals that corrupt the response (Fig. 3.6a). The process noise (w_{k-1}) corrupt the states and the sensor noise (θ_K) corrupt the output. The modified governing equations incorporating the effects of these exogenous inputs can be written as:

$$\begin{aligned}x_k &= Ax_{k-1} + BU_{k-1} + Fw_{k-1} \\y_k &= Cx_k + DU_k + \theta_K\end{aligned}\tag{3.4}$$

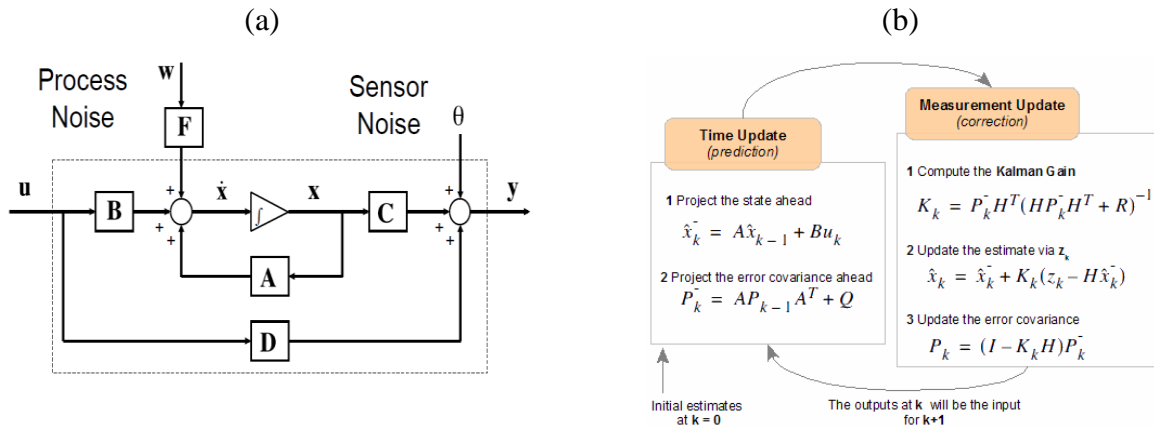


Fig. 3.6: (a) Incorporating the effect of process noise (w) and sensor noise (Θ) in the system dynamics, and (b) a complete picture of the operation of the Kalman filter

We desire to obtain an optimal estimate of the state vector \hat{x}_k , using noisy measurements of the output vector y_k that minimizes the following mean squared error:

$$J = E [(\hat{x}_k - x_k)^T (\hat{x}_k - x_k)] \quad (3.5)$$

where $(\hat{x}_k - x_k)$ is the state estimation error vector.

For the three inputs (U_k , w_k and Θ_k) to the discrete time state-space system:

- U_k is always known because it is the control signal that we are creating (i.e. deterministic process)
- w_k and Θ_k are never known completely because they are not directly measurable nor are they predictable (i.e. stochastic process)
- We almost always know something about w_k and Θ_k such as the mean and covariance statistics. Here they are assumed to be independent (of each other), white, and with normal probability distribution ($p(w) \sim N(0, Q)$, $p(\Theta) \sim N(0, R)$).

Consequently, we have two sources of information that can help us in estimating the state of the system at time k . First, we can use the equations that describe the dynamics of the system.

$$\hat{x}_k = A\hat{x}_{k-1} + BU_{k-1} \quad (3.6)$$

A second useful source of information is our observation y_k .

$$\hat{y}_k = C\hat{x}_k \quad (3.7)$$

We might pick \hat{x}_k so as to minimize $\|y_k - C\hat{x}_k\|$. There's an obvious trade-off between these two methods of estimating x_k . The Kalman filter produces a weighted combination of these two estimates that is optimal in the sense that it minimizes the uncertainty of the resulting estimate.

$$\hat{x}_k = A\hat{x}_{k-1} + BU_{k-1} + K_K(y_k - \hat{y}_k) \quad (3.8)$$

This is achieved in a five step procedure shown below (Fig. 3.6b):

Step 1: Prediction of state

$$\hat{x}_{\bar{k}} = A\hat{x}_{k-1} + BU_{k-1}$$

Step 2: Prediction of covariance

$$\hat{P}(\hat{x}_{\bar{k}}) = A\hat{P}(\hat{x}_{k-1})A^T + Q$$

Where Q is the covariance of w_{k-1}

Step 3: Calculate the Kalman gain matrix

$$K_K = \hat{P}(\hat{x}_{\bar{k}})H^T(H\hat{P}(\hat{x}_{\bar{k}})H^T + R)^{-1}$$

Where R is the covariance of Θ_K

Step 4: Update the state estimate

$$\hat{x}_k = \hat{x}_{\bar{k}} + K_K(y_k - \hat{y}_k)$$

Where $\hat{y}_k = C\hat{x}_{\bar{k}}$

Step 5: Update the covariance matrix

$$\hat{P}(\hat{x}_k) = (1 - K_K H)\hat{P}(\hat{x}_{\bar{k}})$$

3.2.2.3. Estimator Performance

The performance of the Kalman filter based estimator was examined under a simulated double lane change (Fig. 3.7a) and fishhook maneuver (Fig. 3.7b) to verify the effectiveness under aggressive driving conditions.

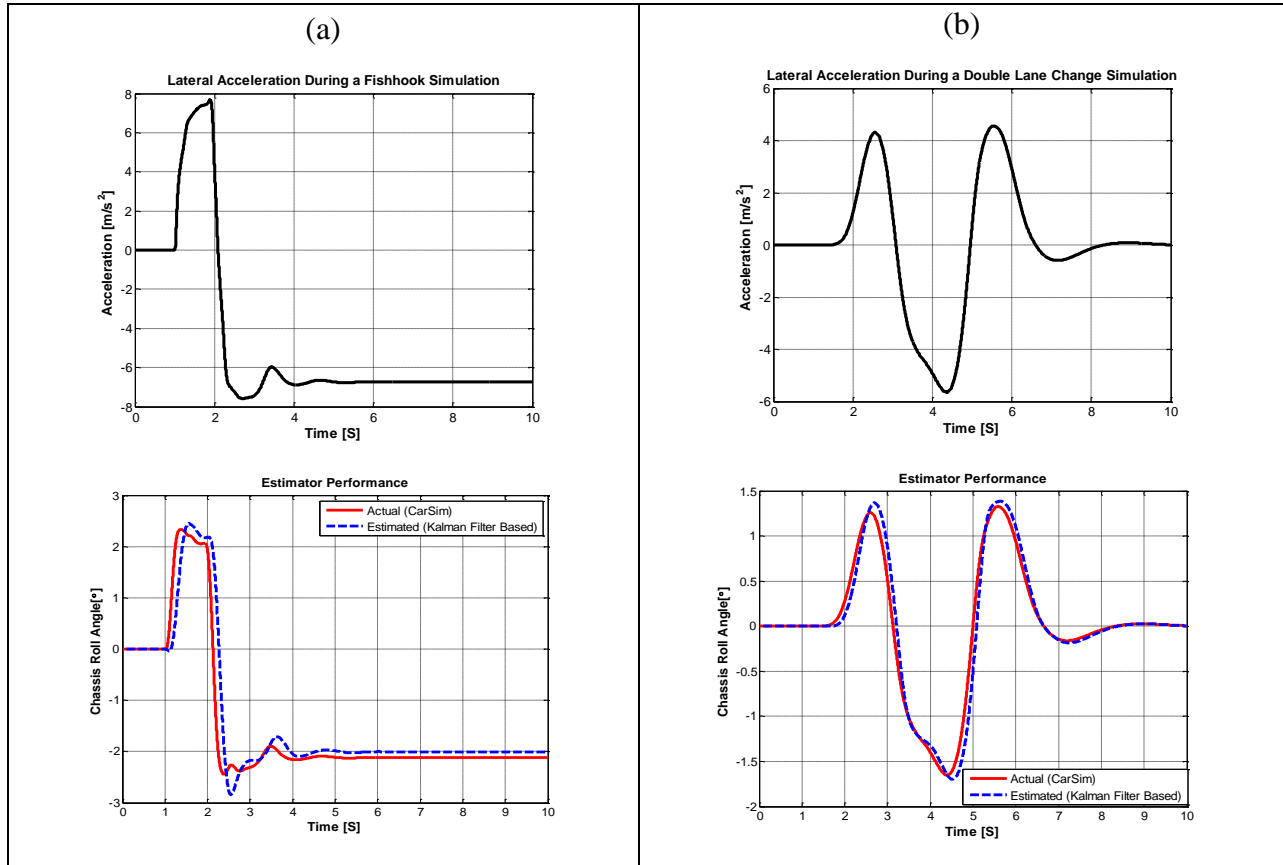


Fig. 3.7: Estimator performance: (a) fishhook maneuver, and (b) double lane change maneuver

It was observed from this study that an accurate estimate of the vehicle chassis roll angle could be achieved using the above mentioned approach, even under aggressive driving conditions.

3.2.3 Vehicle Chassis Pitch Angle Estimator

3.2.3.1 Modeling Approach

During a strong deceleration (acceleration) phase, the vehicle experiences a load transfer from the rear to the front axle (or the opposite), which causes, due to suspensions elasticity, a non zero vehicle pitch angle (Fig. 3.8).

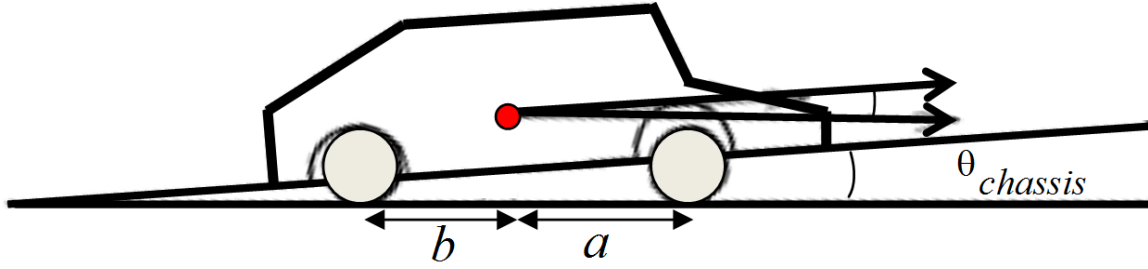


Fig. 3.8: Longitudinal vehicular load transfer under acceleration

According to Hooke's law, we can compute the suspension springs compression (Δx) due to load variation (ΔF_z) as $\Delta x = \Delta F_z/k$, where k is the spring elastic constant. Hence, the pitch angle can be approximated by its tangent as:

$$\theta_{chassis} = \frac{2 \cdot \Delta x}{(a + b)} = \frac{2 \cdot \Delta F}{k \cdot (a + b)} \quad (3.9)$$

The longitudinal load transfer (axle load variation) can be estimated using the vehicle's longitudinal acceleration as:

$$\Delta F = \frac{m_s \cdot h_{cg}}{(a + b)} a_{x,c} \quad (3.10)$$

where $a_{x,c}$ is the bias-compensated longitudinal acceleration signal and is given by the expression $a_{x,c} = a_{x,m} + g \cdot \sin(\theta_{chassis})$. A methodology to compensate the measured acceleration signal for the gravity component is given in Section 3.2.5. Substituting Equation (3.10) in (3.9), we get an expression for the chassis pitch angle as:

$$\theta_{chassis} = \frac{2 \cdot m_s \cdot h_{cg}}{k \cdot (a + b)} a_{x,c} \quad (3.11)$$

Since chassis pitch angle is calculated through a linear model, the parameters used in the model are functions of characteristics such as the height of the c.g. and the sprung mass. One challenge with using these parameters in computing $\theta_{chassis}$ is that they vary with the vehicle loading

conditions (Fig. 3.9). If the above parameters are fixed at certain nominal values, it is conceivable that optimal estimation performance may not be achieved under a different loading condition. For example, if the parameters in the chassis pitch angle model are determined based on nominal vehicle loading condition assumptions, without considering variations due to loading, the chassis pitch angle may be under estimated for vehicles with load that raises the c.g. On the other hand, if the parameters in the chassis pitch angle model are determined based on a certain loading condition that raises the c.g., it may be over estimated for vehicles without load. In order to improve the overall performance of the estimation process, it is desirable to estimate and update the vehicle parameters periodically or adaptively adjust them in real time based on the actual behavior of the vehicle.

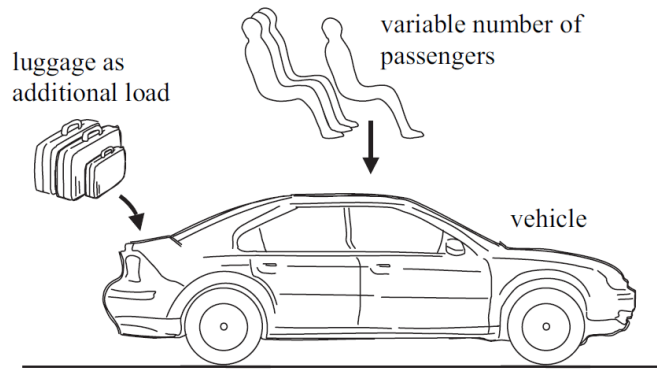


Fig. 3.9: Parameter variations: mass can change

3.2.3.2 Vehicle Sprung Mass Estimation

The estimation approach proposed here is a model-based approach (using equations for the longitudinal motion of the vehicle (Fig. 3.10a). Vehicle's acceleration is a result of a combination of wheel drive and braking torques and the road loads on the vehicle. The dynamic equation for the vehicle motion is:

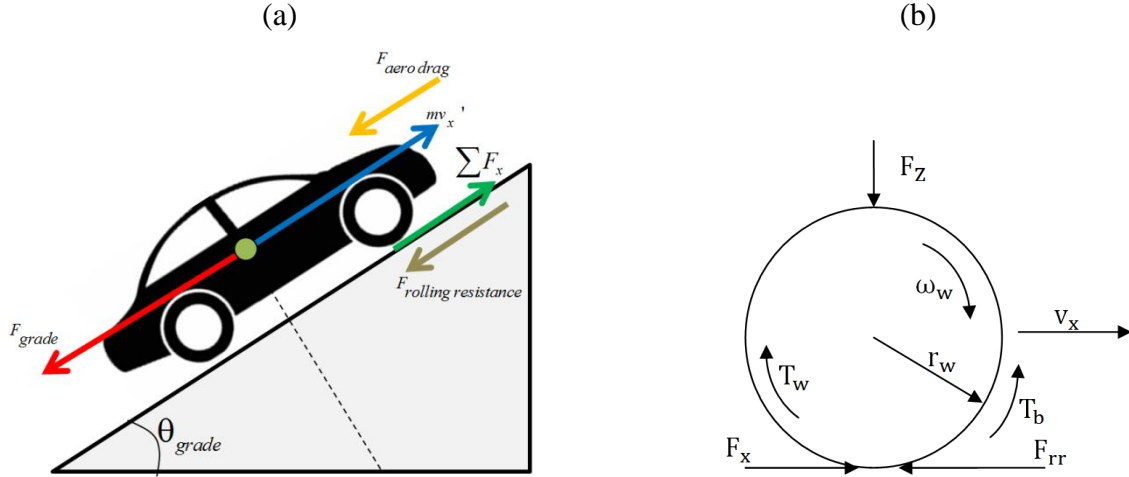


Fig. 3.10: (a) Longitudinal vehicle dynamics model, and (b) simplified wheel dynamics model

$$m\dot{v}_x = \sum F_x - F_{aero\ drag} - F_{grade} - F_{rolling\ resistance} \quad (3.12)$$

where:

$\sum F_x$: summation of the tire forces generated at all the four tires

$F_{aero\ drag}$: aerodynamic drag force ($\frac{1}{2}\rho C_d A_f v_x^2$)

F_{grade} : road grade force ($mg\sin\theta_{grade}$)

$F_{rolling\ resistance}$: rolling resistance ($f_r mg\cos\theta_{grade}$)

$$or\ m\dot{v}_x = (F_{x_{fl}} + F_{x_{fr}} + F_{x_{rl}} + F_{x_{rr}}) - \frac{1}{2}\rho C_d A_f v_x^2 - mg\sin\theta_{grade} - f_r mg\cos\theta_{grade}$$

Rearranging the above Equation yields an expression for the vehicle mass as:

$$m = \frac{(F_{x_{fl}} + F_{x_{fr}} + F_{x_{rl}} + F_{x_{rr}}) - \frac{1}{2}\rho C_d A_f v_x^2}{\dot{v}_x + g\sin\theta_{grade} + f_r g\cos\theta_{grade}} \quad (3.13)$$

From the above expression, we can see that an estimate of the vehicle mass can be made by using information about the longitudinal tire forces, vehicle longitudinal velocity and road grade. To achieve the aforementioned objective of estimating vehicle mass, an integrated estimation scheme is proposed (Fig. 3.11). The estimation scheme consists of three key estimator blocks: 1)

tire longitudinal force estimator; 2) vehicle longitudinal velocity estimator; 3) road bank-grade angle estimator. The tire longitudinal force estimator is based on a simplified wheel dynamics model (Fig. 3.10b). The dynamic equation for the angular motion of the wheel is given as:

$$J\dot{\omega}_w = (T_w - T_b) - F_x r_w - F_{rr} r_w \quad (3.14)$$

where the subscripts have been omitted for convenience. The same estimator and equations hold for all the wheels. Rearranging Equation (3.14) yields an expression for the longitudinal force as:

$$F_x = \frac{(T_w - T_b) - J\dot{\omega}_w}{r_w} - F_{rr} \quad (3.15)$$

Here the wheel drive torque (T_w) can be estimated by using the turbine torque, the turbine angular velocity, and the wheel angular velocity [53]. It is assumed that the brake pressure of each wheel is an available signal. Therefore, the brake torque (T_b) can be computed by the brake gain (k_{bf}, k_{br}). F_{rr} , the wheel rolling resistance force is given by the expression:

$$F_{rr} = 0.005 + 3.24 \cdot 0.01 \cdot (r_w \cdot \omega_w)^2 \quad (3.16)$$

In a previous work [54] it has been shown that the accuracy of longitudinal force estimation using Eq. (3.15) heavily depends on the accuracy of the effective tire radius (r_w), and therefore, obtaining an accurate estimate of r_w is crucial. The effective tire radius (r_w) can be determined by the vertical load (estimation methodology for the vertical load is explained in Section 3.2.7) as:

$$r_{w,i} = r_o - \frac{F_{z,i}}{k_t} \quad (3.17)$$

Even though Equation (3.15) presents a relatively simple (open-loop) method to estimate the longitudinal tire force (i.e. we can calculate the longitudinal tire force directly using Eq. (3.15), or use a recursive least squares (RLS) method for a smoother estimation), it is not advisable to use this approach, since in real-world conditions, finding the time derivative of angular wheel speed signals ($\dot{\omega}_w$) can pose some challenges.

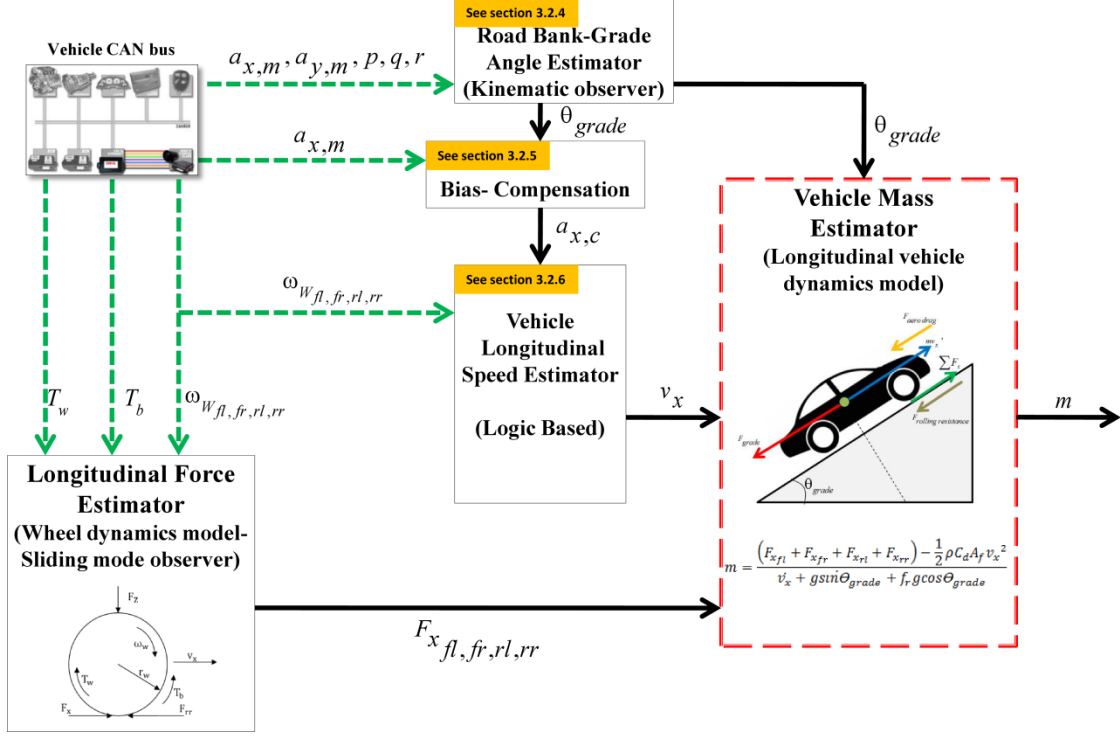


Fig. 3.11: Schematic diagram of the vehicle mass estimation process

To avoid the need to take derivatives of ω_w , a sliding mode observer (SMO) based estimation scheme is proposed. The SMO uses a sliding mode structure, with the state estimate ($\hat{\omega}_w$) evolving according to the wheel dynamics model (ref. Eq. (3.14)), the force model ($\dot{\hat{F}}_x = 0$; *i.e. tire forces are modelled with a random walk model*) and the sign of the measurement estimation error (difference between actual (ω_w) and estimated ($\hat{\omega}_w$) angular wheel speed) as:

$$J\dot{\hat{\omega}}_w = (T_w - T_b) - \hat{F}_x r_w - F_{rr} r_w + k_1 \text{sgn}(\omega_w - \hat{\omega}_w) \quad (3.18)$$

$$\dot{\hat{F}}_x = k_2 \text{sgn}(\omega_w - \hat{\omega}_w) \quad (3.19)$$

Here k_1 & k_2 are the observer gains and $\text{sgn}(\cdot)$ denotes signum function defined as:

$$\text{sgn}(s(t)) = \begin{cases} 1, & \text{if } s(t) > 0 \\ 0, & \text{if } s(t) = 0 \\ -1, & \text{if } s(t) < 0 \end{cases} \quad (3.20)$$

It is known that the discontinuous switching functions can be approximated by their continuous switching functions to avoid the chattering of the control force and to achieve the exponential stability. Instead of signum function, a saturation function has been used via introducing a thin boundary layer around the sliding surface to avoid chattering. For a more smooth change of the switching signal, a hyperbolic tangent function has also been used to improve the switching control effort.

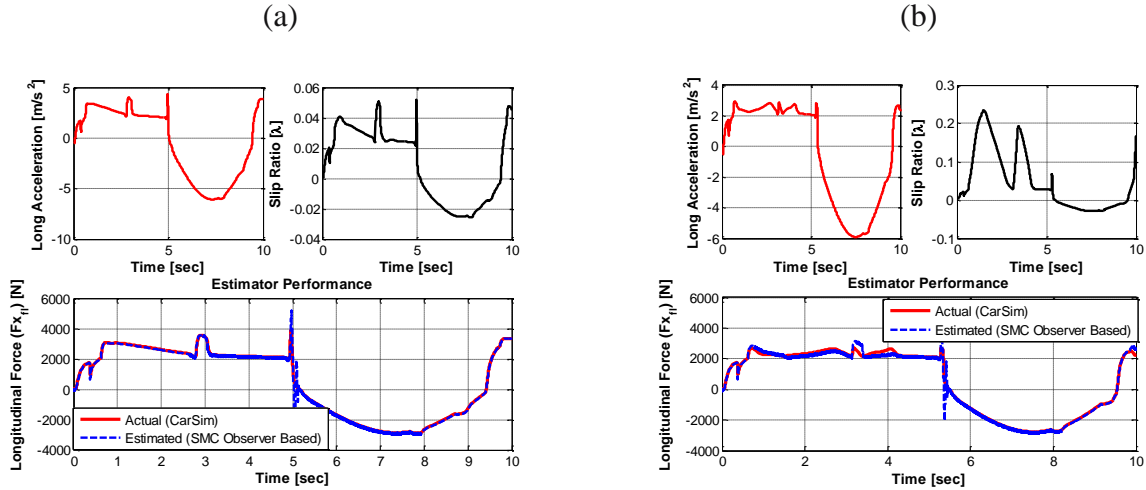


Fig. 3.12: Longitudinal force (individual tire) estimator performance: a) high μ surface condition, and (b) low μ surface condition

The results (Fig. 3.12a-Fig. 3.12b) show that the estimated longitudinal forces match the simulated forces very well. The proposed observer based on Equations (3.18) and (3.19) thus ensures stable estimation of the longitudinal tire force.

As previously mentioned, apart from the longitudinal tire force, the other variables required to estimate the vehicle mass include (ref. Eq. (3.13)): road grade angle and vehicle longitudinal velocity. The road grade angle (θ_{grade}) can be determined using a kinematics-based observer, as explained in Section 3.2.5. The vehicle longitudinal velocity (v_x) can be determined using the measurement of the four wheel rotational speed and longitudinal vehicle acceleration, as explained in Section 3.2.6. Finally, using information from the three aforementioned estimators, vehicle mass can be estimated using Equation (3.13). Even though we can directly use Equation (3.13), using a Recursive Least Squares (RLS) algorithm (by rewriting Equation (3.13) into a standard parameter identification form) results in smoother

estimates of the vehicle mass, as shown in Fig. 3.13. Details regarding the Recursive Least Squares (RLS) algorithm are given in Section 3.2.8.1.

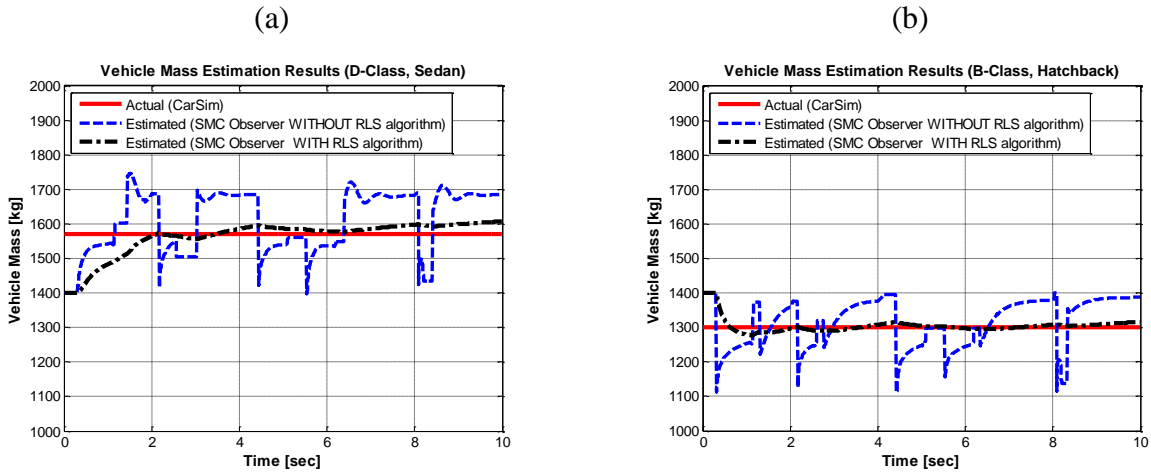


Fig. 3.13: Vehicle mass estimation results (a) D-class vehicle (sedan) driving on low μ surface, and (b) B-class vehicle (hatchback) driving on high μ surface

3.2.3.3 Estimator Performance

The performance of the chassis pitch angle estimator (ref. Eq. (3.11), with vehicle mass adaptation) was evaluated for a high speed straight-line braking maneuver (100-0 kph) for constant friction coefficient ($\mu_{constant}$) (Fig. 3.14a), and varying friction coefficient ($\mu_{varying}$) (Fig. 3.14b) conditions.

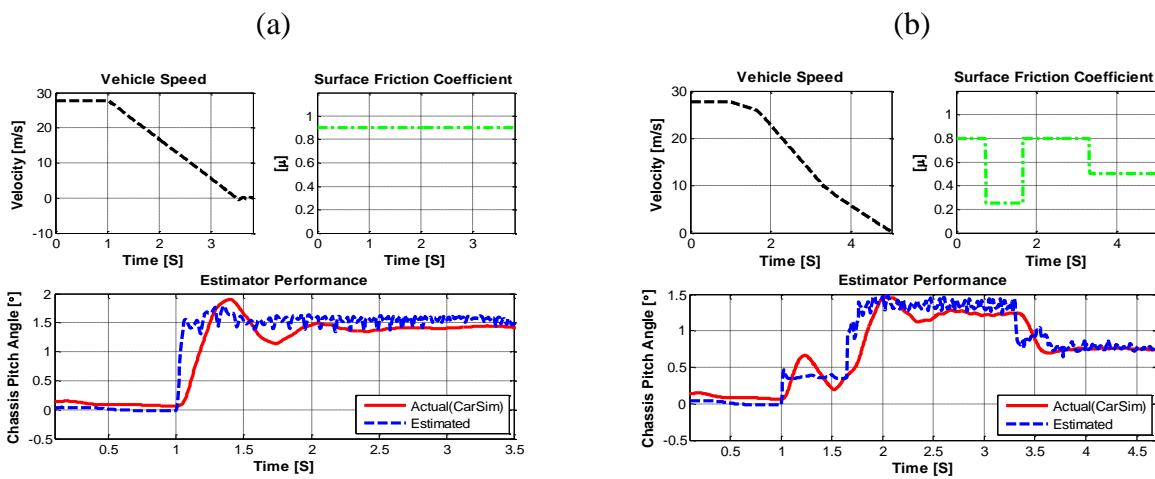


Fig. 3.14: Estimator performance: (a) straight-line braking maneuver (constant μ condition), and (b) straight-line braking maneuver (varying μ condition)

Satisfactory results were obtained in both the cases, as shown in Fig. 3.14.

3.2.4 Vehicle Roll and Pitch Angle Estimator

Knowledge of the vehicle roll and pitch angle is very important for satisfactory control performance. Analysis presented in Sections 3.2.2 and 3.2.3 described a methodology to estimate the vehicle chassis roll (local roll) and chassis pitch (local pitch) angle. The vehicle roll angle (global roll) consists of a combination of vehicle chassis roll angle and road bank angle (Fig. 3.15):

$$\phi_{vehicle\ roll} = \phi_{chassis} + \phi_{road\ bank} \quad (3.21)$$

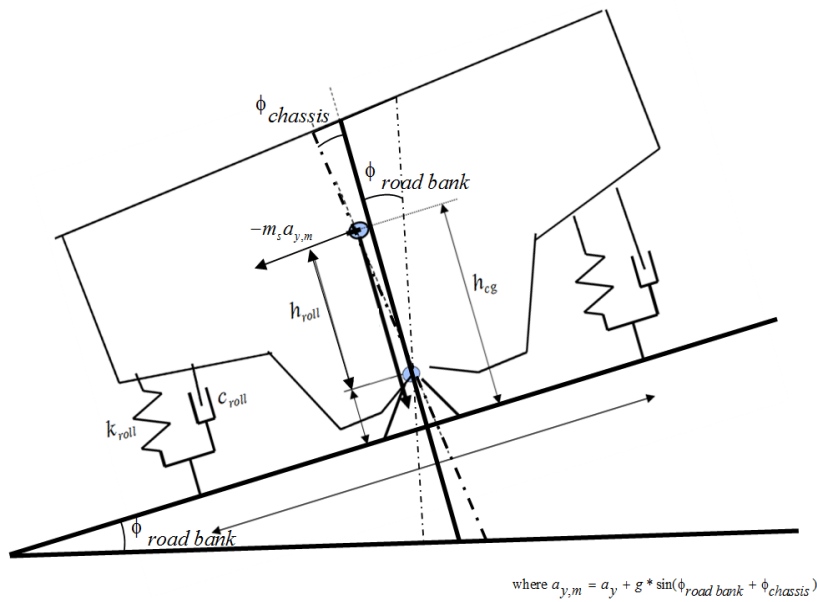


Fig. 3.15: Vehicle roll model

Similarly, the vehicle pitch angle consists of the combination of vehicle chassis pitch angle and road grade angle (Fig. 3.16):

$$\theta_{vehicle\ pitch} = \theta_{chassis} + \theta_{road\ grade} \quad (3.22)$$

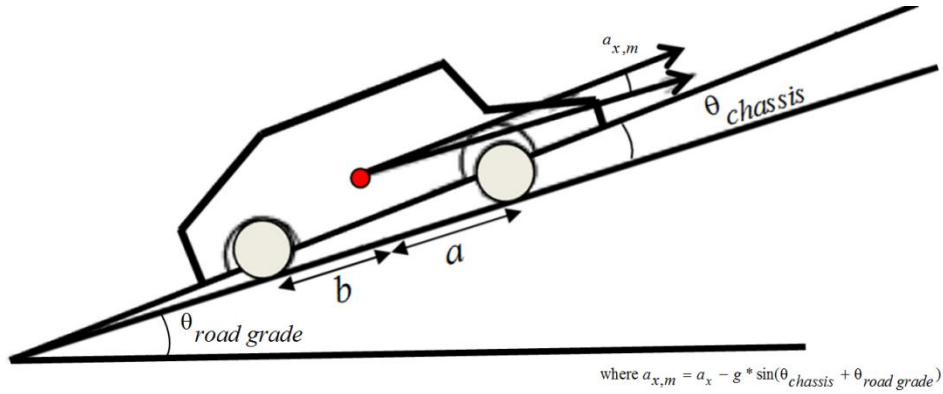


Fig. 3.16: Vehicle pitch model

The effect of vehicle chassis roll and pitch, as well as the dynamically changing road bank and road grade is significant, because they directly lead to the gravity components measured by the accelerometers, as shown below:

$$\begin{aligned}
 a_{x,m} &= a_x - g \cdot \sin(\theta_{vehicle\ pitch}) \\
 \Rightarrow a_{x,m} &= (v_x \dot{} - r \cdot v_y) - (g \cdot \sin(\theta_{vehicle\ pitch}))
 \end{aligned}
 \tag{3.23}$$

$$\begin{aligned}
 a_{y,m} &= a_y + g \cdot \sin(\phi_{vehicle\ roll}) \cdot \cos(\theta_{vehicle\ pitch}) \\
 \Rightarrow a_{y,m} &= (v_y \dot{} + r \cdot v_x) + (g \cdot \sin(\phi_{vehicle\ roll}) \cdot \cos(\theta_{vehicle\ pitch}))
 \end{aligned}
 \tag{3.24}$$

Rearranging the above equations, we have expressions for the vehicle chassis roll and pitch angles as:

$$\begin{aligned}
 \theta_{vehicle\ pitch} &= \arcsin \left(\frac{v_x \dot{} - r \cdot v_y - a_{x,m}}{g} \right) \\
 \phi_{vehicle\ roll} &= \arcsin \left(\frac{a_{y,m} - v_y \dot{} - r \cdot v_x}{g \cdot \cos(\theta_{vehicle\ pitch})} \right)
 \end{aligned}
 \tag{3.25}$$

In the following section, a methodology to estimate the vehicle roll and pitch angles under steady state conditions is presented.

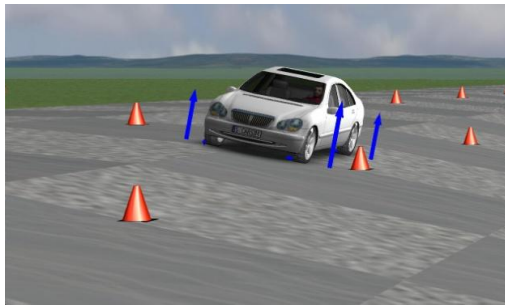
3.2.4.1 Steady State Vehicle Roll and Pitch Angle Estimator

In this section, steady state estimates of the vehicle pitch and roll angles are presented by utilizing the sensors typically available on vehicles equipped with electronic stability control or yaw stability control. As seen from Equation (3.25), vehicle pitch and roll angles can be calculated if $v_x, v_y, \dot{v}_x, \dot{v}_y$ were available. Although it is possible to obtain fairly accurate v_x and thus \dot{v}_x from wheel speed sensors when the wheel slip is small (see Section 3.2.6 for details), v_y and \dot{v}_y are generally not available on current production vehicles. Thus Equation (3.25) cannot be implemented. Fortunately, during many maneuvers, v_y or \dot{v}_y is fairly small and can be neglected. In such cases, the so-called steady state pitch and roll angles, $\theta_{vehicle\ pitch_{SS}}$ and $\phi_{vehicle\ roll_{SS}}$, respectively, are given by the following equations:

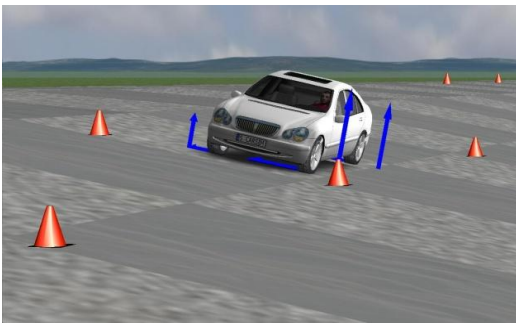
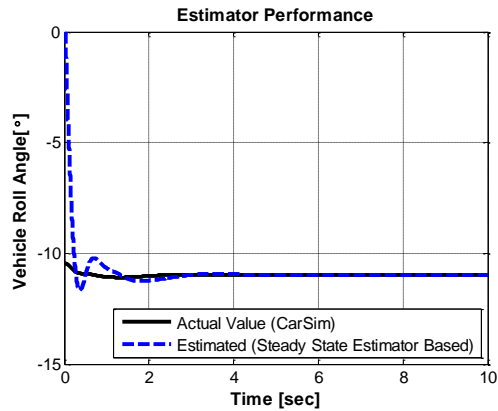
$$\theta_{vehicle\ pitch_{SS}} = \arcsin\left(\frac{\dot{v}_x - a_{x,m}}{g}\right) \tag{3.26}$$

$$\phi_{vehicle\ roll_{SS}} = \arcsin\left(\frac{a_{y,m} - r \cdot v_x}{g \cdot \cos(\theta_{vehicle\ pitch_{SS}})}\right)$$

Steady state means that the lateral motion of a vehicle is almost nonexistent (v_y or \dot{v}_y is fairly small and can be neglected), because the steering input is nearly constant or the variation of it is very small enough to neglect. The steady state estimate obtained from the algebraic manipulation of the kinematic laws only captures the low-frequency component of the vehicle attitude (Fig. 3.17)



(a)



(b)

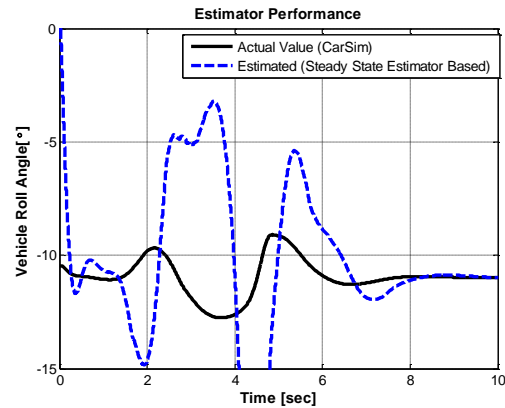


Fig. 3.17: Performance of the steady state vehicle roll angle estimator: (a) constant speed straight-line driving (steady state) on a banked road, and (b) double lane change maneuver (transient state) on a banked road

The underlying reason for the poor performance of the steady state estimator (Fig. 3.17b) is the assumption ($v_y \approx 0$ or $\dot{v}_y \approx 0$) on which the estimator works. This assumption is often violated during real life driving situations. For example, a vehicle performs an object avoidance maneuver on a highway ramp or a vehicle negotiating a mountain road may experience significant bank angle variation during the transient maneuver. Hence this estimate would contain significant bias in transient maneuvers. In the following section, a methodology to estimate the vehicle roll and pitch angles under transient state conditions is presented.

3.2.4.2 Transient State Vehicle Roll and Pitch Angle Estimator

Without loss of generality, it is assumed that the IMU is placed at the vehicle center of gravity, and there is no misalignment with respect to the vehicle body frame. Using the kinematic relationship between IMU output (vehicle-fixed frame) and the derivatives of the Euler angles (inertial frame), and assuming that the rotation rate of the earth is negligible, the equations of vehicle motion can be written as [55]:

$$\begin{aligned}
 \dot{\phi}_{vehicle\ roll} &= p + (q \cdot \sin \phi_{vehicle\ roll} + r \cdot \cos \phi_{vehicle\ roll}) \cdot \tan(\theta_{vehicle\ pitch}) \\
 \dot{\theta}_{vehicle\ pitch} &= q \cdot \cos \phi_{vehicle\ roll} - r \cdot \sin \phi_{vehicle\ roll} \\
 \dot{\psi}_{vehicle\ yaw} &= (q \cdot \sin \phi_{vehicle\ roll} + r \cdot \cos \phi_{vehicle\ roll}) \cdot \sec(\theta_{vehicle\ pitch})
 \end{aligned} \tag{3.27}$$

From the above relationships we can see that, theoretically, the vehicle roll ($\phi_{vehicle\ pitch}$) and pitch angles ($\theta_{vehicle\ pitch}$) can be computed via mathematical integration (open-loop integration), if the initial condition is known and angular rates (p, q, r) are measured by the gyro sensors. In practice, however, direct integration tends to drift due to sensor bias and inevitable numerical errors. To overcome limitations of an open-loop integration process, an alternative method is proposed. With the addition of an observer feedback term, $k(\theta_{chassis} - \hat{\theta}_{chassis})$, a new closed-loop observer is designed, motivated by [49], to estimate the vehicle roll-pitch angle under transient state conditions as:

$$\begin{aligned}
 \dot{\phi}_{vehicle\ roll_{TS}} &= p + (q \cdot \sin \phi_{vehicle\ roll_{TS}} + r \cdot \cos \phi_{vehicle\ roll_{TS}}) \tan(\theta_{vehicle\ pitch_{TS}}) \\
 &+ k(\theta_{chassis} - \hat{\theta}_{chassis}) \\
 \dot{\theta}_{vehicle\ pitch_{TS}} &= q \cdot \cos \phi_{vehicle\ roll_{TS}} - r \cdot \sin \phi_{vehicle\ roll_{TS}}
 \end{aligned} \tag{3.28}$$

where the subscript TS denotes transient state. The observer feedback term ($k(\theta_{chassis} - \hat{\theta}_{chassis})$), basically consists of a measurement estimation error, i.e. difference between actual $\theta_{chassis}$ and estimated $\hat{\theta}_{chassis}$ chassis roll angles. Here $\theta_{chassis}$ is obtained using a 1DOF roll dynamics model in conjunction with a Kalman filter (details given in Section 3.2.2). $\hat{\theta}_{chassis}$, is

obtained using information about the lateral load transfer ratio (LTR) (details given in Section 3.2.7.4), where the LTR is estimated using dynamic tire load estimates (details given in Section 3.2.7).

To fuse the steady state (ref. Eq. (3.26)) and transient state (ref. Eq. (3.28)) estimates, an index known as the vehicle transient state factor (*VTSF*) is defined, which represents the state of the vehicle (i.e. *VTSF*=1 (Transient State); *VTSF*=0 (Steady State)). The vehicle transient state factor (*VTSF*) is characterized as a function of the vehicle roll rate, derivative of the steering wheel angle and yaw rate.

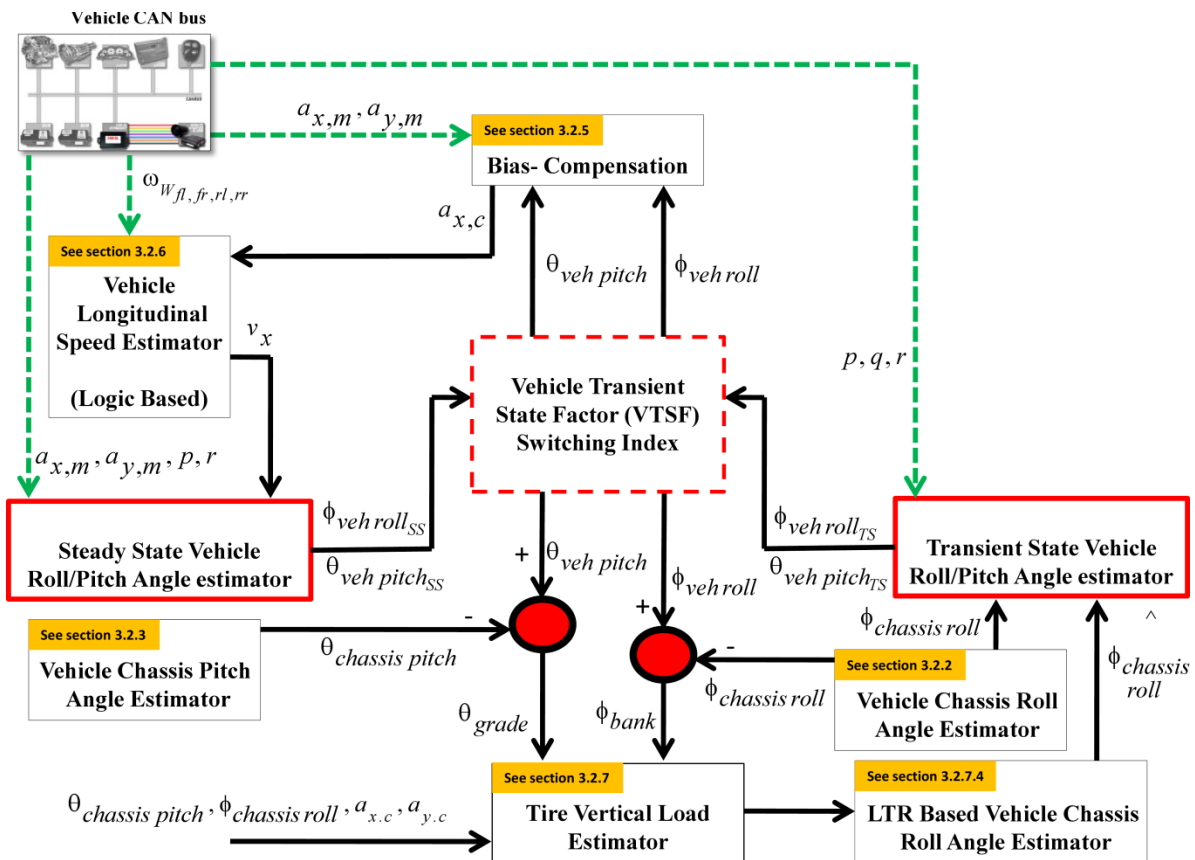


Fig. 3.18: Schematic diagram of the proposed vehicle roll/pitch angle estimation process

Finally, the vehicle roll angle is estimated using the vehicle steady state and transient state roll angles based on the vehicle state index switching (Fig. 3.18) as:

$$\phi_{vehicle\ roll} = \left[VTSF * \left(\int \left(\begin{aligned} & p + (q \cdot \sin \phi_{vehicle\ roll_{TS}} + r \cdot \cos \phi_{vehicle\ roll_{TS}}) \\ & \cdot \tan(\theta_{vehicle\ pitch_{TS}}) \\ & + k(\theta_{chassis} - \theta_{chassis}) \\ & + (\phi_{vehicle\ roll_{SS}}^*) \end{aligned} \right) \right) \right] + \left[(1-VTSF) \cdot \phi_{vehicle\ roll_{SS}} \right] \quad (3.29)$$

where $\phi_{vehicle\ roll_{SS}}^*$ is the vehicle steady state roll angle when the state index switches from 1 to 0. It is used as an initial condition for the vehicle transient roll angle estimator.

An updated estimate of the vehicle pitch angle is derived using the following expression (ref. Eq. (3.27)):

$$\dot{\theta}_{vehicle\ pitch} = q \cdot \cos \phi_{vehicle\ roll} - r \cdot \sin \phi_{vehicle\ roll} \quad (3.30)$$

3.2.4.3 Estimator Performance

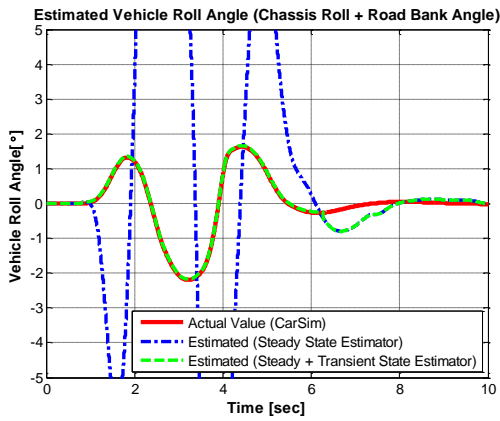
The performance of the designed roll/pitch angle estimator was evaluated for a range of different simulations cases (Table 3.2).

Table 3.2: Simulation cases

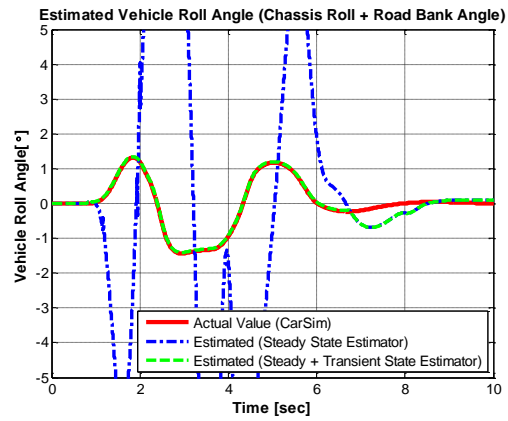
	Vehicle Speed (kph)	Friction Coefficient (μ)	Test Maneuver	Road Bank Angle ($^{\circ}$)	Road Grade Angle ($^{\circ}$)
Case 1	140 kph	0.85	Double lane change	0°	0°
Case 2	140 kph	Varying (high- low-high)	Double lane change	0°	0°
Case 3	80 kph	0.85	Fishhook	0°	0°
Case 4	70 kph	0.20	Slalom	0°	0°
Case 5	120 kph	0.85	Straight and	0° - 18° - 0°	0°

			Bank Turn		
Case 6	140 kph	0.85	Double lane change	0°-18°- 0°	0°
Case 7	100 kph	Varying (high-low-high)	Straight-line braking	0°	≈2.5°

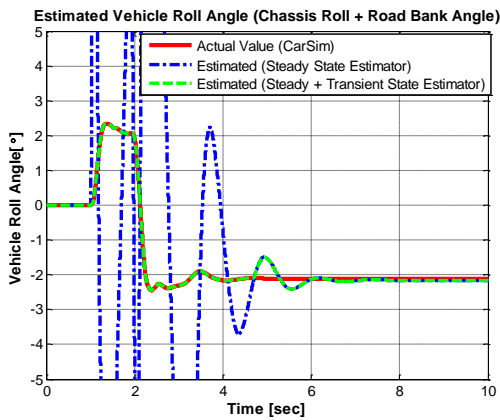
Case 1



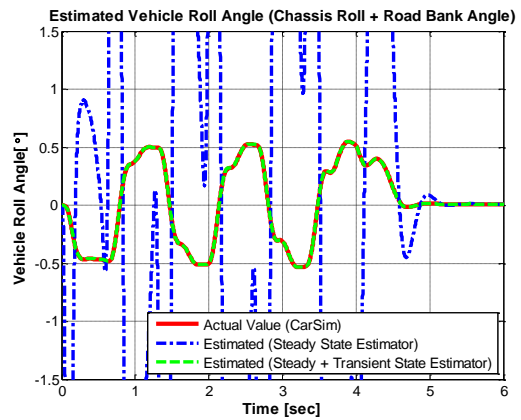
Case 2



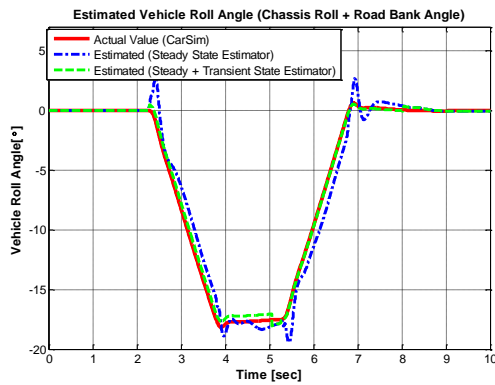
Case 3



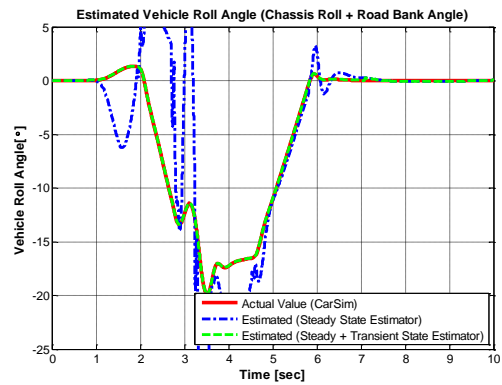
Case 4



Case 5



Case 6



Case 7

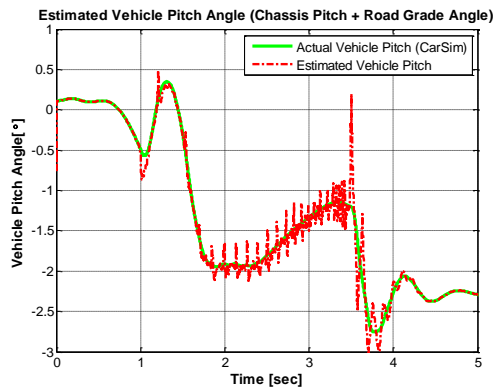


Fig. 3.19: Vehicle roll/pitch angle estimator performance (ref. Table 3.2 for a description of the simulation conditions)

Fig. 3.19 shows that the proposed observer is able to estimate the vehicle states (roll/pitch angle) successfully even for challenging (aggressive maneuvering) operating conditions.

3.2.5 Bias Compensation

The measured lateral/longitudinal acceleration has both lateral/longitudinal dynamics components and gravity components (Fig. 3.20) due to road bank/grade and chassis angles, as described in Fig. 3.15-Fig. 3.16.

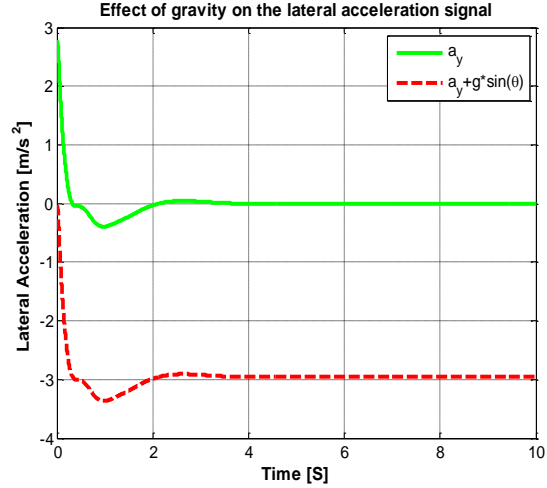
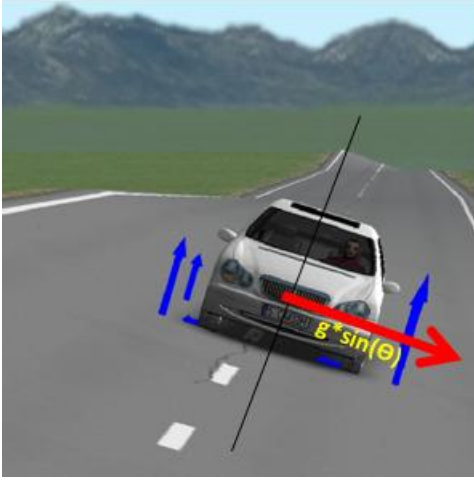


Fig. 3.20: Effect of gravity bias on the lateral acceleration signal

Using the real-time vehicle roll and pitch angle estimates (as described in Section 3.2.4), the measured acceleration signals are compensated for the gravity components using:

$$a_{x,c} = a_{x,m} + g \cdot \sin(\theta_{vehicle\ pitch}) \quad (3.31)$$

$$a_{y,c} = a_{y,m} - g \cdot \sin(\phi_{vehicle\ roll}) \cdot \cos(\theta_{vehicle\ pitch}) \quad (3.32)$$

Vehicle side-slip angle is estimated using a simple integration method to verify whether the compensation of the lateral acceleration is useful to estimate the side-slip angle. The integration method to estimate the side-slip angle is as follows (obtained by rearranging Equation (3.24)):

$$\beta = \frac{v_y}{v_x} = \int \left(\frac{a_{y,m} - (g \cdot \sin(\phi_{vehicle\ roll}) \cdot \cos(\theta_{vehicle\ pitch})) - r \cdot v_x}{v_x} \right) dt \quad (3.33)$$

$$or \beta = \frac{v_y}{v_x} = \int \left(\frac{a_{y,c} - r \cdot v_x}{v_x} \right) dt \quad (3.34)$$

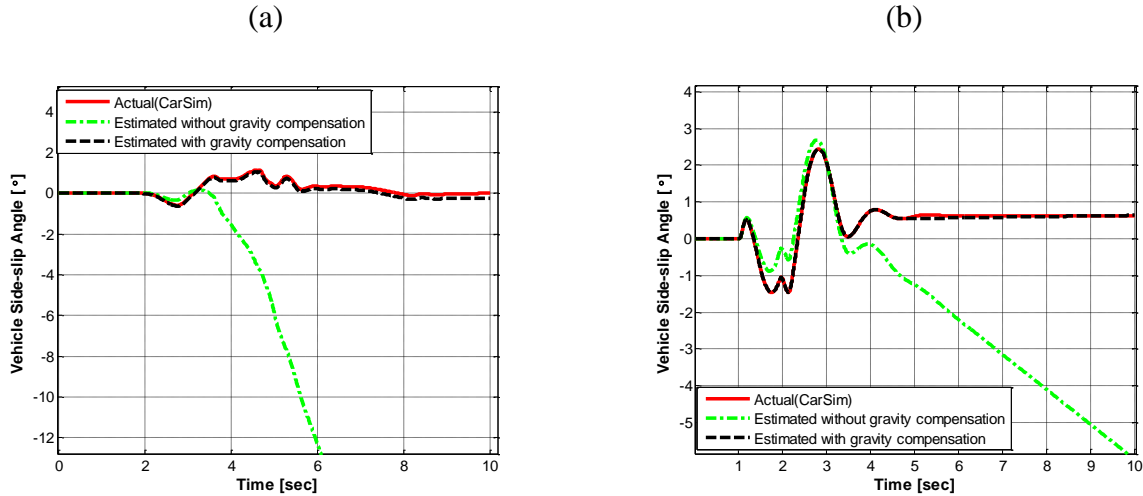


Fig. 3.21: Vehicle sideslip angle estimation using a simple integration method: (a) double lane change steering/high $\mu(0.85 / 120\text{kph} / \text{bank}(0 - 18- 0 \text{ deg}))$, and (b) fishhook steering/high $\mu(0.85 / 80\text{kph} / \text{flat surface})$

The simulation results show (Fig. 3.21) that the compensated lateral acceleration can be used directly to estimate the vehicle side-slip angle.

3.2.6 Vehicle Longitudinal Velocity Estimator

3.2.6.1 Estimation Methodology

An integrated state estimation scheme (ref. Fig. 3.3) requires reliable vehicle speed information. It is much harder to estimate the vehicle speed during braking than in traction, since in the former case all four wheels are slipping. The proposed vehicle speed estimation algorithm (Fig. 3.22) is based on the measurement of the four wheel rotational speed and longitudinal vehicle acceleration. The estimator uses a structure based on the work of reference [34]. The main advantage of this approach are the low computation burden, as compared some of the previous work proposed in literature [56-59], which suffer from high computational complexity.

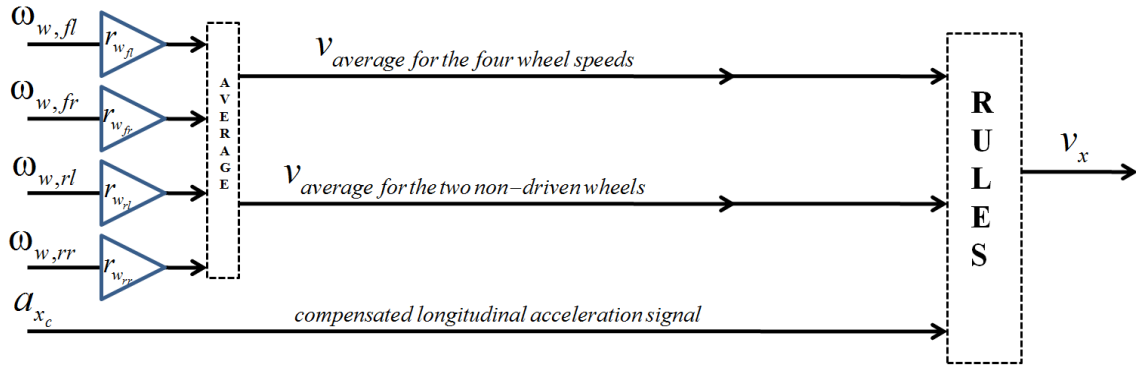


Fig. 3.22: Estimation algorithm data flow chart

The longitudinal acceleration signal is supposed to have been properly corrected according to the discussion given in Section 3.2.5 as:

$$a_{x,c} = a_{x,m} + g \cdot \sin(\theta_{vehicle\ pitch}) \quad (3.35)$$

The effective tire radius (r_w) required to estimate the linear wheel speed can be determined using the tire vertical load information (load estimation methodology described in Section 3.2.7) as:

$$r_{w,i} = r - \frac{F_{z,i}}{k_t} \quad (3.36)$$

At each sampling instant, the following auxiliary signals are computed:

- $v_{average}$: average of the four wheel speeds
- $v_{non-driven\ average}$: average of the two non - driven wheels speed

The estimation algorithm behavior changes according to the status of the vehicle, which is represented by the following four states:

State 1: Low Speed

State 2: Accelerating

State 3: Constant speed or is softly braking

State 4: Braking

The status of the vehicle is determined using the following threshold values:

v_{min} : vehicle speed threshold

a_{acc} : vehicle acceleration threshold

a_{dcc} : vehicle deceleration threshold

Table 3.3: Estimation algorithm rules

Rule Chart : Vehicle Status and Velocity Estimation

Case 1	Case 2	Case 3	Case 4
<p>if $v_{average} < v_{min}$</p> <p>"Vehicle status : Low speed"</p> <p>$v_x = v_{average}$</p>	<p>if $v_{average} > v_{min}$ & $a_x > a_{acc}$</p> <p>"Vehicle status : Accelerating"</p> <p>$v_x = v_{non-driven\ average}$</p>	<p>if $v_{average} > v_{min}$ & $a_{dcc} < a_x < a_{acc}$</p> <p>"Vehicle status : Constant speed or softly braking"</p> <p>$v_x = v_{average}$</p>	<p>if $v_{average} > v_{min}$ & $a_x < a_{dcc}$</p> <p>"Vehicle status : Braking"</p> <p>$v_x(t) = v_x(t-1) + a_x(t) * T_s$</p> <p><i>Speed is estimated using a recursive rule (i.e., discrete time integrator of vehicle acceleration)</i></p>

Thresholds :

$$v_{min} = 2\text{ m / s}; a_{acc} = 0.1\text{ m / s}^2; a_{dcc} = -0.8\text{ m / s}^2$$

When the vehicle has very low or constant speed, the estimated vehicle speed is obtained as the average of the four wheel speeds. When the car is accelerating, instead, as the driving wheels have a non-null longitudinal slip due to traction force, the estimated vehicle speed is obtained as the average of the non-driving wheels. During an extreme braking maneuver, the estimated vehicle speed is obtained via an open-loop integration of the corrected accelerometer signal, augmented with a backward integration phase to cope with initialization errors (ref. Table 3.3).

3.2.6.2 Estimator Performance

The performance of the velocity estimator was evaluated for an aggressive straight-line braking maneuver (Fig. 3.23).

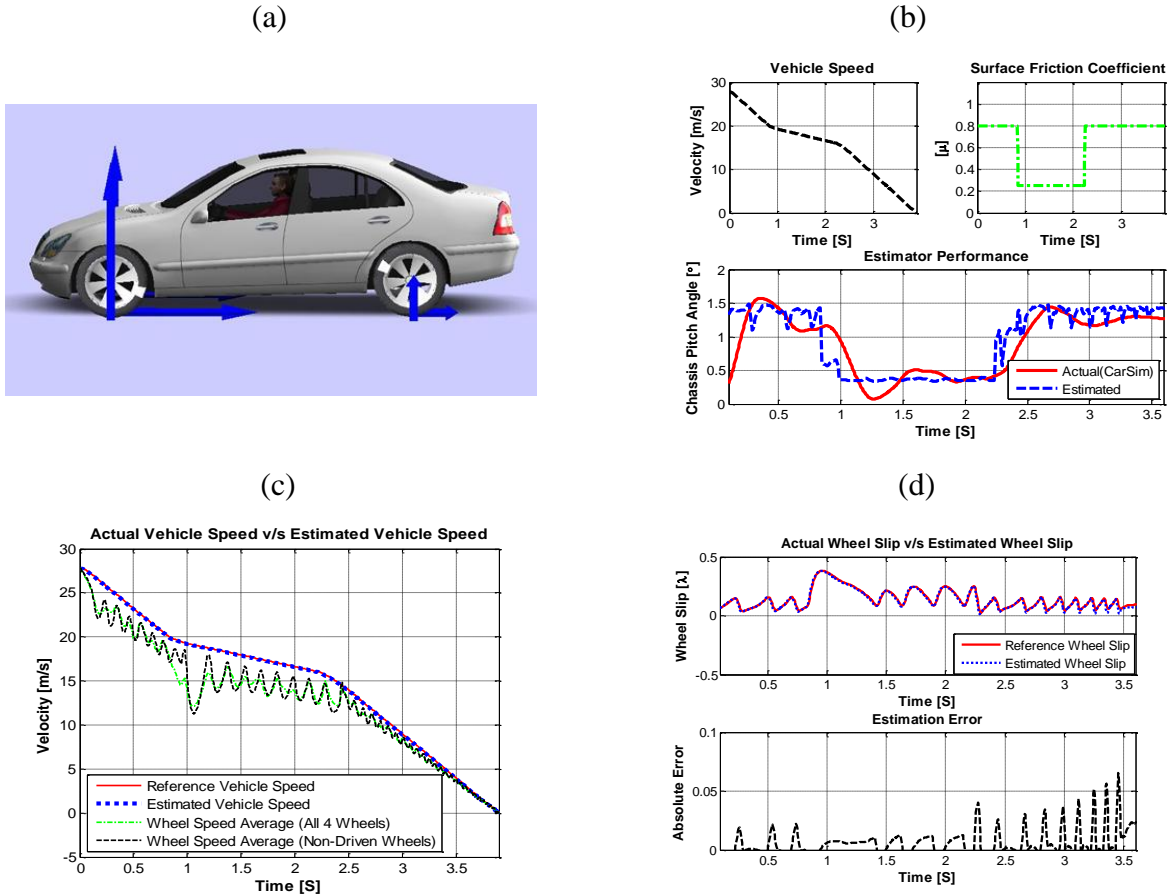


Fig. 3.23: (a) Test conditions: straight-line braking maneuver (varying μ condition), (b) estimated vehicle speed compared with the reference vehicle speed, and (c) estimated wheel slip (top) and absolute error (bottom) compared with the reference wheel slip

According to these encouraging results (Fig. 3.23c), the output of the longitudinal vehicle speed estimation algorithm could also be employed for reliably computing the longitudinal wheel slip (Fig. 3.23d).

3.2.7 Tire Vertical Load Estimator

The vertical tire forces can be estimated by the summation of longitudinal load transfer, lateral load transfer and the static normal force. The estimates of the vertical tire forces can be represented as follows:

$$\begin{aligned}
Fz_{fl} &= \frac{Fz_{front\ axle}}{2} - W_{Lateral\ Load\ Transfer} - W_{Longitudinal\ Load\ Transfer} \\
Fz_{fr} &= \frac{Fz_{front\ axle}}{2} + W_{Lateral\ Load\ Transfer} - W_{Longitudinal\ Load\ Transfer} \\
Fz_{rl} &= \frac{Fz_{rear\ axle}}{2} - W_{Lateral\ Load\ Transfer} + W_{Longitudinal\ Load\ Transfer} \\
Fz_{rr} &= \frac{Fz_{rear\ axle}}{2} + W_{Lateral\ Load\ Transfer} + W_{Longitudinal\ Load\ Transfer}
\end{aligned} \tag{3.37}$$

where the axle load distribution is strictly a function of the vehicle geometry, and is given as:

$$\begin{aligned}
Fz_{front\ axle} &= mg \cdot \frac{b}{a+b} \\
Fz_{rear\ axle} &= mg \cdot \frac{a}{a+b}
\end{aligned} \tag{3.38}$$

The vehicle mass (m) can be estimated adaptively using an estimation scheme described in Section 3.2.3.2. The lateral and longitudinal load transfer terms can be estimated using the vehicle's roll model (Fig. 3.4a) and longitudinal models (Fig. 3.10a) as:

$$\begin{aligned}
W_{Lateral\ Load\ Transfer} &= \left(\frac{(m_s \cdot h_r + m_u \cdot h_a)}{t} \cdot a_{y,c} \right) + \left(\frac{k_{roll} \cdot \phi_{chassis} + c_{roll} \cdot \dot{\phi}_{chassis}}{t} \right) \\
W_{Longitudinal\ Load\ Transfer} &= \frac{m_s \cdot h_{cg}}{2(a+b)} \cdot a_{x,c}
\end{aligned} \tag{3.39}$$

The roll rates ($\phi, \dot{\phi}$) required to estimate the lateral load transfer term can be obtained by the use of a vehicle roll state estimator, as described in Section 3.2.4.

3.2.7.1 Effect of Grade Angle on the Load Distribution

In this case, the lower tires become more heavily loaded (Fig. 3.24).

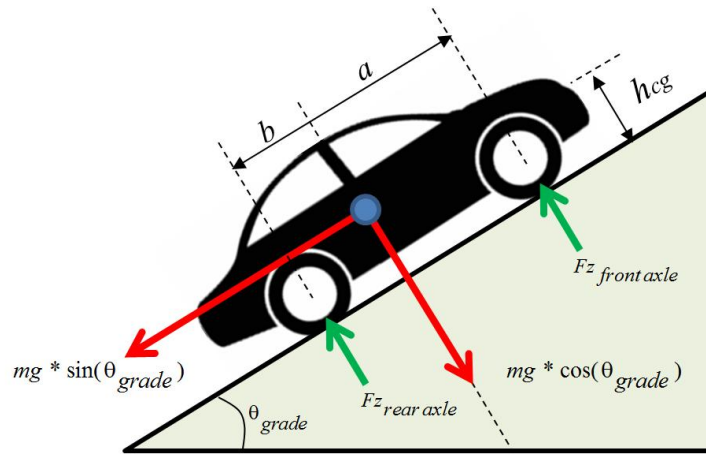


Fig. 3.24: Load distribution of a vehicle on a graded road

Load distribution can be determined by summing the moments around the tire-road contact points, leading to equations:

$$\begin{aligned}
 Fz_{front\ axle} &= mg \cdot \frac{b}{a+b} \cdot \cos \theta_{road\ grade} - mg \cdot \frac{h_{cg}}{a+b} \cdot \sin \theta_{road\ grade} \\
 Fz_{rear\ axle} &= mg \cdot \frac{a}{a+b} \cdot \cos \theta_{road\ grade} + mg \cdot \frac{h_{cg}}{a+b} \cdot \sin \theta_{road\ grade}
 \end{aligned}
 \tag{3.40}$$

3.2.7.2 Effect of Bank Angle on the Load Distribution

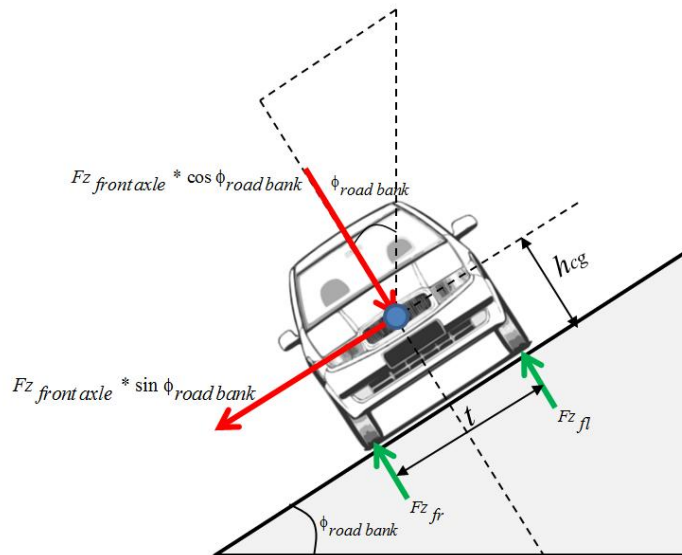


Fig. 3.25: Load distribution of a vehicle on a banked road

A bank causes the load on the interior (lower) tires to increase, while the load on the exterior (upper) tires decreases (Fig. 3.25). The formulas for the change in loads on the tire are:

$$\begin{aligned}
 Fz_{fl} &= \frac{Fz_{front\ axle}}{2} \cdot \cos \phi_{vehicle\ roll} - \frac{Fz_{front\ axle} \cdot h_{cg}}{t} \cdot \sin \phi_{vehicle\ roll} \\
 Fz_{fr} &= \frac{Fz_{front\ axle}}{2} \cdot \cos \phi_{vehicle\ roll} + \frac{Fz_{front\ axle} \cdot h_{cg}}{t} \cdot \sin \phi_{vehicle\ roll} \\
 Fz_{rl} &= \frac{Fz_{rear\ axle}}{2} \cdot \cos \phi_{vehicle\ roll} - \frac{Fz_{rear\ axle} \cdot h_{cg}}{t} \cdot \sin \phi_{vehicle\ roll} \\
 Fz_{rr} &= \frac{Fz_{rear\ axle}}{2} \cdot \cos \phi_{vehicle\ roll} + \frac{Fz_{rear\ axle} \cdot h_{cg}}{t} \cdot \sin \phi_{vehicle\ roll}
 \end{aligned} \tag{3.41}$$

3.2.7.3 Combined Effects of Banked and Graded Road Surface Conditions on the Load Distribution

Studying the combined effects of banked and graded road surface conditions, the formulas for the change in loads on the tire are:

$$\begin{aligned}
 Fz_{fl} &= \frac{mg \cdot \frac{b}{a+b} \cdot \cos \theta_{road\ grade} - mg \cdot \frac{h_{cg}}{a+b} \cdot \sin \theta_{road\ grade}}{2} \cdot \cos \phi_{vehicle\ roll} \\
 &\quad - \frac{mg \cdot \frac{b}{a+b} \cdot \cos \theta_{road\ grade} - mg \cdot \frac{h_{cg}}{a+b} \cdot \sin \theta_{road\ grade} \cdot h_{cg}}{t} \cdot \sin \phi_{vehicle\ roll}
 \end{aligned}$$

$-W_{Lateral\ Load\ Transfer} - W_{Longitudinal\ Load\ Transfer}$

$$\begin{aligned}
Fz_{fr} &= \frac{mg \cdot \frac{b}{a+b} \cdot \cos \theta_{road\ grade} - mg \cdot \frac{h_{cg}}{a+b} \cdot \sin \theta_{road\ grade}}{2} \cdot \cos \phi_{vehicle\ roll} \\
&+ \frac{mg \cdot \frac{b}{a+b} \cdot \cos \theta_{road\ grade} - mg \cdot \frac{h_{cg}}{a+b} \cdot \sin \theta_{road\ grade} \cdot h_{cg}}{t} \cdot \sin \phi_{vehicle\ roll} \\
&+ W_{Lateral\ Load\ Transfer} - W_{Longitudinal\ Load\ Transfer} \\
Fz_{rl} &= \frac{mg \cdot \frac{a}{a+b} \cdot \cos \theta_{road\ grade} + mg \cdot \frac{h_{cg}}{a+b} \cdot \sin \theta_{road\ grade}}{2} \cdot \cos \phi_{vehicle\ roll} \\
&- \frac{mg \cdot \frac{a}{a+b} \cdot \cos \theta_{road\ grade} + mg \cdot \frac{h_{cg}}{a+b} \cdot \sin \theta_{road\ grade} \cdot h_{cg}}{t} \cdot \sin \phi_{vehicle\ roll} \\
&- W_{Lateral\ Load\ Transfer} + W_{Longitudinal\ Load\ Transfer} \\
Fz_{rr} &= \frac{mg \cdot \frac{a}{a+b} \cdot \cos \theta_{road\ grade} + mg \cdot \frac{h_{cg}}{a+b} \cdot \sin \theta_{road\ grade}}{2} \cdot \cos \phi_{vehicle\ roll} \\
&+ \frac{mg \cdot \frac{a}{a+b} \cdot \cos \theta_{road\ grade} + mg \cdot \frac{h_{cg}}{a+b} \cdot \sin \theta_{road\ grade} \cdot h_{cg}}{t} \cdot \sin \phi_{vehicle\ roll} \\
&+ W_{Lateral\ Load\ Transfer} + W_{Longitudinal\ Load\ Transfer}
\end{aligned}$$

(3.42)

The tire vertical load information can be used to estimate the load transfer ratio (LTR), given by the expression:

$$LTR = \frac{(Fz_{fl} + Fz_{rl}) - (Fz_{fr} + Fz_{rr})}{(Fz_{fl} + Fz_{rl}) + (Fz_{fr} + Fz_{rr})} \quad (3.43)$$

3.2.7.4 Estimator Performance

To investigate the performance of the proposed vertical load estimator, simulations have been conducted for a wide range of driving maneuvers (Table 3.4), without including any road disturbances.

Table 3.4: Simulation cases

	Vehicle Speed (kph)	Friction Coefficient (μ)	Test Maneuver	Road Bank Angle ($^{\circ}$)	Road Grade Angle ($^{\circ}$)
Case 1	140 kph	Varying (high-low-high)	Double lane change	0°	0°
Case 2	80 kph	0.85	Fishhook	3°	3°
Case 3	70 kph	0.20	Slalom	0°	0°
Case 4	100-0 kph	Varying (high-low-high)	Straight-line braking	0°	3°

Case 1

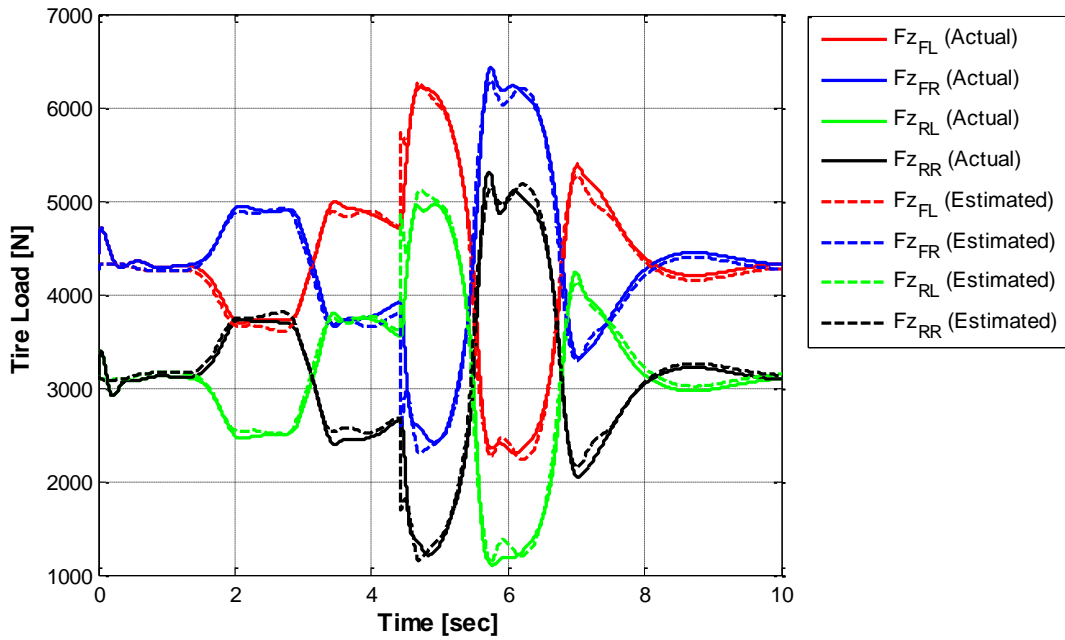
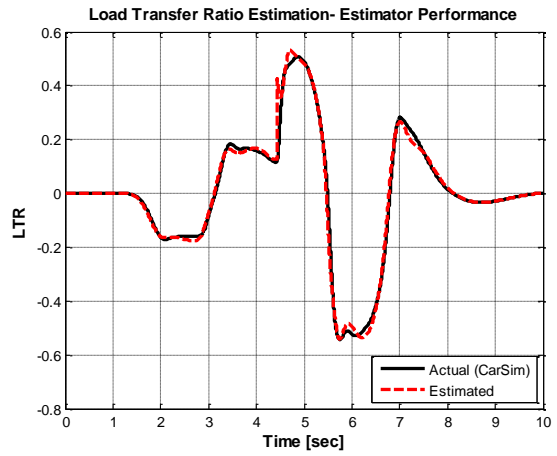
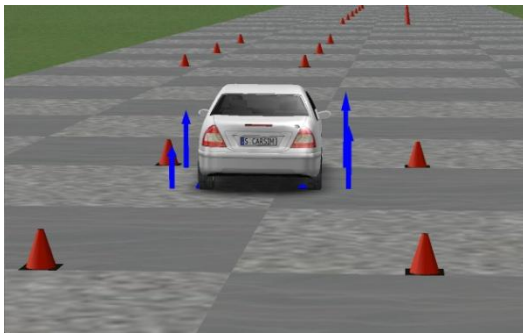


Fig. 3.26: Test condition: double lane change maneuver (varying μ condition)

Case 2

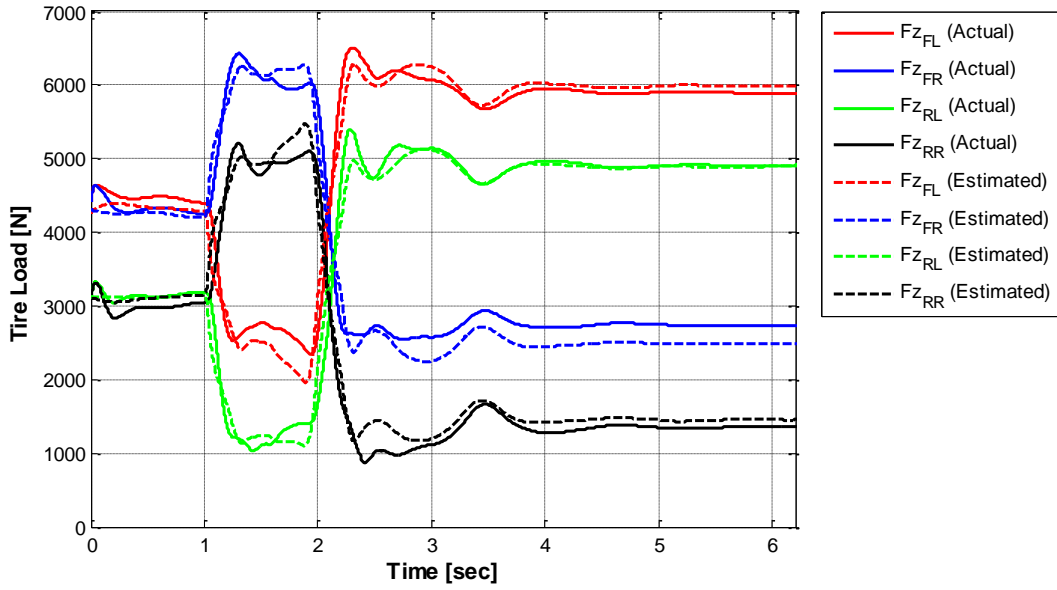
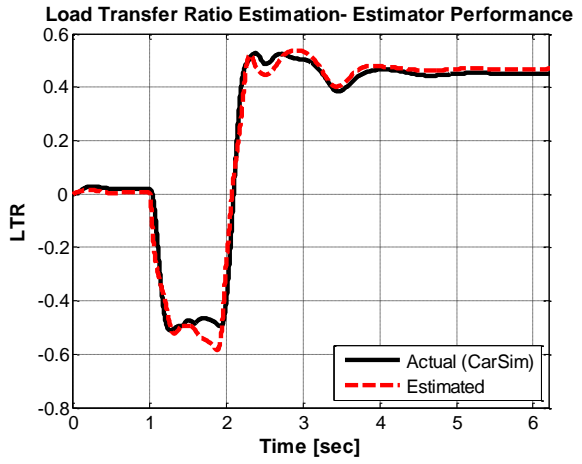
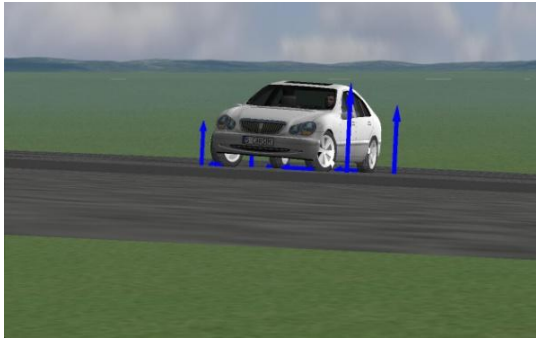


Fig. 3.27: Test condition: fishhook maneuver (constant μ , banked (3°) and graded road (2°) condition)

Case 3

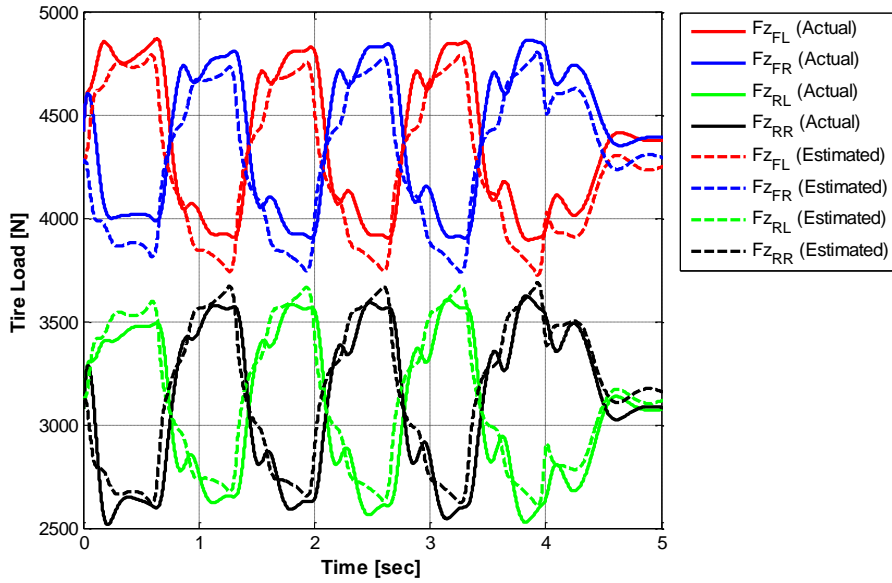
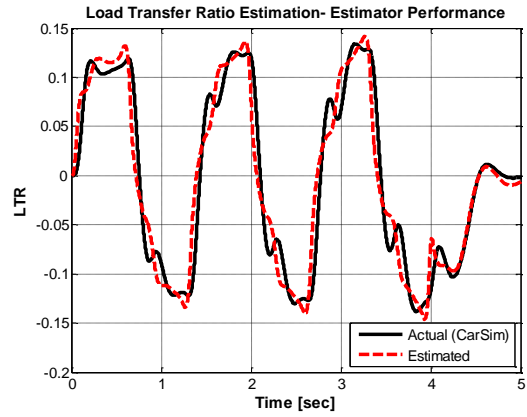
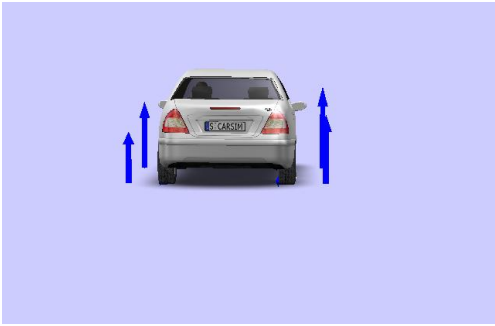


Fig. 3.28: Test condition: slalom steering maneuver (low μ condition)

Case 4

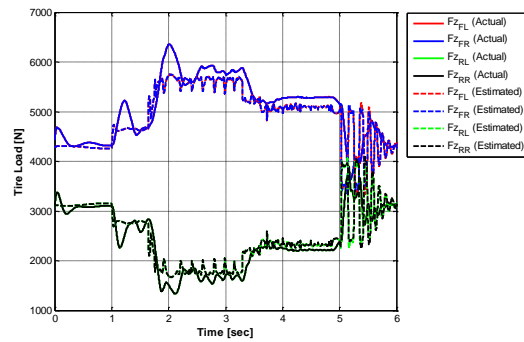
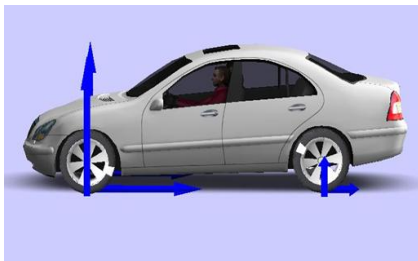


Fig. 3.29: Test condition: straight-line braking maneuver (varying μ condition)

The comparison of the estimated vertical forces using the algorithm described in Section 2.7.3 and actual forces using the CarSim software is presented in Fig. 3.26 to Fig. 3.29. Results show that the estimated vertical forces match the simulated forces well.

3.2.7.5 LTR Based Chassis Roll Angle Estimator

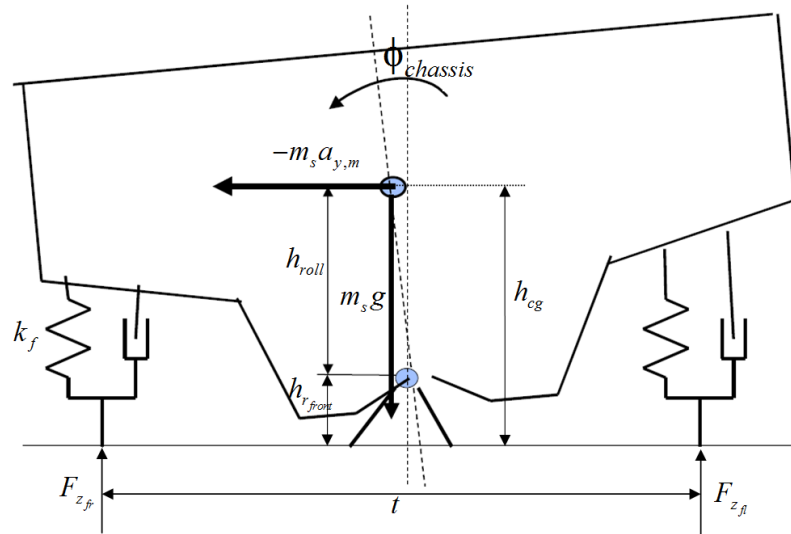


Fig. 3.30: Simplified roll dynamics model

Summing moments about the front and rear roll centers:

$$(F_{z_{fl}} - F_{z_{fr}}) \cdot \frac{t}{2} = k_f \cdot \phi_{chassis} + m_s \cdot a_y \cdot \frac{b}{a+b} \cdot h_{f_{front}} \quad (3.44)$$

$$(F_{z_{rl}} - F_{z_{rr}}) \cdot \frac{t}{2} = k_r \cdot \phi_{chassis} + m_s \cdot a_y \cdot \frac{a}{a+b} \cdot h_{r_{rear}} \quad (3.45)$$

Adding equations (44) & (45), we get:

$$\begin{aligned} & \left((Fz_{fl} + Fz_{rl}) - (Fz_{fr} + Fz_{rr}) \right) \cdot \frac{t}{2} = (k_f + k_r) \cdot \phi_{chassis} \\ & + m_s \cdot a_y \cdot \left(\frac{b}{a+b} \cdot h_f + \frac{a}{a+b} \cdot h_r \right) \end{aligned} \quad (3.46)$$

Dividing above equation by mg

$$\begin{aligned} & \left(\frac{(Fz_{fl} + Fz_{rl}) - (Fz_{fr} + Fz_{rr})}{mg} \right) \cdot \frac{t}{2} = (k_f + k_r) \cdot \frac{\phi_{chassis}}{mg} \\ & + \frac{m_s \cdot a_y}{mg} \cdot \left(\frac{b}{a+b} \cdot h_{f_{front}} + \frac{a}{a+b} \cdot h_{r_{rear}} \right) \end{aligned} \quad (3.47)$$

$$\text{where } \left(\frac{(Fz_{fl} + Fz_{rl}) - (Fz_{fr} + Fz_{rr})}{mg} \right) = \left(\frac{(Fz_{fl} + Fz_{rl}) - (Fz_{fr} + Fz_{rr})}{(Fz_{fl} + Fz_{rl}) + (Fz_{fr} + Fz_{rr})} \right) = LTR$$

Rearranging Equation (3.47), we get an expression for the chassis roll angle as:

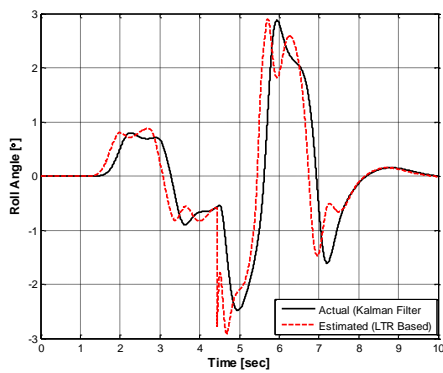
$$\phi_{chassis} = \frac{LTR \cdot \frac{t}{2} - \frac{m_s \cdot a_y}{mg} \cdot \left(\frac{b}{a+b} \cdot h_{f_{front}} + \frac{a}{a+b} \cdot h_{r_{rear}} \right)}{(k_f + k_r)} \quad (3.48)$$

The performance of the load transfer ratio (LTR) based chassis roll angle estimator was evaluated for a range of different simulations cases (Table 5).

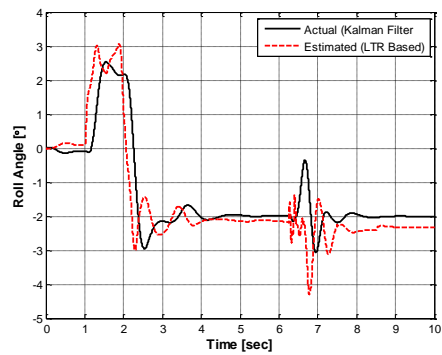
Table 3.5: Simulation cases

	Vehicle Speed (kph)	Friction Coefficient (μ)	Test Maneuver	Road Bank Angle ($^{\circ}$)	Road Grade Angle ($^{\circ}$)
Case 1	140 kph	Varying (high-low-high)	Double lane change	0°	0°
Case 2	80 kph	0.85	Fishhook	0°	0°
Case 3	120 kph	0.85	Straight and Bank Turn	0° - 18° - 0°	0°

Case 1



Case 2



Case 3

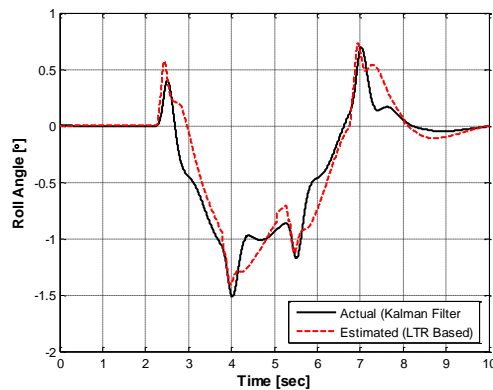


Fig. 3.31: LTR based chassis roll angle estimates (ref. Table 5 for a description of the simulation conditions)

3.2.8 Tire Longitudinal and Lateral Force Estimator

3.2.8.1 Longitudinal Force Estimator

In the case of a normal driving situation, longitudinal force estimators designed at the previous time instant (i.e. wheel dynamics based observer, ref. Eq. (3.18) and (3.19)) show good performance. However, during extreme maneuvering conditions, where the slip-ratio is large, the performance of the estimator is not satisfactory, since the longitudinal tire-force estimator based on wheel dynamics model does not take into consideration the effects of deformation slip or wheel slip. To overcome this drawback (unsatisfactory performance under high-slip conditions) of a wheel dynamics based observer, a tire model - based closed-loop feedback observer is proposed. In the case of pneumatic tires, there are three distinct ranges of force generation: linear, transient and saturation ranges, as shown in Fig. 3.32a-Fig. 3.32b. In the linear range the force generation curves can be modeled as a linear function and the gradient of the linear function is believed to be dependent on the friction coefficient. In the saturation range, the force generation becomes insensitive to the slip and is mostly dependent on the friction coefficient and the tire normal force. In the transient range, the force curves are affected by not only the friction coefficient but also vehicle dynamic states and road surface materials which are not represented only by the friction coefficient. There are many models available that describe this complex nonlinear behavior of a tire (Fig. 3.33).

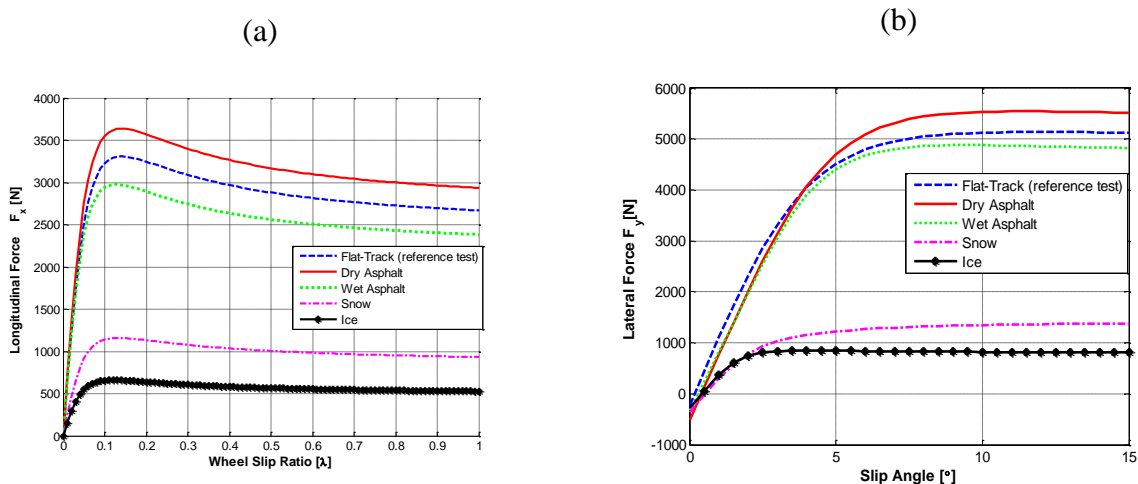


Fig. 3.32: (a) Simulated longitudinal force curves as a function of wheel slip-ratio (λ) for varying surface conditions, and (b) simulated lateral force curves as a function of slip-angle (α) for varying surface conditions

It is possible to use the commonly used tire models such as the Magic Formula (MF for short) tire model for accurate modeling, but this would result in heavy computation work which is usually beyond the computation authority of the on-board microprocessors.

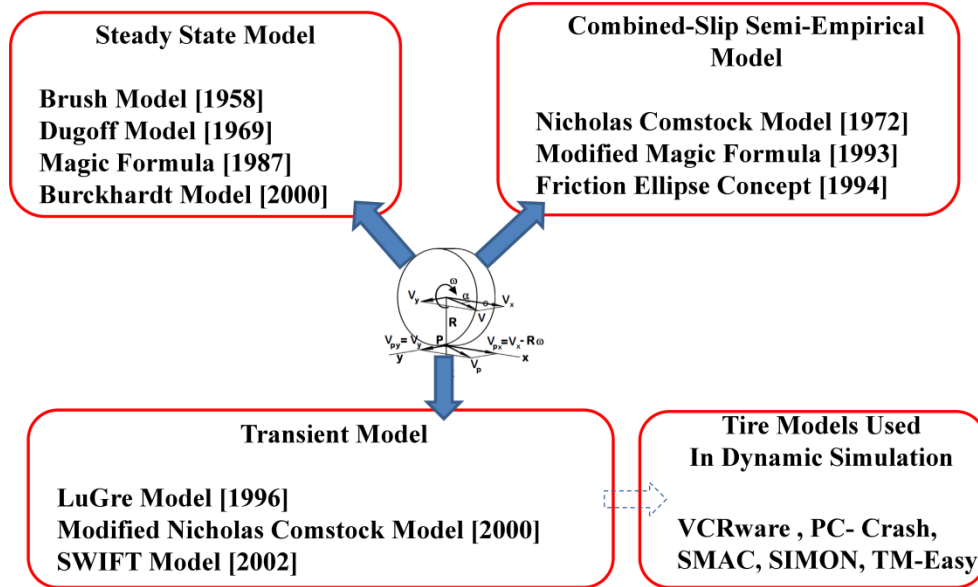


Fig. 3.33: Some representative tire-road friction models

The estimator concept used here relies on a physically derived tire model called the Dugoff tire model. In its simplest formulation, the model describes the relationship between the tire force and the slip as a function of two parameters, the tire stiffness ($C_{x,y}$) and the tire to road friction coefficient (μ). The tire stiffness describes the inclination of the force-slip relation at small slips whereas the friction coefficient describes its curvature and peak value.

Dugoff-tire model can be expressed as follows:

$$F_x = C_x \frac{s}{1+s} f(\lambda) \quad (3.49)$$

$$F_y = C_y \frac{\tan(\alpha)}{1+s} f(\lambda) \quad (3.50)$$

where λ is related to tire-road friction coefficient (μ). λ and function $f(\lambda)$ are defined, as follows:

$$\lambda = \frac{\mu F_z (1+s)}{2\sqrt{(C_x s)^2 + (C_y \tan \alpha)^2}} \quad (3.51)$$

$$f(\lambda) = \begin{cases} (2-\lambda)\lambda, & \lambda < 1 \\ 1, & \lambda \geq 1 \end{cases} \quad (3.52)$$

Under pure longitudinal slip conditions, the above equations simplify to:

$$F_x = C_x \frac{s}{1+s} f(\lambda)$$

$$f(\lambda) = \begin{cases} (2-\lambda)\lambda, & \text{if } \lambda < 1 \\ 1, & \text{otherwise} \end{cases} \quad (3.53)$$

$$\lambda = \frac{\mu_x F_z (1+s)}{2C_x |s|}$$

$$s = \frac{\omega \cdot r_w - v_x}{\max(\omega \cdot r_w, v_x)}$$

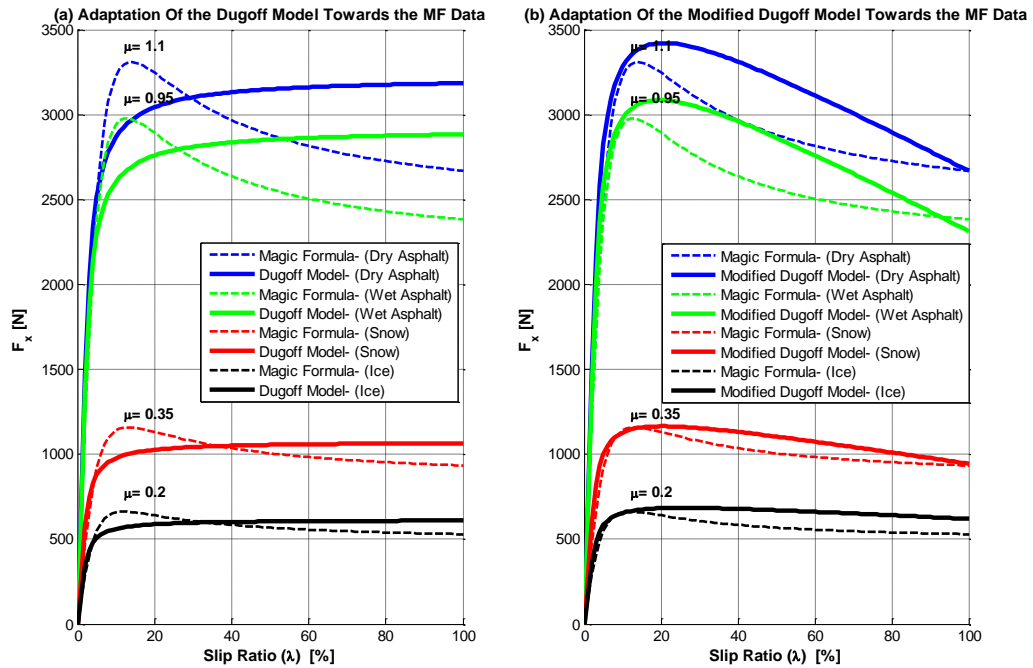


Fig. 3.34: (a) Tire forces calculated by the Dugoff and MF model, and (b) Tire forces calculated by the Modified Dugoff and MF model

Shown in Fig. 3.34a is a comparison of the longitudinal forces calculated by the Dugoff and MF tire model. Comparing results from Fig. 3.34a, we see that, there is no peak point in the Dugoff model, and the peak value is much smaller than the MF model. Also, the difference in the two models is larger when the slip-ratio is high (i.e. a larger difference in the unstable/saturation region can be seen).

Previous publications [60] have shown that the above-stated discrepancies between Dugoff-tire and MF-tire models can be reduced if different tire/road friction coefficients are taken for different magnitudes of slip-ratio. The slip-dependent friction coefficient is expressed as [60]:

$$\mu_x = \mu_{xp}(1-s) + \mu_{xs}s, \quad \text{for pure longitudinal slip}$$

where

$$\begin{aligned} \mu_{xp} &= \frac{c_l}{k_l} \mu \\ \mu_{xs} &= 0.5545\mu_{xp}^3 - 0.9697\mu_{xp}^2 + 1.0424\mu_{xp} \end{aligned} \tag{3.54}$$

where $c_l = 1.125$ and $k_l = 0.925$. c_l and k_l are compensation factor and attenuation factor, respectively. Force calculations based on the modified Dugoff tire model are shown in Fig. 3.34b. The results are seen to be coincident to the MF tire model. The modified Dugoff model has the virtues of the original model, and the precision in nonlinear condition is much improved. Hence, the estimator concept proposed here is based on the modified Dugoff tire model.

As mentioned previously, the Dugoff model describes the relationship between the tire force and the slip as a function of two parameters, the tire stiffness and the tire to road friction coefficient. In the small-slip range, the longitudinal force increases proportional to the slip and the gradient of the force-slip curve is defined as the tire longitudinal stiffness. Thus, the longitudinal force model in the small-slip range can be expressed as follows:

$$F_x = C_x \cdot \lambda, \quad \text{for } |\lambda| < 3\% \tag{3.55}$$

Satisfactory performance of the wheel dynamics based observer in the small slip region ($|\lambda| < 3\%$) provides us with an opportunity to adaptively estimate the longitudinal stiffness of the tire using an on-line parameter estimation algorithm. Equation (55) can be rewritten into a standard parameter identification form as follows:

$$y(t) = \varphi^T(t) \cdot \theta(t) \quad (3.56)$$

where $y(t) = F_x$ is the system output (from the wheel dynamics based observer, $\theta(t) = C_x$, is the unknown parameter, and $\varphi^T(t) = \lambda$ is the measured slip ratio. The unknown parameter $\theta(t)$ can be identified in real-time using parameter identification approach.

The recursive least squares (RLS) algorithm [61] provides a method to iteratively update the unknown parameter at each sampling time to minimize the sum of the squares of the modeling error using the past data contained within the regression vector, $\varphi(t)$. The procedure for solving the RLS problem is as follows:

Step 0: Initialize the unknown parameter $\theta(0)$ and the covariance matrix $P(0)$; set the forgetting factor λ .

Step 1: Measure the system output $y(t)$ and compute the regression vector $\varphi(t)$.

Step 2: Calculate the identification error $e(t)$:

$$e(t) = y(t) - \varphi^T(t) \cdot \theta(t-1) \quad (3.57)$$

Step 3: Calculate the gain $k(t)$:

$$k(t) = P(t-1)\varphi(t) \left[\lambda + \varphi^T(t)P(t-1)\varphi(t) \right]^{-1} \quad (3.58)$$

Step 4: Calculate the covariance matrix:

$$P(t) = \left(1 - k(t)\varphi^T(t) \right) \lambda^{-1} P(t-1) \quad (3.59)$$

Step 5: Update the unknown parameter:

$$\theta(t) = \theta(t-1) + k(t)e(t) \quad (3.60)$$

Step 6: Repeat Steps 1~5 for each time step.

The performance of the RLS algorithm is evaluated with simulations where the road surface is designed to have sudden friction coefficient changes, and the vehicle maneuver is straight driving with intermittent gas pedal presses (Table 3.6).

Table 3.6: Simulation cases

	Vehicle Speed (kph)	Friction Coefficient (μ)	Test Maneuver
Case 1	≈ 65 kph	High-low-high (jump- μ)	Straight driving with intermittent gas pedal presses
Case 2	≈ 65 kph	High-low	Straight driving with intermittent gas pedal presses

Case 1

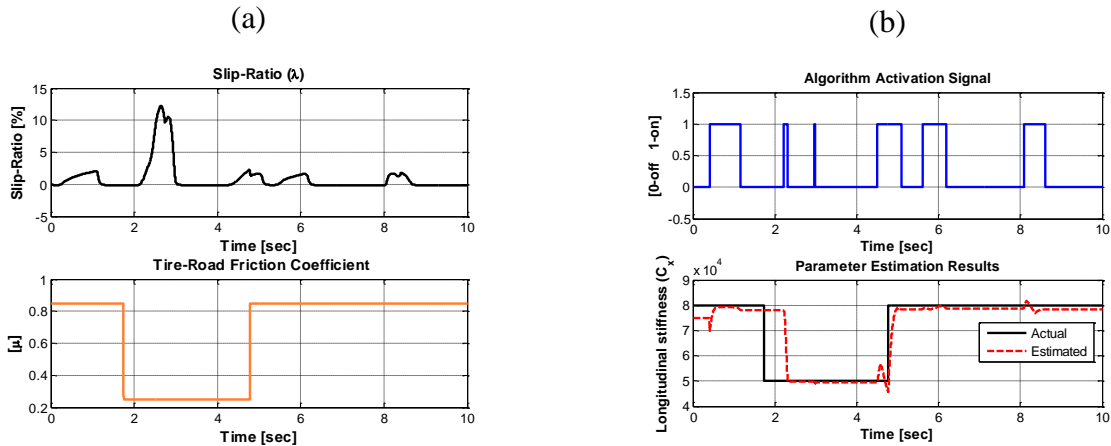


Fig. 3.35: (a) Road surface condition (bottom) and the tire slip-ratio (top) during the simulation, and (b) longitudinal stiffness estimation result (bottom) and corresponding activation signal (top)

Case 2

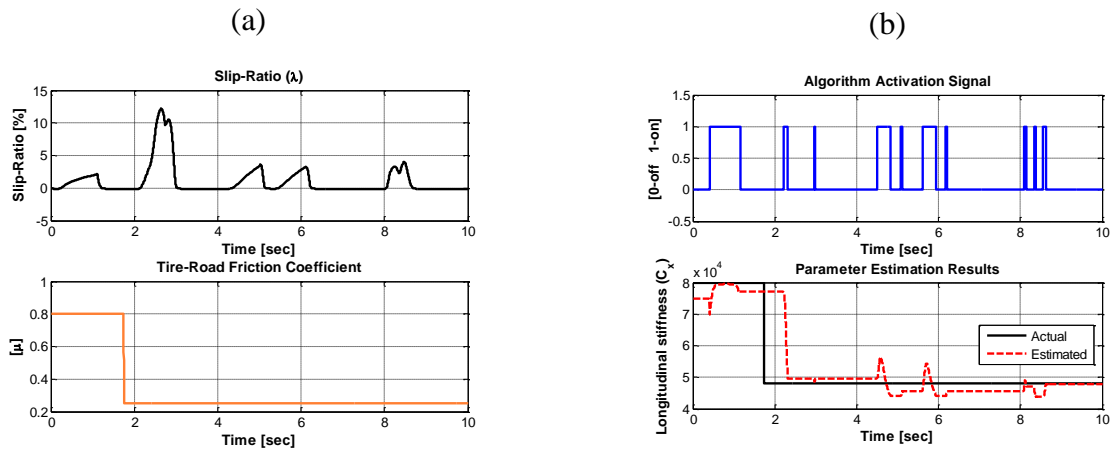


Fig. 3.36: (a) Road surface condition (bottom) and the tire slip-ratio (top) during the simulation, and (b) longitudinal stiffness estimation result (bottom) and corresponding activation signal (top)

From Fig. 3.35 and Fig. 3.36, it can be seen that, the estimator shows delayed estimation at the first change due to lack of excitation at that time. Once excitation occurs at 2.2 seconds, the estimator updates the longitudinal stiffness. In Fig. 3.35b, at the time of the second surface change (4.8 seconds), the excitation duration is coincident with the change so that the estimated friction coefficient tracks the actual value immediately.

The second parameter of interest required to describe the relationship between the tire force and the slip using the Dugoff model is the tire- road friction coefficient (μ). As shown previously in [62-67], there is a co-variation between the friction coefficient and the longitudinal stiffness (C_x) of a tire, as shown in Fig. 3.37.

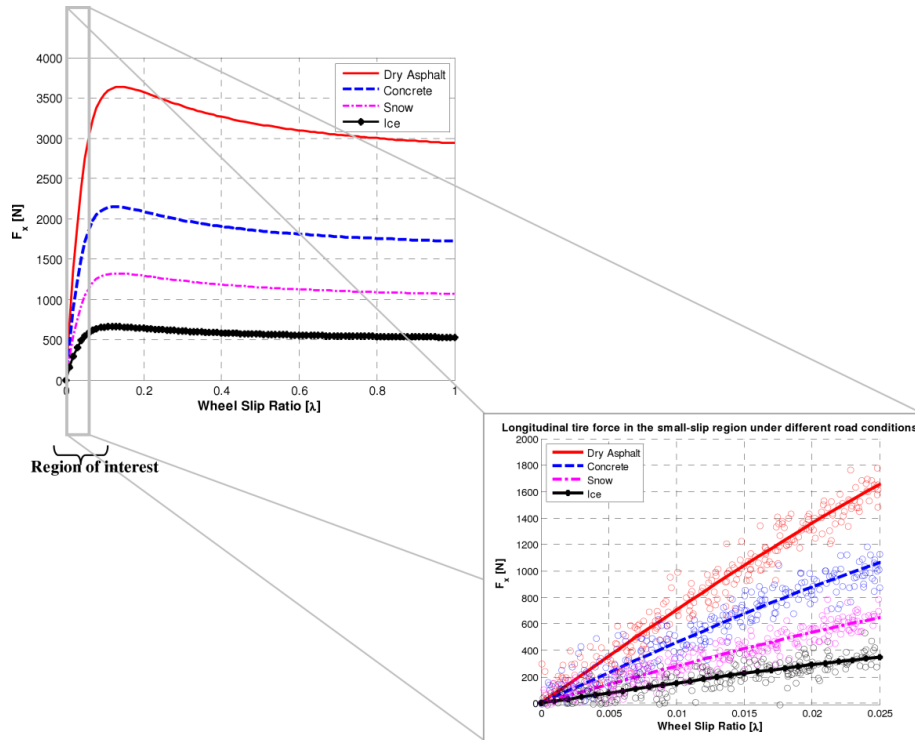


Fig. 3.37: Longitudinal tire force in the small-slip region under different road conditions

Hence a popular and in many circumstances successful approach to assess the friction is to estimate the longitudinal stiffness, i.e. the incline of the tire force relative to slip at low slips and from this value distinguishing between different surface conditions.

Contrary to this popular belief, some recent studies [68] show that the longitudinal stiffness depends on many factors and a generic relation between the slope and the exact friction coefficient is therefore not possible to obtain. The relation is physically difficult to explain and does not always hold. The longitudinal stiffness has been shown to be sensitive to many other factors, namely, tire inflation pressure, vertical load, wear and temperature, and a change of the stiffness might not guarantee a change in friction.

To develop a tire-road friction coefficient (μ) estimation technique robust against these uncertainties, it is proposed here to use an observer based parameter estimation scheme. The general formulation of the estimation scheme is as follows:

Consider the following nonlinear dynamic system and nonlinear measurement:

$$\begin{aligned} \dot{x} &= f(x, u, \theta) \\ y &= h(x, u, \theta) \end{aligned} \quad (3.61)$$

where x is the state of the system, y is the measurement, u is the control input, and θ is a vector of constant parameters to be estimated. For the system shown in (61), the following parameter and state estimation algorithm [69] can be applied:

$$\begin{aligned} \dot{\hat{x}} &= f(\hat{x}, \hat{u}, \hat{\theta}) + k_1(\hat{x}, \hat{u}, \hat{\theta}) \cdot (y - \hat{y}) \\ \dot{\hat{\theta}} &= k_2(\hat{x}, \hat{u}, \hat{\theta}) \cdot (y - \hat{y}) \end{aligned} \quad (3.62)$$

where the observer gains (k_1, k_2) can be determined using a optimization routine that maximizes robust stability against plant uncertainties.

Applying the above design methodology for our friction estimation problem, the estimation scheme proposed here is based on equations for the longitudinal motion of the vehicle (Ref. Fig. 3.10(a)). The equation of motion can be derived by force equilibrium as shown in Fig. 3.10a and the resulting equation is:

$$m\dot{v}_x = \sum F_x - F_{aero\ drag} - F_{grade} - F_{rolling\ resistance} \quad (3.63)$$

where:

$\sum F_x$: summation of the tire forces generated at all the four tires

$F_{aero\ drag}$: aerodynamic drag force ($\frac{1}{2}\rho C_d A_f v_x^2$)

F_{grade} : road grade force ($mg\sin\theta_{grade}$)

$F_{rolling\ resistance}$: rolling resistance ($f_r mg\cos\theta_{grade}$)

$$\begin{aligned} \text{or } m\dot{v}_x &= (F_{x_{fl}} + F_{x_{fr}} + F_{x_{rl}} + F_{x_{rr}}) - \frac{1}{2}\rho C_d A_f v_x^2 - mg\sin\theta_{grade} \\ &\quad - f_r mg\cos\theta_{grade} \end{aligned} \quad (3.64)$$

$$\begin{aligned} \text{or } (F_{x_{fl}} + F_{x_{fr}} + F_{x_{rl}} + F_{x_{rr}}) &= mv_x + \frac{1}{2}\rho C_d A_f v_x^2 + mg \sin \theta_{grade} \\ &+ f_r mg \cos \theta_{grade} \end{aligned} \quad (3.65)$$

The longitudinal force ($\sum F_x = F_{x_{fl}} + F_{x_{fr}} + F_{x_{rl}} + F_{x_{rr}}$) evolution is modeled with a random walk model, with derivative equal to random noise as:

$$\hat{F}_x = 0 \quad (3.66)$$

Using Eq. (3.66) and the formulation given by Eq. (3.62), and applying principles of sliding mode observer, an estimator can be designed as:

$$\sum \hat{F}_x = k_1 \cdot \tanh \left(\begin{array}{l} \left(mv_x + \frac{1}{2}\rho C_d A_f v_x^2 + mg \sin \theta_{grade} + f_r mg \cos \theta_{grade} \right) \\ - \left(\hat{F}_{x_{fl}} + \hat{F}_{x_{fr}} + \hat{F}_{x_{rl}} + \hat{F}_{x_{rr}} \right) \end{array} \right) \quad (3.67)$$

$$\begin{aligned} \hat{\mu} &= k_2 \cdot \tanh \left(\begin{array}{l} \left(mv_x + \frac{1}{2}\rho C_d A_f v_x^2 + mg \sin \theta_{grade} + f_r mg \cos \theta_{grade} \right) \\ - \left(\hat{F}_{x_{fl}} + \hat{F}_{x_{fr}} + \hat{F}_{x_{rl}} + \hat{F}_{x_{rr}} \right) \end{array} \right) \\ &+ k_3 \cdot \tanh(\mu_{c_x} - \hat{\mu}) \end{aligned} \quad (3.68)$$

where the system state and parameter to be estimated are $\sum \hat{F}_x$ and $\hat{\mu}$. $F_{x_{fl},fr,rl,rr}$ is the longitudinal force estimate for the individual wheels obtained using the modified Dugoff model, updated at each time step using the tire stiffness (from Eq. (3.56)) and the tire-road friction coefficient estimates (from Eq. (3.68)).

A summary of the estimation scheme is given below:

Step 1: Estimate tire forces under low slip conditions ($|\lambda_i| < 3\%$) using the wheel dynamics model.

Step 2: Using the low-slip force information from Step 1, update the tire longitudinal stiffness (C_{x_i}) and vehicle mass (m) estimates using a recursive least square (RLS) parameter estimation algorithm.

RLS algorithm 1: Longitudinal stiffness estimation

$$\text{Governing equation: } F_{x_i} = C_{x_i} \cdot \lambda_i, \text{ for } |\lambda_i| < 3\% \quad (3.69)$$

The above equation can be rewritten into a standard parameter identification form as follows:

$$y(t) = \varphi^T(t) \cdot \theta(t) \quad (3.70)$$

By comparing (69) and (70), we can configure a RLS problem as follows:

$$\begin{aligned} y(t) &= F_{x_i} \\ \varphi^T(t) &= \lambda_i \\ \theta(t) &= C_{x_i} \end{aligned} \quad (3.71)$$

RLS algorithm 2: Vehicle mass estimation

$$\text{Governing equation: } m = \frac{(F_{x_{fl}} + F_{x_{fr}} + F_{x_{rl}} + F_{x_{rr}}) - \frac{1}{2} \rho C_d A_f v_x^2}{v_x + g \sin \theta_{grade} + f_r g \cos \theta_{grade}} \quad (3.72)$$

The above equation can be rewritten into a standard parameter identification form as follows:

$$y(t) = \varphi^T(t) \cdot \theta(t) \quad (3.73)$$

By comparing (3.72) and (3.73), we can configure a RLS problem as follows:

$$\begin{aligned} y(t) &= \frac{(F_{x_{fl}} + F_{x_{fr}} + F_{x_{rl}} + F_{x_{rr}}) - \frac{1}{2} \rho C_d A_f v_x^2}{v_x + g \sin \theta_{grade} + f_r g \cos \theta_{grade}} \\ \varphi^T(t) &= 1 \\ \theta(t) &= m \end{aligned} \quad (3.74)$$

Step 3: Using the longitudinal stiffness term (C_{x_i}) identified in Step 2, calculate the tire-road friction coefficient (μ_{c_x}) through an interpolation process (based on the assumption that there is a co-variation between the friction coefficient and the longitudinal stiffness (C_{x_i}) of a tire).

Step 4: Using the modified Dugoff model, make an estimate of the tire longitudinal force using the cornering stiffness (C_{x_i}) estimate (from Step 2) and tire-road friction estimate (from Step 3 for the first iteration ($\mu_x = \mu_{c_x}$), otherwise from Step 6 for the subsequent iterations ($\mu_x = \hat{\mu}$).

$$F_x = C_x \frac{s}{1+s} f(\lambda)$$

where

$$\lambda = \frac{\mu_x F_Z (1+s)}{2C_K s} \quad (3.75)$$

$$f(\lambda) = \begin{cases} (2-\lambda)\lambda, & \text{if } \lambda < 1 \\ 1, & \text{otherwise} \end{cases}$$

Step 5:

$$\Sigma \hat{F}_x = k_1 \cdot \tanh \left(\begin{array}{l} \left(mv_x \dot{} + \frac{1}{2} \rho C_d A_f v_x^2 + mg \sin \theta_{grade} + f_r mg \cos \theta_{grade} \right) \\ - \left(\hat{F}_{x_{fl}} + \hat{F}_{x_{fr}} + \hat{F}_{x_{rl}} + \hat{F}_{x_{rr}} \right) \end{array} \right) \quad (3.76)$$

$$e(t) = \Sigma \hat{F}_x - \left(\hat{F}_{x_{fl}} + \hat{F}_{x_{fr}} + \hat{F}_{x_{rl}} + \hat{F}_{x_{rr}} \right)$$

Step 6:

If $e(t) > \text{threshold error}$

$$\hat{\mu} = k_2 \cdot \tanh \left(\begin{array}{l} \left(mv_x \dot{} + \frac{1}{2} \rho C_d A_f v_x^2 + mg \sin \theta_{grade} + f_r mg \cos \theta_{grade} \right) \\ - \left(\hat{F}_{x_{fl}} + \hat{F}_{x_{fr}} + \hat{F}_{x_{rl}} + \hat{F}_{x_{rr}} \right) \end{array} \right) \quad (3.77)$$

else if $e(t) \leq \text{threshold error}$

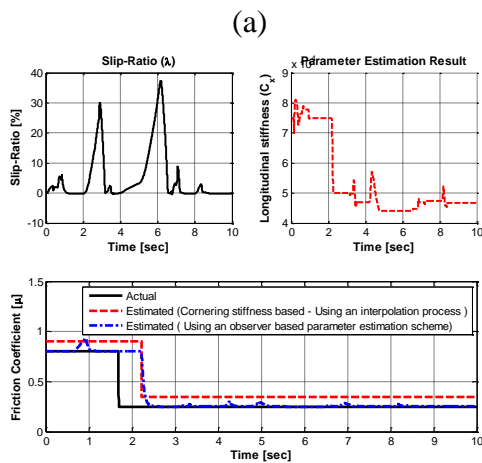
$$\begin{aligned} \hat{\mu}' = k_3 \cdot \tanh & \left(\left(mv_x \dot{\cdot} + \frac{1}{2} \rho C_d A_f v_x^2 + mg \sin \theta_{\text{grade}} + f_r mg \cos \theta_{\text{grade}} \right) \right. \\ & \left. - \left(\hat{F}_{x_{fl}} + \hat{F}_{x_{fr}} + \hat{F}_{x_{rl}} + \hat{F}_{x_{rr}} \right) \right) \\ & + k_4 \cdot \tanh \left(\mu_{C_x} - \hat{\mu} \right) \end{aligned} \quad (3.78)$$

Step 7: Repeat Steps 1-6 for each time step.

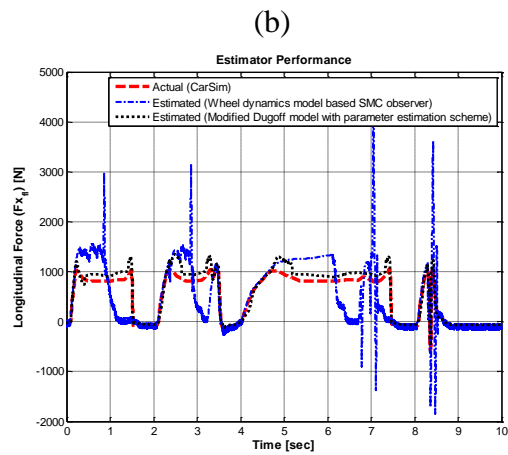
The performance of the observer was evaluated with simulations where the road surface is designed to have sudden friction coefficient changes (Table 7).

Table 3.7: Simulation cases

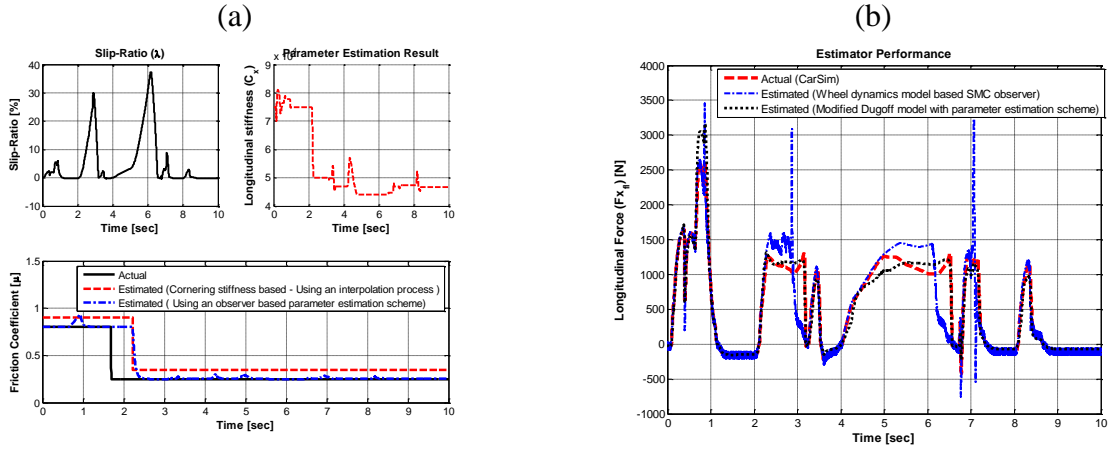
	Friction Coefficient (μ)
Case 1	Low mu
Case 2	Jump mu (high-low)
Case 3	Jump mu (high-low-high)



Case 1



Case 2



Case 3

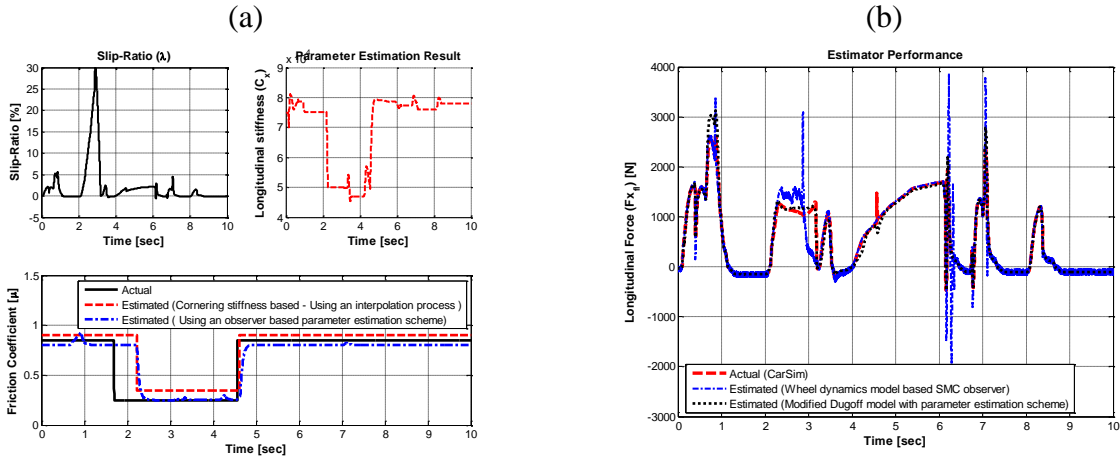


Fig. 3.38: Observer Performance (ref. Table 7 for a description of the simulation conditions)

Fig. 3.38 shows that the proposed observer is able to estimate the longitudinal forces successfully even under high-slip conditions.

3.2.8.2 Lateral Force Estimator

A sliding mode observer (SMO) methodology is proposed to observe the tire lateral forces. The observer estimates lateral forces per axle ($F_{y_{front}}, F_{y_{rear}}$) and then calculates lateral force on each tire according to the distribution of the estimated vertical forces as:

$$\begin{aligned}
F_{y_{fl}} &= \frac{F_{z_{fl}}}{F_{z_{fl}} + F_{z_{fr}}} \cdot F_{y_{front}} \\
F_{y_{fr}} &= \frac{F_{z_{fr}}}{F_{z_{fl}} + F_{z_{fr}}} \cdot F_{y_{front}} \\
F_{y_{rl}} &= \frac{F_{z_{rl}}}{F_{z_{rl}} + F_{z_{rr}}} \cdot F_{y_{rear}} \\
F_{y_{rr}} &= \frac{F_{z_{rr}}}{F_{z_{rl}} + F_{z_{rr}}} \cdot F_{y_{rear}}
\end{aligned} \tag{3.79}$$

The observer is built in such a way that it requires no tire force model or prior knowledge of road friction. The tire forces (axle forces) are modeled with a random walk model:

$$\begin{aligned}
\dot{F}_{y_{front}} &= 0 \\
\dot{F}_{y_{rear}} &= 0
\end{aligned} \tag{3.80}$$

The vehicle dynamics are described by the following state and measurement equations:

$$\begin{aligned}
X &= [x_1, x_2, x_3] = [F_{y_{front}}, F_{y_{rear}}, r] \\
Y &= [y_1, y_2] = [a_y, r]
\end{aligned} \tag{3.81}$$

Vectors $\hat{X} = [\hat{x}_1, \hat{x}_2, \hat{x}_3]$ and $\hat{Y} = [\hat{y}_1, \hat{y}_2]$ represent the state and measurement estimations. The measurement model is:

$$\hat{y}_1 = \frac{\hat{x}_1 + \hat{x}_2}{m}; \hat{y}_2 = \hat{x}_3 \tag{3.82}$$

where m is the vehicle mass. The estimation errors for states and measurements are denoted respectively as:

$$\begin{aligned}
e_x &= [x_1 - \hat{x}_1, x_2 - \hat{x}_2, x_3 - \hat{x}_3] \\
e_y &= [y_1 - \hat{y}_1, y_2 - \hat{y}_2]
\end{aligned} \tag{3.83}$$

The state estimates evolve according to the four-wheel vehicle model, the force model and the sign of the measurement estimation errors as:

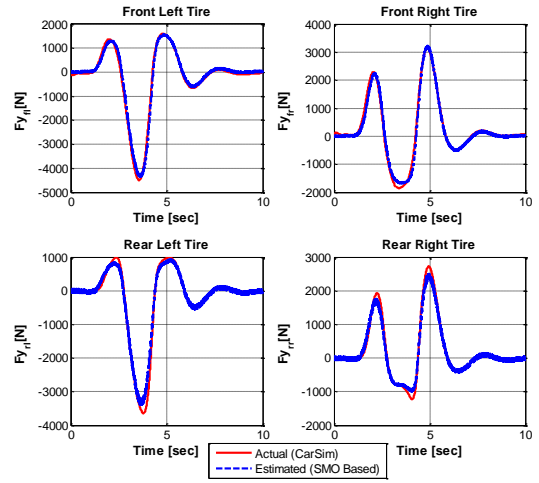
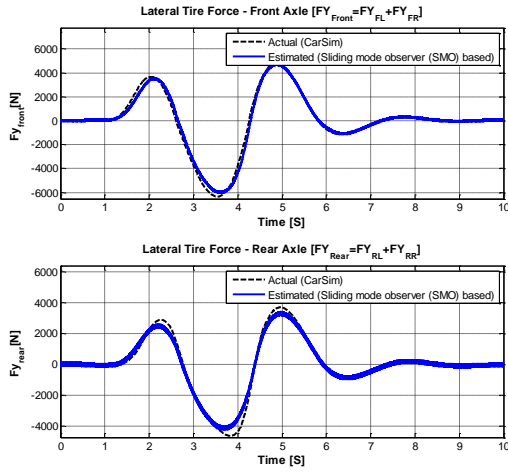
$$\begin{aligned}
\dot{\hat{x}}_1 &= k_{11} \text{sign}(e_{y_1}) + k_{12} \text{sign}(e_{y_2}) \\
\dot{\hat{x}}_2 &= k_{21} \text{sign}(e_{y_1}) + k_{22} \text{sign}(e_{y_2}) \\
\dot{\hat{x}}_3 &= \frac{1}{I_z} [a * \hat{x}_2 - b * \hat{x}_1 + \frac{t}{2} \left((F_{x_{fr}} \cos \delta + F_{x_{rr}}) - (F_{x_{fl}} \cos \delta + F_{x_{rl}}) \right)] + k_{31} \text{sign}(e_{y_2})
\end{aligned} \tag{3.84}$$

where $k_{11}, k_{12}, k_{21}, k_{22}, k_{31}$ are the observer gains. $F_{x_{ij}}$ is the longitudinal force estimate for the individual wheels obtained using the estimation scheme proposed in Section 2.8.1. The force balance equations also include any additional forces and moments generated from longitudinal drive traction or braking forces at the wheels. The longitudinal force terms should be included so the lateral estimation does not become corrupted, especially in situations when the vehicle is undergoing significant acceleration or braking. The drive and traction forces of the front wheels contribute to the lateral force of the steered wheels, and any ESC differential braking produces an additional moment that must be included in the moment equation. A complete study for the convergence of the SMO is presented in [70]. The performance of the observer was evaluated for a range of different simulations cases (Table 3.8).

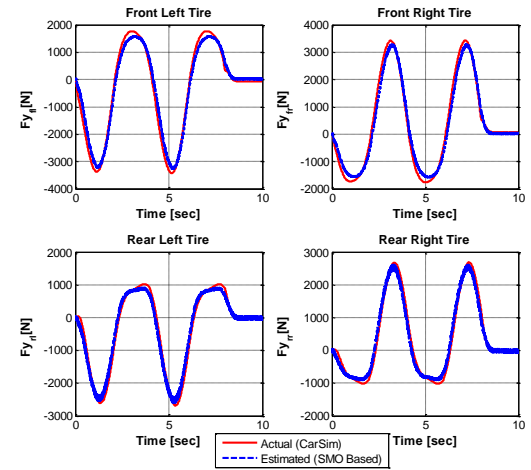
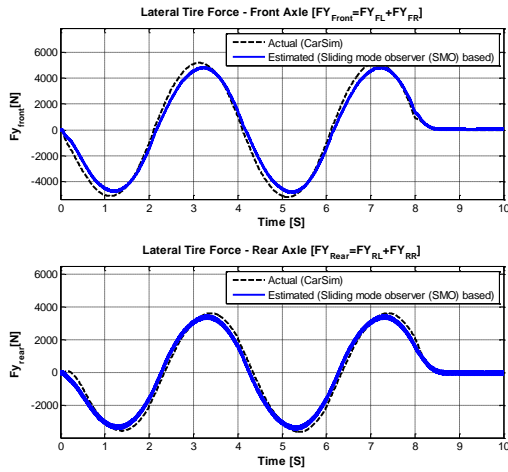
Table 3.8: Simulation cases

	Vehicle Speed (kph)	Test Maneuver
Case 1	≈ 120 kph	Double lane change
Case 2	≈ 70 kph	Slalom steering maneuver (55 deg/0.25 Hz)
Case 3	≈ 80 kph	Fishhook Maneuver

Case 1



Case 2



Case 3

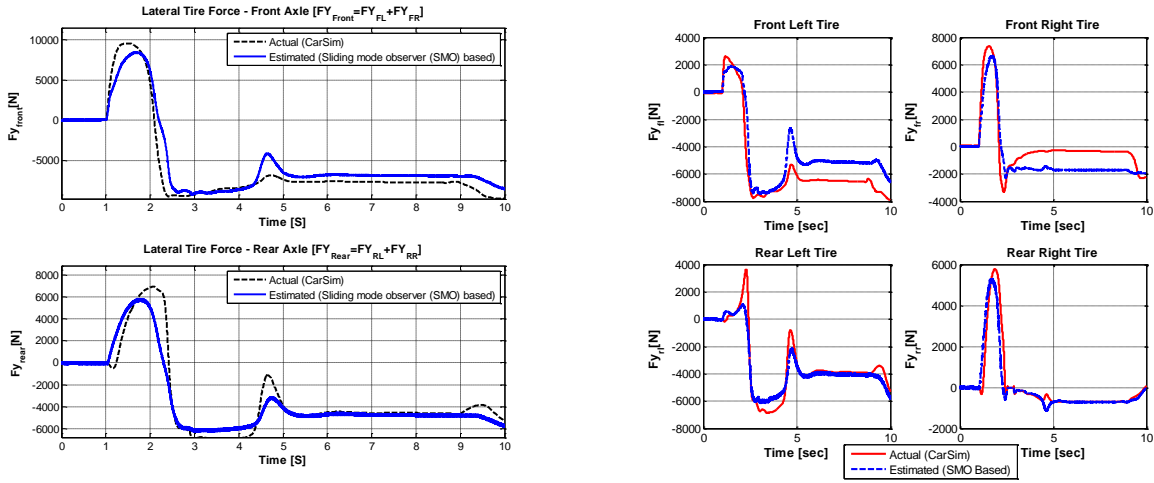


Fig. 3.39: Observer Performance (ref. Table 3.8 for a description of the simulation conditions)

From Fig. 3.39 we see that the SMO observer produces satisfactory estimations close to the actual value.

3.2.9 Vehicle Lateral and Longitudinal Velocity Estimator

3.2.9.1 Estimation Concept

Longitudinal and lateral vehicle velocities are important information for active vehicle stability control. But for both technical and economical reasons, these vehicle states cannot be measured directly in a standard car. As a result, the problem of longitudinal and lateral vehicle velocities estimation has attracted considerable attentions of many researchers, and several works have already been conducted over the past few years. Kalman filter based techniques (KF, EKF...) have become a standard technique used in a number of nonlinear estimation and machine learning applications. KF is only applied to linear systems, and EKF is developed for state estimation in non-linear systems. But as linearization of EKF algorithm requires the evaluation of a Jacobian matrix at each time step, the computational complexity is enlarged. To avoid this problem, [71] proposes Unscented Kalman Filter (UKF), which avoids the linearization errors and improves filtering accuracy. The UKF acts directly on the nonlinear model and approximates the states by using a set of sigma points, avoiding the linearization made by the EKF [72]. This study proposes to estimate longitudinal and lateral velocity based on UKF using vehicle dynamics model.

In most vehicle handling and stability studies, two degrees of freedom vehicle model is usually used, which need to make a great linear hypothesis. To obtain a more realistic simulation of vehicle performance, a nonlinear model with four wheels (coupled model very largely used in simulation) is selected in this study (Fig. 3.40). The different equations for the calculation of longitudinal, lateral and yaw motion are as follows:

$$\dot{v}_x = \frac{F_{xfl} \cos \delta + F_{xfr} \cos \delta + F_{xrl} + F_{xrr}}{m} + r \cdot v_y - g \cdot \sin(\theta_{pitch}) \quad (3.85)$$

$$\dot{v}_y = \frac{F_{yfront} + F_{yrear}}{m} - r \cdot v_x - g \cdot \sin(\phi_{roll}) \quad (3.86)$$

$$\dot{r} = \frac{a \cdot F_{yfront} - b \cdot F_{yrear} + \left((F_{xfr} \cos \delta + F_{xrr}) - (F_{xfl} \cos \delta + F_{xrl}) \right) \cdot \frac{t}{2}}{I_z} \quad (3.87)$$

Where, m is the vehicle mass; δ is the steering angle of front wheel; a and b are the distances from front and rear axle respectively to centre of gravity; t is the vehicle track-width; v_x is longitudinal velocity; v_y is lateral velocity; r is yaw rate; θ_{pitch} is the vehicle pitch (global) angle (see Fig. 3.16); ϕ_{roll} is the vehicle roll (global) angle (see Fig. 3.15); F_{xij} are tire longitudinal forces, and F_{yfront} and F_{yrear} are the lateral forces at the front and rear axles, respectively.

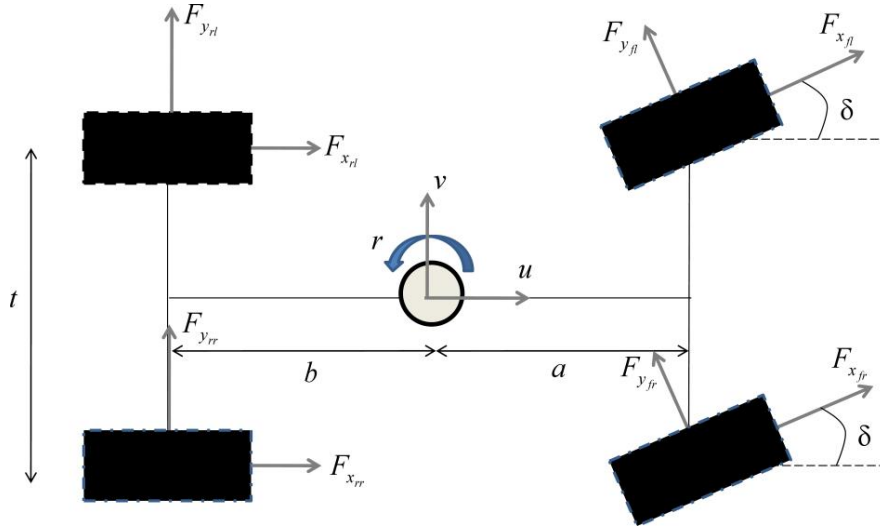


Fig. 3.40: Four wheel vehicle model

The nonlinear model can be transformed into standard state-space form with state vector (x) composed of longitudinal speed, lateral speed and yaw rate:

$$x = [v_x, v_y, r] \quad (3.88)$$

The input vector (u) comprises the measured steering angle, tire forces (considered estimated beforehand, see Section 3.2.7), and vehicle global roll and pitch angles (considered estimated beforehand, see Section 3.2.4):

$$u = [\delta, F_{x_{fl}}, F_{x_{fr}}, F_{x_{rl}}, F_{x_{rr}}, F_{y_{front}}, F_{y_{front}}, \theta_{pitch}, \phi_{roll}] \quad (3.89)$$

The measurement vector (y) comprises vehicle longitudinal velocity (considered estimated beforehand, see Section 3.2.6), measured yaw rate, and lateral accelerations:

$$y = [v_x, r, a_{y,m}] \quad (3.90)$$

The process and measurement noise vectors are assumed to be white, zero mean and uncorrelated. The schematic simulation block diagram is represented in Fig. 3.41.

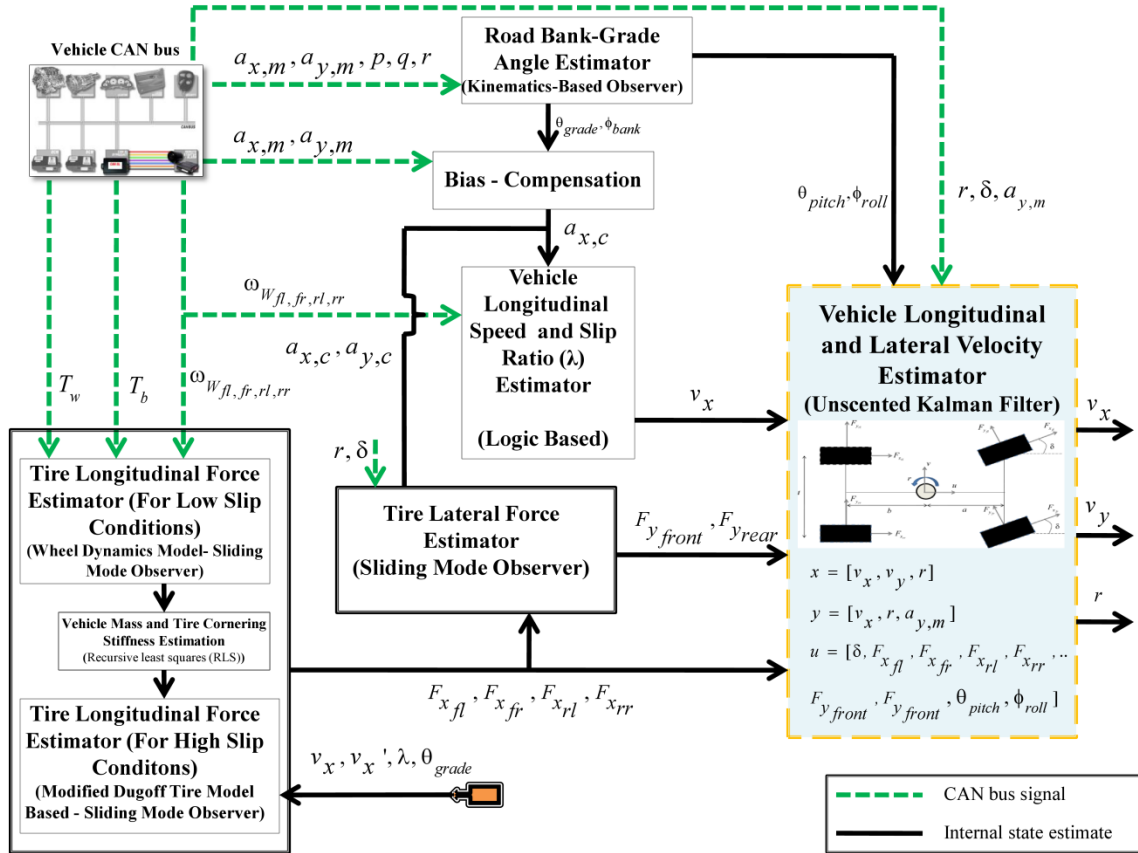


Fig. 3.41: Schematic diagram of the vehicle longitudinal and lateral velocity estimation process

3.2.9.2 UKF ALGORITHM

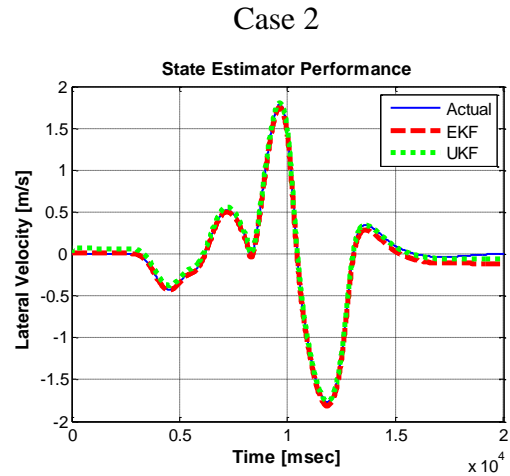
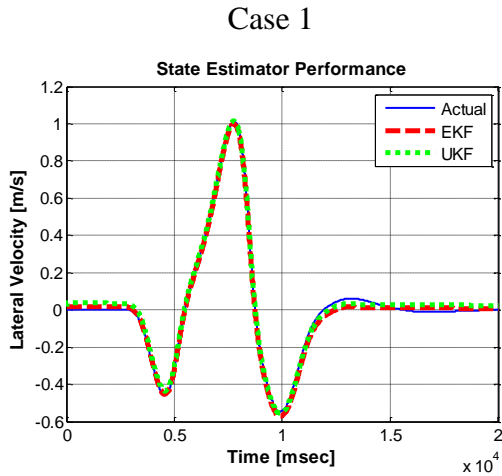
UKF [73] (unscented Kalman filter) adopts a sampling method based on EKF to solve the Gaussian random variable (GRV) propagation in the nonlinear system. UT (unscented transformation) is the core and basis of UKF method, which is founded on the intuition that it is easier to approximate a Gaussian distribution than it is to approximate an arbitrary nonlinear function. A set of sigma sample points are chosen so that their sample mean and sample covariance are the mean and covariance of GRV. The nonlinear function is applied to each point in turn to yield a cloud of transformed points and the statistics of the transformed points (posterior mean and covariance). Details regarding the UKF algorithm formulation can be found in [73].

3.2.9.3 Simulation Analysis

The performance of the observer was evaluated for a range of different simulations cases (Table 3.9).

Table 3.9: Simulation cases

	Vehicle Speed (kph)	Friction Coefficient (μ)	Test Maneuver
Case 1	140 kph	0.85	Double lane change
Case 2	140 kph	Varying (high-low-high)	Double lane change
Case 3	80 kph	0.85	Fishhook
Case 4	70 kph	0.20	Slalom



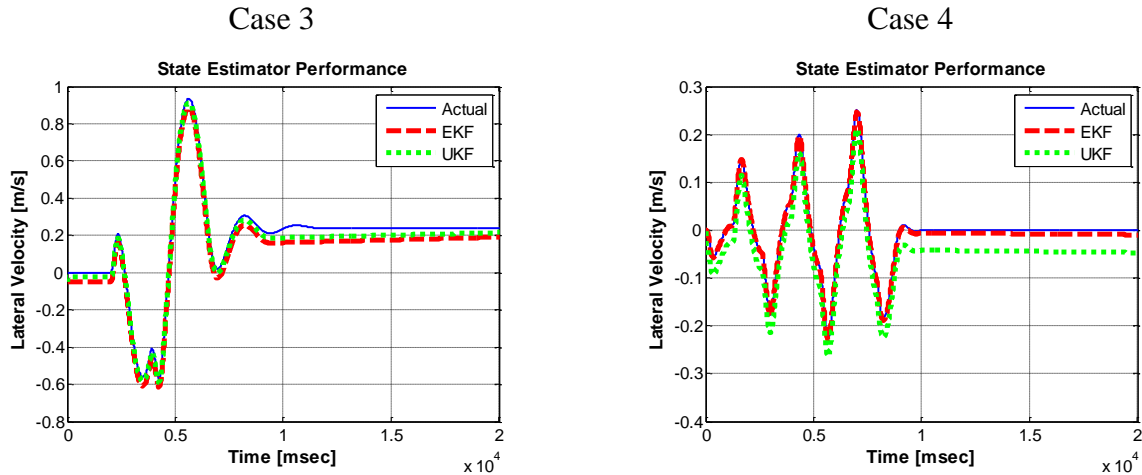


Fig. 3.42: Observer Performance (ref. Table 3.9 for a description of the simulation conditions)

3.2.10 Tire slip-ratio and slip-angle estimator

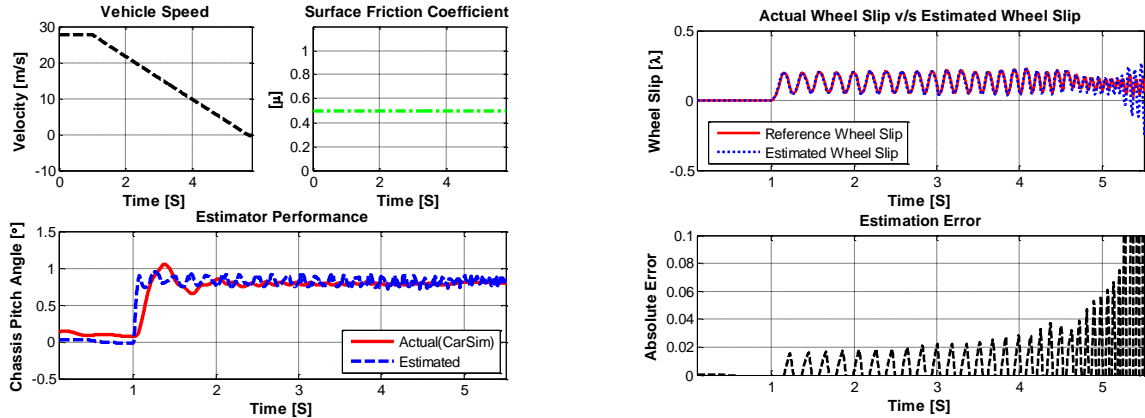
3.2.10.1 Slip ratio Estimator

As shown in Section 3.2.6, the output of the longitudinal vehicle speed estimation algorithm could also be employed for reliably computing the longitudinal wheel slip. Performance of the observer under extreme braking conditions (Table 3.10) is demonstrated in Fig. 3.43

Table 3.10: Simulation cases

	Vehicle Speed (kph)	Friction Coefficient (μ)	Test Maneuver
Case 1	100-0 kph	0.5	Straight-line braking
Case 2	100-0 kph	Varying	Straight-line braking

Case 1



Case 2

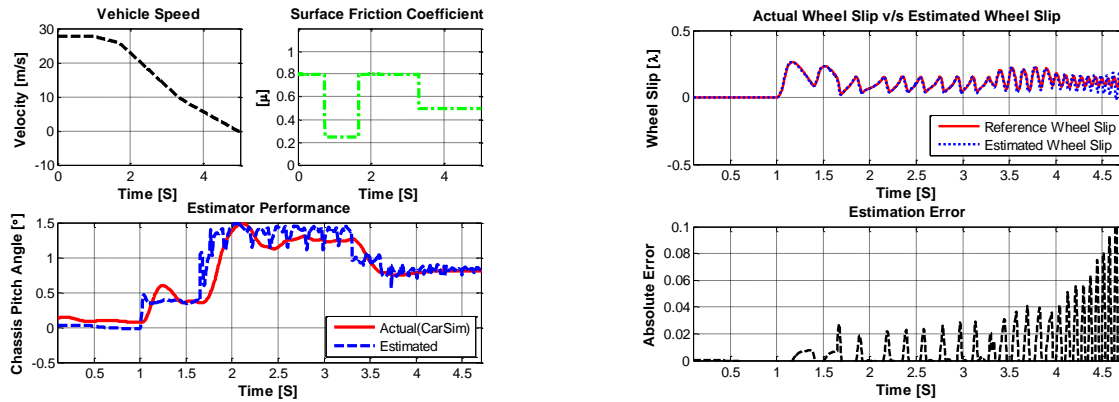


Fig. 3.43: Observer Performance (ref. Table 3.10 for a description of the simulation conditions)

3.2.10.2 Slipangle Estimator

3.2.10.2.1 Estimation Concept and Observer Update Law

To estimate the tire slipangle, an update equation for the front slip angle is derived as a function of the tire forces. A four-wheel vehicle model is employed to simulate the vehicle rigid body dynamic (Fig. 3.40). The dynamic equations of motion of the vehicle model are presented in Eq. (3.91) - Eq. (3.93):

$$\dot{v}_x = \frac{F_{xfl} \cos \delta + F_{xfr} \cos \delta + F_{xrl} + F_{xrr}}{m} + r \cdot v_y - g \cdot \sin(\theta_{pitch}) \quad (3.91)$$

$$\dot{v}_y = \frac{F_{y_{front}} + F_{y_{rear}}}{m} - r \cdot \dot{v}_x - g \cdot \sin(\phi_{roll}) \quad (3.92)$$

$$\dot{r} = \frac{a \cdot F_{y_{front}} - b \cdot F_{y_{rear}} + \left((F_{x_{fr}} \cos \delta + F_{x_{rr}}) - (F_{x_{fl}} \cos \delta + F_{x_{rl}}) \right) \cdot \frac{t}{2}}{I_z} \quad (3.93)$$

where $F_{y_{front}} = \left(F_{y_{fl}} \cos \delta + F_{x_{fl}} \sin \delta \right) + \left(F_{y_{fr}} \cos \delta + F_{x_{fr}} \sin \delta \right)$ and

$F_{y_{rear}} = F_{y_{rl}} + F_{y_{rr}}$ are the lateral forces at the front and rear axles, respectively.

Using kinematics, the front and rear tire slip angles are linearized to be:

$$\alpha_f = \frac{v_y + a \cdot r}{v_x} - \delta \quad (3.94)$$

$$\alpha_r = \frac{v_y - b \cdot r}{v_x} \quad (3.95)$$

The update equation for the front slip angle is derived by taking the derivative of Eq. (3.94)

$$\dot{\alpha}_f = \frac{v_y \dot{} + a \cdot \dot{r}}{v_x} - \dot{\delta} \quad (3.96)$$

Substituting expressions for v_y (Ref. Eq. (3.92)), and r (Ref. Eq. (3.93)) in Equation (3.96), we get:

$$\dot{\alpha}_f = \frac{1}{v_x} \left(\begin{array}{c} \frac{F_{y_{front}} + F_{y_{rear}}}{m} - r \cdot v_x \\ a \cdot F_{y_{front}} - b \cdot F_{y_{rear}} + \left((F_{x_{fr}} \cos \delta + F_{x_{rr}}) - (F_{x_{fl}} \cos \delta + F_{x_{rl}}) \right) \cdot \frac{t}{2} \\ + a \cdot \frac{\phantom{a \cdot F_{y_{front}} - b \cdot F_{y_{rear}} + \left((F_{x_{fr}} \cos \delta + F_{x_{rr}}) - (F_{x_{fl}} \cos \delta + F_{x_{rl}}) \right) \cdot \frac{t}{2}}}{I_z} \end{array} \right) - \dot{\delta} \quad (3.97)$$

Rearranging above equation, we get:

$$\begin{aligned} \dot{\alpha}_f &= \left(\frac{1}{mv_x} + \frac{a^2}{I_z v_x} \right) \cdot F_{y_{front}} + \left(\frac{1}{mv_x} - \frac{ab}{I_z v_x} \right) \cdot F_{y_{rear}} \\ &+ \frac{t \cdot a}{2I_z v_x} \left((F_{x_{fr}} \cos \delta + F_{x_{rr}}) - (F_{x_{fl}} \cos \delta + F_{x_{rl}}) \right) - r - \dot{\delta} \end{aligned} \quad (3.98)$$

Thus, to update $\hat{\alpha}_f$, we may integrate the following observer update law:

$$\begin{aligned} \dot{\hat{\alpha}}_f &= \left(\frac{1}{mv_x} + \frac{a^2}{I_z v_x} \right) \cdot F_{y_{front}} + \left(\frac{1}{mv_x} - \frac{ab}{I_z v_x} \right) \cdot F_{y_{rear}} \\ &+ \frac{t \cdot a}{2I_z v_x} \left((F_{x_{fr}} \cos \delta + F_{x_{rr}}) - (F_{x_{fl}} \cos \delta + F_{x_{rl}}) \right) - r - \dot{\delta} + k(ma_y - F_{y_{front}} - F_{y_{rear}}) \end{aligned} \quad (3.99)$$

where k is the observer feedback gain and a_y is the measured lateral acceleration. Once $\hat{\alpha}_f$ is updated, the rear slipangle estimate ($\hat{\alpha}_r$) can be updated using the kinematic relationship described by Eq. (3.95).

From Equation (3.99), we can see that an estimate of the tire slipangle can be made, provided we have real-time information about the tire longitudinal/lateral forces. To successfully achieve the aforementioned objective of estimating the tire slipangle, an integrated estimation scheme is proposed (Fig. 3.44). The estimation scheme consists of two key blocks: 1) tire longitudinal force estimator; 2) tire lateral force estimator.

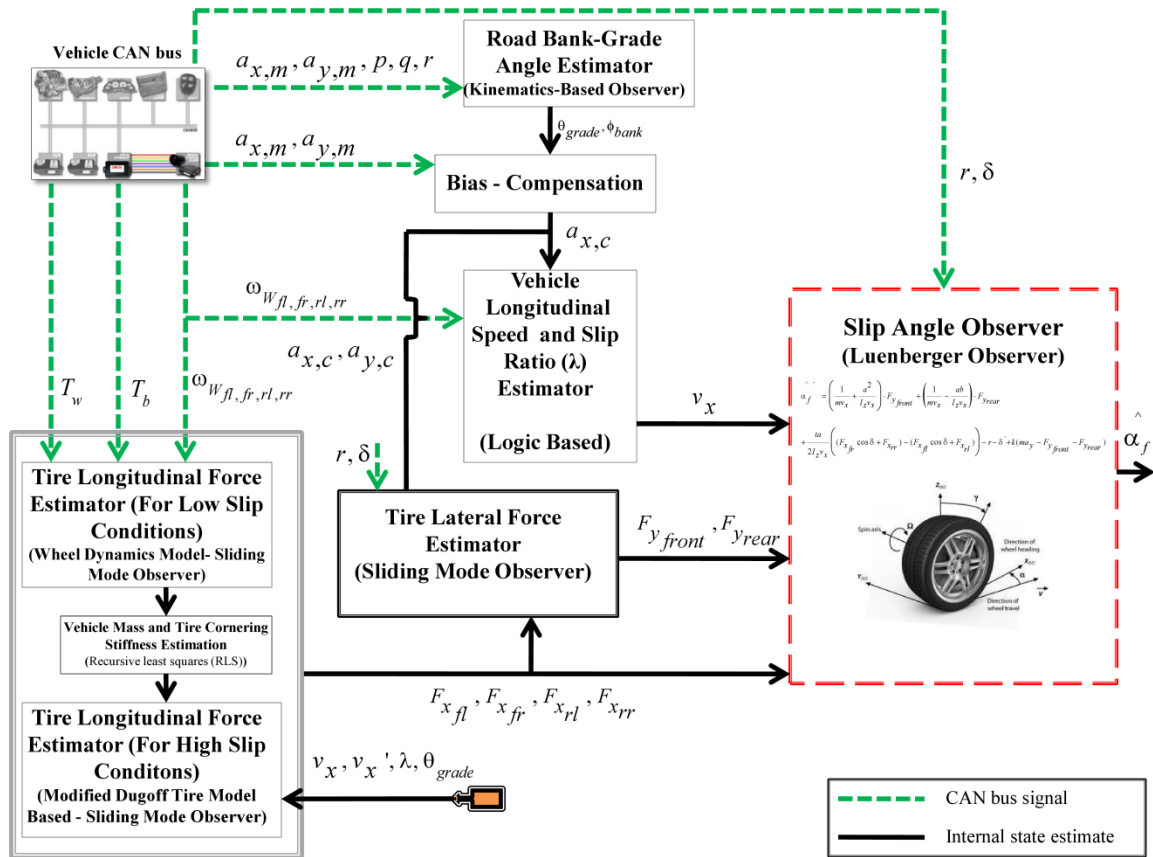


Fig. 3.44: Schematic diagram of the tire slipangle estimation process

3.2.10.2.2 Slipangle Estimator Performance

Using the tire longitudinal/lateral force estimates (considered estimated beforehand, see Section 3.2.8), the performance of the slipangle observer (Eq. (3.99)) was evaluated for range of different aggressive steering maneuvers (Table 3.11). Fig. 3.45 shows that the proposed observer is able to estimate the tire slipangle successfully even for challenging (aggressive maneuvering) operating conditions.

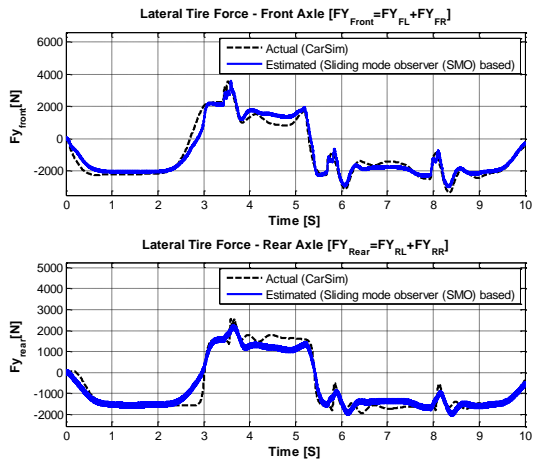
Table 3.11: Simulation cases

	Vehicle Speed (kph)	Friction Coefficient	Test Maneuver
Case 1	80 kph	$\mu=0.2$	Slalom steering maneuver (55 deg/0.25 Hz)
Case 2	80 kph	$\mu=0.5$	Slalom steering maneuver (55

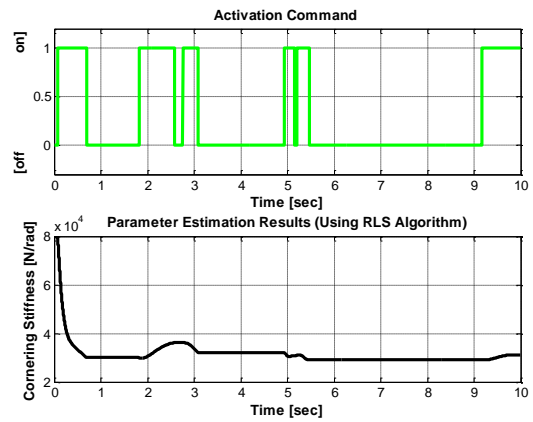
			deg/0.25 Hz)
Case 3	120 kph	$\mu=0.4$	Double lane change maneuver
Case 4	120 kph	$\mu=0.85$	Double lane change maneuver
Case 5	60 kph	Jump μ (high-low)	Double lane change maneuver

Case 1

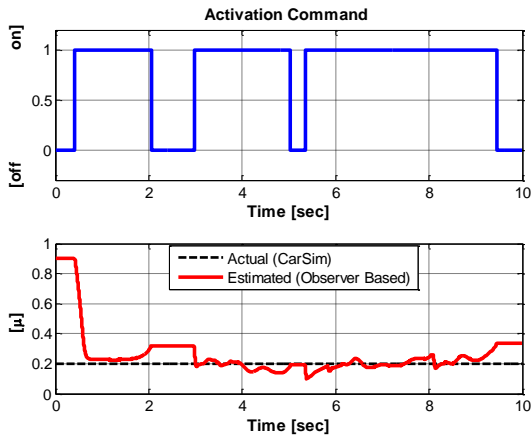
Axle lateral force estimation



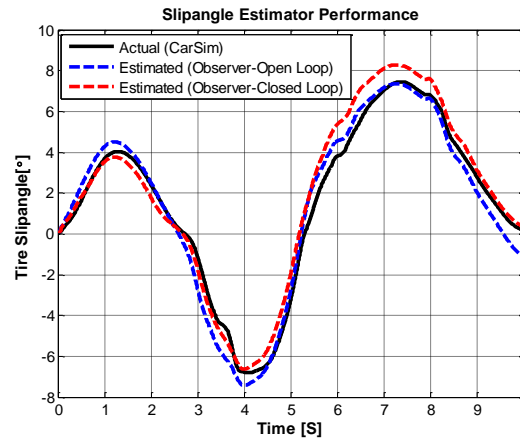
Cornering Stiffness Estimation



Friction Estimation

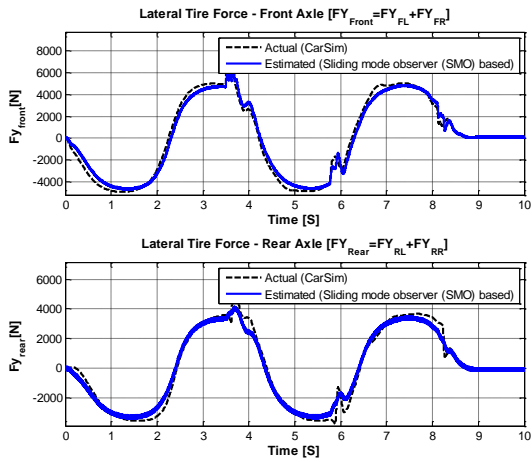


Slipangle Estimation

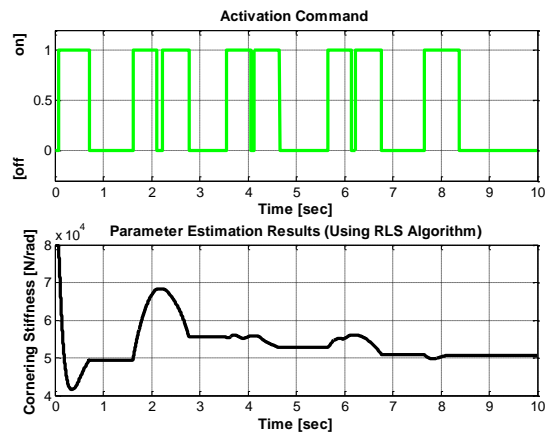


Case 2

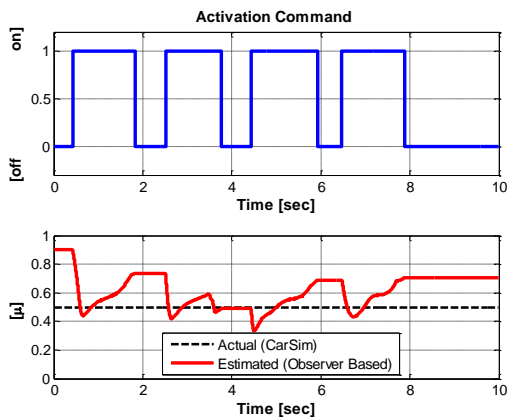
Axle lateral force estimation



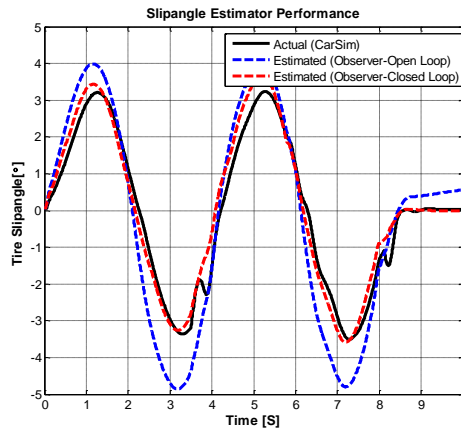
Cornering Stiffness Estimation



Friction Estimation

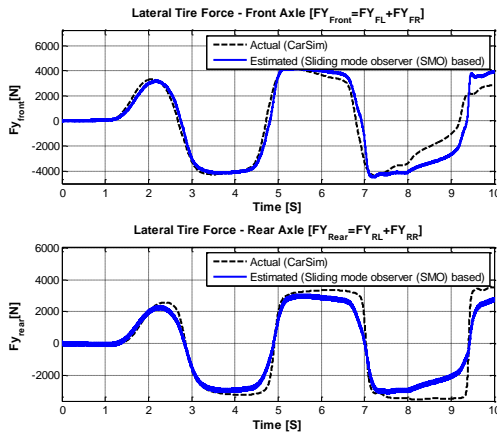


Slipangle Estimation

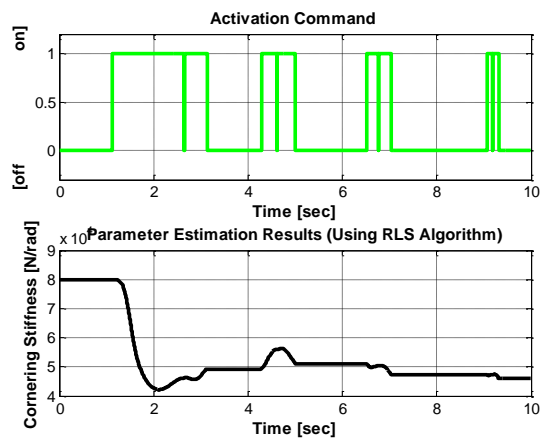


Case 3

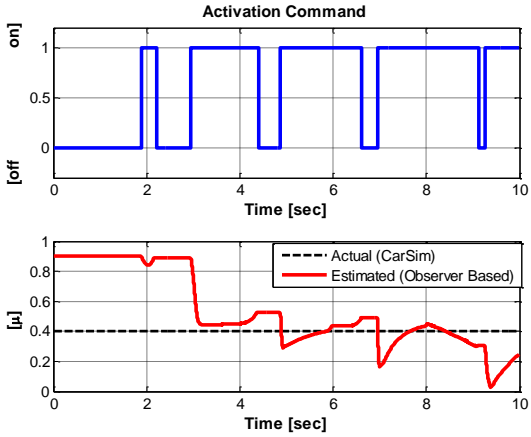
Axle lateral force estimation



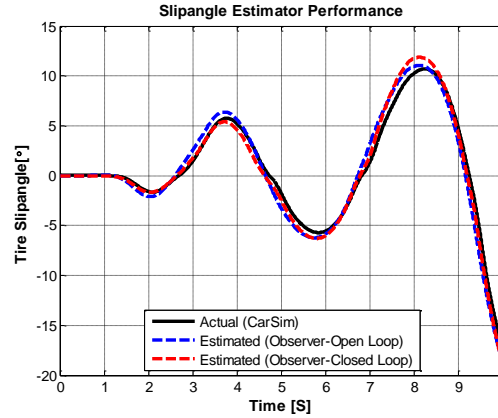
Cornering Stiffness Estimation



Friction Estimation

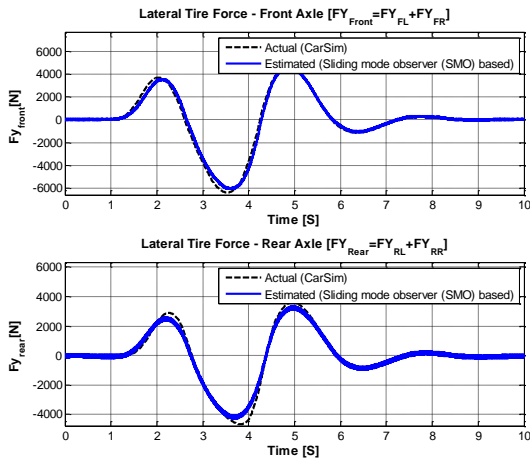


Slipangle Estimation

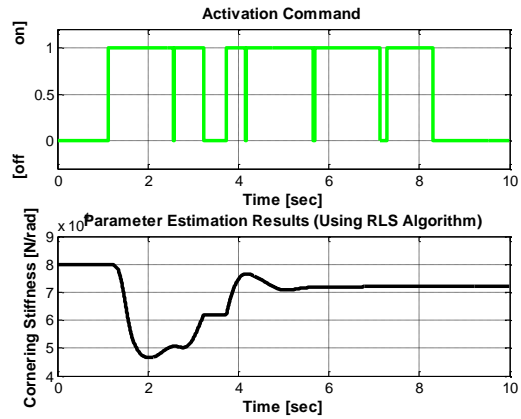


Case 4

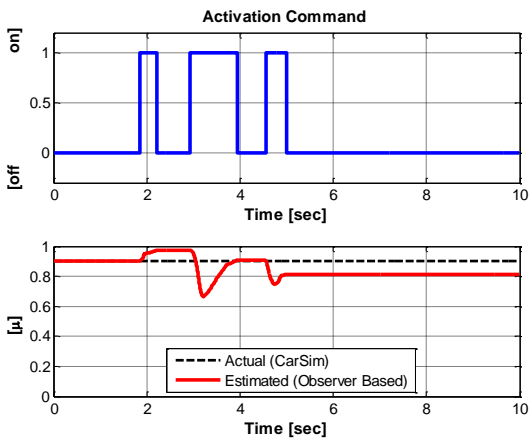
Axle lateral force estimation



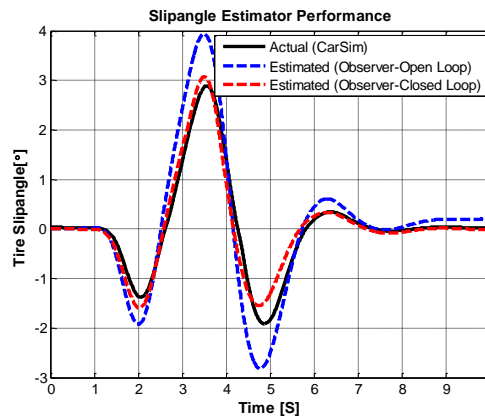
Cornering Stiffness Estimation



Friction Estimation

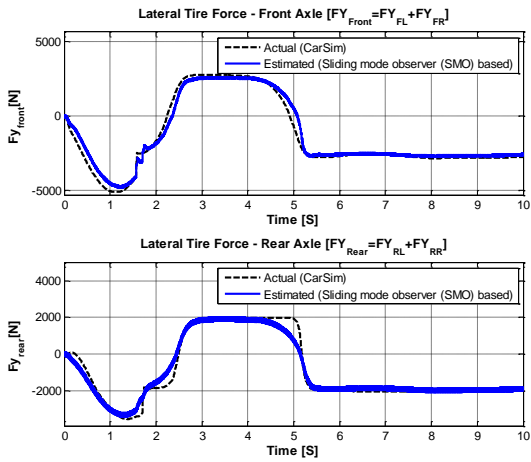


Slipangle Estimation

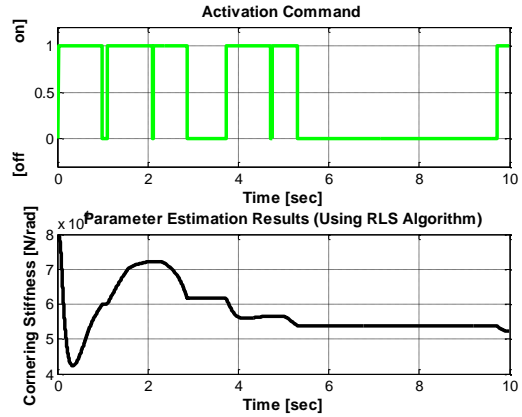


Case 5

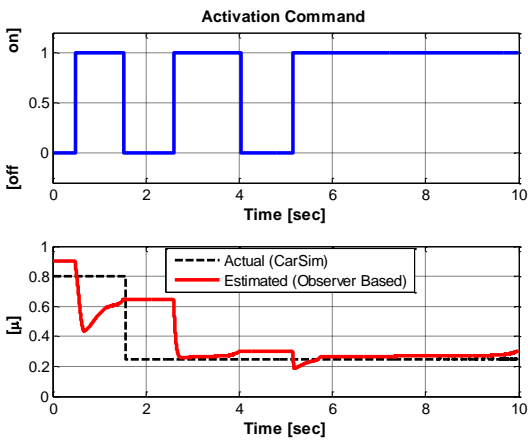
Axle lateral force estimation



Cornering Stiffness Estimation



Friction Estimation



Slipangle Estimation

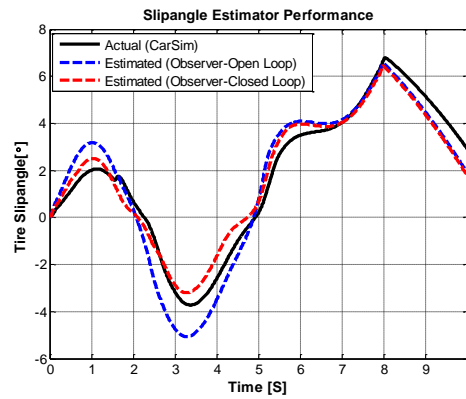


Fig. 3.45: Observer Performance (ref. Table 3.11 for a description of the simulation conditions)

3.3 Conclusion

This study introduces an integrated vehicle state estimator, comprising of a series of model-based and kinematics-based observers. The estimator is implemented in the Matlab/Simulink and CarSim software environment. Results presented here show the ability of cascaded estimators to provide accurate estimates of vehicle states. Moreover, it shows good robustness with respect to road friction variations. These improved state estimates can be used to develop a more reliable and robust vehicle stability control system.

Nomenclature

F_{y_f} : front axle lateral force (in vehicle body axis)

F_{y_r} : rear axle lateral force (in vehicle body axis)

$\sum F_x$: summation of tire longitudinal forces (in vehicle body axis)

ϕ : roll angle

θ : pitch angle

ψ : yaw angle

v_x : longitudinal velocity at C.G.

v_y : lateral velocity at C.G.

v_z : vertical velocity at C.G.

a_x : longitudinal acceleration measured at C.G.

a_y : lateral acceleration measured at C.G.

a_z : vertical acceleration measured at C.G.

p : roll rate measured at C.G.

q : pitch rate measured at C.G.

r : yaw rate measured at C.G.

m : total vehicle mass

m_s : sprung mass of the vehicle

m_u : unsprung mass of the vehicle

g : gravitational constant

h_{cg} : vehicle C.G. height

h_r : height of the roll center from the ground

$h_{r_{front}}$: height of the front roll center from the ground

$h_{r_{rear}}$: height of the rear roll center from the ground

h_a : height of the unsprung mass from the ground

h_{roll} : height of the sprung mass from the roll axis

a : distance between C.G. and front axle
 b : distance between C.G. and rear axle
 l : distance between front and rear axle
 I_z : moment of inertia about z - axis / yaw axis
 I_x : moment of inertia about x - axis / roll axis
 β : vehicle sideslip angle
 δ_{sus} : suspension deflection
 λ : tire slip – ratio
 α : tire slip – angle
 T_e : engine torque
 T_b : brake torque
 T_w : wheel torque
 ω_w : wheel angular speed
 θ_w : angular position of the wheel
 k_{roll} : roll stiffness
 c_{roll} : roll damping coefficient
 $\phi_{chassis}$: vehicle chassis roll angle
 $\theta_{chassis}$: vehicle chassis pitch angle
 $\phi_{road\ bank}$: road bank angle
 $\theta_{road\ grade}$: road grade angle
 t : track width
 $\phi_{vehicle\ roll}$: vehicle roll angle
 $\phi_{vehicle\ roll_{SS}}$: vehicle steady state roll angle
 $\phi_{vehicle\ roll_{TS}}$: vehicle transient state roll angle
 $\theta_{vehicle\ pitch}$: vehicle pitch angle
 $\theta_{vehicle\ pitch_{SS}}$: vehicle steady state pitch angle
 $\phi_{vehicle\ pitch_{TS}}$: vehicle transient state pitch angle
 $a_{x,m}$: measured longitudinal acceleration of the vehicle

$a_{y,m}$: measured lateral acceleration of the vehicle
 $a_{x,c}$: bias – compensated longitudinal acceleration of the vehicle
 $a_{y,c}$: bias – compensated lateral acceleration of the vehicle
 r_o : original wheel radius
 r_w : effective wheel radius
 v_w : linear velocity of the four wheels
 $v_{average}$: average of the four wheel speeds
 $v_{non-driven\ average}$: average of the two non - driven wheel speeds
 v_{min} : vehicle speed threshold
 a_{acc} : acceleration threshold
 a_{dcc} : deceleration threshold
 $Fz_{front\ axle}$: normal force of the front axle
 $Fz_{rear\ axle}$: normal force of the rear axle
 Fx_{fl} : longitudinal force of the front - left wheel
 Fx_{fr} : longitudinal force of the front - right wheel
 Fx_{rl} : longitudinal force of the rear - left wheel
 Fx_{rr} : longitudinal force of the rear - right wheel
 Fy_{fl} : lateral force of the front - left wheel
 Fy_{fr} : lateral force of the front - right wheel
 Fy_{rl} : lateral force of the rear - left wheel
 Fy_{rr} : lateral force of the rear - right wheel
 Fz_{fl} : vertical force of the front - left wheel
 Fz_{fr} : vertical force of the front - right wheel
 Fz_{rl} : vertical force of the rear - left wheel
 Fz_{rr} : vertical force of the rear - right wheel
 F_{rr} : rolling resistance force

$W_{Lateral Load Transfer}$: vehicle lateral load transfer
 $W_{Longitudinal Load Transfer}$: vehicle longitudinal load transfer
 LTR :load transfer ratio
 k_f : front suspension stiffness
 k_r : rear suspension stiffness
 k_{bf} : brake gain of the front wheel $\mu\mu$
 k_{br} : brake gain of the rear wheel
 J_w : spin inertia for each wheel
 k_t : spring rate of the tire
 δ :tire steer angle
 C_x : tire longitudinal stiffness
 C_y : tire cornering stiffness
 μ :tire road friction coefficient
 C_d : vehicle drag coefficient
 A_f : frontal area of the vehicle
 ρ :density of air
 A : state matrix
 B :input matrix
 C :output matrix
 D : feedthrough matrix
 P :covariance matrix

References

[1] G. Baffet, A. Charara and D. Lechner, *Estimation of Tire-Road Forces and Vehicle Sideslip Angle*, in: J. Aramburo, A.R. Trevino (Eds.) *Advances in Robotics, Automation and Control*, 2008, pp. 472.

- [2] G. Baffet, A. Charara and D. Lechner, *Estimation of vehicle sideslip, tire force and wheel cornering stiffness*, Control Engineering Practice. 17 (2009), pp. 1255-1264.
- [3] Z. Wei, D. Nenggen, Y. Guizhen and Z. Wei, *Virtual sensors design in vehicle sideslip angle and velocity of the centre of gravity estimation*, in: Electronic Measurement & Instruments, 2009. ICEMI '09. 9th International Conference on, 2009, pp. 3-652-653-656.
- [4] M. Doumiati, A. Victorino, A. Charara, G. Baffet and D. Lechner, *An estimation process for vehicle wheel-ground contact normal forces*, in: Proceedings of the 17th World Congress The International Federation of Automatic Control, 2008.
- [5] M. Doumiati, A. Victorino, A. Charara and D. Lechner, *Lateral load transfer and normal forces estimation for vehicle safety: experimental test*, Vehicle System Dynamics. 47 (2009), pp. 1511-1533.
- [6] M. Doumiati, A. Victorino, A. Charara and D. Lechner, *Virtual sensors, application to vehicle tire-road normal forces for road safety*, in: American Control Conference, 2009. ACC '09., 2009, pp. 3337-3343.
- [7] H.K. Fathy, K. Dongsoo and J.L. Stein, *Online vehicle mass estimation using recursive least squares and supervisory data extraction*, in: American Control Conference, 2008, 2008, pp. 1842-1848.
- [8] A. Vahidi, A. Stefanopoulou and H. Peng, *Recursive least squares with forgetting for online estimation of vehicle mass and road grade: theory and experiments*, Vehicle System Dynamics. 43 (2005), pp. 31-55.
- [9] C. Wanki, Y. Jangyeol, Y. Seongjin, K. Bongyeong and Y. Kyongsu, *Estimation of Tire Forces for Application to Vehicle Stability Control*, Vehicular Technology, IEEE Transactions on. 59 (2010), pp. 638-649.
- [10] M. Doumiati, A. Victorino, A. Charara and D. Lechner, *Unscented Kalman filter for real-time vehicle lateral tire forces and sideslip angle estimation*, in: Intelligent Vehicles Symposium, 2009 IEEE, 2009, pp. 901-906.

- [11] M. Doumiati, A. Victorino, A. Charara and D. Lechner, *A method to estimate the lateral tire force and the sideslip angle of a vehicle: Experimental validation*, in: American Control Conference (ACC), 2010, 2010, pp. 6936-6942.
- [12] M. Doumiati, A.C. Victorino, A. Charara and D. Lechner, *Onboard Real-Time Estimation of Vehicle Lateral Tire-Road Forces and Sideslip Angle*, Mechatronics, IEEE/ASME Transactions on. 16 (2011), pp. 601-614.
- [13] M. Doumiati, A.C. Victorino, A. Charara and D. Lechner, *Estimation of vehicle lateral tire-road forces: a comparison between extended and unscented Kalman filtering*, in: Proceedings of the European Control Conference, Budapest, Hungary, 2009.
- [14] M. Doumiati, A. Victorino, A. Charara, G. Baffet and D. Lechner, *Observers for vehicle tyre/road forces estimation: experimental validation*, Vehicle System Dynamics. 48 (2010), pp. 1345-1378.
- [15] R. Ghandour, A. Victorino, M. Doumiati and A. Charara, *Tire/road friction coefficient estimation applied to road safety*, in: Control & Automation (MED), 2010 18th Mediterranean Conference on, 2010, pp. 1485-1490.
- [16] R. Ghandour, A. Victorino, A. Charara and D. Lechner, *A vehicle skid indicator based on maximum friction estimation*, in: 18th IFAC World Congress, 2011.
- [17] R. Ghandour, F.H.R. da Cunha, A. Victorino, A. Charara and D. Lechner, *Risk indicators prediction based on the estimation of tire/road forces and the maximum friction coefficient: Experimental validation*, in: Control & Automation (MED), 2011 19th Mediterranean Conference on, 2011, pp. 700-705.
- [18] M. Doumiati, A. Victorino, A. Charara and D. Lechner, *Estimation of road profile for vehicle dynamics motion: Experimental validation*, in: American Control Conference (ACC), 2011, pp. 5237-5242.

- [19] H.F. Grip, L. Imsland, T.A. Johansen, J.C. Kalkkuhl and A. Suissa, *Vehicle sideslip estimation*, Control Systems, IEEE. 29 (2009), pp. 36-52.
- [20] L.R. Ray, *Nonlinear state and tire force estimation for advanced vehicle control*, Control Systems Technology, IEEE Transactions on. 3 (1995), pp. 117-124.
- [21] B. Samadi, R. Kazemi, K.Y. Nikravesh and M. Kabganian, *Real-time estimation of vehicle state and tire-road friction forces*, in: American Control Conference, 2001. Proceedings of the 2001, 2001, pp. 3318-3323 vol.3315.
- [22] A. Rabhi, N.K. M'Sirdi and A. Elhajjaji, *Estimation of contact forces and tire road friction*, in: Control & Automation, 2007. MED '07. Mediterranean Conference on, 2007, pp. 1-6.
- [23] N.K. M'Sirdi, A. Rabhi, M. Ouladsine and L. Fridman, *First and High-Order Sliding Mode Observers to Estimate the Contact Forces*, in: Variable Structure Systems, 2006. VSS'06. International Workshop on, 2006, pp. 274-279.
- [24] T. Hsiao, N.-C. Liu and S.-Y. Chen, *Robust estimation of the friction forces generated by each tire of a vehicle*, in: American Control Conference (ACC), 2011, 2011, pp. 5261-5266.
- [25] J. Dakhllallah, S. Glaser, S. Mammar and Y. Sebsadji, *Tire-road forces estimation using extended Kalman filter and sideslip angle evaluation*, in: American Control Conference, 2008, 2008, pp. 4597-4602.
- [26] Y. Sebsadji, S. Glaser, S. Mammar and J. Dakhllallah, *Road slope and vehicle dynamics estimation*, in: American Control Conference, 2008, 2008, pp. 4603-4608.
- [27] Z. Tianjun and Z. Hongyan, *Application of Unscented Kalman Filter to Vehicle State Estimation*, in: Computing, Communication, Control, and Management, 2008. CCCM '08. ISECS International Colloquium on, 2008, pp. 135-139.
- [28] P. Zhao, Z. Changfu, Z. Jiahao, X. Xujun and D. Yiliang, *UKF and EKF estimator design based on a nonlinear vehicle model containing UniTire model*, in: Mechatronics and Automation, 2009. ICMA 2009. International Conference on, 2009, pp. 4780-4784.

- [29] B.-C. Chen and F.-C. Hsieh, *Sideslip angle estimation using extended Kalman filter*, *Vehicle System Dynamics*. 46 (2008), pp. 353-364.
- [30] C. Qi, A. Correa-Victorino and A. Charara, *A new nonlinear observer using unscented Kalman filter to estimate sideslip angle, lateral tire road forces and tire road friction coefficient*, in: *Intelligent Vehicles Symposium (IV)*, 2011 IEEE, 2011, pp. 709-714.
- [31] K. Nam, S. Oh, H. Fujimoto and Y. Hori, *Vehicle state estimation for advanced vehicle motion control using novel lateral tire force sensors*, in: *American Control Conference (ACC)*, 2011, 2011, pp. 4853-4858.
- [32] C. Liang, S. Yanru, Z. Yongsheng, L. Hongwei and X. Mingfa, *Vehicle lateral and longitudinal velocity estimation based on Adaptive Kalman Filter*, in: *Advanced Computer Theory and Engineering (ICACTE)*, 2010 3rd International Conference on, 2010, pp. V3-325-V323-329.
- [33] C. Liang, Z. Yongsheng, S. Yanru, X. Mingfa and L. Minghui, *Vehicle lateral and longitudinal velocity estimation based on Unscented Kalman Filter*, in: *Education Technology and Computer (ICETC)*, 2010 2nd International Conference on, 2010, pp. V3-427-V423-432.
- [34] M. Tanelli, S.M. Savaresi and C. Cantoni, *Longitudinal vehicle speed estimation for traction and braking control systems*, in: *Computer Aided Control System Design, 2006 IEEE International Conference on Control Applications, 2006 IEEE International Symposium on Intelligent Control*, 2006 IEEE, 2006, pp. 2790-2795.
- [35] C. Liang, C. LiBo, Z. YongSheng and S. YanRu, *Design of longitudinal vehicle velocity observer using fuzzy logic and Kalman filter*, in: *Electronic and Mechanical Engineering and Information Technology (EMEIT)*, 2011 International Conference on, 2011, pp. 3225-3228.
- [36] S.-K. Chen, N. Moshchuk, F. Nardi and J. Ryu, *Vehicle Rollover Avoidance*, *Control Systems, IEEE*. 30 (2010), pp. 70-85.
- [37] R. Jihan, N.K. Moshchuk and C. Shih-Ken, *Vehicle State Estimation for Roll Control System*, in: *American Control Conference, 2007. ACC '07*, 2007, pp. 1618-1623.

- [38] J.-I. Park, J.-Y. Yoon, D.-S. Kim and K.-S. Yi, *Roll state estimator for rollover mitigation control*, Proceedings of the Institution of Mechanical Engineers, Part D: Journal of Automobile Engineering. 222 (2008), pp. 1289-1312.
- [39] Y. Kyongsu, Y. Jangyeol and K. Dongshin, *Model-based Estimation of Vehicle Roll State for Detection of Impending Vehicle Rollover*, in: American Control Conference, 2007. ACC '07, 2007, pp. 1624-1629.
- [40] A. Hac, T. Brown and J. Martens, *Detection of Vehicle Rollover*, in: SAE 2004 World Congress & Exhibition, Detroit, MI, 2004.
- [41] R. Rajamani, D. Piyabongkarn, V. Tsourapas and J.Y. Lew, *Real-time estimation of roll angle and CG height for active rollover prevention applications*, in: American Control Conference, 2009. ACC '09., 2009, pp. 433-438.
- [42] R. Rajamani, D. Piyabongkarn, V. Tsourapas and J.Y. Lew, *Parameter and State Estimation in Vehicle Roll Dynamics*, Intelligent Transportation Systems, IEEE Transactions on. PP (2011), pp. 1-10.
- [43] V. Tsourapas, D. Piyabongkarn, A.C. Williams and R. Rajamani, *New method of identifying real-time Predictive Lateral load Transfer Ratio for rollover prevention systems*, in: American Control Conference, 2009. ACC '09., 2009, pp. 439-444.
- [44] J. Oh and S.B. Choi, *Design of a New Composite Observer for Vehicle Velocity and Attitude Estimation*, in: IASTED International Conference on Control and Applications, Vancouver, BC, Canada, 2011.
- [45] H.E. Tseng, *Dynamic Estimation of Road Bank Angle*, Vehicle System Dynamics. 36 (2001), pp. 307-328.
- [46] H. Eric Tseng, L. Xu and D. Hrovat, *Estimation of land vehicle roll and pitch angles*, Vehicle System Dynamics. 45 (2007), pp. 433-443.
- [47] A. Rehm, *Estimation of vehicle roll angle*, in: Communications, Control and Signal Processing (ISCCSP), 2010 4th International Symposium on, 2010, pp. 1-4.

- [48] H.F. Grip, L. Imsland, T.A. Johansen, J.C. Kalkkuhl and A. Suissa, *Estimation of road inclination and bank angle in automotive vehicles*, in: American Control Conference, 2009. ACC '09., 2009, pp. 426-432.
- [49] C. Kwanghyun, S. Hyunwoo, S.B. Choi and K. Sukchang, *Lateral acceleration compensation of a vehicle based on roll angle estimation*, in: Control Applications (CCA), 2010 IEEE International Conference on, 2010, pp. 1363-1368.
- [50] A. Hac, D. Nichols and D. Sygnarowicz, *Estimation of Vehicle Roll Angle and Side Slip for Crash Sensing*, in: SAE 2010 World Congress & Exhibition, Detroit, MI, USA, 2010.
- [51] Y.H.J. Hsu, S.M. Laws and J.C. Gerdes, *Estimation of Tire Slip Angle and Friction Limits Using Steering Torque*, Control Systems Technology, IEEE Transactions on. 18 (2010), pp. 896-907.
- [52] G. Welch and G. Bishop, *An Introduction to the Kalman Filter*, in: Department of Computer Science, University of North Carolina at Chapel Hill, 2001.
- [53] R.A. Masmoudi and J.K. Hedrick, *Estimation of Vehicle Shaft Torque Using nonlinear Observers*, Journal of Dynamic Systems, Measurement, and Control. 114 (1992), pp. 394-400.
- [54] R. Hoseinnezhad and A. Bab-Hadiashar, *Efficient Antilock Braking by Direct Maximization of Tire-Road Frictions* Industrial Electronics, IEEE Transactions on. 58 (2011), pp. 3593-3600.
- [55] D.T. Greenwood, *Principles of dynamics*, Prentice-Hall, 1998.
- [56] J. Fangjun and G. Zhiqiang, *An adaptive nonlinear filter approach to the vehicle velocity estimation for ABS*, in: Control Applications, 2000. Proceedings of the 2000 IEEE International Conference on, 2000, pp. 490-495.
- [57] K. Watanabe, K. Kinase and K. Kobayashi, *Absolute Speed Measurement Of Vehicles From Noisy Acceleration And Erroneous Wheel Speed*, in: Intelligent Vehicles '93 Symposium, 1993, pp. 271-276.

- [58] R. Klein, A. Daiss and H. Eichfeld, *Antilock braking system and vehicle speed estimation using fuzzy logic*, in: Proceedings of the 1st Embedded Computing Conference, Paris, 1996.
- [59] K. Kobayashi, K.C. Cheok and K. Watanabe, *Estimation of absolute vehicle speed using fuzzy logic rule-based Kalman filter*, in: American Control Conference, 1995. Proceedings of the, 1995, pp. 3086-3090 vol.3085.
- [60] N. Ding and S. Taheri, *A Modified Dugoff Tire Model for Combined-slip Forces*, Tire Science & Technology. 38 (2010), pp. 228-244.
- [61] S. Sastry and M. Bodson, *Adaptive Control: Stability, Convergence, and Robustness*, Prentice Hall, Englewood Cliffs, N.J, 1989.
- [62] S. Germann, M. Wurtenberger and A. Daiss, *Monitoring of the friction coefficient between tyre and road surface*, in: Control Applications, 1994., Proceedings of the Third IEEE Conference on, 1994, pp. 613-618 vol.611.
- [63] L.R. Ray, *Nonlinear tire force estimation and road friction identification: simulation and experiments*, Automatica. 33 (1997), pp. 1819-1833.
- [64] F. Gustafsson, *Slip-based estimation of tire - road friction*, Automatica. 33 (1997), pp. 1087-1099.
- [65] S. Muller, M. Uchanski and K. Hedrick, *Estimation of the Maximum Tire-Road Friction Coefficient*, Journal of Dynamic Systems, Measurement, and Control. 125 (2003), pp. 607-617.
- [66] L. Chankyu, K. Hedrick and Y. Kyongsu, *Real-time slip-based estimation of maximum tire-road friction coefficient*, Mechatronics, IEEE/ASME Transactions on. 9 (2004), pp. 454-458.
- [67] K. Li, J.A. Misener and K. Hedrick, *On-board road condition monitoring system using slip-based tyre-road friction estimation and wheel speed signal analysis*, Proceedings of the Institution of Mechanical Engineers, Part K: Journal of Multi-body Dynamics. 221 (2007), pp. 129-146.

- [68] J. Svendenius, *Tire modeling and friction estimation*, in: Department of Automatic Control, Lund University, Lund, 2007.
- [69] F. Bernard, *A nonlinear observer for estimating parameters in dynamic systems*, Automatica. 33 (1997), pp. 1525-1530.
- [70] G. Baffet, A. Charara and D. Lechner, *Experimental evaluation of a sliding mode observer for tire-road forces and an extended Kalman filter for vehicle sideslip angle*, in: Decision and Control, 2007 46th IEEE Conference on, 2007, pp. 3877-3882.
- [71] S.J. Julier, J.K. Uhlmann and H.F. Durrant-Whyte, *A new approach for filtering nonlinear systems*, in: American Control Conference, 1995. Proceedings of the, 1995, pp. 1628-1632 vol.1623.
- [72] S. Julier and J. Uhlmann, *A New Extension of the Kalman Filter to Nonlinear Systems*, in: In Int. Symp. Aerospace/Defense Sensing, Simul. and Controls, 1997, pp. 182-193.
- [73] E.A. Wan and R. Van Der Merwe, *The unscented Kalman filter for nonlinear estimation*, in: Adaptive Systems for Signal Processing, Communications, and Control Symposium 2000. ASSPCC. The IEEE 2000, 2000, pp. 153-158.

Chapter 4

Model-Based Tire-Road Friction Estimation

Executive Summary

Current vehicle chassis control systems such as ABS and ESC participate in vehicle stability control only when the maximum friction has exceeded. Future safety systems such as collision mitigation systems (CMS) would benefit from a more continuous friction estimation system. Also, some of the existing systems could be supported with high quality real-time information about tire-road friction coefficient. Tire-road friction coefficient information would enable, for example, ABS to start braking with the optimal brake pressure based on the current maximum coefficient of friction, meaning the early cycles of operation are more efficient, resulting in shorter stopping distance. In addition, it may be useful to present the driver with friction information.

From the discussions above it is clear that some method of estimating friction, using existing onboard vehicle sensor information and with a minimum of assumptions, would be desirable. Many approaches for estimating tire-road friction estimation have been proposed in the literature, with different requirements for sensors and levels of excitations. The estimation methods can be categorized into “Cause-based” and “Effect-based” approaches. “Cause-based” strategies try to measure factors that lead to changes in friction and then attempt to predict what μ_{max} will be based on past experience or friction models. “Effect-based” approaches, on the other hand, measure the effects that friction has on the vehicle or tires during driving. They then attempt to extrapolate what the limit friction will be based on this data.

This study aims at estimating the value of the friction coefficient by using a well-defined accurate model for the “effect of the friction on the tire behavior”. The model adopted for this purpose is the physically based brush-tire model. In its simplest formulation, the brush model describes the relationship between the tire force and the slip as a function of two parameters, the tire stiffness ($C_{x,y}$) and the tire -road friction coefficient (μ). Knowledge of the shape of the friction characteristic, possibly obtained through estimation of both friction and tire stiffness

using the brush model, provides information on the slip values for which maximum friction is obtained. This information could be used to generate slip references for slip controllers, for example in ABS. Tire stiffness estimates can also be used in vehicle models, such as the bicycle model, which are often used for reference generation and estimation.

Keywords: friction estimation, brush model, nonlinear least squares (NLLS), Levenberg-Marquardt

4.1 Introduction

Tire friction forces, as primary forces affecting planar vehicle motions, are physically limited by the surface coefficient of friction (μ) of the road in the contact patch of the tire and the instantaneous tire normal forces (Fig. 4.1). Therefore, the ability to reliably estimate tire- road friction coefficient is important for maximizing the performance of vehicle control systems, which work well only when the tire force command computed by the safety systems is within the friction limit.

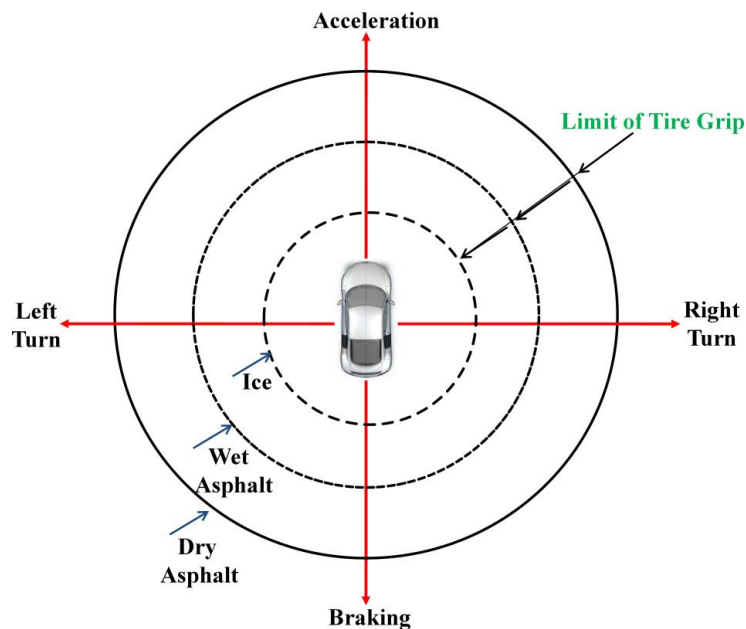


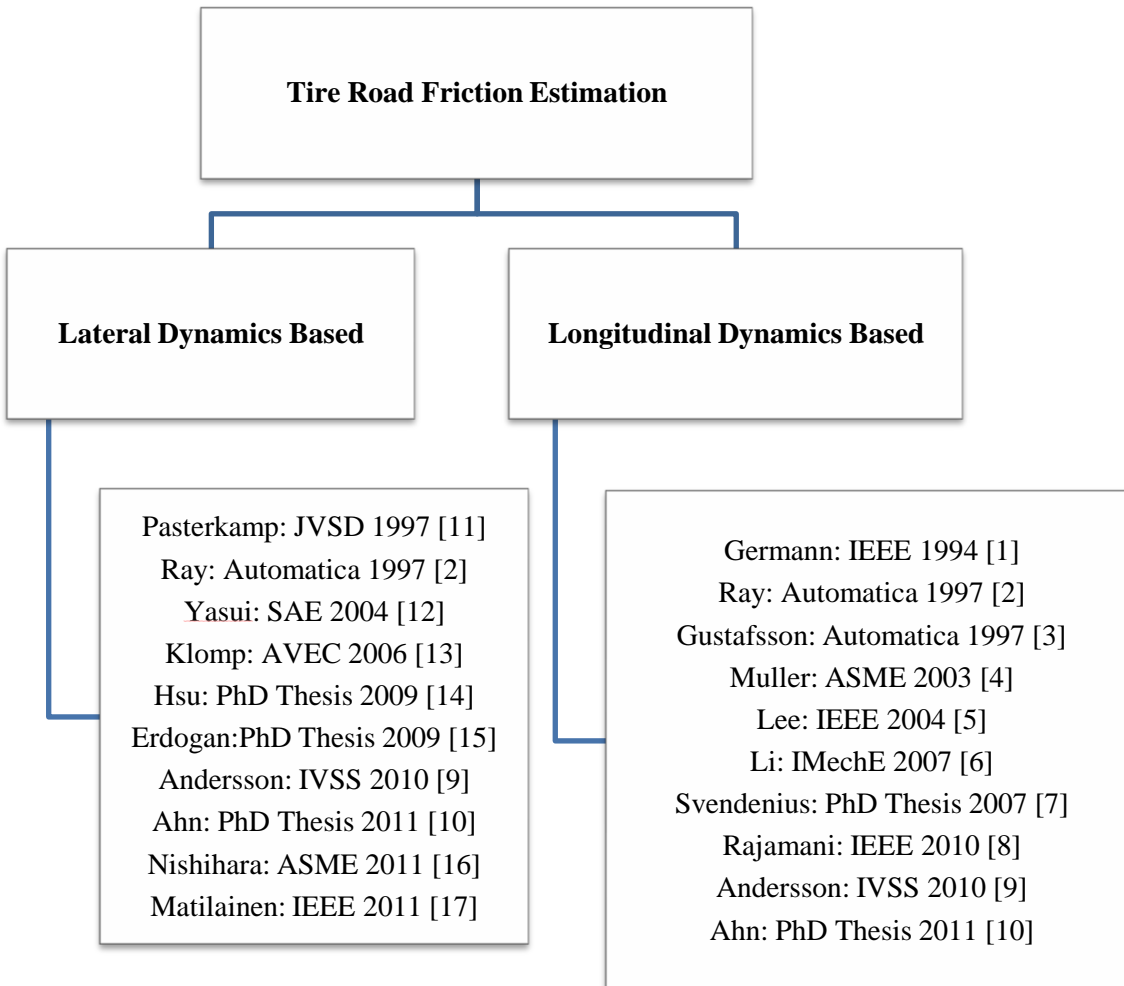
Fig. 4.1: Friction circle of a tire

Knowing the friction value of tire-road interaction, it is possible to improve the traffic safety in several ways, where some examples are:

1. Enhancement of active safety systems of the vehicle. This includes improved performance of systems such as anti-lock braking system (ABS) and electronic stability control (ESC). Adaptive cruise control could adjust to an adequate safety distance and a collision mitigation system could expedite intervention in slippery conditions.
2. The output from a road friction estimator might be used as a detecting device that warns the driver about a bad or suddenly changed road condition.
3. Enhanced road maintenance by communication of estimated friction value to the road authorities. In this way individual vehicles act as sensors, providing information about friction at specific points in the road network.

The importance of friction estimation is reflected by the considerable amount of work that has been done in the area (see Table 4.1).

Table 4.1: State-of-the-Art Literature Review



In normal driving conditions the frictional force is not fully utilized and the developed tire force will be somewhere in the interior of the circle. When force is applied to a tire, a relative motion arises between the tire structure and the road. This relative motion is referred to as tire slip. The relation between the resulting tire force and the slip depends on many factors, namely, tire inflation pressure, vertical load, tire wear, temperature, etc., and contains information about the available friction. When the tire is exposed to excitation with high utilization, beyond the point corresponding to the maximum available friction force, the tire is sliding and the resulting tire force directly corresponds to the friction coefficient. Hence, determination of friction coefficient is straightforward in cases where tire forces are saturated, such as under hard braking. The difficulty lies in obtaining a friction estimate under more normal driving circumstances, in which the tire slip is smaller (lower utilization conditions). In these cases a model-based approach can be advantageous. By fitting data to a model of the tire, the model parameters, including μ , may be estimated. This approach may allow the estimation of friction without requiring tire force saturation.

This study investigates the use of a model-based approach to estimate tire-road friction coefficient, and more importantly determine the level of tire force excitation necessary to provide an estimate within a specified range of accuracy. This method is based on the assumption that the lateral force, traction/braking force, aligning torque, and vertical load can be measured or estimated.

4.2 Mechanics of Pneumatic Tire

This section gives a brief introduction to tire mechanics. In addition to providing a comfortable ride, the purpose of the tire is to transfer forces from the vehicle to the road. Two kinematic variables typically are used with tire force models and with the measurement of tire forces. These are the slip ratio, defined by λ and slip angle, defined by α . Slip ratio is what causes longitudinal force generation and slip angle causes lateral force generation of the tire. Slip ratio is the relative motion between the tire and the road. Slip ratio is expressed as a percentage and is represented by Equation (4.1), where v_x is the free rolling vehicle longitudinal speed, ω is the angular velocity of the wheel, and r is the effective rolling radius of the tire.

$$\lambda = \begin{cases} \frac{v_x - r \cdot \omega}{r \omega} & \text{for acceleration} \\ \frac{v_x - r \cdot \omega}{v_x} & \text{for braking} \end{cases} \quad (4.1)$$

Slip angle is defined in Equation (4.2) as:

$$\alpha_f = \frac{v_y + a \cdot r}{v_x} - \delta$$

$$\alpha_r = \frac{v_y - b \cdot r}{v_x}$$
(4.2)

where δ is the steering angle, v_y is the lateral velocity of the wheel and v_x is the forward velocity of the wheel, a and b are the longitudinal distances from the center of gravity to the front and rear wheels and r is the vehicles yaw rate.

At small levels of slip, the forces depend mainly on elastic deformation of the tire and are associated with a linear trend. At higher levels of slip, the horizontal forces are limited by the friction between the tire and the road.

4.2.1 Longitudinal Tire Characteristics

Longitudinal characteristics of the tire play an important role in both vibration characteristics of the car and its tractive performance in acceleration and braking. Initially, longitudinal force increases linearly with slip ratio, goes through transition, reaches a maximum value then saturates, as shown in Fig. 4.2. During acceleration/deceleration, as the slip ratio increases, the longitudinal force increases linearly. As the slip ratio continues to increase, the tire horizontal force will eventually reach its maximum, and the wheel will begin to spin (during acceleration)/lock (during deceleration), causing a reduction in longitudinal force.

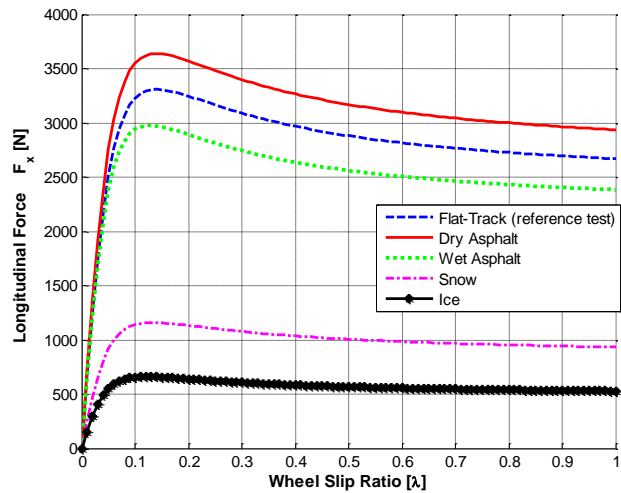


Fig. 4.2: Simulated longitudinal force curves as a function of wheel slip-ratio (λ) for varying surface conditions

4.2.2 Lateral Tire Characteristics

Fig. 4.3 shows lateral force versus slip angle plots for a passenger car tire. Initially, the lateral force increases linearly with slip angle (the linear range of the tire), then curves, reaches a peak value and saturates in the non-linear region of the tire. Assuming a constant vehicle speed, the linear region of the tire corresponds to small slip angles, in which the tire experiences more predictable behavior. As the slip angle increases, the tire moves into the transitional region, in which the cornering stiffness of the tire, or slope of the lateral force versus slip angle curve, becomes less predictable. As the slip angle continues to increase, it will reach a point where the tire lateral force reaches its maximum value for the given road surface. Due to the lateral properties of the tire, the vehicle response to driver input can change abruptly when the maximum limit of adhesion is reached. For example, during cornering maneuvers, the vehicle yaw rate remains proportional to the steering input while the tires operate in the linear range. Once the tires move into the transitional and frictional range, this relationship no longer holds and the vehicle can no longer follow the driver's desired path.

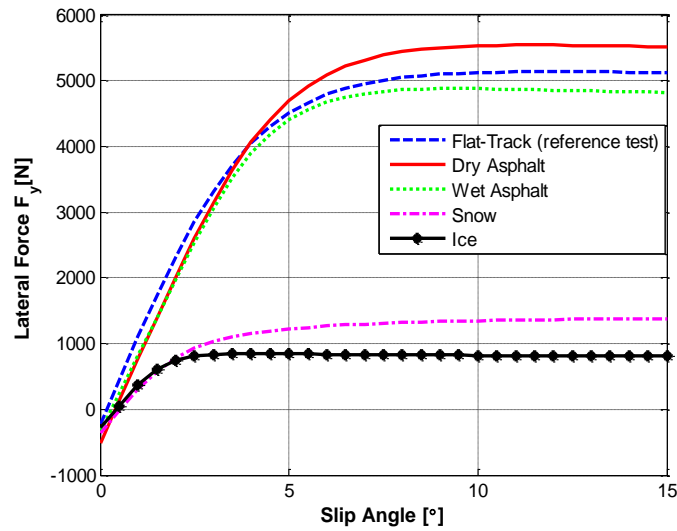
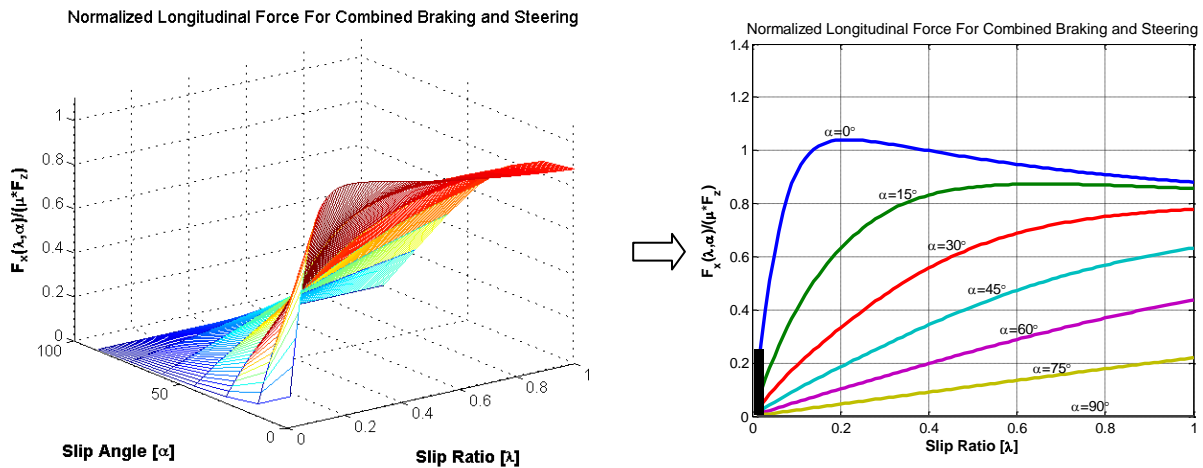


Fig. 4.3: Simulated lateral force curves as a function of slip-angle (α) for varying surface conditions

4.2.3 Combined-slip Forces

Under combined braking and cornering conditions, the magnitude and direction of the resulting tire force depends on the magnitude and direction of the total slip vector. Fig. 4.4a shows the resulting tire forces, where the lateral slip is held fixed and the longitudinal slip is varied from free rolling ($\lambda = 0$) to locked wheel ($\lambda = 1$) condition. Fig. 4.4b shows the resulting tire forces, where the longitudinal slip is held fixed and the lateral slip is varied from $\alpha = 0^\circ$ to $\alpha = 50^\circ$.

(a)



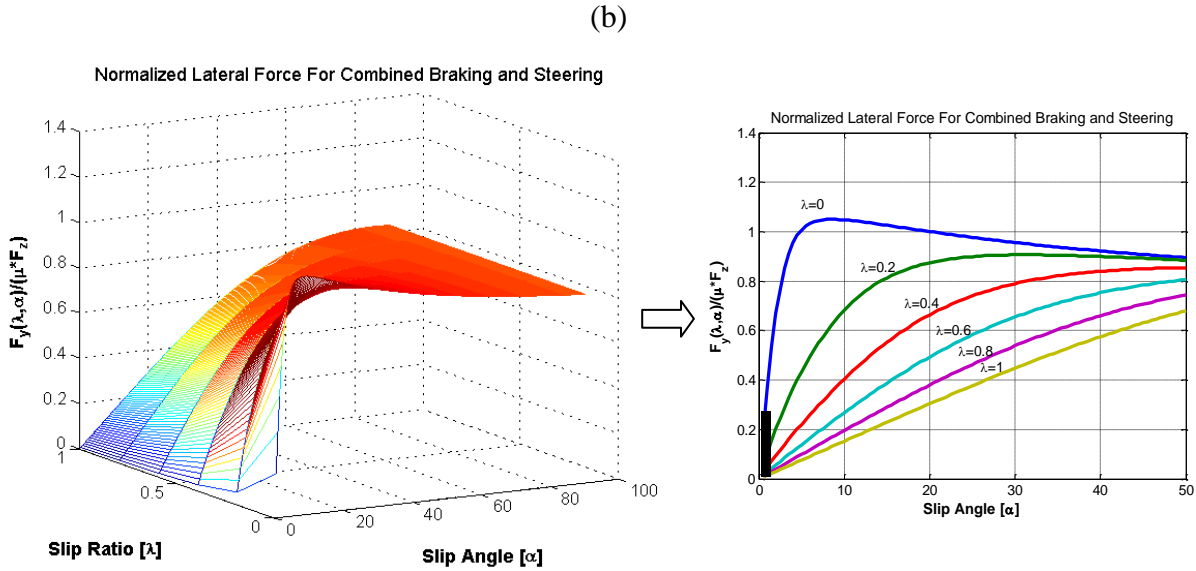


Fig. 4.4: (a) Normalized longitudinal tire force for combined braking and steering, and (b) normalized lateral tire force for combined braking and steering

The maximum available tire forces at pure braking or cornering reflects the maximum available tire/road adhesion. Since the road adhesion provide a bound also on combined forces, the envelope of all possible curves (Fig. 4.5) describes a circle like shape. This envelope is commonly denoted as the friction circle (For a real-world tire, the circle is likely to be closer to an ellipse, with the y axis slightly longer than the x axis).

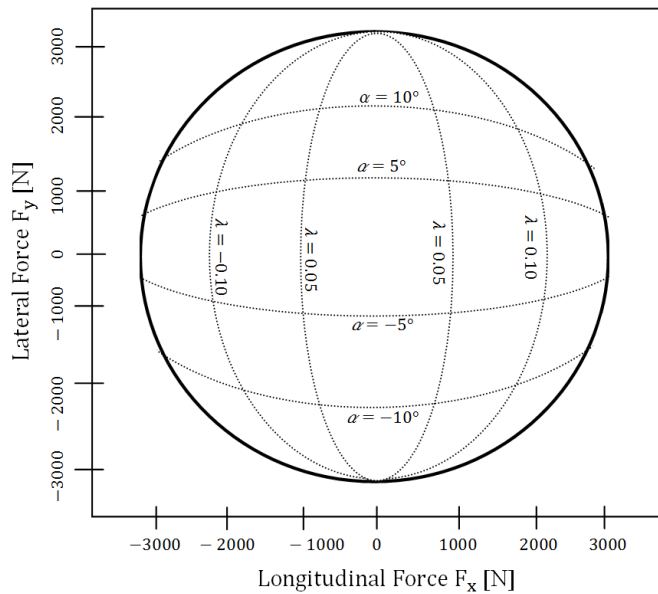


Fig. 4.5: Friction circle diagram at a vertical load of 3000 N

4.3 Tire Model Selection

Critical to the success of a model-based approach is the choice of model structure. There are many models available that describe the complex nonlinear behavior of a tire [18]. Some models are based on first principles where the physical principles that determine the forces such as tire deformation and tire stiffness, are modeled. Some models are empirical, where the tire characteristic is measured and using a set of coefficients, a curve is fitted to the tire characteristic. Since parameter estimation is to be performed, it is desirable to choose a model with a small number of parameters. The brush model [19] is well suited to these requirements, containing only stiffness and friction parameters. The basic concept of the brush model is that a tire consists of a row of elastic bristles which touch the road plane and can deflect in a direction that is parallel to the road surface (Fig. 4.6).

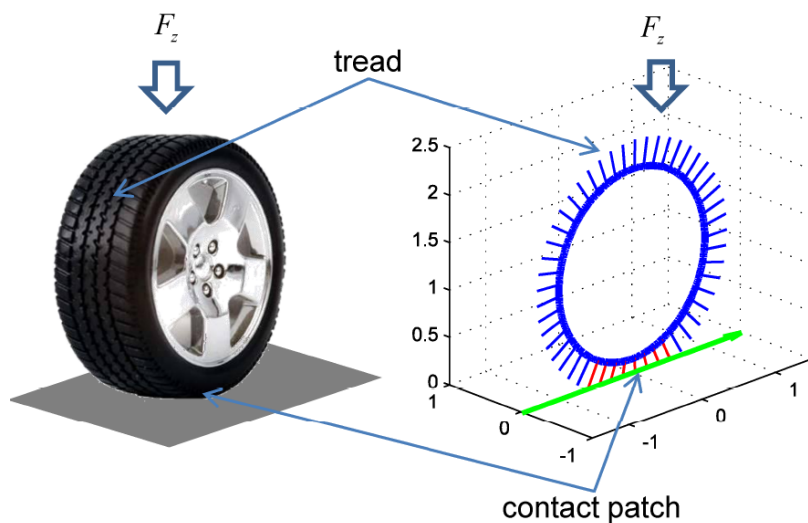


Fig. 4.6: Tire and Brush model [10]

As a result, a tire can be modeled as a thin disk with brushes along the circumference that represent the tire treads. Treads in the contact patch are compressed and experience vertical stresses. The distribution of vertical stress is assumed to be parabolic. The generated forces or moment can be computed by integrating the stress of all brushes in the contact patch. The model is built with some assumptions. The elasticity of the bristles is assumed to be linearly even though rubber isn't. The carcass of the tire is also assumed to be stiff, which results in the carcass deformation effects to be neglected. A thorough coverage of the brush model is included in [19].

In a pure longitudinal slip case, the tire longitudinal force, F_x , can be represented as follows:

$$F_x = \begin{cases} C_x \left(\frac{\lambda}{\lambda+1} \right) - \left(\frac{1}{3} \frac{C_x^2 \left| \frac{\lambda}{\lambda+1} \right| \left| \frac{\lambda}{\lambda+1} \right|}{\mu F_z} \right) - \left(\frac{1}{27} \frac{C_x^3 \left(\frac{\lambda}{\lambda+1} \right)^3}{(\mu F_z)^2} \right) & \text{for } |\lambda| \leq |\lambda_{sl}| \\ \mu F_z \text{sign}(\lambda) & \text{for } |\lambda| > |\lambda_{sl}| \end{cases} \quad (4.3)$$

where

F_x : tire longitudinal force

F_z : tire normal force

C_x : tire longitudinal stiffness

μ : tire – road friction coefficient

λ : slip ratio

λ_{sl} : slip ratio where transition from partial to full sliding occur

In a pure lateral slip case, the tire lateral force, F_y , and tire aligning moment, τ_a , can be represented as follows:

$$F_y = \begin{cases} -C_y \tan(\alpha) + \left(\frac{1}{3} \frac{C_y^2 |\tan(\alpha)| \tan(\alpha)}{\mu F_z} \right) - \left(\frac{1}{27} \frac{C_y^3 \tan^3(\alpha)}{(\mu F_z)^2} \right) & \text{for } |\alpha| \leq |\alpha_{sl}| \\ -\mu F_z \text{sign}(\alpha) & \text{for } |\alpha| > |\alpha_{sl}| \end{cases} \quad (4.4)$$

$$\tau_a = \begin{cases} \frac{C_y \tan(\alpha) a_{cpl}}{3} \left(1 - \left| \frac{C_y \tan(\alpha)}{3\mu F_z} \right| \right)^3 & \text{for } |\alpha| \leq |\alpha_{sl}| \\ 0 & \text{for } |\alpha| > |\alpha_{sl}| \end{cases} \quad (4.5)$$

where

F_y : tire lateral force

τ_a : tire aligning moment

F_z : tire normal force

C_y : tire cornering stiffness

μ : tire – road friction coefficient

α : slip angle

α_{sl} : slip angle where transition from partial to full sliding occur

a_{cpl} : half of tire contact patch length

The force and moment equations in combined slip cases are similar to the equations for pure slip cases. If both lateral slip and longitudinal slip exist, the treads are deformed in the direction determined by the magnitudes of both slips. The Brush model for the combined slip case is shown in the following equation:

$$F_x = F \frac{\sigma_x}{\sigma}, F_y = F \frac{\sigma_y}{\sigma}, M_z = -t(\sigma) \times F_y \quad (4.6)$$

where

$$F(\lambda, \alpha, \mu) = \begin{cases} \mu F_z (1 - \rho^3) & \text{for } |\sigma| \leq |\sigma_{sl}| \\ \mu F_z \operatorname{sgn}(\alpha) & \text{for } |\sigma| > |\sigma_{sl}| \end{cases},$$

$$\sigma_x = \frac{\lambda}{\lambda+1}, \sigma_y = \frac{\tan(\alpha)}{\lambda+1}, \sigma = \sqrt{\sigma_x^2 + \sigma_y^2}$$

$$a_{cpl} = a_{cpl0} \sqrt{\frac{F_z}{F_{z0}}}, C = 2c_p a_{cpl}^2, \theta = \frac{C}{3\mu F_z}, \sigma_{sl} = \frac{1}{\theta}, \rho = 1 - \theta\sigma$$

$$t(\sigma) = \frac{l(1 - |\theta\sigma|)^3}{(3 - 3|\theta\sigma| + |\theta\sigma|^2)}$$

Here c_p is the tread stiffness in unit length given at a nominal contact patch length a_{cpl_0} and normal load F_{z_0} , and the model assumes isotropic tire properties ($C_x = C_y = C$).

4.4 Brush Model Validation

In order to use the brush model as a basis for friction estimation, it is desirable to validate the model. This section presents an experimental validation of the brush-tire model. The longitudinal tire data was generated by applying a braking torque on the wheel as a ramp function from free rolling to $\sim 15\text{-}20\%$ slip conditons. The lateral tire data was generated by testing the tire under slip angle sweep conditions. The model fitting algorithm is based on storing data points in the force-slip/moment-slip plane and using those points to compute the tire longitudinal/cornering stiffness and the tire-road friction coefficient by optimization. In other words, it is a method for the identification of parameters through determining the best fit between modeled and observed data. The optimization algorithm used is the method of Levenberg-Marquardt [21-22]. The algorithm of Levenberg- Marquardt (LM) is an iterative technique to locate the minimum of a function with several variables, which is expressed as the sum of squares of real valued non-linear functions. It has become a standard technique for non-linear least-squares problems, widely adopted in a broad spectrum of disciplines. The LM method can be thought of as a combination of steepest descent method and the method of Gauss-Newton. When the current solution is far from the correct one, the algorithm behaves like a steepest descent method: it is slow, but guaranteed to converge. When the current solution is close to the correct solution, it becomes a Gauss-Newton method.

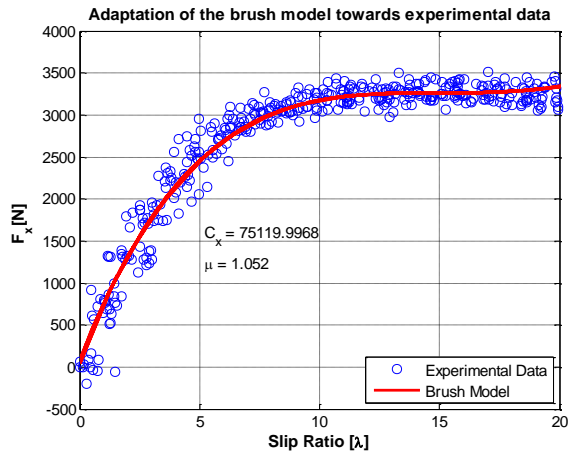
In Fig. 4.7 are shown the results of adaptation of the brush model to tire measurement data for different test conditions (Table 4.2).

Table 4.2: Tire test conditions

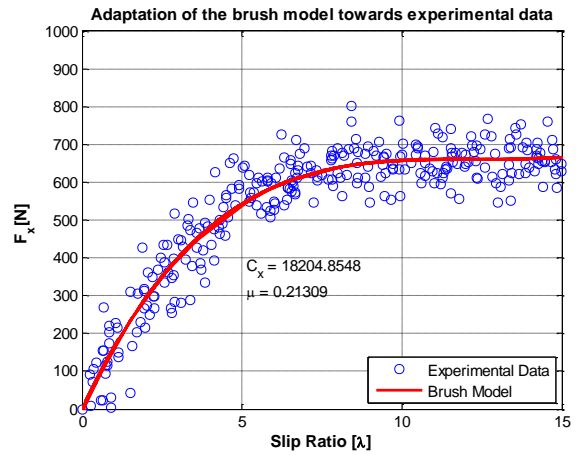
	Test Description	Surface Condition	Measured/Estimated Signals	Estimated Parameters
Case 1	Longitudinal force test	High μ	F_x, F_z, λ	C_x, μ
Case 2	Longitudinal force test	Low μ	F_x, F_z, λ	C_x, μ
Case 3	Lateral force test	High μ	F_y, F_z, α	C_y, μ

Case 4	Lateral force test	Low μ	F_y, F_z, α	C_y, μ
Case 5	Self aligning moment test	High μ	τ_a, F_z, α	C_y, μ
Case 6	Self aligning moment test	Low μ	τ_a, F_z, α	C_y, μ

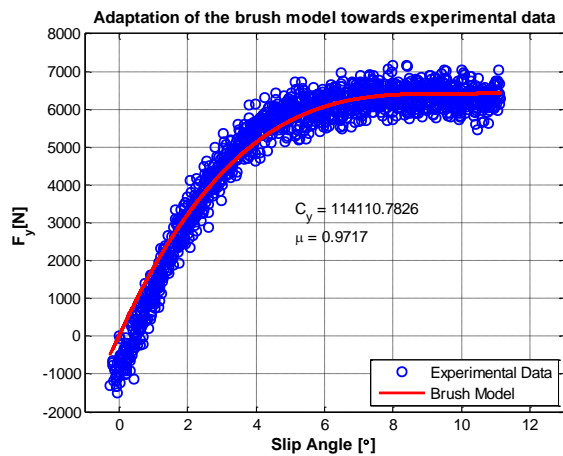
(a) Case 1: Longitudinal force test-High μ



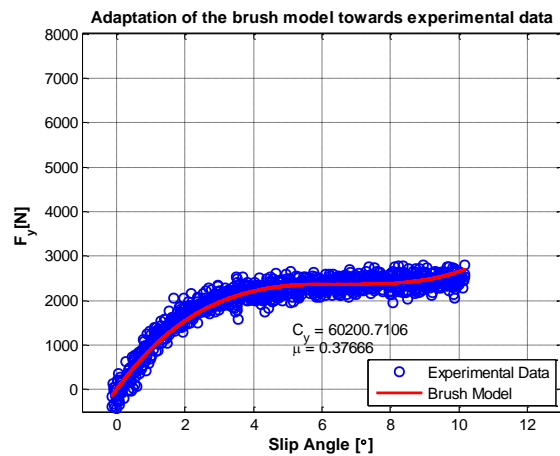
(b) Case 2: Longitudinal force test-Low μ



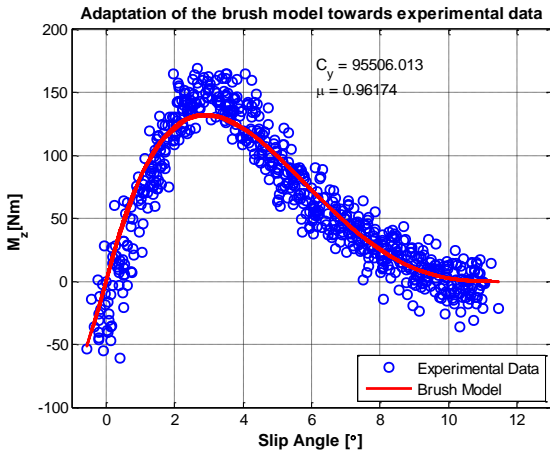
(c) Case 3: Lateral force test-High μ



(d) Case 4: Lateral force test-Low μ



(e) Case 5: Self aligning moment test-High μ



(f) Case 6: Self aligning moment test-Low μ

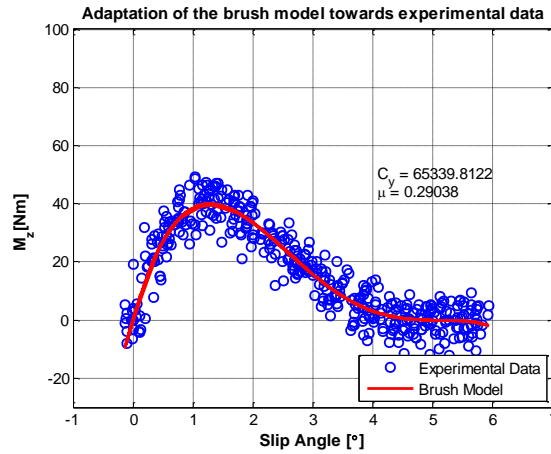


Fig. 4.7: Adaptation of the brush-tire model to tire measurement data (ref.

for a description of the test conditions)

From the shown figures (Fig. 4.7), it can be seen that, for the pure longitudinal slip the coherence between the brush model and the reference curve is good. For the pure lateral slip there are discrepancies in the lateral force and the self aligning torque. As mentioned in previous research [20], the main reason for this discrepancy is the assumption of a stiff carcass.

4.5 Real-Time Implementation

The real-time parameter estimation algorithm used in this study is similar to the one presented in [14].

The complete real-time estimation algorithm is outlined below:

- Iteratively perform NLLS to the brush model on the batch of force-slip/moment-slip data, starting with initial estimates of braking/cornering stiffness and friction coefficient.
- To ensure that there is enough data for the NLLS fit to be meaningful, first initialize the process by placing a tire slip level threshold. The tire slip must exceed the threshold value before parameter estimation begins.

- The next step is to determine whether the tire force/moment has saturated sufficiently to estimate μ . In parallel to NLLS fit, apply the method of LS to the data points to find the slope of the line through the origin. Calculate the incremental mean squared error (MSE) of both fits from the most recent vector of data points of length N. If the force-slip/moment-slip data is sufficiently nonlinear, update the value of μ . Otherwise, hold the coefficient of friction estimate at its previous value.
- As new data is collected and appended to the existing batch, repeat the above algorithm.

A schematic representation of the Lateral Force-Slip regression method is shown in Fig. 4.8.

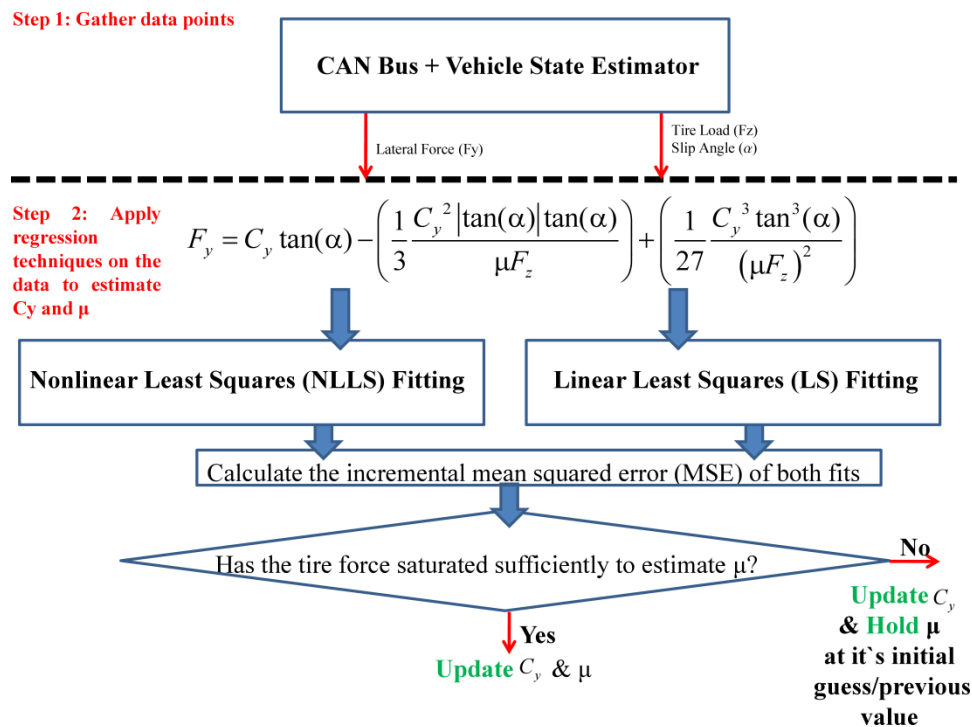


Fig. 4.8: Tire parameter estimation algorithm - Lateral Force-Slip regression method

4.6 Parameter Estimation Results

Friction estimation using the real-time estimation technique presented in Section 4.5 has been tested on tire measurement data. This section investigates how the value of the highest available slip (tire force utilization level) affects the accuracy of the friction estimation. The following sub-sections present the results for each of the estimation methods, namely, Longitudinal Force-

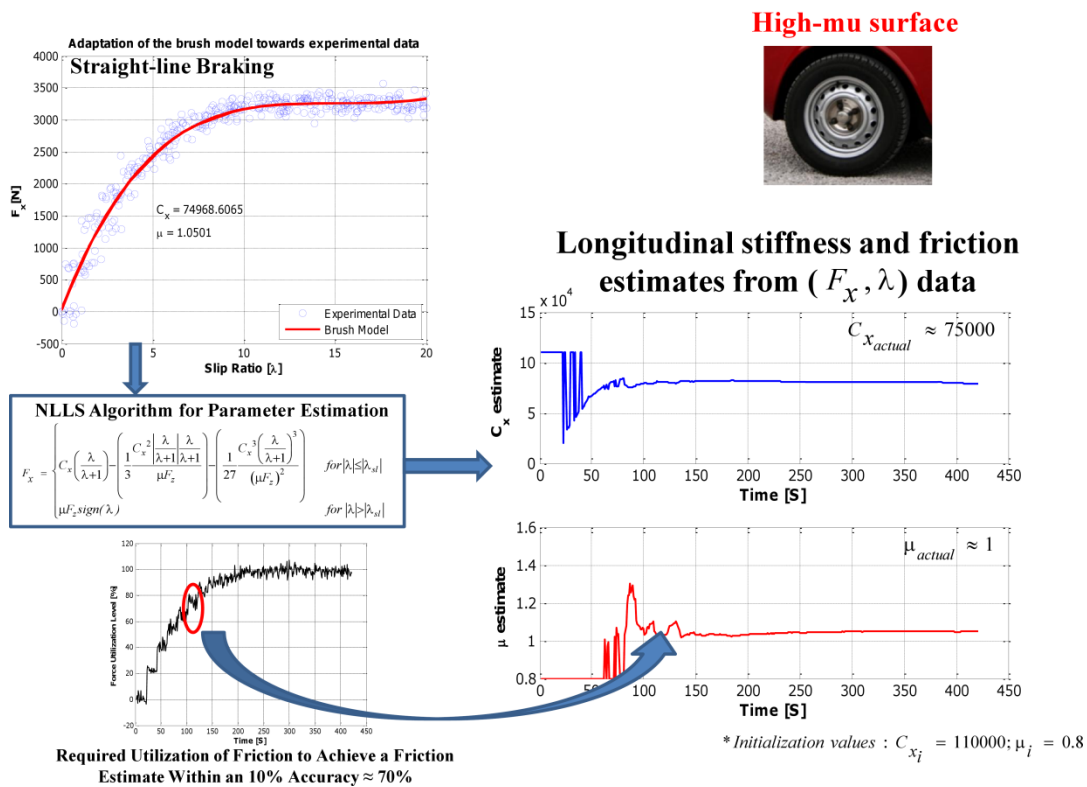
Slip Regression Method’, ‘Lateral Force-Slip Regression Method’, and ‘Moment-Slip Regression Method’.

4.6.1 Estimation Based on Longitudinal Force-Slip Regression Method

Using the estimation algorithm described previously with $\lambda_{thres} = 0.1$, $\mu_{initial} = 0.8$, $C_{x_{initial}} = 110000$, force and slip ratio data is post-processed to yield longitudinal stiffness and friction coefficient estimates (Fig. 4.9).

(a) Case 1: High μ

Real-time Implementation - Friction Estimation Results



(b) Case 2: Low μ

Real-time Implementation - Friction Estimation Results

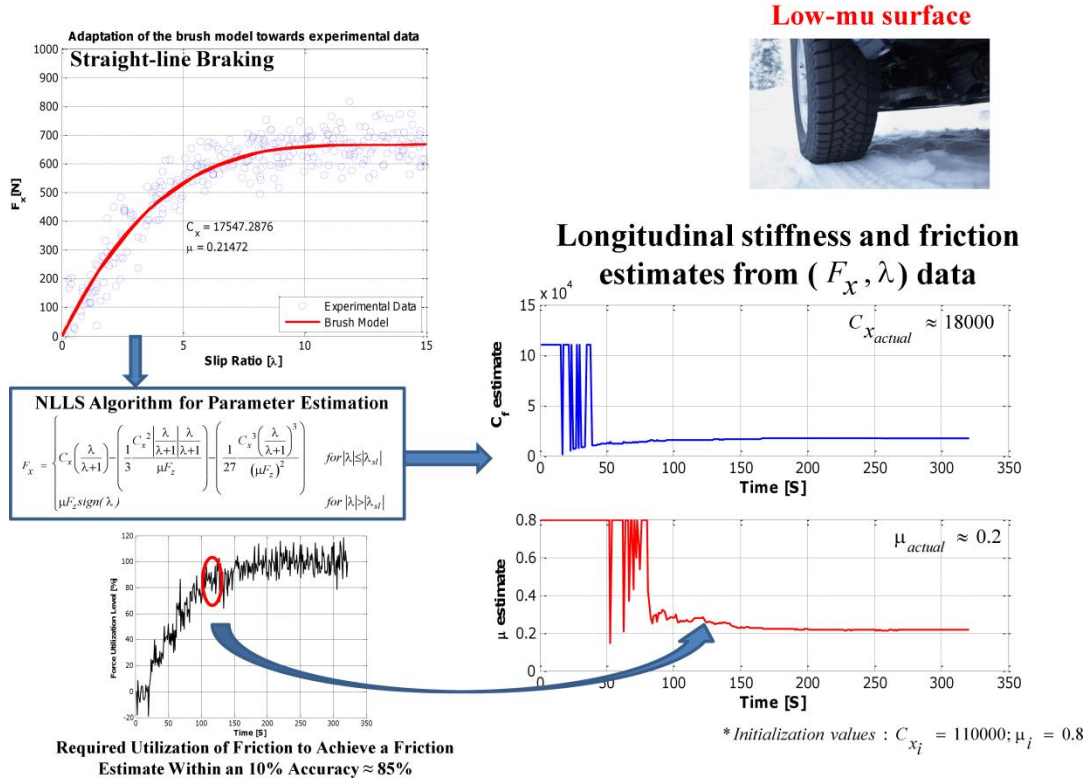


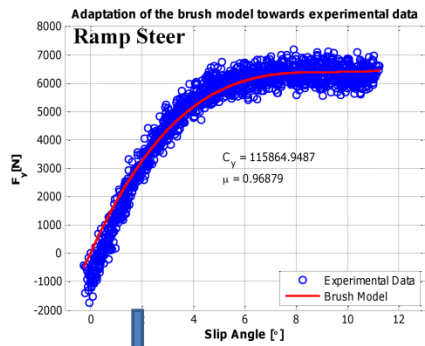
Fig. 4.9: Longitudinal stiffness and friction coefficient estimates from (F_x, λ) data: (a) high μ conditions, and low μ conditions

4.6.2 Estimation Based on Lateral Force-Slip Regression Method

With $\alpha_{thres} = 2^\circ$, $\mu_{initial} = 0.8$, $C_{y_{initial}} = 110000$, force and slip angle data is post-processed to yield cornering stiffness and friction coefficient estimates (Fig. 4.10).

(a) Case 1: High μ

Real-time Implementation - Friction Estimation Results

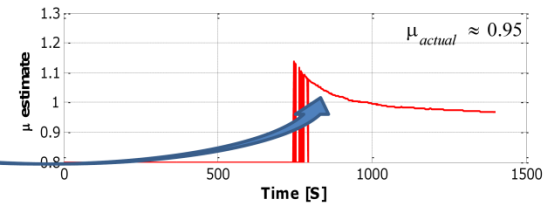
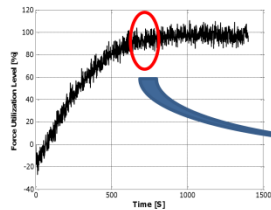
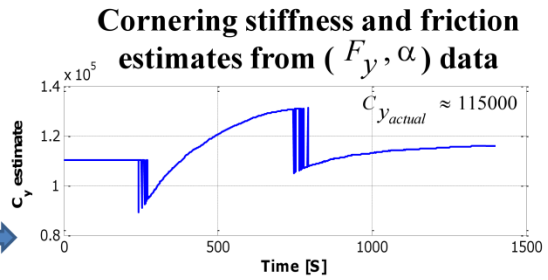


High-mu surface



NLLS Algorithm for Parameter Estimation

$$F_y = \begin{cases} -C_y \tan(\alpha) + \left(\frac{1}{3} C_y^2 |\tan(\alpha)| \tan(\alpha) \right) \left(\frac{1}{27} C_y^3 \tan^3(\alpha) \right) & \text{for } |\alpha| \leq |\alpha_d| \\ -\mu F_z \text{sign}(\alpha) & \text{for } |\alpha| > |\alpha_d| \end{cases}$$



Required Utilization of Friction to Achieve a Friction Estimate Within an 10% Accuracy $\approx 85\%$

* Initialization values : $C_{y_i} = 110000; \mu_i = 0.8$

(b) Case 2: Low μ

Real-time Implementation - Friction Estimation Results

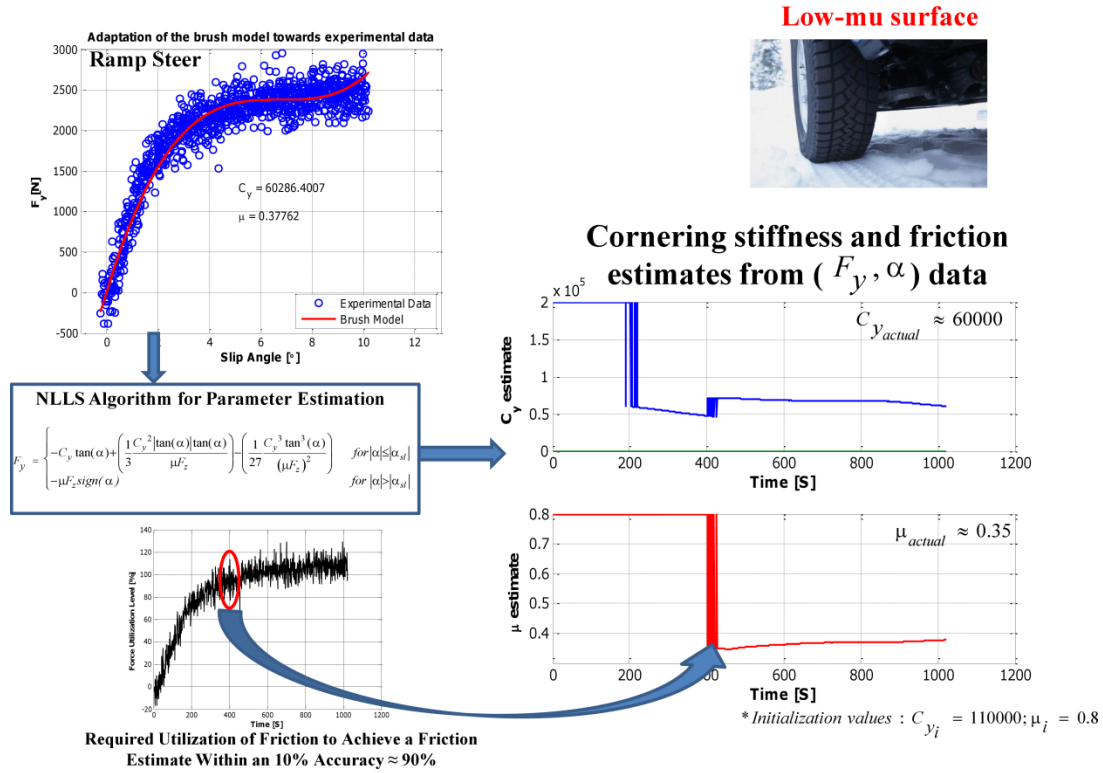


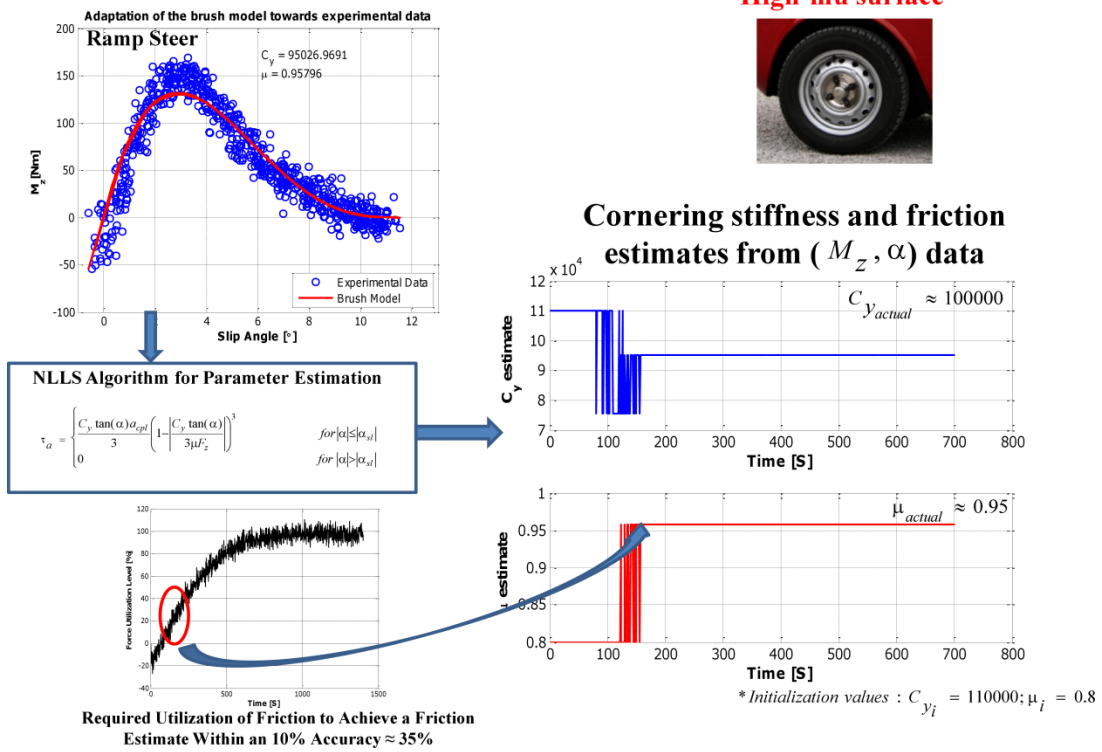
Fig. 4.10: Cornering stiffness and friction coefficient estimates from (F_y, α) data: (a) high μ conditons, and low μ conditons

4.6.3 Estimation Based on Moment-Slip Regression Method

With $\alpha_{thres} = 0.5^\circ$, $\mu_{initial} = 0.8$, $C_{y_{initial}} = 110000$, moment and slip angle data is post-processed to yield cornering stiffness and friction coefficient estimates (Fig. 4.11).

(a) Case 1: High μ

Real-time Implementation - Friction Estimation Results



(b) Case 2: Low μ

Real-time Implementation - Friction Estimation Results

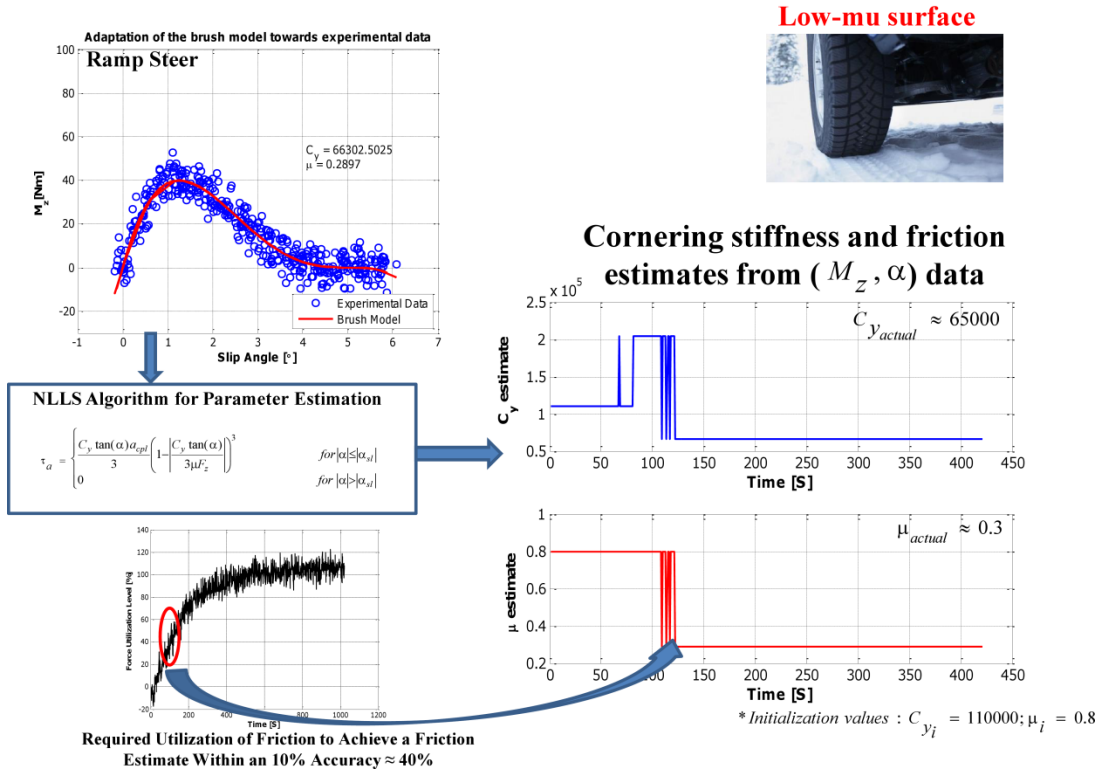


Fig. 4.11: Cornering stiffness and friction coefficient estimates from (M_z, α) data: (a) high μ conditions, and low μ conditions

Based on the results shown in Fig. 4.9 - Fig. 4.11, the required utilization of friction necessary to provide a friction estimate within the specified accuracy of $\pm 10\%$ is presented in Table 4.3. In the case of the ‘Force-Slip Regression Method’, more than 75-80% of the available friction force must be generated before an accurate estimate can be derived. However, it is possible to estimate the tire road friction coefficient for lower levels of utilization ($\sim 30\text{-}40\%$) if self aligning torque (‘Moment-Slip Regression Method’) is used as a basis for the estimator instead of the lateral force (‘Lateral Force-Slip Regression Method’).

Table 4.3: Required utilization of friction (in percent) to achieve a friction estimate within an accuracy of $\pm 10\%$

Estimation Methodology	Friction Coefficient (μ)	Required Utilization of Friction (%)
Longitudinal Force-Slip Regression Method	High μ	70
	Low μ	85
Lateral Force-Slip Regression Method	High μ	85
	Low μ	90
Moment-Slip Regression Method	High μ	35
	Low μ	40

4.7 Conclusion

In this chapter, a model-based approach to friction estimation has been developed. Using the brush model, a relatively simple parameter estimation problem can be posed, allowing estimation of the friction and tire stiffness parameters. The nonlinear least squares (NLLS) optimization method used shows best performance by increasing the size of the data set and guessing good initial values. However, using a long data set induces delay and increases computation load. The primary shortcoming of the ‘Force-Slip Regression Method’ identified is, it necessitates waiting until the vehicle enters the nonlinear region of handling before friction can be estimated. Thus, in the case of the ‘Force-Slip Regression Method’, an estimation algorithm based on the brush model will work, but high friction utilization is required for an accurate friction estimate. To be of greatest use to stability control systems, an estimation method needs to offer earlier knowledge of the limits. The ‘Moment-Slip Regression Method’ based off total aligning moment has the benefit of knowing the coefficient of friction earlier—before the tire forces reach their maximum grip on the road. Given that these methods process data in batches, we expect a delayed sensitivity to quickly changing road friction properties.

References

- [1] S. Germann, M. Wurtenberger and A. Daiss, *Monitoring of the friction coefficient between tyre and road surface*, in: Control Applications, 1994., Proceedings of the Third IEEE Conference on, 1994, pp. 613-618 vol.611.
- [2] L.R. Ray, *Nonlinear tire force estimation and road friction identification: simulation and experiments*, Automatica. 33 (1997), pp. 1819-1833.
- [3] F. Gustafsson, *Slip-based estimation of tire - road friction*, Automatica. 33 (1997), pp. 1087-1099.
- [4] S. Muller, M. Uchanski and K. Hedrick, *Estimation of the Maximum Tire-Road Friction Coefficient*, Journal of Dynamic Systems, Measurement, and Control. 125 (2003), pp. 607-617.
- [5] L. Chankyu, K. Hedrick and Y. Kyongsu, *Real-time slip-based estimation of maximum tire-road friction coefficient*, Mechatronics, IEEE/ASME Transactions on. 9 (2004), pp. 454-458.
- [6] K. Li, J.A. Misener and K. Hedrick, *On-board road condition monitoring system using slip-based tyre-road friction estimation and wheel speed signal analysis*, Proceedings of the Institution of Mechanical Engineers, Part K: Journal of Multi-body Dynamics. 221 (2007), pp. 129-146.
- [7] J. Svendenius, *Tire modeling and friction estimation*, in: Department of Automatic Control, Lund University, Lund, 2007.
- [8] R. Rajamani, N. Piyabongkarn, J. Lew, K. Yi and G. Phanomchoeng, *Tire-Road Friction-Coefficient Estimation*, Control Systems, IEEE. 30 (2010), pp. 54-69.
- [9] M. Andersson, F. Bruzelius, J. Casselgren, M. Hjort, S. Löfving, G. Olsson, J. Rönnerberg, M. Sjöodahl, S. Solyom, J. Svendenius and S. Yngve, *Road Friction Estimation, part II - IVSS Project Report*, in, 2010.

- [10] C.S. Ahn, *Robust Estimation of Road Friction Coefficient for Vehicle Active Safety Systems*, in: Department of Mechanical Engineering, The University of Michigan, Ann Arbor, 2011.
- [11] W.R. Pasterkamp and H.B. Pacejka, *The Tyre as a Sensor to Estimate Friction*, *Vehicle System Dynamics*. 27 (1997), pp. 409-422.
- [12] Y. Yasui, W. Tanaka, Y. Muragishi, E. Ono, M. Momiyama, H. Katoh, H. Aizawa and Y. Imoto, *Estimation of Lateral Grip Margin Based on Self-aligning Torque for Vehicle Dynamics Enhancement*, in: SAE 2004 World Congress & Exhibition, SAE, Detroit, MI, 2004.
- [13] M. Klomp and M. Lidberg, *Safety Margin Estimation in Steady State Maneuvers*, in: Proceedings of AVEC '06 - The 8th International Symposium on Advanced Vehicle Control, Taipei, Taiwan, 2006.
- [14] Y.-H.J. Hsu, *Estimation and Control of Lateral Tire Forces Using Steering Torque*, in: Department of Mechanical Engineering, Stanford University, 2009.
- [15] G. Erdogan, *New Sensors and Estimation Systems for the Measurement of Tire-Road Friction Coefficient and Tire Slip Variables*, in: Mechanical Engineering, University of Minnesota, 2009.
- [16] O. Nishihara and K. Masahiko, *Estimation of Road Friction Coefficient Based on the Brush Model*, *Journal of Dynamic Systems, Measurement, and Control*. 133 (2011), pp. 041006-041009.
- [17] M.J. Matilainen and A.J. Tuononen, *Tire friction potential estimation from measured tie rod forces*, in: Intelligent Vehicles Symposium (IV), 2011 IEEE, 2011, pp. 320-325.
- [18] L. Li, W. Fei-Yue and Z. Qunzhi, *Integrated longitudinal and lateral tire/road friction modeling and monitoring for vehicle motion control*, *Intelligent Transportation Systems, IEEE Transactions on*. 7 (2006), pp. 1-19.
- [19] H.B. Pacejka, *Tyre brush model*, in: *Tyre and Vehicle Dynamics*, Elsevier, Oxford, U.K, 2005, pp. 93-134.

[20] J. Svendenius, *Tire Models for Use in Braking Applications*, in: Department of Automatic Control, Lund Institute of Technology, Lund, Sweden, 2003.

[21] S. Roweis, *Levenberg-Marquardt Optimization*, Toronto, 1996.

[22] M.I.A. Lourakis, *A brief description of the Levenberg–Marquardt algorithm implemented by Levmar*, 2005. Available online at: <http://www.ics.forth.gr/~lourakis/levmar/levmar.pdf>

Chapter 5

An Intelligent Tire Based Tire-Road Friction Estimation Technique and Adaptive Wheel Slip Controller for Anti-lock Brake System

Executive Summary

The contact between the tire and the road is the key enabler of vehicle acceleration, deceleration and steering. However, due to changes to the road conditions, the driver's ability to maintain a stable vehicle maybe at risk. In many cases, this requires intervention from the chassis control systems onboard the vehicle. Although these systems perform well in a variety of situations, their performance can be improved if a real-time estimate of the tire-road friction coefficient is available. Existing tire-road friction estimation approaches often require certain levels of vehicle longitudinal and/or lateral motion to satisfy the persistence of excitation condition for reliable estimations. Such excitations may undesirably interfere with vehicle motion controls. This study presents a novel development and implementation of a real-time tire-road contact parameter estimation methodology using acceleration signals from an intelligent tire. The proposed method characterizes the terrain using the measured frequency response of the tire vibrations and provides the capability to estimate the tire road friction coefficient under extremely lower levels of force utilization. Under higher levels of force excitation (high slip conditions), the increased vibration levels due to the stick/slip phenomenon linked to the tread block vibration modes make the proposed tire vibrations based method unsuitable. Therefore for high slip conditions, a brush model-based nonlinear least-squares (NLLS) parameter estimation approach is proposed. Hence an integrated approach using the intelligent tire based friction estimator and the model based estimator gives us the capability to reliably estimate friction for a wider range of excitations. Considering the strong interdependence between the operating road surface condition and the instantaneous forces and moments generated; this real time estimate of the tire-road friction coefficient is expected to play a pivotal role in improving the performance of a number of vehicle control systems. In particular, this study focuses on the possibility of enhancing the performance of the ABS control systems. In order to achieve the aforementioned

objectives, the design and implementation of a Fuzzy/Sliding Mode/Proportional Integral (Fuzzy-SMC-PI (FSP)) control methodology is proposed. Fuzzy-SMC-PI is basically a combination of Sliding Mode Control (SMC) and PI control methodologies through fuzzy logic. The fuzzy controller acts as a supervisory controller for a sliding mode controller and a classical PI controller. Lyapunov functions are used to ensure the stability of the overall system. The proposed regulator solves the problems of overshoot and slow transient responses associated with fast response PI controllers in transient state and the chattering problem associated with robust sliding mode controllers in the steady state. The mathematical model of the vehicle-wheel system and the Fuzzy-SMC-PI control algorithm to regulate the wheel slip are presented. The results show significant improvements in the stopping distance of a vehicle equipped with an intelligent tire based FSP controller as compared to a vehicle equipped with a standard ABS.

Keywords: *intelligent tire, friction estimation, Fuzzy-SMC-PI (FSP), nonlinear least-squares (NLLS), artificial neural network (ANN)*

5.1 Introduction

Locking-up the wheels during the braking process has a marked negative effect on the stability of a vehicle, potentially putting driver and passengers at risk. For this reason, ABS has become one of the most important automotive safety technologies. The control target of ABS is to keep the wheels from locking, thus guaranteeing good controllability of the vehicle and exploiting maximally the coefficient of friction between the tire and the road. ABS algorithms must guarantee that the friction coefficient between the tire and road is exploited. As stated by the friction ellipse theory [1], the total friction force acting between the tire and the road cannot exceed the maximum value determined by the friction coefficient (μ) and the vertical load (F_z). A decrease in the lateral force is expected as the longitudinal force increases, and vice versa.

Conventional ABS controllers utilize a rule-based method to maintain longitudinal wheel slip in a certain range on the information provided by angular wheel speed sensors [2-4]. The generic control approach is based on wheel slip and wheel angular acceleration control. The principle of the algorithm implemented in conventional ABS is based on limited cycling of longitudinal wheel slip in a desired range [5]. The algorithm sets certain bounds for wheel angular acceleration and wheel angular speed and uses a complex rule set to decide for the

pressure mode of the actuator. Nonetheless, these conventional ABS systems do not take into consideration the characteristics of different types of road surfaces, which naturally have their own appropriate operating conditions. This can ultimately lead to inefficient braking performance as well as unexpected consequences as the car encounters a road surface that is not defined in the ABS system’s default settings. Therefore, it may be technically preferable if the ABS system is able to operate at different operating points that are most appropriate to the road surface type the vehicle travelling on.

In this work, an adaptive intelligent tire based ABS system is proposed as a procedurally viable option to address the problem of unpredictable road surface conditions. The proposed ABS system is capable of differentiating various types of road surfaces, deriving the most suitable information for the road surface, and providing an appropriate amount of brake force, which prevents wheel lockup, essential to bringing the car to a complete stop in a minimal amount of time and distance. The details of the vehicle model used in this study can be found in Section 5.2. Section 5.3 provides details on the ABS controller architecture, which comprises of two subsystems: (1) the proposed road surface identification system, and (2) the FSP based wheel slip control mechanism. All simulation results obtained are presented and discussed in Section 5.4. Section 5.5 provides the concluding remarks of our work.

5.2 System Dynamics

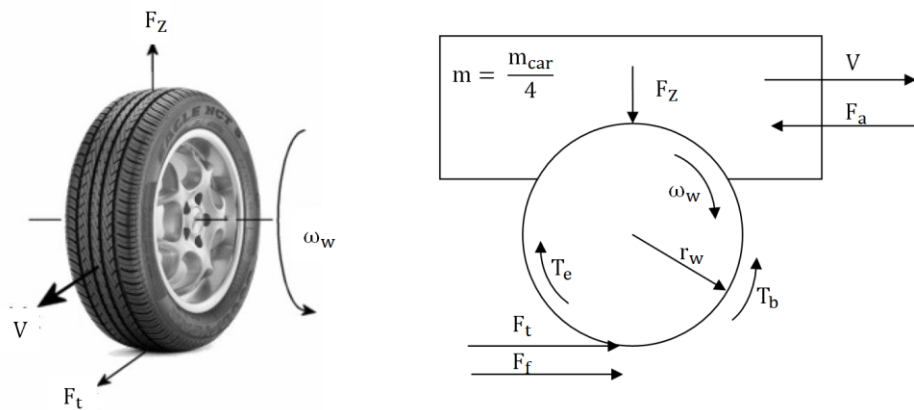


Fig. 5.1: Free body diagram of the quarter car model

In this section, a simplified model of the quarter vehicle undergoing braking maneuver is developed (Fig. 5.1). This model will then be used for system analysis, design of control laws and computer simulations. The following assumptions are considered in the modeling process:

1. Zero steering input.
2. Motion only along longitudinal axis.
3. Motion dynamics arising from rotation of the vertical axis is not considered.
4. The sprung mass is assumed to be connected to unsprung mass (no suspension effects).
5. Approximating the vertical forces as a static value.

5.2.1 Wheel Dynamics

The dynamic equation for the angular motion of the wheel is given as:

$$J\dot{\omega}_w = (T_e - T_b) - F_t r_w - F_f r_w \quad (5.1)$$

where $(T_e - T_b)$ represents the net torque (T_{net}) on the wheel, with T_e as the engine/driving torque and T_b as the braking torque. Applying a driving torque or a braking torque to a pneumatic tire produces a tractive force at the tire-road contact patch [1]. The driving torque produces compression at the tire tread in front and within the contact patch. Consequently, the tire travels less distance than it would if it were free rolling. Similarly, when a braking torque is applied, it produces a tension at the tire tread within the contact patch and at the front. Because of this tension, the tire travels more distance than it would during free rolling. This phenomenon is called the deformation slip or wheel slip (λ) [6]. Mathematically, the wheel slip is defined as:

$$\lambda = \frac{r_w \omega_w - V}{\max\{r_w \omega_w, V\}} \quad (5.2)$$

where V is the vehicle velocity. The tractive force, F_t , is given by:

$$F_t = \mu(\lambda) F_z \quad (5.3)$$

where the friction coefficient $\mu(\lambda)$, which is the ratio between the tire tractive force F_t and the normal load F_z , depends on the tire-road conditions and the value of the wheel slip (λ). In this study, the function:

$$\mu(\lambda) = 2\mu_p\lambda_p \left(\frac{\lambda}{\lambda_p^2 + \lambda^2} \right) \quad (5.4)$$

is used for a nominal curve [7], where μ_p and λ_p are the peak values. This function gives values compatible with experimental data given in the literature [1], especially in the range $\lambda \in [0 \ 0.3]$. For various road conditions, the curves have different peak values and slopes (Fig. 5.2).

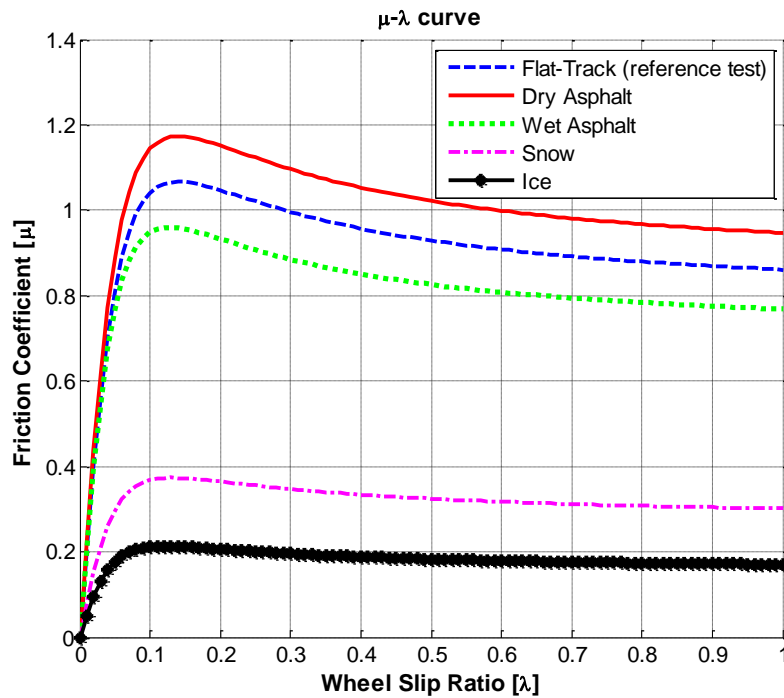


Fig. 5.2: Simulated adhesion/friction coefficient (μ) versus longitudinal slip-ratio (λ) curve for varying surface conditions

The friction coefficient-wheel slip characteristics are also influenced by operational parameters like speed and vertical load. The peak value for friction (μ_p) may have values between 0.10 and 0.95 as shown in

Table 5.1.

Table 5.1: Typical roads parameters

Road	λ_p	μ_p
Dry Asphalt	0.2	0.95
Wet Asphalt	0.15	0.60
Snow	0.11	0.35
Ice	0.06	0.10

The maximum of the friction curve lies at $\frac{d\mu}{d\lambda} = 0$ (Fig. 5.2). This point will be called λ_p and separates the two zones of the curve known as the stable zone and the unstable zone. At any absolute slip value larger than λ_p , one is in the unstable zone of the tire curve. At any absolute slip value smaller than λ_p , one is in the stable zone of the tire curve. Within the stable zone, as the brake force is increased, the longitudinal force on the road increases. In the unstable zone, increasing the brake force will lead to a decrease in the exerted longitudinal force. The maximum force drop from λ_p to wheel lock at $\lambda=1$ is typically up to 30%.

The total vertical load on the tire (F_z) is given by the expression [8]:

$$F_z = \left(mg - \frac{m_{car} h_c \dot{V}}{2L} \right) \quad (5.5)$$

The wheel rolling resistance force (F_f) is given by the expression [8]:

$$F_f = 0.005 + 3.24 \cdot 0.01 \cdot (r_w \cdot \omega_w)^2 \quad (5.6)$$

The block diagram representation of the wheel dynamics is shown in Fig. 5.3.

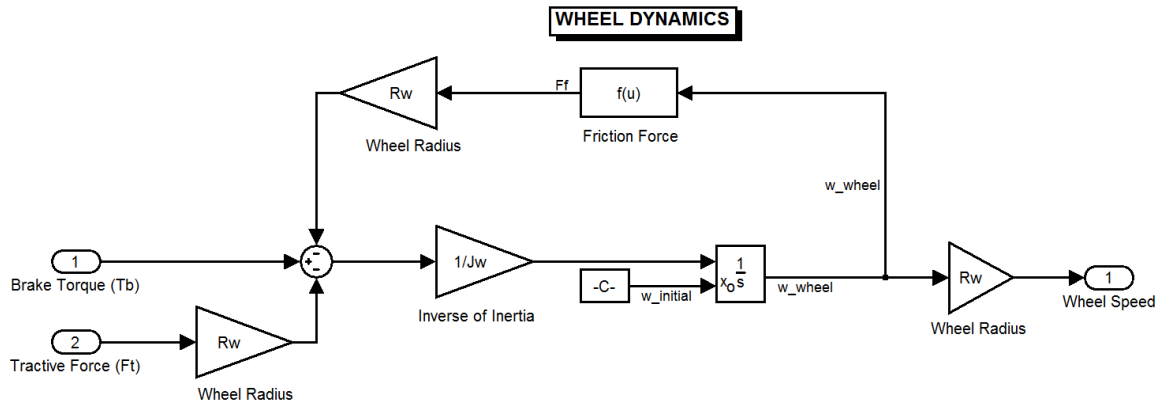


Fig. 5.3: Wheel dynamics (refer to Equations (5.1)-(5.6))

5.2.2 Vehicle Dynamics

The linear acceleration of the vehicle is governed by the tractive forces (F_t) from the wheels and the aerodynamic friction force (F_a). The tractive force is the average friction force of the driving wheels for acceleration and the average friction force of all wheels for deceleration. The dynamic equation for the vehicle motion is:

$$m\dot{V} = F_t - F_a \quad (5.7)$$

Equation (5.8) defines the aerodynamic force experienced by the vehicle, where ρ is the density of air, C_d is the measured drag coefficient of the vehicle being tested, A_f is the total frontal area of the vehicle and V is the vehicle speed.

$$F_a = \frac{1}{2} \rho C_d A_f V^2 \quad (5.8)$$

The block diagram representation of the vehicle dynamics is shown in Fig. 5.4.

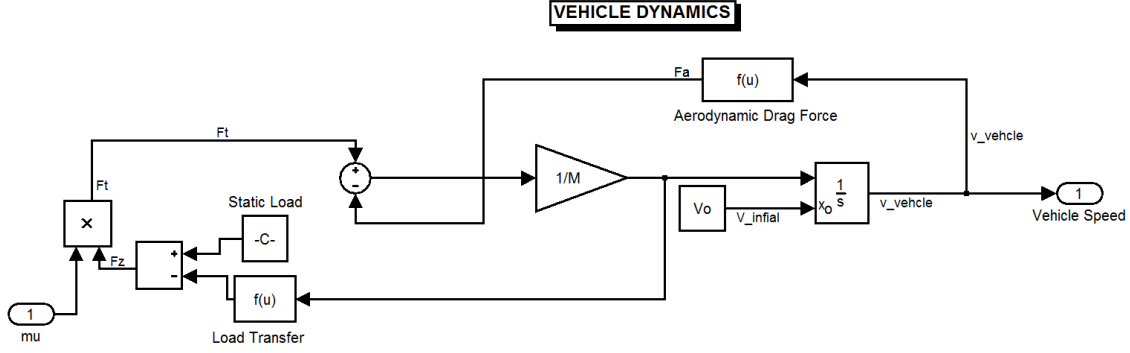


Fig. 5.4: Vehicle dynamics (refer to Equations (5.7)-(5.8))

5.2.3 Coupled Wheel and Vehicle Dynamics

The dynamic equation of the system can be written in state variable form by defining wheel and vehicle angular velocities as state variables:

$$x_1 = \omega_v \left(= \frac{V}{r_w} \right), x_2 = \omega_w \quad (5.9)$$

Now we can rewrite Equations (5.1) and (5.7) as:

$$\dot{x}_1 = \frac{-F_a}{mr_w} + \frac{\mu F_z}{mr_w} \quad (5.10)$$

$$\dot{x}_2 = \frac{-F_f r_w}{J} - \frac{\mu F_z r_w}{J} + \frac{T}{J} \quad (5.11)$$

Hence, the state equations of the system can be described by the following nonlinear form:

$$\begin{bmatrix} \dot{x}_1 \\ \dot{x}_2 \end{bmatrix} = \begin{bmatrix} -f_1(x_1) + b_1(\mu(x_1, x_2)) \\ -f_2(x_2) - b_2(\mu(x_1, x_2)) \end{bmatrix} + \begin{bmatrix} 0 \\ b_3 \end{bmatrix} T \quad (5.12)$$

where

$$f_1(x_1) = \frac{F_a}{mr_w}, f_2(x_2) = \frac{F_f r_w}{J},$$

$$b_1(\mu(x_1, x_2)) = \frac{\mu F_z}{mr_w}, b_2(\mu(x_1, x_2)) = \frac{\mu F_z r_w}{J}, b_3 = \frac{1}{J}$$

The control input (T) is the applied torque at the wheels which is equal to the difference of the shaft torque from the engine and the braking torque. The block diagram representation of the combined dynamic system is shown in

Fig. 5.5.

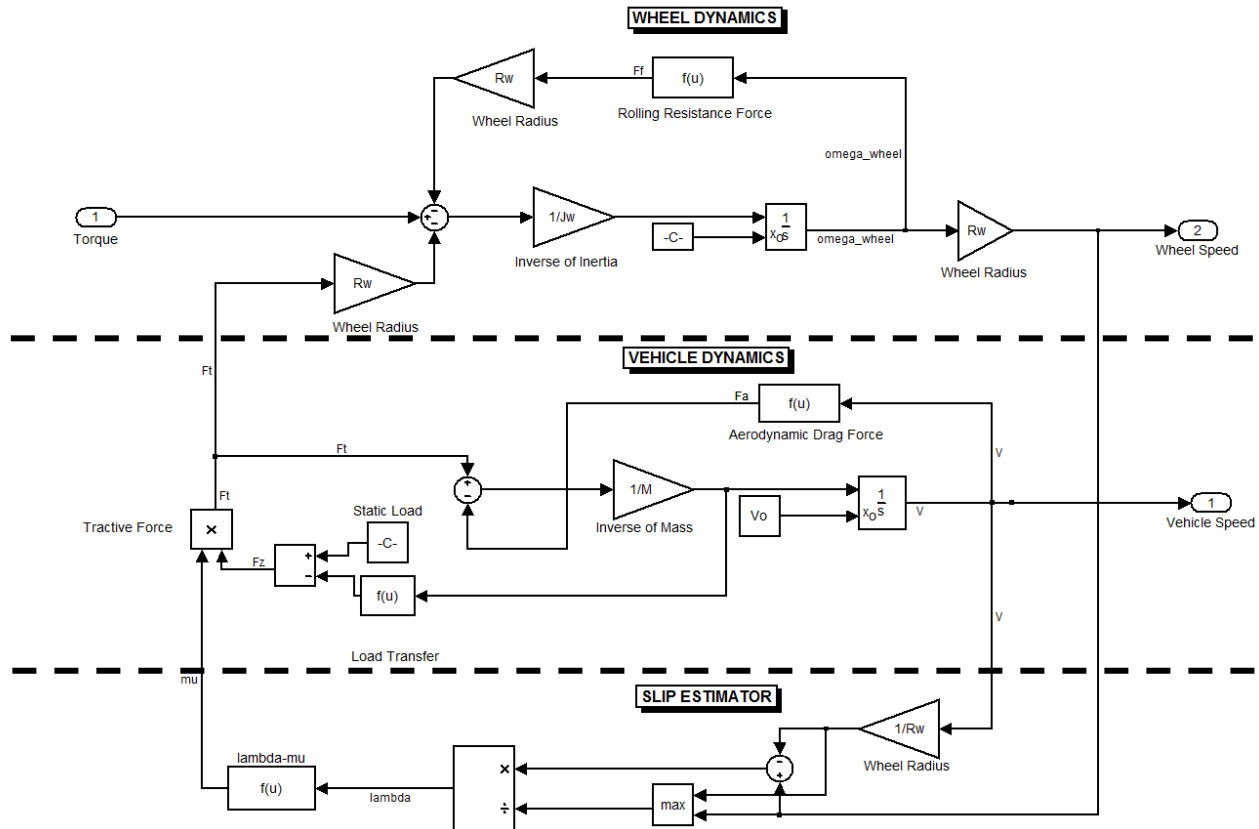


Fig. 5.5: Combined system dynamics

During acceleration, engine torque is the primary input, whereas during deceleration, it is the braking torque. The wheel slip is chosen here as the controlled variable for traction control algorithms because of its strong influence on the tractive force between the tire and the road. In order to control the slip, it is convenient to have the system dynamic equations in terms of the wheel slip. Since the functional relationship between the wheel slip and the state variables is different for acceleration and deceleration, we will only derive the equations for the deceleration case. During deceleration the condition $\omega_w < \omega_v$ is satisfied, and therefore the wheel slip is defined as:

$$\lambda = \frac{\omega_w - \omega_v}{\omega_v} = \frac{x_2 - x_1}{x_1} \quad (5.13)$$

Taking the time derivative we obtain:

$$\dot{\lambda} = \frac{\dot{x}_2 - (1 + \lambda)\dot{x}_1}{x_1} \quad (5.14)$$

Substituting Equations (5.10)-(5.11) into Eq. (5.14), we get Eq.(5.15):

$$\dot{\lambda} = \frac{1}{x_1} \left[\frac{T_e - T_b}{J} - \frac{F_t r_w}{J} - \frac{F_f r_w}{J} - (1 + \lambda) \frac{F_t - F_a}{m r_w} \right] \quad (5.15)$$

This gives the wheel slip equation for deceleration (braking) case.

5.2.4 Hydraulic Brake Dynamics

The braking torque depends on the hydraulic pressure of the wheel cylinder. The pressure is controlled by solenoid valves through the combination of pressure build-up, hold and reduces states [5]. The brake system including the solenoid valves can be approximated by a second order transfer function [9]:

$$H(s) = \frac{\omega_n^2}{s^2 + 2\zeta\omega_n s + \omega_n^2} \quad (5.16)$$

Here, s is the Laplace operator, ζ is the damping ratio and ω_n is the undamped natural frequency of the brake system.

5.3 Controller Design

In this study, a cascade form of the controller is realized. The cascade control form is applicable to the ABS problem because the disk brake system dynamics are independent of the vehicle and tire dynamics. This approach will simplify the individual control design. The ABS control scheme is designed based on the vehicle model as the plant, independent of the brake system dynamics. The brake hydraulic system is regarded as unmodelled dynamics in the design of the

sliding mode control. The output of the ABS control scheme, which is the desired brake torque, will serve as the desired input to the brake system.

5.3.1. Road Surface Condition Estimation Algorithm

The implementation strategy for a road surface condition estimation algorithm that utilizes sensor signals from an instrumented tire is presented in this section. A method that characterizes the terrain using the measured frequency response of the tire vibrations has been developed. To do this, the tire vibration signals in a predetermined domain were extracted. The predetermined domain represents a certain portion of the tire signal per tire revolution. The vibration levels of a predetermined frequency band within these domains are then calculated using the frequency spectrum of the time signal by passing the signals through a band-pass filter. Based on the calculated vibration level, the road surface condition can be estimated. Details regarding the procedure adopted to instrument the tire, outdoor tire testing, methodology for sensor data analysis and the classification algorithm are explained in the sections to follow.

5.3.1.1 Tire Instrumentation and Testing

The instrumented tire system was developed by placing accelerometers [10] on the inner liner of a tire (Fig. 5.6a).

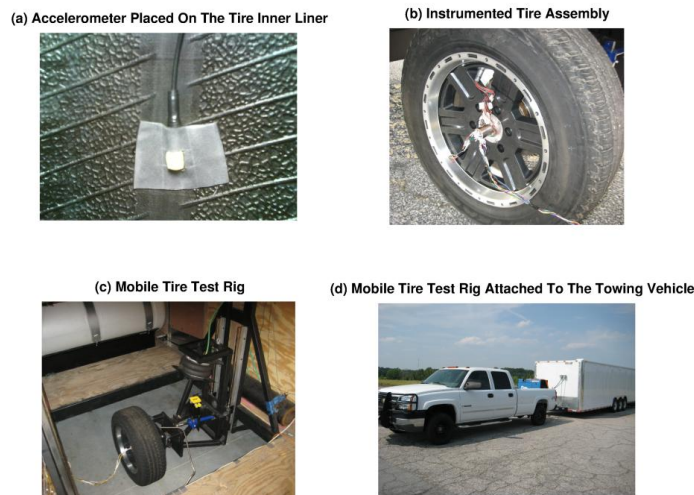


Fig. 5.6: Intelligent tire application: (a) sensor mounting location, (b) instrumented tire assembly, (c) mobile tire test rig, and (d) test rig attached to the towing vehicle

Fig. 5.6b shows the final assembly of the instrumented tire with a high speed slip ring attached to the wheel. Extensive dynamic tests of the tire were conducted using the in-house mobile tire test rig [11] shown in Fig. 5.6c and 6d. An example of the acceleration signal is shown in Fig. 5.7.

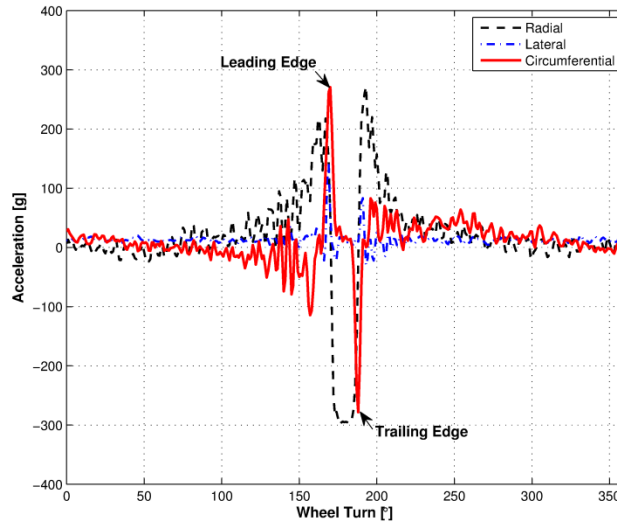


Fig. 5.7: Measured acceleration signal for one rotation

5.3.1.2 Sensor Data Analysis and Algorithm Development

The effect of tire load, translational speed, varying pressure conditions, and road surface roughness on the tire vibration spectra were studied by varying each of these parameters by carrying out extensive outdoor testing of the instrumented tire under free-rolling, traction/braking and steering conditions (Fig. 5.8).

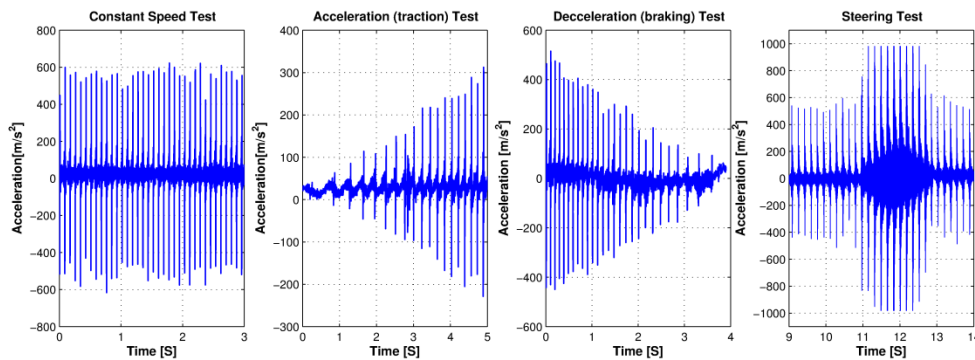


Fig. 5.8: Measured circumferential acceleration signal under free-rolling, traction, braking, and steering conditions

The power spectrum of each accelerometer signal from these tests was computed using Welch's averaged modified periodogram method [12] for spectral estimation (Fig. 5.9). Analyzing the dynamic test results, it was concluded that, a marked difference was noticed in the concentration of the higher frequencies on the spectrum of the circumferential acceleration signal of the tire tested on different surface conditions (Fig. 5.9d). This variation in the circumferential acceleration signal PSD on different road surface conditions presented an opportunity to characterize the road condition using the tire vibration pattern information.

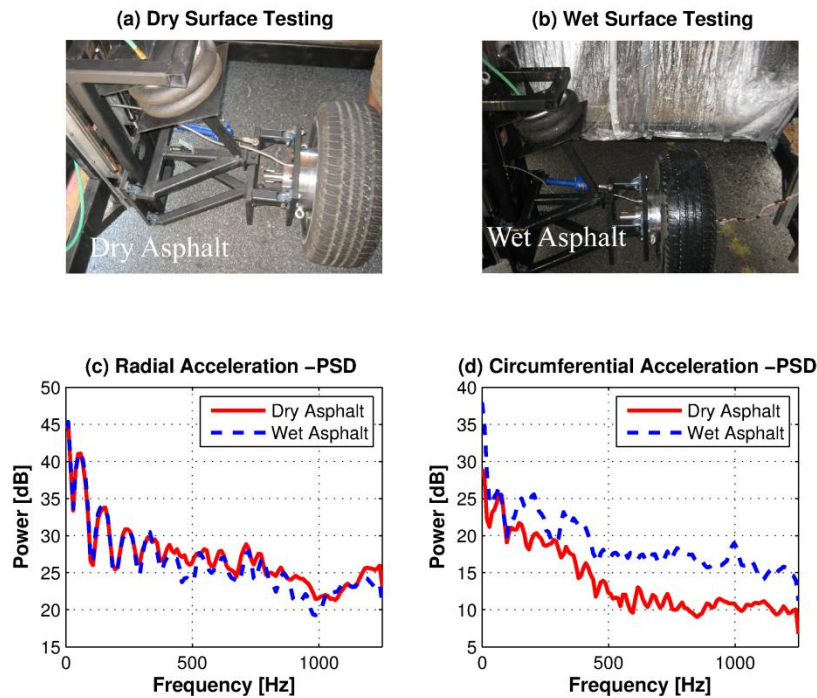


Fig. 5.9: Tire tested on different road surface conditions: (a) dry surface testing, and (b) wet surface testing; Roughness dependence study: (c) radial signal PSD, and (d) circumferential signal PSD

The proposed intelligent tire based road surface condition estimating algorithm (Fig. 5.10) consists of detecting the circumferential vibration of a tire of a running vehicle; dividing the detected tire vibration into vibration in a pre-trailing domain, the domain existing before a trailing edge position; and vibration in a post-trailing domain, the domain existing after a trailing edge position as shown in Fig. 5.11a. Thereafter extracting signals of tire vibration only from the pre-trailing domain; obtaining a time-series waveform of tire vibration including only the

frequencies in a predetermined frequency band by passing the extracted signals through a band-pass filter of the predetermined frequency band; calculating a vibration level in the predetermined frequency band; and estimating a road surface condition based on the calculated vibration level.

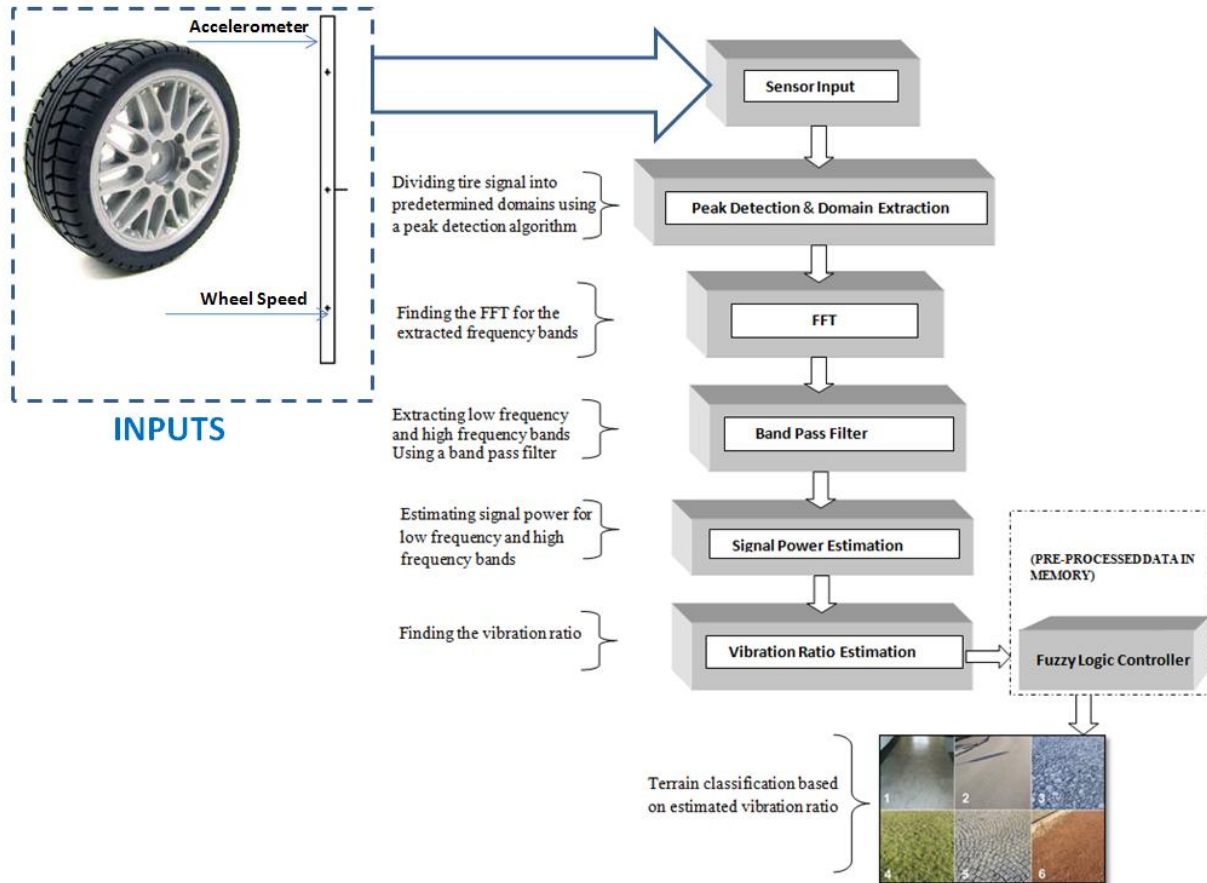


Fig. 5.10: Algorithm flowchart

The predefined frequency domains being a low frequency band (e.g. 10-500 Hz band) and a high frequency band (e.g. 600 to 2500 Hz), as shown in Fig. 5.12. The motivation for only using the pre-trailing domain signal is the larger difference in the PSD of the pre-trailing domain signal as shown in Fig. 5.11c, as compared to the PSD's obtained using the entire signal (Fig. 5.11b) or using the signal from the post-trailing domain (Fig. 5.11d).

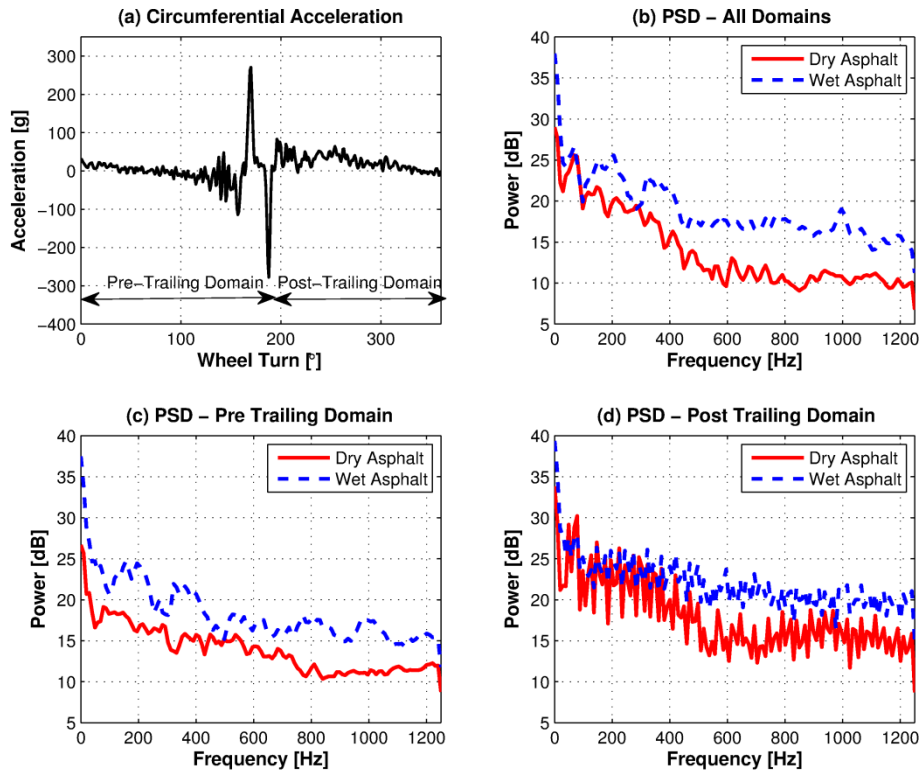


Fig. 5.11: (a) Accelerometer signal domains; PSD waveforms using: (b) all the domains, (c) only the pre-trailing domain, and (d) only the post-trailing domain

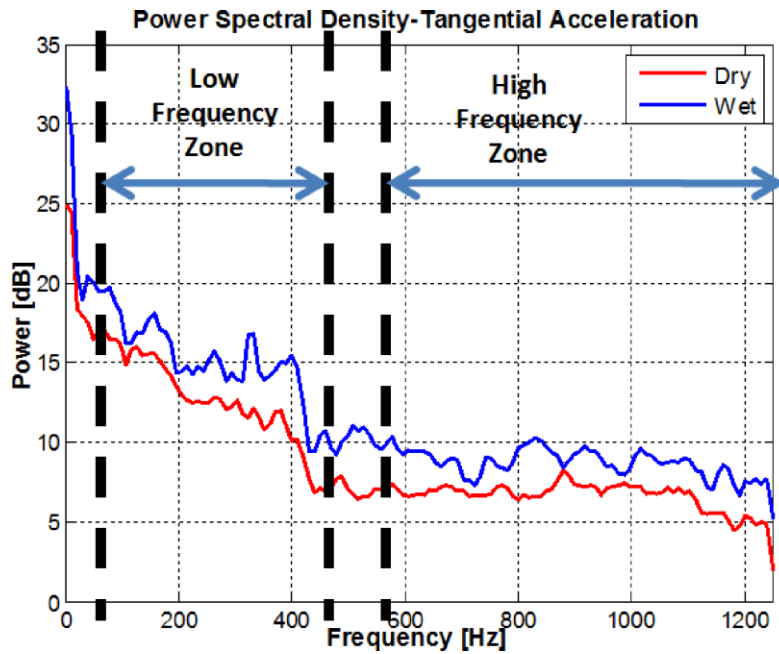


Fig. 5.12: High and low frequency domains in the circumferential acceleration PSD

To determine these differences, the instrumented tire was first driven on a dry surface and then on a wet road surface at different speeds and the change in the vibration level ratio was measured. It is evident from Fig. 5.13 that the vibration level ratio R increased as the tire was tested on the wet road surface. This change in the vibration level ratio can be attributed to the increased slippage of the tire, and thus it has been confirmed that the slipperiness of a road surface can be decided by setting a proper threshold value.

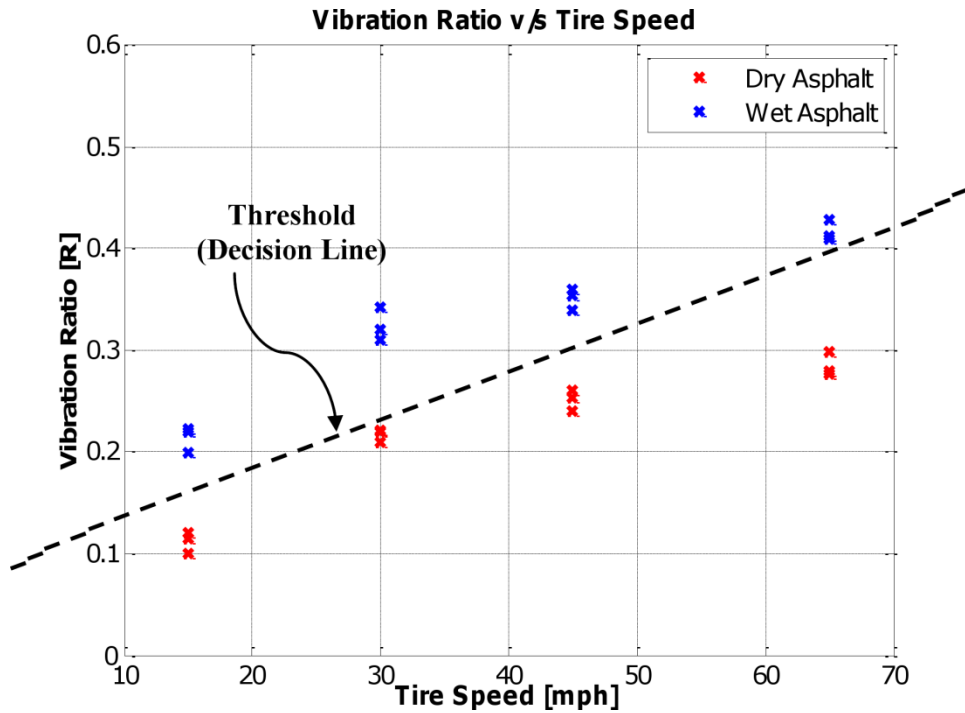


Fig. 5.13: Vibration ratio on dry and wet surface conditions for a range of tire speeds

For this purpose, a fuzzy logic classification approach [13-14] was developed for the real-time implementation of the proposed algorithm. The application of fuzzy logic to solve the classification problem is motivated by its noise tolerance to the vibration data retrieved from sensors, and its ability for real-time implementation while ensuring robustness with respect to imprecise or uncertain signal interpretation. Fuzzy logic provides a linguistic-based method for modeling the relationship between vibration data input values and the terrain surface information. In fact, fuzzy logic is ideally suited for this application because it naturally copes with ambiguities and imprecision's. This is accomplished by representing terrain information using ranges of values that are sectored into several linguistic classes that have smooth overlapping boundaries. Fuzzy logic rule evaluation involves only simple arithmetic calculations

that can be performed very rapidly. Therefore, the computational time is very small, making it feasible for real-time implementation. Fig. 5.14 shows the fuzzy controller architecture.

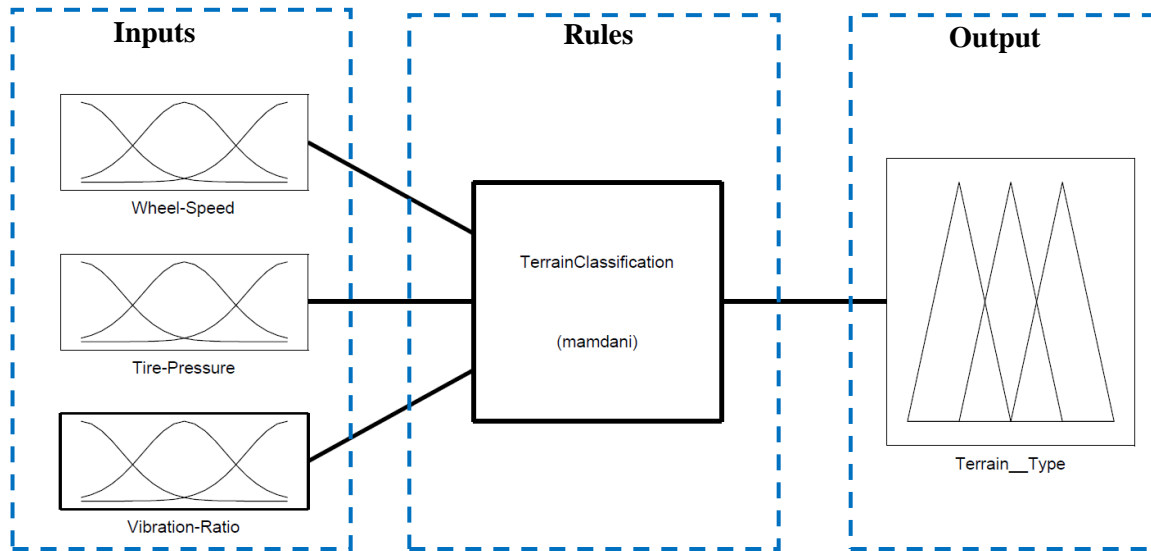


Fig. 5.14: Fuzzy logic based controller architecture

The input block has three variables, which have been identified based on the factor dependence study. Details regarding the fuzzy membership functions for the input and output variables are presented below.

Membership function for input set:

A) Wheel Speed

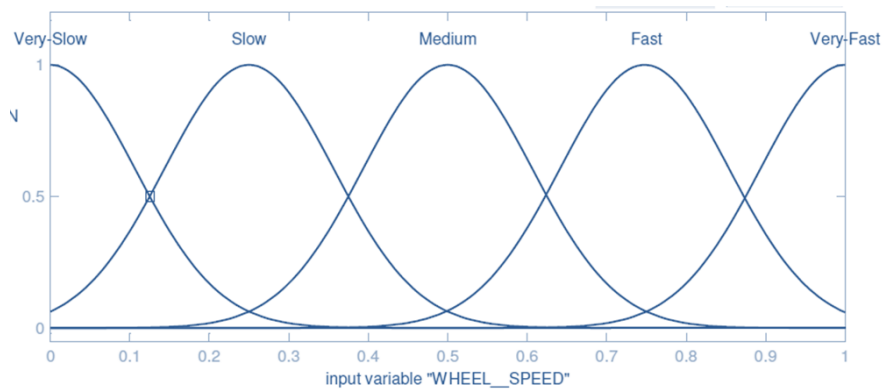


Fig. 5.15: Membership functions for input variable-speed

There are six membership functions for the input variable-speed (Fig. 5.15).

B) Tire Pressure

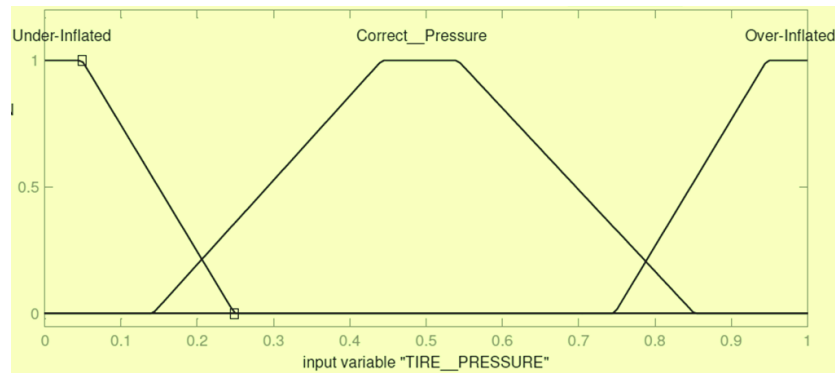


Fig. 5.16: Membership functions for input variable-tire pressure

There are three membership functions for the input variable-tire pressure (Fig. 5.16).

C) Vibration Ratio

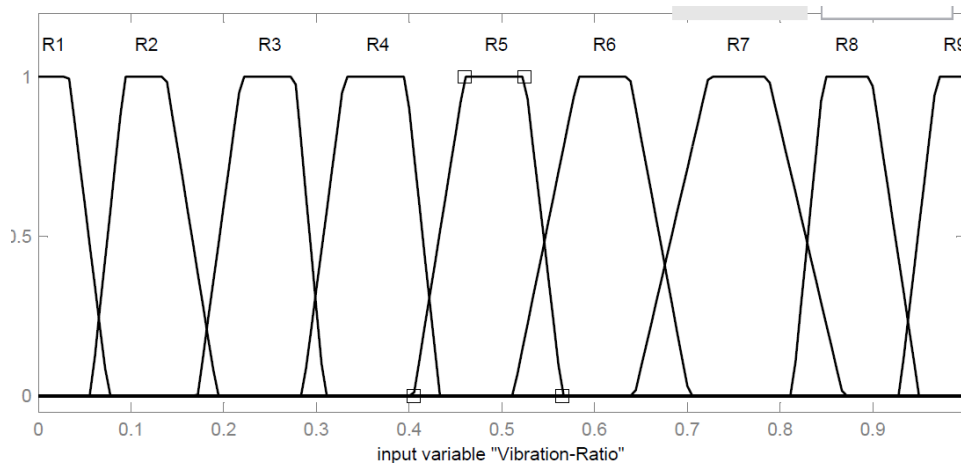


Fig. 5.17: Membership functions for input variable-vibration ratio

There are nine membership functions for the input variable-Vibration-Ratio (Fig. 5.17).

Membership function for output set:

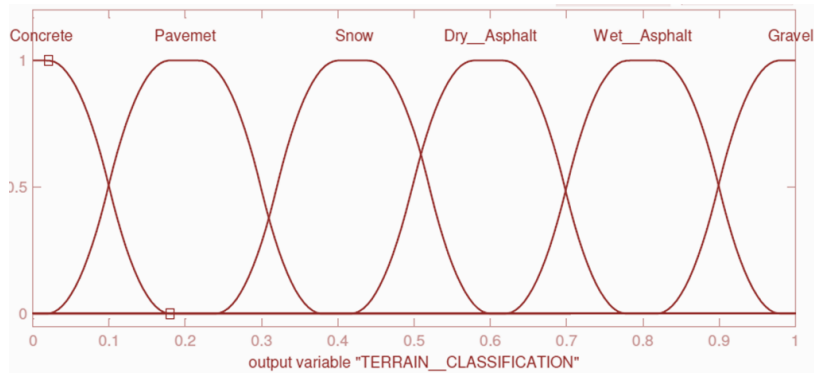


Fig. 5.18: Membership functions for output variable-terrain classification

There are six membership functions for the output variable-Terrain-Classification (Fig. 5.18).

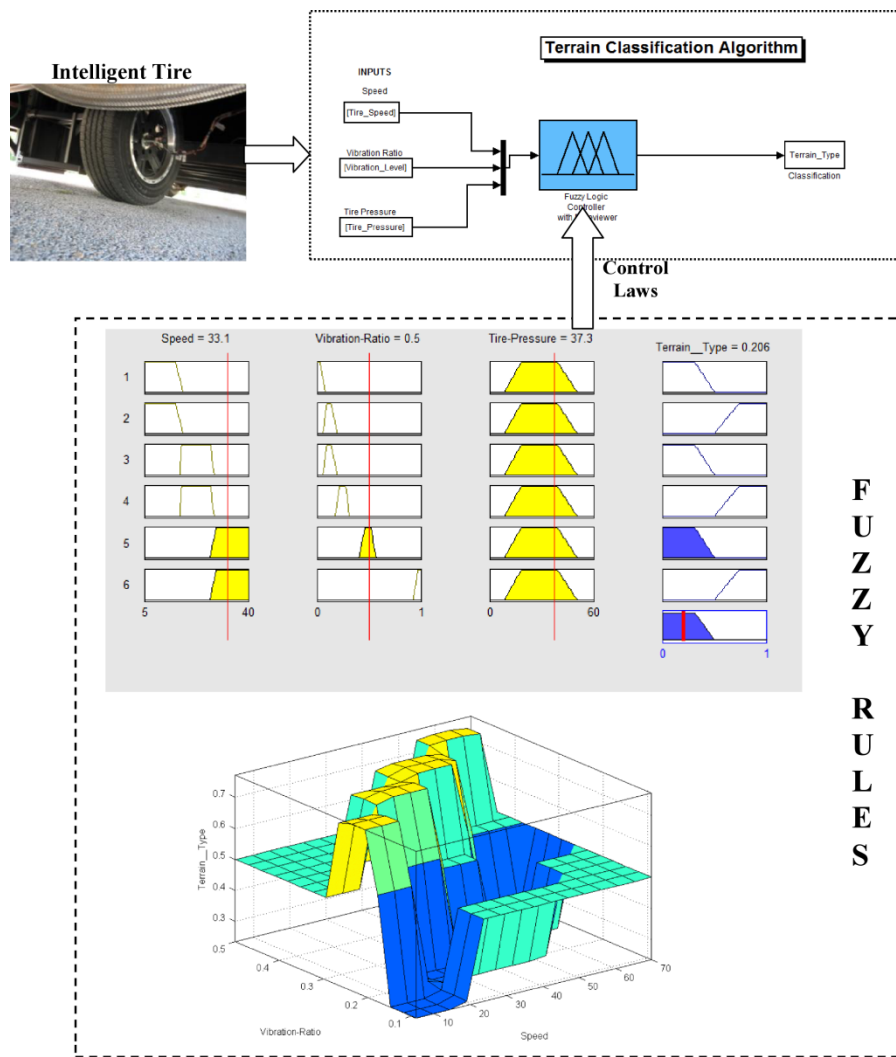


Fig. 5.19: Flowchart of the proposed terrain classification algorithm

Based on the interdependence of all the inputs for a given road surface condition and the way they effect the vibration spectra of a tire, a set of linguistic rules were developed to identify the road surface condition. Fig. 5.19 shows these rules.

The classifier performance was validated on smooth asphalt, regular asphalt, rough asphalt and wet asphalt (Fig. 5.20). Two different tests were performed to study the classifier performance. The first test involved testing the tire under free-rolling and low-slip conditions (low force utilization). The second test involved testing the tire under high-slip conditions (high force utilization). For the first test (free-rolling and low-slip conditions), the classifier was successfully able to distinguish between the different road surface conditions as shown in Fig. 5.21.

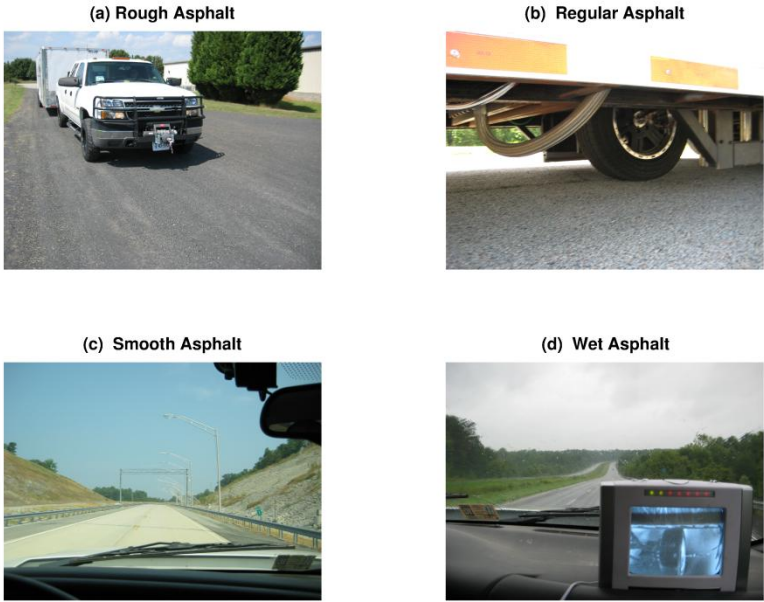


Fig. 5.20: Tire tested on different road surface conditions: (a) rough asphalt, (b) regular asphalt, (c) smooth asphalt, and (d) wet asphalt

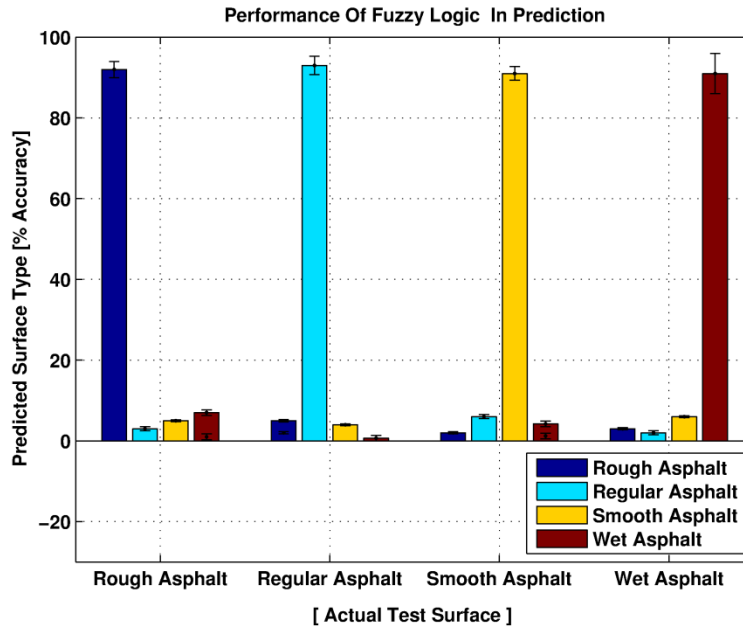


Fig. 5.21: Performance of the fuzzy logic classifier - low-slip conditions

However, for the second test (high-slip conditions), classifier performance was unsatisfactory (Fig. 5.22). Higher misclassification rates under high slip conditions were attributed to the increased vibration levels in the circumferential acceleration signal due to the stick/slip phenomenon linked to the tread block vibration modes (Fig. 5.23).

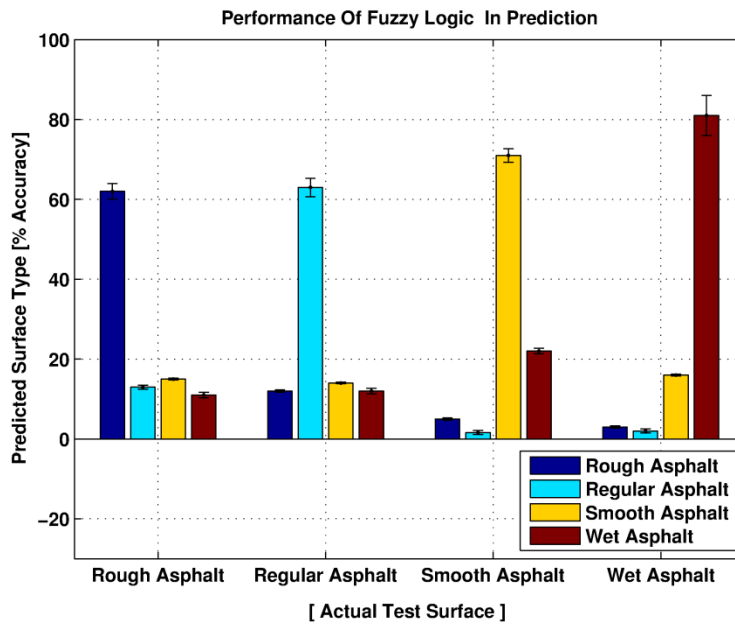


Fig. 5.22: Performance of the fuzzy logic classifier - high-slip conditions

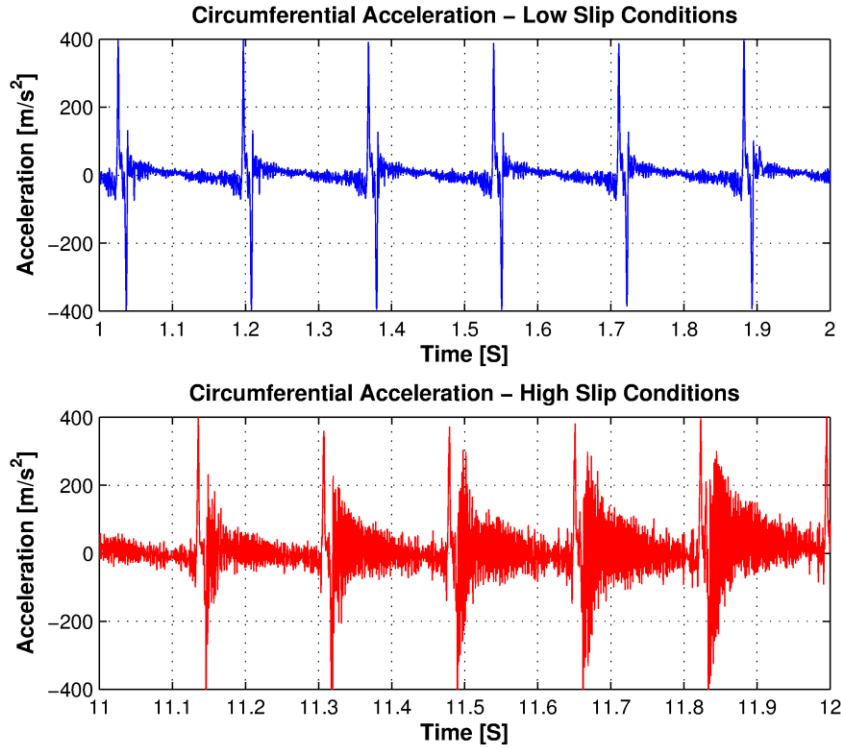


Fig. 5.23: Circumferential acceleration signal under low-slip conditions (top), and increased vibration levels in the circumferential acceleration signal under high-slip conditions (bottom)

The requirement of a more complex event detection algorithm for distinguishing the high frequency content of a signal due to the tread block mobility effects, under high-slip conditions, makes the proposed fuzzy logic classifier unsuitable for friction estimation under high-slip conditions. Hence it was proposed to use a model based approach to estimate road surface friction under high-slip conditions.

5.3.1.3 Model Based Friction Estimation Algorithm

If we assume that a tire consists of a row of elastic bristles that touches the road plane and can deflect in a direction parallel to the road surface [15], the tire longitudinal force can be modeled by simple equations, e.g. brush model. Tire brush model is proper for estimation or control purposes because it has fewer parameters compared with many other tire models [15]. The pure-slip longitudinal tire force model is:

$$F_x = \begin{cases} -C_x \frac{\lambda}{\lambda + 1} + \frac{1}{3} \left(\frac{C_x^2 \left| \frac{\lambda}{\lambda + 1} \right| \frac{\lambda}{\lambda + 1}}{\mu F_z} \right) & \text{for } |\lambda| \leq |\lambda_{sliding}| \\ -\frac{1}{27} \left(\frac{\left(C_x \frac{\lambda}{\lambda + 1} \right)^3}{(\mu F_z)^2} \right) & \\ \mu F_z \text{sign}(\lambda) & \text{for } |\lambda| > |\lambda_{sliding}| \end{cases} \quad (5.17)$$

To validate the agreement of the brush tire model towards magic formula [16] data, the brush model was adapted to the magic formula data. From Fig. 5.24, it can be seen that the brush model mostly fits the magic formula data well.

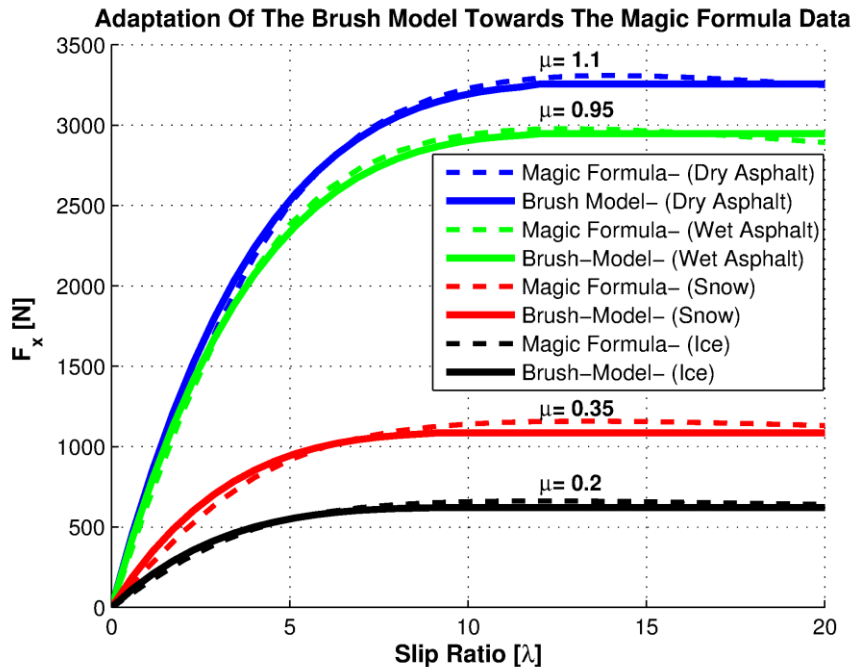


Fig. 5.24: Adaption of the brush model towards the magic formula

For the real-time implementation of the high-slip condition friction estimation algorithm, a nonlinear least-squares (NLLS) parameter estimation approach was developed and implemented. The least squares method can be seen as a method for the identification of parameters through determining the best fit between modeled and observed data.

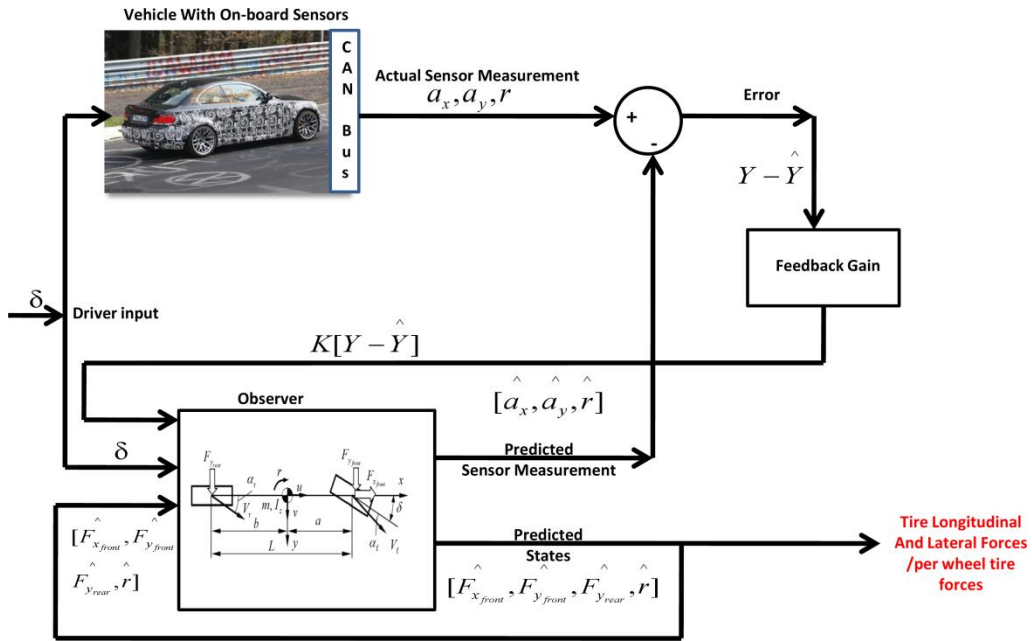


Fig. 5.25: Tire force estimator architecture

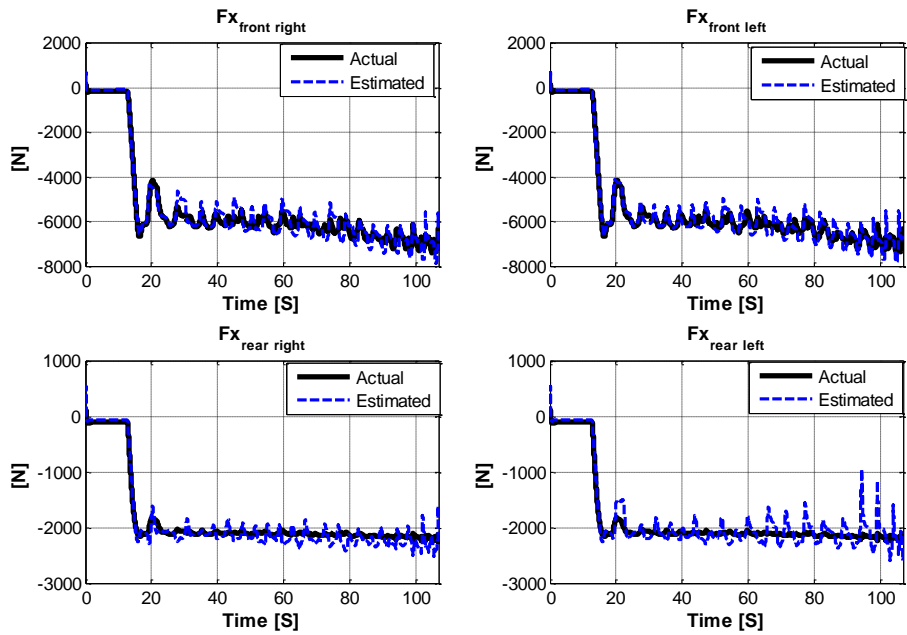


Fig. 5.26: Straight-line braking test - SMC observer - tire force estimates

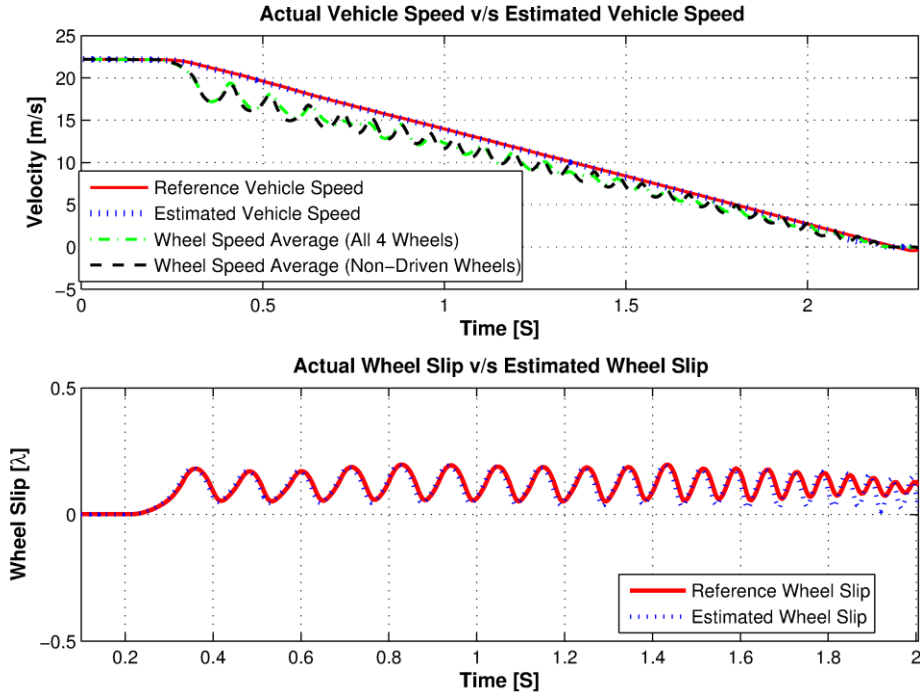


Fig. 5.27: Straight-line braking test - estimated vehicle speed compared with the reference vehicle speed (top), and estimated wheel slip compared with the reference wheel slip (bottom)

The required brush model parameters for the estimation algorithm include longitudinal force (F_x), tire load (F_z) and tire slip ratio (λ) and the unknown parameters being estimated include tire longitudinal stiffness (C_x) and friction coefficient (μ). For estimating the longitudinal force, a sliding-mode control (SMC) observer [17] based dynamic tire longitudinal/lateral force estimator was developed and implemented (Fig. 5.25). The tire slip-ratio was estimated using a rule-based approach, utilizing the four wheel rotational speeds (ω_w) and of the longitudinal vehicle acceleration (a_x) signals [18]. The performance of the SMC longitudinal/lateral force estimator and the slip-ratio estimator was validated using a commercial software package CarSim (Fig. 5.26-Fig. 5.27). To estimate the tire load, a novel signal processing algorithm using the intelligent tire radial acceleration signal was developed. Through extensive outdoor tests, a parametric sensitivity analysis was conducted to study the effect of changing operating conditions of the tire on the radial acceleration signal (Table 5.2).

Table 5.2: Results for the parameter sensitivity analysis

S. No	Parameter Under Study	Frequency Domain	Time Domain	
		Variation in Frequency Spectra	Variation in Signal Power	Variation in Contact Patch Length
1	Rolling Speed	Significant	Significant	Significant
2	Inflation Pressure	Negligible	Significant	Significant
3	Load	Marginal	Significant	Significant
4	Camber Angle	Negligible	Marginal	Marginal
5	Slip Angle	Marginal	Marginal	Marginal
6	Road Surface	Negligible	Negligible	Negligible

The goal of this analysis was to determine parameters that were sensitive only to normal load. The two parameters identified were: (a) the contact patch length (CPL) and (b) the radial acceleration signal amplitude (Table 5.2). A strong dependence of both these parameters was seen on the tire rolling speed and inflation pressure.

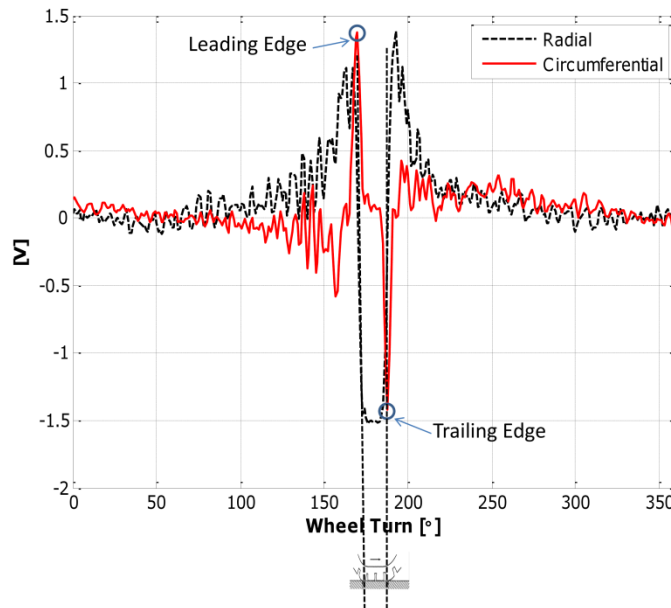


Fig. 5.28: Measured radial and circumferential acceleration signal for one tire rotation

The contact patch length information was extracted from the radial acceleration signal by determining the distance between the zero crossing points of the signal, where the crossing points correspond to the leading and the trailing edge of the tire (Fig. 5.28).

Having identified parameters that were sensitive to the tire normal load, the next task was to establish a relationship between these system inputs/parameters (rolling speed, inflation pressure, contact patch length and signal amplitude) and the system output (tire normal load). To achieve the aforementioned objective, an explicit artificial neural network (ANN) [19] based formulation was developed to estimate the tire normal load in terms of tire rolling speed, inflation pressure, contact patch length and signal power (Fig. 5.29). The neural network structure was selected by using an evolutionary algorithm. The selected ANN was trained for various learning rate and termination criteria [20]. The neural network model was able to make highly complex, nonlinear and multidimensional associations between selected input parameters and output to allow acceptable degree of accuracy in the predictions of the tire load across the full range of the tire operating conditions (Fig. 5.30)

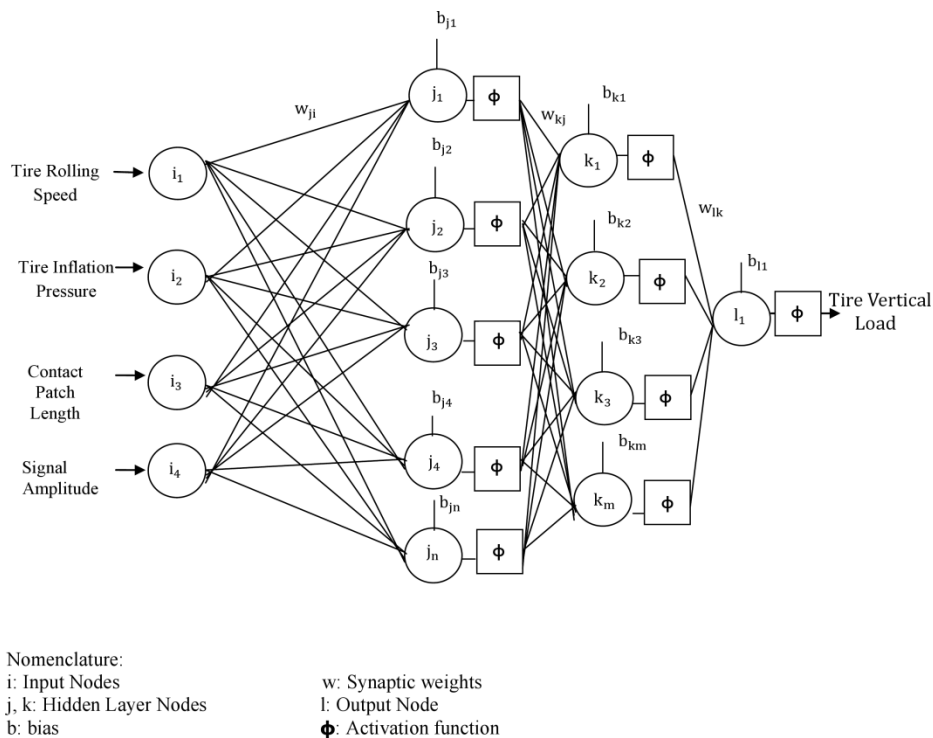


Fig. 5.29: Architecture of the proposed artificial neural network (ANN) model

Finally, the performance of the high-slip condition nonlinear least-squares (NLLS) parameter estimation algorithm was evaluated with simulation where the road surface is designed to have sudden friction coefficient changes, a so called jump- μ surface and the vehicle maneuver is straight driving with intermittent gas pedal presses, sufficient to generate a large slip-ratio. Fig. 5.31 shows the estimation results. The algorithms work well for high-slip conditions.

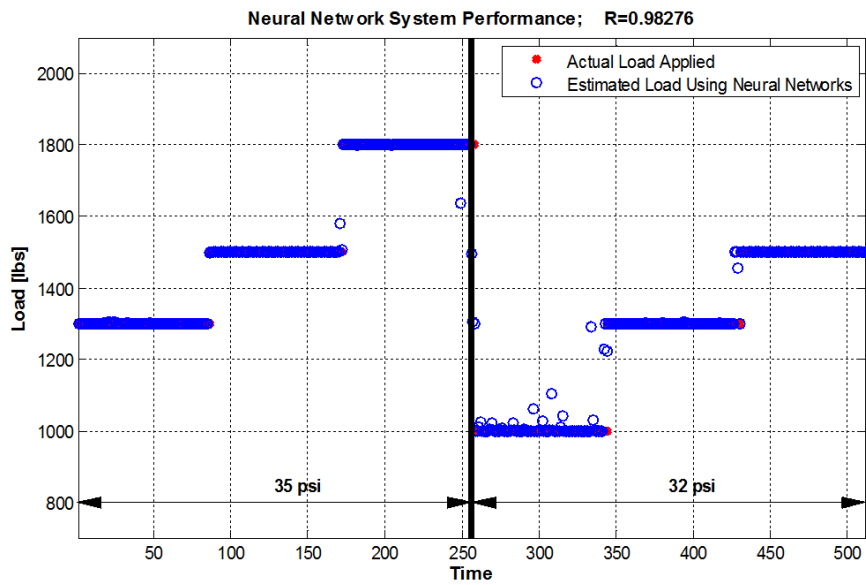


Fig. 5.30: Artificial neural network (ANN) performance

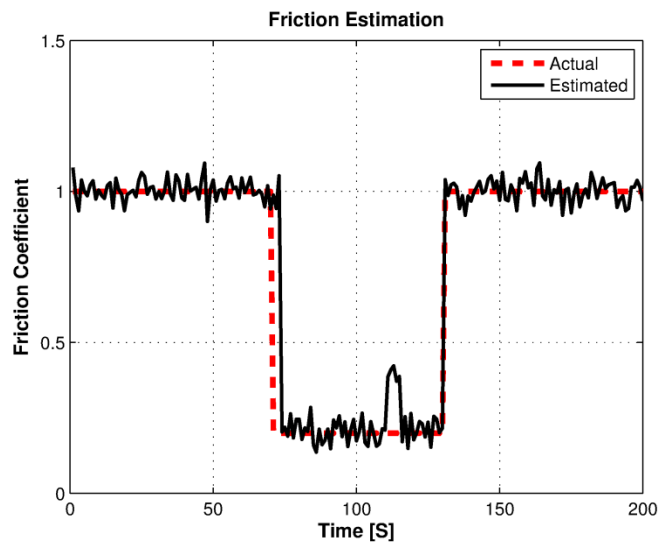


Fig. 5.31: Friction estimation results using the brush model based algorithm under high-slip

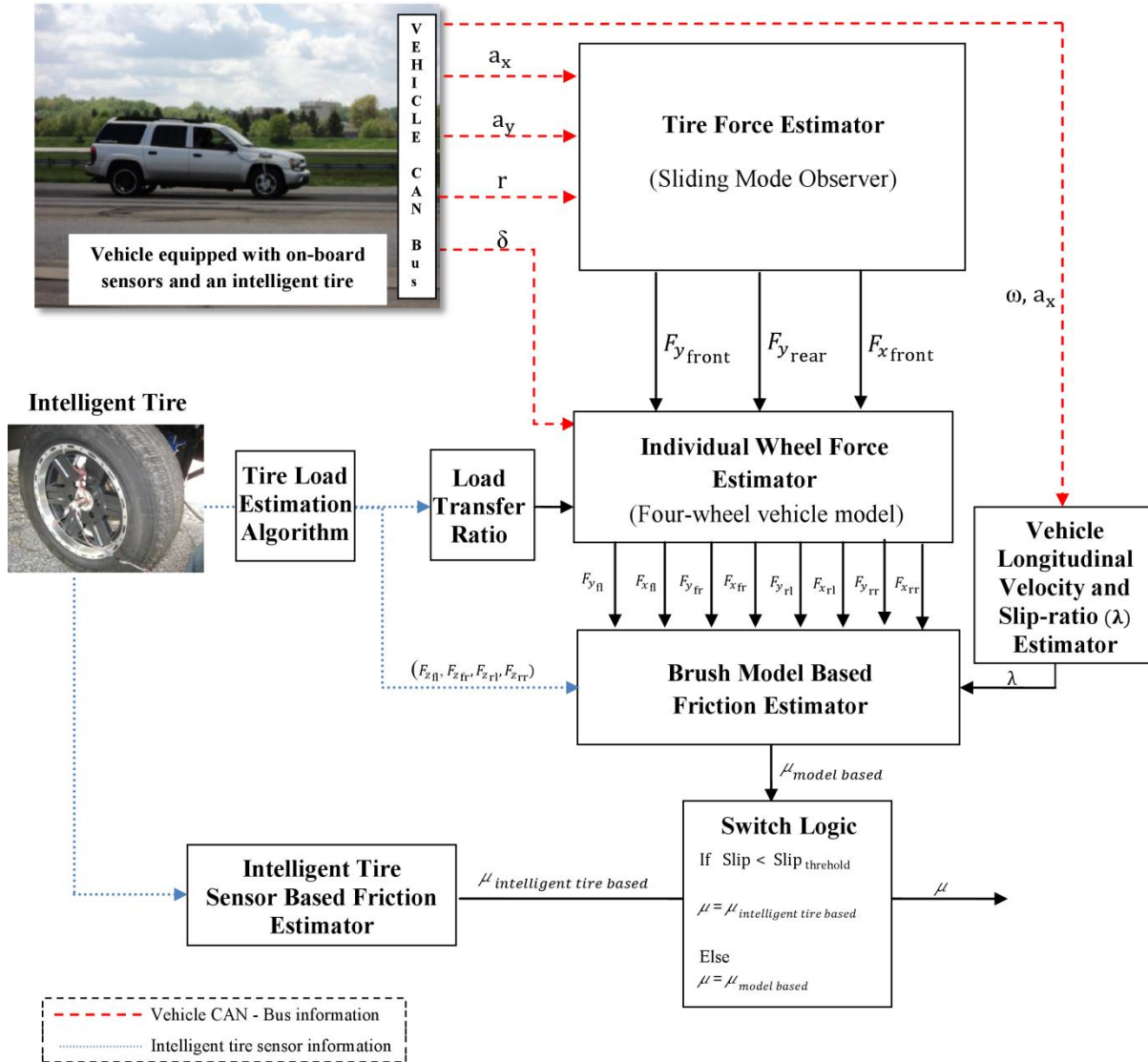


Fig. 5.32: Architecture of the proposed integrated approach using an intelligent tire based friction estimator and the model based estimator

Hence, an integrated approach using the intelligent tire based friction estimator (Fig. 5.32) and the model based estimator gives us the capability to reliably estimate friction for a wider range of excitations (both low-slip and high slip conditions).

5.3.2 Wheel Slip Controller

For wheel slip control, a nonlinear control strategy based on sliding mode is designed. Sliding mode control (SMC) technique is one of the general form of nonlinear control paradigms and an

effective and robust method of controlling nonlinear plants [21]. It is insensitive to parametric uncertainty and external disturbances [22]. As generally known, ABS is a nonlinear plant, so SMC provides an effective method to control it. There are three important steps to design a sliding mode controller [23], designing switching surface, guaranteeing the existence of the sliding mode and designing the controller. The following is the derivation of the sliding mode control law for wheel slip regulation. Equation (5.15) gives the slip dynamic equation for deceleration. Since the system is of first order, the switching surface is defined by equating sliding variable to zero.

$$s(t) = \left(\frac{d}{dt} + \lambda \right)^{(n-1)} \times (\lambda - \lambda_d) \quad (5.18)$$

Applying the SMC technique [24], the equivalent control algorithm providing the brake torque such that the slip ratio (λ) tracks the desired slip ratio (λ_d) can be found.

Equivalent Control Law: The dynamics along the sliding surface are given by:

$$s(t) = 0 \quad (5.19)$$

Therefore the equivalent control law is obtained when:

$$\begin{aligned} s(t) &= 0 \\ \Rightarrow \lambda(t) - \lambda_d(t) &= 0 \\ \Rightarrow \dot{\lambda}(t) &= 0 \end{aligned} \quad (5.20)$$

Equating Eq. (5.15) to zero then gives the equivalent control law $U_{eq}(t)$ as follows:

$$U_{eq} = \frac{(1 + \lambda)J\mu F_t}{mr_w} - \frac{(1 + \lambda)J\mu F_a}{mr_w} + \mu F_z r_w + F_f r_w \quad (5.21)$$

If the initial output trajectory is not on the sliding surface $s(t)$, or there is a deviation of the representative point from $s(t)$ due to parameter variations and disturbances, the controller must be designed such that it can drive the output trajectory to the sliding mode $s(t) = 0$. The output trajectory under the condition that will move toward and reach the sliding surface is said to be on the reaching phase. For this purpose, a Lyapunov function [21] can be chosen as:

$$V(t) = \frac{1}{2} s(t)^2 \quad (5.22)$$

with $V(0) = 0$ and $V(t) > 0$ for $s(t) \neq 0$. A sufficient condition to guarantee that the trajectory of the error will translate from reaching phase to sliding phase is to select the control strategy, also known as reaching condition as:

$$\begin{aligned} \dot{V}(t) (= s(t)\dot{s}(t)) &< 0 \\ s(t) &\neq 0 \end{aligned} \quad (5.23)$$

To satisfy the reaching condition, the equivalent condition $U_{eq}(t)$ given in Equation (5.20) is augmented by a switching control term $U_{sw}(t)$ to be determined.

Switching Control Law: The switching control law can be chosen as:

$$U_{sw}(t) = K_s \times \text{sgn}(s) \quad (5.24)$$

where K_s is a positive constant and $\text{sgn}()$ denotes signum function defined as:

$$\text{sgn}(s(t)) = \begin{cases} 1 & \text{if } s(t) > 0 \\ 0 & \text{if } s(t) = 0 \\ -1 & \text{if } s(t) < 0 \end{cases} \quad (5.25)$$

It is known that the discontinuous switching functions can be approximated by their continuous switching functions to avoid the chattering of the control force and to achieve the exponential stability [25-26]. Instead of signum function, a saturation function has been used via introducing a thin boundary layer around the sliding surface to avoid chattering. For a more smooth change of the switching signal, a hyperbolic tangent function has also been used to improve the switching control effort as:

$$U_{sw}(t) = K_s \tanh (s(t)/\Omega) \quad (5.26)$$

where Ω is a positive constant and it defines the thickness of the boundary layer that affects the steady-state accuracy and robustness. Thus, the control input of the sliding mode control for the ABS can be written as:

$$U(t) = U_{eq}(t) + U_{sw}(t) \quad (5.27)$$

$$U(t) = \frac{(1 + \lambda)J\mu F_t}{mr_w} - \frac{(1 + \lambda)J\mu F_a}{mr_w} + \mu F_z r_w + F_f r_w + K_s \tanh (s(t)/\Omega) \quad (5.28)$$

The block diagram representation of the sliding model control law is shown in Fig. 5.33.

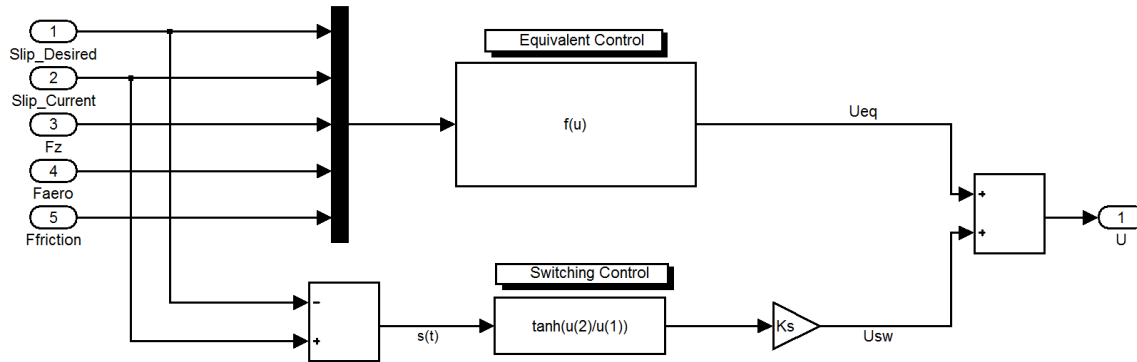


Fig. 5.33: Sliding mode control law($U(t) = U_{eq} (t) + U_{sw} (t)$) model

5.4 Simulation Results

To get a measure of the improvements in the performance of the proposed intelligent tire based ABS algorithm, it is compared to the standard ABS algorithm being employed in modern day vehicles.

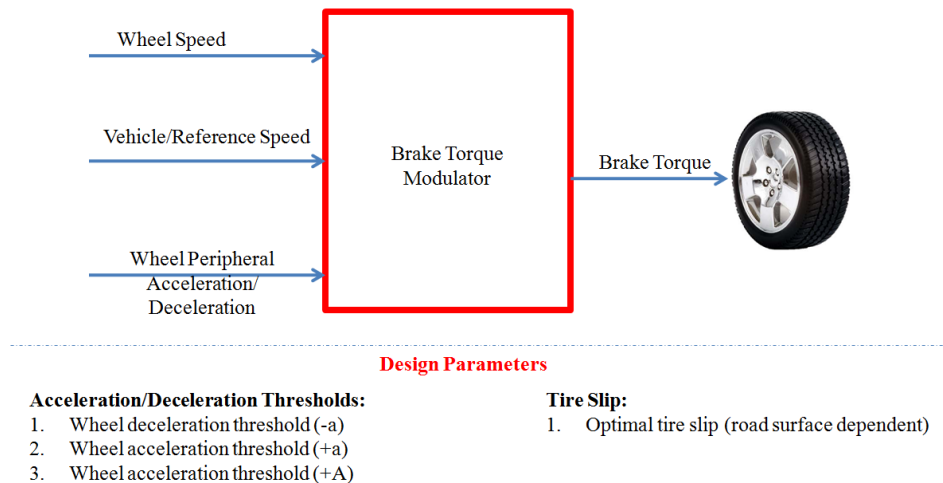


Fig. 5.34: Baseline ABS model - design parameters

Conventional ABS controllers utilize a rule-based method to maintain longitudinal wheel slip in a certain range on the information provided by angular wheel speed sensors. The operation sequence of a conventional rule based ABS system is depicted in [5] (Fig. 5.34 - Fig. 5.35).

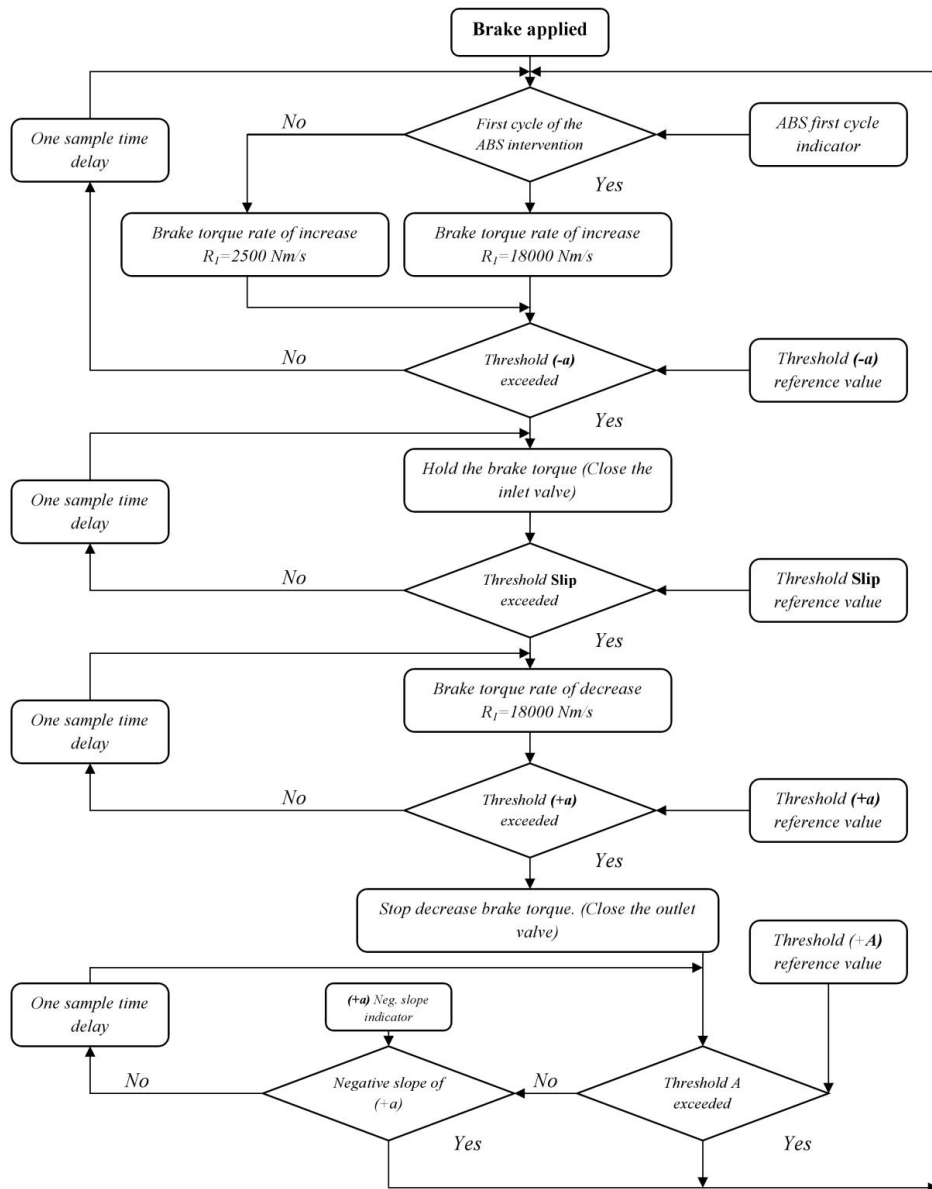


Fig. 5.35: Operation flowchart -baseline ABS algorithm

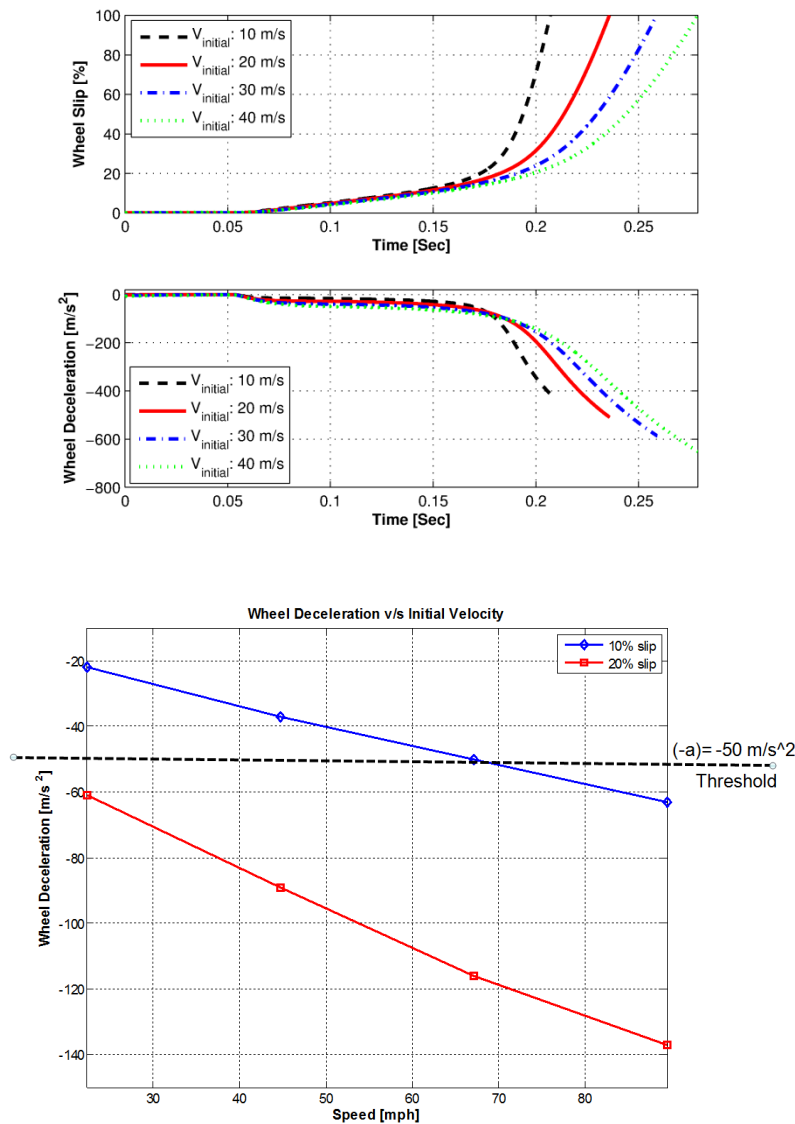


Fig. 5.36: Threshold value selection for the baseline ABS model - wheel-deceleration and slip curves for different initial braking velocities (top), and wheel-deceleration thresholds (bottom)

The following methodology was adopted to select the acceleration/deceleration thresholds:

1. **Wheel deceleration threshold (-a):** The relationship between the wheel-deceleration and slip curves for different initial braking velocities (10- 40 m/s) was studied (Fig. 5.36). Clearly, for high velocities, the deceleration threshold should be set at higher values. In contrast for low initial velocities the threshold should be decreased. A reasonable selection for this threshold could be the 10% slip value. Such a selection will

be able to provide 10% slip for high initial braking velocities and slip exceeding 10%, but still lower than 20% for lower velocities.

2. **Wheel acceleration threshold (+a):** This threshold is used to mark a positive tendency in the wheel acceleration. Appropriate threshold values are $3 - 6 m/s^2$.

3. **Wheel acceleration threshold (+A):** This threshold denotes a recovery from the predicted lock and is higher than (+a). Selection of too high values of (+A) threshold results in higher recovered wheel speed and lower slip values. Suitable threshold values are $9 - 12 m/s^2$.

The summary of the triggering signals and threshold values are given in Table 5.3.

Table 5.3: Triggering signals and threshold values

Command	Triggering Signal	Threshold Value
Hold	$-a$	$-50m/s^2$
Decrease	$> slip$	20% High- μ
		15% Low- μ
Stop Decrease	$+a$	$4m/s^2$
Increase	$+A$	$10m/s^2$

5.4.1 Baseline ABS Controller Model - Straight-Line Braking Simulation Results

The vehicle used for the basis of this simulation is a small size sport utility vehicle (SUV) (vehicle parameters used for the simulation are given in Table 5.4).

Table 5.4: Vehicle simulation parameters

Parameter	Units	Symbol	Value
Total vehicle mass	kg	m_{car}	1950
Tire mass	kg	m_t	40

Radius of wheel	m	r_w	0.3215
Moment of inertia	$kg.m^2$	J	1.8
Frontal area	m^2	A_f	2.25
C.G height	m	h_{cg}	0.59
Drag coefficient	-	C_d	0.3
Maximum value of brake torque	Nm	T_b	2500

The wheel & vehicle longitudinal speed and the control of the longitudinal slip ratio over time are known as the two key parameters in quantifying ABS performance. Each of these key parameters will be presented to show the system performance for both a high- μ surface, representative of dry asphalt and a low- μ surface, representative of an icy surface.

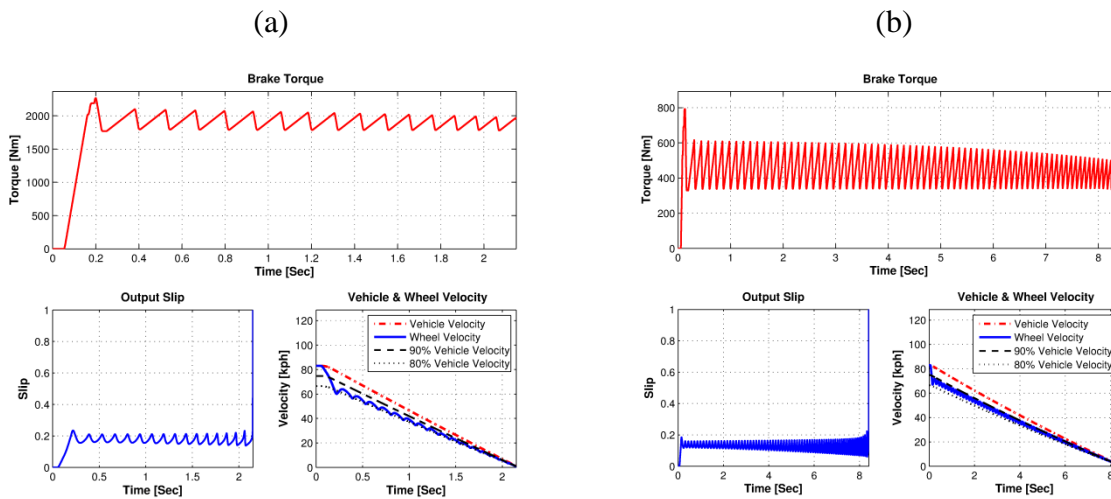


Fig. 5.37: Baseline ABS model performance: (a) high- μ condition, and (b) low- μ condition

Fig. 5.37a - Fig. 5.37b show the performance of the baseline ABS model on high- μ and low- μ surfaces, respectively. Given an initial velocity of 83kph, the results show that the vehicle requires 26.13m to come to a complete stop on the high- μ surface, whereas on the low- μ surface this distance is 94.56m.

5.4.2 Proposed Intelligent Tire Based ABS Control Model - Straight-Line Braking Simulation Results

Using the same vehicle parameters to repeat the simulations for the SMC based ABS model, the results in Fig. 5.38a - Fig. 5.38b are obtained. With the SMC-ABS algorithm employed, the distance required to stop becomes 25.92m on the high- μ surface and 93.97m on the low- μ surface.

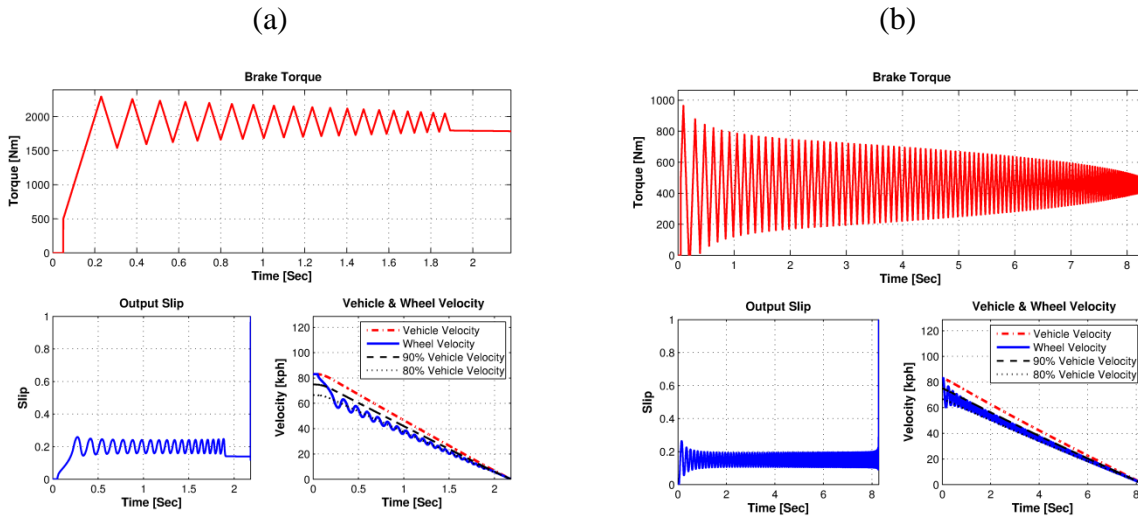


Fig. 5.38: SMC based ABS model performance: (a) high- μ condition, and (b) low- μ condition

Clearly, executing the described SMC based ABS control algorithm shows a good braking dynamic response. The longitudinal slip quickly reaches the calculated desired slip ratio after brake application and oscillates about this point for the remainder of the braking maneuver, until the ABS cut-off speed is reached. The slip ratio is maintained within a close proximity to the desired slip. The proportional gains for the switching control law were chosen so that the ABS operated at approximately 14 Hz and experienced a constant oscillation value around the desired longitudinal slip value. The SMC based ABS controller shows excellent control of the longitudinal slip ratio, resulting in a slip range that operates between 0.18 and 0.22 for the high- μ surface (Fig. 5.39b) and 0.12 and 0.17 for the low- μ surface (Fig. 5.39d).

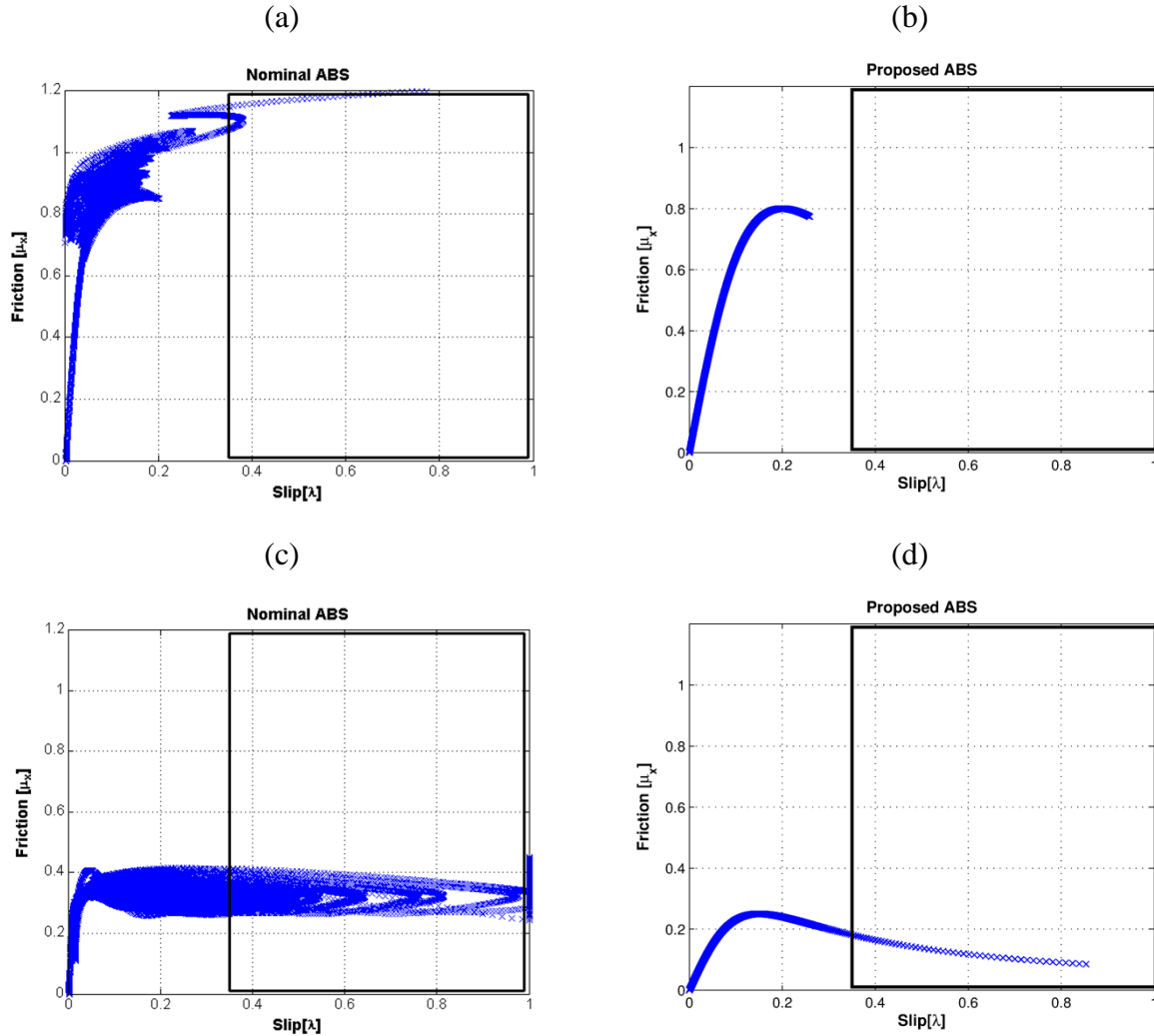


Fig. 5.39: Comparison of performance of the two ABS algorithms: (a)-(b) high- μ condition, and (c)-(d) low- μ condition

The result of staying within these close boundaries is an increase in the average longitudinal braking force available to the tire. For the baseline ABS simulation, there is a wider variation in the slip ratio range; a range about 3 times larger than for SMC based controller (Fig. 5.39a and Fig. 5.39c). This equates to a lower average longitudinal braking force and therefore longer braking distances. Hence the proposed control algorithm minimizes the time spent in the unstable zone of the μ - λ curve by exploiting the friction coefficient very close to its maximum.

5.4.3 Drawbacks of a Pure Sliding Mode Controller and Proposed Controller Modifications to Overcome These Drawbacks

In order for the sliding surface to be attractive, the reaching condition has to be met and this requires the use of discontinuous switching function, which causes chattering of the control signals. This chattering control signal involves high control activity which may excite neglected high-frequency dynamics in the system and also to cause possible damages to the actuators. However, eliminating the chattering also has other drawbacks in which in some application, the discontinuous switching input is necessary in order to maintain the characteristic of the systems. Many methods have been proposed such that a continuous control term is used to replace the discontinuous term such as the saturation function and boundary layer technique [26]. These methods are proven to be advantageous in eliminating, or at least minimizing chattering to certain acceptable degree, but at the expense of the robustness property of SMC. Besides, both of these methods require the use of thin boundary layer around the sliding surface in which magnitude of the boundary layer determines the control accuracy. The larger the boundary layer width, the smoother the control signal, however, it no longer drives the system to the origin, but to within the chosen boundary layer instead. These conflicting requirements to fulfill, which are the smoothness of the input signal and the control accuracy, have attracted our research to propose a method that can overcome the chattering effect while retaining the property of the SMC. A Fuzzy-SMC-PI methodology is proposed for an ABS application. Fuzzy SMC-PI is basically a combination of SMC and PI through fuzzy logic (Fig. 5.40).

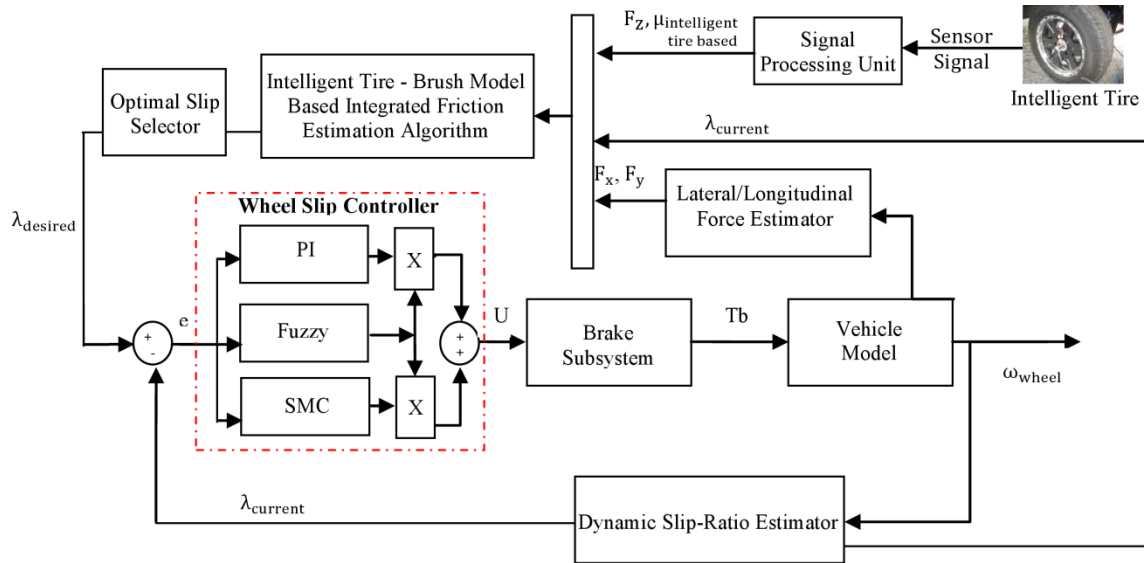


Fig. 5.40: Implementation of the proposed FSP ABS

The advantage of such a strategy is as follows: The SMC is responsive during transient state, but, it has an inherent chattering problem, as shown in Fig. 5.41. This chattering phenomenon continuously creates noise even under steady state. Thus zero steady state error is not attainable with control strategy using SMC methodology alone. On the other hand, with PI control strategy, zero steady state error is achievable but the PI control strategy is not all that ideal too. It has a significant overshoot problem and has a longer settling time and rise time. Comparatively, it is less responsive to SMC control strategy.

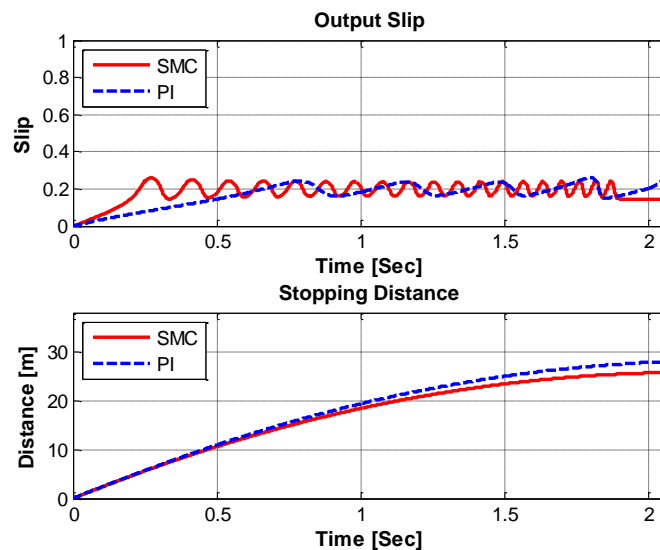


Fig. 5.41: ABS performance- PI v/s SMC

The combination of both control strategies through fuzzy logic provides a mean to create a hybrid control strategy that produce minimum overshoot, faster settling time and an almost chatter free system (Fig. 5.42).

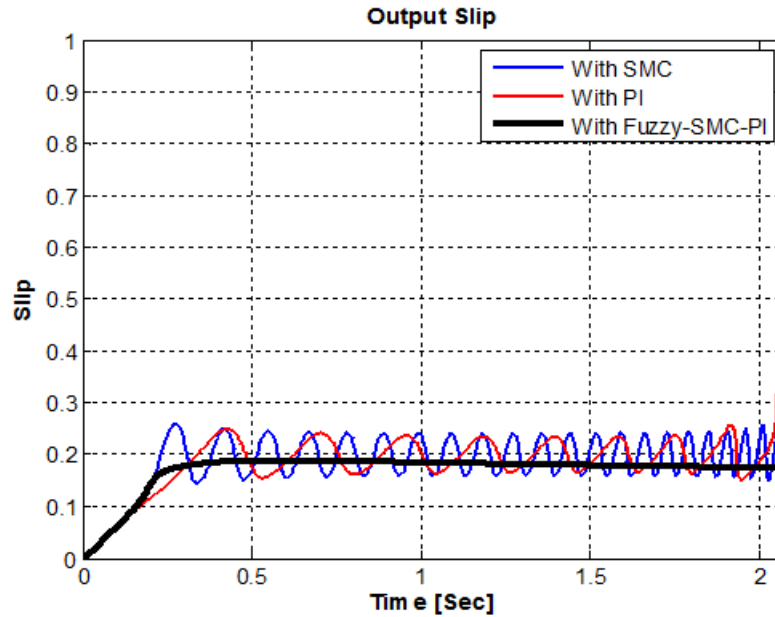


Fig. 5.42: Performance of Fuzzy-SMC-PI controller compared to SMC and PI controllers

The resulting hybrid system operates by sliding between SMC and PI mode depending on the condition imposed by external factors such as load. Fuzzy-SMC-PI strategy is developed by dividing the control region into three different regions, where e is the system's error. The first region involves pure SMC strategy. This region is responsible in bringing the system state to the targeted state as quickly as possible. This is followed by mixed strategy region which consists of SMC and PI strategies working in tandem through fuzzy logic to produce a single controller output. The objective of this region is to subdue any probable over-shoot prior to the steady state. The third and the final region is the pure PI strategy region. The output from this region serves to keep the steady error to a minimum or eliminates it totally. From the previous definition of the controller, it follows that the linguistic rules of the fuzzy logic supervisory controller should be defined as follows:

Rule 1: IF e is SMALL, Then $U = U_{pi}$

Rule 2: IF e is LARGE, Then $U = U_{SMC}$

where e is the error and the input of the fuzzy logic controller, SMALL and LARGE are defined to be its membership functions, as shown in Fig. 5.43.

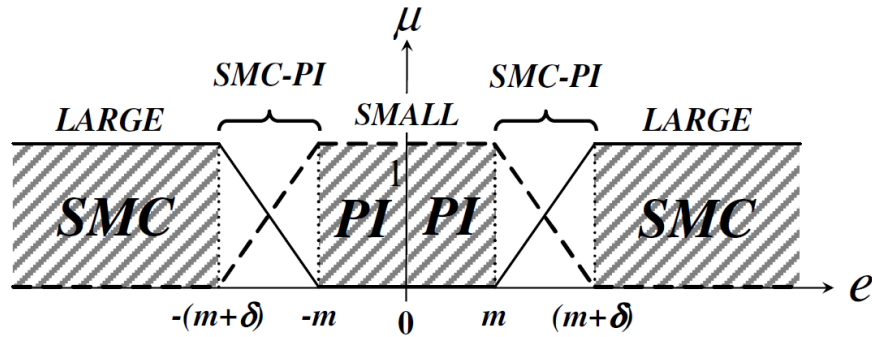


Fig. 5.43: Fuzzy logic membership functions

U_{pi} and U_{SMC} are the calculated control input commands of the PI and SMC controllers respectively. Note that the proposed sliding surface is designed to be the system's error, i.e. $s = e$. The controller implementation blocks are shown in Fig. 5.44 and Fig. 5.45.

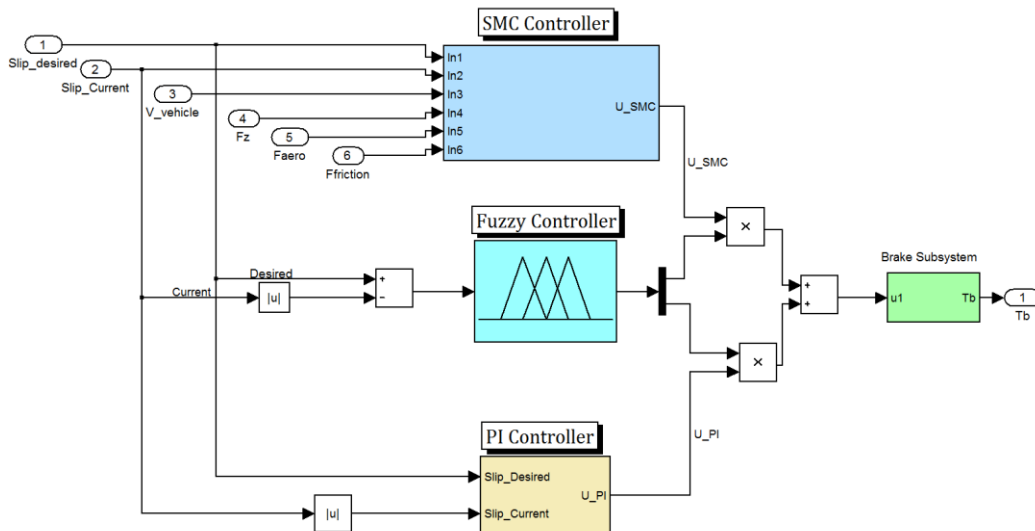


Fig. 5.44: Fuzzy-SMC-PI controller implementation block diagram

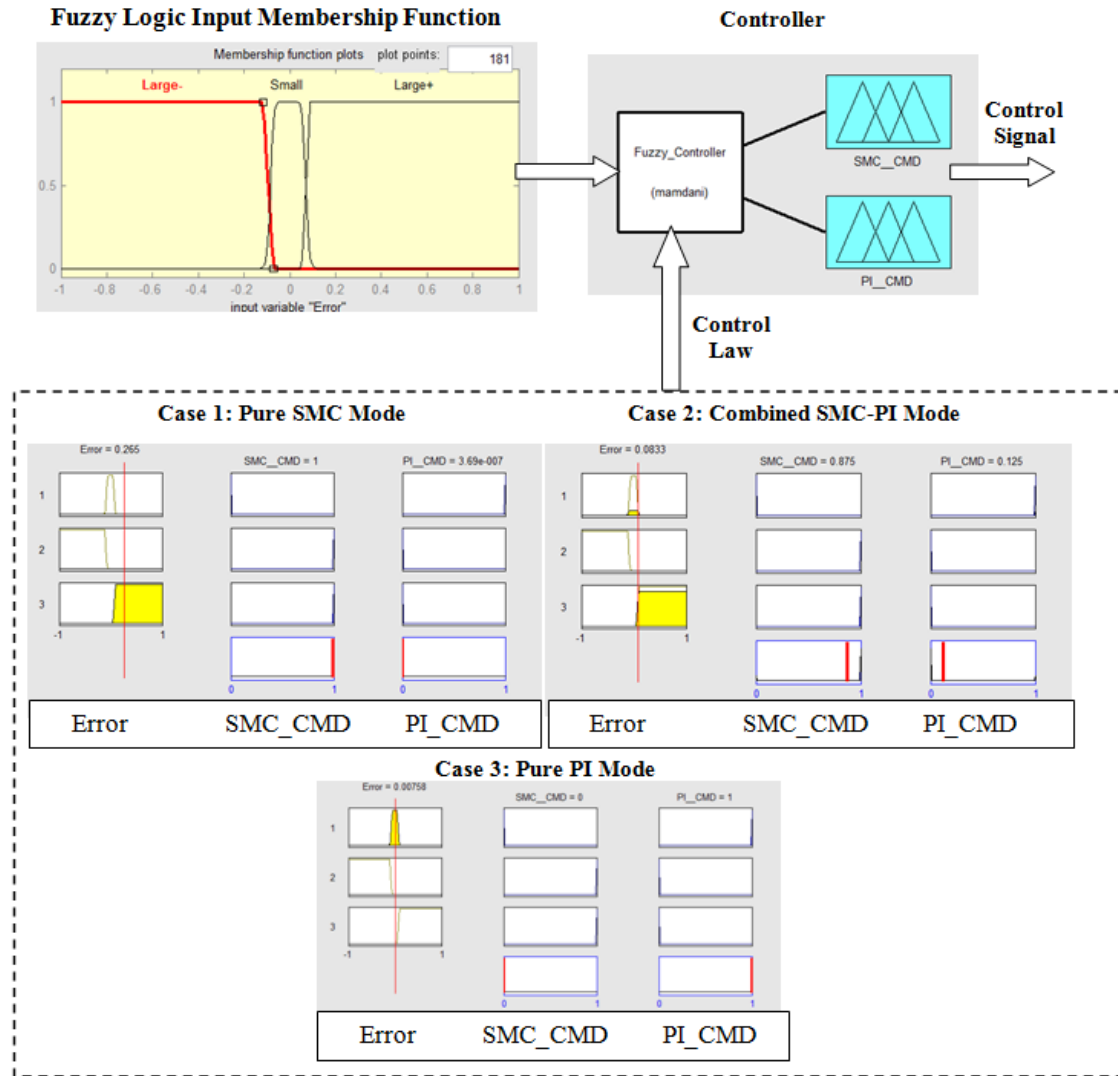


Fig. 5.45: Supervisory Fuzzy controller block diagram

Same simulations are repeated for the chatter-free FSP algorithm and similar comparisons are made with the baseline model. Results for the performance of the FSP controller for a straight line braking maneuver on dry and wet surface conditions are shown in Fig. 5.46a and Fig. 5.46b. Table 5.5 summarizes and compares the results for all of the above systems. The results of the proposed SMC based and FPS based ABS controllers reflect a robust performance, especially the results of the FSP based ABS controller indicate a promising future for the strategy considering its chatter-free characteristics.

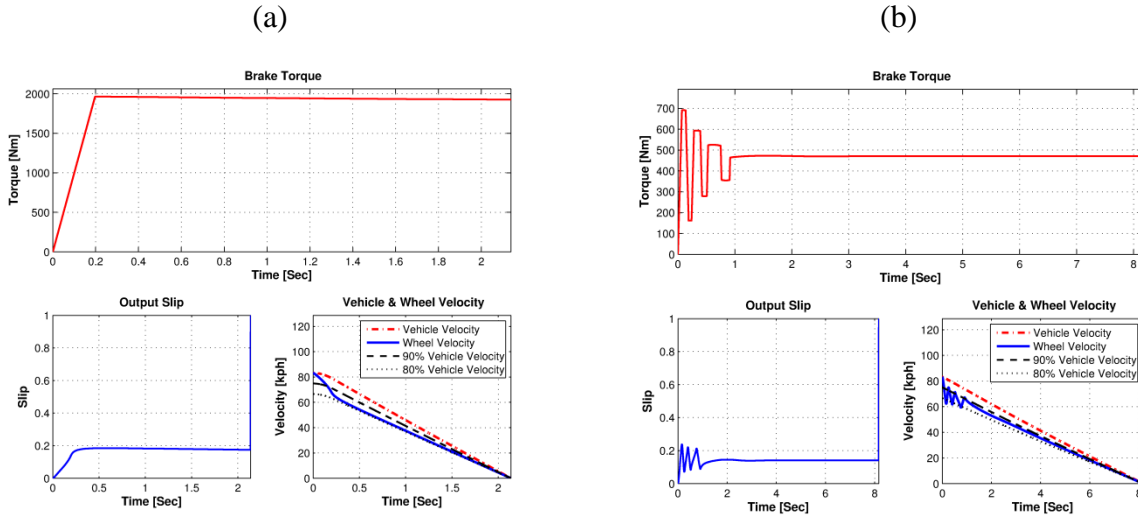


Fig. 5.46: FSP based ABS performance: (a) high- μ condition, and (b) low- μ condition.

Table 5.5: Straight line braking results comparison

	Dry surface [$\mu=0.8$]		Wet surface [$\mu=0.25$]	
	Stopping Distance [m]	Improvement over baseline system [%]	Stopping Distance [m]	Improvement over baseline system [%]
Baseline ABS	26.13	-	94.56 m	-
SMC based ABS	25.92	0.82	93.97 m	0.62
Fuzzy-SMC-PI based ABS	25.56	2.18	92.43 m	2.25

5.4.4 Jump - μ Simulation Results

A parametric analysis aimed at evaluating the benefits induced by introduction of friction information from the intelligent tire has been carried out. Furthermore a brake pressure preconditioning methodology is implemented to adapt the system on changing surface conditions. The performance of the ABS control system was evaluated through a series of

braking maneuvers on straight track focusing the attention on jump- μ conditions (Fig. 5.47). This maneuver can be extremely harsh for many rule-based ABS logics.

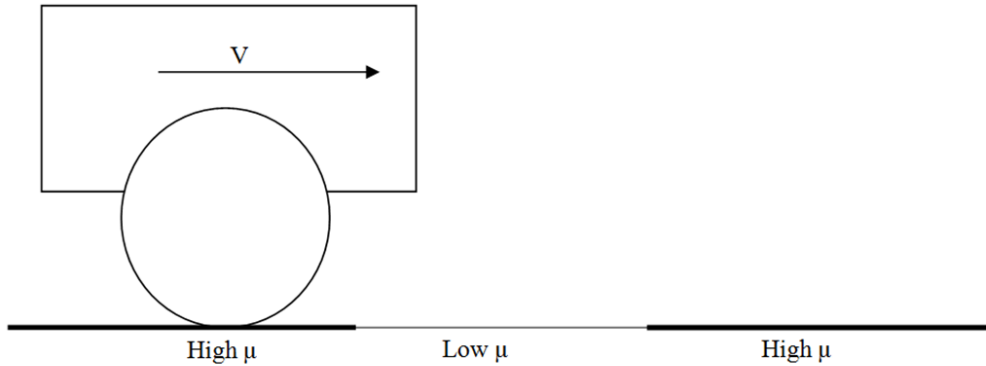


Fig. 5.47: Jump- μ test

Fig. 5.48 shows the overall flow of the intelligent tire implemented ABS algorithm.

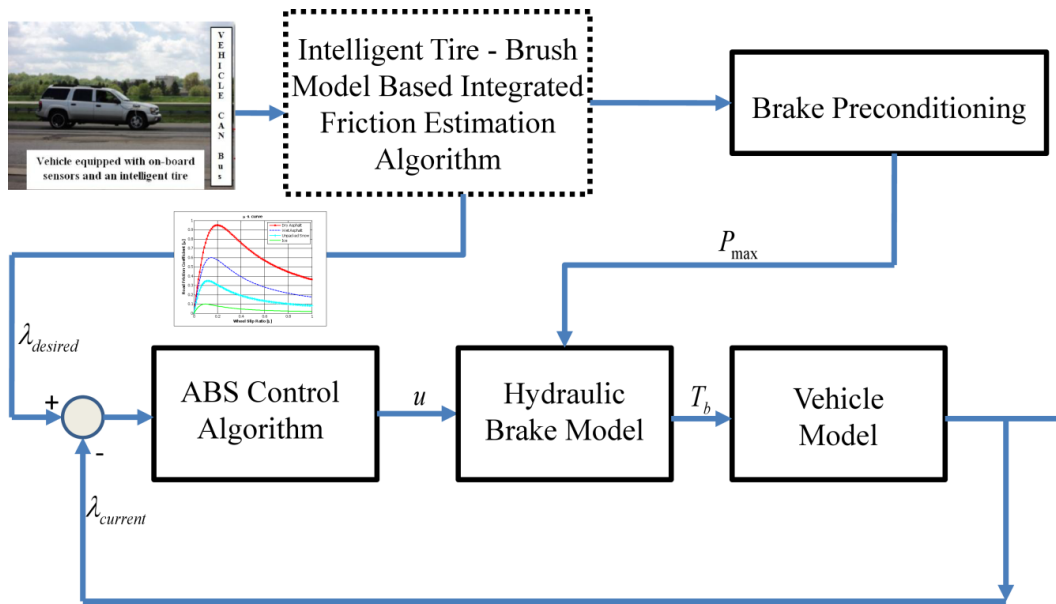
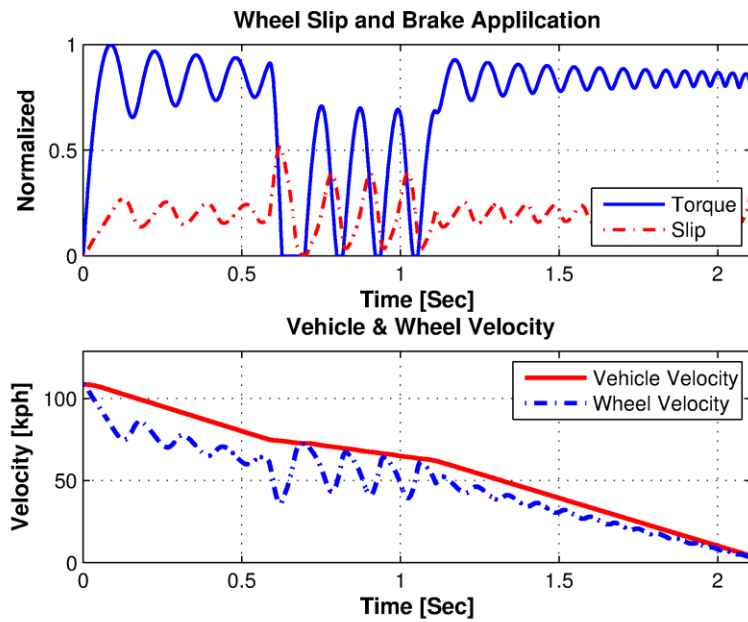


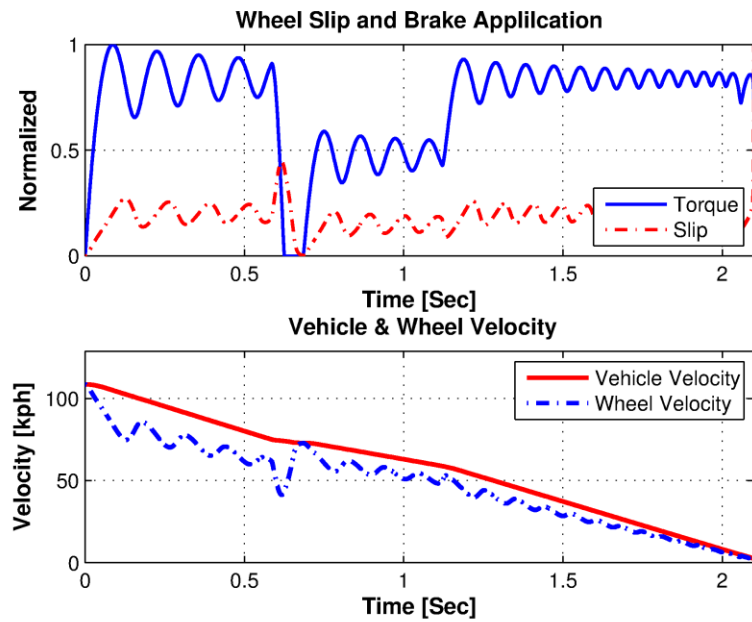
Fig. 5.48: Intelligent tire based ABS with road-condition estimator and brake preconditioning module

The results obtained for a vehicle while driving on a high- μ surface for the first 15m and then suddenly changing on a low- μ surface for 10m and finally going back to the initial high- μ surface are reported in Fig. 5.49a - Fig. 5.49c.

(a) No intelligent tire & no brake pre-conditioning



(b) With intelligent tire & no brake pre-conditioning



(c) With intelligent tire & brake pre-conditioning

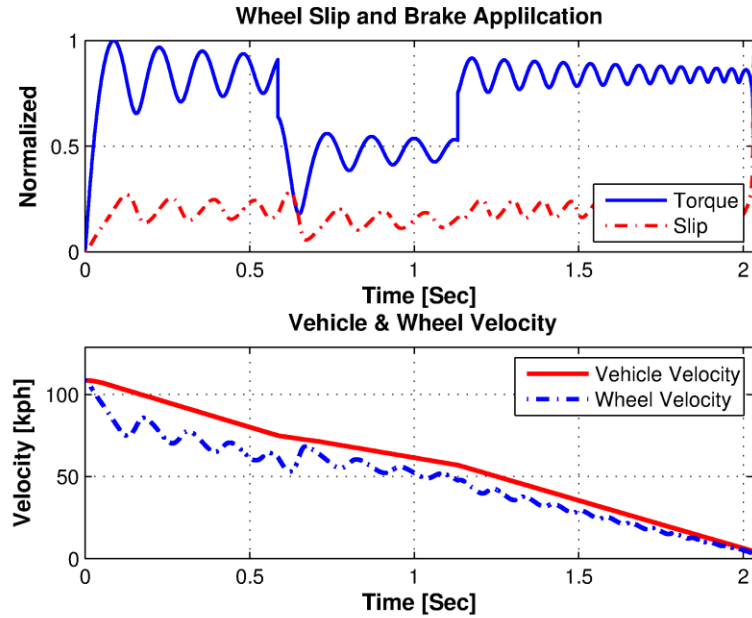


Fig. 5.49: Jump- μ test results

Table 5.6 summarizes the results for the above simulations.

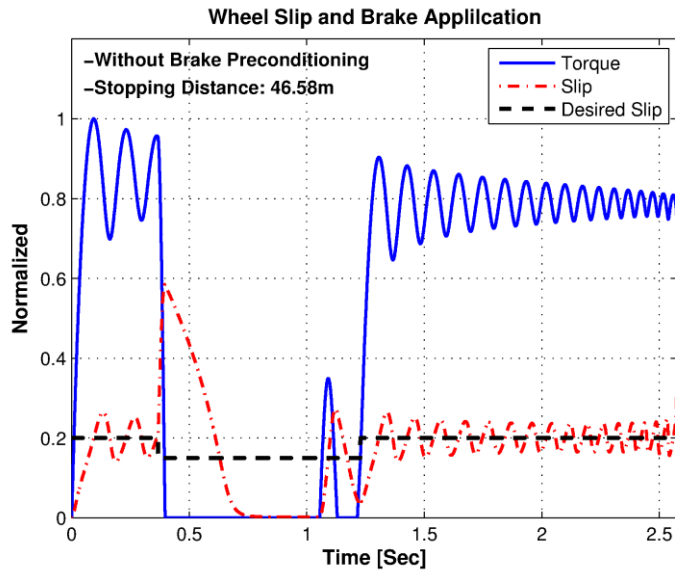
Table 5.6: Jump- μ tests- results comparison

ABS Methodology	Stopping distance [m]	Improvement over baseline system [%]
SMC Without An Intelligent Tire	34.33	-
SMC With An Intelligent Tire	33.49	2.44
SMC With An Intelligent Tire And Brake Preconditioning	32.91	4.13

It is clear from the proposed simulations that the effect of the jump- μ is significant, but the proposed algorithm handles quite well unexpected changes in the road surface conditions. Next,

the proposed system with an intelligent tire was tested under extreme friction conditions. The comparison between the time histories of tire slip (Fig. 5.50a and Fig. 5.50b) clearly shows how the instantaneous information about the change of friction coefficient allows the ABS controller to prevent the wheel lock-up during the jump from high friction to low friction.

(a) No intelligent tire & no brake pre-conditioning



(b) With intelligent tire & brake pre-conditioning

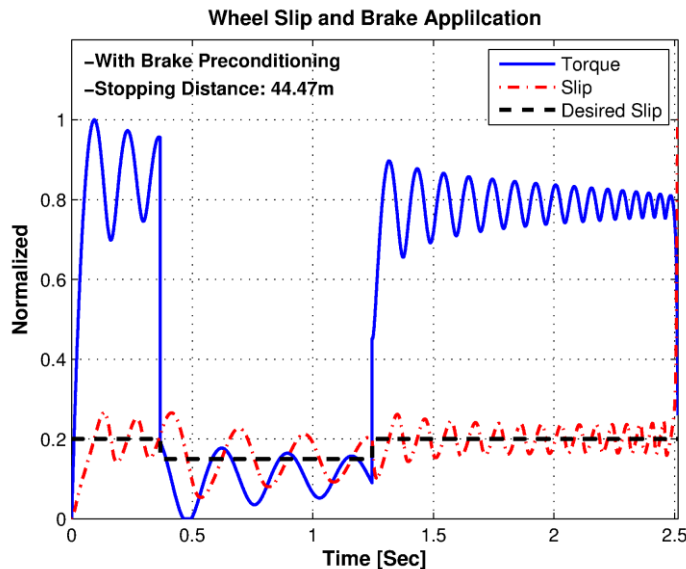
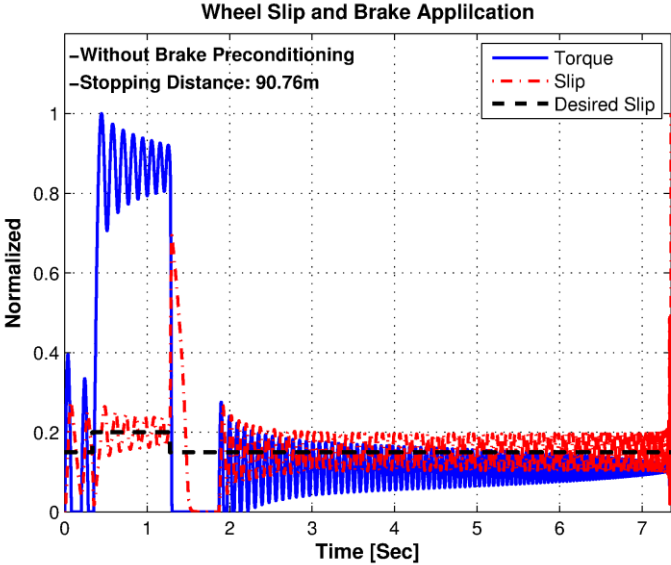


Fig. 5.50: Jump- μ results for extreme surface friction conditions (high=1-low=0.2-high=1)

A more significant improvement is visible in the low-high-low jump- μ case (Fig. 5.51a and Fig. 5.51b). This can be attributed to the fact that the pressure build-up phase that follows the jump from low friction to high friction starts in advance with respect to a standard ABS.

(a) No intelligent tire & no brake pre-conditioning



(b) With intelligent tire & brake pre-conditioning

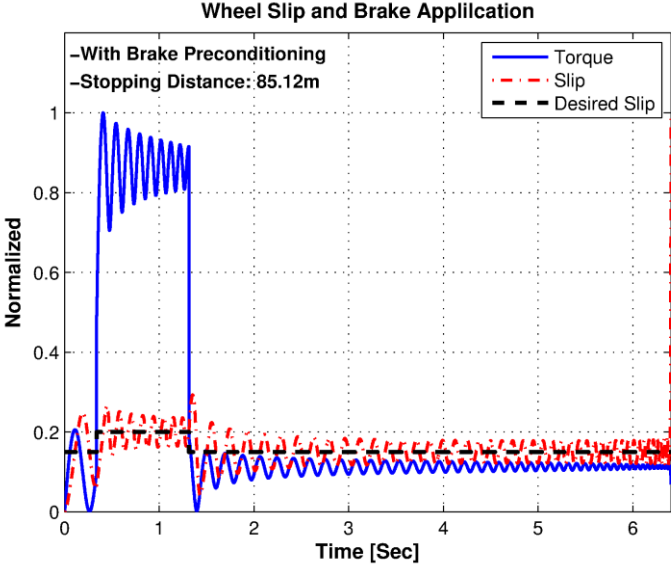


Fig. 5.51: Jump- μ results for extreme surface friction conditions (low=0.2-high=1-low=0.2)

It can therefore be concluded that the knowledge of tire-road friction conditions obtained using the intelligent tire leads to reductions in the stopping distance in case of jump- μ conditions.

5.5 Conclusion

This study presents a road surface condition/terrain classification system through an intelligent tire which is later employed in a FSP based ABS algorithm. Simulations are carried out on a series of braking maneuvers to examine the possible improvements in the ABS system performance, assuming that the additional information concerning road surface condition could be provided by an intelligent tire. The results reveal that the presence of an intelligent tire allows for a considerable decrease in the stopping distance. Most impressive improvements are obtained for the μ -jump tests where a reduction of 2.4% in stopping distance is possible. Furthermore, using the surface condition information from the intelligent tire makes it possible to apply a brake preconditioning algorithm. Implementing this preconditioning method into the FSP based ABS model, the percentage of the reduction in the stopping distance scales up to 4.1%. In the light of these results, we conclude that knowing the actual road surface condition can be quite favorable for enhancing the current ABS models.

Nomenclature

$+A$	<i>Wheel acceleration threshold (m/s^2)</i>
C_x	<i>Longitudinal stiffness of the tire (N/m)</i>
$F_{x_{front}}$	<i>Total longitudinal force on the front axle (N)</i>
$F_{y_{front}}$	<i>Total lateral force on the front axle (N)</i>
$F_{y_{rear}}$	<i>Total lateral force on the rear axle (N)</i>
$F_{x_{fl}}$	<i>Longitudinal force of the front-left wheel (N)</i>
$F_{x_{fr}}$	<i>Longitudinal force of the front-right wheel (N)</i>
$F_{x_{rl}}$	<i>Longitudinal force of the rear-left wheel (N)</i>
$F_{x_{rr}}$	<i>Longitudinal force of the rear-right wheel (N)</i>
$F_{z_{fl}}$	<i>Vertical force of the front-left wheel (N)</i>

$F_{z_{fr}}$	<i>Vertical force of the front-right wheel (N)</i>
$F_{z_{rl}}$	<i>Vertical force of the rear-left wheel (N)</i>
$F_{z_{rr}}$	<i>Vertical force of the rear-right wheel (N)</i>
F_t	<i>Tractive force (N)</i>
F_a	<i>Aerodynamic drag force (N)</i>
F_f	<i>Rolling resistance force (N)</i>
I_z	<i>Vehicle moment of inertia about yaw axis (kg.m²)</i>
J	<i>Moment of inertia (kg.m²)</i>
L	<i>Wheel base (m)</i>
R	<i>Vibration level ratio</i>
T_{net}	<i>Net torque (Nm)</i>
T_e	<i>Engine torque (Nm)</i>
T_b	<i>Brake torque (Nm)</i>
V	<i>Vehicle velocity (m/s)</i>
a_{hpl}	<i>Half of the contact patch length (m)</i>
$-a$	<i>Wheel deceleration threshold (m/s²)</i>
$+a$	<i>Wheel acceleration threshold (m/s²)</i>
a_x	<i>Vehicle longitudinal acceleration (m/s²)</i>
a_y	<i>Vehicle lateral acceleration (m/s²)</i>
g	<i>Gravitational acceleration (m/s²)</i>
h_c	<i>Center of gravity height (m)</i>
m_{car}	<i>Total vehicle mass (kg)</i>
m_t	<i>Tire mass (kg)</i>
m	<i>Total mass of quarter vehicle (kg)</i>
r_w	<i>Radius of the wheel (m)</i>
r	<i>Vehicle yaw rate (rad/sec)</i>

x_1	<i>State vector-Vehicle angular velocity (rad/sec)</i>
x_2	<i>State vector- Wheel angular velocity (rad/sec)</i>
δ	<i>Steering wheel angle (rad)</i>
λ	<i>Longitudinal slip ratio</i>
λ_d	<i>Reference/desired longitudinal slip ratio</i>
λ_p	<i>Peak longitudinal slip ratio</i>
$\lambda_{sliding}$	<i>Slip ratio at which the tire loses its longitudinal slip</i>
μ	<i>Surface friction coefficient</i>
μ_p	<i>Peak surface friction coefficient</i>

References

- [1] J.Y. Wong, *Theory of Ground Vehicles*, John Wiles and Sons, Inc., New York, NY, 2001.
- [2] H. Leiber and A. Czinczel, *Four Years of Experience with 4-Wheel Antiskid Brake Systems (ABS)*, in: SAE, 1983.
- [3] H. Leiber and A. Czinczel, *Antiskid System for Passenger Cars with a Digital Electronic Control Unit*, in: SAE, 1979.
- [4] R.B. Gmbh, *Automotive Handbook*, in, Troy, MI, 2000.
- [5] T.D. Day and S.G. Roberts, *A simulation model for vehicle braking systems fitted with ABS*, in: SAE 2002 World Congress & Exhibition, Detroit, MI, USA, 2002.
- [6] J.J. Taborek, *Mechanics of Vehicle*, Cleveland, OH, 1957.
- [7] H.S. Tan and M. Tomizuka, *An Adaptive Sliding Mode Vehicle Traction Controller Design*, Proceedings of the American Control Conference. 2 (1990), pp. 1856-1861.
- [8] T.D. Gillespie, *Fundamentals of Vehicle Dynamics*, Society of Automotive Engineers, Warrendale, PA, 1992.

- [9] Y. Kyongsu and C. Jintai, *Nonlinear brake control for vehicle CW/CA systems*, *Mechatronics*, IEEE/ASME Transactions on. 6 (2001), pp. 17-25.
- [10] *Dytran. Mini-triaxial accelerometers specification sheet*. Available online at: <http://www.dytran.com>.
- [11] IALR, 2010. *Institute researchers develop new way to test tires*. In the news, Institute for Advanced Learning and Research, Danville, VA. Available online at: <http://www.ialr.org>.
- [12] H. Ebrahimirad, M.J. Yazdanpanah and R.J. Kazemi, *The Use of Fast Fourier Transform for the Estimation of Power Spectra: A Method Based on Time-Averaging Over Short, Modified Periodograms*, *IEEE Transactions on Audio and Electroacoustics*. (1967), pp. 70 - 73.
- [13] G.J. Klir and B. Yuan, *Fuzzy Sets and Fuzzy Logic: Theory and Applications*, Prentice Hall, Upper Saddle River, NJ, 1995.
- [14] G.J. Klir, *On fuzzy-set interpretation of possibility theory*, *Fuzzy Sets Syst.* 108 (1999), pp. 263-273.
- [15] H.B. Pacejka, *Tyre and Vehicle Dynamics*, 2nd ed., Elsevier.
- [16] H.B. Pacejka and E. Bakker, *The Magic Formula Tyre Model*, *Vehicle System Dynamics*. 21 (1992), pp. 1 - 18.
- [17] G. Baffet, A. Charara and D. Lechner, *Estimation of vehicle sideslip, tire force and wheel cornering stiffness*, *Control Engineering Practice*. 17 (2009), pp. 1255-1264.
- [18] S.M. Savaresi and M. Tanelli, *Active braking control systems design for vehicles*, Springer-Verlag, London, UK, 2010.
- [19] R.O. Duda, P.E. Hart and D.G. Stork, *Pattern Classification*, 2nd ed., John Wiley & Sons Inc.
- [20] M.T. Hagan and M.B. Menhaj, *Training feedforward networks with the Marquardt algorithm*, *Neural Networks*, *IEEE Transactions on*. 5 (1994), pp. 989-993.

- [21] J.J. Slotine and W. Li, *Applied Nonlinear Control*, Prentice Hall, Upper Saddle River, NJ, 1991.
- [22] S.H. Zak, *Systems and Control*, Oxford University Press, 2002.
- [23] Y.S. Kueon and J.S. Bedi, *Fuzzy-neural sliding mode controller and its applications to the vehicle anti-lock braking systems*, Proc. IEEE/IAS Conf. Industrial Automation and Control: Emerging Technology. (1995), pp. 391-398.
- [24] C. Edwards and K.S. Spurgeon, *Sliding Mode Control: Theory and Applications*, Taylor and Francis, London, UK, 1998.
- [25] P. Kachroo and M. Tomizuka, *Chattering reduction and error convergence in the sliding-mode control of a class of nonlinear systems*, Automatic Control, IEEE Transactions on. 41 (1996), pp. 1063-1068.
- [26] H. Ebrahimirad, M.J. Yazdanpanah and R. Kazemi, *Sliding mode four wheel slip-ratio control of anti-lock braking systems*, in: IEEE International Conference on Industrial Technology, 2004, pp. 1602-1606.

Chapter 6

Piezoelectric Vibration Energy Harvesting System with an Adaptive Frequency Tuning Mechanism for Intelligent Tires

Executive Summary

The environment inside an automobile tire is typically harsh, with temperature extremes ranging from -25°C to 140°C. Often, these temperature extremes preclude the use of batteries for sensor nodes embedded inside an intelligent tire. The high vibration levels inside a tire have the potential to generate electrical power using vibration based energy harvesting techniques. In this study, the feasibility of using an inertial vibrating energy harvester unit to power a sensor module inside the tire is assessed. The harvester unit is adapted to the tire vibration spectra and the superimposed acceleration signal. First prototypes demonstrate power generation capabilities sufficient enough to transmit tire sensor data multiple times per minute. To optimize the harvester performance with changing dominant tire vibration frequencies, a novel artificial neural network (ANN) based closed loop system capable of ensuring broad band operations has been proposed. By presenting a battery-less power supply unit, the proposed system addresses one of the key challenges in the realization of the intelligent tire concept. These harvesters designed for the harsh tire environment provide a distinct advantage in cost and flexibility of installation, while extending the lifetime of the power supply for sensor data acquisition and communication. Results indicate the viability of the procedure outlined in this study.

Keywords: *Broadband vibration energy harvesting, intelligent tire, frequency tuning, artificial neural network (ANN)*

6.1 Introduction

While current vehicle safety systems are unquestionably lifesaving technologies, they unfortunately are limited by the lack of knowledge about the tire - vehicle states and operating conditions. Classical observer based indirect measurement techniques exhibit unsatisfactory results during severe maneuvering conditions. Although the forces maneuvering a vehicle are

generated inside the tire contact patch, the modern day state-of-the-art control systems have no feedback directly from the tires. Tires really are placed in a very privileged position, and it is easy to imagine the possible improvements in vehicle handling and comfort characteristics that could be achieved by having a thorough understanding of the tire-road interaction forces, and other parameters at the contact patch. Knowledge about these additional tire-vehicle states can significantly reduce the risk of accidents, through effective design and implementation of advanced chassis control systems [1-2]. However, at present, the commercially available tire monitoring systems are not equipped to sense and transmit high speed dynamic variables used for real-time active safety control systems. To address this problem, researchers have been developing certain sensor based advanced tire concepts [3-4]. The new terms "Intelligent Tires" and "Smart Tires", which mean online tire monitoring, are thus enjoying increasing popularity among automotive manufacturers [5]. The Intelligent tire concept as envisioned by the tire researchers would have the capability to monitor in real time, the forces at tire-road interface, contact patch length, friction coefficient, slip angle, road condition and tire wear (Fig. 6.1).

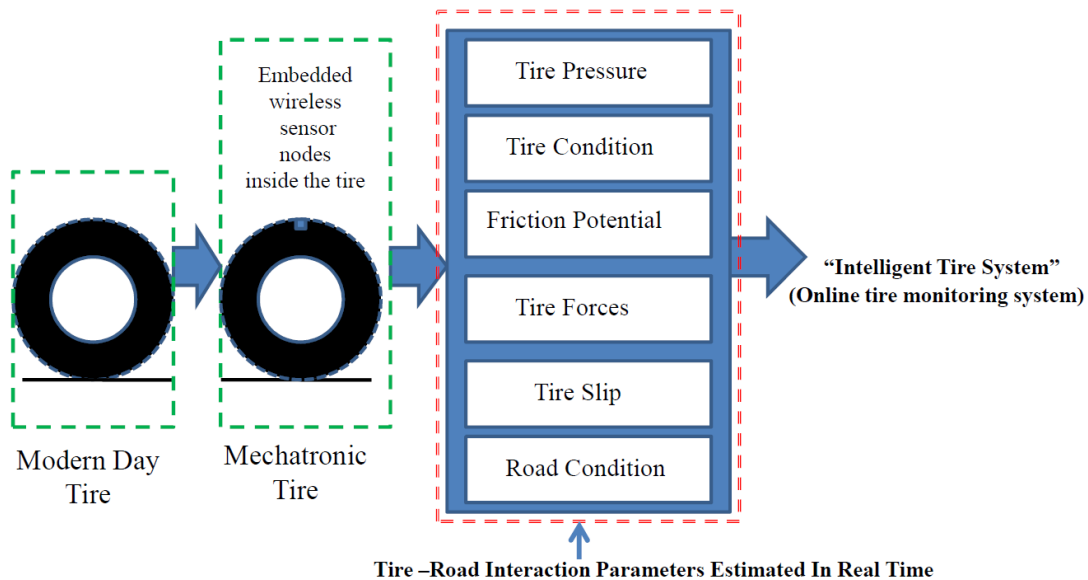


Fig. 6.1: Intelligent tire system for online tire monitoring

This is expected to improve safety and reliability of tires and also improve the performance of vehicle control systems that are rapidly becoming common equipment on all vehicles. However, for the installation of sensors in a tire, many problems have to be considered, such as compatibility of the sensors with tire rubber i.e. stiffness issues, harsh internal environmental

conditions, wireless transmission of gathered data, economic issues relating to the use of expensive sensors in a comparatively inexpensive product and above all meeting the power requirements of all the electronic components.

One of the major issues in using battery powered wireless sensor nodes inside tires arises when the battery is drained of all its power. In such a scenario, the sensor has to be retrieved and the battery has to be replaced. Due to the remote placement of these devices within the tire carcass, battery replacement is not feasible. So even though a battery has the advantage of a fixed, stable voltage supply, its disadvantages are its limited total energy availability, its temperature dependency and its relatively short life span. To address this problem, over the past few years a number of novel energy harvesting systems have been proposed which have the capability to capture energy that otherwise would be lost. In the case of tires, harvesting the wheel's vibration energy to power the sensing and wireless communication devices is an attractive proposition [6]. The high vibration levels inside a tire have the potential to generate electrical power using vibration based energy harvesting techniques. However, in the case of tires, vibration based power harvesting techniques can be very demanding because of the dynamically varying vibration spectra of a tire. A vibration spectrum with varying frequency may severely limit the power harvested by a single-degree-of-freedom resonance-based device, and hence a frequency agile or broadband device is required to maximize the energy harvested. In this study, the feasibility of using an inertial vibrating energy harvester unit to power a sensor module for tire use is assessed. To ensure broadband operation of the harvester, a novel artificial neural network (ANN) based closed loop system optimized for different tire operating conditions has been proposed. The proposed closed loop system would enable the harvester to be under resonance conditions over a suitable frequency range and thus generate power at a broad spectrum of vibrations.

This chapter is organized as follows: The principle of operation of the energy harvesting device is presented in Section 6.2. The design procedure adopted to develop a tire specific harvester unit is presented in Section 6.3. Harvester fabrication details and experimental performance results are presented in Section 6.4. The main performance shortcomings of the fabricated harvester unit along with details about the proposed power processing techniques to

overcome these shortcomings are presented in Section 6.5, before concluding this study in Section 6.6.

6.2 Principle of Operation

While the tire rotates around its axis, the external surface of the tire is subjected to high deformations around the point of contact of the tire and road surface. These deformations lead to accelerations in three different directions, which are circumferential, lateral and radial (Fig. 6.2).

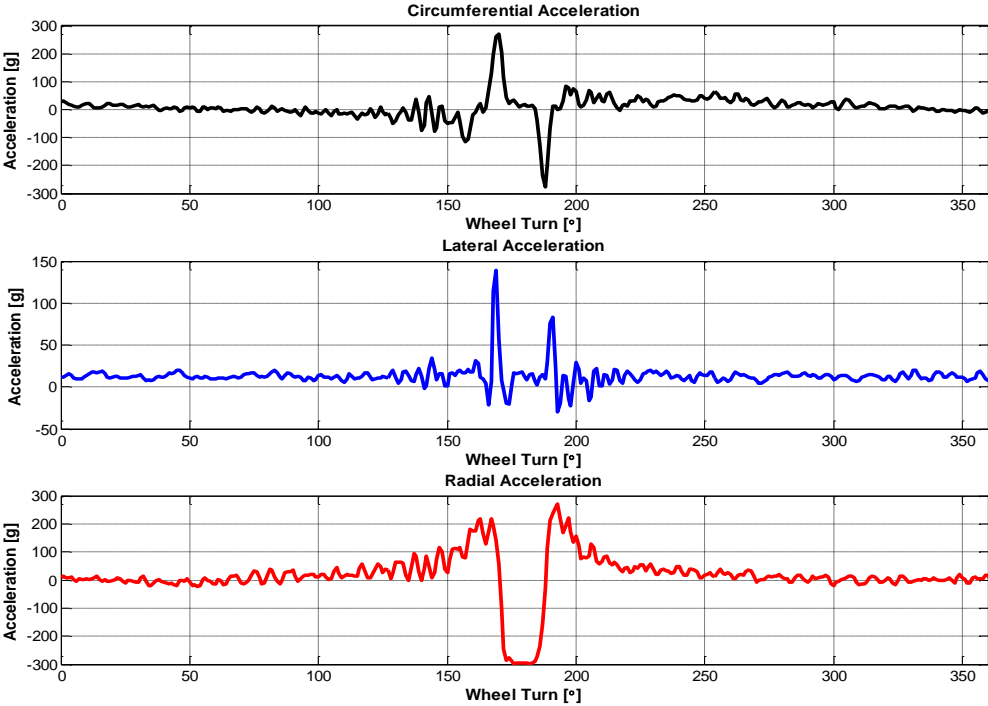


Fig. 6.2: Tire vibration waveform arranged in time series: (top) circumferential, (middle) lateral, and (bottom) radial signals

Although accelerations in lateral and longitudinal directions are possible alternatives, those in radial direction contain most energy and were therefore preferred in this study. When that point on the tire comes into contact with the ground, the radial acceleration goes to zero for the short time that the point is translating (pure linear motion) along the surface of the ground. This happens after an initial increase in the acceleration levels due to deformation to which the tire is subjected during passage from a circumferential to a flat configuration, at the beginning of the

contact region between the tire and the ground. It is during the flat region (contact patch, footprint), where a vibrating device (harvester) would oscillate freely around its equilibrium position. A further increase in the acceleration levels are encountered when the tire exits from the contact region. As soon as the passage in the contact patch terminates, the centrifugal acceleration causes a forced stopping of the oscillations.

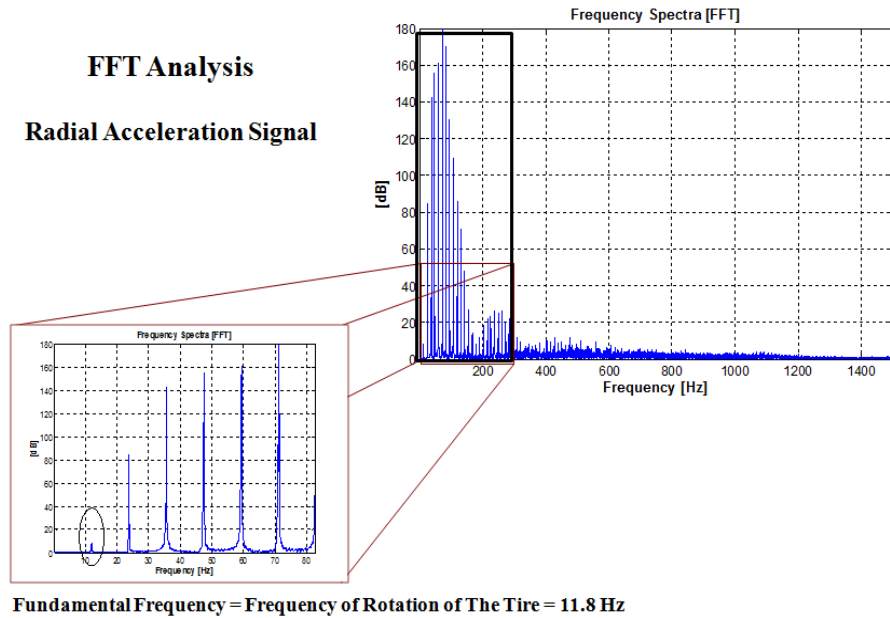


Fig. 6.3: Radial acceleration signal in frequency domain

The Fourier spectra of the radial acceleration signal are characterized by high amplitudes around the first multiples of the fundamental frequency (Fig. 6.3). The dominant excitation frequency for a tire, as it travel over the road generally lies reasonably close to the fundamental frequency of the tire or one of its higher natural frequencies. Since resonant mechanical vibration energy harvesting is the scheme under investigation here, the resonant frequency of the harvester unit can be matched to this dominant frequency of excitation of the tire to maximize the power output. Taking advantage of the piezoelectric material's ability to produce voltage in response to a deformation of the material, electrical power is generated by converting the mechanical strain due to tire flexure during rolling, to electric charge that is made available to an electronic device disposed within the tire.

6.3 Energy Harvester Design

6.3.1 Target Energy Levels

An intelligent tire system generally requires a distributed system comprising of a remote sensing module and a receiver module. Shown below (Fig. 6.4) is the schematic of a typical wireless transmission system one can expect to see in the next generation intelligent tires. Depending on the amount of information that must be acquired and transmitted for each tire revolution, the level of power consumption would vary as a function of the tire translational speed.

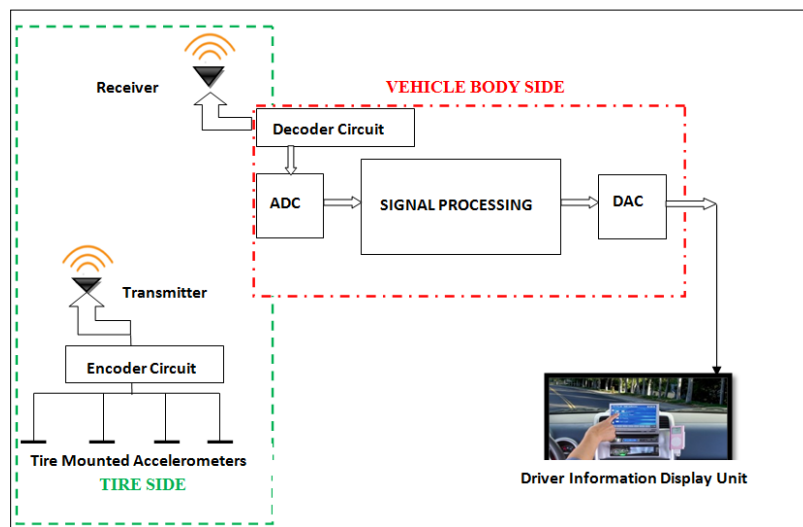


Fig. 6.4: Typical wireless data transmission system for intelligent tires

For a battery-less tire mounted system, one would need to cater to the power supply needs of all the equipment mounted on the tire side. For a typical passenger car tire, the minimum energy per revolution for different translational speeds of the tire has been estimated. The time required for one rotation based on the tire speed is given by:

$$\text{Time for one rotation} = \frac{\text{Tire circumference}}{\text{Translational Speed}} \quad (6.1)$$

The number of samples to be processed per rotation is given by the relationship:

$$\text{Number of samples per revolution} = \text{Time for one rotation} * \text{sampling rate} \quad (6.2)$$

Then by [7], the minimum energy requirements for an intelligent tire equipped with accelerometers, with a data transfer rate of 15 bytes per revolution for different tire translational speeds is summarized below (Table 6.1):

Table 6.1: Minimum energy required per tire revolution for different tire translational speeds

Tire Speed	Time for one revolution (sec)	Number of data samples acquired per revolution (samp_freq=10kHz)	Minimum energy required per tire revolution ($\mu\text{J}/\text{rev}$)
10 mph	0.529	5290	8.374 $\mu\text{J}/\text{rev}$
30 mph	0.176	1760	6.256 $\mu\text{J}/\text{rev}$
45 mph	0.117	1170	5.902 $\mu\text{J}/\text{rev}$
65 mph	0.0813	813	5.680 $\mu\text{J}/\text{rev}$

To get a more realistic picture about the energy consumptions levels, the average energy demand on a per mile basis was estimated using the federal drive cycles [8], which represent actual driving conditions. Two standard drive cycles - the ‘Urban Dynamometer Driving Schedule’ (UDDS), which represents city driving conditions (Fig. 6.5a) and the ‘Highway Fuel Economy Driving Schedule’ (HWFET), which represents highway driving conditions (Fig. 6.6a), were used for this analysis.

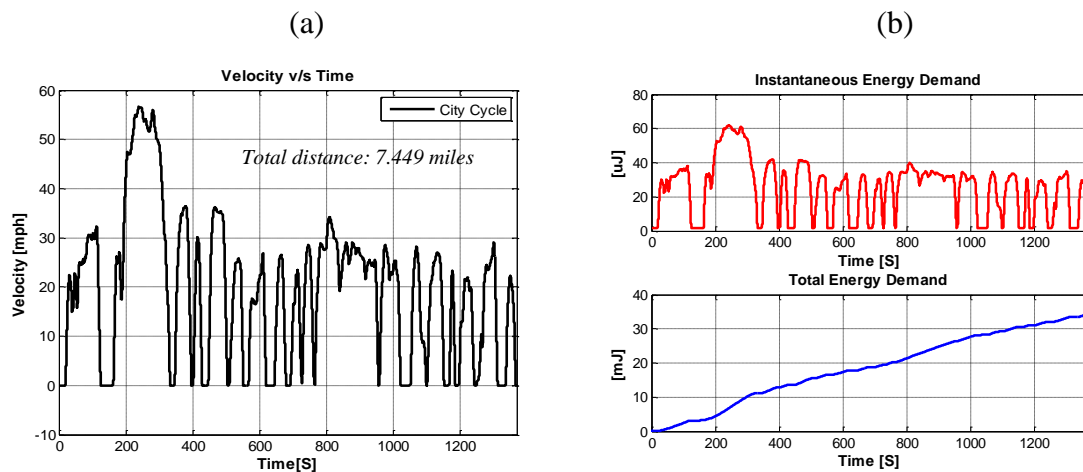


Fig. 6.5: (a) Velocity profile for the city driving schedule, and (b) energy demand analysis for the city cycle

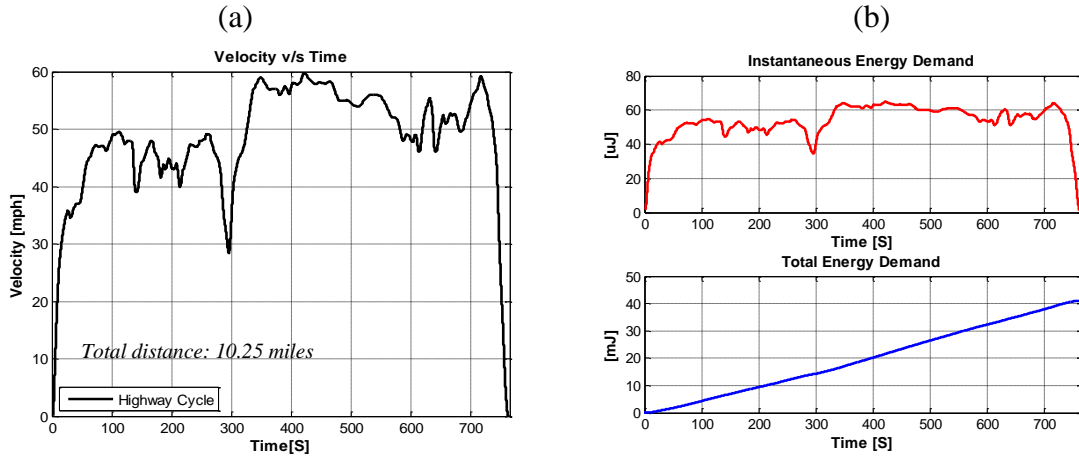


Fig. 6.6: (a) Velocity profile for the hwy driving schedule, and (b) energy demand analysis for the hwy cycle

The average energy demand for the city driving conditions was estimated to be 4.27mJ/mile (Fig. 6.5b). For the highway driving schedule, the average energy demand was estimated to be 3.99mJ/mile (Fig. 6.6b).

The first intelligent tires are expected to arrive in the next 2-3 years and are likely to use batteries [9]. For a battery based system, the current consumption is the most critical issue. The amount of current consumed by a wireless sensor module determines the size, weight, cost, and life time of the of the power source. The percentage of current consumed by different processes of a battery-based TPMS module is illustrated below (Table 6.2):

Table 6.2: Distribution of the power consumption for a TPMS [10]

S. No	Operation	Percentage Consumption
1	Power down current	57%
2	Motion detection	13%
3	Pressure measurement	3%
4	CPU execution	11%
5	RF transmission	10%
6	LF Sampling	6%

A battery based TPMS module in the power down mode consumes more than 50% of the total current [10]. The large amount of current consumed is mainly due to the leakage currents within

the module. Based on the above analysis, for a battery powered intelligent tire system, the ideal battery capacity for it to last the life of a vehicle (10yr / 150000 miles) can be estimated as follows:

$$\text{Battery Capacity} = \frac{((\text{Average energy demand per mile}) * (\text{Total number of miles driven}))}{((\text{Battery loss factor}) * (\text{Battery Depth of discharge}))} \quad (6.3)$$

$$\approx 2700 \text{ J or } 0.75 \text{ Wh}$$

The majority of the commercially available direct TPMS units are using lithium- based primary batteries (type 2450) [11]. Theoretically speaking, in the case of intelligent tires, lithium-based coin cells of the type 2450 (24 mm diameter and 5 mm height), having a battery capacity of about 450-600 mAh can be utilized to fulfill the total energy requirements. In practice, they really don't present a viable option for a high power load like the wireless transmission system of an intelligent tire. The key limiting factor is the maximum discharge current/power capability of a battery. This fact can be better understood by analyzing the effect of state of charge (SOC) on the power limits of a battery, using a mathematical model for a lithium ion cell (Fig. 6.7). Specifications of the battery used for our analysis are shown below (Table 6.3):

Table 6.3: Battery specifications used for power analysis [12]

<p>Model ER2450 (lithium-thionyl chloride batteries)</p> <p>*Current Application: Being used as a power source for most wireless TPM systems</p>	<p>Max Dimension : 24mm * 5mm</p> <p>Nominal Capacity: 500mAh</p> <p>Nominal Voltage: 3.6V</p> <p>Weight:10g</p> <p>Operating temperature range:- 55°C to +85°C</p>
--	---

The equations used to estimate maximum power limits are as follows:

$$\text{Terminal Voltage : } V_T = V_{oc} - I * R_{int} \quad (6.4)$$

$$\text{Maximum Discharge Power : } (V_{oc} - V_{min}) * V_{min} * \text{Modules} / R_{dis} \quad (6.5)$$

$$\text{Maximum Charging Power} : (V_{oc} - V_{min}) * V_{max} * \text{Modules} / R_{chg} \quad (6.6)$$

Notation used: V_{oc} : Open circuit voltage V_{min} : Minimum voltage
 V_{max} : Maximum voltage Modules : Total number of modules
 R_{dis} : Discharge resistance R_{chg} : Recharging resistance

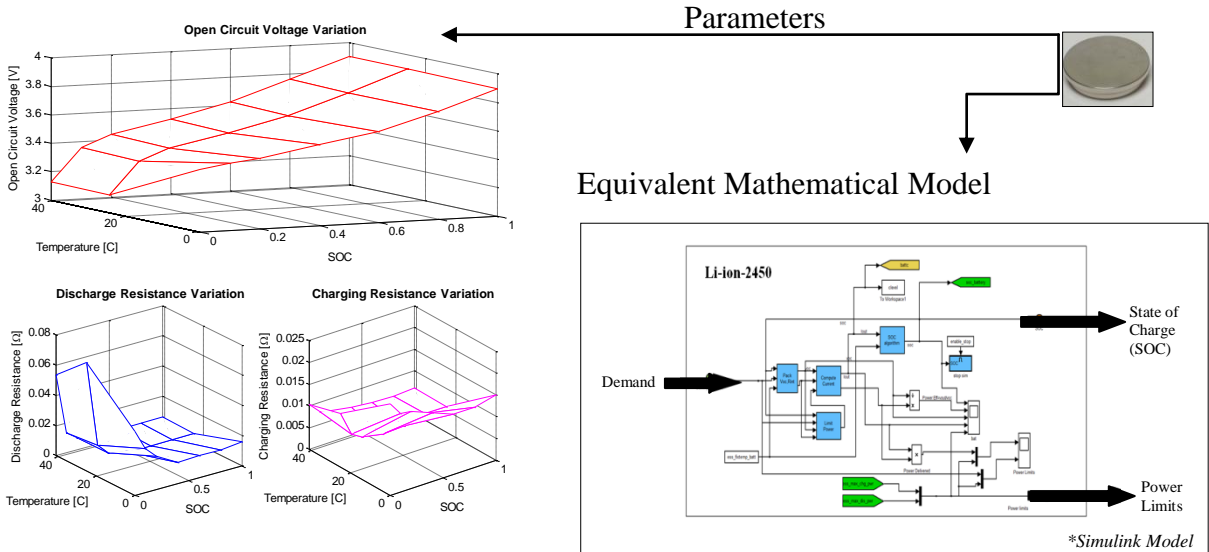


Fig. 6.7: Equivalent battery model for a Li-ion cell created in matlab-simulink for analysis

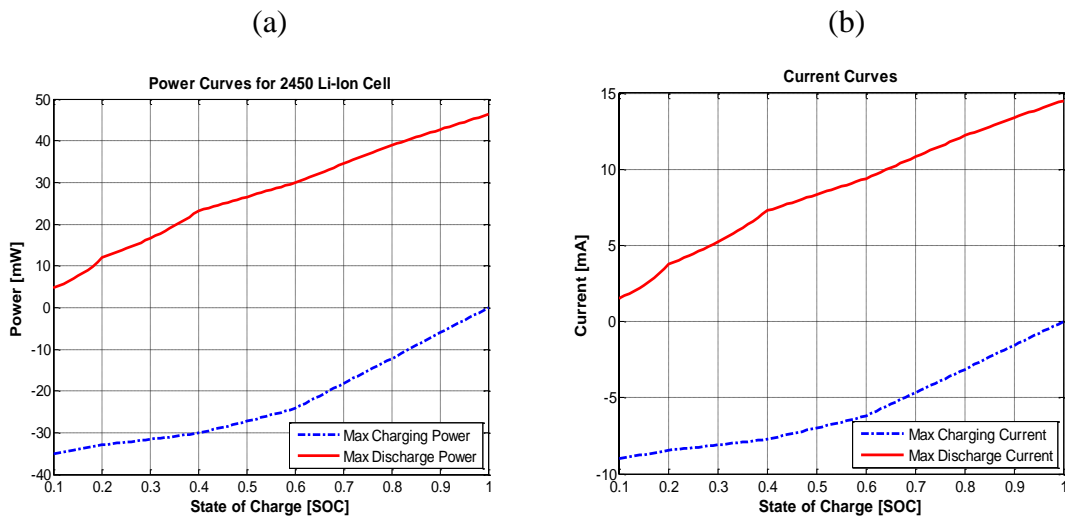


Fig. 6.8: (a) Power limits as a function of the state of charge (SOC) of the cell, and (b) Charge-discharge current limits as a function of the state of charge (SOC) of the cell

Based on the above analysis, the average discharge current rating of the cell was found to be close to 10mA (Fig. 6.8). Analyzing the peak current requirements for an intelligent tire system (Table 6.4), the peak current requirements (ON condition) were estimated to be as high as 30-35mA. This was much higher than the discharge current rating of a Li-ion cell under consideration.

Table 6.4: Current consumption for sensors, microcontroller and wireless transmitter [13]

Component	Action	Power supply	Current consumption	
Sensor (e.g. Accelerometers)	Measure	5V	5mA	
Microcontroller	Compute	5V	ON- 2.5mA	Sleep- 50 μ A
Wireless Transmitter	Transmit	3.3V	ON- 25mA	Sleep-10 μ A

So, in the case of intelligent tires, a battery with a much higher energy capacity would be needed for being able to meet the peak current requirements. In case of a battery, a higher energy capacity translates to a larger volume. Increasing the battery volume won't be an ideal solution in the case of tires, due to the size constraint for this application because of the high curvature of the tire at the point where the tire comes into contact with the ground. Hence, in addition to meeting the average energy demand requirements (≈ 4 mJ/mile), we would need certain power processing circuits for the harvester, which would have the capability to handle high power loads (power/current surges), like the wireless transmission unit of an intelligent tire system.

6.3.2 Design Considerations

Like all other resonance based vibration energy harvesting systems, even in this case, one of the key design parameters was to select the ideal operating frequency for the harvester. To identify this optimal resonance frequency, the vibration spectra of the tire was analyzed under static and dynamic operating conditions using an instrumented tire. The instrumented tire system was developed by placing accelerometers on the inner liner of a tire (Fig. 6.9). The accelerometers used were triaxial with a 5000g peak measurement range and rated up to 10000 Hz [14].

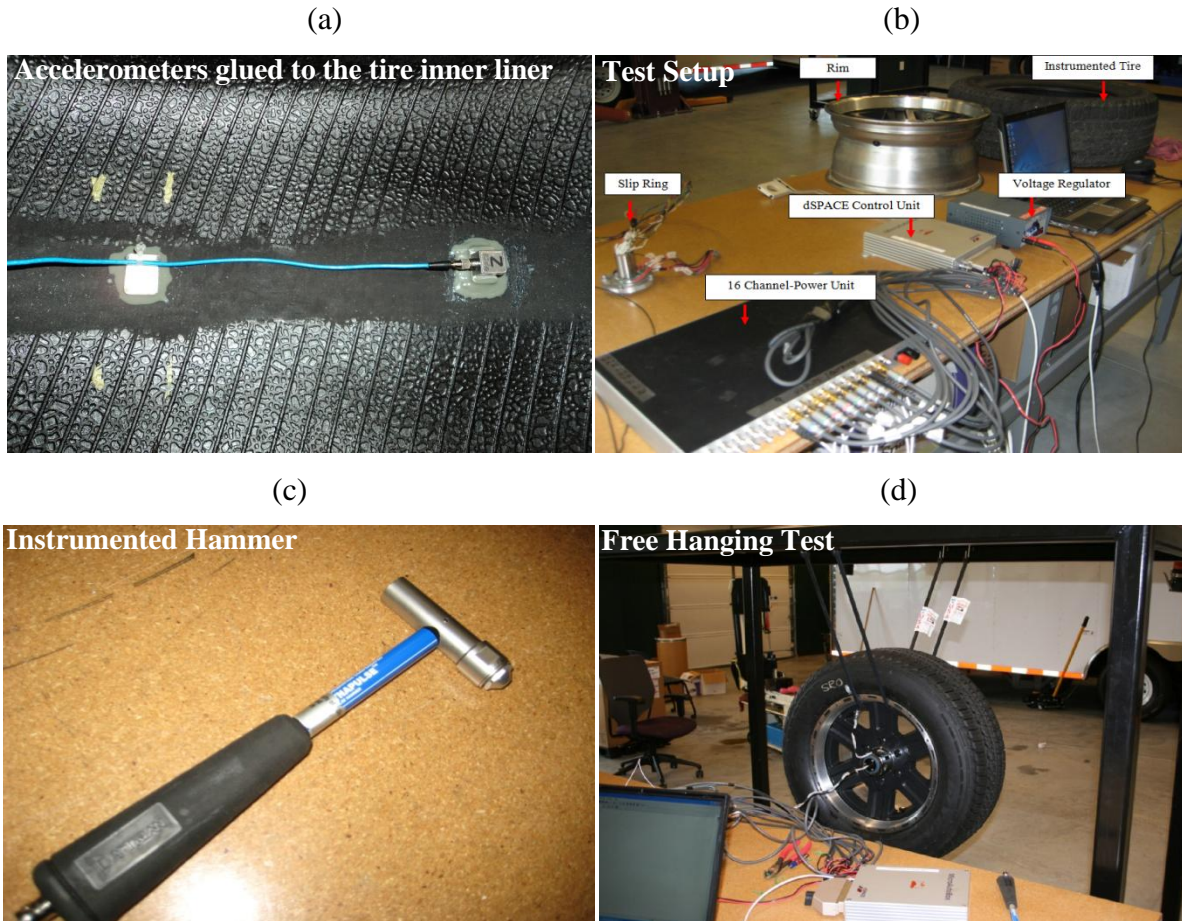


Fig. 6.9: (a) Accelerometer glued to the inner liner, (b) static testing setup equipment, (c) instrumented hammer, and (d) free hanging hammer test setup

For the static free hanging tests, an impulse was applied with an instrumented hammer (Fig. 6.9c) and the corresponding accelerations were recorded from the different accelerometers.

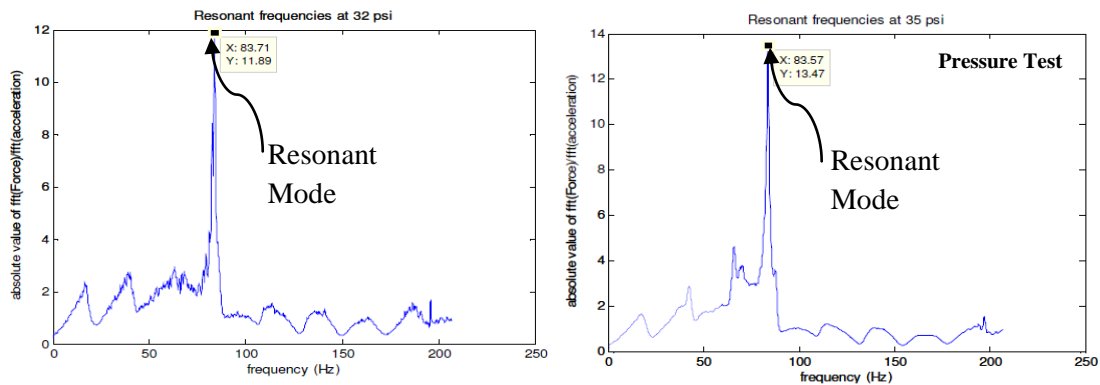


Fig. 6.10: Hammer test results for different pressure

The frequency content of the hammer and accelerometers were found and the frequency response function plotted (Fig. 6.10). These tests were carried out at different tire pressures to study the variation of resonant frequency with inflation pressure. For the static load tests, the tire was attached to a hub that had a wheel force transducer for measuring the load. The tire and hub assembly were loaded using an airspring filled with nitrogen gas. Fig. 6.11 shows how the airspring is mounted. Once the test assembly was lowered to the road surface using the screw actuator, the nitrogen tank forced nitrogen into the airspring until the desired vertical load was achieved.

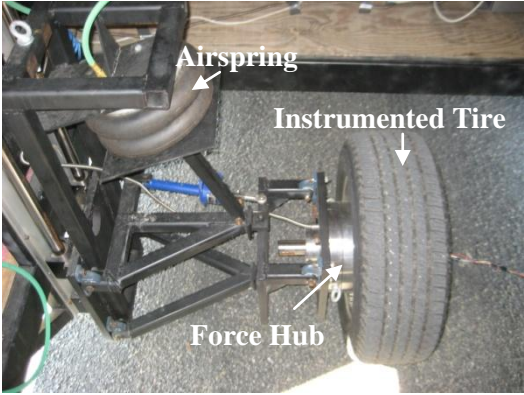


Fig. 6.11: Test setup used to determine the natural modes of vibrations of the tire under static loading conditions

The instrumented impact hammer was used to strike the loaded tire and the same procedure as described above for the free-hanging condition was used to obtain the frequency response function.

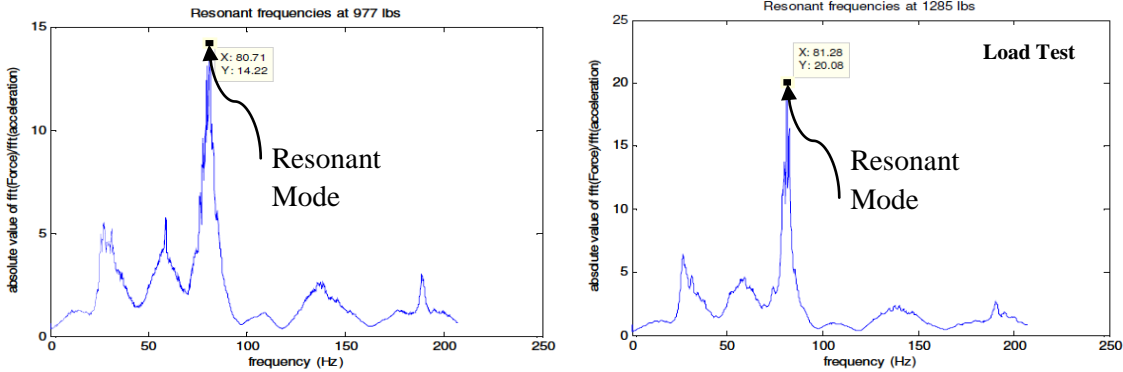


Fig. 6.12: Hammer test results for different tire vertical loading conditions

It was noticed that the peaks in the frequency response function (FRF) were shifted up to a higher value as the pressure in the tire was increased and increasing the load on the tire increased the resonant modes. Based on the hammer test results (Fig. 6.10 and Fig. 6.12), the resonant frequency range of the tire was identified to be in the range 80 Hz - 83 Hz.

For the dynamic tests, the instrumented tire was tested by varying the tire vertical load, translational speed, pressure and road surface conditions using the in-house mobile tire test rig shown below (Fig. 6.13).



Fig. 6.13: Data for the dynamic tests collected using the in-house mobile tire test rig at the Intelligent Transportation Laboratory (ITL), Virginia Tech

A plot of the typical time series data collected for the tire under dynamic test conditions is presented in Fig. 6.14.

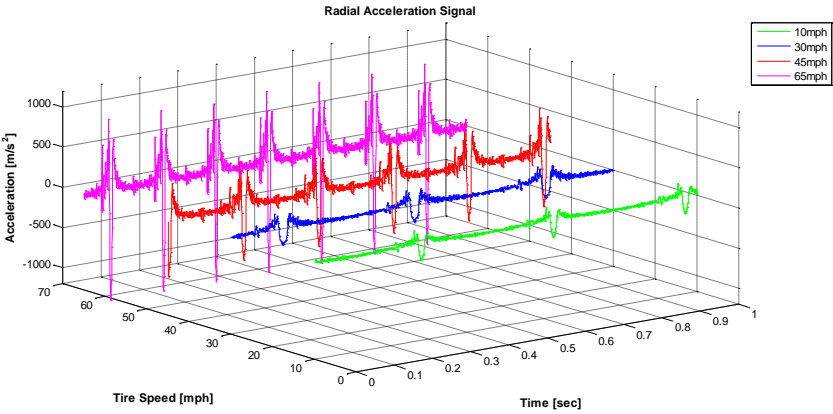


Fig. 6.14: Cascade diagram showing the time series data for the tire radial acceleration at different translational speeds

There was a fair amount of pre-processing of the raw data necessary before it could successfully be used for any kind of analysis. It was necessary to filter the input signal to ensure that we were looking at frequency ranges at which the equipment is capable of making meaningful measurements. After analyzing the bandwidth of the accelerometer, it was seen that the sensor attenuated signals above 10 kHz. The raw sensor data from the accelerometers was filtered using a low pass second order Butterworth filter with a cutoff frequency equal to 10 kHz. By analyzing the FFT of the filtered data (Fig. 6.15), the fundamental natural frequencies at different translational speeds of a tire were identified. Analyzing the dynamic test results, it was concluded that, increasing the tire translational speeds resulted in higher vibration levels. Also, a shift in the spectrum to higher frequencies was noticed, with an increase in the tire speed.

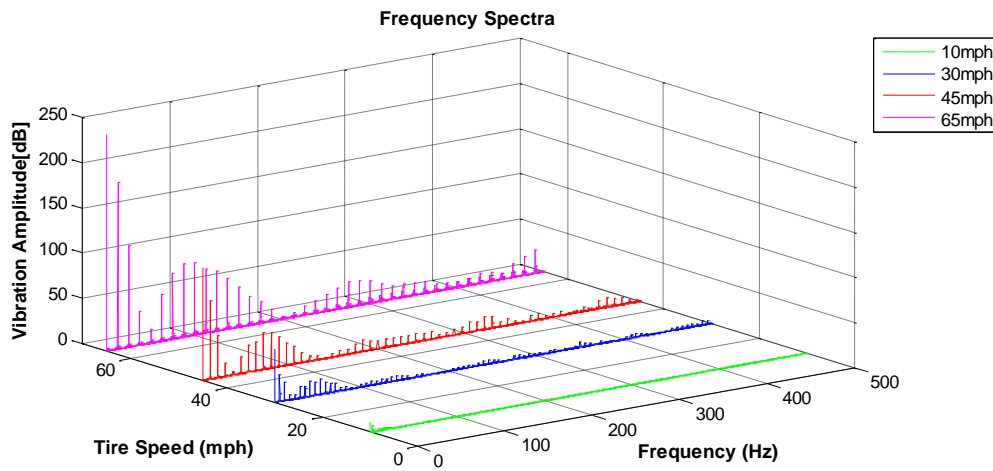


Fig. 6.15: Cascade diagram showing the dependency of the tire vibration spectra on the translational speed

The most important outcome of this analysis was being able understand the fact that there no longer was a dominant driving frequency to which the natural frequency of the harvester unit could be matched. Hence an acceleration-based power harvesting technique from tires can be very demanding as compared to other methods because the vibration spectrum of a tire varies dynamically with operating conditions as seen from the dynamic test results. A vibration spectrum with varying frequency may severely limit the power harvested by a single-degree-of-freedom resonance-based device, and hence a frequency agile or broadband device is required to maximize the energy harvested. To identify the optimum operating range for a broad band

harvester, the effect of tire load, translational speed, varying pressure conditions and road surface roughness on the tire vibration spectra were studied by varying each of these parameters by carrying out extensive outdoor testing of the instrumented tire on different road surface conditions (Fig. 6.16). The power spectrum of each accelerometer signal from these tests was computed using Welch’s averaged modified periodogram method for spectral estimation [15]. The signal was divided into windows of length 256 and windowed using a hamming window with 50% overlap.

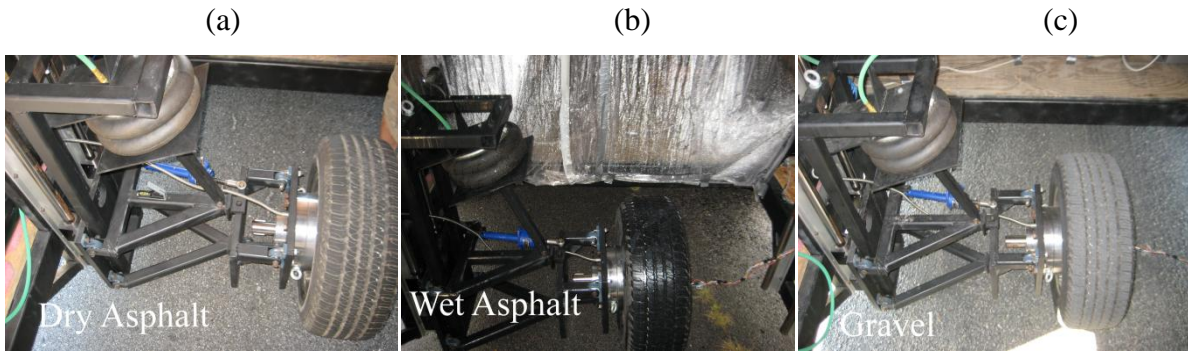


Fig. 6.16: Tire tested on different road surface conditions: (a) dry Asphalt, (b) wet Asphalt, and (c) gravel

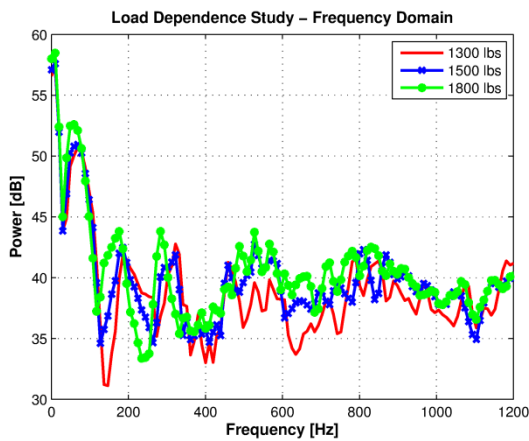


Fig 6.17: Load dependence study

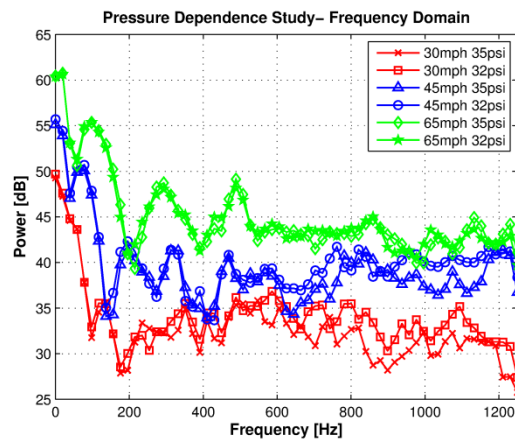


Fig. 6.18: Pressure dependence study

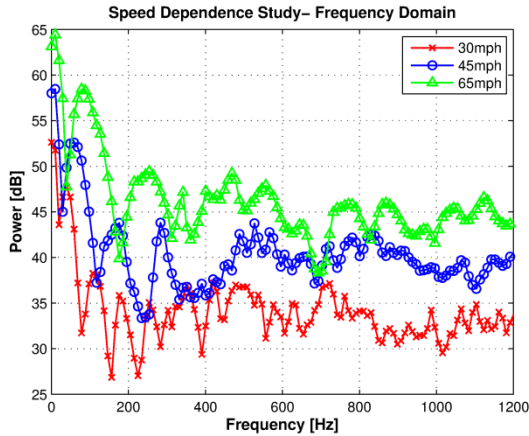


Fig. 6.19: Speed dependence study

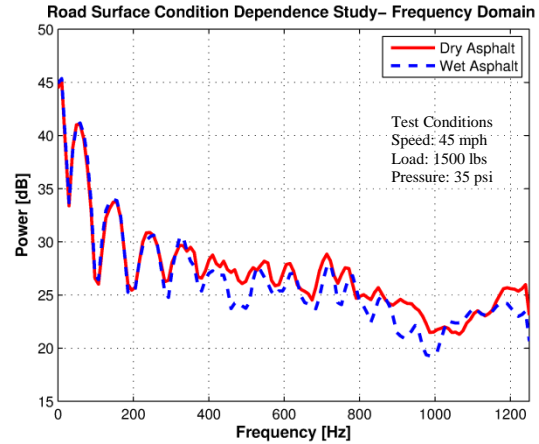


Fig. 6.20: Roughness dependence study

Analyzing the dynamic test results, it was concluded that the fundamental frequencies showed very little dependence on the vertical load (Fig 6.17) and tire pressure (Fig. 6.18), as long as the variation was within an admissible range. A marked difference was noticed in the concentration of the higher frequencies on the spectrum of the tire tested on different surface conditions.

Based on this analysis, the two key parameters identified that majorly were affecting the tire vibration pattern were the tire translational speed (Fig. 6.19) and road surface roughness (Fig. 6.20). Another key parameter which would affect the total energy output of the harvester would be the passage time of the harvester through the contact patch region. This can be attributed to the fact that, it is during this region where the harvester oscillates freely around its equilibrium position, and in turn generates electric charge. As soon as the passage in the contact patch terminates, the centrifugal acceleration causes a forced stopping of the oscillations. To better understand the effect of tire operating conditions on the passage time, the total passage time through the tire-road contact region, for each tire revolution was estimated. This was done by first estimating the contact patch length of the tire under different dynamic test conditions. Using the patch length information, the total passage time was estimated (Fig. 6.21).

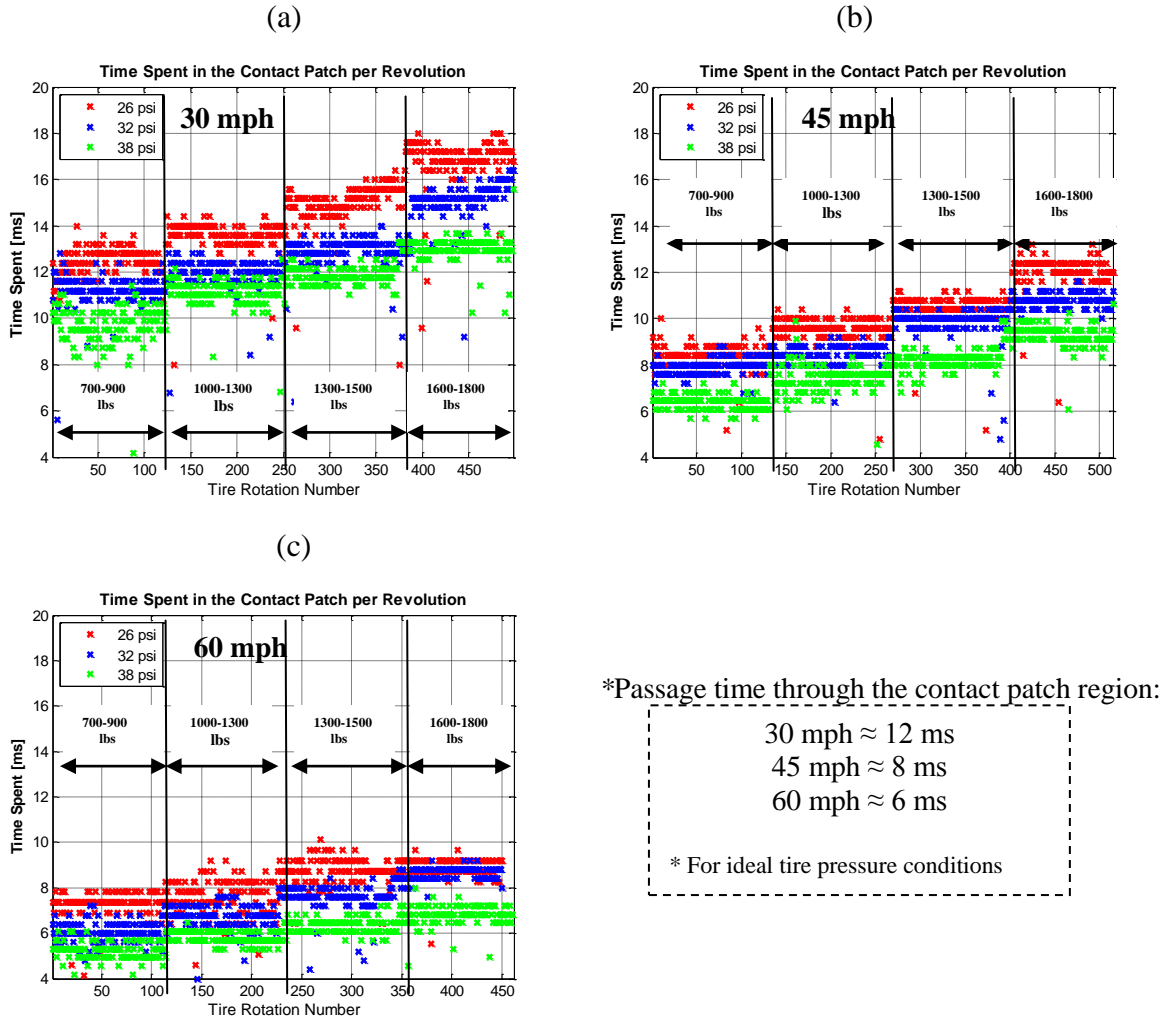


Fig. 6.21: Time spent in the contact patch per revolution for different tire speeds, under different tire pressure and vertical load conditions: (a) 30 mph, (b) 45 mph, and (c) 60 mph

At lower speeds, even though the extent of oscillations would be lower, the total passage time through the contact region was seen to be longer (Fig. 6.21a) as compared to the passage time at higher speeds (Fig. 6.21c). This would translate to a higher number of oscillations at lower tire speeds as compared to those during higher speeds and in turn higher energy output. The frequency associated to such contributions vary in the low frequency range (Table 6.5), corresponding to the number of passages through the contact patch in one second.

Table 6.5: Number of passages through the contact patch region in one second

Tire Speed	Time for one revolution (sec)	Frequency (Hz)
10 mph	0.529	≈ 2 Hz
30 mph	0.176	≈ 6 Hz
45 mph	0.117	≈ 9 Hz
65 mph	0.0813	≈ 12 Hz

Due to such low frequency contributions, a pulsed generation of electric charge may be obtained, as a result of the pulsed oscillating behavior of the harvester unit with a pulse frequency depending on the tire rotation speed. To ensure a continuous generation of electric charge, one can take advantage of the high frequency components of the radial acceleration signal. These components are due to the vibration modes of the tire structure (torsion and vibration modes) as a whole or due to the tire–road interaction that may be dependent on the road surface condition. This would ensure that the harvester unit oscillates not only in contact patch region but also in the non-contact region. This may only be possible for low tire speeds, when the centrifugal acceleration developed due to the tire rotation is not so strong to practically cancel out all other components of the radial acceleration signal. At higher tire speeds, electric charge would only be generated in the contact patch region because the high centrifugal acceleration magnitudes in the non- contact region would impede the oscillations of the harvester.

To select the optimal operating range, the PSD plots for different tire speeds were normalized and the mean power estimated at each frequency bin (Fig. 6.22). Using the mean power curves, the ideal operating range for the harvester, to ensure sufficient power generation, over a wide range of tires speeds was estimated to be in the range 60-80 Hz.

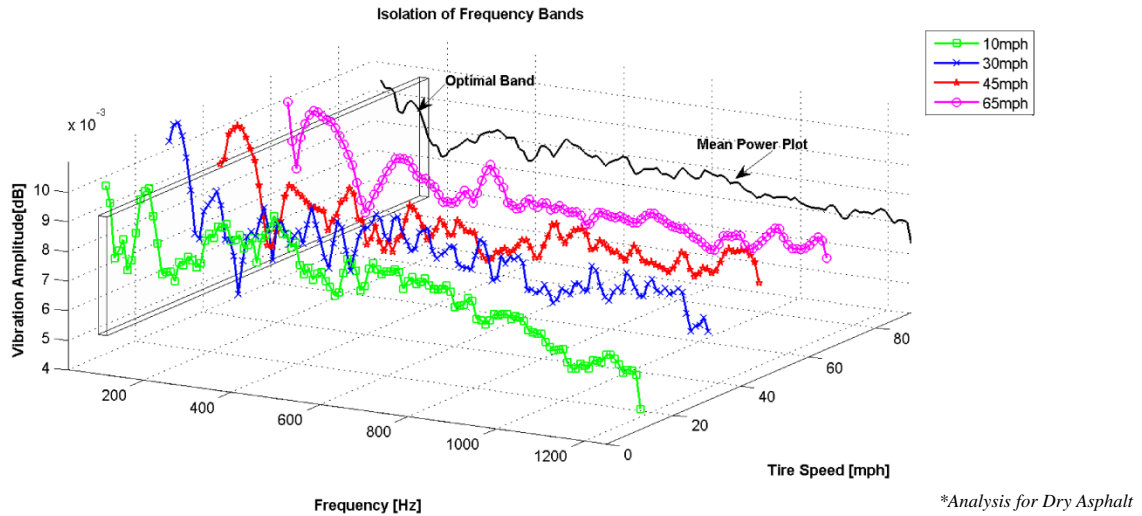


Fig. 6.22: Identifying ideal operating frequency band for the harvester

To ensure the selected range was the optimal range for all possible road surface conditions, a comparison was made between the radial acceleration PSD plots for different road surface conditions in the range of interest (Fig. 6.23).

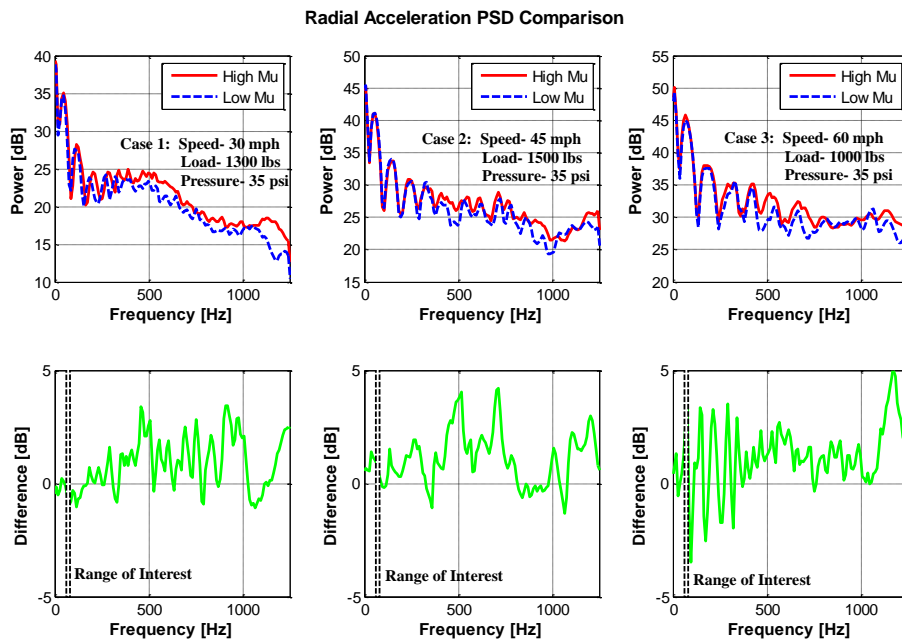


Fig. 6.23: Comparison between radial acceleration PSD plots for low and high- μ surface conditions

It was seen that throughout the chosen optimal frequency band range, the data sets were statistically similar. Hence, the selected operating band for the harvester was the ideal operating range for different road surface conditions and tire speeds.

6.3.3 Harvester Configuration and Mounting Location

Extremely large accelerations present inside a tire pose certain key issues in designing a harvester unit for tires. Based on the harvester design constraints identified (Fig. 6.24), the harvester configuration selected for our analysis was a two layer bender (bimorph) mounted as a cantilever beam with a mass placed on the free end (Fig. 6.25). A bending element was chosen as the basis for a generator since this configuration results in the highest average strain, and the power output is closely related to the average strain developed in the bender.

**Key Design Guidelines for
Tire Mounted Harvesters**



- **Broad band operation** – To ensure sufficient power outputs levels under varying tire speed and road surface conditions.
- **Low weight** – So as not to adversely affect a wheel's balance.
- **Small volume-** Because of the high curvature of the tire at the point where the tire comes in contact with the ground.

Fig. 6.24: Key design guidelines for selecting an appropriate harvester configuration for tires

The cantilever mounting also results in the lowest resonance frequency for a given size, which is important because the target input vibrations inside a tire are in the low frequency range (1–100 Hz).

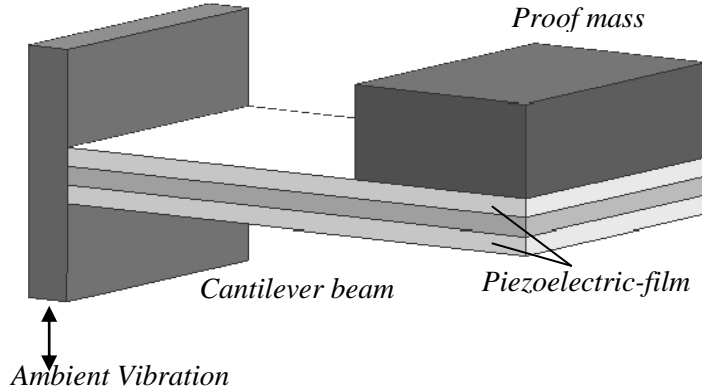


Fig. 6.25: Cantilever beam with a tip mass under translational base motion

The harvester element would be disposed on the tire inner liner, along a plane orthogonal to the radial direction (Fig. 6.26). Ideally, one could dispose the leg of the piezoelectric element in the axial direction to ensure uniform stress distribution along the piezo film. This might not be a viable option in this case due to the limitations in the tire dimensions in the width direction. Alternatively, the leg can be disposed in the tangential direction.

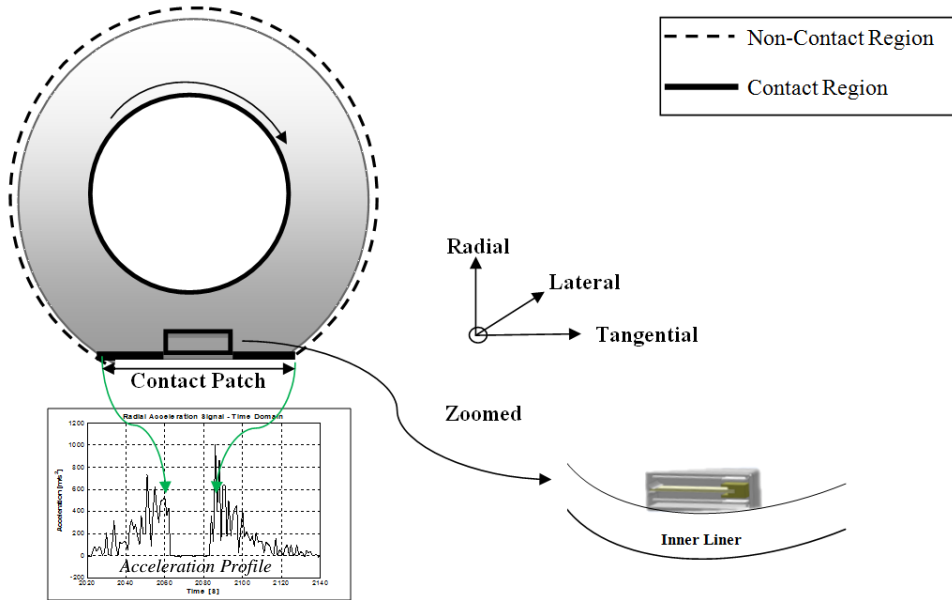


Fig. 6.26: The planned mounting location of the harvester is demonstrated

Since the tire experiences high amplitude accelerations during the rotation, it was proposed to incorporate limit stops into the harvester casing design (Fig. 6.27a-Fig. 6.27c). The limit stops would reduce the occurrence of cracks in the piezoelectric material that could be caused by continuously large oscillations of the piezoelectric element.

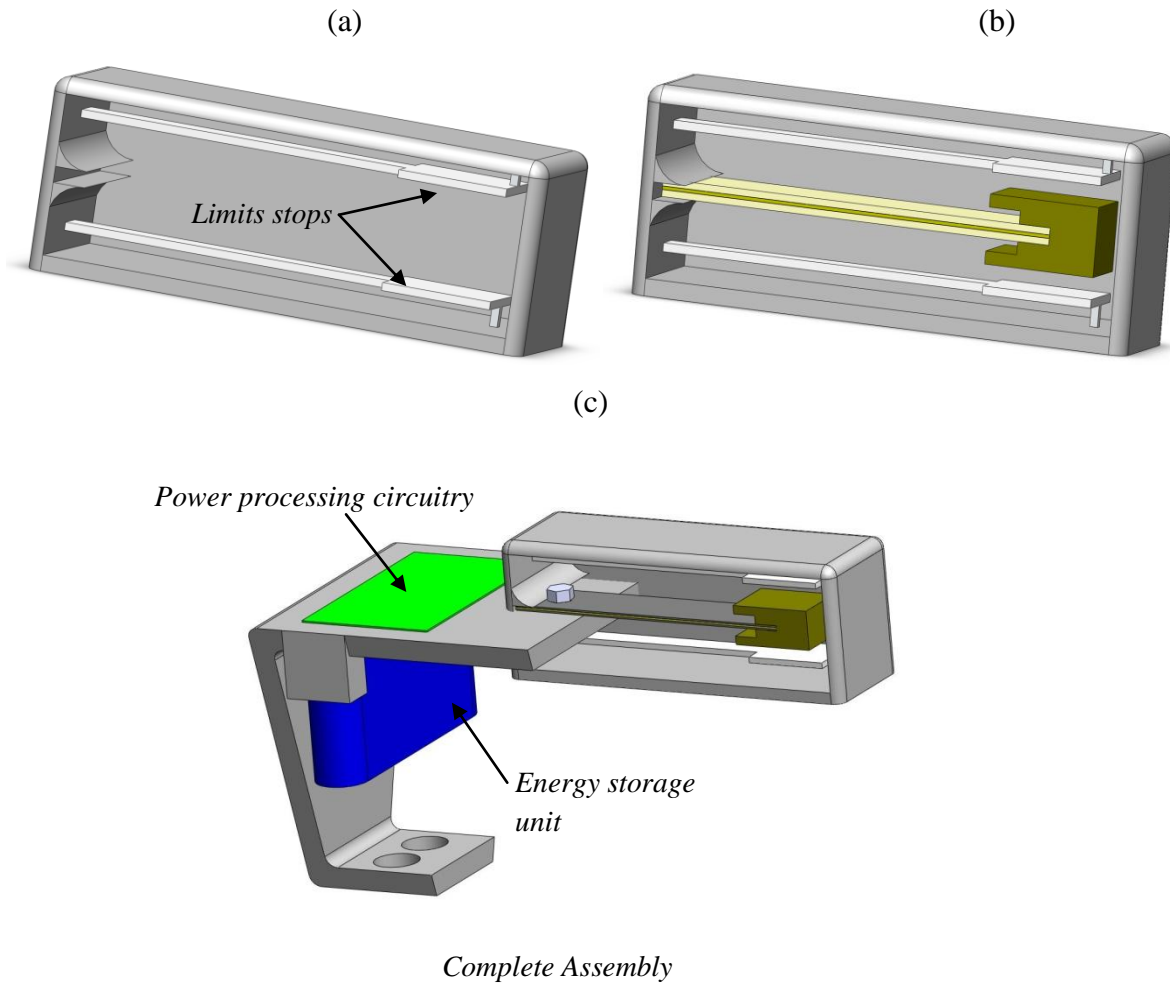


Fig. 6.27: (a) CAD drawing of the harvester casing, (b) drawing of the harvester placed inside the casing, and (c) drawing of the complete assembly. (Note: some components removed from model for clarity)

The spacing between the limits stop and the cantilever tip mass can be optimized depending on the estimated tip mass deflection under different tire operating conditions. For the analysis presented in this paper, the spacing was selected so as to limit the harvester motion under extreme tire operating conditions, namely high tire speeds, underinflated pressure conditions, to

avoid damage to the piezoelectric film due to excessively high stress levels induced because of the beam motion.

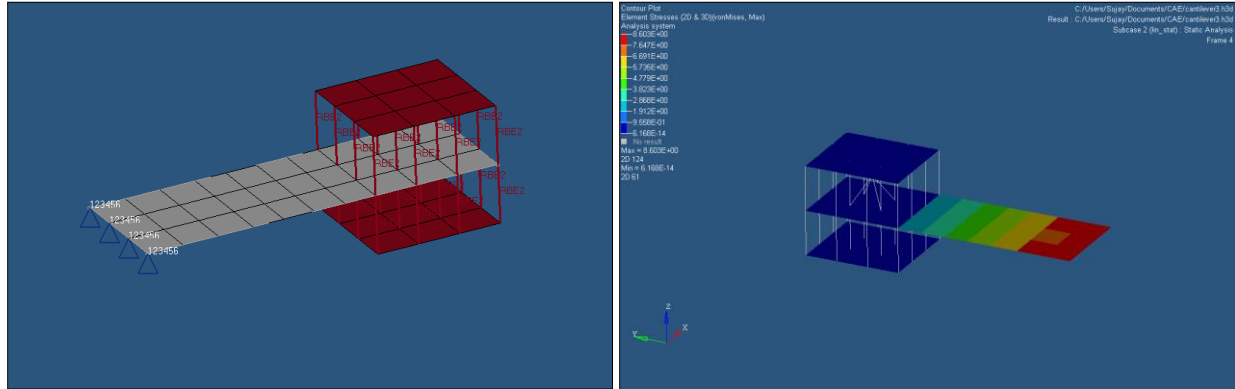


Fig. 6.28: Stress distribution along the length of the beam

The measured acceleration levels on the inner liner under extreme tire operating conditions were used to estimate the beam deflection and the corresponding stress levels generated along the beam length (Fig. 6.28). Based on the maximum allowable stress levels for a piezo-film, the tip mass - limit stop spacing was optimized.

6.3.4 System Modeling

An analytical model of the harvester is important not only for estimating the amount of power possible from a given vibration source, but also for making explicit relationships that give the designer of the system some intuition about how to improve its performance. With these goals in mind, the development of an analytical model for the harvester configuration selected was undertaken. For the purpose of modeling, it was assumed that the piezoelectric patches were perfectly bonded to the beam and showed linear elastic behavior. In addition, the beam of the energy harvesting device was modeled as an Euler-Bernoulli beam. The aspect ratios of the harvester beam used in the literature allow neglecting the effects of shear deformation and rotary inertia, and make it reasonable to use the Euler–Bernoulli beam model. The established constitutive equations for a piezoelectric material can be expressed as [16]:

$$\begin{aligned} \{T\} &= [c^E]\{S\} - [e^T]\{E\} \\ \{D\} &= [e]\{S\} + [\varepsilon^S]\{E\} \end{aligned} \quad (6.7)$$

where: $\{T\}$ is the vector of stresses

$\{S\}$ is the strain vector,

$\{D\}$ is the electric displacement vector

$\{E\}$ is the electric field vector

$[c^E]$ is the modulus of elasticity matrix evaluated at constant electric field

$[e]$ is the matrix of piezoelectric coupling coefficient

$[\varepsilon^T]$ is the dielectric constant matrix evaluated at constant stress.

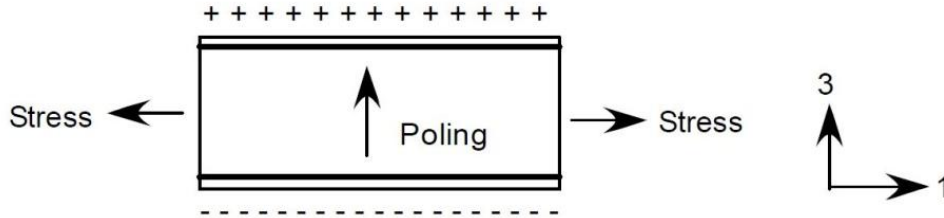


Fig. 6.29: 31-direction: Charge collection in 3 direction and stress in 1 direction

For a cantilever beam on which is bonded with a d31- type PZT material (Fig. 6.29), if the driving vibrations are applied to the beam only in the 3 direction (transverse vibrations) and the poling direction is along the 3 direction, then the beam experiences a 1D stress along the 1 direction. Equation (6.7) can then be simplified to scalar equations as follows:

$$\begin{aligned} \{T_1\} &= [c_{11}^E]\{S_1\} + [e_{31}]^t\{E\} \\ \{D_3\} &= [e_{31}]\{S_1\} + [\varepsilon_{33}^T]\{E\} \end{aligned} \quad (6.8)$$

The dynamic equations of motion of the energy harvesting beam were derived using Hamilton's variational principle [17-19]. This states that the variational indicator must be zero at all time, as shown below in Equation (6.9):

$$\int_{t_1}^{t_2} [\delta T - \delta U + \delta W] dt = 0 \quad (6.9)$$

Where: δT is the variation of the kinetic energy

δU is the variation of the potential energy

δW is the variation of the work done by an external force

In order to solve Equation (6.9) for a cantilever beam with bimorph piezoelectric elements, the following assumptions were made. The first assumption follows the Rayleigh–Ritz procedure, which defines the displacement $U(x, t)$ of the beam as the summation of modes in the beam and a temporal coordinate

$$\text{Displacement } (U(x, t)) = \sum_{n=1}^p \phi_n(x)r_n(t) \quad (6.10)$$

where : $\phi_n(x)$ is the assumed mode shape

$r_n(t)$ is the time-dependent generalized mechanical coordinate &

p is the number of modes to be included in the analysis

In this study, the first mode shape of the cantilever beam was used for the assumed mode method. The generalized expression for the mode shape function for a cantilever beam with a tip mass can be expressed as:

$$\phi_n(x) = D_n[(\cosh(\beta_n x)\cos(\beta_n x)) \left(\frac{\cos\beta_n l + \cosh\beta_n l}{\sin\beta_n l + \sinh\beta_n l} \right) (\sinh(\beta_n x)\sin(\beta_n x))] \quad (6.11)$$

The second assumption made is to apply the Euler–Bernoulli beam theory, which assumes that the strain is linearly related to the distance (y) from the neutral axis.

$$\text{Strain } (S) = -y \frac{\partial^2 u(x,t)}{\partial x^2} \quad (6.12)$$

$$S = -y \phi(x)'' r(t)$$

The third assumption is made is to assume that the electric potential across the piezoelectric element is constant. This assumption also indicates that no field is applied to the beam, which designates the beam to be inactive material.

$$E = \begin{cases} -\frac{v}{t_p} & \frac{t_s}{2} < y < \frac{t_s}{2} + t_p \\ 0 & \frac{t_s}{2} < y < \frac{t_s}{2} + t_p \\ \frac{v}{t_p} & -\frac{t_s}{2} - t_p < y < -\frac{t_s}{2} \end{cases} \quad (6.13)$$

Using these assumptions, variational function Equation (6.9) was simplified to get the governing equations of motion of the energy harvesting beam as:

$$\begin{aligned} Mr''(t) + Kr(t) + Cr'(t) - \Theta v(t) &= F(t) \\ \Theta^T r(t) + C_p v(t) &= Q(t) \end{aligned} \quad (6.14)$$

The effective system parameters, M , mass, K , stiffness, C , damping, Θ , coupling, C_p capacitance, are defined as:

$$M = \int_{V_s} \rho_s \phi(x) \phi(x) dV_s + \int_{V_p} \rho_p \phi(x) \phi(x) dV_p \quad (6.15)$$

$$K = \int_{V_s} y^2 \phi''(x) c_s \phi''(x) dV_s + \int_{V_p} y^2 \phi''(x) c^E \phi''(x) dV_s \quad (6.16)$$

$$\Theta = -\int_{V_p} y \phi''(x) e^T \varphi(y) dV_p \quad (6.17)$$

$$C_p = -\int_{V_p} \varphi^T(y) \varepsilon^S \varphi(y) dV_p \quad (6.18)$$

$$C = \alpha M + \beta K \quad (6.19)$$

The subscripts p and s denote the piezoelectric material and the substrate, respectively. The superscript $()^S$ signifies that the parameter was measured at constant strain, superscript $()^T$ signifies that the parameter was measured at constant stress, and the superscript $()_E$ indicates that the parameter was measured at constant electric field. The x , y , and z coordinates are used to represent the length, thickness, and width directions of the beam, respectively. $\varphi(y)$ denotes the electrical field over the thickness of the piezoelectric. Proportional structural damping is added to the model through constants α and β . When the energy harvesting beam is connected to the

external load resistance, R , the voltage harvested from the vibration can be expressed in terms of the load resistance as:

$$v = -RQ \quad (6.20)$$

Using Equations (6.20) and (6.14), the governing equations of the harvesting beam can be obtained as follows:

$$\begin{aligned} Mr''(t) + Kr(t) + Cr(t) - \Theta v(t) &= F(t) \\ \Theta^T r'(t) + C_p v'(t) + \frac{v}{R} &= 0 \end{aligned} \quad (6.21)$$

From Equation (6.21), the harvested DC voltage for the energy harvesting beam is obtained:

$$\begin{aligned} V_{DC}(\omega) &= \left(\frac{\Theta R F}{\sqrt{2} M} \right) \frac{1}{\sqrt{\left(\frac{\Theta^2 R}{M} + C_p R (\omega_n^2 - \omega^2) + 2\zeta \omega_n \right)^2 + \left(\frac{\omega_n^2}{\omega} - \omega - 2\zeta \omega_n C_p R \right)^2}} \end{aligned} \quad (6.22)$$

where:

$$\omega_n = \sqrt{\frac{K}{M}} \quad \text{and} \quad \zeta = \frac{c}{2\sqrt{KM}}$$

The power in frequency domain is given by:

$$\begin{aligned} P_{DC}(\omega) &= \frac{V_{DC}^2}{R} \\ &= \left(\frac{\Theta^2 R F^2}{2M^2} \right) * \frac{1}{\left(\frac{\Theta^2 R}{M} + C_p R (\omega_n^2 - \omega^2) + 2\zeta \omega_n \right)^2 + \left(\frac{\omega_n^2}{\omega} - \omega - 2\zeta \omega_n C_p R \right)^2} \end{aligned} \quad (6.23)$$

If the excitation frequency, ω , is equal to the resonance frequency, ω_n , the maximum voltage $V_{DC}(\omega_n)$ in frequency domain is obtained:

$$V_{DC}(\omega_n) = \left(\frac{\Theta R F}{\sqrt{2} M} \right) \frac{1}{\sqrt{\left(\frac{\Theta^2 R}{M} + 2\zeta\omega_n \right)^2 + (2\zeta\omega_n C_p R)^2}} \quad (6.24)$$

The maximum power, $P_{DC}(\omega_n)$, in the frequency domain is given by:

$$P_{DC}(\omega) = \left(\frac{\Theta^2 R F^2}{2M^2} \right) * \frac{1}{\left(\frac{\Theta^2 R}{M} + 2\zeta\omega_n \right)^2 + (2\zeta\omega_n C_p R)^2} \quad (6.25)$$

For energy harvesting beam with two PZT patches (one bonded at the top of the beam and the other at the bottom), its governing equations can be obtained as follows:

$$Mr''(t) + Kr(t) + Cr(t) - \sum_{i=1}^2 \Theta_i v(t)_i = F(t) \quad (6.26)$$

$$\sum_{i=1}^2 \Theta_i^T r_i(t) + \sum_{i=1}^2 C_{p_i} v_i(t) = \sum_{i=1}^2 Q_i(t)$$

From Equation (6.26), the harvested DC voltage for the energy harvesting beam is obtained:

$$V_{DC}(\omega) = \left(\frac{\sqrt{2}\Theta^2 R F^2}{M^2} \right) * \frac{1}{\left(\frac{4\Theta^2 R}{M} + 2\zeta\omega_n \right)^2 + (4\zeta\omega_n^2 C_p R)^2} \quad (6.27)$$

The maximum power, $P_{DC}(\omega_n)$, in the frequency domain is given by:

$$P_{DC}(\omega) = \left(\frac{2\Theta^2 R F^2}{2M^2} \right) * \frac{1}{\left(\frac{4\Theta^2 R}{M} + 2\zeta\omega_n \right)^2 + (4\zeta\omega_n^2 C_p R)^2} \quad (6.28)$$

6.3.5 Numerical Studies

Fig. 6.30 shows the geometry of the simulated cantilever beam. A brass substrate with thickness t_s is sandwiched between two PZT elements with equal thickness t_p , creating a bimorph configuration. The piezoelectric layer is used to actuate or produce energy and a non-

piezoelectric layer is used to add stiffness as well as make the device more durable. For the case studied, the PZT material was assumed to be poled in the 31 direction, ‘3’ denoting the direction of charge collection and the ‘1’ the direction of applied stress.

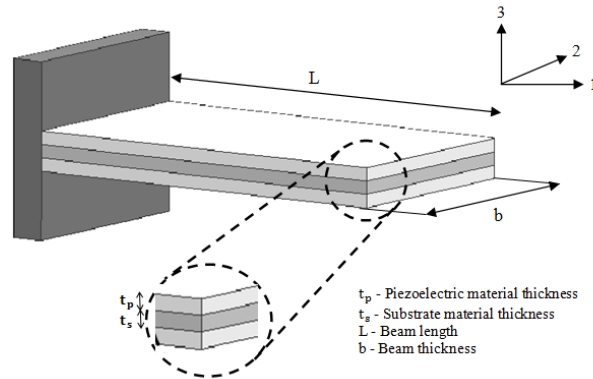


Fig. 6.30: Schematic of the beam showing the parameters used in the simulations

The resonance frequency of the harvester unit was tuned using a tip mass. The operating frequency was intentionally selected to lie in the range of optimal frequency range identified for tire mounted harvester (Fig. 6.22). Shown below (Table 6) are the geometry and material properties of the simulated system.

Table 6.6: Geometry and material properties of the simulated system

Property	Symbol	Value
Length	L	10 mm
Width	b	3.2 mm
Brass thickness	t_s	0.2 mm
PZT thickness	t_p	0.1 mm
Brass density	ρ_s	8000 kg/m ³
Brass modulus	c_s	100 GPa
PZT density	ρ_p	7800 kg/m ³
PZT modulus	c_p	62 GPa
PZT dielectric	K_3^T	2800
PZT strain constant	d_{31}	-300 *10 ⁻¹² m/V

The resonance frequency of the harvester under study was set to 66.2 Hz. Two kinds of wire connection were studied as shown in Fig. 31. One was serial connection between top and bottom piezo layers (Fig. 6.31a), the other was parallel connection (Fig. 6.31b). In series, the 2 piezoelectric layers are oppositely polarized and the output terminals are the outside electrodes of the piezoelectric layers. In this case, an electric potential exists between the output terminals when the structure is subjected to a vibration at the fixed end of the beam. In parallel, the 2 piezoelectric layers are polarized in the same direction, and the outside electrodes are joined to make one terminal. The central layer constitutes the other terminal. In this configuration, the same amount of charge exists on each outside electrode when the structure is subjected to vibration at the fixed end.

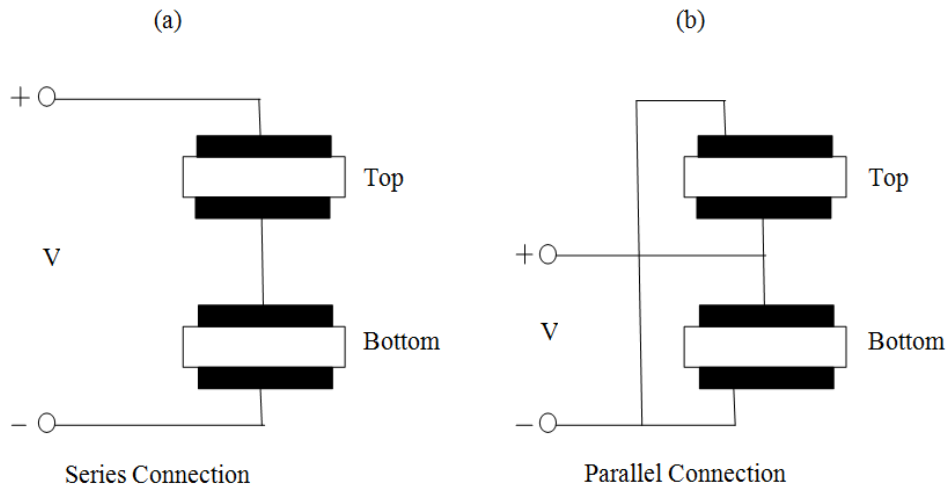


Fig. 6.31: Connection method between the energy harvesting device and the rectification circuitry

Fig. 6.32 presents the results for the predicted characteristics of the energy harvesting unit. The maximum power was located in the electrical load range of 20-200 k Ω (Fig. 6.32a). The serial connection exhibited peak power levels at a higher electrical resistance than the parallel connection. The generated current decreased, as the electrical resistance increased (Fig. 6.32b). In addition, the parallel connection produced higher current than the serial connection. For the aforementioned simulation conditions, the ideal load resistance to maximize the system power output (Fig. 6.32c) was estimated to be ≈ 200 k Ohms. The harvester was able to produce sufficient power levels under the assumption that the source excitation frequency was tuned to the resonant frequency for the harvester unit. However, the output power levels were seen to

drop exponentially around either side of the system resonance frequency (Fig. 6.32c). This kind of a behavior was expected from a device working on the principle of resonant mechanical vibration energy harvesting.

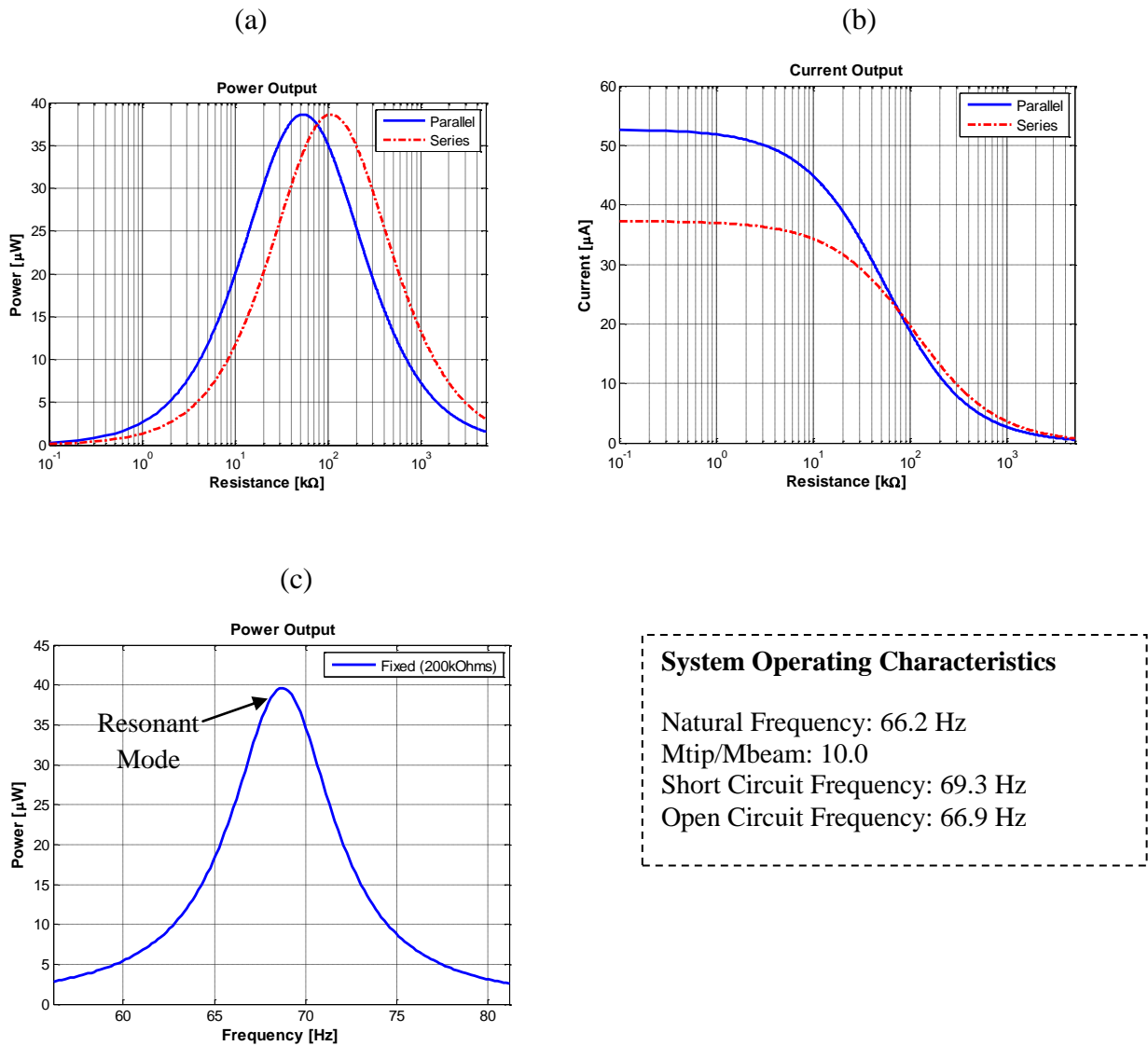


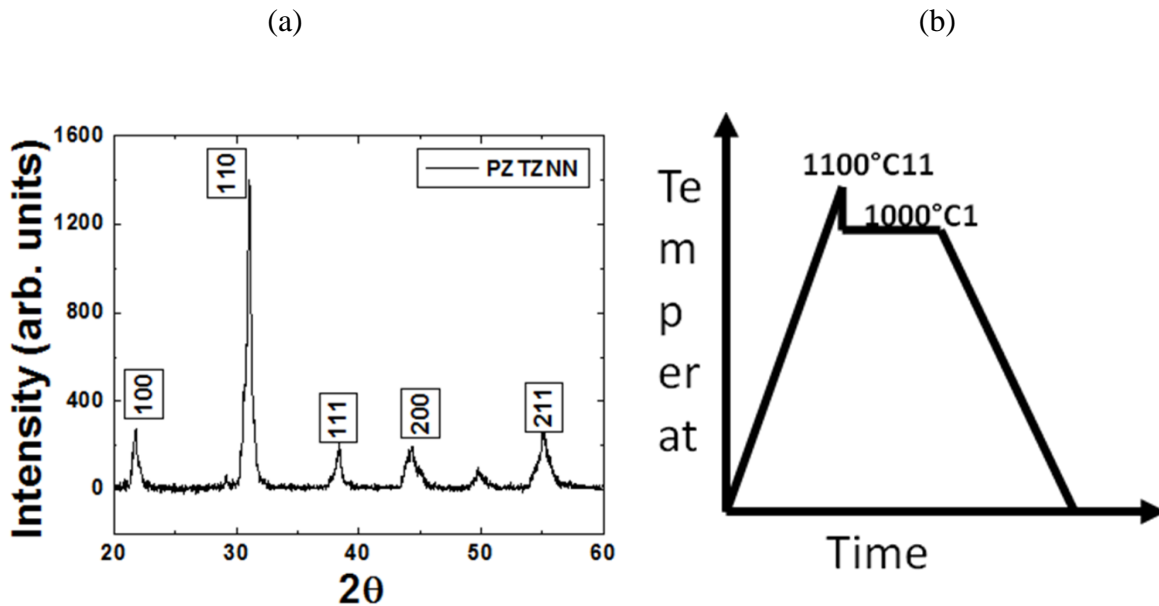
Fig. 6.32: (a) Output power v/s electrical resistance, (b) output current v/s electrical resistance, and (c) output power v/s frequency

6.4 Harvester Fabrication and Performance Results

6.4.1 Fabrication Details

The work presented in this section was performed under a collaborative research project with the Center for Energy Harvesting Materials and Systems (CEHMS), Virginia Tech.

Based on the design specification for a tire specific harvester unit presented in Section 6.3, a vibration energy harvesting unit using piezoelectric bimorph transducers was fabricated. High energy density piezoelectric ceramic composition $0.9Pb(Zr_{0.56}Ti_{0.44})O_3 - 0.1Pb[(Zn_{0.8/3}Ni_{0.2/3})Nb_{2/3}]O_3 + 2 \text{ mol}\% MnO_2$ (PZTZNN) was synthesized using a conventional mixed oxide ceramic processing route explained in detail elsewhere [20-25]. Sieved powders were pressed in to plates with the dimensions of $40 \times 15 \text{ mm}^2$ using a hardened steel die and hydraulic press under a pressure of 1.5 ksi. The green body was next pressed in cold isostatic press (CIP) operating at 20 ksi for 10 – 15 min in order to improve the density of the green body. After CIP, the samples were sintered in air atmosphere using a Sentrotech furnace with two-step sintering profile. It is well known that two step sintering technique results in smaller grain size and higher density of the polycrystalline ceramic. Samples were heated to 1100°C and held for 5 minutes followed by rapid cooling to 1000°C and holding for 4 hours.



(c)

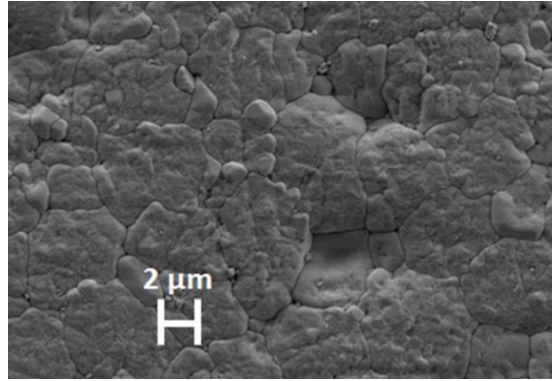


Fig. 6.33: (a) X-ray diffraction pattern of PZTZNN plates showing single phase perovskite structure, (b) sintering profile, and (c) microstructure of sintered PZTZNN plates

The sintered samples were then polished and electroded using Ag-Pd electrode that was fired at 650°C. The samples were poled at 3-4 kV/mm using a high voltage supply in an oil bath maintained at 120°C. X-ray Diffraction (XRD) was used in order to confirm the perovskite phase of the synthesized powder, as shown in Fig. 6.33a. Scanning electron microscopy was performed using LEO (Carl Zeiss SMT, Inc.) 1550 high-performance Schottky field-emission SEM. The piezoelectric constant of the synthesized composites was measured by APC YE 2730A d_{33} meter. Resonance characteristics were determined by HP 4194A impedance analyzer (Hewlett Packard Co., USA). Table 6.7 summarizes the piezoelectric properties of material.

Table 6.7: Piezoelectric properties of the synthesized material

Dielectric constant	k_p	Q_m	d_{33} (pC/N)	g_{33} ($\times 10^{-3}$) (Vm/N)	d.g	N
475	0.45	673	167	42	6646	1.167
S_{11}^E	ρ_p (kg/m ³)	k_{31}	d_{31} (pC/N)	g_{31} ($\times 10^{-3}$) (Vm/N)		
1.05×10^{-11}	7800	0.25	53	12		

In order to fabricate the bimorphs, rectangular plates were pressed and sintered and then polished along the thickness to 0.4 mm. The final dimensions of the fabricated bimorph were 25 x 5 x 0.4 mm³. Two polished plates were electroded, poled and attached to brass foil in sandwich configuration, as shown in Fig. 6.34a. Fabricated bimorph was mounted on a Ling dynamic shaker, as shown in Fig. 6.34b using a custom clamp. A tip mass of 11.45 grams was attached at the free end of bimorph for dynamic force excitation at the mechanical resonance, as shown in Fig. 6.34b. In order to obtain a wide range of resonance frequencies, the tip mass was varied from 9 gm to 12 gm while keeping all the other parameters constant.

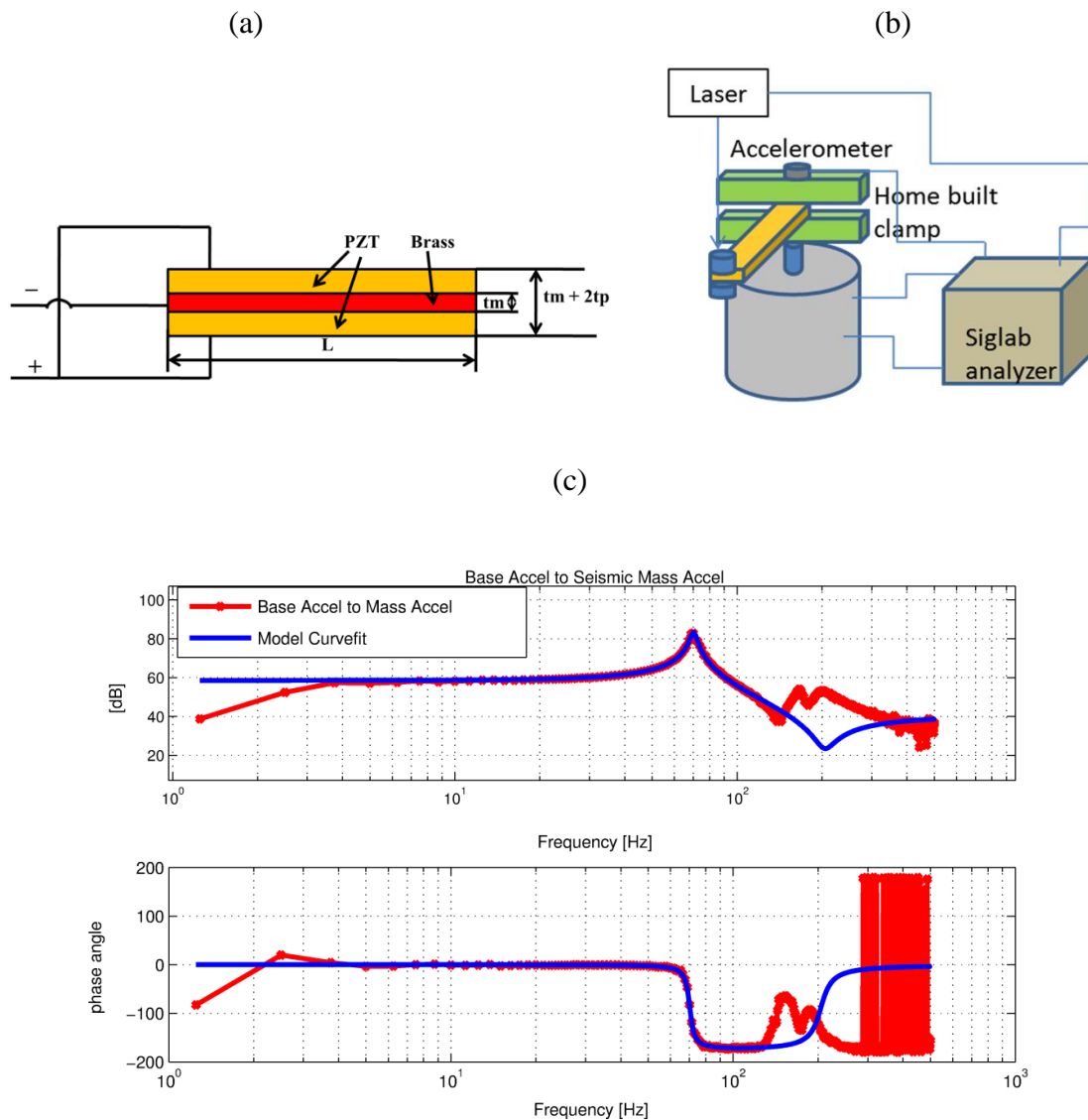


Fig. 6.34: (a) parallel bimorph configuration, (b) experimental setup, and (c) Frequency response function

Acceleration measurements were taken on the base of the structure and tip mass by using a shear accelerometer (Piezotronics, Inc.), OFV 303 Laser vibrometer (Polytech, Inc.) and a spectral analyzer (Siglab Model 20-42). The output from the accelerometer was sent through a sensor signal conditioner (Piezotronics Inc. Series 481). The output from laser vibrometer was recorded using Siglab. A small breadboard was used to vary the load resistors across the output of bimorph electrical terminals. The Siglab analyzer was used for collecting the time traces, power spectrums of acceleration and output voltage, and the transfer function from base acceleration to tip mass acceleration.

6.4.2 Performance Results and discussion

6.4.2.1 Microstructural characterization

The piezoelectric and dielectric properties of the fabricated bimorphs are summarized in Table 6.7. Two step sintering process results in smaller grain size and higher density [21]. The grain size was determined from the SEM micrographs by using linear intercept method and was found to be 2.5 μm . Fig. 6.33c shows the microstructure of sintered plates. The density of the polycrystalline ceramic was calculated to be 96% of the theoretical value. The dielectric constant was 475 whereas piezoelectric charge constant (d_{33}) was measured to be 167 pC/N.

6.4.2.2 Theoretical analysis of bimorph

The bimorph transducer consists of one metal plate (substructure) sandwiched between the two PZTZNN plates as shown in Fig. 6.34a. The effective moment of inertia (M.I.) of the composite beam can be defined as [22, 25]:

$$I_{eff} = 2 I_p + \frac{E_m}{E_p} \quad (6.29)$$

$$I_p = \frac{b t_p \left(\frac{t_p}{2} - y \right)^2}{12} \quad (6.30)$$

$$I_m = \frac{b (t_m)^2}{12} \quad (6.31)$$

where I_p is the moment of inertia of piezoelectric plate, b is the width of bimorph, E_m and E_p are Young's modulus of metal (substructure) and PZT respectively, and t_m , and t_p are thickness of metal substructure and PZT respectively. The centroid position of beam is given by Eq. (6.32) as:

$$y = \frac{\int y dA}{\int dA} \quad (6.32)$$

where, y is the distance of centroid from the base reference plane, and A is the cross sectional area of the plate. Due to the symmetric geometry of bimorph, centroid is located at the center of total thickness of beam and neutral plane passes through the centroid. Therefore $y = 0$ for this study. Wang and Cross [23] have proposed the analytical solution for resonance frequency of bimorph as following:

$$f_r = \frac{3.52t}{4\pi L^2} \sqrt{\frac{E_p}{3\rho_p}} \sqrt{\frac{1 + 3(1 + 2B)^2 + 4AB^3}{4(1 + B)^2(BC + 1)}} \quad (6.33)$$

Using parameters from Table 6.7 for PZTZNN bimorphs fabricated as: $A = E_s/E_p = 1.667$, $B = tm/2tp = 0.0625$, $C = 1.114$, $t = tm + 2tp = 8.5 \cdot 10^{-4} m$ and $L = 25 \times 10^{-3} m$, the analytical resonance frequency for PZTZNN bimorph was calculated to be 633 Hz. For a clamped-free beam with a tip mass of M , and length L , the fundamental natural frequency of the beam is given as [25]:

$$f_1 = \frac{1}{2\pi} \left(\frac{3EI}{L^3 (M + 0.24M_b)} \right) \quad (6.34)$$

where M_b is the mass of the beam. The mass of beam can be calculated as follows: density of PZT (ρ_p) = 7900 kg/m³, volume of PZT (V_p) = $1.1 \times 10^{-7} m^3$, density of brass (ρ_s) = 8800 kg/m³, volume of brass (V_s) = $6.25 \cdot 10^{-6} m^3$, and hence; $M_b = \rho_p V_p + \rho_s V_s = 0.935 gm$. Using Eq. (6.34), the natural frequency was calculated to be 88 Hz for PZTZNN plates for a tip mass of 11.5 gm.

As discussed earlier, a frequency range of 60 – 80 Hz was chosen for energy harvesting based on the tire vibration spectrum. Fig. 6.34c shows the transfer function between

base acceleration and tip mass acceleration measured using an accelerometer mounted on the structure and a laser vibrometer focused on the tip of cantilever beam. From this transfer function, the resonance frequency and damping ratio of the structure were calculated [25].

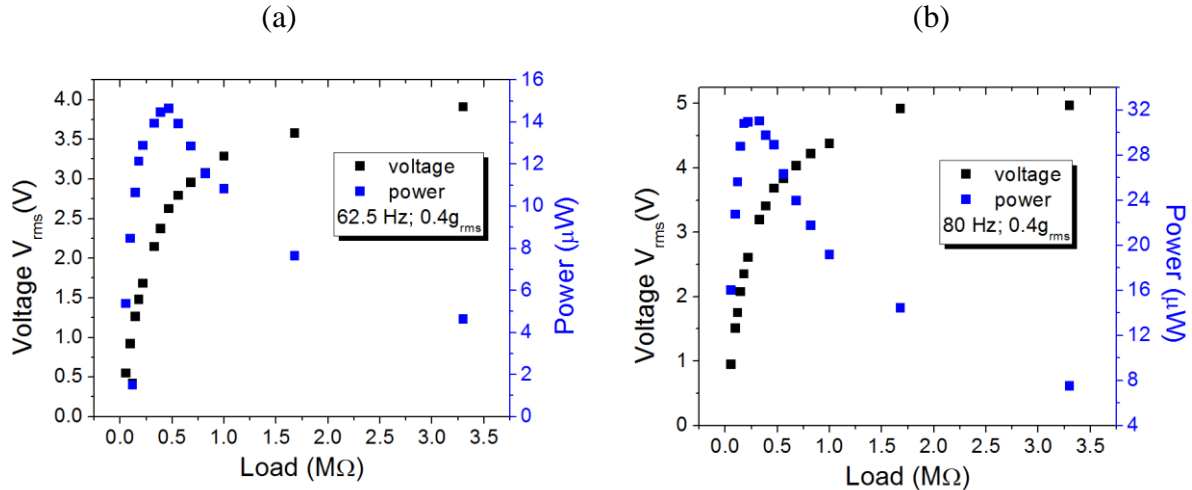


Fig. 6.35: Voltage and power characteristics of the bimorph energy harvester at $1g_{rms}$ base excitation with a tip mass of 11.45 gm at: (a) 62.5 Hz, and (b) 80 Hz

The maximum available power was calculated to be $25.4 \mu W$ at 62.5 Hz with base excitation of $0.4 g_{rms}$. The bimorph generated $15 \mu W$ of power across a load of $470 k\Omega$ with $0.4 g_{rms}$ base excitation and a damping ratio of 0.023 at frequency of 62.5 Hz (Fig. 6.35a). At a frequency of 80 Hz and $0.4 g_{rms}$ base excitation, the generated power was $31 \mu W$ across an electrical load of $330 k\Omega$ (Fig. 6.35b). Thus, the piezoelectric vibration based energy harvester can be an attractive alternative for energy generation inside a tire with a feedback mechanism for the given broadband frequency range maintaining the efficiency of conversion of mechanical vibrations into electrical power.

6.5 Power Processing Circuitry for Broad-Band Harvesting

The harvester performance results shown in Section 6.4 clearly indicate their ability to produce sufficient power under the assumption that the source excitation frequency is tuned to the resonant frequency for the harvester unit. However, the output power levels were seen to drop exponentially on either side of the system resonance frequency. To be able to generate sufficient power levels for a range of frequencies, one would need to explore the possibility of using a

broad band harvester. In the case of broad band harvesting, the device frequency matches the source frequency, enabling it to be in resonance to generate maximum power output over a suitable frequency range. The need for a broad band harvesters, one intends on using in tires becomes even more critical since the frequency of excitation for the harvester system changes with a change in the tire operating conditions, as seen during our analysis in Section 6.3. This high variation in the operating frequency range poses serious problems to the output power levels of the resonance based harvester unit. Hence, to get an expanded harvesting bandwidth, one needs to employ certain adaptive power management techniques. For simplicity, most harvesting devices have frequently been modeled as a current source in parallel with their intrinsic piezoelectric capacitance. The assumption made in this method is that, the displacement amplitude of the piezoelectric structure is independent of the impedance value of the externally connected power processing circuit. However, in reality, the vibration amplitude and in turn the power transfer from the piezoelectric material is highly affected by the load impedance connected to the piezo material. Therefore the power management circuitry needs to present the optimal load impedance to the generator to maximize the power output. The optimal load impedance expression [19] is given as:

$$R_{optimal} = \frac{1}{\omega C_p} \sqrt{\frac{(C_c \omega)^2 + (K - M \omega^2)^2}{(C_c \omega)^2 + (K + \frac{\Theta^2}{C_p} - M \omega^2)^2}} \quad (6.35)$$

From Equation (6.35), it can be seen that for a fixed set of geometrical properties of the harvester, the optimal resistance is a function of the operating frequency and the electromechanical coupling factor.

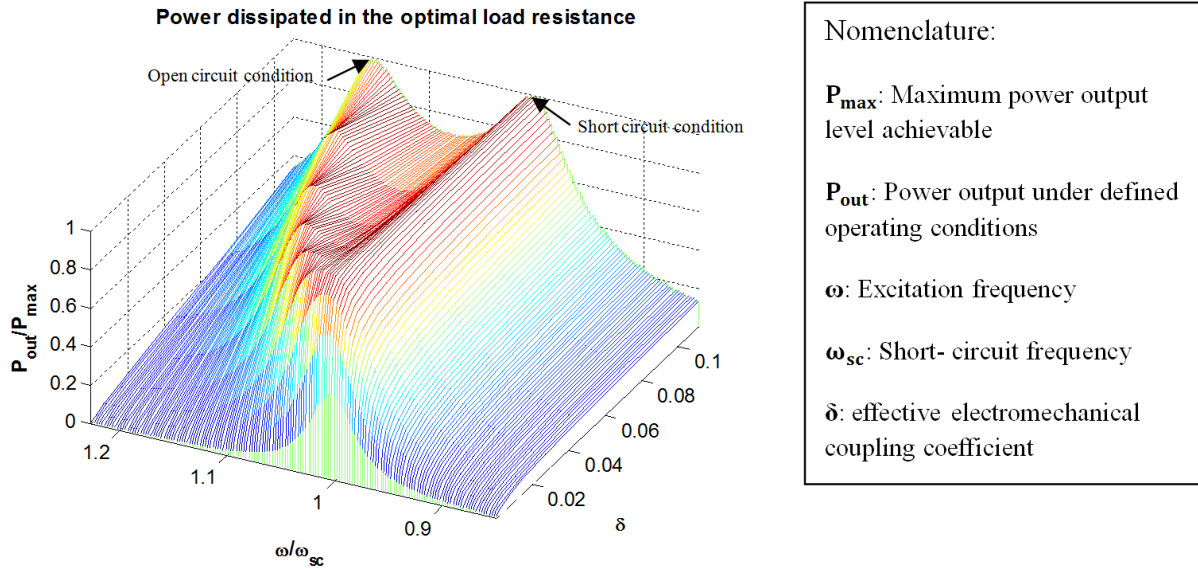


Fig. 6.36: Harvester power dissipated in the optimal resistive load versus operating frequency and squared coupling factor

Fig. 6.36 shows a plot of the harvested output power for a varying operating frequency and with varying coupling factor δ ($\delta = \Theta^2/C_p K$). At both open and short circuit resonance frequencies, the output power tends to the maximum available power (P_{max}) for larger coupling factor. The open-circuit resonance frequency of a piezoelectric generator is the frequency which results in the output voltage maximum as the load resistance tends to infinity (open-circuit condition). In contrast, the short-circuit resonance frequency is the one that makes the output current maximum as the load resistance tends to zero (short-circuit condition). In the case of wireless sensor nodes powered by energy harvesters, continuity of power supply must be ensured. In most modern power processing circuits, this is achieved by using a rechargeable battery or by a supercapacitor. However, these energy storage cells don't exhibit the voltage/current properties of a resistor and they can't intrinsically ensure an optimal power generation if directly connected to the rectifier output. Researchers [26] have considered using buck-boost topology to effectively realize resistive impedance matching (Fig. 6.37).

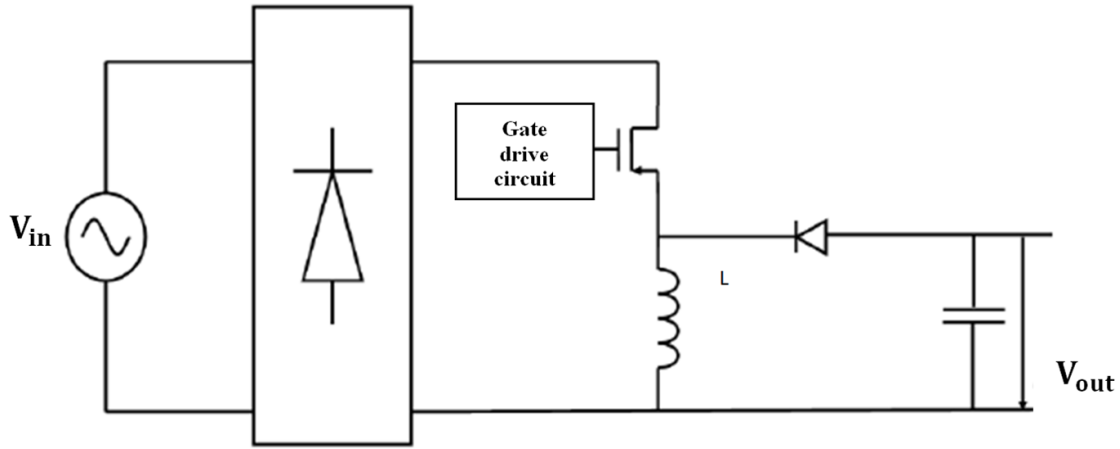


Fig. 6.37: Basic Buck-Boost AC-DC switch-mode power converter

The circuit performs an AC-DC conversion as well as presents the correct electrical impedance to the energy harvester to maximize its power output. This is achieved by working a buck-boost topology in discontinuous conduction mode. The input impedance of the processing circuit is adjusted using duty cycle (D) control.

$$R_{in} = \frac{2Lf_s}{D^2} \quad (6.36)$$

In the case of tires, for selecting the optimal duty cycle, one would need an adaptive system, which would have the capability to sense the changing dominant tire vibration frequencies with a change in the tire operating conditions and accordingly adjust the duty cycle to ensure the impedance across the harvester is the optimal impedance. To achieve the above mentioned objectives, a closed loop system capable of ensuring broad band operations for the tire mounted harvester was developed (Fig. 6.38). The key objective of the tuning device was to enable the harvester to be under resonance conditions over a suitable frequency range by matching the load impedance.

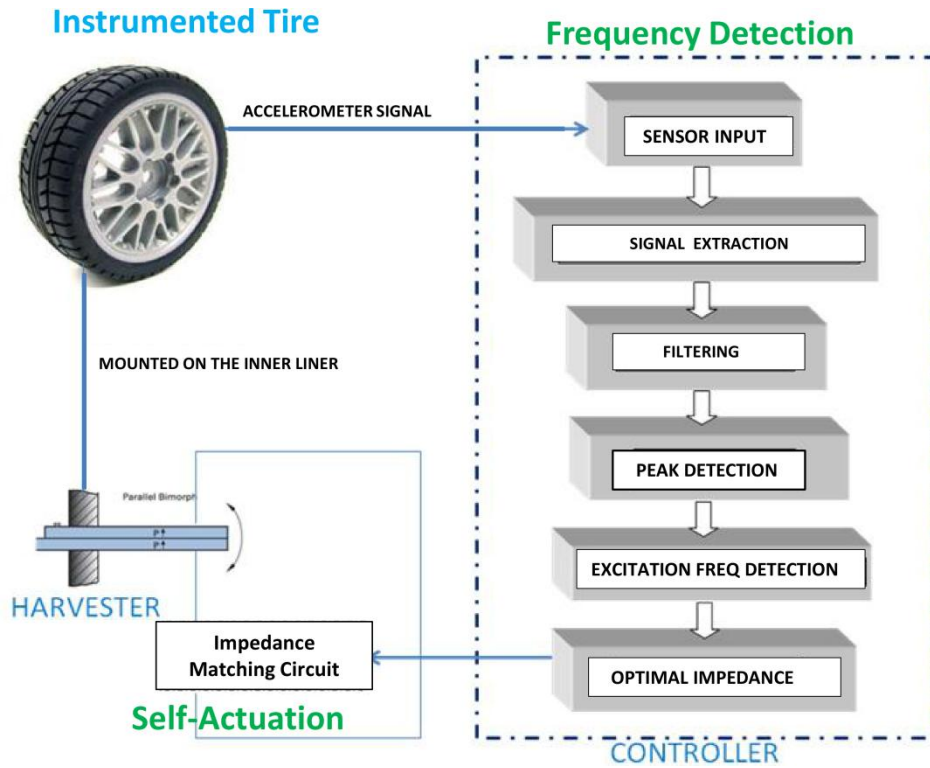
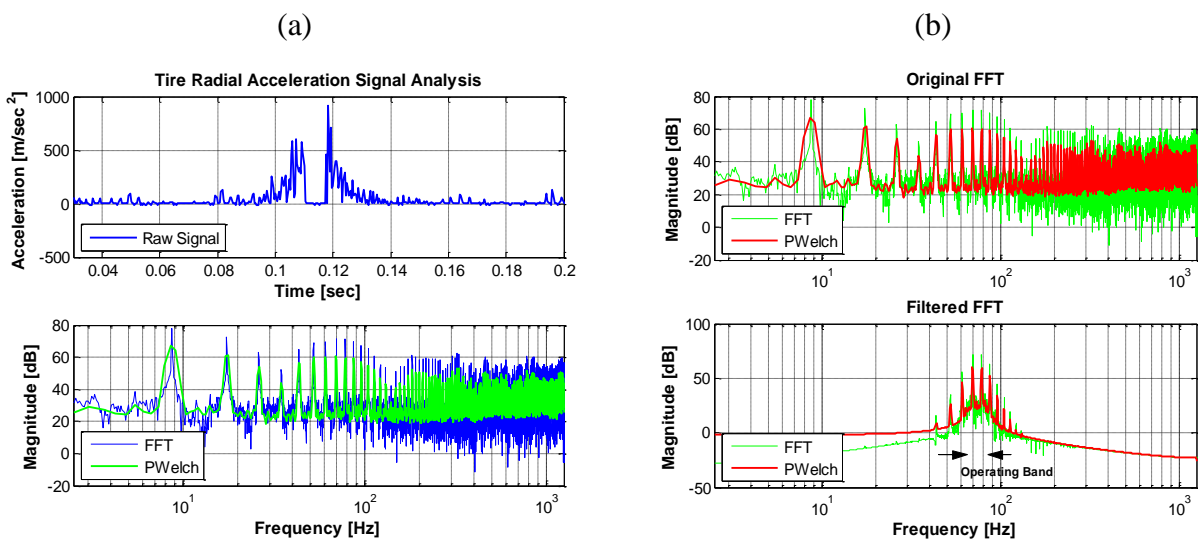
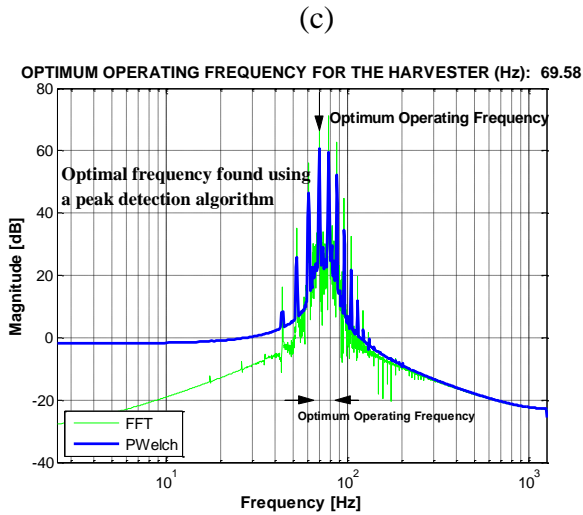


Fig. 6.38: Proposed system architecture for real time control- A self-tunable system, combining both frequency detection and self-actuation

This system was developed specifically for application in intelligent tire systems equipped with accelerometers. The input to this system was the raw radial acceleration signal from the accelerometer (Fig. 6.39a).





Optimum load impedance as a function of tire speed:

Tire Speed	Optimum Frequency	Optimal Load Impedance
10 mph	61.02 Hz	110 K Ω
30 mph	64.09 Hz	75 K Ω
45 mph	69.58 Hz	400 K Ω
65 mph	75.07 Hz	210 K Ω

Fig. 6.39: Optimal load impedance selection

The time domain signal was converted to a frequency domain signal on a per revolution basis by computing the FFT. This signal was thereafter passed through a band pass filter (Fig. 6.39b). The range of the band pass filter was selected based on the desired range of operation of the harvester identified in Section 6.3. The optimum operating frequency within this filtered range was found using a peak detection algorithm (Fig. 6.39c).

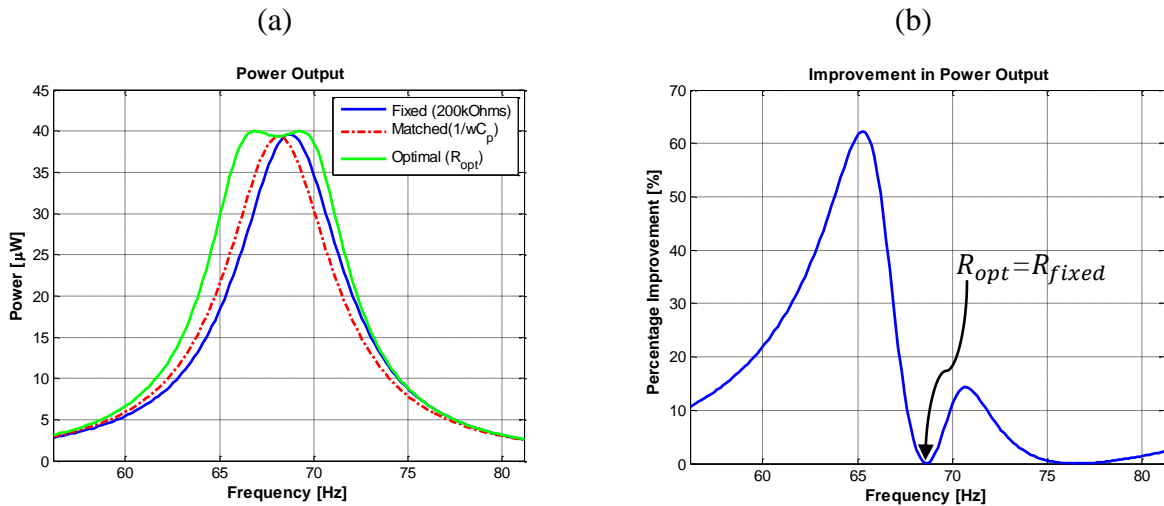


Fig. 6.40: (a) Power versus frequency for three cases, a constant resistance, the resistance matched to the capacitive piezoelectric materials, and the optimal resistance, and (b) additional power obtained (percentage) by using the optimal resistance instead of the matched resistance

The peak detection algorithm was able to determine the optimum frequency in real time. Finally depending on the optimum frequency estimated, the optimal load impedance was estimated. The use of the optimal impedance allowed for higher power levels to be generated at or around the open-circuit resonance or the short-circuit resonance (Fig. 6.40a). This improvement in the power output levels were estimated to be as high as 50-60% for frequencies close to the open circuit frequency (Fig. 6.40b).

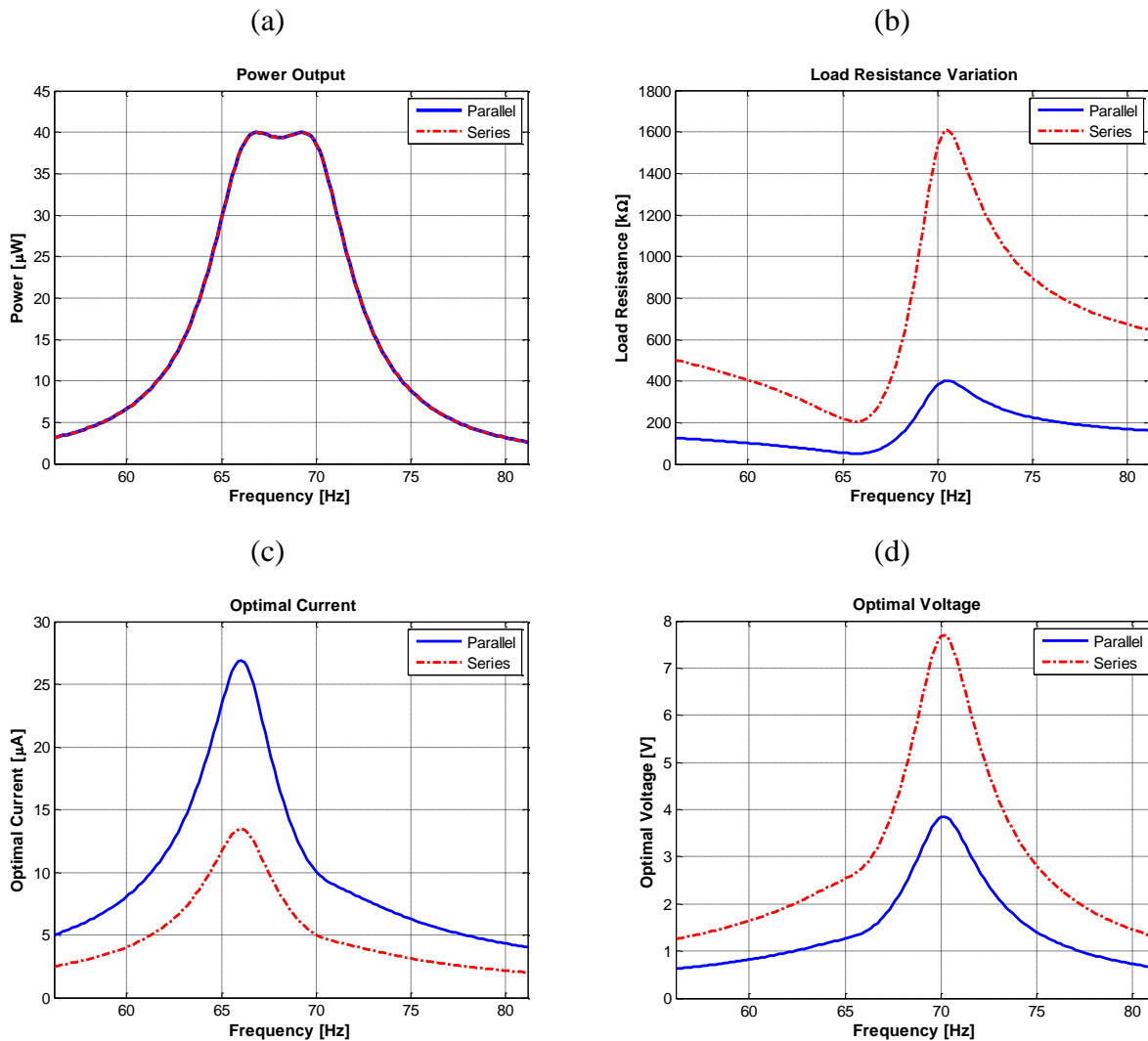


Fig. 6.41: (a) Power output, (b) optimal resistance, (c) optimal current, and (d) voltage vs frequency of the parallel-connected and serial-connected systems

Analyzing the operating characteristics of the parallel and the series wire connections under the influence of the impedance matching circuit, it was noticed that the same amount of power was

harvested from the parallel system (Fig. 6.41a) as that obtained from the serial system by using a resistance four times the parallel resistance (Fig. 6.41b). Hence the configurations only changed the distribution of the electric current and voltage at the output terminals but did not change the power output when the structure was subjected to the same excitations.

Although the use of the optimal impedance in the aforementioned power processing technique substantially improved the performance of the power harvesting system, one of the key limitations in using this technique would be the dependence of this system on the power spectrum (PSD) of the radial acceleration signal. The “true” PSD of a signal can only be estimated from a finite batch of data. This can be attributed to the fact that these techniques rely on a lot of averaging to remove noise. In the case of tires, it was estimated that, acceleration signal data for about 5 or more seconds was required to estimate the tire PSD correctly. To overcome this shortcoming, an artificial neural network (ANN) based controller was developed. Artificial Neural Networks is a class of flexible nonlinear models that can discover patterns adaptively from the data. The motivation behind developing such a system was to have the capability of estimating the optimal load impedance on a real time basis i.e. estimating the optimal impedance on a per revolution basis. Rather than determine an optimum neural network structure for this specific problem, the scope of this work was to design a network capable of estimating the optimal impedance for all possible tire operating conditions. Based on the analysis presented in Section 6.3, it was important to consider the effect of pressure, load and speed while training the neural network. The inputs for training the neural network were chosen accordingly (Fig. 6.42).

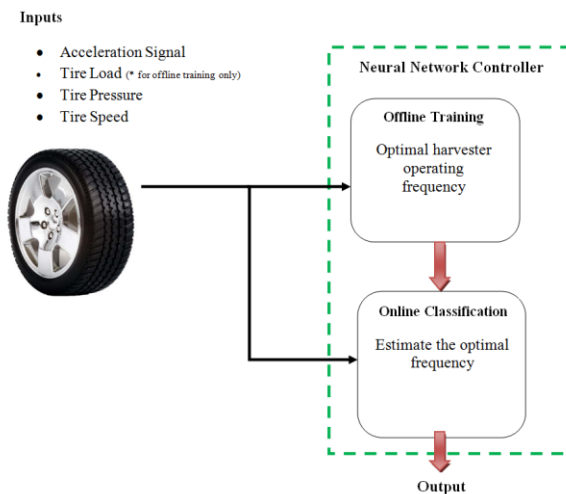


Fig. 6.42: Load impedance estimation via neural networks

Tire speed and pressure information is readily available on most modern vehicles. The tire speed information is available from the wheel speed sensor and the tire pressure information from the TPMS module. Information about the tire load is something which isn't available on most modern automobiles. During the offline training of the neural network, the load information was available from the measured data. The load on the tire was modulated using an airspring (Fig. 6.43).

(a)



(b)

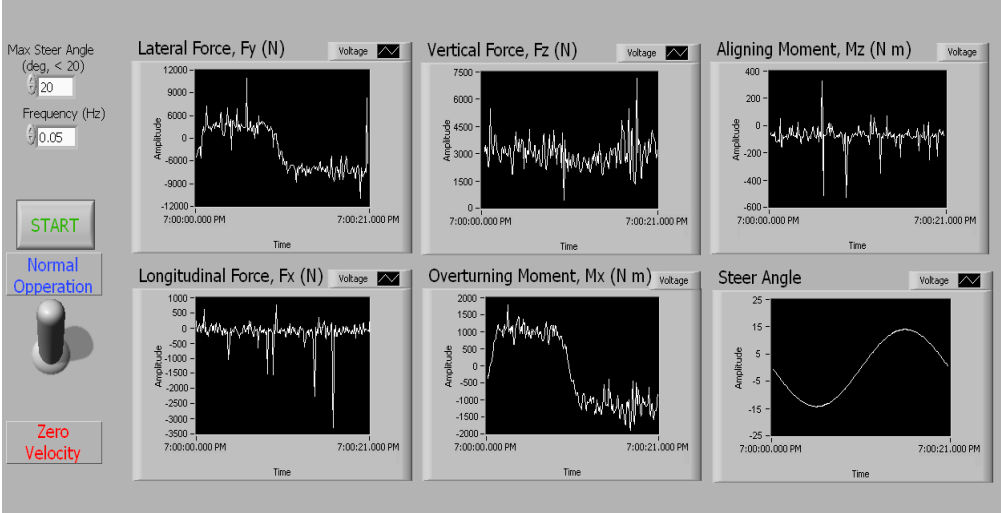


Fig. 6.43: (a) Tire testing setup, and (b) Front panel of LabView VI - Instantaneous Force – Moment- Slip Angle Information

Table 6.8: Test Matrix for creating the training data set

Speed Range	Pressure Range	Vertical Load Range
10- 65 mph	25-38 psi	800-1800 lbs

In the absence of the vertical load information during the online classification procedure, it became necessary to correlate the accelerometer signal to the instantaneous vertical load. To achieve this objective, the total radial acceleration signal power was estimated on a per revolution basis (Fig. 6.44) using the test data collected under a range of vertical loading conditions.

Effect of Vertical Load on the Radial Acceleration

* Signal power estimated on a per revolution basis

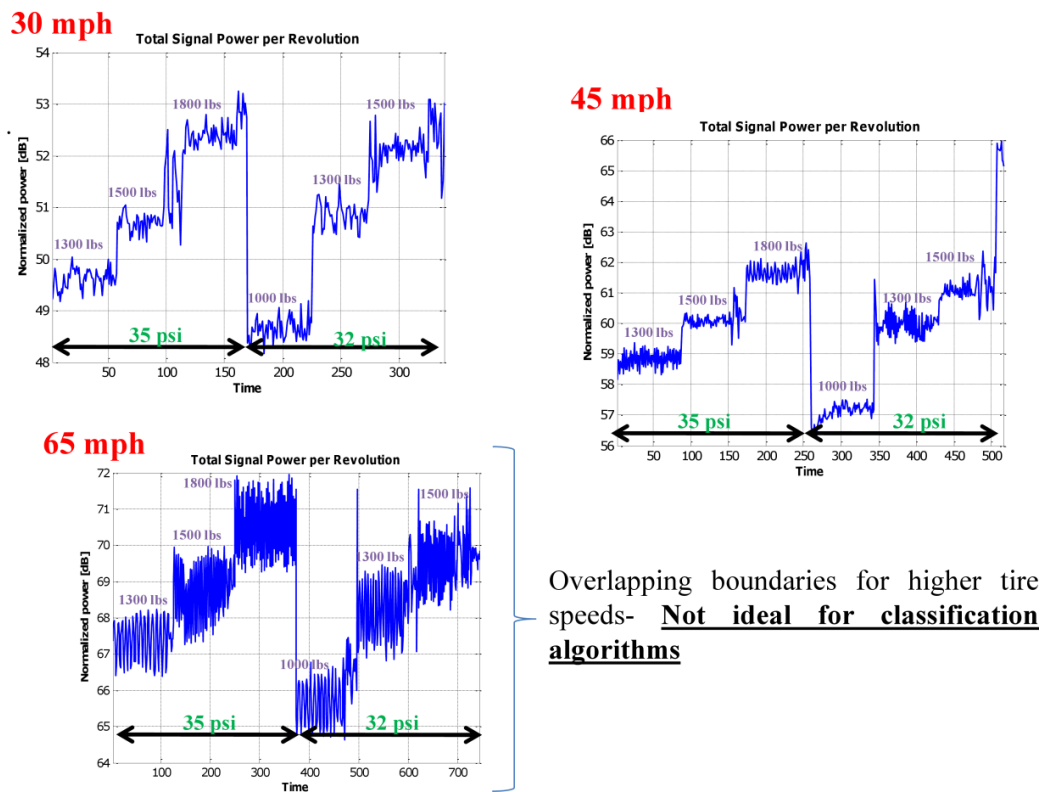


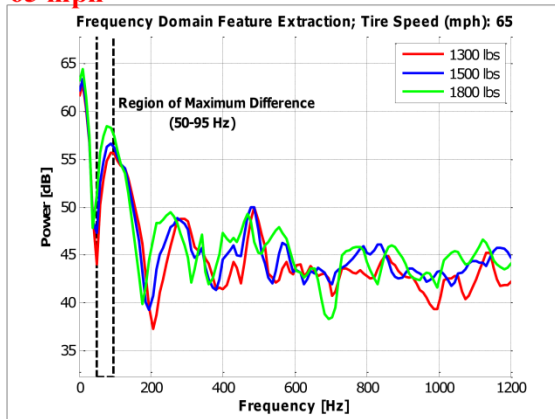
Fig. 6.44: Radial acceleration signal power on a per revolution basis: at 30 mph, 45mph and 65 mph

For the low speed tests (10-50 mph) (Fig. 6.44), the signal power estimates were seen to correlate to the applied vertical load with distinct boundaries demarcating the change in the

instantaneous load. For the high speed tests (>50 mph) (Fig. 6.44), certain overlapping boundaries were noticed, which did not present an ideal scenario for a classification algorithm. To resolve this issue, the effect of change in the instantaneous load on the frequency domain radial acceleration signal was analyzed (Fig. 6.45). The sole purpose of this analysis was to try and analyze the regions showing maximum difference in the PSD with changing vertical load conditions on the tire. For each tire speed, a range of maximum difference was identified. The raw radial accelerometer signal was filtered using a band pass filter, with the filter range being same as the range identified in the aforementioned analysis and being changed adaptively as function of the tire speed.

Isolation of Frequency Bands

65 mph



Identifying regions of maximum difference in the frequency domain

Test Results:

Tire Speed	Range of maximum difference
30	20-50 Hz
45	30-70 Hz
65	50- 95 Hz

Modified Power Estimation Technique:

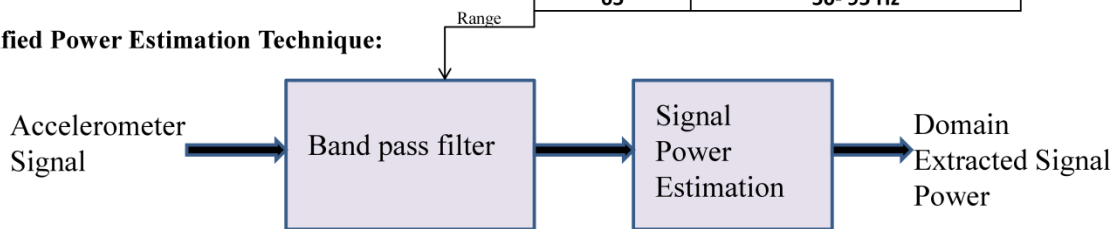
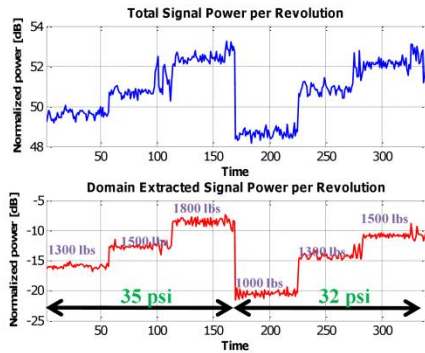


Fig. 6.45: Identifying regions of maximum difference in the frequency domain

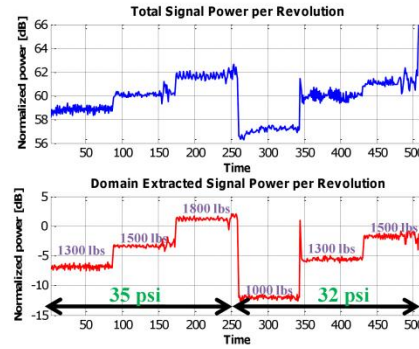
Using this filtered signal, the signal power of this domain extracted signal was estimated on a per revolution basis (Fig. 6.46). Distinct boundaries demarcating the change in the instantaneous vertical load were noticed even for the high speed tests.

Domain Extracted Signal Power: Results

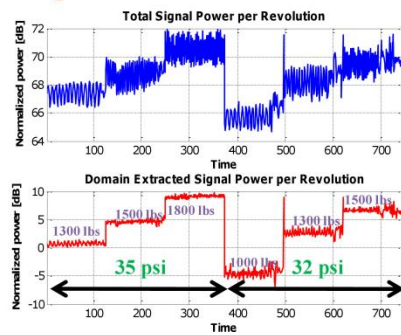
30 mph



45 mph



65 mph

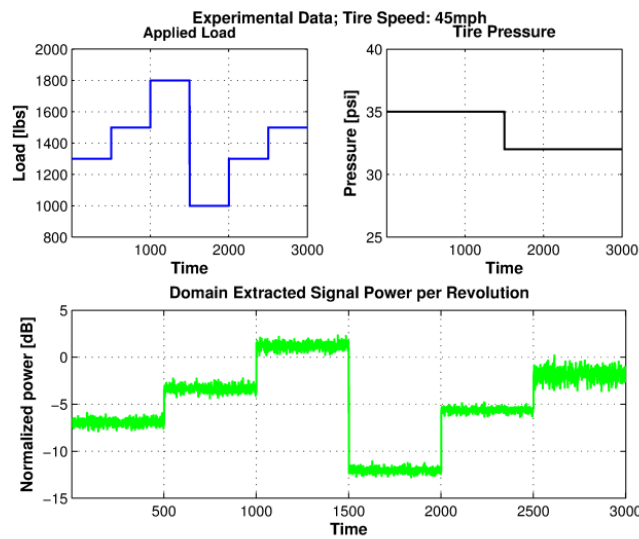


➤ No overlapping boundaries even for higher tire speeds- **Ideal for classification algorithms**

Fig. 6.46: Identifying regions of maximum difference in the frequency domain

Using this analysis, the vertical load information needed as an input to the neural network was captured indirectly using the domain extracted radial acceleration signal (Fig. 6.47a-Fig. 6.47b)

(a)



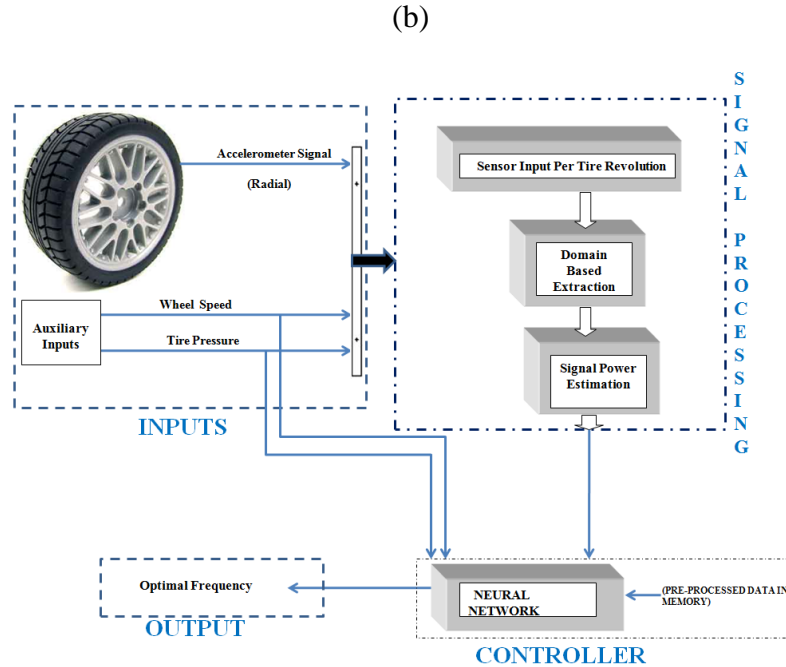


Fig. 6.47: (a) Sample experimental data set, and (b) System architecture for the ANN system

Extensive testing of the instrumented tire under a wide range of operating conditions, along with an artificial training data, based on statistical properties of a significantly smaller test data set, were used to train the neural network. The motivation for creating an artificial training data was to create enough data where the error seen with the training subset of the network approached that of what was seen with the testing subset.

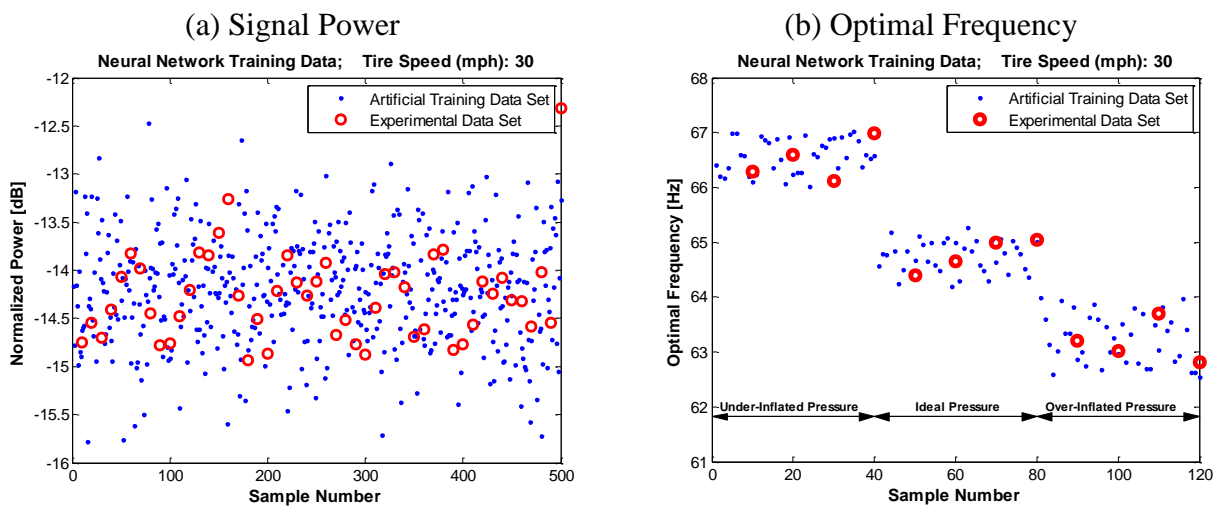


Fig. 6.48: Artificial training data set creation

The artificial data set created, also would help minimize the effect that bad inputs, or outliers, on the network training [23]. The method chosen to accomplish these two goals was to create a normal (Gaussian) distribution of random data points about the respective mean values (Fig. 6.48a-Fig. 6.48b).

A random sampling of the training data was used to divide the training data into three groups. The first group (60% of data) was used for the neural network training, the second group (20% of data) was used to cross-validate the results of the training and the third group (20% of the data) was used to test the neural network or generalize the error of the network. A two layer feed forward back-propagation network was used. Fig. 6.49a is representative of each node with the output of each neuron being a function of the activation function, weights (w), biases (b) and inputs. The differentiable activation function was specified as the tan sigmoid or hyperbolic tangent (Fig. 6.49b), for all nodes: hidden layer, and output layer.

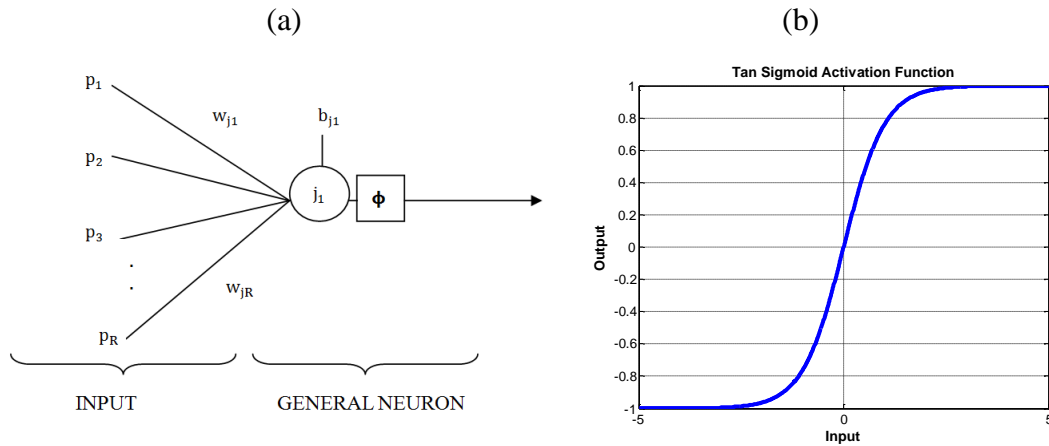


Fig. 6.49: (a) Neuron model with R inputs, and (b) Tan-Sigmoid activation function

The ANN was trained by adjusting the values of connections (synaptic weights) (Fig. 6.50). The ANN parameters (weights and biases) were adjusted to minimize the sum of the squares of the differences between the actual values and network output values.

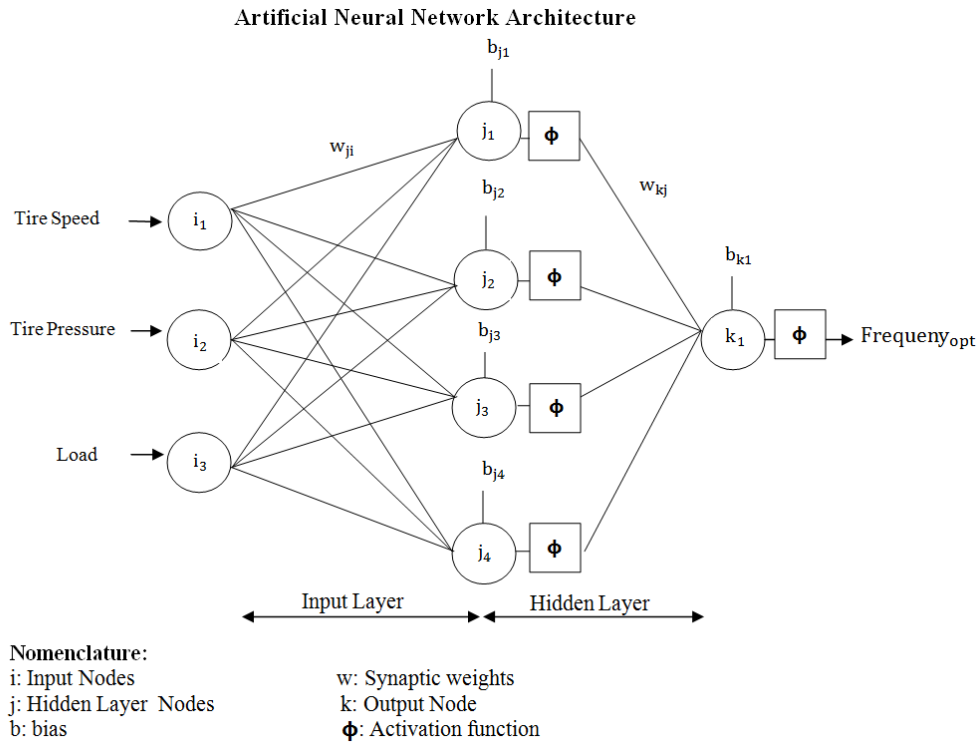


Fig. 6.50: Multi-layer Perceptron (Neural Network)

The ANN was trained in a batch mode where its parameters were only updated after all the input-output pairs were presented. The Levenberg-Marquardt (L-M) algorithm [28] was employed for the training and the target performance goal (mean square difference between ANN output and target output) was set at 0.001. The maximum number of epochs (representation of the input/output pairs and the adjustment of ANN parameters) was set at 200. Effect of the number of neurons in the hidden layer in the ANN performance was analyzed. The performance was measured in terms of the fraction of variance (R^2). The criteria followed for selecting the architecture choice was to choose the one with the highest averaged R^2 . The resulting ANN architecture selected was with 8 neurons in the hidden layer and 0.998 averaged R^2 . Having trained the neural network, extensive testing of the mobile test trailer with the prototype tire was carried out to create a new test data set so as to evaluate the performance of the trained neural network. Fig. 6.51b shows the control setup inside the passenger compartment of the tow vehicle. The remote laptop control enabled complete control of the vertical loading, steer control and data acquisition from the cab of the tow vehicle.

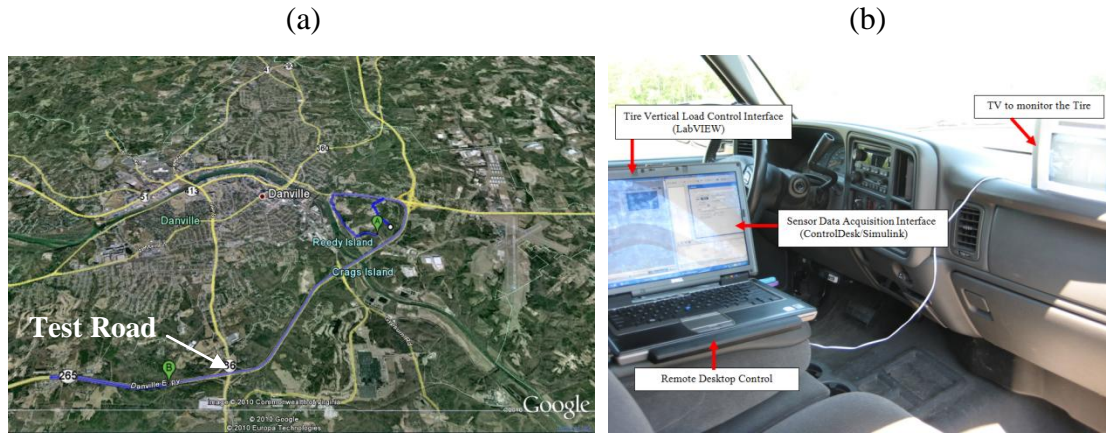


Fig. 6.51: (a) Test Road in the Map, and (b) Remote desktop control setup

Tests were carried out under both dry and wet surface conditions (Fig. 6.52).

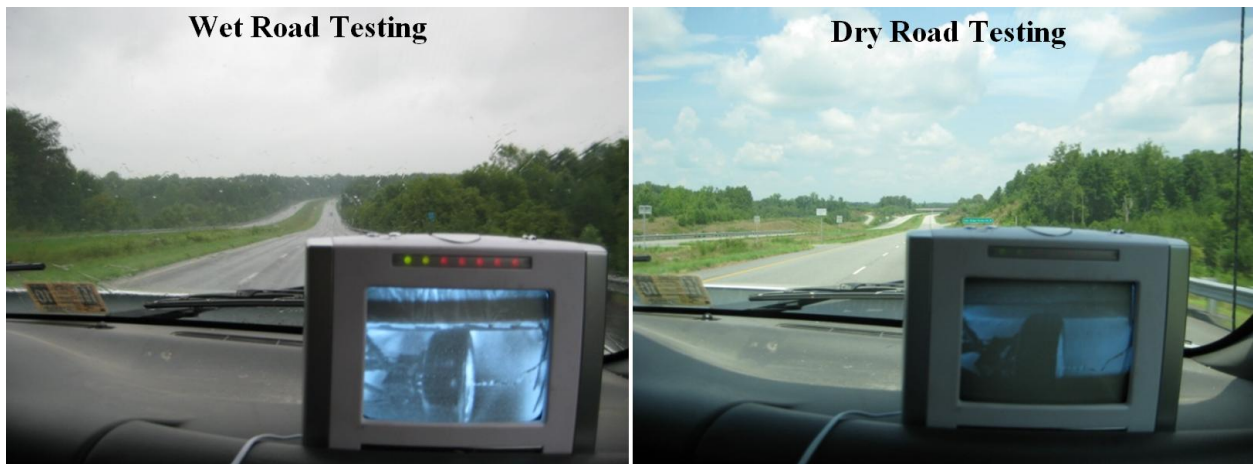


Fig. 6.52: Testing under dry and wet road surface conditons

The neural network model was able to make highly complex, nonlinear and multidimensional associations between selected input parameters and output to allow acceptable degree of accuracy in the predictions of the optimal frequency across the full range of the tire operating conditions (Fig. 6.53). However, there was an appreciable error in the predicted optimal frequency under lower speed conditions.

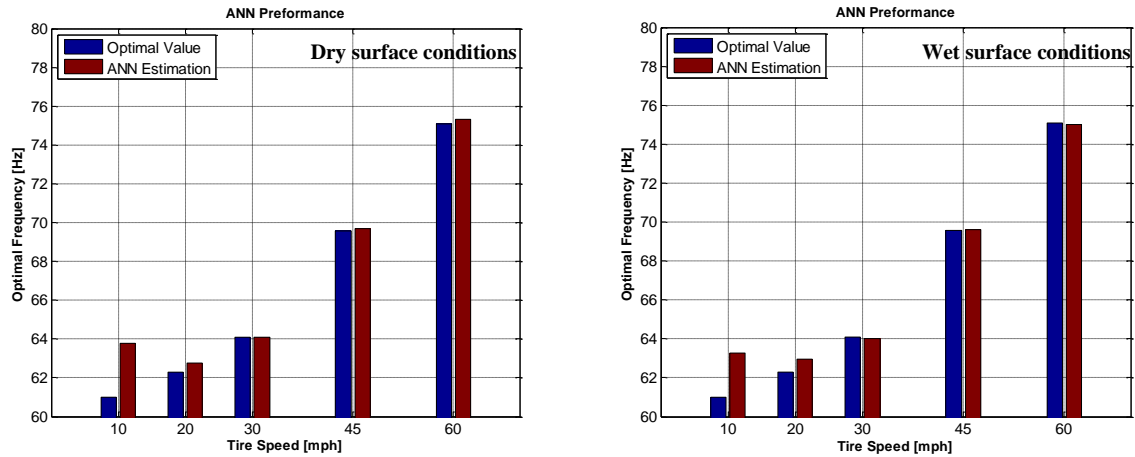


Fig. 6.53: Comparison of experimental and ANN predicted results

Hence, the proposed neural network based power conversion circuitry would present the correct electrical impedance to the harvester to maximize its power output (Fig. 6.54).

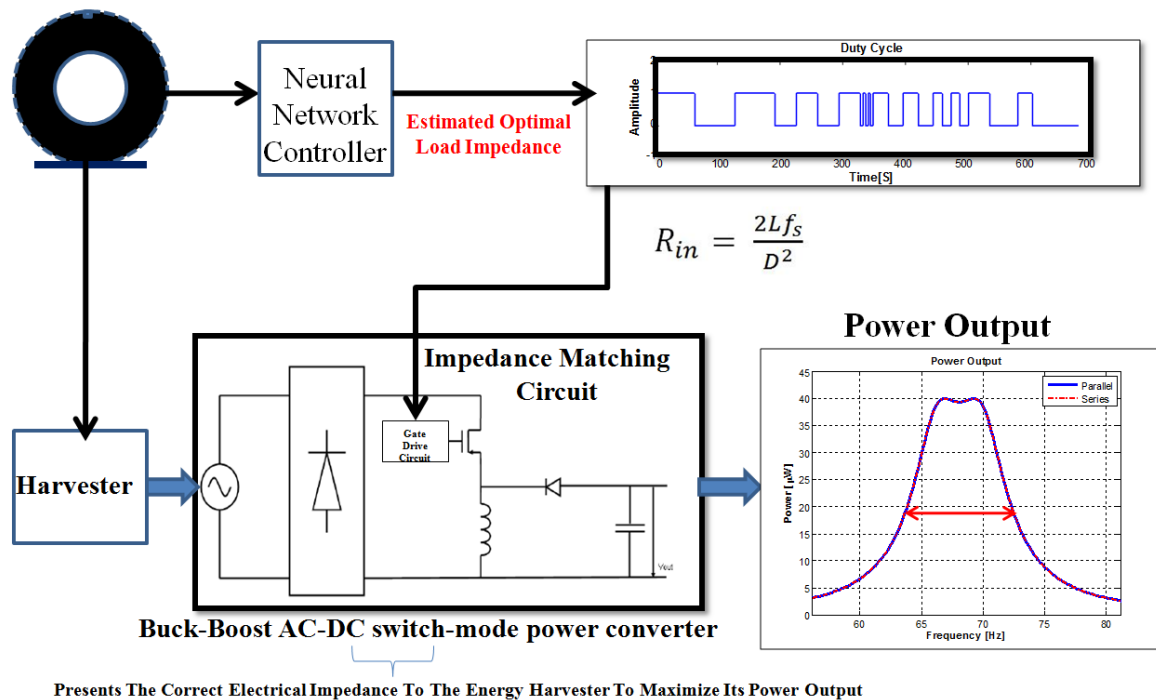


Fig. 6.54: Neural network based impedance matching system for tire energy harvesting

6.6 Conclusion

In this study, the feasibility of an onboard vibration energy harvesting system for a tire is presented. Various parameters such as tire speed, load, pressure and road roughness conditions were investigated based on real-time accelerations measured inside a tire. To optimize the frequency band of operation, a novel artificial neural network (ANN) based feedback loop control system was developed. High energy density piezoelectric ceramic materials based bimorph harvesters were designed and characterized for the chosen frequency range.

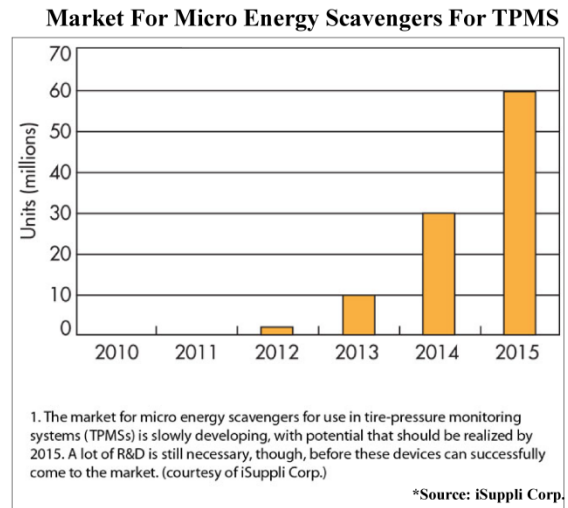
- **Power generation in a tire sensor application has been demonstrated over a wide speed range using a broad band piezoelectric energy harvester.**

- **Piezo based harvesters:**

- Ideal for low Duty cycle system.
- For a high duty Cycle system: Have limitations due to the max ‘g’ levels they can handle.

- **Future Work:**

- For a high duty Cycle system: Developing a multi modal harvester. (Piezoelectric + electromagnetic)



“This Technology Has The Potential Of Being A Game Changer”

Fig. 6.55: Key conclusions

Acknowledgements

The energy harvester fabrication and performance validation work (Section 6.4) was performed under a collaborative research project with the Center for Energy Harvesting Materials and Systems (CEHMS), Virginia Tech. The author would like to thank Dr. Shashank Priya and Dr. Vishwas Bedekar for their interest and support of this work.

Nomenclature

ϵ *dielectric constant*

n	<i>materials parameter</i>
I_p	<i>moment of inertia of piezoelectric plate</i>
I_m	<i>moment of inertia of substructure plate</i>
I_{eff}	<i>effective moment of inertia of the composite beam</i>
E_p	<i>young's modulus of PZT</i>
E_m	<i>young's modulus of substructure (metal)</i>
t_p	<i>thickness of piezoceramic</i>
t_m	<i>thickness of metal (brass)</i>
y	<i>distance of centroid from the base plate</i>
A_p	<i>cross sectional area of the plate</i>
ρ_m	<i>density of metal (brass)</i>
ρ_p	<i>density of PZT</i>
f_r	<i>resonance frequency</i>
A	$= e_s/e_p$
B	$= h_s/2h_p$
C	$= \frac{\rho_s}{\rho_p}$
Tt	$= tm + 2tp$
f_1	<i>fundamental natural frequency of clamped beam with tip mass</i>
V_m	<i>volume of substructure</i>
V_p	<i>volume of PZT</i>
M_b	<i>mass of beam</i>
M	<i>tip mass of cantilever</i>
L	<i>free length of the cantilever beam</i>
b	<i>width of beam/bimorph</i>
C_p	<i>capacitance of bimorph layer</i>
d_{31}	<i>piezoelectric constant</i>
s_{11}^E	<i>elastic compliance of the piezoelectric layer at constant electric field</i>
ζ_m	<i>damping ratio</i>
ω_n	<i>natural frequency</i>

P_{avg} average power
 $P_{e,max}$ maximum electrical power
 R_{opt} optimal load impedance
 ω excitation frequency
 D duty cycle
 R_{in} input impedance
 $d(n)$ desired output
 $y(n)$ predicted output
 $e(n)$ error

References

- [1] M. Gobbi, J. Botero and G. Mastinu, *Improving the active safety of road vehicles by sensing forces and moments at the wheels* Vehicle System Dynamics. Volume 46, Supplement 1 (2008), pp. 957-968.
- [2] M. Gobbi, J. Botero and G. Mastinu, *Global chassis control by sensing forces/moments at the wheels*, International Journal of Vehicle Autonomous Systems. Volume 7 (2009), pp. 221 - 242.
- [3] APOLLO - Final Report including Technical Implementation Plan. Deliverable 22/23 for the European Commission, Tampere, Finland (2005). Available online at: http://virtual.vtt.fi/virtual/proj3/apollo/deliverables/apollo_final%20report.pdf.
- [4] FRICTI@N- Final Report including Technical Implementation Plan. Deliverable13 (2009). Available online at: http://friction.vtt.fi/FRICTION_FinalReport_D13.pdf.
- [5] Pirelli's Intelligent Cyber Tire 'Speaks to the Car', in, 2010. Available online at: http://www.tirereview.com/article/72778/pirellis_intelligent_cyber_tire_speaks_to_the_car.aspx.
- [6] S. Roundy, *Energy harvesting for tire pressure monitoring systems: design considerations*, Technical Digest PowerMEMS 2008, Sendai, Japan. (2008), pp. 1–6.

- [7] L. Doherty, B.A. Warneke, B.E. Boser and K.S.J. Pister, *Energy and performance considerations for smart dust*, International Journal of Distributed Systems & Networks. 4 (2001), pp. 121-133.
- [8] Available online at: <http://www.epa.gov/nvfel/testing/dynamometer.htm>.
- [9] Available online at: http://wardsauto.com/ar/Intelligent_tires_debut_100624/.
- [10] *Intelligent Low-Power Management and Concepts for Battery-less Direct Tire Pressure Monitoring Systems (TPMS)*, *Advanced Microsystems for Automotive Applications 2007*, in: J. Valldorf, W. Gessner (Eds.), Springer Berlin Heidelberg, 2007, pp. 237-249.
- [11] Available online at: <http://www.be-power.de/german/downloads/TPMS.pdf>.
- [12] Available online at: <http://www.gmbattery.com/dl/cp1/eng/ER2450.pdf>.
- [13] *Texas Instruments, TI/Chipcon CC2430, 2.4 GHz IEEE 802.15.4/ZigBee™ low cost, low power System-on-Chip (SoC) solution.* Available online at: <http://www.ti.com/lit/ds/symlink/cc2430.pdf>.
- [14] *Dytran - Mini triaxial accelerometers specification sheet.* Available online at: <http://www.dytran.com/img/products/3023A.pdf>.
- [15] P.D. Welch, *The Use of Fast Fourier Transform for the Estimation of Power Spectra: A Method Based on Time-Averaging Over Short, Modified Periodograms*, IEEE Transactions on Audio and Electroacoustics. June (1967), pp. 70-73.
- [16] IEEE Standard on Piezoelectricity 1987 (New York: IEEE).
- [17] N.W. Hagood, W.H. Chung and A. Von Flotow, *Modelling of Piezoelectric Actuator Dynamics for Active Structural Control*, Journal of Intelligent Material Systems and Structures. 1 (1990), pp. 327-354.
- [18] H.A. Sodano, G. Park and D.J. Inman, *Estimation of Electric Charge output for Piezoelectric Energy Harvesting*, Strain Journal. 40 (2004), pp. 49-58.

- [19] Y. Liao and H.A. Sodano, *Model of a single mode energy harvester and properties for optimal power generation* Smart Materials and Structures. 17 (2008), pp. 065026.
- [20] R.A. Islam and S. Priya, *High Energy Density Ceramic Composition in the System $Pb(Zr,Ti)O_3 - Pb[(Zn,Ni)_{1/3}Nb_{2/3}]O_3$* , Journal of the American Ceramic Society. 89 (2006), pp. 3147-3156.
- [21] I.W. Chen and X.H. Wang, *Sintering dense nanocrystalline ceramics without final-stage grain growth*, Nature. 404 (2002), pp. 168–171.
- [22] T. Wu and P.I. Ro, *Dynamic peak amplitude analysis and bonding layer effects of piezoelectric bimorph cantilevers* Smart Materials and Structures. Volume 13, Number 1 (2004), pp. 203-210.
- [23] Q.-M. Wang and L.E. Cross, *Performance analysis of piezoelectric cantilever bending actuators* Ferroelectrics 215 (1998), pp. 187 – 213.
- [24] R.D. Blevins, *Formulas for natural frequency and mode shape*, New York : Van Nostrand Reinhold Co, 1979.
- [25] V. Bedekar, J. Oliver and S. Priya, *Design and Fabrication of Bimorph Transducer for Optimal Vibration Energy Harvesting*, IEEE Transactions on Ultrasonics Ferroelectrics and Frequency Control. 57 (2010), pp. 1513-1523.
- [26] R. D'hulst and J. Driesen, *Power processing circuits for vibration-based energy harvesters*, Power Electronics Specialists Conference, 2008. PESC 2008. IEEE. (2008), pp. 2556 – 2562
- [27] R. Duda, P. Hart and D.G. Stork, *Pattern Classification*, 2nd. New York: John Wiley & Sons Inc., 2001.
- [28] M.T. Hagan and M.B. Menhaj, *Training feedforward networks with the Marquardt algorithm*, IEEE Transactions on Neural Networks 5(1994), pp. 989-993.

Chapter 7

Conclusions and Future Work

7.1 Summary of the Work

The increasing worldwide use of automobiles has brought about a dramatic increase in number of accidents. The high number of accidents and their root cause in human error has motivated the need to develop driver assistance systems. A variety of active safety control systems such as traction control, electronic stability control (ESC), rollover prevention, lane departure avoidance systems, collision avoidance systems, and adaptive cruise control (ACC) are being developed to reduce driver burden, partially automate normal driving operations, and reduce accidents. The effectiveness of these driver assistance systems can be significantly enhanced if the values of several tire-vehicle parameters and state variables can be known in real-time. In order to achieve the aforementioned objective, this research has developed an ‘Intelligent Tire Based Tire - Vehicle State Estimator for Application to Global Chassis Control’.

In Chapter 2, an innovative approach to obtain real-time information about the tire-road contact parameters from “in-tire” acceleration measurements is presented. This chapter provides a detailed description of the signal processing algorithms that can be used to extract features of interest from the data provided by an intelligent tire. Experimental results show that the developed signal processing methodologies provide good estimates of tire normal load, tire slip angle, tire slip ratio and tire-road friction coefficient.

Chapter 3 provides details about the design and implementation of an integrated vehicle state estimator. The estimator is implemented in the Matlab/Simulink and CarSim software environment. An effectively designed merging scheme ensures robust estimation performance even during the vehicle maneuvers which show highly nonlinear tire characteristics, and in the existence of road inclination or bank angle. Results presented in this chapter show the ability of cascaded estimators to provide accurate estimates of vehicle states.

Knowledge of the coefficient of friction is critical for the performance of vehicle dynamics control systems. In Chapter 4, a model-based approach to friction estimation is presented. The physically-derived yet simple brush model is used. This model is well suited for

friction estimation because it contains only two parameters, namely the tire stiffness and friction coefficient. This allows a relatively simple estimation problem to be posed. The proposed method has been tested on experimental tire data sets, and found to work reliably.

Considering the strong interdependence between the operating road surface condition and the instantaneous forces and moments generated; real time estimate of the tire-vehicle parameters and state variables is expected to play a pivotal role in improving the performance of a number of vehicle control systems. Chapter 5 presents a study that focuses on the possibility of enhancing the performance of the ABS control by using the additional information provided by the intelligent tire. In order to achieve the aforementioned objectives, the design and implementation of a Fuzzy/Sliding Mode/Proportional Integral (Fuzzy-SMC-PI (FSP)) control methodology is proposed. The performance of the proposed system has been evaluated through simulations on a series of braking maneuvers, emphasizing on jump - μ conditions. The results show significant improvements in the stopping distance of a vehicle equipped with an intelligent tire based FSP controller as compared to a vehicle equipped with a standard ABS.

In Chapter 6, the feasibility of using an inertial vibrating energy harvester unit to power a sensor module being used to monitor the tire road interaction parameters is assessed. To predict the electrical power output of the generator, a generic analytical model based on the transfer of energy within the system has been derived. The vibration measurements taken from the test conducted using accelerometers embedded in the tire have been applied as an excitation to the model to predict the power output for a device of suitable dimensions and to study the feasibility of this concept. The power generator unit is adapted to the tire vibration spectra and the superimposed acceleration signal. The harvester utilizes the radial accelerations, which are impacts resulting from the tire-road contact and are present even at constant vehicle speeds. For the intelligent tire applications, a special compact harvester design has been proposed that is able to withstand large shocks and vibrations. Suitable mathematical models for different harvester configurations have been developed to identify the best configuration suited for use inside a tire. The harvester unit demonstrates power generation over a wide speed range and enables sensor systems to transmit tire information at desired rates. The proposed concept addresses one of the key challenges in the realization of the intelligent tire system concepts, by presenting a battery-less power supply unit which can generate power that is sufficient for a multitude of wireless

platforms such as ZigBee and Wi-Fi protocols which are expected to find their way in the next generation intelligent tires.

7.2 Future Work

There are several lines of research arising from the work presented in this thesis. Some key research areas identified are listed below. These research projects are located at the Intelligent Transportation Laboratory (ITL), Virginia Tech and they are currently in active status.

1. Development of Multi-Sensor Signal Fusion Schemes for Intelligent Tire Applications

Description: Due to unavoidable power consumption limitations, a multi-sensor network system doesn't seem a viable option for tire applications. Consequently, in the case of a single sensor intelligent tire system, "meaningful" data from a tire embedded sensor would only be available once every tire revolution ($\approx 5\text{Hz}$). The sampling frequency available on most communication buses (*e.g.*, TTCAN and TTP) used in vehicles is $\approx 200\text{ Hz}$. This mismatch in the intelligent tire system and Vehicle CAN –bus operating frequency renders the tire sensor information worthless for application to vehicle stability control systems. To overcome this limitation, this study explores the feasibility of developing novel sensor signal fusion schemes, combining the tire and vehicle sensor information, so as to overcome bandwidth limitations of a single sensor intelligent tire system (Fig. 7.1).

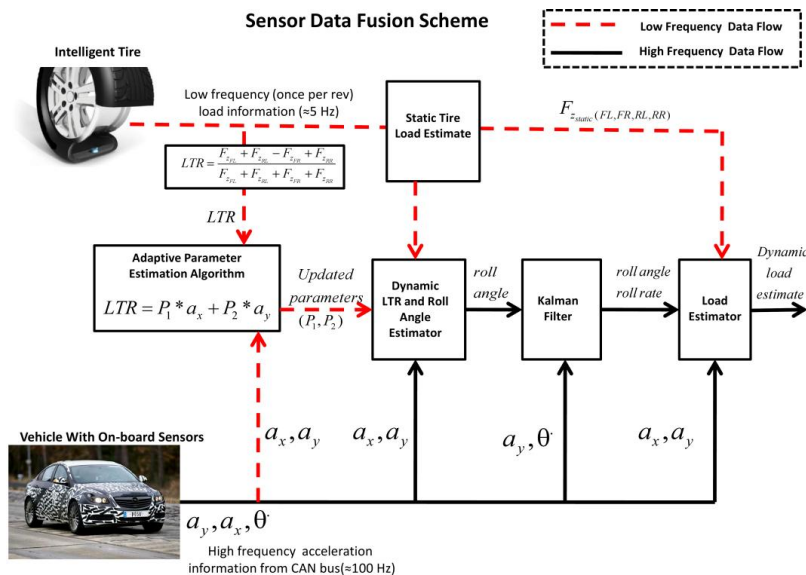


Fig. 7.1: Sensor data fusion scheme

2. Development of a Simplified Vehicle Stability Control (VSC) System Based on Tire Force Feedback

Description: This study aims to integrate the vehicle state estimation scheme developed as part of the work presented in this thesis into a chassis control algorithm based on active front steering (AFS) and direct yaw moment control (DYC). It is expected that a new control strategy aiming to use all of the information available from the vehicle state estimator would significantly enhance vehicle stability during emergency evasive maneuvers on various road conditions ranging from dry asphalt to very slippery packed snow road surfaces.

3. Tire- Road Friction Coefficient Estimation Based on Extended Kalman Filter

Description: Current control algorithms are usually designed to be conservative due to the lack of road friction information. Knowledge of the friction coefficient can enable more sophisticated and precise control algorithms. This study aims to develop a new predictive methodology for the estimation of tire-road friction coefficient by using the modified Dugoff tire model and an extended Kalman filter. The key objectives of this study are to: produce accurate estimations in a wide range of vehicle states, be robust to plant uncertainties, and use sensors that are available on typical passenger cars.

4. Development of a Rotary Broadband Energy Harvester for Tire Applications

Description: Presently, technology for harvesting energy from tire vibrations uses non resonant or narrow bandwidth resonant approaches, which exhibit low efficiency power generation. This study aims to develop a self-tuning broadband energy harvester for extracting energy from the rotational motion of a tire. The proposed self tuning broadband energy harvester can be an attractive alternative for energy generation, maintaining the efficiency of conversion of mechanical vibrations into electrical power for the given broadband frequency range of the tire.